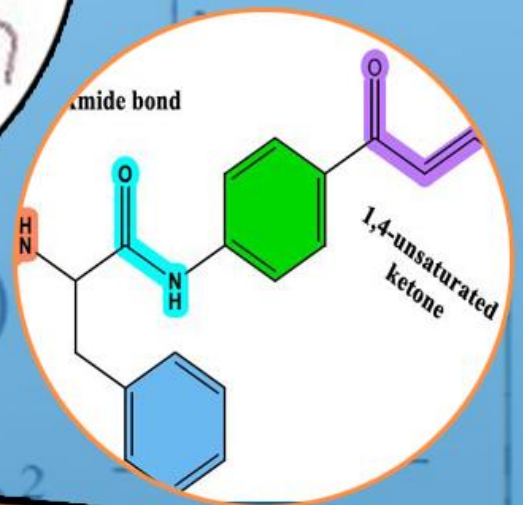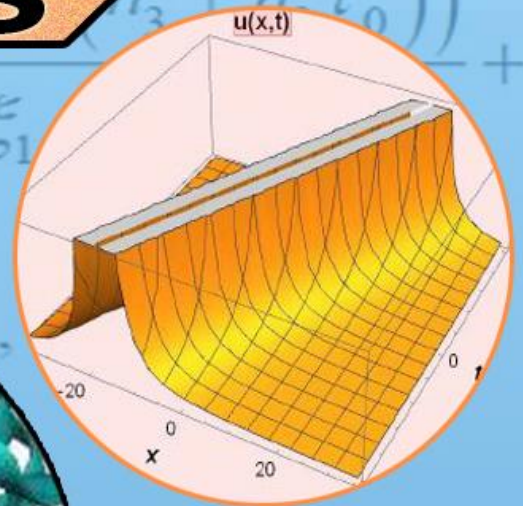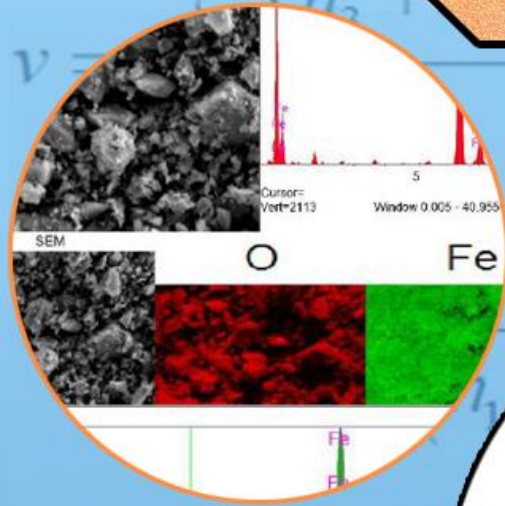# TDFD
TÜRK DOĞA ve FEN DERGİSİ

TURKISH JOURNAL OF NATURE AND SCIENCE

TJNS

TÜRK DOĞA VE FEN DERGİSİ

Amaç

Türk Doğa ve Fen Dergisi, Dergipark tarafından yayınlanan Bingöl Üniversitesi Fen Bilimleri Enstitüsüne ait ulusal ve hakemli bir dergidir. Türk Doğa ve Fen Dergisi, Türkiye ve dünyanın her yerinden gelen doğa ve fen bilimlerinin her alanında özgün, yayımlanmamış, yayımlanmak üzere başka yere gönderilmemiş makale, derleme ve sempozyum değerlendirmesi gibi çalışmaların bilim alemine sunulması amacıyla kurulmuştur.

Kapsam

Türk Doğa ve Fen Dergisinde Mühendislik, Ziraat, Veterinerlik, Fen ve Doğa Bilimleri alanlarından olmak üzere Türkçe ve İngilizce hazırlanmış orijinal makale, derleme ve sempozyum değerlendirmesi gibi çalışmalar yayımlanır. Türk Doğa ve Fen Dergisi sadece online sistemde yayınlanmakta olup ayrıca kağıt baskısı bulunmamaktadır.

Merhaba…

Türk Doğa ve Fen Dergisi, Dergipark tarafından yayınlanmakta olup Bingöl Üniversitesi Fen Bilimleri Enstitüsüne aittir. Bahar ve güz dönemi olmak üzere yılda iki defa çıkarılan ulusal hakemli bir dergi olarak ilk sayısını 2012 bahar döneminde yayımlamıştır. Türk Doğa ve Fen Dergisi, Türkiye ve dünyanın her yerinden gelen doğa ve fen bilimlerinin her alanında özgün, yayımlanmamış, yayımlanmak üzere başka yere gönderilmemiş makale, derleme ve sempozyum değerlendirmesi gibi çalışmaların bilim alemine sunulması amacıyla kurulmuştur. İlk sayısından bugüne kesintisiz olarak faaliyetlerini sürdürmektedir.

Türk Doğa ve Fen Dergisi sadece online sistemde yayınlanmakta olup ayrıca kağıt baskısı bulunmamaktadır. Dergimize gelen her çalışma öncelikle Turnitin intihal programında taranmaktadır. Dergimizde editörlerin, hakemlerin ve yazarların, uluslararası yayım etik kurallarına uyması ve makalelerin yazım kurallarına uyumlu olması zorunluluğu vardır.

Yazarlar yayımlanmak üzere dergimize gönderdikleri çalışmaları ile ilgili telif haklarını zorunlu olarak Bingöl Üniversitesi Türk Doğa ve Fen Dergisi'ne devretmiş sayılırlar. Yazarlardan herhangi bir ücret talep edilmemektedir. Yazarların değerlendirmeleri, dergimizin resmi görüşü olarak kabul edilemez. Çalışmaların her türlü sorumluluğu yazarlarına aittir. Araştırma ürünleri için etik kurul raporu gerekli ise, çalışma üzerinde bu raporun alınmış olduğu belirtilmeli ve kurul raporu sisteme kaydedilmelidir. Araştırma ile ilgili intihal, atıf manipülasyonu, sahte veri uydurma vb. suistimallerin tespit edilmesi halinde yayım ve etik ilkelerine göre davranılır. Bu durumda çalışmanın yayımlanmasını önlemek, yayımdan kaldırmak ya da başka işlemler yapmak için gerekli işlemler takip edilmektedir.

Dergimizde, kaynak gösteriminde uluslararası Vancouver sistemine geçilmiştir. Ayrıca dergimiz, Creative Commons ile lisanslanmak suretiyle dergimizde yayımlanan makalelerin paylaşımı, kaynak gösterimi ve yayımlanmasında dergi ve yazar haklarını korumaya almıştır. 2018 yılı güz döneminden itibaren makaleler, uluslararası yazar kimlik numarası ORCID No'su ile yayımlanmaktadır.

Dergi ekibi, dergimizin ulusal ve uluslararası indekslerce taranan bir dergi olması yönünde çalışmalarını titizlikle sürdürmektedir. Dergimize gösterilen ilgi bu yönde bizleri teşvik etmeye devam edecektir.

Prof. Dr. Zafer ŞİAR

Bingöl Üniversitesi, Fen-Edebiyat Fakültesi, Matematik Bölümü
E-Mail: zsiar@bingol.edu.tr

Prof. Dr. Uğur ÇAKILCIOĞLU

Munzur Üniversitesi, Pertek Sakine Genç Meslek Yüksekokulu, Bitki Morfolojisi
ve Anatomisi Bölümü
E-Mail: ucakilcioglu@yahoo.com

Doç. Dr. Kamuran DİLSİZ

Bingöl Üniversitesi, Fen-Edebiyat Fakültesi, Fizik Bölümü
E-Mail: kdilsiz@bingol.edu.tr

Doç. Dr. Şükran KONCA

Bakırçay Üniversitesi, Mühendislik ve Mimarlık Fakültesi, Temel Bilimler,
Matematik Bölümü
E-Mail: sukran.konca@bakircay.edu.tr

Doç. Dr. İdris YAZGAN

Kastamonu Üniversitesi, Fen Edebiyat Fakültesi, Biyoloji

E-Mail: idrisyazgan@gmail.com

Doç. Dr. Abdulcabbar YAVUZ

Gaziantep Üniversitesi, Mühendislik Fakültesi, Metalurji ve Malzeme Mühendisliği
E-Mail: ayavuz@gantep.edu.tr

Doç. Dr. Bünyamin ALIM

Bayburt Üniversitesi, Teknik Bilimler Meslek Yüksekokulu, Elektrik ve Enerji
Bölümü
E-Mail: balim@bayburt.edu.tr

Dr. Öğr. Üyesi Mustafa Şükrü KURT

Erzurum Teknik Üniversitesi, Fen Fakültesi, Temel Bilimler
E-Mail: mustafa.kurt@erzurum.edu.tr

Dr. Öğr. Üyesi Sinan SAĞIR

Karamanoğlu Mehmetbey Üniversitesi, Fizik

E-Mail: sinansagir@kmu.edu.tr / sinan.sagir@cern.ch

Doç. Dr. Murat AYDEMİR

Erzurum Teknik Üniversitesi, Fen Fakültesi, Temel Bilimler

E-Mail: murat.aydemir@erzurum.edu.tr

Mühendislik Bilimleri

Doç. Dr. Özgür ÖZGÜN

Bingöl Üniversitesi, Sağlık Bilimleri Fakültesi, İş Sağlığı ve Güvenliği Bölümü
E-Mail: oozgun@bingol.edu.tr

Prof. Dr. Figen KOREL

İzmir Yüksek Teknoloji Enstitüsü, Gıda Mühendisliği Bölümü
E-Mail: figenkorel@iyte.edu.tr

Prof. Dr. Kubilay ASLANTAŞ

Afyon Kocatepe Üniversitesi, Teknoloji Fakültesi, Makine Mühendisliği Bölümü
E-Mail: aslantas@aku.edu.tr

Prof. Dr. Hamit Özkan GÜLSOY

Marmara Üniversitesi, Teknoloji Fakültesi, Metalurji ve Malzeme Mühendisliği
Bölümü
E-Mail: ogulsoy@marmara.edu.tr

Prof. Dr. Ali Adnan HAYALOĞLU

İnönü Üniversitesi, Mühendislik Fakültesi, Gıda Mühendisliği Bölümü
E-Mail: adnan.hayaloglu@inonu.edu.tr

Prof. Dr. Barbara SAWICKA

University of Life Sciences in Lublin, Department of Plant Production Technology
and Commodities Sciences
E-Mail: barbara.sawicka@gmail.com

Prof. Dr. İbrahim GÜNEŞ

Giresun Üniversitesi, Mühendislik Fakültesi, İnşaat Mühendisliği Bölümü
E-Mail: ibrahim.gunes@giresun.edu.tr

Doç. Dr. Sırma YEĞİN

Ege Üniversitesi, Mühendislik Fakültesi, Gıda Mühendisliği Bölümü
E-Mail: sirma.yegin@ege.edu.tr

Doç. Dr. Hasan OĞUL

Sinop Üniversitesi, Mimarlık ve Mühendislik Fakültesi, Nükleer Enerji
Mühendisliği
E-Mail: hogul@sinop.edu.tr

Doç. Dr. Murat YILMAZTEKİN

İnönü Üniversitesi, Mühendislik Fakültesi, Gıda Mühendisliği Bölümü
E-Mail: murat.yilmaztekin@inonu.edu.tr

Doç. Dr. Ferhat AYDIN

Sakarya Uygulamalı Bilimler Üniversitesi, Teknoloji Fakültesi, İnşaat
Mühendisliği Bölümü
E-Mail: ferhata@subu.edu.tr

Dr. Öğr. Üyesi Nurullah DEMİR

Bingöl Üniversitesi, Mühendislik ve Mimarlık Fakültesi, Gıda Mühendisliği
Bölümü
E-Mail: ndemir@bingol.edu.tr

Dr. Öğr. Üyesi Ahmet GÜNER

Bingöl Üniversitesi, Mühendislik ve Mimarlık Fakültesi, Elektrik ve Elektronik
Mühendisliği Bölümü
E-Mail: aguner@bingol.edu.tr

Dr. Öğr. Üyesi Tahir AKGÜL

Sakarya Uygulamalı Bilimler Üniversitesi, Teknoloji Fakültesi, İnşaat
Mühendisliği Bölümü
E-Mail: tahirakgul@subu.edu.tr

Dr. Erhan Sulejmani

University of Tetova, Faculty of Food Technology and Nutrition
E-Mail: erhan.sulejmani@unite.edu.mk

Dr. Hacène Medjoudj

Larbi Ben M'Hidi University of Oum El Bouaghi, Food Science Department
E-Mail: medjoudjh@yahoo.com

Dr. Avinash Lakshmikanthan

Nitte Meenakshi Institute of Technology, Department of Mechanical Engineering,
Karnataka, India
E-Mail: avinash.laks01@gmail.com

Dr. Manjunath Patel GC

PES Institute of Technology and Management, Department of Mechanical
Engineering, Karnataka, India
E-Mail: manju09mpm05@gmail.com

Sağlık Bilimleri

Doç. Dr. Aydın Şükrü BENGÜ

Bingöl Üniversitesi, Sağlık Hizmetleri Meslek Yüksekokulu, Tıbbi Hizmetler ve
Teknikler
E-Mail: abengu@bingol.edu.tr

Dr. Öğr. Üyesi Dilhun Keriman ARSERİM UÇAR

Bingöl Üniversitesi, Sağlık Bilimleri Fakültesi, Beslenme ve Diyetetik Bölümü
E-Mail: dkucar@bingol.edu.tr

Dr. Öğr. Üyesi Abdullah TUNÇ

Bingöl Üniversitesi, Sağlık Bilimleri Fakültesi, İş Sağlığı ve Güvenliği Bölümü
E-Mail: atunc@bingol.edu.tr

Dr. Öğr. Üyesi Ramazan GÜNDOĞDU

Bingöl Üniversitesi, Sağlık Hizmetleri Meslek Yüksekokulu, Eczane Hizmetleri
E-Mail: rgundogdu@bingol.edu.tr

Dr. Alexander HERGOVICH

UCL Cancer Institute, Faculty of Medical Sciences, Department of Cancer Biology,
UCL, London, UK
E-Mail: a.hergovich@uc.ac.uk

Dr. Valenti GOMEZ

UCL Cancer Institute, Faculty of Medical Sciences, Department of Oncology, UCL, London, UK
E-Mail: valentin.gomez@ucl.ac.uk

Veterinerlik Bilimleri

Doç. Dr. Cüneyt ÇAĞLAYAN

Bilecik Şeyh Edebali Üniversitesi, Tıp Fakültesi, Temel Tıp Bilimleri Bölümü, Tıbbi Biyokimya Anabilim Dalı
E-Mail: cuneyt.caglayan@bilecik.edu.tr

Prof. Dr. Fatih Mehmet KANDEMİR

Atatürk Üniversitesi, Veteriner Fakültesi, Veteriner Hekimliği Temel Bilimler
E-Mail: fmehmet.kandemir@atauni.edu.tr

Doç. Dr. Akın KIRBAŞ

Bozok Üniversitesi, Veteriner Fakültesi, Klinik Bilimler Bölümü
E-Mail: akindahiliye55@yahoo.com

Doç. Dr. Emrah Hicazi AKSU

Atatürk Üniversitesi, Veteriner Fakültesi, Klinik Bilimler Bölümü
E-Mail: emrahaksu@atauni.edu.tr

Ziraat Bilimleri

Prof. Dr. Kağan KÖKTEN

Bingöl Üniversitesi, Ziraat Fakültesi, Tarla Bitkileri Bölümü
E-Mail: kahafe1974@yahoo.com

Prof. Dr. Mustafa SÜRMEN

Adnan Menderes Üniversitesi, Ziraat Fakültesi, Tarla Bitkileri Bölümü
E-Mail: mustafa.surmen@adu.edu.tr

Prof. Dr. Banu YÜCEL

Ege Üniversitesi, Ziraat Fakültesi, Hayvan Yetiştirme Anabilim Dalı, Zootekni Bölümü
E-Mail: banu.yucel@ege.edu.tr

Doç. Dr. Hakan İNCİ

Bingöl Üniversitesi, Ziraat Fakültesi, Zootekni Bölümü
E-Mail: hinci@bingol.edu.tr

TEKNİK EDİTÖRLER

Dr. Öğr. Üyesi Mücahit ÇALIŞAN

Bingöl Üniversitesi, Teknik Bilimler Meslek Yüksekokulu, Bilgisayar Teknolojileri
E-Mail: mcalisan@bingol.edu.tr

Dr. Ersin KARAKAYA

Bingöl Üniversitesi, Ziraat Fakültesi, Tarım Ekonomisi Bölümü
E-Mail: karakayaersin1982@gmail.com

Dr. Nimetullah KORKUT

Bingöl Üniversitesi, BİNUZEM, Bilgisayar Teknolojileri
E-Mail: nkorkut@bingol.edu.tr

DİL EDİTÖRÜ
Öğr. Gör. Dr. Ahmet KESMEZ
Bingöl Üniversitesi, Yabancı Diller Yüksekokulu, İngilizce Bölümü
E-Mail: akesmez@bingol.edu.tr

Türk Doğa ve Fen Dergisi
Turkish Journal of Nature and Science

İÇİNDEKİLER/CONTENTS

Cloneable Jellyfish Search Optimizer Based Task Scheduling in Cloud Environments

Mücahit BÜRKÜK[1], Güngör YILDIRIM[1*]

[1]Firat University, Engineering Faculty, Department of Computer Engineering, Elazig, Türkiye
Mucahit BÜRKÜK ORCID No: 0000-0002-4974-0590
Güngör YILDIRIM ORCID No: 0000-0002-4096-4838

Corresponding author: gungor.yildirim@firat.edu.tr

| | 35 |

Thermal Conductivity and Thermal Rectification in Various Sequences of Monolayer Hexagonal Boron Nitride/Aluminum Nitride Superlattice Nanoribbons

Yenal KARAASLAN[1,2*]

[1]Department of Fundamental Sciences, Air NCO Vocational HE School, Turkish National Defence University, 35415 İzmir, Türkiye
[2]Department of Mechanical Engineering, Eskisehir Technical University, 26555 Eskişehir, Türkiye
Yenal KARAASLAN ORCID No: 0000-0001-8483-4819

Corresponding author: ykaraaslan@msu.edu.tr, yenalkaraaslan@gmail.com

| | 44 |

Evaluation of the Levels of Metalloproteinases as well as Markers of Oxidative Stress and Apoptosis in Lung Tissues After Malathion and Rutin Administrations to Rats

Cihan GÜR[1*], Fatih Mehmet KANDEMİR[2]

[1] Atatürk University, Veterinary Faculty, Biochemistry Department, Erzurum, Türkiye
[2] Aksaray University, Medicine Faculty, Medical Biochemistry Department, Aksaray, Türkiye
Cihan GÜR ORCID No: 0000-0001-6775-7858
Fatih Mehmet KANDEMİR ORCID No: 0000-0002-8490-2479

Corresponding author: cihan.gur@atauni.edu.tr

| | 51 |

Utilization of Demolition Waste for Treatment of Acid Mine Drainage and Immobilization of Heavy Metals Released from Copper Flotation Tailings

Gulsen TOZSIN[1*], Ercument KOC[1], Banu YAYLALI[2], Haci DEVECI[3]

[1]Ataturk University, Faculty of Engineering, Department of Metallurgical and Materials Engineering, Erzurum, Türkiye
[2]Ataturk University, Faculty of Engineering, Department of Mechanical Engineering, Erzurum, Türkiye
[3]Karadeniz Technical University, Faculty of Engineering, Department of Mining Engineering, Trabzon, Türkiye
Gulsen TOZSIN ORCID No: 0000-0001-5653-9919
Ercument KOC ORCID No: 0000-0002-9804-4620
Banu YAYLALI ORCID No: 0000-0002-9488-3910
Haci DEVECI ORCID No: 0000-0003-4105-0912

Corresponding author: gulsentozsin@gmail.com

| | 58 |

Evaluations on the Use Potential of Some Woody Plants Naturally Growing in Elazığ Flora in Landscape Architecture **Musa Denizhan ULUSAN[1*], Rıdvan POLAT[2]** [1]Süleyman Demirel University, General Secretariat Unit, Isparta, Türkiye [2]Bingöl University, Faculty of Agriculture, Department of Landscape Architecture, Bingöl, Türkiye Musa Denizhan ULUSAN ORCID No: 0000-0001-9040-5025 Rıdvan POLAT ORCID No: 0000-0003-0261-3671 *Corresponding author: rpolat@bingol.edu.tr* 	**84**
The Antinociceptive Effect of Adalimumab, A TNF-Alpha Inhibitor, in a Formalin Induced Inflammatory Pain Model in Mice **Mehmet ÖZ[1*], Hasan ŞİMŞEK[1]** [1] Department of Physiology, Faculty of Medicine, University of Aksaray, Aksaray, Türkiye Mehmet ÖZ ORCID No: 0000-0003-4167-2623 Hasan ŞİMŞEK ORCID No: 0000-0001-5573-4923 *Corresponding author: ozmhmt@gmail.com* 	**89**
The Use of *Rheum Ribes* (Işgın) Extracts for Copper Protection in Acidic Media **Fatma KAYA[1], Ramazan SOLMAZ[2*], İbrahim Halil GEÇİBESLER[2]** [1] Bingöl University, Science and Letters Faculty, Chemistry Department, 12000, Bingöl, Türkiye [2] Bingöl University, Health Sciences Faculty, Occupational Health and Safety Department, 12000, Bingöl, Türkiye Fatma KAYA ORCID No: 0000-0003-0783-5652 Ramazan SOLMAZ ORCID No: 0000-0002-9295-1203 Halil İbrahim GEÇİBESLER ORCID No: 0000-0002-4473-2671 *Corresponding author: rsolmaz@bingol.edu.tr; rsolmaz01@gmail.com* 	**94**
Determination of Silage Quality of Fenugreek (*Trigonella foenum-graecum* L.) with Oat (*Avena sativa* L.) and Rye (*Secale cereale* L.) Mixtures **Mehmet Arif ÖZYAZICI[1*], Seyithan SEYDOŞOĞLU[1], Semih AÇIKBAŞ[1]** [1]Siirt University, Faculty of Agriculture, Department of Field Crops, Siirt, Türkiye Mehmet Arif ÖZYAZICI ORCID No: 0000-0001-8709-4633 Seyithan SEYDOŞOĞLU ORCID No: 0000-0002-3711-3733 Semih AÇIKBAŞ ORCID No: 0000-0003-4384-3908 *Corresponding author: arifozyazici@siirt.edu.tr* 	**102**

Biosynthesis, Characterization and Determination of Sun Protection Factor (SPF) of Iron Nanoparticles With Bee Bread **Büşra BILDIR[1], Zeynep DEMİRKAN[1], Bülent KAYA[2*]** [1] Bee and Bee Products Department, Institute of Science, Bingöl University, Bingöl, Türkiye [2] Molecular Biology and Genetics Department, Science and Art Faculty, Bingol University, Bingöl, Türkiye Büşra BILDIR ORCID No: 0000-0002-5631-1946 Zeynep DEMİRKAN ORCID No: 0000-0002-8101-8194 Bülent KAYA ORCID No: 0000-0002-1216-6441 *Corresponding author: bkaya@bingol.edu.tr 	**110**
Influence of Layer Thickness on Magnetoresistance Properties of Multilayered Thin Films **Taner KALAYCI[1*]** [1] Bandırma Onyedi Eylül University, Medical Services and Technique Department, Bandırma, Türkiye Taner KALAYCI ORCID No: 0000-0002-6374-2373 *Corresponding author: tanerkalayci@bandirma.edu.tr 	**118**
A Generalized Thermoelastic Behaviour of Isotropic Hollow Cylinder **Mehmet EKER[1*], Durmuş YARIMPABUÇ[2]** [1] Tarsus University, Faculty of Engineering, Department of Mechanical Engineering, Mersin, Türkiye [2] Osmaniye Korkut Ata University, Faculty of Arts and Sciences, Department of Mathematics, Osmaniye, Türkiye Mehmet EKER ORCID No: 0000-0002-6785-1710 Durmuş YARIMPABUÇ ORCID No: 0000-0002-8763-1125 *Corresponding author: mehmeteker@tarsus.edu.tr 	**123**
Topographic, Morphological and Morphometric Investigation of Mandible in Norduz Sheep **Semine DALGA[1*], Uğur AYDIN[2], Tansel ÇAL[1]** [1]Kafkas University, Veterinary Faculty, Anatomy Department, Kars, Türkiye [2]Kafkas University, Veterinary Faculty, Surgery Department, Kars, Türkiye Semine DALGA ORCID No: 0000-0001-7227-2513 Uğur AYDIN ORCID No: 0000-0001-5756-4841 Tansel ÇAL ORCID No: 0000-0002-3034-5814 *Corresponding author: seminedalga@kafkas.edu.tr 	**129**

On Travelling Wave Solutions of Dullin-Gottwald-Holm Dynamical Equation and Strain Wave Equation **Seyma TULUCE DEMIRAY[1*], Merve DAVARCI YALCIN[2]** [1] Osmaniye Korkut Ata University, Department of Mathematics, Osmaniye, Türkiye [2] Osmaniye Korkut Ata University, Department of Mathematics, Osmaniye, Türkiye Seyma TULUCE DEMIRAY ORCID No: 0000-0002-8027-7290 Merve DAVARCI YALCIN ORCID No: 0000-0002-4862-7836 *Corresponding author: seymatuluce@gmail.com* 	**134**
Railway Security System Design Using Unmanned Aerial Vehicle Image Processing and Deep Learning Methods **Muzaffer EYLENCE[1], Mehmet YÜCEL[1], M. Melikşah ÖZMEN[1], Bekir AKSOY[1*]** [1] Isparta University of Applied Sciences, Technology Faculty, Mechatronic Engineering Department, Isparta, Türkiye Muzaffer EYLENCE ORCID No: 0000-0001-7299-8525 Mehmet YÜCEL ORCID No: 0000-0002-4100-5831 Mustafa Melikşah ÖZMEN ORCID No: 0000-0003-3585-0518 Bekir AKSOY ORCID No: 0000-0001-8052-9411 *Corresponding author: bekiraksoy@isparta.edu.tr* 	**150**
New Amino Acid Chalcone Conjugates: Synthesis, Characterization and Dielectric Properties **Eray ÇALIŞKAN*[1]** [1] Bingol University, Faculty of Science and Arts, Chemistry Department, Bingöl, Türkiye Eray ÇALIŞKAN ORCID No: 0000-0003-2399-4100 *Corresponding author: ecaliskan@bingol.edu.tr* 	**155**
Fabric Defect Detection Using Customized Deep Convolutional Neural Network for Circular Knitting Fabrics **Mahdi HATAMI VARJOVI*[1], Muhammed Fatih TALU [1], Kazım HANBAY[2]** [1] Inonu University, Engineering Faculty, Computer Engineering Department, Malatya, Türkiye [2] Inonu University, Engineering Faculty, Software Engineering Department, Malatya, Türkiye Mahdi HATAMI VARJOVI ORCID No: 0000-0001-6442-7175 Muhammed Fatih TALU ORCID No: 0000-0003-1166-8404 Kazım HANBAY ORCID No: 0000-0003-1374-1417 *Corresponding author: mahdi.hatami.v@gmail.com* 	**160**

Evaluation of the Biological Activities of Royal Jelly on Prostate and Breast Cancer Cells

Adnan AYNA[1]*, Ekrem DARENDELİOĞLU[2]

[1] Bingöl University, Science and Letter Faculty, Chemistry Department, Bingöl, Türkiye
[2] Bingöl University, Science and Letter Faculty, Molecular Biology and Genetics Department, Bingöl, Türkiye
Adnan AYNA ORCID No: 0000-0001-6801-6242
Ekrem DARENDELİOĞLU ORCID No: 0000-0002-0630-4086

Corresponding author: aayna@bingol.edu.tr

166

Viscometric Investigation of Compatibilizer Effect on Polyvinyl chloride/Polystyrene Blends

Ersen YILMAZ[1]*, Ali BOZTUĞ[2]

[1] Munzur University, Tunceli Vocational School, Machinery Department, Tunceli, Türkiye
[2] Cumhuriyet University, Science Faculty Chemistry Department, Sivas, Türkiye
Ersen YILMAZ ORCID No: 0000-0002-8567-1668
Ali BOZTUĞ ORCID No: 0000-0003-2922-4481

Corresponding author: ersenyilmaz@munzur.edu.tr

171

Comparison of traditional Zivzik pomegranate vinegar against commercial pomegranate vinegar: antioxidant activity and chemical composition

Abdulkerim AYBEK[1], Ebru AKKEMİK[1,2]*

[1] Siirt University, Faculty of Engineering, Food Engineering Department, Siirt, Türkiye
[2] Siirt University, Science and Technology Application and Research Center, Siirt,Türkiye
Abdulkerim AYBEK ORCID No: 0000-0002-9543-8659
Ebru AKKEMİK ORCID No: 0000-0002-4177-4884

Corresponding author: eakkemik@siirt.edu.tr

178

Sweet Plant Proteins and Their Recombinant Production

Shokoufeh Yazdanıan ASR[1], Nergiz YÜKSEL[2,3], Seyhan İÇİER[3], Burcu KAPLAN TÜRKÖZ*[4]

[1] Ege University, Graduate School of Natural and Applied Sciences, Department of Food Engineering, İzmir, Türkiye
[2] Aydın Adnan Menderes University Germencik Yamantürk Vocational School Aydın, Türkiye
[3] Ege University, Graduate School of Natural and Applied Sciences, Department of Biotechnology, İzmir, Türkiye
[4] Ege University, Faculty of Engineering, Department of Food Engineering, İzmir, Türkiye
Shokoufeh Yazdanıan ASR ORCID No: 0000-0002-3468-7045
Nergiz YÜKSEL ORCID No: 0000-0002-1334-051X
Seyhan İÇİER ORCID No: 0000-0002-0627-733X
Burcu KAPLAN TÜRKÖZ ORCID No: 0000-0003-3040-3321

Corresponding author: burcu.kaplan.turkoz@ege.edu.tr

186

Türk Doğa ve Fen Dergisi
Turkish Journal of Nature and Science

www.dergipark.gov.tr/tdfd

Investigation of Bread Wheat Genotypes with Different Characteristics by Physiological and Quality Traits

Mehmet KARAMAN[1*], Fırat KURT[1], Yaşar KARADAĞ[1], Mahir BAŞARAN[2]

[1]Muş Alparslan University, Faculty of Applied Sciences, Muş, Türkiye
[2]GAP International Agricultural Research and Traning Center, Diyarbakir, Türkiye
Mehmet KARAMAN ORCID: 0000-0002-6176-9580
Fırat KURT ORCID: 0000-0003-0172-1953
Yaşar KARADAĞ ORCID: 0000-0002-0523-9470
Mahir BAŞARAN ORCID: 0000-0002-9655-0992

*Corresponding author: m.karaman@alparslan.edu.tr

Abstract: Instruments measuring spectral reflectance are very important to determine the relationship between grain yield (GY), quality and physiological traits of bread wheat genotypes at different developmental stages. This study was carried out under rain-fed conditions in 2019-2020 and 2020-2021 growing seasons in Muş province. The experiment was set up in a Randomized Blocks Experimental Design with 3 replicates. Except to flowering stage chlorophyll content (FSC), statistically significant differences were determined among genotypes at the level of p≤0.01 in all examined characteristics. More explicitly, G6, G8, G10, Müfitbey, Hanlı and Metin in terms of GY; Cemre, Kenanbey and Bezostaja 1 as regards quality traits; Ekiz, G8, and G9 with regard to physiological traits were found as significant genotypes. Biplot model analysis, used to determine the relationship genotype-trait and stability, showed that thousand grain weight (TGW) and plant height (PH) were positively associated with both GY and Normalized Difference Vegetation Index (NDVI). GY was found to be related to canopy temperature (CT) and heading time (HT) negatively. Notably, NDVI were positively related to protein ratio. Hanlı, Metin, G6, G8, and G10 were established as the high-yielded stabile genotypes which are least affected from environmental conditions.

Farklı Karakterli Ekmeklik Buğday Genotiplerinin Fizyolojik ve Kalite Özellikleri yönüyle İncelenmesi

Öz: Buğdayın farklı gelişim dönemlerinde, fizyolojik özellikler ile tane verimi ve kalite özellikleri arasındaki ilişkiyi belirlemek amacıyla spektral yansıma aletleri farklı araştırıcılar tarafından yoğun bir şekilde kullanılmaktadır. Çalışma, Muş ilinde yağışa dayalı koşullarda 2019-2020 ve 2020-2021 sezonlarında yürütülmüştür. Deneme, Tesadüf Blokları Deneme Deseninde 3 tekrarlamalı olarak kurulmuştur. Çiçeklenme dönemi klorofil içeriği (FSC) hariç, incelenen tüm özelliklerde genotipler arasında p≤0.01 düzeyinde istatistiki olarak önemli farklılıklar belirlenmiştir. Varyans analizi sonuçlarına göre, tane veriminde (GY); G6, G8, G10, Müfitbey, Hanlı ve Metin, Kalitede; Cemre, Kenanbey ve Bezostaja 1, Fizyolojik özelliklerde; Ekiz, G8 ve G9 genotipleri öne çıkmıştır. Genotip-özellik ve stabilite biplot modeline göre; bin tane ağırlığı (TGW) ve bitki boyu (PH)'nun hem GY ile hem de Normalize Edilmiş Vejatasyon İndeksi (NDVI) ile pozitif ilişkili olduğu görülmüştür. GY'nin bitki örtüsü sıcaklığı (CT) ve başaklanma süresi (HT) ile negatif ilişkili olduğu belirlenmiştir. NDVI ile protein oranı (PR) arasında pozitif ilişki görülmesi dikkate değerdir. Güncel çalışmada; Hanlı, Metin, G6, G8 ve G10 hem yüksek verimli hemde değişen çevre koşullarından en az etkilenen kararlı genotipler olarak öne çıkmıştır.

1. INTRODUCTION

Bread wheat (2n= 42) is one of most cultivated staple crops in Turkey and around the world because it has higher adaptive capacity and grows in various soils and environmental conditions. It is known that grain yield (GY) and quality traits of wheat show a considerable variation in terms of years and ecological factors [1-3]. In order for wheat genotypes to be classified at best category, the traits such as GY, thousand grain weight (TGW), and protein ratio (PR) should be in a certain range.

TGW and PR are affected by ecological conditions along with inheritance and the results of the studies conducted in various ecologies indicated that PRs of the wheat changes between 9.8 and 16.2 % [4-6, 1, 3]. The measurement these mentioned parameters along with physiological traits in plant breeding programs increase the success of the breeding [7, 8].

Chlorophyll content (represented as SPAD readings), normalized difference vegetation index (NDVI), and canopy temperature (CT) are used widely in field studies as selection parameters to determine the relationships between physiological traits, and GY and quality trait (QT) [9-13]. SPAD readings under stress conditions help determine the performances of genotypes and flag-leaf chlorophyll content in plant breeding studies since there is a positive correlation between increase of GY and chlorophyll content [14, 15]. Likewise, the highest CT values are observed before heading time and the CT values show higher correlations in determining the GY potential during grain filling stage [16, 17].

The effects of morphological, physiological, phenological, agronomic, genetic and ecological factors over GY, NDVI, CT, SPAD values are taken into consideration in the wheat cultivation and affect the success of the wheat breeding programs [17]. Therefore, in the present study, it is aimed to identifying the best genotypes for Muş ecological conditions based on GY, physiological, and quality traits.

2. MATERIALS AND METHODS

The study was conducted in 2019-2020 and 2020-2021 growing seasons under rain-fed conditions in Yildiz Farm in Muş, Turkey (Figure 1).

Figure 1. The map showing the location of the trial area

The materials used in the trial were consisted of 25 wheat genotypes with different characters (winter, alternative, spring) (Table 1). The trial was setup on the 6 m^2 plots which are comprised of 6 rows having 20 cm row spacing in 5 m long. The seeds were sown between 15 October and 15 November. According to soil analysis, the trial area had insufficient organic matter with moderately alkaline pH. Also, it was determined that the soil structure was clayey and the phosphorus content was insufficient (Table 2). Therefore, 9 kg da^{-1} N and 5 kg da^{-1} P$_2$O$_5$ were applied to the soil. Nitrogen fertilization was given in two stages as 2.3 kg da^{-1} during sowing and as 6.7 kg da^{-1} at the end of tillering stage Zadoks 26 [18], respectively, whilst all phosphorus fertilization was applied at once during sowing. Each plot was harvested during July with a plot combine.

Table 1. The origins and pedigrees of the genotypes used in the study

Genotypes	Character	Origin
Cemre	Spring	GAP International Agricultural Research and Traning Center
Bezostaja 1	Winter	Maize Research Institute
Hanlı	Spring	Maize Research Institute
Metin	Alternative	Maize Research Institute
Konya-2002	Winter	Bahri Dağdaş International Agricultural Research Institute
Beşköprü	Alternatif	Maize Research Institute
Syrena odes'ka	Winter	Yıldız Plant Productions, Seed, and Agricultural Industry Crop
Yıldırım	Winter	East Anatolian Agricultural Research Institute
Müfitbey	Alternative	Transitional Zone Agricultural Research Institute
Ahmetağa	Winter	Bahri Dağdaş International Agricultural Research Institute
Sönmez 2001	Winter	Transitional Zone Agricultural Research Institute
Ayyıldız	Winter	East Anatolian Agricultural Research Institute
Bayraktar 2000	Alternative	Field Crops Central Research Institute
Kenanbey	Winter	Field Crops Central Research Institute
Ekiz	Winter	Bahri Dağdaş International Agricultural Research Institute
G1	Winter	IWWIP
G2	Winter	IWWIP
G3	Winter	IWWIP
G4	Winter	IWWIP
G5	Alternative	IWWIP
G6	Winter	IWWIP
G7	Alternative	IWWIP
G8	Alternative	IWWIP
G9	Alternative	IWWIP
G10	Alternative	IWWIP

IWWIP: International Winter Wheat Improvement Program

Table 2. The soil properties of trial area

Texture	Salt (%)	pH	$CaCO_3$ (%)	P_2O_5 (kg da^{-1})	Organic Matter (%)	Saturation (%)
Clay	0.2	8.2	7.96	3.21	1.74	77

Source: Anonymous [19]

3

The precipitation and temperature data are given in Table 3. The precipitation in 2019-2020 (749.6 mm) was similar the long-term average (762.9 mm) while lower (386.6 mm) than the long-term average in 2020-2021. Notably, the precipitation of March and May during 2019-2020 growing season was approximately two-fold the long-term average. The temperature values, other than observed in October, December, and January of 2020-2021, were higher than those in 2019-2020.

Table 3. The climate data of experimental area during 2019-2021 seasons

Months	Precipitation of Muş (mm)			Temperature of Muş (^{0}C)		
	2019-2020	2020-2021	Long-Term	2019-2020	2020-2021	Long-Term
September	0.0	1.2	14.7	19.9	23.8	20.0
October	37.0	0.0	63.5	16.7	16.2	12.6
November	27.2	38.2	94.1	6.9	9.8	4.5
December	74.4	16.6	89.7	4.2	-2.3	3.0
January	36.8	94.0	86.0	-7.7	-8.1	-7.4
February	89.2	49.8	100.4	-3.8	2.7	-6.1
March	198.0	166.4	103.3	3.7	3.9	0.6
April	117.0	7.8	107.4	11.2	14.6	9.0
May	113.2	11.6	69.0	17.6	19.1	14.9
June	29.0	0.6	28.2	20.5	23.0	20.2
July	27.8	0.4	6.6	25.4	27.5	25.3
Total	749.6	386.6	762.9	-	-	-

Source: Anonymous [20]

2.1. The Investigated Parameters

2.1.1. Grain yield (GY): After harvesting and threshing of each plot, the grains were weighted in a scale (±0.001 g) and the yields were expressed as kg da^{-1}.

2.1.2. Heading time (HT): Heading time was the total number of days beginning from the emergence of the plants until the 70% of the plants in each plot were spiked at the rate of ½.

2.1.3. Plant height (PH): After selecting plants with 10 spikes in dough developmental stage, each plant's height

was measured from soil surface to the upper most spikelet and expressed as cm.

2.1.4. Flag-leaf chlorophyll content (represented as SPAD values): A total of two chlorophyll content were measured made during flowering (FSC) and milk stages (MSC) to determine the chlorophyll content of flag leaf using SPAD 502 Chlorophyll-Meter (Minolta, Osaka, Japan). Values were determined by reading from the middle of the flag leaf between 10.00-12.00 hours of the day [21].

2.1.5. Normalized Difference Vegetation Index (NDVI): It was measured using GreenSeeker (Handheld crop) instrument between 11.00-15.00 in a day of flowering stage when weather was open, without wind and sunny, and plant surface was dry.

2.1.6. Plant canopy temperature (CT): it was measured using infrared thermometer (91KB JPG) between 12.00-14.00 in a day of flowering stage and expressed in Celsius (°C) [22].

2.1.7. Thousand grain weight (TGW): Four samples each of which consisted of 100 seeds were weighted in grams

(g). After the mean weight of all samples were calculated, it was multiplied by 10.

2.1.8. Protein ratio (PR) (%): PR was measured on wheat grains using NIT (IM 550) instrument.

2.2. Statistical Analyses

The statistical analyses were conducted using JMP 13.0. The differences among means were determined by LSD method ($p \leq 0.01$ and $p \leq 0.05$) [23]. Genstat 12th was employed for graphical visualization.

3. RESULTS AND DISCUSSION

ANOVA results of GY, physiological traits, and other agricultural parameters obtained from the trial which was conducted with 25 genotypes (15 varieties and 10 lines) with three replicates in 2019-2020 and 2020-2021 growing seasons are given in Table 4. Except to FSC, In terms of the genotypes all parameters were found significant at $p \leq 0.01$ level, while year and year*genotype interaction was significant only in some parameters ($p \leq 0.05$ or $p \leq 0.01$) (Table 4).

Table 4. Analysis of variance results for traits of the examined in bread wheat genotypes

Variance Resources	df	GY		HT		PH		FSC		NDVI	
		MS	F	MS	F	MS	F	MS	F	MS	F
Year	1	34132.4	11.9*	10651.3	4318.1**	15080.1	440.3**	4201.9	8.0*	0.038	11.0*
Rep.[Year]&Random	4	2861.1	2.6	2.5	2.0	34.3	1.6718	524.1	56.9	0.003	2.0
Genotype	24	8083.5	7.4**	44.5	35.7**	174.3	8.5**	11.9 n.s	1.3	0.006	3.3**
Year * Genotype	24	8856.1	8.1**	1.6	1.3	52.9	2.6**	10.6	1.1	0.003	1.5
Error	96	1089.6	-	1.2	-	20.5	-	9.3	-	0.002	-
CV(%)		13.8		0.6		6.4		6.8		6.4	
		CT		MSC		TGW		PR			
		MS	F	MS	F	MS	F	MS	F		
Year	1	240.3	2.6	923.1	27.7**	5925.2	607.3**	360.6	106.6**		
Rep.[Year]&Random	4	93.2	57.5	33.3	5.9	9.8	2.5	3.4	19.5		
Genotype	24	4.8	3.0**	17.0	3.0**	25.7	6.5**	2.5	14.1**		
Year * Genotype	24	2.5	1.5	8.8	1.6	8.9	2.3**	2.4	14.0**		
Error	96	1.6	-	5.6	-	3.9	-	0.2	-		
CV(%)		4.0		4.9		6.3	-	2.8			

GY: Grain yield; HT: Heading time; PH: Plant height; FSC: Flowering stage chlorophyll content; NDVI: Normalized difference vegetation index; CT: Canopy temperature; MSC: Milk stage chlorophyll content; TGW: Thousand grain weight; PR: Protein ratio; Rep.: Replication; df: degrees of freedom; MS: Mean of squares; *: $p \leq 0.05$; **: $p \leq 0.01$; n.s: not significant

Table 5. Mean values of wheat genotypes tested in different years with relation to parameters of GY, HT and PH

Genotype	GY			HT			PH		
	2019-2020	2020-2021	Mean	2019-2020	2020-2021	Mean	2019-2020	2020-2021	Mean
Cemre	281.3 abc	180.8 ij	231.1 e-ı	209.0 def	193.3 efg	201.2 cde	84.0 b-g	65.7 bcd	74.8 b-e
Bezostaja 1	240.8 c-g	123.1 k	181.9 k	210.7 bcd	192.0 g-j	201.3 cde	85.7 b-f	64.7 b-e	75.2 bcd
Hanlı	266.3 b-e	307.5 a-d	286.9 b	207.7 f	191.0 h-k	199.3 fg	76.3 g-j	61.0 d-h	68.7 f-ı
Metin	237.1 c-ı	309.2 a-d	273.1 bc	207.7 f	192.7 fgh	200.2 ef	80.3 c-ı	57.3 ghı	68.8 f-ı
Konya-2002	174.6 jkl	239.7 e-h	207.2 g-k	210.7 bcd	192.3 f-ı	201.5 cd	73.7 hıj	62.3 d-g	68.0 f-ı
Beşköprü	184.6 h-l	282.1 cde	233.3 d-ı	208.0 ef	189.0 lm	198.5 g	80.7 c-ı	62.7 c-g	71.7 c-g
Syrena odes'ka	264.4 cde	208.1 hı	236.3 c-h	209.7 de	192.0 g-j	200.8 de	70.0 j	57.7 ghı	63.8 ıj
Yıldırım	195.4 f-k	280.6 cde	238.0 c-h	210.0 cd	193.0 fg	201.5 cd	86.7 bcd	56.7 ghı	71.7 c-g

Müfitbey	321.3	ab	248.3	e-h	284.8	b	211.7	abc	195.7	abc	203.7	b	97.0	a	64.7	b-e	80.8	a
Ahmetağa	169.2	jkl	210.6	hı	189.9	k	212.0	ab	195.0	b-e	203.5	b	75.3	hıj	56.7	ghı	66.0	hı
Sönmez 2001	271.7	a-d	134.4	jk	203.1	h-k	210.3	bcd	194.0	c-f	202.2	c	86.3	b-e	53.0	ij	69.7	e-h
Ayyıldız	185.3	g-l	272.2	c-f	228.8	f-j	213.0	a	196.0	ab	204.5	ab	92.0	ab	66.7	bcd	79.3	ab
Bayraktar 2000	182.8	ı-l	348.3	a	265.6	b-f	201.7	l	186.0	n	193.8	l	85.0	b-f	73.0	a	79.0	ab
Kenanbey	242.1	c-f	257.2	d-h	249.7	b-f	213.0	a	197.3	a	205.2	a	87.3	bc	62.7	c-g	75.0	bcd
Ekiz	213.3	e-k	300.8	a-d	257.1	b-f	211.7	abc	195.3	bcd	203.5	b	78.7	d-ı	59.0	e-ı	68.8	f-ı
G1	135.0	l	268.8	c-g	201.9	h-k	209.7	de	193.7	d-g	201.7	cd	81.7	c-h	62.7	c-g	72.2	c-f
G2	263.8	cde	241.7	e-h	252.7	b-f	209.7	de	193.0	fg	201.3	cde	72.3	ij	48.3	j	60.3	j
G3	160.8	kl	223.8	f-ı	192.3	jk	207.7	f	190.7	ı-l	199.2	fg	78.0	e-j	54.7	ı	66.3	hı
G4	196.9	f-k	218.3	ghı	207.6	g-k	210.3	bcd	193.3	efg	201.8	cd	77.3	f-j	55.0	hı	66.2	hı
G5	211.7	e-k	273.8	c-f	242.7	c-g	209.7	de	193.0	fgh	201.3	cde	87.7	bc	70.3	ab	79.0	ab
G6	239.4	c-h	304.4	a-d	271.9	bc	207.7	f	190.3	jkl	199.0	fg	74.3	hıj	59.0	e-ı	66.7	ghı
G7	222.5	d-j	312.1	abc	267.3	b-e	207.7	f	189.3	klm	198.5	g	74.7	hıj	58.0	f-ı	66.3	hı
G8	322.9	a	334.2	ab	328.5	a	205.7	g	188.0	m	196.8	h	85.0	b-f	68.7	abc	76.8	abc
G9	180.0	jkl	212.1	hı	196.0	ıjk	212.7	a	195.3	bcd	204.0	ab	75.7	g-j	58.0	f-ı	66.8	ghı
G10	257.5	cde	282.9	b-e	270.2	bcd	203.7	h	188.3	m	196.0	h	78.0	e-j	64.0	c-f	71.0	d-e
Min. value	135.0		123.1		189.9		201.7		186.0		194		70.0		48.3		60.3	
Max. value	322.9		348.3		328.5		213.0		197.3		205		97.0		73.0		80.8	
General Mean	224.8		255.0		239.9		209.2		192.4		201		80.9		60.9		70.9	
LSD (0.05)	56.2**		52.1**		37.8**		1.9**		1.8**		1.3**		8.5**		6.2**		5.2**	
CV(%)	15.2		12.4		13.8		0.6		0.6		0.6		6.4		6.1		6.4	

3.1. Grain Yield (kg da^{-1})

Significant differences were found between years and genotypes in terms of GY (Table 4 and 5). G8 yielded the highest GY (322.9 kg da^{-1}) in 2019-2020. Cemre, Müfitbey, Sönmez 2001 were placed in the same group with G8. Bayraktar 2000 (348.3 kg da^{-1}) yielded the best GY in 2020-2021 and was in the same group with Hanlı, Metin, Ekiz, G6, G7, and G8. When the means of GY was evaluated by years, 30.2 kg da^{-1} less GY was obtained despite the higher rainfall in 2019-2020 growing season (Table 3 and 5). This situation is probably stemmed from the water logging (or flooding) stress occurred as a result of rainfalls which are accompanied by snow-melting of March and May in the first growing season. The combined analysis results indicated that G8, Hanlı, and Müfitbey were significant genotypes with relation to GY. GY results in this study were similar to those of Fagnano et al. [24], Aydoğan ve Soylu [6], and Ülker [25], who obtained 213-362 kg da^{-1}, 154.58-258.43 kg da^{-1}, and 164-301 kg da^{-1}, respectively.

3.2. Heading Time (day)

The earliest heading variety was identified as Bayraktar 2000 (201.7 and 186.0 day) in both growing seasons whereas the latest heading varieties were Ayyıldız (213.0 and 196.0 days) and Kenanbey (213.0 and 197.3 days), which were in the same group. The heading time was shortened 16.8 day, when the means of growing seasons were compared, due to the drought conditions in 2020-2021. Combined means of HT showed that there was a considerable variation (194-205 day) among genotypes. Moreover, Bayraktar 2000 was the earliest variety whereas Kenanbey, Ayyıldız, and G9 were the latest genotypes sharing the same group (Table 5). When HT is compared to GY, the inheritance was more effective over HT than ecological conditions [26]. In regions where heat or drought stress is seen in the late period, early varieties may be more productive with the advantage of escaping from stress. Indeed, some researchers reported that early varieties were more productive [27, 28].

3.3. Plant Height (cm)

Year (environment) and genotype were found to be effective over PH and a wide-range variation among genotypes were established (Table 4 and 5). Müfitbey (97.0 cm) were identified as the tallest genotype whereas Syrena odes'ka (70 cm) was the shortest in 2019-2020. Bayraktar 2000 (73.0 cm) were found to be the tallest whereas G2 (48.3 cm) was the shortest genotype in 2020-2021. When mean values of PH were compared by years, PHs in 2020-2021 were 20 cm were shorter. This may be originated from the drought effect in the season. According to the results of the combined analysis, PHs changed in a range of 60.3 cm - 80.8 cm. Müfitbey,

Ayyıldız, Bayraktar 2000, G5, and G8 were the tallest genotypes involved in the same group whereas G2 was the shortest genotype. In the studies conducted in different regions by different authors related to the PH, a wide range results were obtained. In this regard, Aydın et al. [29], Aydoğan and Soylu [6], Çağlar et al. [30], and Demirel et al. [31] found bread wheat PHs as follows: 68.1-95.6 cm, 79.5-108.2 cm, 72.5-99.3 cm, and 52.16-96.66 cm, respectively.

Table 6. Mean values of wheat genotypes tested in different years with relation to parameters of FSC, NDVI, and CT

Genotype	FSC 2019-2020	FSC 2020-2021		FSC Mean	NDVI 2019-2020	NDVI 2020-2021		NDVI Mean		CT 2019-2020		CT 2020-2021		CT Mean	
Cemre	39.20	46.10	k	42.65	0.677	0.623	e-ı	0.650	c-f	37.60	a	31.73	ab	34.67	a
Bezostaja 1	43.30	49.77	d-j	46.53	0.643	0.677	a-e	0.660	b-e	32.38	b-e	30.80	b-e	31.59	b-h
Hanlı	43.57	52.33	a-d	47.95	0.660	0.700	ab	0.680	a-d	34.90	ab	30.42	c-f	32.66	bcd
Metin	42.17	49.17	e-k	45.67	0.673	0.617	e-j	0.645	c-g	33.47	bcd	32.18	a	32.83	bc
Konya-2002	37.13	50.03	c-j	43.58	0.643	0.560	ıj	0.602	gh	32.42	b-e	30.48	c-f	31.45	b-h
Beşköprü	41.33	49.20	e-k	45.27	0.707	0.647	b-f	0.677	a-d	33.45	bcd	30.25	c-f	31.85	b-h
Syrena odes'ka	39.23	53.57	ab	46.40	0.600	0.647	b-f	0.623	e-h	34.45	bcd	30.08	c-f	32.27	b-g
Yıldırım	39.10	48.13	ıjk	43.62	0.667	0.603	f-j	0.635	d-h	30.47	e	30.48	c-f	30.48	h
Müfitbey	39.67	51.70	a-f	45.68	0.690	0.693	abc	0.692	abc	31.92	cde	30.17	c-f	31.04	fgh
Ahmetağa	38.83	51.23	b-ı	45.03	0.643	0.603	f-j	0.623	e-h	34.00	bcd	31.82	ab	32.91	b
Sönmez 2001	41.90	48.30	h-k	45.10	0.663	0.623	e-ı	0.643	d-h	32.25	b-e	30.20	c-f	31.23	d-h
Ayyıldız	38.87	49.13	e-k	44.00	0.713	0.690	a-d	0.702	ab	32.22	b-e	29.87	ef	31.04	fgh
Bayraktar 2000	38.13	51.43	a-g	44.78	0.623	0.623	e-ı	0.623	e-h	32.60	b-e	29.78	ef	31.19	e-h
Kenanbey	37.77	48.60	f-k	43.18	0.680	0.670	a-e	0.675	a-d	32.33	b-e	30.07	c-f	31.20	d-h
Ekiz	38.97	49.23	d-j	44.10	0.710	0.717	a	0.713	a	32.88	b-e	30.98	bc	31.93	b-h
G1	39.60	47.97	jk	43.78	0.673	0.580	g-j	0.627	e-h	34.67	bc	30.62	cde	32.64	b-e
G2	37.50	50.37	c-j	43.93	0.673	0.623	e-ı	0.648	c-g	34.03	bcd	30.97	bc	32.50	b-f
G3	35.97	51.40	a-h	43.68	0.617	0.627	d-h	0.622	e-h	31.75	de	30.60	cde	31.18	fgh
G4	39.73	50.17	c-j	44.95	0.683	0.620	e-j	0.652	c-f	32.40	b-e	31.08	bc	31.74	b-h
G5	36.80	48.40	g-k	42.60	0.660	0.613	e-j	0.637	d-h	33.30	bcd	29.45	f	31.38	c-h
G6	40.13	52.23	a-e	46.18	0.657	0.630	c-g	0.643	d-h	32.32	b-e	29.75	ef	31.03	gh
G7	40.23	53.00	abc	46.62	0.660	0.557	j	0.608	fgh	32.50	b-e	29.78	ef	31.14	fgh
G8	40.83	49.07	f-k	44.95	0.670	0.667	a-f	0.668	a-e	32.28	b-e	29.88	def	31.08	fgh
G9	40.07	49.70	d-j	44.88	0.700	0.653	a-f	0.677	a-d	32.17	b-e	30.95	bcd	31.56	b-h
G10	40.03	54.47	a	47.25	0.630	0.563	hıj	0.597	h	32.68	b-e	29.75	ef	31.22	d-h
Min. value	36.00	46.10		42.60	0.665	0.557		0.649		30.47		29.45		30.48	
Max. value	43.60	54.47		47.95	0.713	0.717		0.713		37.60		32.18		34.67	
General Mean	39.60	50.19		44.90	0.665	0.633		0.649		33.02		30.49		31.75	
LSD $_{(0.05)}$	n.s	3.1**		n.s	n.s	0.07**		0.05**		2.8*		1.1**		1.5**	
CV(%)	9.7	3.8		6.8	6.4	6.3		6.4		5.1		2.2		4.0	

n.s: not significant

3.4. Flowering Stage Chlorophyll Content (FSC)

There is no statistical difference among genotypes in term of the results of combined analysis and of 2019-2020 season. However, the differences among genotypes were found significant in 2020-2021 and the G10 was identified as the genotype with the highest FSC (54.47 mg/m²). FSC in 2020-2021 was found 10.59 mg/m² higher compared to the previous year and it changed from 42.60 to 47.95 mg/m² in terms of two-year data (Table 6). In a study carried out by Dalkılıç et al. [17] in Kahramanmaraş, it was reported that FSC in durum wheat showed a variation between 46.9 and 52.3 mg/m². FSCs were found between 42.6-47.95 mg/m² in the present study.

3.5. Normalized Difference Vegetation Index (NDVI)

NDVI values of genotypes showed no statistical significance in 2019-2020. Nonetheless, a significant differences was found among genotypes in 2020-2021 growing season and combined analysis. Ekiz (0.717 and 0.713) variety had the highest NDVI value (Table 6). When means of the years were compared, the NDVI

values during 2019-2020 were 0.032 higher. Before flowering 20 days and after 10 days, the maximum leaf area forms in wheat and therefore, it is stated that there is a positive relationship between NDVI readings and GY [32, 33]. Nevertheless, no relationship was established between NDVI readings and GY in this study (Figure 2).

3.6. Canopy Temperature (ºC)

Genotypes showed significant differences in terms of CT. Yıldırım variety (30.47 ºC) in 2019-2020, and G5 (29.45) genotype in 2020-2021 were significantly kept their leaves cool. CT values in 2019-2020 growing period were 2.53 ºC higher than those in 2020-2021 (Table 6). According to the results of combined analysis, Yıldırım, Müfitbey, Ayyıldız, G6, and G8 were the significant genotypes in keeping their leaves cool. These results were similar to those of the study carried out by Fahlani and Assad in Iran [34], in which CT values of bread wheat genotypes showed significant difference at the stem elongation, booting, and flowering stages. In another study, conducted with 15 bread wheat genotypes under Mediterranean conditions for three years, CTs did not differ significantly in the period between the beginning of the heading and of the milk stages [35, 17]. However, in a study conducted in Diyarbakir conditions in landraces bread wheat, it was reported that there was a negative and significant relationship between CT and GY during the heading time period [36].

3.7. Milk Stage Chlorophyll Content (MSC)

The flag leaf chlorophyll content is an important indicator in showing photosynthetic activity and GY potential [37]. The effects of years and the genotypes were found significantly different in the present study. Sönmez 2001 in 2019-2020 (49.10 mg/m^2), G7 (53.37 mg/m^2) and G9 (53.57 mg/m^2) in 2020-2021 had significantly more high MSC (Table 7). The comparison of the means of the growing years indicated that MSC was 4.96 mg/m^2 higher at the milk stage in 2020-2021. According to the combined analysis results, Beşköprü, G4, G7, G9, and G10 were in the same group and having the highest chlorophyll content. In a study conducted on durum wheat in rainfed and irrigated conditions in Diyarbakır province, a positive and significant relationship was found in both environments between the chlorophyll content in the milk stage and grain yield [38]. In our study, no relationship was found between the chlorophyll content of the milk production period and the grain yield (Figure 2).

3.8. Thousand Grain Weight (TGW) (g)

TGW was found significantly different in terms of years and genotypes. G8 (43 g) had the highest TGW, followed by G1 which was involved in the same group in 2019-2020. On the other hand, Konya-2002 (29.25 g) genotype had the highest TGW in 2020-2021. It shared the same group with Cemre, Müfitbey, Ayyıldız, Ekiz, G5, and G8 (Table 7). According to the means of the TGW, lower value 12.6 g was obtained in 2020-2021 (Table 7). This result may be explained by the effect of the drought. The combined analysis showed that Cemre, Konya-2002, Yıldırım, Müfitbey, Ayyıldız, G5, and G8 were shared the same group with the highest TGWs. In a study conducted with 14 bread wheat genotypes for three years in Yozgat, Turkey, TGW values showed changes between 29.2 and 38.4 g [39]. TGW values in this study was ranged between 27.63 - 34.58 g. The differences among genotypes are usually explained by inheritance and environmental factors. Additionally, genotypes benefiting from the ecological conditions after heading stage usually have better TGWs [40, 41].

3.9. Protein Ratio (PR) (%)

PR is an important quality parameter for flour mill owners to make decision to which product of (flour, semolina, pasta, and etc.) wheat will be processed [42, 43, 41]. According to the PRs of genotypes, Cemre in 2019-2020 and Kenanbey in 2020-2021 had the highest PR as 15.57 % and 19.57 %, respectively. The comparison of the means by years showed that PR was 3.10 % higher in 2020-2021 compared to the previous year. Moreover, Cemre and Kenanbey had the highest PRs as 16.45 % and 16.32 % at the combined analyse, respectively (Table 7). PRs of the wheat genotypes are affected by ecological conditions and are genotype-specific, and range between 6-22 % depending on the ecological conditions [44, 39]. In the present study, PRs of the studied genotypes were between 13.97 % and 16.45 %.

7

Table 7. Mean values of wheat genotypes tested in different years with relation to parameters of MSC, TGW, and PR

Genotype	MSC			TGW			PR		
	2019-2020	2020-2021	Mean	2019-2020	2020-2021	Mean	2019-2020	2020-2021	Mean
Cemre	42.37 def	48.03 def	45.20 fg	37.83 bcd	29.00 a	33.42 abc	15.57 a	17.33 bc	16.45 a
Bezostaja 1	46.50 a-d	50.73 a-e	48.62 a-d	37.83 bcd	24.92 b-g	31.38 c-f	14.17 cd	17.43 b	15.80 b
Hanlı	46.27 a-e	49.50 b-f	47.88 a-f	35.50 d-g	23.75 e-h	29.63 fgh	13.23 h-k	16.17 e-h	14.70 f-ı
Metin	42.50 c-f	48.77 c-f	45.63 efg	33.92 gh	24.67 c-g	29.29 fgh	12.57 lmn	16.03 fgh	14.30 ijk
Konya-2002	46.30 a-e	51.13 a-d	48.72 a-d	39.92 b	29.25 a	34.58 a	12.80 klm	16.03 fgh	14.42 h-k
Beşköprü	47.90 ab	52.07 abc	49.98 a	34.83 e-h	24.42 c-g	29.63 fgh	13.07 ijk	15.77 ghı	14.42 h-k
Syrena odes'ka	41.30 f	52.80 ab	47.05 b-f	38.25 bcd	24.67 c-g	31.46 c-f	13.63 e-h	16.27 e-h	14.95 efg
Yıldırım	45.73 a-e	47.47 ef	46.60 d-g	40.08 b	25.00 b-g	32.54 a-d	13.77 d-g	16.63 b-f	15.20 cde

Müfitbey	47.60	ab	51.03	a-e	49.32	abc	39.92	b	28.50	ab	34.21	ab	11.80	o	17.27	bcd	14.53	g-j
Ahmetağa	46.63	abc	51.43	a-d	49.03	a-d	32.67	h	23.25	e-h	27.96	gh	12.23	no	15.70	h1	13.97	k
Sönmez 2001	49.10	a	50.03	a-e	49.57	ab	36.83	c-f	25.00	b-g	30.92	def	12.43	mn	16.57	c-g	14.50	g-j
Ayyıldız	47.70	ab	51.53	a-d	49.62	ab	37.50	b-e	27.75	a-d	32.63	a-d	12.50	lmn	17.17	bcd	14.83	e-h
Bayraktar 2000	44.67	b-f	48.77	c-f	46.72	c-g	39.17	bc	24.67	c-g	31.92	cde	13.23	h-k	14.93	1	14.08	jk
Kenanbey	46.37	a-e	50.97	a-e	48.67	a-d	36.92	c-f	21.75	gh	29.33	fgh	13.07	ijk	19.57	a	16.32	a
Ekiz	47.07	ab	51.50	a-d	49.28	a-d	36.67	c-g	26.25	a-f	31.46	c-f	12.83	klm	16.91	b-e	14.87	e-h
G1	46.97	ab	49.10	c-f	48.03	a-e	40.25	ab	24.25	d-h	32.25	b-e	14.80	b	16.50	c-h	15.65	bc
G2	42.30	ef	51.77	abc	47.03	b-f	38.67	bc	23.08	e-h	30.88	def	12.93	jkl	16.77	b-f	14.85	e-h
G3	42.60	c-f	51.57	a-d	47.08	b-f	34.17	fgh	20.75	h	27.46	h	14.23	c	16.10	e-h	15.17	def
G4	48.50	ab	51.33	a-d	49.92	a	35.75	d-g	24.25	d-h	30.00	efg	14.30	c	16.70	b-f	15.50	bcd
G5	42.40	def	46.00	f	44.20	g	39.25	bc	27.92	abc	33.58	abc	13.87	c-f	16.47	d-h	15.17	def
G6	47.23	ab	51.40	a-d	49.32	abc	39.75	b	24.33	c-h	32.04	b-e	13.37	g-j	14.97	1	14.17	jk
G7	47.70	ab	53.37	a	50.53	a	38.17	bcd	23.75	e-h	30.96	def	13.30	hij	16.13	e-h	14.72	f-1
G8	44.90	b-f	51.77	abc	48.33	a-e	43.00	a	26.50	a-e	34.75	a	13.50	f-1	16.43	d-h	14.97	efg
G9	46.43	a-e	53.57	a	50.00	a	32.50	h	22.75	fgh	27.63	h	12.93	jkl	16.87	b-f	14.90	efg
G10	47.47	ab	52.90	ab	50.18	a	38.25	bcd	22.92	e-h	30.58	def	14.07	cde	14.97	1	14.52	g-j
Min. value	41.3		46.0		44.2		32.50		20.8		27.63		11.8		14.97		13.97	
Max. value	49.1		53.37		50.5		43.00		29.00		34.58		15.6		19.57		16.45	
General mean	45.78		50.74		48.3		37.50		24.90		31.22		13.37		16.47		14.92	
LSD $_{(0.05)}$	4.18**		3.58**		2.7**		2.8**		3.6**		2.3**		0.5**		0.9**		0.5**	
CV(%)	5.6		4.3		4.9		4.6		8.8		6.30		2.0		3.2		2.80	

3.10. The Stability of Yield and The Associations Among Traits by Using the GGE Biplot Model

The relationships genotype-trait, GY, GY stability, and many binary or multiple comparisons, made by using many parameters, can be visualized and presented using GGE biplot. The angle (<90º positive relationship, >90º negative relationship, =90º no relationship) between vectors and the positions of the vectors are important for interpretation of genotype-trait relationships the model [45]. Additionally, the lengths of the vectors give ideas about the variations among genotypes. In this regard, whilst the short vector indicates lower variation, the long vector shows higher [46-48].
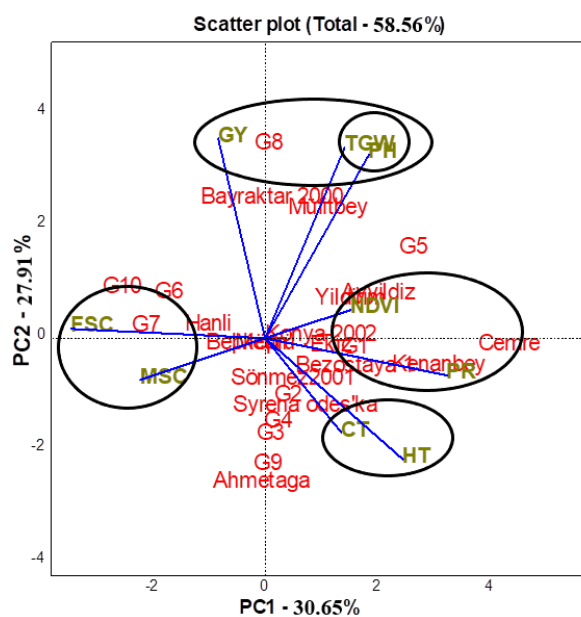
Figure 2. GGE biplot model show the relationships genotype-trait.

Figure 3 . Ranking biplot model show the stability of genotypes based on GY

The GGE biplot model is given in Figure 2 and it accounts for genotype-trait relationships in the study as 30.65 %, 27.91 %, and 58.56 % for PC1, PC2, and PC1+PC2, respectively (Figure 2). According to Figure 2, a positive relationship was observed among GY, TGW, and PH. The relationship between TGW and PH were found stronger. On the other hand, there was a negative relation GY, and HT, CT, PR. FSC and MSC

8

had the negative relationship with NDVI. In terms of quality parameters, PR was negatively associated with GY, FSC and MSC. When yield and quality parameters were taken into consideration, the genotypes G8, Bayraktar 2000, and Müfitbey were prominent according to GY whilst Cemre stood out in terms of PR.

The ranking biplot, the stability plot of the examined genotypes, indicates that genotypes above x axis have higher GY whereas below *x* axis have lower GY than the average of GY (Table 5 and Figure 3). The G8 genotype, located in the utmost right side of the stability line, was found as moderately stabile genotype with the highest GY. Müfitbey, Hanlı, Metin, G6, and G10 were established as genotypes with higher GYs following G8. G1, Bezostaja 1, and Sönmez 2001 were found as instable genotypes with lower GYs.

Ideal genotype was described as a stabile genotype with higher GY which does not change from one experimental field to another (Yan and Kang, 2003) [40]. Müfitbey was found as a genotype having higher GY with low stability. On the other hand, although Hanlı and G10 genotypes are not as high yielding as G8, they were established as genotypes with higher stability. G9 and Ahmetağa genotypes were stabile genotypes; however, their GYs were much below the trial averages.

4. CONCLUSION

Negative or positive relationships were found between GY and other traits in the study conducted with 25 genotypes having different characters in rain-fed conditions in Muş. G8, Hanlı, Müfitbey, G10, G6, Metin and Kenanbey were the best genotypes in terms of GY. Cemre, Kenanbey, Bezostaja 1, Konya-2002, Müfitbey, and G8 were the established as significant genotypes according to quality traits. GYs of Cemre, Bezostaja 1, Beşköprü, Yıldırım, Sönmez 2001, Ay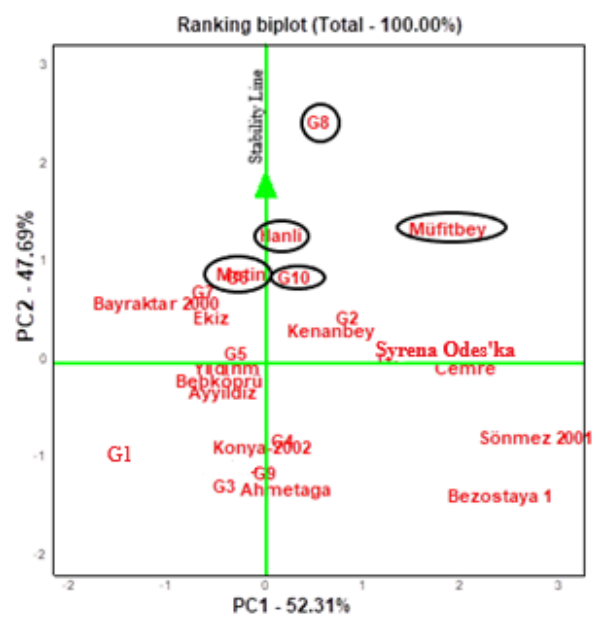yıldız and G1 genotypes were below averages and instabile. Metin, Ekiz, G5, G6, and G7 had GYs above the trial averages and were found as moderately stabile under environmental conditions. Although Bayraktar 2000 had higher GY above the trial average, it was highly affected by environmental conditions. Hanlı, Kenanbey, G6, G8, and G10 were the most stabile genotypes whose GYs were above the trial average. Notably, NDVI readings were found correlated with PR in the study. The genotypes with higher GYs were found to keep CT lower levels compared to other genotypes. To elaborate this important result, different studies should be conducted examining the relationship between CT and GY at different stages of the generative period.

Acknowledgement

REFERENCES

[1] Güngör H, Dumlupınar Z. Evaluation of some bread wheat *(Triticum aestivum L.)* cultivars for yield, yield components and quality traits in bolu conditions. Turkish J. of Agric. and Natural Sci. 2019;6(1):44-51.

[2] Çay F. Morphological and molecular characterization of synthetic hexaploid bread wheat lines and wheat varieties. Tekirdağ Namık Kemal University Graduate School of Natural and Applied Sciences Department of Field Crops. PhD Thesis. 157 p. 2020.

[3] Kahraman T, Güngör H, Öztürk İ, Yüce İ, Dumlupınar Z. Evaluating the effects of genotype and environment on yield and some quality parameters in bread wheat *(Triticum aestivum L.)* genotypes using principal component and GGE biplot analyses. KSU J. Agric Nat. 2021;24 (5):992-1002.

[4] Schular SF. Bacon RK. Gbur EE. Kernel and spike character influence on test weight of soft red winter wheat. Crop Sci. 1994;34:1309-1313.

[5] Miadenow N. Przulj N. Hristov N. Djuricand V. Milovanovic M. Cultivar by enviroment interactions for wheat quality traits in semiarid conditions. Cereal Chemistry. 2001;78:363-367.

[6] Aydoğan S, Soylu S. Determination of yield, yield components and some quality properties of bread wheat varieties. J. of Field Crop. Cent. Res. Inst. 2017;26(1):24-30.

[7] Jackson P, Robertson M, Cooper M, Hammer G. The role of physiological understanding in plant breeding. from a breeding perspective. Field Crops Res. 1996;49:11-37.

[8] Karaman M, Akıncı C, Yıldırım M. Investigation of the relationship between grain yield with physiological parameters in some bread wheat varieties. Trakya Univ. J. of Natural Sci. 2014;15(1):41-46.

[9] Giunta F, Motzo R, Deidda M. SPAD readings and associated leaf traits in durum wheat. barley and triticale cultivars. Euphytica. 2002;125(2):197-205.

[10] Yıldırım M, Akıncı C, Koç M, Barutçular C. Applicability of canopy temperature depression and chlorophyl content in durum wheat breeding. Anadolu J. Agric. Sci. 2009;24(3):158-166.

[11] Talebi R. Evaluation of chlorophyll content and canopy temperature as indicators for drought tolerance in durum wheat *(Triticum durum Desf.)*. Aust. J. Basic Appl. Sci. 2011;5:1457-1462.

[12] Islam MR, Haque KMS, Akter N, Karim MA. Leaf chlorophyll dynamics in wheat based on SPAD meter reading and its relationship with grain yield. Sci Agric. (2014;4: 13-18.

[13] Kızılgeçi F, Yıldırım M. The relationship of some physiological traits measured at heading stage with yield and quality properties of durum wheat. Turkish J. of Agric. and Natural Sci. 2019;6(4):777-785.

[14] Rosyara URR, Sharma C, Duveiller E. Variation of canopy temperature depression and chlorophyll content in spring wheat genotypes and association with foliar blight resistance. J. of Plant Breeding Gr. 2006;1:45-52.

[15] Özseven İ, Gençtan T. The effect of long-term waterlogging on flag leaf chlorophyll content in some bread wheat *(Triticum aestivum L.)* genotypes. Anadolu, J. of AARI. 2018; 28(2):1-16.

[16] Reynolds MP, Singh RP, Ibrahim A, Ageeb OAA. Larqué-Saavedra A, Quick JS. Evaluating physiological traits to complement empirical selection for wheat in warm environments. Euphytica. 1998;100:84-95.

[17] Dalkılıç AY, Kara R, Yürürdurmaz C, Şimşek B, Aldemir Y, Akkaya A. The effects on sowing density to physiological parameters in durum wheat. J. of Field Crops Cent. Res. Inst. 2016;25(1):78-87.

[18] Zadoks JC, Chang TT, Konzak CF. A decimal code for the growth stages of cereals. Weed Res. 1974;14:415-421.

[19] Anonymous. Yıldız Plant Manufacturing, Seed and Agriculture Industry Inc. soil analysis laboratory records. [cited 2020 September 05].

[20] Anonymous. Yıldız Plant Productions, Seed, and Agricultural Industry Corp weather station records. [cited 2022 January 07].

[21] Adamsen FJ, Pinter PJ, Barnes EM, Lamorte RL, Wall GW, Leavitt SW, Kimball BA. Measuring wheat senescence with a digital camera. crop ecology, production and management. Crop. Sci. 1999;39:719-724.

[22] Reynolds MP, Nagarajan S, Razzaque MA Ageeb OAA. Heat tolerance. application of physiology in wheat breeding. Mexico, DF, CIMMYT; 2001.

[23] Kalaycı M. Using JMP with examples and variance analysis models for agricultural research. anatolian agricultural research Institute Directorate Publications. Publication Number: 21, Eskişehir; 2005.

[24] Fagnano M, Fiorentino N, D'Egidio M, Quaranta F, Ritieni A., Ferracane R, Raimondi G. Durum wheat in conventional and organic farming: yield amount and pasta quality in Southern Italy. The Sci.World J. 2012;1-9.

[25] Ülker H. Genetic improvement in yield and some agronomic traits of bread wheat cultivars under Central Anatolian rainfed conditions. Ahi Evran University Institute of Science, Master of Science Thesis; 2017.

[26] Reif, JC, Maurer HP, Korzun V, Ebmeyer E, Miedaner T, Würschum T. Theor Appl. Genet. 2011;123:283-292.

[27] Motzo, R., Giunta, F., Deiddia, M. Relationships between grain-yield-filling parameters, fertility, earliness and grain protein of durum wheat in a mediterranean environment. Field-Crops Research. 1996 47(2-3): 129-142.

[28] Jiang, D., Dai,T., Jing, G., Cao, W., Zhou, G., Zhao, H.,Fan, X. Effects of longterm fertilization on leaf photosynthetic characteristics and grain yield in winter wheat. Photosynthetica. 2004;42: 439-446.

[29] Aydın N, Bayramoğlu HO, Mut Z, Özcan H. Determination of yield and quality characters of bread wheat *(Triticum aestivum L.)* cultivars and lines under Black Sea Region Conditions of Turkey. J. of Agric. Sci. 2005;11(3):257-262.

[30] Çağlar Ö, Öztürk A, Bulut S. Adaptation of some bread wheat cultivars in Erzurum plain conditions. J. of Atatürk Univ. Facult. of Agric. 2006;37(1):1-7.

[31] Demirel F, Kumlay AM, Yıldırım B. Evaluation of agromorphological characteristics of some bread wheat *(Triticum aestivum L.)* genotypes by biplot, clustering and path analysis methods. European J. of Sci. and Tech. 2021;23:304-311.

[32] Fischer RA. Yield potential in a dwarf spring wheat and theeffect of shading. Crop Sci. 1975;15(5):607-13

[33] Lopresti MF, Di Bella CM, Degioanni AJ. Relationship between MODIS-NDVI data and wheatyield: A case study in Northern Buenos Airesprovince, Argentina. Elsevier, Information Processing in Agriculture. 2015;2:73-84.

[34] Fahliani RA, Assad MT. Evaluation of Three physiological criteria for selecting drought resistant wheat genotypes. Proceedings of the Tenth International Wheat Genetics Symposium. 1-6 September. Italy; 2003. p. 664-666.

[35] Koc M, Barutcular C, Tiryakioğlu M. Possible heat-tolerant cultivar improvement through the use of flag leaf gas exchange Traits in a Mediterranean Environment. J. Sci Food Agric. Res. 2008;88:1638-1647.

[36] Kendal, E. Determination of the relationships between the characteristics of the pure lines selected from local bread wheat populations in diyarbakır ecological conditions. KSU J. Agric Nat. 2020; 23(4):1021-1029.

[37] Li P, Wu P, Chen J. Evaluation of flag leaf chlorophyll content index in 30 spring wheat genotypes under three irrigation regimes. Australian J. of Crop Sci. 2012;6(6):1123-1130.

[38] Yıldırım, M., Kılıç, H., Kendal, E., Karahan, T. Applicability of chlorophyll meter readings as yield predictor in durum wheat. Journal of Plant Nutrition. 2011;34:151-164.

[39] Mut Z, Erbaş Köse ÖD, Akay H. Determination of grain yield and quality traits of some bread wheat *(Triticum aestivum L.)* varieties. Anadolu J. of Agric. Sci. 2017; 32:85-95.

[40] Mut Z, Aydın N, Bayramoğlu HO, Özcan H. Investigation of yield and primary quality characteristics of some bread wheat *(Triticum aestivum L.)* genotypes. J. of Fac. of Agric., OMU. 2007; 22(2):193-201.

[41] Erdemci E, Aktaş H, Karaman M. Response of some facultative wheat genotypes to different environments. J. of Ege Univ. Fac. of Agric. 2021;58(3):421-430.

10

[42] Laidig F, Piepho HP, Hüsken A, Begemann J, Rentel, D, Drobek, T, Meyer U. Predicting loaf volume for winter wheat by linear regression models based on protein concentration and sedimentation value using samples from VCU trials and mills. J. of Cereal. Sci. 2018;84:132-141.

[43] Rapp M, Lein V, Lacoudre F, Lafferty J, Müller, E, Vida, G, Bozhanova V, Ibraliu A, Thorwarth P, Piepho HP, Leiser WL, Würschum T, Longin CFH. Simultaneous improvement of grain yield and protein content in durum wheat by different phenotypic indices and genomic selection. Theor. Appl. Genet. 2018;131:1315-1329.

[44] Ünal S. Importance of quality in wheat and methods used in determination. Cereal Products Technology Congress and Exhibition. 3-4 October, Gaziantep; 2002.

[45] Yan W, Tinker NA. An integrated biplot analysis system for displaying, interpreting, and exploring genotype× environment interaction. Crop Sci. 2005;45(3):1004-1016.

[46] Yan W, Kang MS. GGE biplot analysis: a graphical tool for breeders, geneticists, and agronomists. - (CRC Press: Boca Raton, FL); 2003.

[47] Yan W, Kang MS, Ma B, Wood S, Cornelius PL. GGE biplot vs. AMMI analysis of genotype by environment data. - Crop Sci. 2007;47:643-655.

[48] Aktaş H. Tracing Highly Adapted Stable Yielding Bread Wheat *(Triticum aestivum L.)* Genotypes For Greatly Variable South-Eastern Turkey. Applied Ecol. and Env. Res. 2016;14(4):159-176.

11

Türk Doğa ve Fen Dergisi
Turkish Journal of Nature and Science
www.dergipark.gov.tr/tdfd

In silico Prediction and In vitro Antioxidant Activities of Two Jujube Fruits from Different Regions

Fatih UCKAYA[1*]

[1] Alanya Alaaddin Keykubat University, Health Science Faculty, Nursing Department, Antalya, Türkiye

Fatih UCKAYA ORCID No: 0000-0003-0905-2010

Corresponding author: fatih.uckaya@alanya.edu.tr

Abstract: Jujube is a fruit rich in antioxidant compounds and vitamin C. In this way, it can prevent cell damage by fighting free radicals. In the study, antioxidant activities, total phenolic and total flavonoid compound amounts of methanolic extracts of jujube fruits were determined. In addition, their biochemical compositions were determined using HPLC. Also, an in silico prediction study of the identified active ingredients was performed to evaluate antioxidant, antiradical, antibacterial, antifungal, anti-inflammatory, antimutagenic, and membrane integrity antagonist properties. For the determination of antioxidant capacity, ferric reducing power (FRAP) and cupric ion reducing capacity (CUPRAC), DPPH radical scavenging activity and β-carotene-linoleic acid assay were used. The amounts of total phenolic and the total flavonoid compounds of the extracts were determined as gallic acid equivalent (GAE) and as quercetin equivalent (QE). The methanolic extract of jujube collected from Antalya contains 580 μg GAE.mg^{-1} and 240 μg QE.mg^{-1}, and the methanolic extract of jujube collected from Denizli contains 900 μg GA.mg^{-1} and 380 μg QE.mg^{-1}. The IC$_{50}$ values of Antalya and Denizli methanolic extracts according to the DPPH scavenging assay were 10.34 and 9.82, respectively. Gallic acid, catechin, caffeic acid, coumaric acid, ferulic acid and cinnamic acid were detected by HPLC. In addition, the in silico effects of these molecules were estimated with the PASS online prediction program. As a result, it was seen that Denizli jujube had a higher antioxidant effect than Antalya jujube.

12

Farklı Bölgelerden İki Hünnap Meyvesinin In silico Tahmin ve In vitro Antioksidan Aktiviteleri

Öz: Hünnap, antioksidan bileşikler ve C vitamini açısından zengin bir meyvedir. Bu sayede serbest radikallerle savaşarak hücre hasarını önleyebilir. Çalışmada hünnap meyvelerinin metanolik ekstraktlarının antioksidan aktiviteleri, toplam fenolik ve toplam flavonoid bileşik miktarları belirlendi. HPLC kullanılarak biyokimyasal bileşimleri belirlendi. Ayrıca, antioksidan, antiradikal, antibakteriyel, antifungal, antienflamatuar, antimutajenik ve membran bütünlüğü antagonist özelliklerini değerlendirmek için tanımlanan aktif bileşenlerin in silico tahmin çalışması yapıldı. Antioksidan kapasitenin belirlenmesi için ferrik indirgeme gücü (FRAP) ve bakır iyonu indirgeme kapasitesi (CUPRAC), DPPH radikal süpürme aktivitesi ve β-karoten-linoleik asit testi kullanıldı. Ekstraktların toplam fenolik ve toplam flavonoid bileşik miktarları gallik asit eşdeğeri (GAE) ve kersetin eşdeğeri (QE) olarak belirlendi. Antalya'dan toplanan hünnapın metanolik ekstraktı 580 μg GAE.mg^{-1} ve 240 μg QE.mg^{-1}, Denizli'den toplanan hünnapın metanolik ekstraktı ise 900 μg GA.mg^{-1} ve 380 μg QE.mg^{-1} içerir. DPPH süpürme tahliline göre Antalya ve Denizli metanolik ekstraktlarının IC$_{50}$ değerleri sırasıyla 10.34 ve 9.82'dir. HPLC ile gallik asit, kateşin, kafeik asit, kumarik asit, ferulik asit ve sinnamik asit tespit edildi. Ayrıca bu moleküllerin in silico etkileri PASS online tahmin programı ile tahmin edilmiştir. Sonuç olarak Denizli hünnabının Antalya hünnabına göre daha yüksek antioksidan etkiye sahip olduğu görüldü.

1. INTRODUCTION

Free radicals are one of the most emphasized issues in recent years. Cellular sources of free radicals, the reactions they take place in, and the resolution of antioxidant mechanisms that prevent free radical damage are extremely important for many diseases. A free radical is an atom or molecule with an odd number of electrons in its outer orbit [1]. They exist as both organic and inorganic molecules. Free radicals cause the atom they affect, and accordingly, the substance in which that atom is located to not be able to function. Depending on the biological significance of the affected substance and whether it can be repaired, temporary or permanent effects are observed [2, 3].

The importance given to antioxidants is increasing day by day due to their positive contributions to health. Antioxidants, which are one of the most popular supplements of the last period, have become used by everyone thanks to their effects that prolong life, reduce the risk of diseases such as cancer and heart diseases, and delay aging. Oxygen, which is indispensable for our life, can harm our body in some cases. The reason for this possible damage of oxygen is the formation of reactive oxygen species as a result of metabolic reactions in our body using oxygen. These molecules, known as free radicals, can damage lipid, protein, DNA and similar cell components. Then, problems such as premature aging, cancer, cardiovascular diseases may be encountered [4]. Antioxidant defense systems developed in aerobic respiration organisms control the formation of free radicals that contain an unpaired electron in their structure and prevent the harmful effects of these molecules. Thus, the cell is not damaged and is protected from diseases. However, there may be cases where the existing antioxidant defense system can not completely prevent the effects of free radicals. That's when the condition called oxidative stress occurs due to the increase of free radicals. Antioxidants are widely used to treat brain damage caused by the brain's vulnerability to oxidative stress. It is known that antioxidant compounds that can be used in treatments prevent cell death and neurological damage by preventing oxidative stress in nerve cells [5].

Jujube (Ziziphus jujuba Mill.) is a fragrant, 4-5 m high thorny tree, red bark, hard core, large olive-shaped plant that blooms yellow flowers between April and May. The outermost wall is leathery and thin, the pulp is yellow, sweet and delicious. The trunks of the tree are cylindrical, with brown bark and many branches. The leaves are in two opposite rows, with a short stem, and two small leaflets in the form of thorns. The sepals are five-part and green in color. The petals are yellow, curved and have five parts. It is thought to have spread from North Africa and Syria to India and China. Although the tree is adaptable to many climates, it needs hot summers to bear fruit well. It is located in Marmara, Western and Southern Anatolia in Turkey. In addition, different species are seen in the Eastern Black Sea Region and especially in the Coruh Valley Basin. The plant has been used as an emollient, expectorant and

diuretic since ancient times. It is very useful in diseases such as cardiovascular stiffness and shortness of breath. It is also used as a cholesterol and lipid lowering agent [6, 7].

In the study, ferric ion reducing power (FRAP), cupric ion reducing capacity (CUPRAC), DPPH radical scavenging activity and β-carotene-linoleic acid emulsion methods were used to determine the antioxidant activity of jujube plant. Total phenolic and flavonoid substance amounts of the extracts were determined as equivalent to gallic acid and quercetin, respectively. In addition, the phenolic compounds of the methanolic extract of the fruit were determined by HPLC. Also, in silico some biologic avtivity prediction of the determined active substances was applied with the PASS online program.

The aim of this study is to evaluate the phytochemical structure and antioxidant activity of the methanolic extract of jujube fruit in order to determine the beneficial effects and the components responsible for these effects. In addition, it is to perform in silico study of the identified active ingredients to understand their antioxidant, antiradical, antibacterial, antifungal, anti-inflammatory, antimutagenic, and membrane integrity antagonist properties.

2. MATERIAL AND METHOD

2.1. Materials

2.1.1. Chemicals

The Folin reagent and 1,1-diphenyl-2-picryl-hydrazil (DPPH•) used in the study were from Sigma-Aldrich and Na_2CO_3, methanol, gallic acid, butylated hydroxyanisole (BHA), butylated hydroxytoluene (BHT), chloroform ($CHCl_3$), β-carotene, lineolic acid, Tween 20, $FeCl_3$, potassium ferrocyanate, trichloroacetic acid (TCA), $CuCl_2.2H_2O$, ammonium acetate and trolox were obtained from Merck.

2.1.2. Fruits

The two jujube fruits used in the study were collected from two different regions of Turkey. One was collected from Alanya, Antalya, located in the Mediterranean region, from 36°30'07" north latitude and 31°38'40" east longitude coordinates (ZJA). The other was collected from Çivril, Denizli, which is located in the Aegean region and from 38° 18′ 5″ North latitude and 29° 44′ 19″ east longitude (ZJD). The fruits were identified as Ziziphus jujuba Mill based on the book "Flora of Turkey and the East Aegean Islands" by PH Davis.

2.1.3. Devices

Devices used in the analysis: Shimadzu UV 1700 spectrophotometer for absorption measurements, Inolap brand pH meter for pH measurements, Precisa XB 220A precision balance for weighing, Nüve brand incubator for heating and drying processes, Heidholph brand

13

evaporator and Lancome brand lyophilizer to remove the solvent after extraction.

2.2. Methods

2.2.1. Jujube fruit extraction

Jujube fruits were collected, cut into small pieces and dried. Then approximately 50 g of each was taken and placed in the soxlet cartridge. In the literature review, it was decided to use 100% methanol. It was extracted in methanol solvent at 30ºC for 6 hours. In order to remove the solvent of the obtained extract, it was subjected to 40ºC under vacuum in the evaporator. After evaporation, it was taken into vials and stored at 4ºC for analysis [8].

2.2.2. Determination of total phenolic and total flavonoid contents

The amount of phenolic compounds in the methanolic extract prepared from the jujube fruits used in the study was determined by the Folin Ciocalteu method [9]. Gallic acid was used as the equivalent standard phenolic compound. A calibration graph of gallic acid was drawn. Using the equation obtained from this graph, the total phenolic compound amounts of the jujube samples were determined. In the study, absorbances were read at 760 nm. Results were calculated in μg in gallic acid equivalent (GAE).

The amount of flavonoid compounds in the methanolic extract prepared from jujube fruits was determined by the aluminum nitrate method [10]. Quercetin was used as the standard flavonoid compound. A calibration graph of Quercetin was drawn. The total flavonoid content of the jujube samples was calculated using this calibration graph. Absorbances were read at 415 nm. Results were calculated in μg in quercetin equivalent (QE).

2.2.3. DPPH free radical scavenging activity
DPPH free radical scavenging activities of extracts prepared from jujube fruits used in the study were carried out according to the method developed by Blois [11]. DPPH was used as a free radical. Absorbance measurements were read at 517 nm. Ethanol was used as a control.

$$\text{Inhibition (\%)} = [(A_{control} - A_{sample})/A_{control}] \times 100$$

The plant extract concentration (IC_{50}) values at the time of scavenging half of the DPPH free radical were calculated for each sample. It was compared with the synthetic antioxidants BHT and BHA.

2.2.4. β-Carotene/linoleic acid bleaching method

Lipid peroxidation was carried out according to the method developed by Miller [12]. A solution of β-carotene in chloroform was used. Synthetic antioxidants BHA and BHT were used as standard. Absorbances were read at 470 nm. One measurement was read at the first time and the other measurements were read every 15 minutes for 120 minutes. Based on this absorbance, the rate of change in absorbance and, accordingly, the % oxidation inhibition coefficients were calculated.

R= ln(a/b)
Here; In is the natural logarithm, a is the initial absorbance, b is the absorbance after 120 minutes of incubation.

$$\text{Inhibition (\%)} = [(R_{control} - R_{sample})/R_{control}] \times 100$$

2.2.5. Ferric ion reducing antioxidant power (FRAP)

Ferric ion reducing antioxidant power of extracts prepared from jujube fruits used in the study was applied according to Benzie and Strain [13]. The FRAP reagent was used and freshly prepared before use. Absorbances were read at 593 nm. Ethanol was used as a control. BHA and BHT were used as positive standards.

2.2.6. Cupric ion reducing antioxidant capacity (CUPRAC)

The copper II ion-reducing antioxidant capacities of the extracts prepared from the jujube fruits used in the study were determined according to the method developed by Apak et al. [14]. Absorbances were read at 450 nm. Ethanol was used as a control. BHA and BHT were used as positive standards.

2.2.7. HPLC analysis

For HPLC analysis of phenolic compounds in fruit extracts, an analysis method was developed by drawing the calibration graph of 15 different phenolic compound standards separately [15]. After 20 mg of the samples were weighed and dissolved in 1 mL of methanol, 20 μL of the solutions were injected into the HPLC. First of all, standard phenolic substances were injected. Results are given as μg.g-1 with 95% confidence interval.

2.2.8. In silico toxic risks prediction by PASSonline

A computer-based program PASS (Prediction of Activity Spectra for Substances) was used to screen the antimicrobial and antioxidant potential of the phenolic compounds that the fruit's methanolic extract contains at the highest rate. The software is used to predict the biological activities of chemical structures, including phytochemicals, based on the structure-activity relationship with a known chemical entity. Besides the desired pharmacological effect, it predicts molecular mechanisms of action and undesirable side effects such as mutagenicity, carcinogenicity, teratogenicity and embryotoxicity [16]. It compares the structure by utilizing a library of molecules containing more than 205,000 compounds exhibiting more than 3750 biological activities. Activity is estimated in terms of Pa (probable activity) and Pi (probable inactivity). Structures where Pa is greater than Pi denote compounds considered for a particular pharmacological activity [17].

14

2.2.9. Statistical analysis

Statistical differences between groups were determined by Tukey post-hoc test and one-way ANOVA. Data were expressed as a mean of 7 standard deviations for three independent determinations. In ANOVA tests, $p < 0.05$ values were accepted as the limit of significance. Analyzes were performed using GraphPad Prism 9.0 for Windows (GraphPad Software, San Diego, CA, USA).

3. RESULTS

In recent years, many studies have been carried out on the therapeutic properties of plants. This therapeutic feature of plants is due to the fact that they contain antioxidant substances. Antioxidants provide the removal of radicals formed in normal ways in human metabolism. The most important antioxidants found in plants are flavonoid, carotenoid and phenolic compounds. Various spectroscopic and chromatographic methods have been developed for the identification of these compounds, and many antioxidant substances such as catechin, gallic acid, rutin, quercetin can be determined in plant and food samples. However, these methods are both expensive and it can not be fully commented on whether they can give antioxidant properties after the molecules are defined. For antioxidant determination, total antioxidant activity determination, total reducing capacity, DPPH scavenging, β-carotene and CUPRAC method, total flavonoid substance determination and similar methods are frequently used [18].

The increasing availability of life-saving drugs such as antibiotics has led to advances in the world of advanced medicine. However, the widespread use of these synthetic drugs has led to life-threatening side effects and the development of resistant strains of deadly pathogenic microorganisms [19, 20]. The development of new antimicrobial drugs that overcome these problems is therefore a major imperative for the pharmaceutical industries. Plant-derived antimicrobials and antioxidants have a long history of providing much needed safe and new therapeutics [21–23]. Plants constantly interact with rapidly changing and potentially harmful external environmental factors such as microbial attack and oxidative stress. This interaction involves alternative defense strategies, including the synthesis of a wide variety of chemical metabolites that counteract these stress factors. According to the World Health Organization, plants are the best source of various biologically active drugs [20]. To date, only 10-15% of plant species have been studied for their therapeutic potential for various ailments [17].

3.1. Total Phenolic and Total Flavonoid Substance Results

The most important antioxidant compounds are phenolic compounds. Phenols can donate electrons and hydrogens due to the functional groups they carry in terms of their structure. These groups eliminate radicals and oxidizing groups. Phenolic groups are rich in OH groups. These

groups add polarity to them and increase their antioxidant properties [24].

Table 1. Total phenolic and flavonoid contents of *Ziziphus spp.* and statistic analysis[a]

Samples	Total Phenolic Contents (µg GA.mg⁻¹ extract)[b]	Total Flavonoid Contents (µg QE.mg⁻¹ extract)[c]
ZJA[d]	$580 \pm 0{,}014$	$240 \pm 0{,}27$
ZJD[e]	$900 \pm 0{,}068$	$380 \pm 0{,}55$

[a]Statistical analyzes were performed using One Way Anova test and Tukey test in GraphPad Prism 9.0 program. According to the results, significant differences were found between four groups ($p < 0.05$, $F = 58.17$). [b]GA, gallic acid equivalents. [c]QE, quercetin equivalents. [d]ZJA: *Z. jujuba* extract collected from Antalya. [e]ZJD: *Z. jujuba* extract collected from Denizli.

In this study, the total phenolic substance determination was made according to the Folin-Ciocaltaeu method. The total amount of flavonoid substances was determined by a method based on aluminum chelation. For the calibration curves of gallic acid and quercetin, which are used as standards, solutions of these substances in methanol at five different concentrations were prepared.
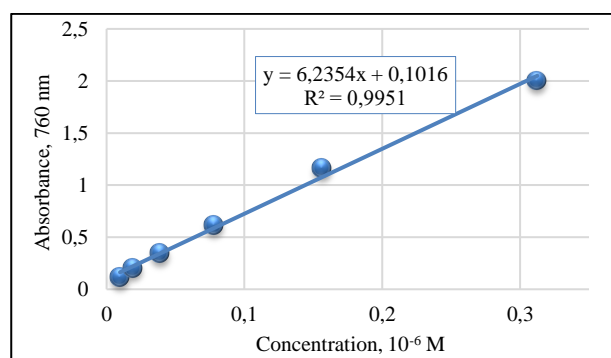
Figure 1. Calibration curve of gallic acid

The concentrations of total phenolic compounds in *Z. jujuba* extracts were calculated as gallic acid equivalent from the graphic equation obtained from the calibration curves of gallic acid methanol solutions given in Figure 1. The resulting graphic equation was found to be $y = 6{,}235x + 0{,}101$. According to the results given in Table 1, it was observed that the methanolic extract of ZJD contained a higher amount of phenolic substances than the methanolic extract collected from ZJA.

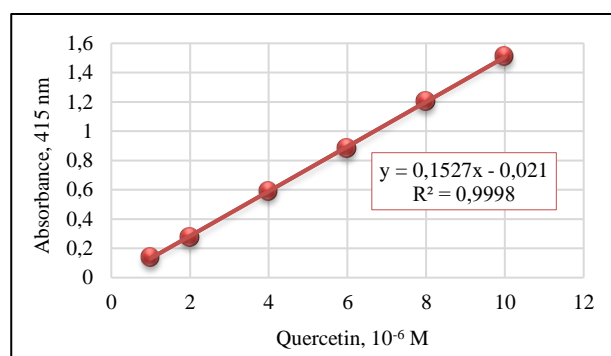**Figure 2.** Calibration curve of quercetin

The concentrations of total flavonoid compounds in Z. jujuba extracts were calculated as equivalent to the total amount of flavonoid substance quercetin from the graphic equation obtained from the calibration curves of quercetin methanol solutions given in Figure 2. The

Tr. Doğa ve Fen Derg. Cilt 11, Sayı 3, Sayfa 12-23, 2022

Tr. J. Nature Sci. Volume 11, Issue 3, Page 12-23, 2022

obtained graphic equation was found as y = 0,152x – 0,021. According to the results given in Table 2, it was observed that the methanolic extract of ZJD contained a higher amount of flavonoid substances than the methanolic extract collected from ZJA. As a result of the examinations, it has been determined that the total phenolic and total flavonoid substance amounts of the ZJD are higher than the ZJA.

3.2. DPPH Free Radical Scavenging Results

The radical scavenging activities of antioxidants are very important for the biological system and the food industry. Excessive formation of free radicals accelerates lipid peroxidation. This is an undesirable situation in foods and causes some diseases in humans. These diseases include premature aging, cancer, and forgetfulness [18].

In this method, DPPH• radical scavenging activity assay of methanol extract of Z. *jujuba* and standard antioxidant compounds which is BHA and BHT were determined. Calibration curve of DPPH in methanol was drawn. From the graph equation obtained (y = 0.013x + 0.006), IC$_{50}$ values of extracts and standarts were calculated.
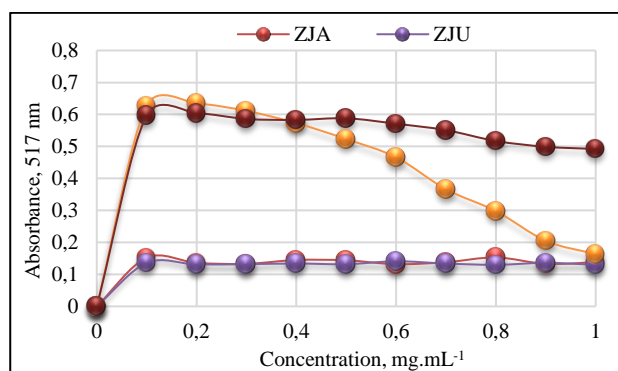

Figure 3. DPPH free radical scvenging activity graph of Z. *jujuba* methanolic extract collected from Antalya (ZJA), Z. *jujuba* methanolic extract collected from Denizli (ZJD), standart BHA and standart BHT.

The DPPH radical scavenging activity was determined for different concentrations of Z. jujuba methanolic extract, BHA and BHT. For this purpose, inhibition values at each concentration were calculated from the absorption values obtained and plotted against the concentration (Figure 3). As seen in Figure 3, there is no significant increase or decrease in the DPPH radical scavenging activities of methanolic extracs of ZJA and ZJD. In addition, it was observed that there was not a very large concentration difference between the two extracts.

3.3. β - Carotene Lineolic Acid Emulsion Assay Results

When free radicals attack the fat molecules in the cell membrane, the fat molecule undergoes a change. When fats are changed in the body, the structure and functions of the cell membrane are damaged. Therefore, the cell membrane cannot transfer nutrients, oxygen and water for a long time. It also cannot regulate the disposal of spent products. Continuing the attacks of free radicals

for a long time causes the breakdown of the oils in the structure of the cell membrane, the rupture of the plant membrane and the disintegration of the cell components [25].
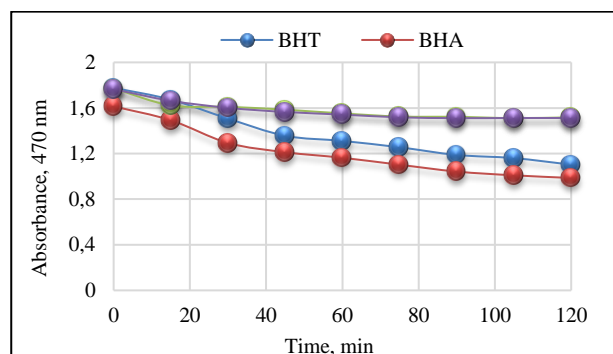
Figure 4. β-Carotene linoleic acid emulsion assay graph of Z. *jujuba* methanolic extract collected from Antalya (ZJA), Z. *jujuba* methanolic extract collected from Denizli (ZJD), standart BHA and standart BHT.

β-Carotene-lineolic acid emulsion method is based on the disappearance of the yellow color over time, which is formed by the reaction of the radicals formed as a result of the oxidation of lineoic acid in the emulsion with β-carotene. The presence of antioxidants prevents the color from lightening. In the β-carotene lineolic acid system, the fact that the yellow color did not fade immediately during the test period (120 min) indicates the presence of a high potential antioxidant (Figure 4).

In this method, antioxidant activities of ZJA extract and ZJD extract were measured and compared with the antioxidant activities of synthetic antioxidants BHA and BHT. As a result of the analyzes, it was found that the methanolic extract of ZJD showed higher antioxidant activity than the methanolic extract of ZJA according to the β-carotene lineoleic acid emulsion method. In addition, it was observed that two extracts showed higher activity than the standards.

3.4. CUPRAC Results

In the method, Cu (II) chloride solution, neocuprine solution and ammonium acetate (pH=7 buffer) solution are mixed. Antioxidant solution to be determined is added to the solution, and after 30 minutes, absorbance values are measured at 450 nm against the reference without antioxidant.

Figure 5. Cupric ions reducing capacity assay graph of Z. *jujuba* methanolic extract collected from Antalya (ZJA), Z. *jujuba* methanolic extract collected from Denizli (ZJD), standart BHA and standart BHT.

16

The cupric ion reduction potential results of Z. jujuba extracts according to the CUPRAC method are given in Figure 5. The results were obtained by measuring the absorbance of methanol solutions of the samples at 450 nm. When Figure 5 is examined, it has been observed that the sample of ZJA reduces more cupric ions to cuprous than the sample of ZJD. It was determined that both extracts had similar reducing power with standard BHA and BHT.

3.5. FRAP Results

In the method, the yellow color of the solution turns into green in different shades due to the reduction activities of the antioxidant substances in the solution. In the presence of antioxidants, the ferricyanide (Fe^{3+}) complex is reduced to its ferrous form (Fe^{2+}). The $K_3Fe(CN)_6$ complex gives a maximum absorbance at 593 nm by forming a complex of $Fe_4[Fe(CN)_6]_3$ with added FeCl3 and Perl's prussian blue (Ak Tuba, 2006).
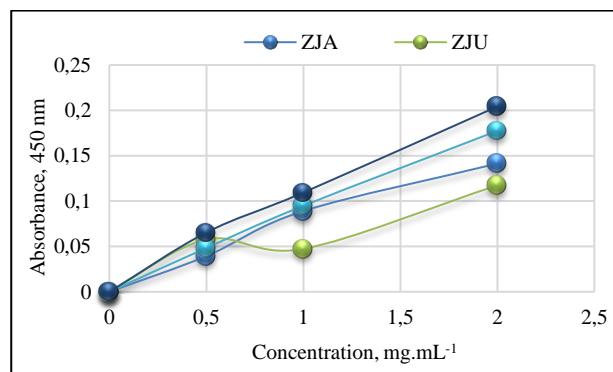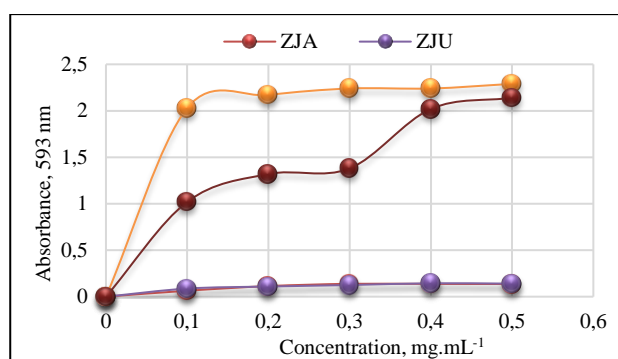

Figure 6. Ferric reducing antioxidant potential assay graph of Z. jujuba methanolic extract collected from Antalya (ZJA), Z. jujuba methanolic extract collected from Denizli (ZJD), standart BHA and standart BHT.

The ferric ion reducing power results of Z. jujuba methanol extracts according to the FRAP method are given in Figure 6. As seen in figure, Z. jujuba extracts showed a lower antioxidant effect than the standard antioxidants BHT and BHA. It was found that there was not much difference in value between the two extracts at a concentration of 1 mg.mL^{-1}, but the methanolic extract of ZJD showed slightly higher antioxidant activity than the methanolic extract of ZJA.

3.6. HPLC Results

Some of the phenolic and flavonoid compounds that provide antioxidant properties to Z. jujuba extracts were determined qualitatively and quantitatively by high performance liquid chromatography. These analyzed components and the amount of these components in each of the methanolic extract are given in Table 2. The chromatogram for the analysis of all standards is given in Figure 7(A). Also, Figure 7(B) shows the chromatogram of ZJA and Figure 7(C) shows the chromatogram of ZJD. As a result, all antioxidant molecules analyzed in Z. jujuba extracts contributed to their antioxidant capacity. The greatest contribution was made by the high levels of gallic acid, catechin, p-coumaric acid, cinnamic acid and ferulic acid molecules.

However, caffeic acid from these molecules was found only in the ZJA extract, while quercetin was not found in any of the extracts. However, it is possible that there are some unanalyzable antioxidant substances in each extract.

Table 2. HPLC results of phenolic compounds from two Z. jujuba species*

Samples	ZJA[a]	ZJD[b]
Gallic acid	6,39	31,20
Catechin	3,90	20,75
Caffeic acid	2,15	ND[c]
p-Coumaric acid	1,36	1,76
Ferulic acid	2,56	5,01
Cinnamic acid	0,43	0,98
Quercetin	ND[c]	ND[c]

*Results are given in µg.g^{-1} with 95% confidence interval. [a]Z. jujuba extract collected from Antalya. [b]ZJD: Z. jujuba extract collected from Denizli. [c]ND, Not detected.

3.7. In Silico Prediction Analysis Results

The hydroxyl and ketone groups in the structures of the molecules enable them to be interactive. The number of these groups and their bonding angles affect reaction rates and activities. The structural formulas of the active ingredients determined by HPLC in the ziziphus sample collected from both places are given in Figure 8.

Calculations using PASS software are widely used to verify and correlate the biological activities of chemical molecules [26, 27]. The results are confirmed by a structural study of the same molecules using software that works on the principle of structure-based comparison of key molecules of jujube fruit with existing antioxidant, antimicrobial, anti-radical, anti-inflammatory, anti-mutagenic and antifungal compounds. Gallic acid showed the highest Pa value for antibacterial activity, cinnamic acid showed the highest Pa value for anti-inflammatory potential, as catechin showed antioxidant activity, antifungal activity, antimutagenic activity, the highest scavenging effect against free radicals and the highest membrane integration antagonist. Significant inhibition effects of these molecules against oxidation, bacteria, fungi, inflammation and mutation have been detected. Catechin was found to be the molecule with the most extensive action. Catechin can be shown as the general factor of biological activities in experimental studies.

4. DISCUSSION AND CONCLUSION

In the study, the total phenolic compound content, total flavonoid compound content, scavenging effect of DPPH• radical, β-carotene lineolic acid emulsion system, copper ion reducing capacity, iron ion reducing power of methanolic extracts of ZJA and ZJD were determined. The results obtained were compared with the synthetic antioxidants BHA and BHT for both extracts separately.

The first study on the determination of total phenolic substances was done in 1965 by Singleton et al [28]. They used the Folin-Ciocalteu Method for determination. Atanassova and colleagues examined the

17

total phenolic content of *Melissa officinalis, Salvia officinalis* and *Mentha piperita*. They found 48.86 mg GAE.100g^{-1} for *Melissa officinalis*, 27.94 mg GAE.100g^{-1} for *Salvia officinalis* and 45.25 mg GAE.100g^{-1} for *Mentha piperita* [29]. Javanmardi et al. studied the total phenolic content of different species of the plant called *Ocimum basilicum*. As a result, they found values ranging from 22.9 mg GAE.g^{-1} to 65.5 mg GAE.g^{-1} [30]. In the study, the amount of phenolic substances contained in 2 mg.mL^{-1} methanol extracts of *Z. jujuba* was calculated as equivalent to gallic acid. The phenolic contents of the ZJD and ZJA were found to be 0.90 mg GAE.g^{-1} and 0.58 mg GAE.g^{-1}, respectively.

The first study on the determination of total flavonoid compound was done by Moreno et al. in 2000 [10]. They applied the calorimetric method for the determination. Atanassova et al. examined the total phenolic content as well as the total flavonoid content of *M. officinalis*, *S. officinalis* and *M. piperita*. They found the total flavonoid contents of 45.06 mg CE.100g^{-1} for M. officinalis, 27.54 mg CE.100g^{-1} for *S. officinalis* and 25.17 mg CE.100g-1 for *M. piperita*, respectively [29]. Chang et al. examined the total flavonoid compound content in propolis, as a result, they found values ranging from 10.38 mg QE.g^{-1} to 24.91 mg QE.g^{-1} [31]. In the study, the amount of flavonoids contained in *Z. jujuba* extracts was calculated as equivalent to quercetin. The flavonoid contents of ZJD and ZJA was found to be 0.38 mg GAE.g^{-1} and 0.24 mg GAE.g^{-1}, respectively.

The determination of DPPH free radical scavenging activity was first made by Blois in 1958 [11]. After Blois, the method was frequently applied because the process was short-lived and easy. Bencheraiet et al. applied the DPPH method to determine the antioxidant activity of *Ammi visnaga*. They found the IC$_{50}$ value of the plant as 8.77±0.2 µg.mL^{-1} and the IC$_{50}$ value of Rutin, a standard, as 3.01±0.2 µg.mL^{-1} and compared with each other. Accordingly, they detected the scavenging activity of DPPH radical [32]. In the study, IC$_{50}$ values of the methanolic extract of *Z. jujuba* were calculated at a concentration of 1 mg.mL^{-1} (ZJA = 5.17 µg.mL^{-1}, ZJD = 4.91 µg.mL^{-1}, BHA = 3 .5 µg.mL^{-1}, BHT = 1.5 µg.mL^{-1}). The DPPH radical scavenging activities of the extracts and synthetic antioxidants were listed as BHT > BHA > ZJD > ZJA.

The β-carotene lineolic acid emulsion method was first performed by Miller in 1971 [12]. In this method, antioxidant activity is determined by measuring the oxidation of linoleic acid in the presence of β-carotene. Türkoğlu et al. applied the β-carotene lineolic acid emulsion method for the determination of the antioxidant activity of *Laetiporus sulphureus* and found the inhibition value of the extract to be 82.2% [33]. In the study, the inhibition value of 1 mg.mL^{-1} *Z. jujuba* methanolic extract was found to be 94.49% for the sample collected from Denizli, and 88.83% for the sample collected from Antalya. In addition, inhibition values of BHT and BHA, which are synthetic antioxidants, were calculated with this method.

Inhibition values for BHT and BHA were obtained as 84.2% and 81.4%, respectively.

Benzie and Strain applied the ferric ion reducing power method for the first time in 1996 [13]. They used the reduction calorimetric method. They determined by measuring the absorption of 100 µmol.L^{-1} bilirubin and 280 µmol.L^{-1} albumin at 593 nm. In the study, the ferric reducing power was determined according to the Oyaizu [34] method. The reducing capacity of the methanolic extract of *Z. jujuba* at 1 mg.mL^{-1} was determined as 20.16 mg TEAC for ZJD and 19.63 mg TEAC for ZJA.

Apak et al. applied the CUPRAC method for the first time in 2004 [14]. The method is based on the reduction of cupric ions to cuprous ions in the presence of antioxidants in the compounds. Cikrikci et al. applied the CUPRAC method to determine the antioxidant activity of *Curcuma longa* [35]. Curcumin and turmeric were used in the determination. The CUPRAC.TEAC^{-1} value for curcumin is 0.8 mg TEAC.g^{-1}, while the CUPRAC.TEAC^{-1} value for turmeric is 0.7 mg TEAC.g^{-1}. In the study, CUPRAC.TEAC^{-1} values of 1 mg.mL^{-1} ZJA methanolic exract and 1 mg.mL^{-1} ZJD methanolic extract were calculated for the determination of antioxidant capacity by CUPRAC method. According to this method, trolox equivalent amounts of ZJA extract and ZJD extract were obtained as 9.15 mg TEAC.g^{-1} and 6.95 mg TEAC.g^{-1}, respectively.

It was observed that the reducing capacity of *Z. jujuba* extracts increased with increasing concentration as well as antioxidant activity. The reducing power may be an important factor in the antioxidant activity of a compound, but the antioxidant property of any pure substance can be explained by different mechanisms. In summary, antioxidant compounds can exhibit their antioxidative properties by different mechanisms such as binding transition metals, breaking down peroxides, and removing radicals.

The β-carotene lineolic acid method is based on hydrogen atom transfer. Electron transfer-based methods measure the capacity of antioxidants as a result of reduction of oxidants that change color when reduced. This event can be in the form of an increase or decrease in absorbance. The degree of color change is related to the total antioxidant concentration of the sample. In fact, reactions based on hydrogen atom transfer and electron transfer are intertwined in a sense and there are no insurmountable boundaries between them.

In this study, gallic acid, catechin, p-coumaric acid, cinnamic acid, ferulic acid, caffeic acid and quercetin were determined qualitatively and quantitatively in the extracts by HPLC analysis. From the obtained chromatograms, it was seen that the HPLC values of the methanolic extract of ZJD were higher than the methanolic extract of ZJA. Gallic acid is the highest in both extracts, followed by catechin. While the gallic acid value in the extract obtained from ZJD is 31.20 µg.g^{-1}, it is 6.39 µg.g^{-1} in the ZJA extract. When the catechin values are examined, ZJD extract is 20.75 µg.g^{-1} and

18

ZJA extract is 3.90 $\mu g.g^{-1}$. Likewise, it was found that the extract obtained from ZJD was higher than that obtained from ZJA in other values.

Gallic acid is an antioxidant and phenolic acid found in varying amounts in most plants. As an antioxidant, gallic acid can defend the body against free radicals and oxidative damage. When cells are exposed to free radicals, they damage their proteins and cell membranes and die faster than normal. The anti-inflammatory property of gallic acid is effective in curing inflammation. The use of ointments containing it for skin diseases such as arthritis and psoriasis significantly reduces inflammation [36, 37]. Caffeic acid is an organic compound belonging to the hydroxycinnamic acid class [38]. Caffeic acid is widely available in the human diet [39]. p-Coumaric acid is an organic compound belonging to the hydroxycinnamic acid class. It has three isomers. 1) ortho-coumaric acid, 2) meta-coumaric acid, 3) para-coumaric acid [40]. p-Coumaric acid is found in esterified or free acid form in the cell wall of grasses, cereals, fruits and vegetables (40, 41). Cinnamic acid is found naturally in most plant sources [42]. It is usually encountered in balms from cinnamon or storax tree [43]. These molecules are phenolic compounds detected in high amounts in methanolic extracts of *Z. jujuba*. Thanks to these molecules, the extract acts against oxidation. In addition to in vitro analyses, some biological effects of these molecules were investigated in silico. As a result of in silico prediction analysis, it was determined that gallic acid and catechin had the highest effect, while the others had potential at certain levels.

Antioxidant molecules have been reported to hold a growing attention owing to their defensive functionalities in food products, fruits, vegetables, bee products and drug products against oxidative damage. Investigation of antioxidant activities of plants and plant derived substances demand appropriate procedures that discourse the machineries of antioxidant oroperties. Several studies evaluating the antioxidant activity of various samples of research interest using different methods in food and human health have been carried out (44, 45, 46, 46, 47).

Consequently, the biochemical composition of the methanolic extracts of ZJA and ZJD was determined by HPLC analysis. The total amount of phenolic substances and total flavonoid substances were determined in the same extracts. As a result of both HPLC and phenolic and flavonoid substance determination methods, it was found that the amount of phenolic substance in plants was higher than the amount of flavonoid substance. For the determination of antioxidant capacity, β-carotene lineolic acid emulsion method and CUPRAC method were applied to the methanolic extracts of ZJA and ZJD, and then the iron ion reducing power and DPPH radical scavenging activities of the extracts were determined. The biological activities of the phenolic compounds contained in the extract were estimated with the PASS online program. When the results obtained are compared with standards and in silico prediction analysis data, it can be said that Z. jujuba methanolic extract is effective

against oxidation, free radicals and lipid peroxidation, as well as metal reduction potentials and its fruits can be used as a potential antioxidant in medicine, pharmaceutical and food industries.

REFERENCES

[1] Halliwell B, Gutteridge JMC. The ımportance of free radicals and catalytic metal ions in human diseases. Mol. Aspects Med. 1985;8(2):89-193.

[2] Halliwell B, Gutteridge JMC. Free radicals in biology and medicine. 3rd ed. New York: Oxford University Press; 1999.

[3] Valko M, Leibfritz D, Moncola J, Cronin MTD, Mazur M, Telser J. Free radicals and antioxidants in normal physiological functions and human disease. Int J Biochem Cell Biol. 2007;39:44-84.

[4] Vinson JA. Oxidative stress in cataracts. Pathophysiology 2006;13:151-162.

[5] Lobo V, Patil A, Phatak A, Chandra N. Free radicals, antioxidants and functional foods: Impact on human health. Pharmacogn Rev. 2010;4(8):118–126.

[6] Davis PH. Flora of Turkey and the east aegean islands. 2nd ed. U.K.: Edinburg University Press, 1967.

[7] Xie B, Wang PJ, Yan ZW, Ren YS, Dong KH, Song ZP, et al. Growth performance, nutrient digestibility, carcass traits, body composition, and meat quality of goat fed Chinese jujube (Ziziphus Jujuba Mill) fruit as a replacement for maize in diet. Anim Feed Sci Technol. 2018;246:127-136.

[8] Uckaya F, Uckaya M. Formulation and evaluation of anti-aging cream using banana peel extract. Int J Pharm Sci. 2022;13(1):1000-11.

[9] Singleton VL, Orthofer R and Lamuela-Raventos RM: Analysis of total phenols and other oxidation substrates and antioxidants by means of Folin-Ciocalteu Reagent. Methods Enzymol. 1999; 299: 152-78.

[10] Moreno MIN, Isla MI, Sampietro AR and Vattuone MA: Comparison of the free radical-scavenging activity of propolis from several regions of Argentina. J Ethnopharmacol. 2000;71:109-14.

[11] Blois MS. Antioxidant determinations by the use of a stable free radical. Nature 1958;181,1199-1200.

[12] Miller HE. A simplified method for evaluation of antioxidant. J Am Oil Chem Soc. 1971;45:91.

[13] Benzie İFF, Strain JJ. The ferric reducing ability of plasma (FRAP) as a measure of "antioxidant power": the FRAP assay. Anal Biochem. 1996;239(1):70-76.

[14] Apak R, Güçlü K, Özyürek M, Karademir SE. Novel total antioxidant capacity index for dietary polyphenols and vitamins c and e, using their cupric ion reducing capability in the presence of neocuproine: CUPRAC Method. J Agric Food Chem. 2004;52:7970-7981.

[15] El-Haci IA, Mazari W, Atik-Bekkara F, Mouttas-Bendimerad F, Hassani F. Bioactive compounds from the flower part of Polygonum maritimum L. collected from Algerian coast. Curr Bioact Compd. 2020;16(4):543-545.

19

[16] Mathew B, Suresh J, Anbazhagan S. Synthesis and PASSassisted in silico approach of some novel 2-substituted benzimidazole bearing a pyrimidine-2,4,6 (trione) system as mucomembranous protector. J Pharm Bioallied Sci. 2013;5:39–43.

[17] Jamkhande PG, Pathan SK, Wadher SJ. In silico PASS analysis and determination of antimycobacterial, antifungal, and antioxidant efficacies of maslinic acid in an extract rich in pentacyclic triterpenoids. Int J Mycobacteriology, 2016;5:417-425.

[18] Pham-Huy LA, He H, Pham-Huy C. Free radicals, antioxidants in disease and health. Int J Biomed Sci. 2008;4(2):89–96.

[19] Reardon S. Antibiotic resistance sweeping developing World. Nature 2014;509:141–142.

[20] Hemalatha M, Thirumalai T, Saranya R, Elumalai EK, Ernest D. A review on antimicrobial efficacy of some traditional medicinal plants in Tamil Nadu. J Acute Dis. 2013;2:99–105.

[21] Kannan RRR, Arumugam R, Thangaradjou T, Anantharaman P. Phytochemical constituents, antioxidant properties and pcoumaric acid analysis in some sea grasses. Food Res Int. 2013;54:1229–1236.

[22] Nain P, Kumar A, Sharma S, Nain J. In vitro evaluation of antimicrobial and antioxidant activities of methanolic extract of Jasminum humile leaves. Asian Pac J Trop Med. 2011;4:804–807.

[23] Rios JL, Recio MC. Medicinal plants and antimicrobial activity. J Ethnopharmacol. 2005;100:80–84.

[24] Brewer MS. Natural antioxidants: sources, compounds, mechanisms of action, and potential applications. Compr Rev Food Sci Food Saf. 2011;10(4):221-247.

[25] Lobo V, Patil A, Phatak A, Chandra N. Free radicals, antioxidants and functional foods: impact on human health. Pharmacogn Rev. 2010;4(8):118–126.

[26] Goel RK, Singh D, Lagunin A, Poroikov V. PASS-assisted exploration of new therapeutic potential of natural products. Med Chem Res. 2011;20:1509–1514.

[27] Khurana N, Ishar MPS, Gajbhiye A, Goel RK. PASS assisted prediction and pharmacological evaluation of novel nicotinic analogs for nootropic activity in mice. Eur J Pharmacol. 2011;661:22–30.

[28] Singleton V, Rossi, J. (1965) Colorimetry of total phenolic compounds with phosphomolybdic-phosphotungstic acid reagents. Am J Enol Vitic. 1965;16:144-158.

[29] Atanassova M, Georgieva S, Ivancheva K. Total phenolic and total flavanoid contents, antioxidant capacity and biological contaminants in medical herbs. J Chem Technol Metall. 2011;46(1):81-88.

[30] Javanmardi J, Stushnoff C, Locke E, Vivanco JM. Antioxidant activity and total phenolic content of Iranian Ocimum accessions. Food Chem. 2003;83(4):547-550.

[31] Chang CC, Yang MH, Wen HM, Chern JC. Estimation of total flavonoid content in propolis by two complementary colorimetric methods. J Food Drug Anal. 2002;10(3):178-182.

[32] Bencheraiet R, Kherrab H, Kabouche Z. Flavonols and antioxidant activity of Ammi visnaga L. (Apiaceae). Rec Nat Prod. 2011;5(1):52-55.

[33] Türkoğlu A, Duru ME, Mercan N, Kıvrak İ, Gezer K. Antioxidant and antimicrobial activity of Laetiporus sulphureus (Bull.: Fr.) Murrill. Food Chem. 2007;101:267-273.

[34] Oyaizu M. Studies on product of browing reaction prepared from glucose amine. Japan Nutr. 1986;44:307-315.

[35] Cikrikci S, Mozioglu E, Yilmaz H. Biological activity of curcuminoids ısolated from Curcuma longa. Rec Nat Prod. 2008;2(1):19-24.

[36] Kiani R, Arzani A, Mirmohammady Maibody SAM. Polyphenols, flavonoids, and antioxidant activity ınvolved in salt tolerance in wheat, Aegilops cylindrica and their amphidiploids. Front. Plant Sci. 2021;12:646221.

[37] Shahidi F, Ambigaipalan P. Phenolics and polyphenolics in foods, beverages and spices: Antioxidant activity and health effects – A review. J Funct Foods, 2015;18(B):820-897.

[38] Espíndola KMM, Ferreira RG, Narvaez LEM, Rosario ACRS, Da Silva AHM, Silva AGB, Vieira APO, Monteiro MC. Chemical and pharmacological aspects of caffeic acid and ıts activity in hepatocarcinoma. Front Oncol. 2019;9:541.

[39] Kępa M, Miklasińska-Majdanik M, Wojtyczka RD, Idzik D, Korzeniowski K, Smoleń-Dzirba J, Wąsik TJ. Antimicrobial potential of caffeic acid against staphylococcus aureus clinical strains. Biomed Res Int. 2018;7413504.

[40] Boz H. p-Coumaric acid in cereals: presence, antioxidant and antimicrobial effects. Int J. Food Sci Technol. 2015;50(11):12898.

[41] Pei K, Ou J, Huang J, Ou S. p-Coumaric acid and its conjugates: dietary sources, pharmacokinetic properties and biological activities. J Sci Food Agric. 2016;96(9):2952-62.

[42] Letsididi KS, Lou Z, Letsididi R, Mohammeda K, Maguy BL. Antimicrobial and antibiofilm effects of trans-cinnamic acid nanoemulsion and its potential application on lettuce. Lebensm Wiss Technol. 2018;94:25-32.

[43] Guzman JD. Natural cinnamic acids, synthetic derivatives and hybrids with antimicrobial activity. Molecules. 2014;19(12):19292-349.

[44] Kucukler S, Benzer F, Yildirim S, Gur C, Kandemir FM, Bengu AS, Ayna A, Caglayan C, Dortbudak MB. Protective effects of chrysin against oxidative stress and inflammation induced by lead acetate in rat kidneys: a biochemical and histopathological approach. Biol Trace Elem Res. 2021;199(4):1501-1514.

[45] Caglayan C, Kandemir FM, Darendelioğlu E, Küçükler S, Ayna A. Hesperidin protects liver and kidney against sodium fluoride-induced toxicity through anti-apoptotic and anti-autophagic mechanisms. Life Sci. 2021;281:119730.

[46] Zengin G, Mahomoodally MF, Aktumsek A, Jekő J, Cziáky Z, Rodrigues MJ, Custodio L, Polat R, Cakilcioglu U, Ayna A, Gallo M, Montesano D, Picot-Allain C. Chemical Profiling and Biological Evaluation of Nepeta baytopii Extracts and Essential Oil: An Endemic Plant from Turkey. Plants. 2021;10(6):1176.

[47] Gulcin I. Antioxidants and antioxidant methods: An updated overview. Arch. Toxicol. 2020;94(3):651-715.

Appendices

Appendix A.
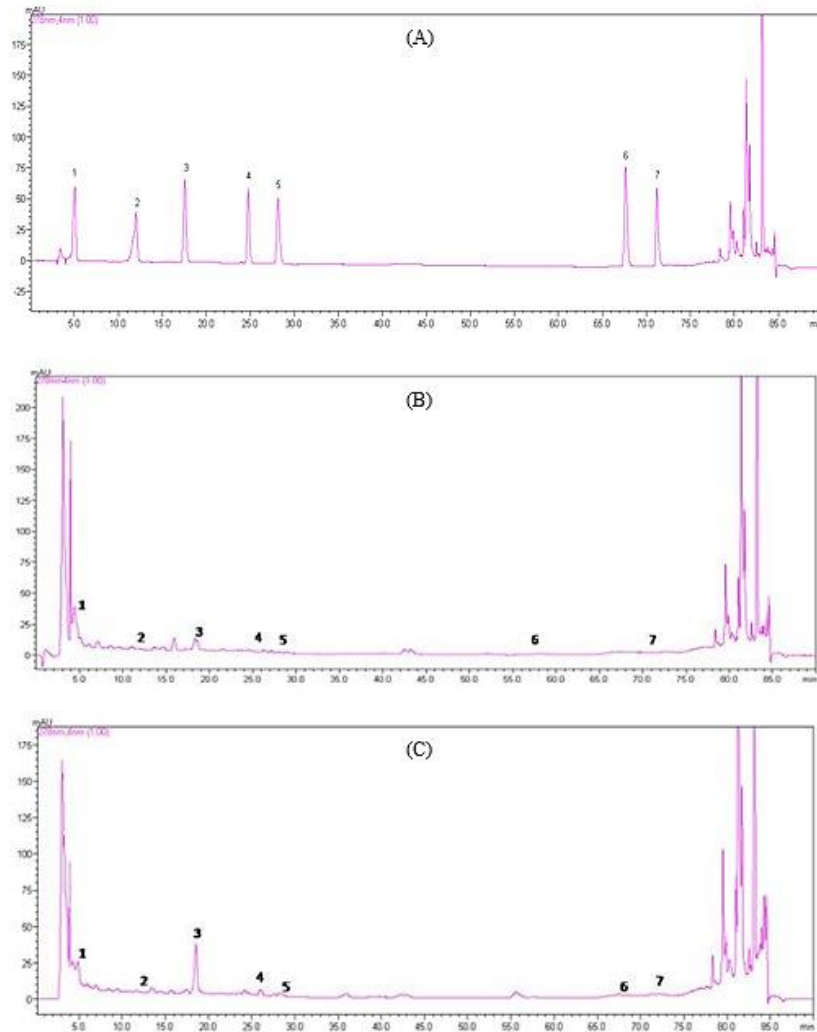
Figure 7. A) Standard chromatogram, B) Chromatogram of *Z. jujuba* collected from Antalya, C) Chromatogram of *Z. jujuba* collected from Denizli. *Molecular numbers given in the chromatogram; 1: Gallik acid, 2: Catechin, 3: Caffeic acid, 4: p-Coumaric acid, 5: Ferulic asid, 6: Cinnamic acid, 7: Quercetin.

Gallic acid	Catechin	Cafeic acid
p-Cumaric acid	Ferulic acid	Cinnamic acid
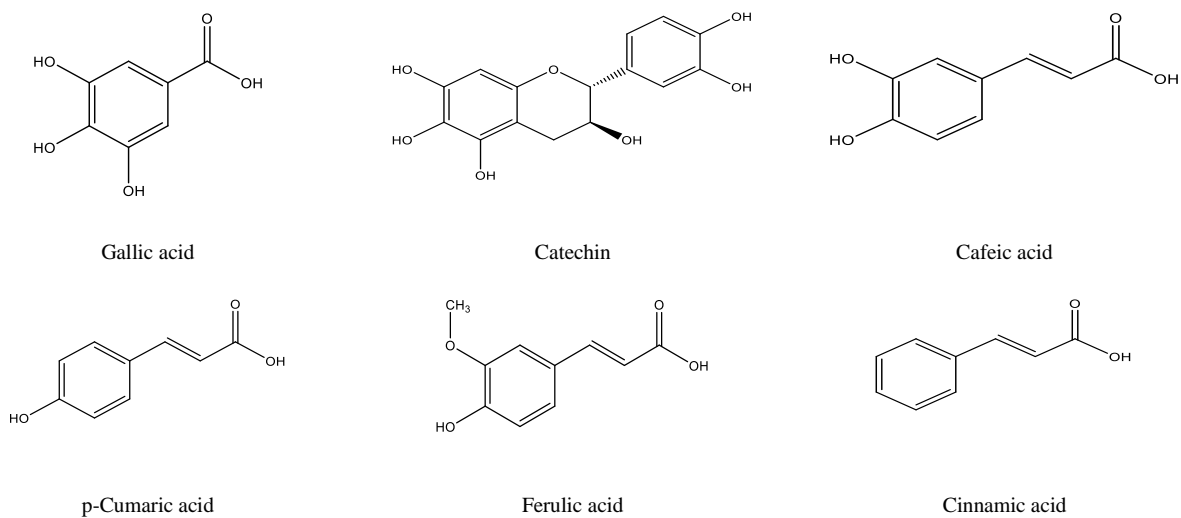
Figure 8. Molecular structures of the major components of both jujube fruits

22

Table 4. Pharmacological activities predicted for major phenolic compounds of *Z. jujuba* methanolic extracts

Activity	Gallic acid		Catechin		Cafeic acid		p-Cumaric acid		Ferulic acid		Cinnamic acid	
	Pa*	Pi**	Pa*	Pi**	Pa*	Pi**	Pa*	Pi**	Pa*	Pi**	Pa*	Pi**
Antioxidant	0,520	0,006	0,847	0,003	0,603	0,005	0,553	0,005	0,540	0,005	0,489	0,007
Free radical scavenger	0,570	0,007	0,827	0,002	0,647	0,005	0,627	0,005	0,731	0,004	0,497	0,010
Antibacterial	0,418	0,026	0,360	0,041	0,358	0,041	0,343	0,045	0,333	0,048	0,312	0,056
Antifungal	0,398	0,050	0,561	0,002	0,450	0,039	0,451	0,039	0,430	0,044	0,401	0,049
Antiinflammatory	0,548	0,044	0,616	0,028	0,651	0,023	0,641	0,024	0,604	0,031	0,656	0,022
Antimutagenic	0,597	0,010	0,917	0,002	0,845	0,003	0,886	0,002	0,900	0,002	0,817	0,004
Membran integrity antagonis	0,543	0,035	0,971	0,002	0,955	0,003	0,954	0,003	0,276	0,130	0,774	0,014

*Pa: Probable activity; **Pi: Probable inactivity. Pa > 700: probable activity greater than 70%. The PASS prediction results were interpreted and used as follows: (i) only activities with Pa > Pi are considered as possible for a particular compound; (ii) if Pa > 0.7, the chance to find the activity experimentally is high.

Prediction of Epidemic Disease Severity and the Relative Importances of the Factors for Epidemic Disease Using the Machine Learning Methods

Hüseyin KUTLU[1*], Cemil ÇOLAK[2], Çağla Nur DOĞAN[3], Mehmet TURGUT[4]

[1] Adıyaman University, Besni Ali Erdemoğlu Vocational School, Computer Tec. Department, Adıyaman, Türkiye
[2] İnönü University, Medical Faculty, Biostatistics and Medical Informatics Department, Malatya, Türkiye
[3] Çukurova University, Medical Faculty, Child Health and DiseasesDepartment, Adana, Türkiye
[4] Adıyaman University, Medical Faculty, Child Health and Diseases Department, Adıyaman, Türkiye

Hüseyin KUTLU ORCID No: 0000-0003-0091-9984
Cemil ÇOLAK ORCID No: 0000-0003-1507-7994
Çağla Nur DOĞAN ORCID No: 0000-0003-1507-7994
Mehmet TURGUT ORCID No: 0000-0002-2155-8113

*Corresponding author: hkutlu@adiyaman.edu.tr

Abstract: Epidemic diseases have been seen frequently in recent years. Today's, thanks to advanced database systems, it is possible to reach the clinical and demographic data of citizens. With the help of these data, machine learning algorithms can predict how severe (at home, hospital or intensive care unit) the disease will be experienced by patients in the risk group before the epidemic begins to spread. With these estimates, necessary precautions can be taken. In this study, during the COVID-19 epidemic, the data obtained from the Italian national drug database was used. COVID-19 severity and the features (Age, Diabetes, Hypertension etc.) that affect the severity was estimated using data mining (CRISP-DM method), machine learning approaches (Bagged Trees, XGBoost, Random Forest, SVM) and an algorithm solving the unbalanced class problem (SMOTE). According to the experimental findings, the Bagged Classification and Regression Trees (Bagged CART) yielded higher accuracy COVID-19 severity prediction results than other methods (83.7%). Age, cardiovascular diseases, hypertension, and diabetes were the four highest significant features based on the relative features calculated from the Bagged CART classifier. The proposed method can be implemented without losing time in different epidemic diseases that may arise in the future.

24

Makine Öğrenimi Yöntemlerini Kullanarak Salgın Hastalık Şiddetinin ve Salgın Hastalık Faktörlerinin Göreceli Önemlerinin Tahmin Edilmesi

Öz: Salgın hastalıklar son yıllarda sıklıkla görülmektedir. Günümüzde gelişmiş veritabanı sistemleri sayesinde vatandaşların klinik ve demografik verilerine ulaşmak mümkündür. Bu veriler yardımıyla makine öğrenme algoritmaları, salgın yayılmaya başlamadan önce risk grubundaki hastaların hastalığın ne kadar şiddetli (evde, hastanede veya yoğun bakım ünitesinde) yaşayacağını tahmin edebilir. Bu tahminler ile gerekli önlemler alınabilir. Bu çalışmada, COVID-19 salgını sırasında İtalya ulusal ilaç veri tabanından elde edilen veriler kullanılmıştır. COVID-19 şiddeti ve şiddeti etkileyen özellikler (Yaş, Diyabet, Hipertansiyon vb.), veri madenciliği (CRISP-DM Metodu), makine öğrenmesi yaklaşımları (Bagged Trees, XGBoost, Random Forest, SVM) ve dengesiz sınıf problemini çözen bir algoritma (SMOTE) kullanılarak tahmin edilmiştir. Deneysel bulgulara göre Torbalı Sınıflandırma ve Regresyon Ağaçları (Bagged CART), diğer yöntemlere göre (%83,7) daha yüksek doğrulukta COVID-19 şiddeti tahmin sonuçları vermiştir. Torbalı CART sınıflandırıcısından hesaplanan göreli özelliklere dayalı olarak yaş, kardiyovasküler hastalıklar, hipertansiyon ve diyabet en önemli dört özellik olarak tahmin edilmiştir. Önerilen yöntem ileride ortaya çıkabilecek farklı salgın hastalıklarda zaman kaybetmeden uygulanabilecektir.

1. INTRODUCTION

An epidemic is when the amount of disease in a population exceeds the expected number [1]. An epidemic can be local (an outbreak of disease), more general (epidemic), or even worldwide (pandemic) [2]. As a result of the destruction of living spaces and climate changes, epidemic and pandemic diseases have been observed frequently in recent years [3]. SARS-COV-2 (2019), ZIKA (2015), EBOLA (2013), MERS (2012), H1N1 (2009), SARS (2002) are some of these diseases [4]. In many of these epidemics, the healthcare community has faced an unheard-of situation. Intensive care units (ICUs) and emergency were full, and doctors had to make extremely difficult decisions. In a situation where resources are limited and doctors have to make fast and accurate decisions for patients, doctors need machine learning-based decision support systems. As the number of infected patients increases, data about the disease increases in parallel. In addition, it is possible to extract information from the patient's past health records, such as the national drug database. By making use of developing software and hardware technologies, this data (demographic and clinical) can be recorded in a database management system. From this data, classification and predictions can be made with the help of machine learning. Epidemics spread from one region (A) to another region (B). Before a disease spreads from region A to region B, necessary measures can be taken in region B with the information obtained from data collected from region A and analyzed by machine learning.

The process of obtaining valuable information from a database, or large datasets, is called data mining. Data mining algorithms are implemented for revealing the covered relationships and hidden patterns in the databases to make accurate predictions about the tasks of interest. Data mining's primary goal is to discover the relevant information for systems called decision support mechanisms after specific methods and processes are performed. Researchers use data mining methods to conduct their studies in many fields such as artificial intelligence, machine learning, database management systems and decision support systems [5]. With rapid technological development, decision support systems have an important place in health sciences [6-8].

The CRISP-DM methodology is a well-established and reliable methodology that provides a systematic approach to designing a data mining project. Cross-Industry Process for Data Mining (CRISP-DM) is an acronym for Cross-Industry Process for Data Mining. The model is an idealized sequence of activities, and some of the tasks can be performed in any order, and it would be appropriate to return to earlier tasks and replicate those acts from time to time. There are several steps to mining data and gaining insights from it. Several procedures were suggested for data mining researchers in order to maximize the likelihood of success in undertaking data mining programs (workflows or basic step-by-step methods) [9-10].

There are many studies in the literature with data mining in epidemic diseases. John et al. [11] aimed to identify the main factors influencing MERS recovery in the KSA (Kingdom of Saudi Arabia). With the demographic and clinical data collected from the website of the KSA Ministry of Health, the main factors affecting recovery MERS disease were determined by machine learning method. In the study, machine learning models such as conditional inference tree support vector machine, J48 and naive Bayesian were modeled to identify important factors. Forna et al. [12] in their study, they used data from the reports of the WHO EBOLA Response Team. In their study with these data, they estimated the case fatality rate (CFR) value and how this value changed according to age and other demographic data with the Boosted regression tree model. Colubri et al. [13] applied multivariate logistic regression to investigate the survival outcomes of 470 patients admitted to five different Ebola treatment units in Liberia and Sierra Leone during 2014–16. They reported that viral load and age were the most important predictors of death. Hu et al. [14] aimed to construct an explainable machine learning (ML) model to predict mortality in influenza patients from clinical/biology data using the real-world severe influenza dataset. The proposed model predicted cumulative feature importance. in the fluid balance domain (0.253), ventilation domain (0.113), laboratory data domain (0.177), demographic and symptom domain (0.140), management domain (0.152) and severity score domain (0.165) respectively. Patel et al. [15] proposed a model for pediatric asthma that predicts disease level and hospital status. Demographic and clinical data obtained from the retrospective analysis of patients from two pediatric emergency departments over 4 years were used in the study. They applied machine learning algorithms to these data. They reported that after patient vital signs and acuity, age and weight, followed by socioeconomic status and weather-related characteristics, were the most important in predicting hospitalization.

After the COVID-19 pandemic was declared, many studies were carried out to combat the virus using data mining and machine learning approaches. Ahamad et al. [16] proposed a method that predicts the COVID-19status (positive or negative) with the XGBoost algorithm with machine learning algorithms (XGBoost, GBM, Random Forest, and SVM). They predicted the COVID-19 situation (positive or negative) with 85% accuracy for age groups and also reported the relative significance values of the chosen important features in the data set. Banerjee et al. [17] proposed a COVID-19 prediction method (positive or-negative) from blood cell count data (monocytes, leukocytes, eosinophils) using machine learning algorithms (Artificial Neural Networks, Random Forest, GLMNET), Logistic Regression). The model they proposed successfully predicted COVID-19 (with AUC 84%) and also predicted where patients (at home - in the normal service) would receive treatment with 94% AUC. In the study conducted in [18], the effect of variables such as temperature, sun exposure time, humidity, wind speed, population, age, density, fertility, Intensive Care Unit, an urban percentage on deaths from COVID-19 was

25

investigated using machine learning algorithms. It has been observed that the relative relationships of temperature, sun exposure and humidity with COVID-19 capture and death are high. In the study conducted in [19], dietary habits on the mortality rate from COVID-19 were investigated with several machine learning algorithms. It has been reported that in countries with a high risk of death, the consumption of animal products, animal fats, milk, sweeteners and meat is higher, and grains are higher in those with a lower risk of death. Kıvrak et al. [20] proposed a method that predicts death status with predictive machine learning using the same data set as the data set used in this study. Random Forest, XGBoost, Knn and deep learning methods were used in the proposed method. In the study, the death status was estimated with 97.5% classification accuracy using the XGBoost algorithm.

In this study, we studied with the data of another pandemic disease, COVID-19. This study aims to predict COVID-19 severity (home, hospital, intensive care) from demographic (age, gender) and clinical data (diabetes, hypertension, Chronic Obstructive Pulmonary Diseases, Cancer, Renal Disease, Cardiovascular Disorders, ACE, ARBs) using the proposed approach integrated with machine learning methods. Another goal of the study is to evaluate the potential impacts of epidemic diseases with data mining and machine learning techniques. We anticipate that the proposed methods that increase the prediction performance in this study can be used in similar data sets and future studies situations.

2. MATERIAL AND METHOD

2.1. CRISP-DM Methodology Implemented in This Study

In this study, CRISP-DM data science management methodology was implemented in predicting the COVID-19 severity based on the demographic and clinical features. The CRISP-DM stages include, Data Understanding, Business Understanding, Data Preparation, Modeling, Deployment and Evaluation. Machine learning algorithms were used in the modeling phase of the methodology [21]. The steps of the CRISP-DM methodology are shown in Figure 1.
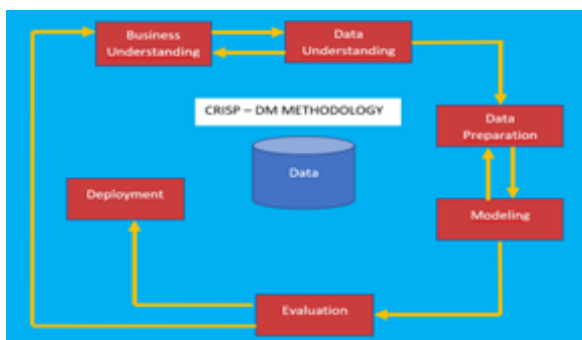
Figure 1. Steps of the CRISP-DM methodology

This study estimates the severity of COVID-19 with demographic and clinical data and evaluates the effect of these data on COVID-19 severity using machine learning techniques. In the reported studies conducted for this purpose, Bravi et al. [23] examined the data presented in their research and concluded that highly accurate COVID-19 severity prediction and the effects on COVID-19 severity could be obtained with data mining techniques. These processes constitute the Business Understanding step, which is the first step of the CRISP-DM methodology. In the Data Understanding step, it was analyzed whether the data was suitable for the targets or not. In the results, it was observed that there was an unbalanced class problem in the data set. However, since the CRISP-DM is a model with possible returns, the next step has been taken. In the Data Preparation phase, the following operations were applied to the data, respectively.

1. Determining the Variable Type and Role (output: COVID-19 Severity; inputs: Factors in Table 1),
2. Processing for missing values (missing value analysis by random forest),
3. Outlier / extreme observation by Local outlier factor (LOF),
4. Data transformation (Z-transform).

For these operations, knowledge discovery process software developed by our team [22] was used in the related stages. In the modelling step, the machine learning methods described in title 3 were applied to the data. In the evaluation step, it was observed that the model did not reach the desired goal according to the metrics described in the title 2.5. Therefore, from this step, the business understanding step has been returned. In the data understanding step, the Random Oversampling process described in title 2.3 was applied to the data. Then the other steps were applied in order. When it comes to the Evaluation step again, the performance of the model was calculated according to the metrics, and it was seen that it reached the desired goal, the model with the highest classification performance was selected, and the next step was taken. In the deployment phase, the recommended method was tested with the validation data set. It has been observed that the model has achieved its purpose. The Diagram of the proposed method is shown Figure 2.

Figure 2. The diagram of proposed method.
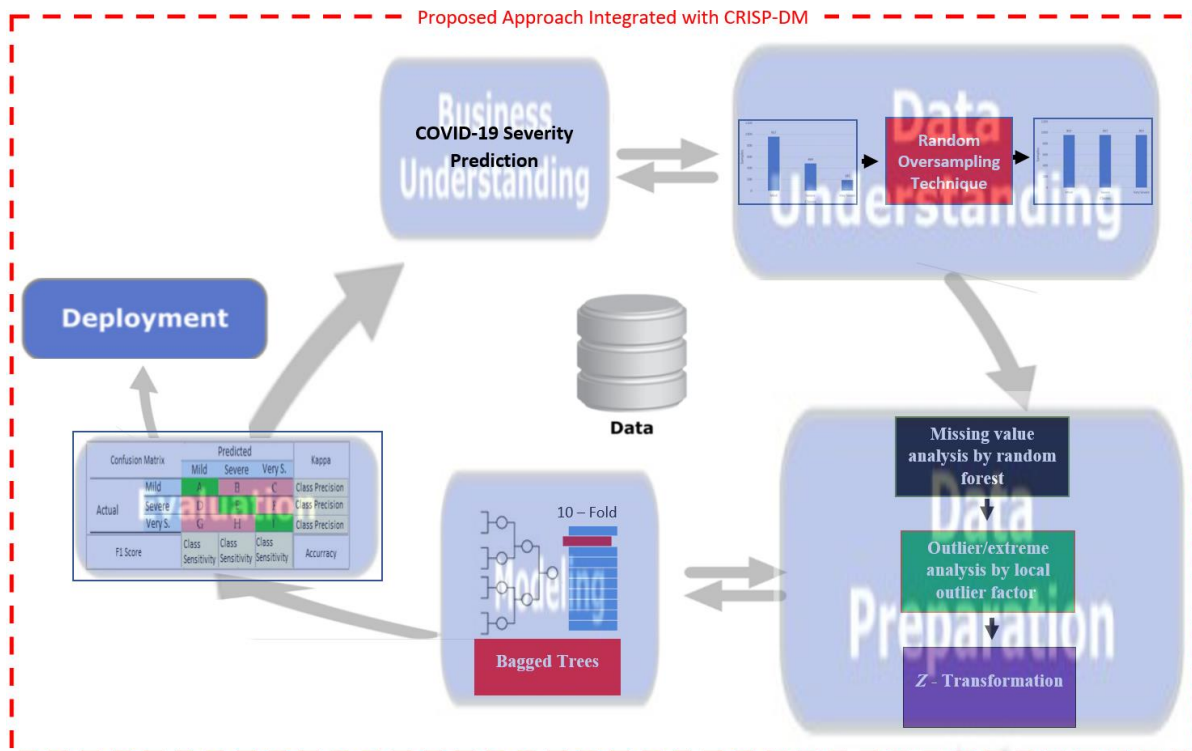
2.2. Dataset

The dataset used in the study was obtained from the survey of Bravi et al. [23]. From this dataset, twelve variables, which are described in Table 1, are used in accordance with the purpose of the study. The data set includes data from 1603 patients suffering from COVID-19-19. The disease information of the patients was obtained from the Italian national drug database. Angiotensin II receptor blockers (ARBs) (C09C and C09D), Angiotensin-converting enzyme (ACE) inhibitors (anatomical therapeutic chemical classes: C09A and C09B) and other anti-diabetic or insulin drugs used by patients in the last two years national drug data set was taken from the base and integrated with the clinical data table. The related data on age, gender, and pre-existing conditions of all subjects were collected via data link with hospital discharge summaries (Italian SDO), which were questioned from the day of diagnosis until January 1, 2015. Two physicians, who are authors of [23], manually analyzed all admission data. The following conditions were included in the analysis: malignant tumours (cancer), major cardiovascular disorders (myocardial infarction, heart failure and stroke [CVD]), renal disease (renal), type II diabetes mellitus (diabetes), and chronic pulmonary obstructive disorders (pneumonia, bronchitis, emphysema [COPD], and asthma)). The variables used in the current study are presented in Table 1. In the data set, the patients were divided into three classes. These classes are described below;

A. Mild (0): asymptomatic infection or mild illness defined as fever or malaise plus at least one of the following: sore throat, myalgia, shortness of breath, dry cough, headache, conjunctivitis, and diarrhoea

B. Severe (1): serious illness requiring hospitalization, not in an intensive care unit;

C. Very Severe (2): A situation that requires admission to an intensive care unit.

Table 1. Variables used in the study

Abbreviation	Explanation	Role
age	Age Information	Input
gender	Gender Information (0=female, 1=male)	Input
Diabetes	Diabetes (1=presence, 0=absence)	Input
hpertension	Hypertension (1=presence, 0=absence)	Input
cvd	Cardiovascular disorders (heart failure, myocardial infarction and stroke-CVD)	Input
copd	Chronic Obstructive Pulmonary Diseases (bronchitis, pneumonia, asthma and emphysema)	Input
cancer	Cancer Diseases (1=presence, 0=absence)	Input
renal	Renal Diseases (1=presence, 0=absence)	Input
ace	Angiotensin-Converting Enzyme (ATC Classes:C09A and C09B)	Input
arbs	Angiotensin II Receptor Blockers (C09C and C09D)	Input
acearbs	ACE or ARBs	Input
COVID-19-Severity	SARS-COV-2 Severity (0=mild, 1=severe, 2=very severe)	Output

27

2.3. Over-sampling Techniques

Unbalanced datasets are a significant challenge in supervised Machine Learning (ML). It is known that the accuracy of many classification algorithms suffers when the data is unbalanced (i.e., when the distribution of instances across classes is severely skewed). Traditional classifiers cause limitations in processing multi-class unbalanced datasets because they are initially designed to handle a balanced distribution.

In this study, Random Oversampling, SMOTE, and ADASYN methods, which are among the three popular oversampling approaches, were applied to the data of interest to solve the class imbalance issue. The data set that was classified with the highest accuracy was the Random Oversampling method.

Random oversampling is a sampling method that increases the number of observations by adding random records to the minority class again. In the first case, the majority class has more data than the minority class, while in the last case, the number of minority class observations increases and becomes equal to the majority class. One of the disadvantages of this method is that it increases the processing time while classifying the target attribute concerning the relevant data. Details of the relevant method are described in the paper of Menardi and Torelli [24].

SMOTE is another method that has been successful in many studies [25 - 26]. Smote technique proposed by Chawla et al. [27] generates artificial data according to the gaps in the property space between the observations of the minority class. Consider k nearest neighbours of a particular observation, each $x_i \in x_{min.class}$ for the subset of $x_{min.class} \in x$. The $n_{min.class-1}$ Euclidean distance between $x_{min.class-1}$ and x_i is calculated. Within this distance $n_{min.class-1}$, the element k of $x_{min.class-\{i\}}$ giving the least distance is the nearest k neighbor. One of these k neighbors is chosen randomly in this process. The vector difference corresponding to the selected neighbor is multiplied by a random number between 0 and 1, and synthetic data are generated. The generation of new data is shown in equation 1.

$$x_{new} = x_i + (\bar{x}_i - x_i) * \delta \qquad (1)$$

It is the observation of minority class $x_i \in x_{min.class}$ in equation 1. $\bar{x}_i$ is one of the closest neighbours found for x_i. δ is a random number between 0 and 1. Synthetic data x_{new} derived in this equation are on a line between x_i and $\bar{x}$. If the sample is created somewhere near rather than above the line, the ADASYN method [28], a particular version of SMOTE, is applied to relevant data.

2.4. Machine Learning Methods for Modeling

Six machine learning methods that stand out in the modelling phase of the study were introduced under subheadings.

2.4.1. Random forest

Random Forest is a classifier developed by Breiman [29] and makes modelling with many decision trees it creates: the ensemble of decision trees. The bootstrap sampling method divides the data set into subsets. It trains each tree that makes up the ensemble with these subsets. Random Forest classifier uses the classification and regression trees (CART) method to generate trees. One of the evaluation criteria of the Random Forest method is the GINI index. Each decision tree that forms the ensemble structure uses a classifier. A prediction is obtained from each classifier, and these predictions are called votes. The majority vote estimates the group, which reduces the error rate and bias in estimates. Random Forest classifiers are fast working classifiers besides being resistant to over-fitting problems. The Random Forest classifier, which is resistant to lost data, can also make a robust classification in missing data. The process steps of the Random Forest classifier are shown in Figure 3.
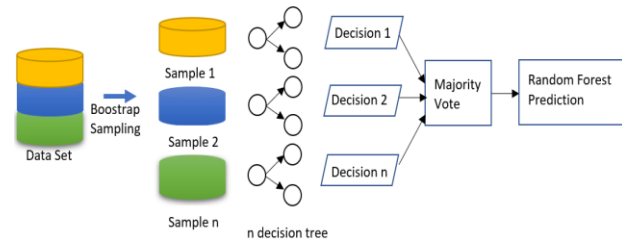
Figure 3. Steps of Random Forest Classifier

2.4.2. Extreme gradient boosting (XGBoost)

Extreme Gradient Boosting (XGBoost) has been proposed by Chen and Guestrin [30] for classification and regression problems. Improved implementation of the Gradient Boosting Trees (GBT) algorithm is designed for speed and performance. The algorithm has been strengthened by adding new trees to correct the trees' errors in the GBT algorithm. XGBoost uses an ensemble of K classification and regression trees (CARTs), each of which has K_E^i nodes (i refers to the numbers 1 to K). The final prediction is the sum of the prediction scores for each tree. The advantages of the XGBoost algorithm over the GBT algorithm are that overfitting can be avoided using both Lasso and Ridge regularization. The hyperparameters of the XGBoost model are the number of segments, maximum depth, and learning speed determined by the grid search optimization algorithm.

2.4.3. Support vector machines

SVM is a machine learning model based on the supervised learning model [31]. The primary purpose of SVM algorithms is to find an optimal hyperplane for classifying new data points. Linear SVM, as shown in Figure 4, creates hyperplanes using the closest training data points of each class. SVM draws a line to separate the data in the plane. It aims at having the maximum distance from the data of the two categories. Besides linear classification, SVMs are also useful in nonlinear

28

classification problems with kernel functions. Many kernel functions such as Radial Basis Function (RBF) kernel, polynomial kernel, and sigmoid kernel are used for the SVM classifier. Also, SVMs can be used in binary and multi-class classifications. For this purpose, many SVM classifier types such as multi-class SVM, radial SVM, and least square SVM have been shown to increase this classifier's ability to distinguish linear and nonlinear data [32].

Figure 4. Diagram of support vector machines

2.4.4. Bagged classification and regression trees (Bagged CART)

CART is a popular machine learning method. Since it is a non-parametric method, it does not depend on the type of distribution of the data and develops binary trees. Breiman [33] introduced bagging used in various classification and regression techniques to improve predictions by reducing the va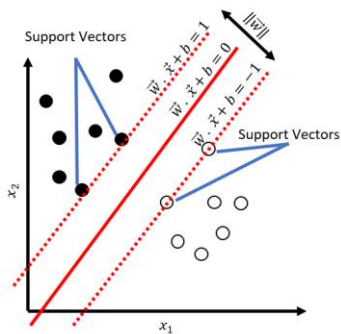riance associated with the prediction. Rather than a weighted averaging method, bagging uses simple averaging of results to improve estimates. Models with an unstable classification process can be packaged for better estimates [34].

2.5. Performance Metrics

In order to evaluate the accuracy of the models, a 10-fold cross-validation method was implemented in the performance evaluation of all classifier models. K-Fold Cross Validation is one way to split the dataset into appropriate parts for evaluating and training the classification models. K-fold cross-validation divides the data into equal portions according to a specified number of k, allowing each component to be used for both training and testing. In 10-fold cross-validation, related models are trained and tested ten different times, and then the average of performance metrics (i.e., accuracy, precision, etc.) is given at the end of the process [35]. Model performances were calculated based on accuracy, precision, sensitivity, specificity, classification error, and kappa metrics [36].

3. RESULTS

First of all, whether there is missing data in the data set was analyzed by the random forest assignment method. The missing data in the data set was completed with this method. Then, whether there were extreme and outlier values in the data set was examined using the local outlier factor (LOF) method. It was determined that there was no outlier in the dataset. Z transformation method was applied to the quantitative variables in the dataset. Table 2 shows the statistical analysis results by variables.

29

Table 2. Baseline characteristics of the sample

Variables	Samples	Mild	Severe	Very Severe
n	1603	957	454	192
Mean age in years (X̄±SD)	58.0±20.9	50.4± 20.2	66.4±16.9	76.2±12.9
Male gender (Count (%))	758 (47.3)	407 (53.7)	241 (31.8)	110 (14.5)
Diabetes (Count (%))	194 (12.1)	65 (34)	75 (37.7)	54 (28.3)
COPD (Count (%))	97 (6.0)	28 (28.9)	42(43.3)	27 (27.8)
Cancer (Count (%))	122 (7.6)	49 (40.2)	46 (37.7)	27 (22.1)
CVD (Count (%))	258 (16.1)	66 (25.6)	122 (47.3)	70 (27.1)
Renal Disease (Count (%))	86 (5.4)	23 (26.7)	40 (46.6)	23 (26.7)
Hypertension (Count (%))	543 (33.9)	207 (38.1)	207 (38.1)	129 (23.6)
ACE inhibitors (Count (%))	251 (15.7)	107 (42.6)	88 (35.1)	56 (22.3)
ARBs (Count (%))	228 (14.2)	86 (37.7)	90 (39.5)	52 (22.8)
ACE and ARBs (Count (%))	450 (28)	183(40.6)	163 (36.2)	104 (23.1)

As a result of the statistical analyses conducted on the data set, it was determined that there was a class imbalance problem in the data set. Classification performances were examined by applying oversampling and undersampling methods to the related data to solve the imbalances between classes. Table 3 shows the performance of random forest classifiers on data sets.

Results obtained from dataset balancing studies are shown in Table 3. According to these results, it was decided to use Random Oversampling method, one of the Oversampling methods, to balance the data set.

After the data set was balanced, the modelling phase was started. Many models have been tested in the modelling phase. Four models, Random Forest, XGBoost, CART and SVM, were constructed for the prediction. The classification accuracy rates of these models are given in Table 4.

The hyperparameter values of the model developed with Random Forest, Bagged CART and XGBoost model were calculated with the grid search optimization algorithm.

Table 3. Random Forest Classification accuracy of different datasets that output of oversampling and undersampling algorithms (z transform is applied to the datasets)

Data Set	Training Data Accuracy (%)	Testing Data Accuracy (%)
Original	82.4	74.7
SMOTE (Oversampling)	85.7	76.8
ADASYN (Oversampling)	84.3	74.0
Borderline SMOTE (Oversampling) [37]	85.2	77.6
SVM SMOTE (Oversampling)	85.4	79.8
SMOTE NC (Oversampling)	80.8	77.3
Random Oversampling	**87.5**	**83.7**
Near Miss (Undersampling) [38]	87,3	74,7
Condensed Nearest Neighbour (Undersampling) [39]	87.3	74.4
Random Undersampling [40]	87.3	74.7

Table 4. Baseline characteristics of the sample

Model	Balanced Accuracy	Accuracy	Precision	Sensitivity	Specificity	F1 Score	Kappa
Bagged CART	**84.7%**	**75.6%**	**90.1%**	**67.0%**	**69.6%**	**71.5%**	**63.4%**
Random Forest	83.5%	74.3%	91.1%	67.5%	64.4%	68.3%	61.5%
XGBoost	82.6%	72.8%	87.4%	67.0%	63.9%	65.6%	59.2%
SVM	80.9%	69.1%	83.2%	67.0%	57.1%	62.4%	53.7%

According to the performance metrics of the models in Table 4, Bagged CART classification algorithm gave the most successful result. Random Forest, XGBoost and SVM are listed after Bagged CART. In kappa statistics that measure statistical fit reliability, Bagged CART and Random Forest approaches represent substantial fit with values of 0.63 and 0.61, described the moderate fit with the XG boost algorithm (0.59) and SVM (0.53) values.

Figure 5 shows the pseudo-codes of the Bagged CART algorithm that gives the best result in predicting COVID-19 severity based on demographic / clinical factors.

Figure 5. Pseudo code of the Bagged CART algorithm

Table 5 shows the importance levels of variables related to COVID-19 severity in SARS-COV-2 patients in bagged CART, XGBoost and random forest modelling.

Bagged CART algorithm calculated the relative importance of variables as follows, respectively. 1. age (100 - 62.41%), 2. cvd (15.84 - 9.88%), 3. hypertension (12.07 - 7.53%), 4. diabetes (9.6- 5.99%), 5. ace arbs (6.80 - 4.24%), 6. Gender (5.52 – 3.44%), 7 arbs (3.15 – 1.96%), 8. ace (2.63 – 1.63%), 9. cancer (2.49 – 1.55%), 10. copd (2.11 – 1.31%) , 11. renal (0 – 0%).

XG BOOST algorithm calculated the relative importance of variables as follows, respectively. 1. age (100 – 80.45%), 2. gender (5.69 – 4.58%), 3.cvd (4.53 – 3.64%), 4. hypertension (4.49 – 3.61), 5. diabetes (4.17 – 3.35%) ,6. acearbs (2.44 – 1.96%), 7. cancer (1.69 – 1.36%), 8.ace (1.06 – 1.07%) ,9. copd (0.10 – 0.11%) ,10. arbs (0.09 – 0.10%) 11. renal (0.0 - 0.0%).

Random Forest classifier calculated the relative importance of variables as fallows, respectively. 1.age (100- 76.15%), 2. gender (7.63- 5.79%), 3. cvd (5.78- 4.41%), 4. diabetes (5.45- 4.16%), 5. hypertension (4.34 – 3.31%), 6. cancer (3.43 – 2.61%),7. copd (1.81 – 1.38%), 8. renal (1.73 – 1.32%), 9. ace (0.78 – 0.60%), 10. arbs (0.35 – 0.27%),11. acearbs (0.0 – 0.0%)

Table 5. Variable importance values for the Bagged CART, XG Boost and Random Forest Algorithms.

Variable	Bagged CART Relative Importance	%	XG BOOST Relative Importance	%	Random Forest Relative Importance	%
age	**100**	**62.41**	**100**	**80.45**	**100**	**76.15**
cvd	**15.84**	**9.88**	**4,53**	**3.64**	**5.78**	**4.41**
hypertension	**12.07**	**7.53**	**4,49**	**3.61**	4.34	3.31
diabetes	**9.60**	**5.99**	4,17	3.35	**5.45**	**4.16**
acearbs	6.80	4.24	2.44	1.96	0.00	0.00
gender	5.52	3.44	**5.69**	**4.58**	**7.63**	**5.79**
arbs	3.15	1.96	0.09	0.10	0.35	0.27
ace	2.63	1.63	1.06	1.07	0.78	0.60
cancer	2.49	1.55	1.69	1.36	3.43	2.61
copd	2.11	1.31	0.10	0.11	1.81	1.38
renal	0.00	0.00	0.00	0.00	1.73	1.32

According to the confusion matrix specified in Table 6, the Bagged CART algorithm's true positive rate is 75.33%, while the true negative rate is 86.29%. While the true positive rate of the random forest algorithm is 74.22%, the true negative rate is 86,02%. While the true positive rate of the XG Boost algorithm is 72.54%, the true negative rate is 84.79%. The true positive rate of the

SVM algorithm is 69.70%, while the true negative rate is 82.28%.

The graphic representation of the confusion matrix for the constructed models is given in Figure 6.

Table 6. Confusion matrix of the models

| Bagged CART	True Mild	True Severe	True Very Severe	Class Precision
Mild	128	42	9	71.508%
Severe	50	133	10	68.912%
Very Severe	13	16	172	85.572%
Class Recall	67.016%	69.634%	90.052%	
RANDOM FOREST				
Mild	129	48	12	68.254%
Severe	33	123	5	76.398%
Very Severe	29	20	174	78.027%
Class Recall	67.539%	64.398%	91.099%	
XG BOOST				
Mild	128	53	14	65.641%
Severe	44	122	10	69.318%
Very Severe	19	16	167	82.673%
Class Recall	67.016%	63.814%	87.435%	
SVM				
Mild	128	52	25	62.439%
Severe	28	109	7	75.694%
Very Severe	35	30	159	70.982%
Class Recall	67.016%	57.068%	83.246%	
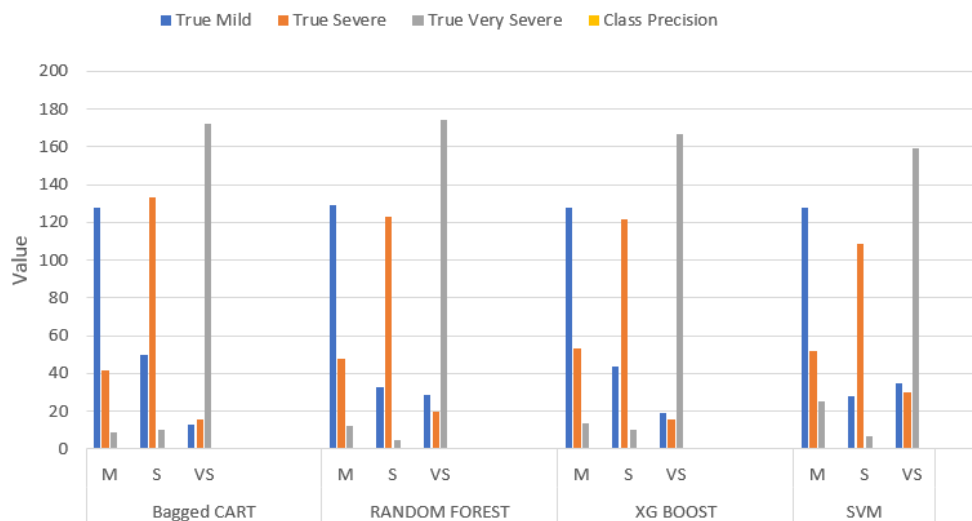
Figure 6. The graphical representation of the confusion matrix for the models.

4. DISCUSSION AND CONCLUSION

As epidemics increase, the occupancy rates of emergency and intensive care units generally increase, and resources become limited. These situations force health managers and doctors to make quick and accurate decisions. Doctors need decision support systems to identify their patients at risk. At this point, data mining and machine learning algorithms come into play. Diseases often arise not from a linear interaction between most specific factors, but from nonlinear interactions between observable determinants (genetic, biological, clinical, demographic, etc.). This creates the application areas of machine learning algorithms. The most important step in traditional machine learning algorithms is the selection of features to enter the model. The relative importance of each of the features included in the model on the course of the disease can be determined by machine learning algorithms. As the number of infected patients increases in an epidemic, information about the disease increases. With the developing technology, both demographic and past clinical data of individuals living in a society are recorded in databases. With these data, the effect of this disease on an individual who has had an epidemic disease can also be recorded. With these data, predictions can be made in another region that is just at the beginning of the epidemic. Outbreak management is not just about estimating the number or condition of patients. The duration and amount of use of medical equipment (respirators, ventilators, etc.) to be used during the epidemic can also be predicted by machine learning algorithms. In order for machine learning algorithms to give accurate results, they need to access sufficient data that is similar to the data expected in the clinical scenario. In some algorithms, the model makes thousands of parameter updates while learning. As the number of parameters to be updated increases, the model needs more training data. In order for machine learning-based systems and software to be used correctly in medical decision making, health institutions need to

Tr. Doğa ve Fen Derg. Cilt 11, Sayı 3, Sayfa 24-34, 2022

Tr. J. Nature Sci. Volume 11, Issue 3, Page 24-34, 2022

store their medical data quickly and accurately by labeling, and make the data public.

The unbalanced dataset is a common problem in healthcare. In the classification of medical data, the number of healthy patients is generally higher than that of unhealthy patients. This situation causes at least one of the classes to be in the minority. It is challenging to train classifiers on unbalanced data because they become biased against a range of classes, resulting in a decrease in classifier performance. Collecting sufficient and equal numbers of data, especially in disease classification problems that occur suddenly, such as COVID-19, will cause both labour and time loss. Many studies with COVID-19 have sought a solution to the unbalanced data set problem. In [25], the authors applied the outlier-SMOTE Oversampling algorithm to Covid-19 data. It has been reported that the performance of the algorithm on the COVID-19 dataset is more successful than the traditional SMOTE method. Yavaş et al. [41] proposed a technique that detects COVID-19 from laboratory test results. In the study, they proposed a technique using SMOTE and Artificial Neural Networks model. At [42], researchers compared the ICU admission rates of hospitalized mild/moderate COVID-19 patients. The authors applied a SMOTE and Bootstrap resampling approach to their data sets and COVID-19 data. In their study, Rohila et al. [43] utilized the random oversampling algorithm while detecting COVID-19 from lung computed tomography images. They achieved 94.9% accuracy with the deep learning-based ReCOV-101 method they suggested.

In this study, the estimation of the severity of the disease and the determination of the relative importance of the disease factors in the treatment of epidemics with machine learning were carried out. The COVID-19 dataset, which is the dataset of the last pandemic, was used as the dataset. A model that predicts COVID-19 severity from demographic and clinical data is proposed. The research was carried out by following the CRISP-DM steps, one of the data mining process models. Within the study's scope, the problem of unbalanced data, one of the main issues of machine learning, is discussed. After the data set is balanced, algorithms such as Bagged CART, XGBoost, Random Forest have been tested. Algorithms were evaluated with performance metrics. THE bagged CART algorithm has achieved the highest performance. Besides, the relative importance of the features has been analyzed within the scope of the study. The variables that determine the COVID-19-19 severity are listed relatively. With the method proposed within the study, health-makers can estimate the severity of the disease and take early precautions on issues such as hospital capacity, intensive care capacity, and personnel needs. People with chronic illnesses or their relatives can take more radical measures against the disease.

Epidemics have emerged frequently in recent years. With the developing technology, demographic and clinical data of individuals are stored in databases. With these data, before the epidemic comes to a region, the people who will suffer from the disease and the severity of the disease can be predicted by machine learning methods. In addition, the importance of the factors that cause the disease can be determined by machine learning methods. Unbalanced data problem is frequently experienced in medical informatics. For example, in a data set that includes cancer and healthy individuals, it can be predicted that the number of cancer patients will be significantly less. In such cases, methods to balance the dataset can be used. Some of the machine learning algorithms update thousands of parameters while updating the network. For this reason, thousands of labeled data may be needed for training. Today, where machine learning methods are used in many fields, it is necessary for doctors and hospital managers to make correctly labeled databases public for developers. In this study, the severity of the disease (at home, hospital, intensive care unit) of people with COVID-19 disease was predicted by machine learning methods from demographic and clinical data obtained from the Italian drug database. In addition, the relative importance of the factors that determine the severity of the disease was calculated. Before a disease comes to a region, it is possible to predict how many people will get the disease in another region and how severely these people will be exposed to the disease, with machine learning methods, with data in a region where it occurs. Doctors and health managers can take the necessary decisions with these estimates. The methods proposed in this study can guide researchers in situations that may arise in the future.

Acknowledgement

REFERENCES

[1] Işık A. SALGIN EKONOMİSİNE GENEL BİR BAKIŞ. Int Anatolia Acad Online J [Internet]. 2021;7(2). Available from: https://dergipark.org.tr/en/download/article-file/1933517

[2] Pandemi [Internet]. 2022. Available from: https://tr.wikipedia.org/wiki/Pandemi

[3] Olgun Eker E. Effects Of Climate Change On Health. 2020;13–23.

[4] Bhadoria P, Gupta G, Agarwal A. Viral pandemics in the past two decades: An overview. J Fam Med Prim Care [Internet]. 2021;10(8):2745. Available from: https://journals.lww.com/jfmpc/Fulltext/2021/10080/Viral_Pandemics_in_the_Past_Two_Decades__An.5.aspx

[5] Ming-Syan Chen, Jiawei Han, Yu PS. Data mining: an overview from a database perspective. IEEE Trans Knowl Data Eng [Internet]. 1996;8(6):866–83. Available from: http://ieeexplore.ieee.org/document/553155/

[6] KARTAL E, BALABAN ME, BAYRAKTAR B. KÜRESEL COVID-19 SALGININININ DÜNYADA VE TÜRKİYE'DE DEĞİŞEN DURUMU VE KÜMELEME ANALİZİ. İstanbul Tıp Fakültesi Derg [Internet]. 2021 Jan 20;84(1). Available from: https://iupress.istanbul.edu.tr/tr/journal/jmed/article/kuresel-covid-19-salgininin-dunyada-ve-turkiyede-degisen-durumu-ve-kumeleme-analizi

[7] Komenda M, Bulhart V, Karolyi M, Jarkovský J, Mužík J, Májek O, et al. Complex Reporting of the COVID-19 Epidemic in the Czech Republic: Use of an Interactive Web-Based App in Practice. J Med Internet Res [Internet]. 2020 May 27;22(5):e19367. Available from: http://www.jmir.org/2020/5/e19367/

[8] Rivai MA. Analysis of Corona Virus spread uses the CRISP-DM as a Framework: Predictive Modelling. Int J Adv Trends Comput Sci Eng [Internet]. 2020 Jun 25;9(3):,2987-2994. Available from: http://www.warse.org/IJATCSE/static/pdf/file/ijatcse76932020.pdf

[9] Utama Id, Sudirman Id. Optımızıng Decısıon Tree Crıterıa To Identıfy The Released Factors Of Covıd-19 Patıents In South Korea. J Theor Appl Inf Technol. 2020;98(16):3305–15.

[10] Jaggia S, Kelly A, Lertwachara K, Chen L. Applying the CRISP-DM Framework for Teaching Business Analytics. Decis Sci J Innov Educ [Internet]. 2020 Oct 21;18(4):612–34. Available from: https://onlinelibrary.wiley.com/doi/10.1111/dsji.12222

[11] John M, Shaiba H. Main factors influencing recovery in MERS Co-V patients using machine learning. J Infect Public Health [Internet]. 2019 Sep;12(5):700–4. Available from: https://linkinghub.elsevier.com/retrieve/pii/S1876034119301297

[12] Forna A, Nouvellet P, Dorigatti I, Donnelly CA. Case Fatality Ratio Estimates for the 2013–2016 West African Ebola Epidemic: Application of Boosted Regression Trees for Imputation. Clin Infect Dis [Internet]. 2020 Jun 10;70(12):2476–83. Available from: https://academic.oup.com/cid/article/70/12/2476/5536742

[13] Colubri A, Hartley MA, Siakor M, Wolfman V, Felix A, Sesay T, et al. Machine-learning Prognostic Models from the 2014–16 Ebola Outbreak: Data-harmonization Challenges, Validation Strategies, and mHealth Applications. EClinicalMedicine. 2019;11:54–64.

[14] Hu C-A, Chen C-M, Fang Y-C, Liang S-J, Wang H-C, Fang W-F, et al. Using a machine learning approach to predict mortality in critically ill influenza patients: a cross-sectional retrospective multicentre study in Taiwan. BMJ Open [Internet]. 2020 Feb 25;10(2):e033898. Available from: https://bmjopen.bmj.com/lookup/doi/10.1136/bmjopen-2019-033898

[15] Patel SJ, Chamberlain DB, Chamberlain JM. A Machine Learning Approach to Predicting Need for Hospitalization for Pediatric Asthma Exacerbation at the Time of Emergency Department Triage. Cloutier R, editor. Acad Emerg Med [Internet]. 2018 Dec 29;25(12):1463–70. Available from: https://onlinelibrary.wiley.com/doi/10.1111/acem.13655

[16] Ahamad MM, Aktar S, Rashed-Al-Mahfuz M, Uddin S, Liò P, Xu H, et al. A machine learning model to identify early stage symptoms of SARS-Cov-2 infected patients. Expert Syst Appl [Internet]. 2020 Dec;160:113661. Available from: https://linkinghub.elsevier.com/retrieve/pii/S0957417420304851

[17] Banerjee A, Ray S, Vorselaars B, Kitson J, Mamalakis M, Weeks S, et al. Use of Machine Learning and Artificial Intelligence to predict SARS-CoV-2 infection from Full Blood Counts in a population. Int Immunopharmacol [Internet]. 2020 Sep;86:106705. Available from: https://linkinghub.elsevier.com/retrieve/pii/S1567576920315770

[18] Malki Z, Atlam E-S, Hassanien AE, Dagnew G, Elhosseini MA, Gad I. Association between weather data and COVID-19 pandemic predicting mortality rate: Machine learning approaches. Chaos, Solitons & Fractals [Internet]. 2020 Sep;138:110137. Available from: https://linkinghub.elsevier.com/retrieve/pii/S0960077920305336

[19] García-Ordás MT, Arias N, Benavides C, García-Olalla O, Benítez-Andrades JA. Evaluation of Country Dietary Habits Using Machine Learning Techniques in Relation to Deaths from COVID-19. Healthcare [Internet]. 2020 Sep 29;8(4):371. Available from: https://www.mdpi.com/2227-9032/8/4/371

[20] Kivrak M, Guldogan E, Colak C. Prediction of death status on the course of treatment in SARS-COV-2 patients with deep learning and machine learning methods. Comput Methods Programs Biomed [Internet]. 2021 Apr;201:105951. Available from: https://linkinghub.elsevier.com/retrieve/pii/S0169260721000250

[21] Schröer C, Kruse F, Gómez JM. A Systematic Literature Review on Applying CRISP-DM Process Model. Procedia Comput Sci [Internet]. 2021;181:526–34. Available from: https://linkinghub.elsevier.com/retrieve/pii/S1877050921002416

[22] Arslan, A. K. & Çolak, C. BKSY: Bilgi Keşfi Süreci Yazılımı [Web-tabanlı yazılım] biostatapps.inonu.edu.tr [Internet]. Available from: http://biostatapps.inonu.edu.tr/BKSY/

[23] Bravi F, Flacco ME, Carradori T, Volta CA, Cosenza G, De Togni A, et al. Predictors of severe or lethal COVID-19, including Angiotensin Converting Enzyme inhibitors and Angiotensin II Receptor Blockers, in a sample of infected Italian citizens. Shimosawa T, editor. PLoS One [Internet]. 2020 Jun 24;15(6):e0235248. Available from: https://dx.plos.org/10.1371/journal.pone.0235248

33

[24] Menardi G, Torelli N. Training and assessing classification rules with imbalanced data. Data Min Knowl Discov [Internet]. 2014 Jan 30;28(1):92–122. Available from: http://link.springer.com/10.1007/s10618-012-0295-5

[25] Turlapati VPK, Prusty MR. Outlier-SMOTE: A refined oversampling technique for improved detection of COVID-19. Intell Med [Internet]. 2020 Dec;3–4:100023. Available from: https://linkinghub.elsevier.com/retrieve/pii/S2666521220300235

[26] Starling JK, Mastrangelo C, Choe Y. Improving Weibull distribution estimation for generalized Type I censored data using modified SMOTE. Reliab Eng Syst Saf [Internet]. 2021 Feb;107505. Available from: https://linkinghub.elsevier.com/retrieve/pii/S0951832021000661

[27] Chawla N V., Bowyer KW, Hall LO, Kegelmeyer WP. SMOTE: Synthetic Minority Over-sampling Technique. 2011 Jun 9; Available from: http://arxiv.org/abs/1106.1813

[28] Haibo He, Yang Bai, Garcia EA, Shutao Li. ADASYN: Adaptive synthetic sampling approach for imbalanced learning. In: 2008 IEEE International Joint Conference on Neural Networks (IEEE World Congress on Computational Intelligence) [Internet]. IEEE; 2008. p. 1322–8. Available from: http://ieeexplore.ieee.org/document/4633969/

[29] Pavlov YL. Random forests. Random For. 2019;1–122.

[30] Chen T, Guestrin C. XGBoost. In: Proceedings of the 22nd ACM SIGKDD International Conference on Knowledge Discovery and Data Mining [Internet]. New York, NY, USA: ACM; 2016. p. 785–94. Available from: https://dl.acm.org/doi/10.1145/2939672.2939785

[31] Weston J, Mukherjee S, Chapelle O, Pontil M, Poggio T, Vapnik V. Feature selection for SVMs. Adv Neural Inf Process Syst. 2001;

[32] Colak C, Colak MC, Ermis N, Erdil N, Ozdemir R. Prediction of cholesterol level in patients with myocardial infarction based on medical data mining methods. Kuwait J Sci [Internet]. 2016;43(Vol. 43 No. 3 (2016): Kuwait Journal of Science):86–90. Available from: https://journalskuwait.org/kjs/index.php/KJS/article/view/875/139

[33] Dd Praagman J. Classification and regression trees. Eur J Oper Res [Internet]. 1985 Jan;19(1):144. Available from: https://linkinghub.elsevier.com/retrieve/pii/0377221785903212

[34] Islam MM, Rahman MJ, Chandra Roy D, Maniruzzaman M. Automated detection and classification of diabetes disease based on Bangladesh demographic and health survey data, 2011 using machine learning approach. Diabetes Metab Syndr Clin Res Rev [Internet]. 2020 May;14(3):217–9. Available from: https://linkinghub.elsevier.com/retrieve/pii/S1871402120300448

[35] Arlot S, Celisse A. A survey of cross-validation procedures for model selection. Stat Surv [Internet]. 2010;4:40–79. Available from: http://projecteuclid.org/euclid.ssu/1268143839

[36] Yaşar Ş, Arslan A, Çolak C, Yoloğlu S. A Developed Interactive Web Application for Statistical Analysis: Statistical Analysis Software. Middle Black Sea J Heal Sci [Internet]. 2020 Aug 31;226–38. Available from: https://dergipark.org.tr/tr/doi/10.19127/mbsjohs.704456

[37] Wang K-J, Adrian AM, Chen K-H, Wang K-M. A hybrid classifier combining Borderline-SMOTE with AIRS algorithm for estimating brain metastasis from lung cancer: A case study in Taiwan. Comput Methods Programs Biomed [Internet]. 2015 Apr;119(2):63–76. Available from: https://linkinghub.elsevier.com/retrieve/pii/S0169260715000577

[38] Koziarski M. Radial-Based Undersampling for imbalanced data classification. Pattern Recognit [Internet]. 2020 Jun;102:107262. Available from: https://linkinghub.elsevier.com/retrieve/pii/S0031320320300674

[39] Zhu Z, Wang Z, Li D, Du W. NearCount: Selecting critical instances based on the cited counts of nearest neighbors. Knowledge-Based Syst [Internet]. 2020 Feb;190:105196. Available from: https://linkinghub.elsevier.com/retrieve/pii/S0950705119305325

[40] Liu B, Tsoumakas G. Dealing with class imbalance in classifier chains via random undersampling. Knowledge-Based Syst [Internet]. 2020 Mar;192:105292. Available from: https://linkinghub.elsevier.com/retrieve/pii/S0950705119305830

[41] Yavaş M, Güran A, Uysal M. Covid-19 Veri Kümesinin SMOTE Tabanlı Örnekleme Yöntemi Uygulanarak Sınıflandırılması. Eur J Sci Technol [Internet]. 2020 Aug 15;258–64. Available from: https://dergipark.org.tr/tr/doi/10.31590/ejosat.779952

[42] Guner R, Hasanoglu I, Kayaaslan B, Aypak A, Akinci E, Bodur H, et al. Comparing ICU admission rates of mild/moderate COVID-19 patients treated with hydroxychloroquine, favipiravir, and hydroxychloroquine plus favipiravir. J Infect Public Health [Internet]. 2021 Mar;14(3):365–70. Available from: https://linkinghub.elsevier.com/retrieve/pii/S1876034120307735

[43] Rohila VS, Gupta N, Kaul A, Sharma DK. Deep Learning Assisted COVID-19 Detection using full CT-scans. Internet of Things [Internet]. 2021 Feb;100377. Available from: https://linkinghub.elsevier.com/retrieve/pii/S2542660521000214

34

Türk Doğa ve Fen Dergisi
Turkish Journal of Nature and Science
www.dergipark.gov.tr/tdfd

Cloneable Jellyfish Search Optimizer Based Task Scheduling in Cloud Environments

Mücahit BÜRKÜK[1], Güngör YILDIRIM[1*]

[1]Firat University, Engineering Faculty, Department of Computer Engineering, Elazig, Türkiye
Mucahit BÜRKÜK ORCID No: 0000-0002-4974-0590
Güngör YILDIRIM ORCID No: 0000-0002-4096-4838

*Corresponding author: gungor.yildirim@firat.edu.tr

Abstract: For cloud environments, task scheduling focusing on the optimal completion time (makespan) is vital. Metaheuristic approaches can be used to produce efficient solutions that will provide important cost savings to both the cloud service provider and the clients. On the other hand, since there is a high probability of getting stuck in local minima in metaheuristic solutions due to the type of problem, it may not always be possible to quickly reach the optimal solution. This study, using a metaheuristic approach, proposes a solution based on the Cloneable Jellyfish Algorithm for optimal task distribution in cloud environments. The unique feature of the proposed algorithm is that it allows dynamic population growth to be carried out in a controlled manner in order not to get stuck in local minima during the exploration phase. In addition, this algorithm, which uses a different cloning mechanism so that similar candidates are not generated in the population growth, has made it possible to achieve the optimal solution in a shorter time. To observe the solution performance, cloud environment simulations created in the Cloudsim simulator have been used. In experiments, the success of the proposed solution compared to classical scheduling algorithms has been proven.

Bulut Sistemlerde Denizanası Arama Optimizasyonu Tabanlı Görev Çizelgeleme

Öz: Bulut ortamlar için optimum tamamlanma süresi (makespan) çözümüne odaklanan görev planlamaları hayati öneme sahiptir. Hem bulut servis sağlayıcı hem de müşteriye ciddi maliyet kazancı sağlayacak çözümlerin üretilmesinde meta-sezgisel yaklaşımlar kullanılabilir. Öte yandan problem tipinden dolayı meta-sezgisel çözümlerde lokal minimumlara takılma olasılığı yüksek olduğundan optimum çözüme hızlıca ulaşmak her zaman mümkün olamayabilir. Meta-sezgisel bir yaklaşım kullanan bu çalışma, bulut ortamlarda optimum görev dağılımı için Klonlanabilir Deniz Anası Algoritması temelli bir çözüm önermektedir. Önerilen algoritmanın özgün özelliği, exploration aşamasında lokal minimumlara takılmamak için dinamik popülasyon artışının kontrollü bir şekilde yapılmasına olanak sağlamasıdır. Ayrıca popülasyon artışında benzer adayların üretilmemesi için farklı bir klonlama mekanizması kullanan bu algoritma, optimum çözüme daha kısa sürede ulaşmayı mümkün kılmıştır. Çözüm performansını gözlemlemek için Cloudsim simülatöründe oluşturulan bulut ortam simülasyonları kullanılmıştır. Farklı senaryolar için yapılan deneylerde, önerilen çözümün klasik scheduling algoritmalarına göre başarısı ispatlanmıştır.

1. INTRODUCTION

Cloud computing technology is the sum of virtualized and scalable resources that allow hosting a large amount of data on the Internet and provide users with a pay-per-use model [1]. Many reasons, such as the development and acceleration of the Internet infrastructure, the spread of IoT (Internet of Things) technology, the rapid growth of big data, and advances in artificial intelligence

studies, have led to the widespread use of cloud technology. Cloud computing allows the users to access various services and resources (CPU, RAM, storage) anytime and anywhere. A cloud system can provide three types of services related to infrastructure, platform, and software. The first service is IaaS (Infrastructure as a Service), which provides infrastructure services such as a storage system and computational resources. The second service is PaaS (Platform as a Service), which allows clients to create their applications on the provided

platform. The third service, on the other hand, is SaaS (Software as a Service), which allows users to use software directly from the cloud instead of on local machines [2]. Cloud service providers must offer resources and services to their clients in a way that does not violate the SLA (Service Level Agreement) and guarantees a certain QoS (Quality of Service). Optimal use of cloud system resources and maintaining performance at the highest level are vital for both service providers and users. Task scheduling is a factor that directly affects cloud system performance and optimal resource utilization. A task or resource scheduling that has not been designed well can lead to an SLA violation, serious loss of revenue, and performance degradation.

One of the most important mechanisms of cloud computing is virtual machines (VMs). VMs are created from resources on the cloud system in accordance with the needs of clients. Depending on the volume of work, the number of clients' VMs and their features may vary. Clients pay a certain fee to the cloud provider based on the characteristics of these VMs and the duration of their use. Incorrect scheduling of tasks that need to be run on VMs leads to an increase in task completion time (makespan) and, naturally, to an increase in costs for the client. This increase in makespan also indirectly negatively affects the energy consumption and maintenance and repair costs of the cloud provider. Therefore, the use of a good task scheduling algorithm on cloud systems is mandatory for both the customer and the cloud provider [4]. Task scheduling is an NP-hard problem [1]. The use of metaheuristic algorithms instead of deterministic solutions is often preferred in solving such problems in terms of performance [5]. But on the other hand, due to the type of problem, the probability of the fact that random search-based metaheuristic algorithms are stuck in local minima is also high. This probability can further increase as the number of tasks and VMs increases. Therefore, it is necessary that the used metaheuristic algorithms use mechanisms that will overcome this problem. For this problem, this study proposes a solution based on Jellyfish Search Optimizer (JSO) [8], which is an up-to-date metaheuristic algorithm that uses a different approach mechanism. The most unique aspect of the proposed method is that it gets rid of local minima more quickly and allows dynamic population growth with a different similarity control. In this way, a more efficient exploration process is realized in the search space. The performance of the proposed method was proven by trying comparatively for different scenarios in the CloudSim simulator.

Other parts of this article are as follows; In Part II, task scheduling strategies in cloud computing systems and similar studies found in the literature are given. Part III contains the details of the used methodology and JSO algorithm. The experiments and comparative evaluations are given in Part IV, and the conclusion is presented in Part V.

2. BACKGROUND AND RELATED WORKS

In cloud systems, virtual machines (VMs) with different properties can be created on physical servers using virtualization techniques. VMs can collaborate to perform a specific task, as well as work independently of each other. Cloud service providers (CSPs) have broker services that conveniently distribute incoming tasks to VMs. Such services can also be developed by the client and run on a separate VM in the cloud. The Task Scheduling algorithm used in both cases is the most important factor that determines performance. Task scheduling has three main mechanisms: resource finding, resource determination, and task allocation [7]. The availability of resources requires that shareable resources can be questionable. Resource determination makes the selection of the most optimal resources depending on the characteristics of the tasks at the end of the resource query. Task allocation, on the other hand, sends the relevant tasks to the determined resources and performs their follow-up. The cloud system has a heterogeneous structure in terms of both resource and customer diversity. This naturally leads to the emergence of different goals in Task Scheduling optimization. Among these goals, the completion time (makespan), energy consumption, and cost stand out. Given this diversity, the strategy to be used in task scheduling should be chosen correctly. In the task scheduling proposed in the literature, strategies can be classified as shown in Figure.1 [11].
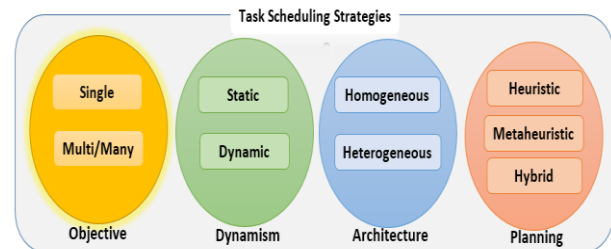
Figure.1 Task scheduling strategies

In the task scheduling strategy by the goal, one of the goals such as makespan, cost, energy consumption, or more than one that contradicts each other can be taken into account. The cloud infrastructure and the incoming task type also determine whether the strategy to be used will be static or dynamic. Static scheduling can be performed in fixed source cloud systems where there is not much workload change. However, since today's cloud technologies have a variable structure, dynamic strategies are usually preferred. This also applies to the heterogeneous structure of the CSP architecture. In terms of planning, heuristic techniques are often used for static scheduling. Metaheuristic algorithms that use heuristics and random search mechanisms together can achieve to create effective solutions for dynamic systems [6, 10, 13]. In this study, the proposed metaheuristic solution was developed for a single objective purpose in a heterogeneous and dynamic CSP system.

Because metaheuristic algorithms contain randomness, initial values are important. In [3], the authors presented a Discrete Symbiotic Organism Search (DSOS)

algorithm, which is a metaheuristic algorithm for the optimal scheduling of tasks in cloud resources. In [9], for the particle swarm optimization (PSO), which is a well-known metaheuristic algorithm, the initial values were found using the heuristic LJFP and MCT algorithms. Thus, success was achieved in makespan and total energy consumption. In [6], makespan optimization conducted with the grey wolf optimizer (GWO) that used the hunting mechanism, CPU, memory, and resource bandwidth parameters were taken into account together. In another study conducted for the purpose of makespan [12], the authors used the Electromagnetism Metaheuristic Algorithm (EMA) and monitored their VM performance comparatively. In [18], the authors used a multi-purpose Task scheduling strategy. For this, they proposed the ICW method that used the metaheuristic whale optimization algorithm (WOA). In [13], transaction cost and makespan optimization were performed with the developed space-shared genetic algorithm, and the superiority of the proposed solution over competitive planning algorithms was proved. Solutions based on ant colony optimization (ACO), which is another well-known metaheuristic algorithm, have also been introduced in the literature. An ACO-based solution taking into account the load balance and the purposes of the makespan was presented in [14]. In [15], a hybrid task scheduling method using the ACO and PSO algorithms was proposed. Another hybrid solution based on ACO was also introduced in [16]. In this study, the authors first ran the GA algorithm to determine the initial values of ACO; thus, they achieved a better execution time. A hybrid solution that performs more metaheuristic algorithm execution in it was proposed by [19]. In this study, GA, ACO, and PSO algorithms were run in the developed framework to obtain the optimum makespan value. In [21], the authors proposed a hyper-heuristic scheduling algorithm by integrating GA, ACO, and PSO into a single framework to reduce the makespan in the cloud. In [22], a minimum makespan task scheduling framework called MMSF and a minimum makespan task scheduling algorithm called MMA were proposed.

In general, in the Metaheuristic Task Scheduling solutions proposed in the literature, it has not been focused on overcoming the emerging local minima problems in a shorter period of time. Unlike the examples in the literature, this study aimed to reach the existing solutions faster with the state-controlled dynamic population variability.

3. MATERIAL AND METHOD

In Task Scheduling, the task scheduler assigns the tasks waiting in the queue to the appropriate VMs according to the output of the JSO algorithm. The used algorithm makes these assignments based on the calculations it makes for certain objective or objectives. In this study, Task Scheduling was performed according to the makespan objective. Makespan is the completion time of a certain number of tasks on the VMs to which they are assigned. The goal of Makespan optimization is to reduce this time to a minimum. As an example, let's

assume that 7 different tasks are assigned to 3 different VMs as in Figure.2. In this case, the makespan value will be equal to the task completion time of the second VM.
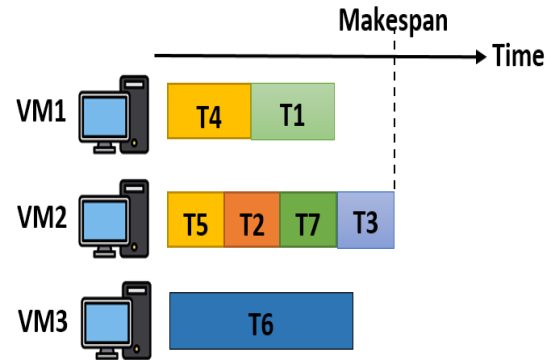

Figure.2 Makespan definition

The JSO tries to reduce makespan to a minimum by trying different assignment variations. In the creation of these variations, calculations made based on the characteristics of tasks and VMs are taken into account. In these calculations, the number of commands of tasks is expressed as a Million Instructions (MI), and the calculation capabilities of VMs are expressed as the number of Million Instructions Per Second (MIPS). Let $T_m = \{MI_0, MI_1, ..., MI_K\}$ be considered as the tasks assigned to the mth virtual machine. In this case, the execution time of the kth task on the mth virtual machine can be calculated using Eq.1. The total execution time for all tasks is found using Eq.2.

$$ET_{km} = \frac{MI_k}{MIPS_m} \tag{1}$$

$$TET_m = \sum_{k=0}^{K} ET_{km} \tag{2}$$

Considering all VMs, the maximum total execution time determined based on the calculation made with Eq.3 will also give the makespan value. The fitness function of the proposed method is to obtain the minimum makespan value, as expressed in Eq.3.

$$Makepsan = max \{TET_m\}, m \in \{VM_1, VM_2, ...\} \tag{3}$$
$$F^{obj} = min \{Makespan\} \tag{4}$$

3.1. Jellyfish Search Optimizer (JSO)

In the proposed method, JSO, the current metaheuristic algorithm of recent years, was used to calculate the optimal Makespan value. JSO is a meta-heuristic optimization algorithm inspired by the movements of jellyfish in the ocean while satisfying their basic needs, such as finding food, and how they affect other individuals in the swarm [8]. In any case, a jellyfish wants to move to a place where the amount of food is more ($the\ best\ F^{obj}$). The amount of food in places visited by jellyfish can vary. In this case, the most favorable location in terms of food is found by comparing the amounts of food. Jellyfish perform two types of movements. These are the movement with the ocean current and the movement within the herd. The transition between these movements is controlled by a

time control mechanism. Since the ocean current contains a lot of nutrients, it always attracts jellyfish. In JSO, the ocean current ($\overrightarrow{OC}$) is found based on the average locations of all candidate solutions (Jellyfish) and the best fitness value. Eq.5 shows the mathematical model of the movement with the ocean current. Here, n_{pop} is the total population and X^* is the jellyfish with the best fitness value so far. In this equation, the random number (r_1) and the hyper-parameter (β) also represent the e_c attractiveness factor of the current ($e_c = \beta \times r_1$, $r \in [0,1]$).

$$\overrightarrow{OC} = \frac{1}{n_{pop}} \sum \overrightarrow{OC_i} = \frac{1}{n_{pop}} \sum (X^* - e_c X_i) = X^* - \beta \times r_1 \times \frac{\sum X_i}{n_{pop}} \tag{5}$$

In the case of movement relative to the ocean current, the next locations of jellyfish ($X_i(t+1)$) are found by using Eq.6. where $X_i(t)$ represents the current state of the ith jellyfish and r_2 represents the number of uniform random.

$$X_i(t+1) = X_i(t) + r_2 \times \overrightarrow{OC} \tag{6}$$

Movements of jellyfish in the swarm are of two types: passive (Type A) and active (Type B) [17]. Initially, most jellyfish exhibit Type A movement while forming a swarm. Over time, Type B movement is exhibited more. In Type A, the jellyfish performs a random movement around its location. The model for this type of movement is given in Eq.7. where γ represents the movement coefficient, and U_b and L_b represent the upper-lower bounds of the search space, respectively.

$$X_i(t+1) = X_i(t) + \gamma \times rand(0,1) \times (U_b - L_b) \tag{7}$$

Type B movement occurs according to the state of the food resources of the ith jellyfish as well as jth jellyfish which is randomly selected in the swarm. The movement will be towards the jellyfish, where there is more food. The jellyfish performs a random movement in the designated direction. In Type B, the direction of movement and the new location of the jellyfish are calculated by Eq.8 and 9. where $\vec{D}$ is the direction of movement and r_3 is the uniform random value.

$$\vec{D} = \begin{cases} X_j(t) - X_i(t) & if \quad f(X_i) \geq f(X_j) \\ X_i(t) - X_j(t) & if \quad f(X_i < f(X_j) \end{cases} \tag{8}$$

$$X_i(t+1) = X_i(t) + r_3 \vec{D} \tag{9}$$

The movements of jellyfish in the swarm initially begin with type A, and over time they switch to type B. In addition, the movement of the ocean current is also taking place over time. In JSO, a time control mechanism is used for all movements of jellyfish. This control mechanism is modelled by Eq.10. In this model, t is the number of iterations, r_4 is the uniform random coefficient, and $max_{iteration}$ is the maximum number of iterations. The result of the control mechanism is compared with a threshold value (usually 0.5). If the

value of the control function is below the threshold value, movement occurs within the swarm, and if it is above the threshold value, movement occurs based on the ocean current. For the movement inside the swarm, the value of $1 - c(t)$ is taken into account. For this purpose, a random value is generated with a uniform generator and this value is compared with $1 - c(t)$. If the generated random value is higher, the type A movement occurs, if not, the type B movement occurs.

$$c(t) = \left| \left(1 - \frac{t}{max_{iteration}} \right) \times (2 \times r_4 - 1) \right| \tag{10}$$

In the fitness tests conducted to determine the coefficients used in the JSO, the effect of the ocean current and the effects of movement types on the results were also observed. As a result of these tests, it was found that the most optimal solutions were obtained for $\beta = 3$ and $\gamma = 0.1$ [8].

3.2. Cloneable JSO and The Proposed Task Scheduling

Similar to other metaheuristic algorithms, the JSO algorithm also has the risk of getting stuck to the local minima in Task Scheduling problems. To overcome this risk, techniques such as increasing iteration or population number or using different random generator functions can be used. High population and iteration numbers are accompanied by time costs. The technique proposed in this study suggests that the optimum value can be reached in a shorter time by increasing the population growth heuristically and dynamically. Accordingly, if there is no change in the best value during a given number of iteration, the current population is increased at a certain rate at run-time. In fact, it was inspired by the biological characteristics of jellyfish for this feature. In nature, jellyfish are creatures that have the ability to clone themselves in a controlled way. However, the critical point here is the positional values of new population candidates (clones). Adding candidates similar to existing candidates to the population will reduce the likelihood of getting out of the local minimum. For a more effective exploration process, the fact that new individuals differ from existing ones is one of the main points of the proposed Cloneable JSO (C-JSO) algorithm [23]. The high computational cost of the function to be used for similarity checks of new candidates will also increase the time cost of the algorithm, especially in high populations. Therefore, it is necessary to use a fast and effective similarity check function. C-JSO uses a fast and effective similarity function to prevent the generation of similar candidates. Task Scheduling, which is used in doing this, benefits from the discrete nature of the problem solving. In the Task Scheduling algorithm, tasks and VMs are usually encoded with integers. Figure.3 shows an example encoding for two candidate solutions (X_i and X_j). Candidate attributes indicate a task. Each attribute value, on the other hand, is an integer code showing the current VMs. The similarity criterion in Task Scheduling is the number of times the same Tasks are assigned to the same VMs in the current and new candidate. C-JSO calculates

38

the similarity ratio by performing a match comparison for each task. In this calculation, the similarity is calculated by the ratio of the total number of zeros, obtained as a result of taking the differences in attributes of the two candidates, to the total number of Tasks. This calculation is expressed in Eq.11 and 12. Accordingly, the similarity ratio of the two candidates in Figure.3 is 50%.

Figure.3 A sample similarity control for task assignment [23]

$$Df = X_i - X_j \tag{11}$$
$$Similarity = \frac{the\ number\ of\ zeroes\ in\ Df}{the\ number\ of\ tasks} \tag{12}$$

In C-JSO, population candidates (jellyfish) have a VM assignment vector as large as the total number of Tasks. Initially, random integer assignments representing VMs are made to these vectors for each candidate. Then the fitness value of each candidate is calculated by Eq.1-4. The candidate with the best fitness value will also represent the ocean current. Throughout the iterations, depending on the value of the time control function, each jellyfish determines its new location within the swarm or relative to the ocean current. In C-JSO, there is a binary variable (φ) that tracks the best value change. If there is no change in the best value in a predefined number (I) at the end of the iteration, this variable gets a value of true. In this case, the current population is increased by a rate of a predefined value (θ). When increasing the population, the similarity of new candidates is calculated by Eq.11-12. As a result of the calculation, candidates below the predefined similarity threshold (ε) are added to the population and the basic steps are repeated. C-JSO's pseudo-code showing these steps is given in Algorithm-1.

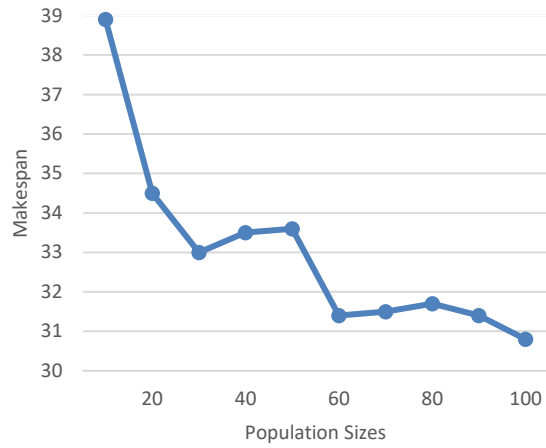**Algorithm 1**. The pseudo code of C-JSO based task scheduling [23]
Initialize the population
Specify $\beta, \gamma, \theta, \varepsilon, I$ and $\varphi \to 0$
While (itr < max iteration)
    Find the fitness values of all candidates by Eq.1-4
    Run time control function by Eq.10
    If c(t) < 0.5 **then** follow $\overrightarrow{OC}$
    Else if 1- c(t) < rand (0,1) **then** make A-type move
    Else make B-type movement
    If there is no change in I iterations ($\varphi \to 1$) **then** increase the population by θ% considering Equation 11-12
    Else $\varphi \to 0$
End while
Return the best solution

4. RESULTS AND DISCUSSION

The success of the C-JSO-based Task Scheduling method was tested in the CloudSim simulator [20] for different Cloud scenarios. The success of the C-JSO was shown in comparison with the results of the default CloudSim Task Scheduling algorithm, the classic JSO, and the ACO algorithm. For simulations, a data center was created primarily in CloudSim. This data center has two main physical servers, each has 16 GB of ram, 10 TB of Storage, 1 GB/s of bandwidth, and time-shared VM scheduling. All VMs are distributed equally on these physical servers. The first of these computers has 4-core and the second has dual-core X86-architecture CPUs. The processing capacity of each processor core is 10000 MIPS. There are Linux operating system and Xen VMM on computers. The VMs have 512 MB of ram, 10 GB of Storage, 10 MB/s of bandwidth, and time-shared task scheduling configuration. The processing capacity of VMs ranges from 1000 to 5000 MIPS, and the command length of tasks ranges from 5000 to 20000 MI. The standard task planning method in CloudSim is "*CloudletSchedulerSpaceShared*". The other parameters used in the experiments are given in Table 1. Statistical results were obtained by running each of the experiments, conducted with 100, 250, 500, and 750 task numbers, 10 times in order to observe the performance of different scenarios.

Table 1. Experiment parameters

PARAMETERS	VALUES
Population sizes	10, 20, 30, 50, 60, 80, 100
Initial population size for C-JSO	10
Maximum Iteration	500
Task Sizes	100 - 750
VM number	20
Task MIs	5000 - 20000
VM MIPSs	1000-5000
Increasing Rate for C-JSO (θ)	13 %
Similarity Rate (ε)	90 %

Metaheuristic approaches achieved results that were close to each other in makespan values and about twice as successful results compared to the default scheduling algorithm. Among themselves, on the other hand, JSO and C-JSO were relatively more successful compared to ACO-based Scheduling. When examined in terms of duration, C-JSO was much more successful than other algorithms. While JSO had the highest values in terms of calculation time, C-JSO achieved the shortest time.

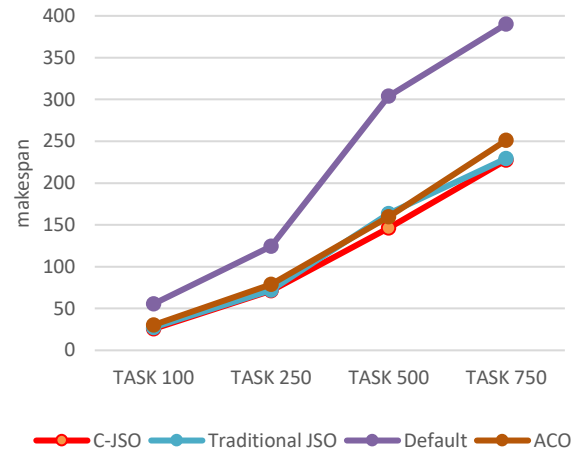**a)** Traditional JSO makespan results
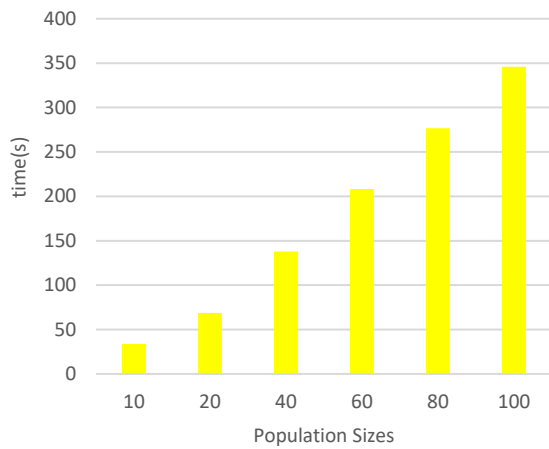
b) Traditional JSO time results

Figure4. The makespan and time results of traditional JSO with different population sizes for 100-task scheduling

In the experiments, first, how population growth affects makespan was examined. For this purpose, classical JSO-based solutions with different population numbers and their durations have been analyzed in a fixed-size Task Scheduling problem. Figure.4a-b shows the results of these experiments. In these experiments, classical JSO algorithms with different population sizes were run for 100 Tasks. As can be seen in Figure.4a, population growth leads to an improvement in the value of makespan. On the other hand, Fig.4b shows that this improvement has a negative effect on the solution time. The proposed method uses dynamic population growth to improve this disadvantage. Thus, at certain task sizes, the optimal result will be achieved in a shorter time with the appropriate number of populations.

Later experiments were conducted for CloudSim scenarios. In these experiments, classical JSO, C-JSO, default Cloud Scheduling, and ACO-based methods were run, and their results were examined. The comparative and statistical results of these experiments are given in Figure.5a-b and Table-2, respectively. In simulation experiments, the worst makespan values were obtained by the default scheduling algorithm.

a) C-JSO, Traditional JSO and Cloudsim makespan results
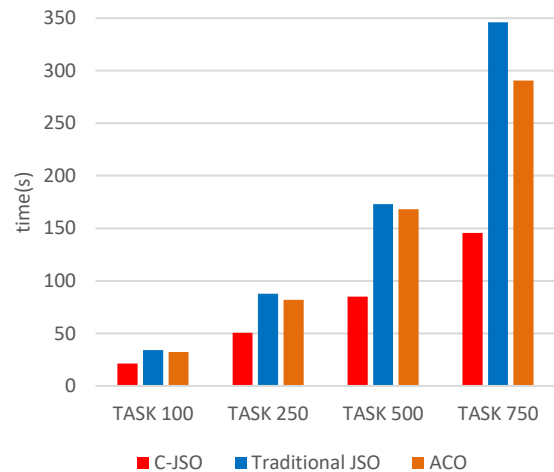
b) C-JSO and Traditional JSO time results

**Figure.5.** Makespan and time comparison for the methods used

According to statistical results, although the ACO algorithm approached the JSO and C-JSO values in terms of the minimum makespan values, the highest makespan values were also obtained by the ACO. Statistical results revealed that the performances of C-JSO and JSO are close to each other. The main superiority of C-JSO manifested itself in the calculation time.

Table 2. Statistical results for the methods used

	Method	100 Task	250 Task	500 Task	750 Task
Minimum		27.38	71.92	163.46	229.43
Maximum		31.05	77.92	201.73	257.34
Mean	JSO	29.33	73.81	179.72	244.08
Median		29.64	75.76	177.28	244.68
Std.		1.26	4.08	12.54	8.96
Minimum		25.61	71.06	146.63	227.45
Maximum		31.42	77.09	161.66	255.74
Mean	C-JSO	27.96	73.64	154.86	242.86
Median		27.88	74.07	154.72	242.46
Std.		1.48	1.79	4.03	6.94
Minimum		30.31	79.02	159.54	251.10
Maximum		35.16	87.33	193.47	287.11
Mean	ACO	34.53	83.18	171.11	267.01
Median		32.14	84.06	177.76	263.74
Std.		2.29	3.12	10.49	9.88
Minimum	CloudSim	55.51	124.43	304.13	390.08
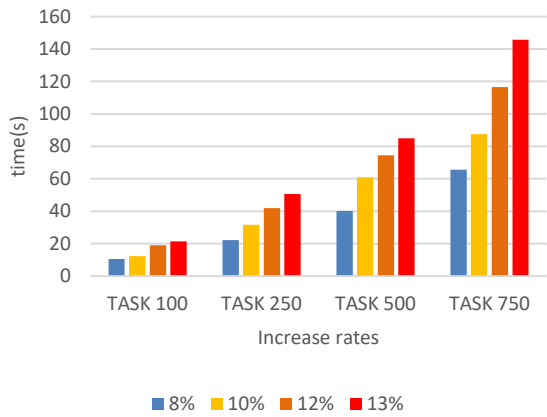
a) The average time results of C-JSO for different increase rates
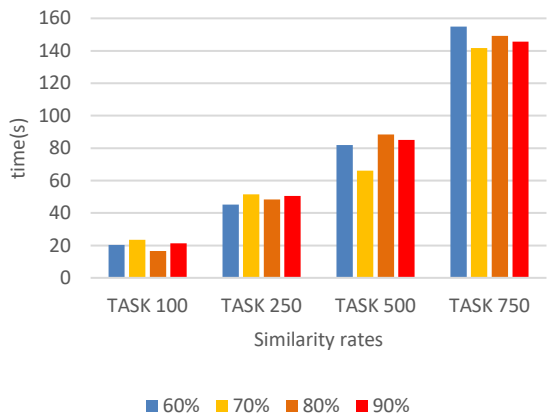
b) The average time results of C-JSO for different similarity rates

Figure.6. Effect of increase and similarity rates in C-JSO on makespan

Important hyper-parameters of C-JSO are the population growth rate and the similarity ratio used in the generation of new candidates. For this reason, parameter experiments were performed for different values, and the

behaviour of C-JSO was examined. In the experiments, 8%, 10%, 12%, and 13% values were selected for the increase rate. In experiments over 13%, there was no improvement in makespan values, and the calculation time approached JSO. Similarity ratios of 60%, 70%, 80%, and 90% were selected. In the experiments, the best results were obtained at the 13% increase rate and 90% similarity rate. The average time performances of these parameters for different scenarios are given in Figure 6a-b and their effects on makespan are given in Figure 7 and 8.
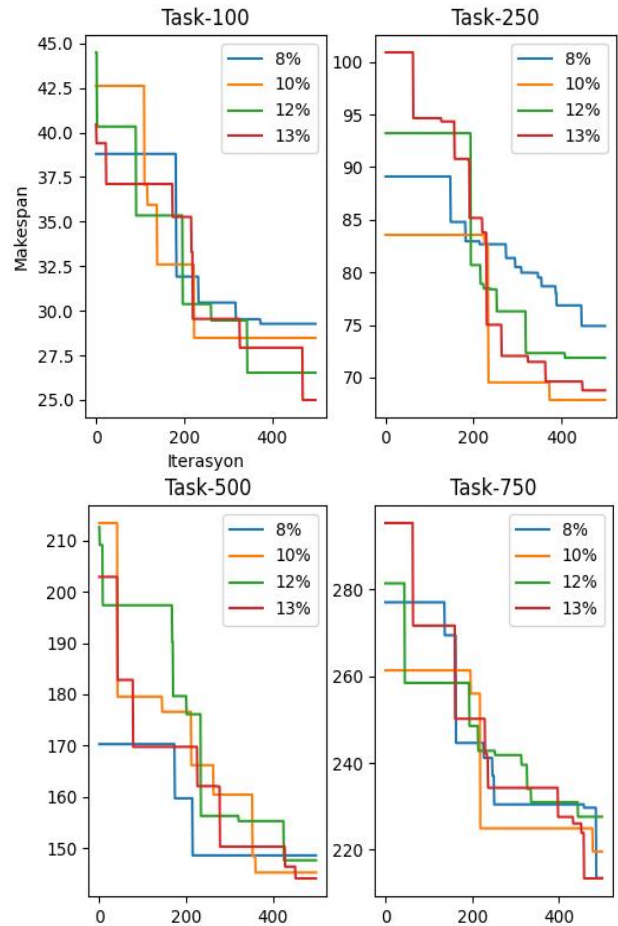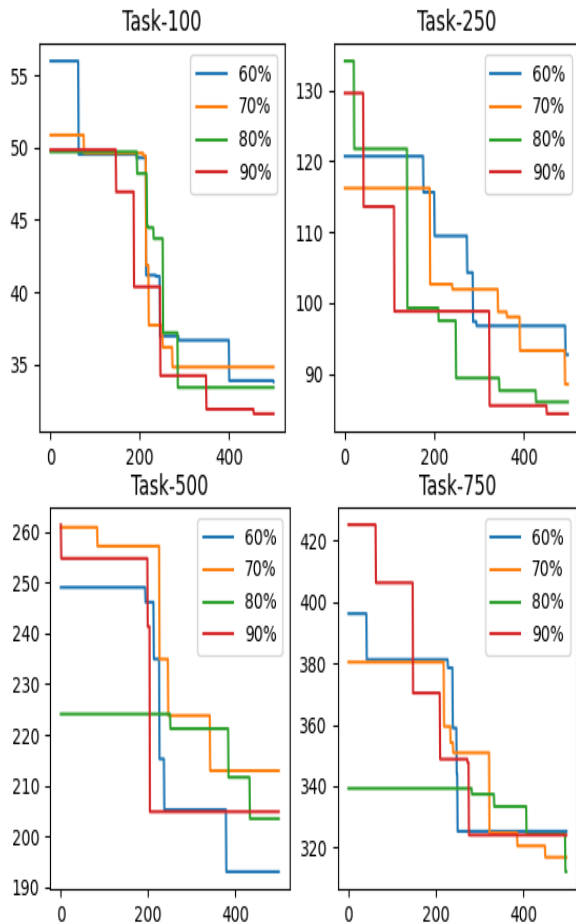

Figure.7. Effect of increase rate in C-JSO on makespan

41

Figure.8. Effect of similarity rate in C-JSO on makespan

4. CONCLUSION

This study focused on the task scheduling process, which is one of the most important problems in cloud computing. To solve this problem, an adapted meta-heuristic algorithm, the C-JSO, which is based on the Jellyfish Search Algorithm (JSO), was developed. C-JSO has functions that can make some mechanisms of traditional JSO more flexible, such as the population structure. The results obtained from the experiments were compared with the CloudSim default task scheduler and the ACO algorithm results. Both classic JSO and C-JSO solutions managed to provide successful results in standard cloud task-sharing methods. It was observed that in Makespan and time comparisons, the C-JSO was more successful than the others. It is clear that cloud systems will remain a topic where different problems will arise for a long time. Therefore, the authors will focus on the solutions of different optimization problems emerging in cloud systems in their next studies.

Acknowledgement

REFERENCES

[1] Strumberger I., Tuba E., Bacanin N., and Tuba, M. Dynamic tree growth algorithm for load scheduling in cloud environments. In 2019 IEEE Congress on Evolutionary Computation. 2019; p. 65-72.

[2] Avram MG. Advantages and challenges of adopting cloud computing from an enterprise perspective. Procedia Technology.2014; 12, 529-534.

[3] Abdullahi M., Ngadi MA. Symbiotic organism search optimization-based task scheduling in cloud computing environment. Future Generation Computer Systems. 2016; 56, 640-650.

[4] Houssein EH., Gad AG., Wazery YM., Suganthan PN. Task scheduling in cloud computing based on meta-heuristics: review, taxonomy, open challenges, and future trends. Swarm and Evolutionary Computation. 2021; 62, 100841.

[5] Mohamed AB. , Laila AF, Arun KS. Computational Intelligence for Multimedia Big Data on the Cloud with Engineering Applications; 2018.

[6] Yildirim G., Alatas B. New adaptive intelligent grey wolf optimizer based multi-objective quantitative classification rules mining approaches. Journal of Ambient Intelligence and Humanized Computing. 2021; 12, 9611–9635. https://doi.org/10.1007/s12652-020-02701-9

[7] Pradhan A., Bisoy SK., Das A. A survey on pso based meta-heuristic scheduling mechanism in cloud computing environment. Journal of King Saud University-Computer and Information Sciences; 2021.

[8] Chou JS., Truong TN. A novel metaheuristic optimizer inspired by behavior of jellyfish in ocean, Applied Mathematics and Computation.2021; 389, 125535.

[9] Alsaidy SA., Abbood AD., Sahib MA. Heuristic initialization of PSO task scheduling algorithm in cloud computing. Journal of King Saud University-Computer and Information Sciences; 2020.

[10] Yıldırım S., Yıldırım G., Alatas B."Anlaşılabilir Sınıflandırma Kurallarının Ayçiçeği Optimizasyon Algoritması ile Otomatik Keşfi", Türk Doğa ve Fen Dergisi. 2021; vol. 10, no. 2, pp. 233-241, doi:10.46810/tdfd.976397

[11] Saurav SK., Benedict S. A Taxonomy and Survey on Energy-Aware Scientific Workflows Scheduling in Large-Scale Heterogeneous Architecture. In 2021 6th International Conference on Inventive Computation Technologies (ICICT). 2021; (pp. 820-826). IEEE.

[12] Belgacem A., Beghdad-Bey K., Nacer H. Task scheduling optimization in cloud based on electromagnetism metaheuristic algorithm. In 2018 3rd International Conference on Pattern Analysis and Intelligent Systems (PAIS) 2018; (pp. 1-7). IEEE.

[13] Yildirim G., Hallac İR., Aydin G., Tatar Y. "Running genetic algorithms on Hadoop for solving high dimensional optimization problems," 2015 9th International Conference on Application of Information and Communication Technologies

(AICT). 2015; pp. 12-16, doi: 10.1109/ICAICT.2015.7338506

[14] Li K., Xu G., Zhao G., Dong Y., Wang D. Cloud task scheduling based on load balancing ant colony optimization. In 2011 sixth annual ChinaGrid conference. 2011; (pp. 3-9). IEEE.

[15] Liu CY., Zou CM., Wu P. A task scheduling algorithm based on genetic algorithm and ant colony optimization in cloud computing. In 2014 13th International Symposium on Distributed Computing and Applications to Business, Engineering and Science 2014; (pp. 68-72). IEEE.

[16] Chen X., Çeng U., Liu K., Liu Q., Liu J., Ying Mao, Murphy J. A WOA-Based Optimization Approach for Task Scheduling in Cloud Computing Systems. 2020; Volume: 14, Issue: 3, 3117 – 3128. IEEE.

[17] Zavodnik D. Spatial aggregations of the swarming jellyfish Pelagia noctiluca (Scyphozoa), Mar. Biol. 1987; 94, 265–269.

[18] Kıran, MS., Fındık O. A directed artificial bee colony algorithm, Appl. Soft Comput. 2015; 26, 454–462.

[19] Kıran M.S., Gündüz M., Baykan ÖK. A novel hybrid algorithm based on particle swarm and ant colony optimization for finding the global minimum, Appl. Math. Comput, 2012; C. 219, 1515–1521.

[20] Calheiros RN., Ranjan R., Beloglazov A., De Rose CA., Buyya R. CloudSim: a toolkit for modeling and simulation of cloud computing environments and evaluation of resource provisioning algorithms. Software: Practice and experience, 2011; 41(1), 23-50.

[21] Tsai CW., Huang WC., Chiang MH., Chiang MC., Yang CS. A hyper-heuristic scheduling algorithm for cloud. IEEE Transactions on Cloud Computing, 2014; 2, 236-250.

[22] Sasikaladevi N. Minimum makespan task scheduling algorithm in cloud computing, International Journal of Advances in Intelligent Informatics ISSN: 2442-6571, 2016; pp. 123-130.

[23] Burkuk M., Developing a Metaheuristic Solution Model to Task Scheduling Problems in Cloud Systems, Master Thesis, Graduate School of Natural and Applied Sciences, Firat University, 2022

43

Türk Doğa ve Fen Dergisi
Turkish Journal of Nature and Science
www.dergipark.gov.tr/tdfd

Thermal Conductivity and Thermal Rectification in Various Sequences of Monolayer Hexagonal Boron Nitride/Aluminum Nitride Superlattice Nanoribbons

Yenal KARAASLAN[1,2*]

[1]Department of Fundamental Sciences, Air NCO Vocational HE School, Turkish National Defence University, 35415 İzmir, Türkiye
[2]Department of Mechanical Engineering, Eskisehir Technical University, 26555 Eskişehir, Türkiye
Yenal KARAASLAN ORCID No: 0000-0001-8483-4819

Corresponding author: ykaraaslan@msu.edu.tr, yenalkaraaslan@gmail.com

Abstract: In this study, the thermal transport properties for various geometries of monolayer *h*-BN/*h*-AlN superlattice nanoribbons are investigated using non-equilibrium molecular dynamics simulations. In this context, the lattice thermal conductivities of the superlattice nanoribbons are obtained for different period lengths, geometries, sample lengths, and temperatures. Results reveal that a decrease in the thermal conductivities of superlattice nanoribbons when compared with those of the pristine nanoribbons, the lattice thermal conductivities decrease with decreasing sample lengths and increasing temperatures, also the formation of the extremum points resulting from the competition between wave-like and particle-like phonon transport in the thermal conductivity of superlattice nanoribbons with the change of the period lengths. Moreover, superlattice nanoribbons with different geometries are created to connect the *h*-BN/*h*-AlN interface, and it is observed that there is a difference between the thermal conductivities calculated in the reverse directions. This difference leads to thermal rectification in the superlattice structures. As the asymmetry between thermal contact areas increases especially at low temperatures, it is found out the thermal rectification ratio increases.

44

Tek Katmanlı Hegzagonal Bor Nitrür/Alüminyum Nitrür Süperörgü Nanoşeritlerinin Çeşitli Dizilerinde Termal İletkenlik ve Termal Doğrultma

Öz: Bu çalışmada, tek-katmanlı h-BN/h-AlN süperörgü nanoşeritlerinin çeşitli geometrileri için termal taşınım özellikleri, denge dışı moleküler dinamik simülasyonları kullanılarak araştırılmıştır. Bu bağlamda, farklı periyot uzunlukları, geometriler, örnek uzunlukları ve sıcaklıklar için süperörgü nanoşeritlerin örgü ısıl iletkenlikleri elde edilmiştir. Sonuçlar, bozulmamış nanoşeritler ile karşılaştırıldığında süperörgü nanoşeritlerin termal iletkenliklerinde bir azalma olduğunu, kafes termal iletkenliklerinin azalan örnek uzunlukları ve artan sıcaklıklar ile azaldığını, ayrıca periyot uzunluklarının değişimi ile süperörgü nanoşeritlerinin termal iletkenliklerinde dalga-benzeri ve parçacık-benzeri fonon taşınımı arasındaki rekabetten kaynaklanan ekstremum noktalarının oluşumunu ortaya koymaktadır. Ayrıca h-BN/h-AlN arayüzünü bağlamak için farklı geometrilere sahip süperörgü nanoşeritler yaratılmıştır ve ters yönlerde hesaplanan termal iletkenlikler arasında fark olduğu gözlemlenmektedir. Bu fark, süperörgü yapılarında termal doğrultmaya sebep olmaktadır. Özellikle düşük sıcaklıklarda termal banyo alanları arasındaki asimetri arttıkça termal doğrultma oranının arttığı tespit edilmiştir.

1. INTRODUCTION

Bulk group III-nitride semiconductor materials (BN, AlN, GaN, and InN) and their alloys have attracted great attention due to different device applications in electronics and optoelectronics as well as in thermoelectrics such as the high electron mobility transistors, laser diodes, light-emitting diodes, photo-detectors, solar cells, electro-optic modulators, and biosensors [1-4]. Nowadays, with the advance of fabrication technologies [5], interest in the hexagonal group-III nitride monolayers which possess graphene-like planar honeycomb structures have increased due to

both their potential in producing alternative solutions to graphene without band-gap (a disadvantage for thermoelectric applications) and their potential to achieve the desired device performances (high computing performance, low power consumption, etc.) for next-generation device applications [6,7]. Recently, the low-dimensional structures of BN [8,9], and AlN [10,11] have been successfully synthesized with high dimensional accuracy. Another class of low-dimensional nanomaterials is quasi-one-dimensional nanoribbons. The nanoribbons can be produced with techniques such as unwrapping of nanotubes [12] or cutting the monolayers, and so the phonons confined in bring novel properties to materials [13,14].

Controlling heat flow provides potential advantages in promising application fields such as thermoelectrics [15,16], thermal management [17,18], information processing [19], and optoelectronics [20]. In particular, the phonon interface scattering in structures such as two-dimensional superlattices is proposed as an alternative option in heat management applications. A superlattice implies a periodic or quasi-periodic arrangement of a certain period length layers composed of two or more crystal structures. In numerous experimental [21-23] and theoretical [24-26] studies, it has been pointed out that a superlattice with various components may indicate quite different thermal transport properties from the ones of its constituents due to due to its new translational symmetry and its capability to produce unusual phenomena [27-29]. Since the phonon mean-free-path is significantly suppressed by the phonon-boundary scattering at the interfaces between the materials, the lower lattice thermal conductivity of these structures compared to their constituents has been predicted [28-30].

One of the most fundamental phenomena associated with thermal manipulation in solid-state device applications is thermal rectification. The thermal rectification arises heterostructures (such superlattices) [31,32] or thermal asymmetry in the heat flow direction of asymmetric structures [33,34] or materials with asymmetric thermal contact [35,36]. For instance, by Chang et al. [37], heavy molecules were externally and in-homogeneously loaded to carbon and BN nanotubes, and about 7% thermal rectification coefficient was experimentally measured between the forward and backward directions by yielding asymmetric axial thermal conductance. In various asymmetric monolayer graphene nanostructures of the micrometer scale samples, the thermal rectification was experimentally measured by Wang et al. [34], and a 10% (26%) thermal rectification factor was reported for pristine monolayer graphene with nanoparticles deposited on one side or with a tapered width (for asymmetric monolayer graphene with nanopores on one side). Moreover, by Duan et al. [38], the interfacial thermal resistance between the carbon nanotube films and copper was experimentally measured, and the thermal rectification coefficient ranges between $57 - 68\%$ were presented. Also, the thermal rectification coefficient originated from phonon confinement in the lateral dimension in asymmetric T-shaped or trapezoidal graphene nanoribbons using

molecular dynamics simulations was predicted around 10% by Wang et al. [39]. Lastly, the thermal rectification coefficient for nozzle-like graphene/boron nitride nanoribbons having various geometries has been estimated at values of up to 25% by Dehaghani et al. [40].

Consequently, knowing and understanding the thermal transport properties of materials by controlling the heat flow is important and necessary for promising next-generation thermal device applications. Therefore, investigation of the thermal behavior of heat carrier phonons in monolayer superlattice nanoribbons is chosen as the subject of this study for both to clearly understand its nature and to indicate can be used as a thermal management tool in low-dimensional layered systems. Here, the thermal transport properties of monolayer hexagonal BN/AlN (*h*-BN/*h*-AlN) superlattice nanoribbons using the non-equilibrium molecular dynamics (NEMD) simulations via the Large-scale Atomic/Molecular Massively Parallel Simulator (LAMMPS) [41,42] are investigated. To this end, the force-field Tersoff potential parameters reported previously are used to model inter-atomic interactions of the *h*-BN/*h*-AlN nanoribbons [43,44].

2. MATERIAL AND METHOD

Schematic representations of monolayer *h*-BN/*h*-AlN superlattice nanoribbons, Boron (B): blue circle, Aluminum (Al): green circle, Nitrogen (N): grey circle) are shown in Fig. 1. Periodic boundary conditions are applied in the *x*-direction where the heat flow direction, while free boundary conditions are put into practice in the *y*-direction. The L_y width is $16a$ ($a = 0.306$ nm is the lattice constant). For L_x eight different length values in the range of $120 - 768$ unit cells ($\sqrt{3}a$) are considered. Simulation cells that the numbers of atoms in materials to be the same are created for six different period lengths ($l_p = l_1, 2l_1, 3l_1, 4l_1, 6l_1, 12l_1$, where $l_1 = 1.060$ nm is the minimum period length). In addition, the simulation cells of nanoribbons, half of which is *h*-BN and the other half which of *h*-AlN, are created to connect the *h*-BN and *h*-AlN interface at four different angles ($\theta = 0°, 30°, 60°,$ and $90°$). The NEMD simulations are performed for 7.5 ns with 0.5 fs time steps. Before applying the thermal gradient, the system is allowed to reach equilibrium at the desired temperature in the NVT ensemble for 1 ns. The thermal conductivity values are provided by using the data collected over the last 5 ns.

The thermal conductivity values of the superlattice nanoribbon simulation cells are obtained via Fourier's law

$$\kappa = -\frac{J}{\partial T/\partial x} \qquad (1)$$

by defining the heat flow, $J = \Delta Q/2A\Delta t$, removed from (or added to) the hot region (cold region) [45]. Here, $\partial T/\partial x$ is the temperature gradient generated between hot and cold regions along the heat flow direction, ΔQ is

45

Tr. Doğa ve Fen Derg. Cilt 11, Sayı 3, Sayfa 44-50, 2022

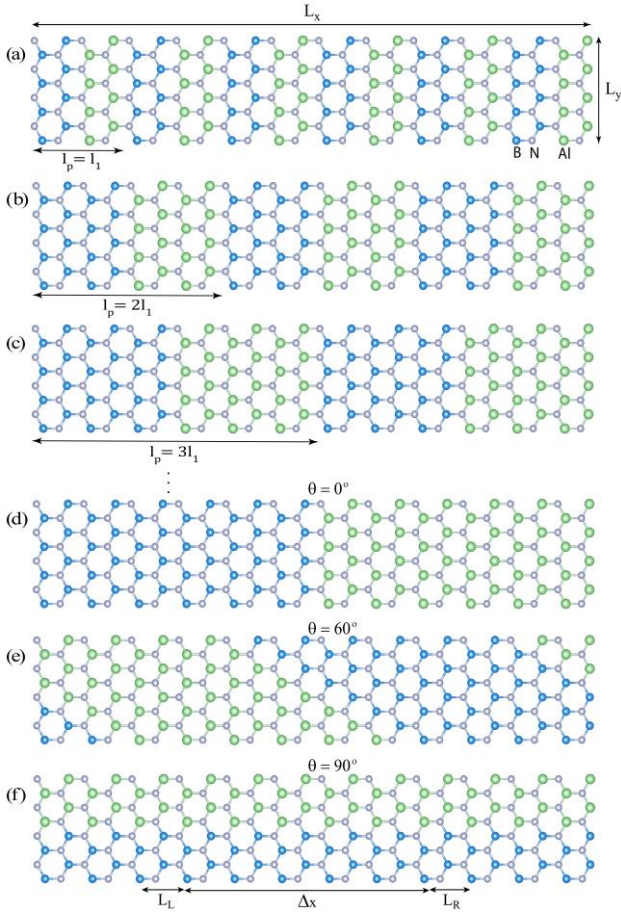**Tr. J. Nature Sci. Volume 11, Issue 3, Page 44-50, 2022**

Figure 1. Some of the schematic representation of the monolayer h-BN/h-AlN superlattice nanoribbon sequences (a) $l_p = l_1$, (b) $l_p = 2l_1$, (c) $l_p = 3 l_1$, (d) $l_p = L_x$ and $\theta = 0^o$, (e) $l_p = L_x$ and $\theta = 60^o$, and (f) $l_p = L_x$ and $\theta = 90^o$. Boron (B): blue circle, Aluminum (Al): green circle, Nitrogen (N): grey circle. Illustrative representation of thermal contacts (L_L and L_R) and sample geometry (width of L_y, length of L_x, symmetrical Δx length between contacts) in the MD simulations.

energy flux, Δt is the simulation time and A is the cross-sectional area that the heat flux passes through along simulation cells. The A is calculated considering $l_z = 0.337$ nm as the effective layer thickness of the monolayer nanoribbons [43]. Langevin thermostat that a stochastic heat bath [46], is used to establish thermal reservoirs in order to control the temperature difference as 60 K. The length of both hot and cold thermal reservoir regions (L_L and L_R, see Fig. 1) is kept constant as 16 unit cells ($16\sqrt{3}a$) to form symmetrical thermal contacts.

The intrinsic lattice thermal conductivity of infinitely long samples is predicted through extrapolation of the finite sample length results determined from the NEMD simulations via [47]:

$$\frac{1}{\kappa(\Delta x)} = \frac{1}{\kappa_\infty}\left(\frac{l_{pmfp}}{\Delta x} + 1\right) \qquad (2)$$

here Δx (see Fig. 1) is the sample length between hot and cold reservoir regions, l_{pmfp} is the phonon mean-free-path, $\kappa(\Delta x)$ is the thermal conductivity value obtained for the selected Δx length, and κ_∞ is the intrinsic lattice

thermal conductivity of the real system with infinite length.

By exchanging the thermal asymmetry, the thermal rectification (TR) is calculated as:

$$TR(\%) = \frac{|\kappa^+ - \kappa^-|}{\kappa^-} \times 100 \qquad (3)$$

where κ^+ is the thermal conductivity while L_L: hot region and L_R: cold region, and κ^- is for the reverse.

3. RESULTS

Intrinsic lattice thermal conductivity of the monolayer h-BN/h-AlN superlattice nanoribbons is estimated using the extrapolation function in Eq. 2 over the thermal conductivities calculated for the simulations of the finite sample lengths along the x-direction. In Fig. 2(a)-(c), the extrapolated data for six different superlattice period lengths of the superlattice nanoribbons are given at 200 K, 300 K, and 600 K temperatures, respectively. In the thermal conductivity results of six different superlattice period lengths, eight different finite simulation sample lengths are taken into account for extrapolations, and only a single NEMD simulation is carried out to determine the thermal conductivities of the finite sample lengths. The increment in nanoribbon sample length contributes to the thermal conduction as brings about an increase in the total phonon life-times along the heat flux direction, and thus the lattice thermal conductivities increase with increasing ribbon length.
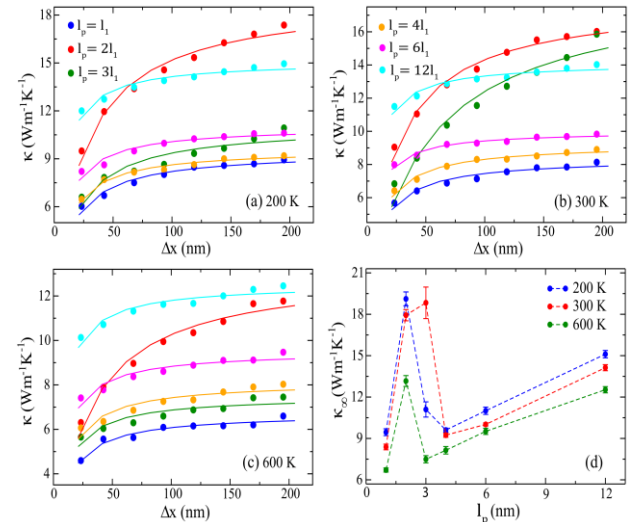
Figure 2. Period length dependent lattice thermal conductivity as a function of the Δx length for the monolayer h-BN/h-AlN superlattice nanoribbons at (a) 200 K, (b) 300 K, and (c) 600 K. Here, the line fit curves drawn in the same color as the data of each period length are generated using Eq. 2. (d) Intrinsic lattice thermal conductivity as a function of the period length at 200, 300, and 600 K temperatures for the monolayer h-BN/h-AlN superlattice nanoribbons.

Fig. 2(d) show the estimated intrinsic lattice thermal conductivity values of the monolayer h-BN/h-AlN superlattice nanoribbons as a function of superlattice period lengths at 200 K, 300 K, and 600 K. The standard deviations are determined from the fit curve of the thermal conductivity data obtained for the

simulations with finite sample lengths, using the function in Eq. 2. The intrinsic thermal conductivities of the superlattice nanoribbons at all the period lengths decrease with increasing temperatures as expected, due to the enhancement of the Umklapp process domination [27,48]. When compared with those of the pristine nanoribbon structures given in Table 1, the reduction in the thermal conductivities of superlattice nanoribbons is observed. Note that, the intrinsic lattice thermal conductivities of the monolayer h-BN and h-AlN pristine nanoribbons given in Table 1 have been calculated by using the same NEMD procedure for comparability [49].

Table 1. Intrinsic lattice thermal conductivity of pristine monolayer h-BN, and h-AlN nanoribbons obtained using the NEMD simulations at 200, 300, and 600 K temperatures [49].

κ_∞/Temperature	200 K	300 K	600 K
h-BN ($Wm^{-1}K^{-1}$)	337.79 ± 3.58	231.46 ± 2.44	122.51 ± 1.60
h-AlN ($Wm^{-1}K^{-1}$)	76.31 ± 0.58	54.66 ± 0.52	30.25 ± 0.63

A remarkable characteristic in the thermal conductivity of superlattice nanoribbons for all temperatures in Fig. 2(d) is the observation of extremum points with the change of the period length of superlattice nanoribbons. This extremum thermal conductivity behavior of the superlattice nanoribbons for the specific superlattice period lengths is consistent with previous results of studies both theoretically [25,26] and experimentally [22,50] performed for bulk and besides low-dimensional [27-30] superlattice structures. The increment of thermal conductivity in different superlattice period lengths implies the incoherent phonon transport where particle-like properties are dominant, while the decrement of thermal conductivity in different superlattice period lengths implies the coherent phonon transport in which wave-like properties are dominant [23].

Fig. 3 presents the temperature profiles of the NEMD simulations belonging to six different period lengths for h-BN/h-AlN superlattice nanoribbons with $L_x = 288$ unit cells at 300 K. The temperature profiles are smoother for shorter superlattice period lengths, and these imply that there is no resistance caused by local scattering, thus the superlattice nanoribbons can behave like a homogeneous structure. The jumping behavior in the temperature at the superlattice interfaces with increasing period lengths can comment as a series of thermal resistors for superlattice nanoribbons [29]. The behavior of the temperature profiles makes meaningful the interpretation of coherent and incoherent phonon transport for different superlattice period lengths.

In addition to superlattice nanoribbons with different period lengths, the superlattices of nanoribbons, half of which is h-BN and the other half which of h-AlN, are created to connect the h-BN and h-AlN interface at four different angles (θ = 0°, 30°, 60°, and 90°). Here, two different thermal conductivity values (κ^+, and κ^-) are calculated for the 0°, 30°, 60° angles, considering that the energy flow from the hot region to the cold region may vary from the energy flow in the inverse
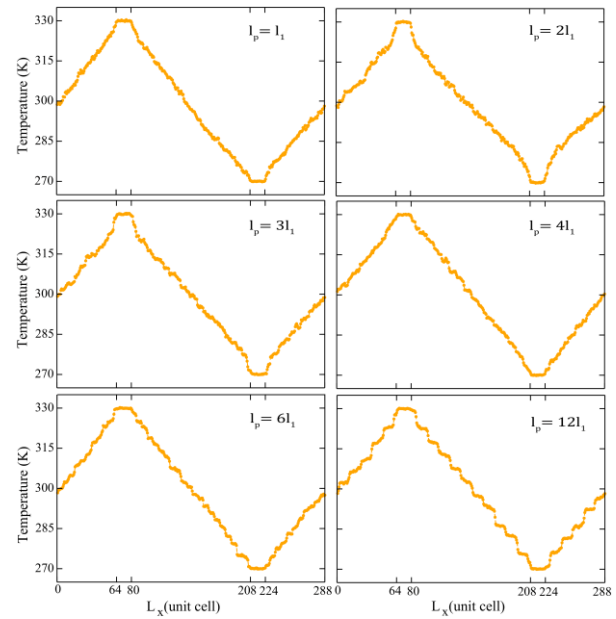
Figure 3. Temperature profiles of the monolayer h-BN/h-AlN superlattice nanoribbons with $L_x = 288$ unit cells for the period lengths $l_p = l_1$, $2l_1$, $3l_1$, $4l_1$, $6l_1$, $12l_1$, at 300 K.
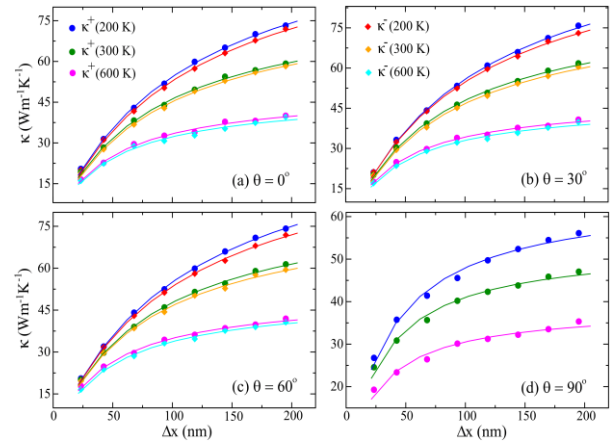
Figure 4. κ^+ and κ^- lattice thermal conductivities of the monolayer h-BN/h-AlN superlattice nanoribbons as a function of the **Δx** length for **θ** values of (a) **0°**, (b) **30°**, (c) **60°**, and (d) **90°**, at **200**, **300**, and **600** K temperatures. The line fit curves drawn in the same color as the data of each temperature are generated using Eq. 2.

case, due to the different atom arrangements at the superlattice interface for these structures. In Fig. 4, the thermal conductivity data determined according to Eq. 1 and extrapolation curves according to Eq. 2 based on these data are given as a function of the nanoribbon sample lengths for four different connect angles of the h-BN/h-AlN superlattice nanoribbon structures at 200 K, 300 K, and 600 K.

Table 2 demonstrates the intrinsic thermal conductivities and thermal rectification results of the monolayer h-BN/h-AlN superlattice nanoribbons for θ = 0°, 30°, 60°, and 90° at 200, 300, and 600 K temperatures. Here, the discussed superlattices should not be considered as different from the superlattices created for the various period lengths discussed above. Because the superlattice created for the 0° is actually a superlattice with $l_p = L_x$ period length. The 30° and 60° angles are superlattices developed to increase the asymmetry at the

47

interface. 90º offers a useful superlattice structure to manipulate thermal conductivity results in a different way. When the calculated thermal conductivity results are evaluated, it is observed that the results for the θ values of 0º, 30º, and 60º at all temperatures are close to each other, but the results for the 90º are approximately 40% lower than the results of other angles. Determining different thermal conductivities in the reverse directions for θ = 0º, 30º, and 60º can be attributed to the differences in phonon transmissivity caused by asymmetric structures. These differences lead to thermal rectification in the superlattice structures. As the rate of asymmetry between connect areas increases at 200 K, and 300 K, the rate of thermal rectification also increases. However, the thermal rectification ratio at 600 K, on the contrary, decreases with increasing angles.

Table 2. Intrinsic lattice thermal conductivity of the monolayer h-BN/h-AlN superlattice nanoribbons for $\theta = 0^o$, 30°, 60°, and 90° at 200, 300, and 600 K temperatures. Thermal rectification rates for the θ values of 0°, 30°, and 60° at all temperatures.

| Angle (°)	Temperature (K)	κ_∞^+ (Wm^{-1}K^{-1})	κ_∞^- (Wm^{-1}K^{-1})	TR (%)
0	200	116.79 ± 1.67	113.33 ± 2.00	3.05
	300	84.36 ± 1.37	83.99 ± 1.59	0.44
	600	49.30 ± 0.99	47.65 ± 1.18	3.46
30	200	117.81 ± 1.67	111.87 ± 1.50	5.31
	300	86.09 ± 1.20	84.10 ± 1.69	2.36
	600	48.32 ± 0.67	47.14 ± 0.91	2.51
60	200	117.55 ± 1.17	110.06 ± 1.04	6.80
	300	86.35 ± 1.33	82.64 ± 1.20	4.49
	600	50.62 ± 0.89	50.08 ± 0.82	1.08
90	200	65.39 ± 1.57	-	-
	300	53.40 ± 1.31	-	-
	600	38.70 ± 1.27	-	-

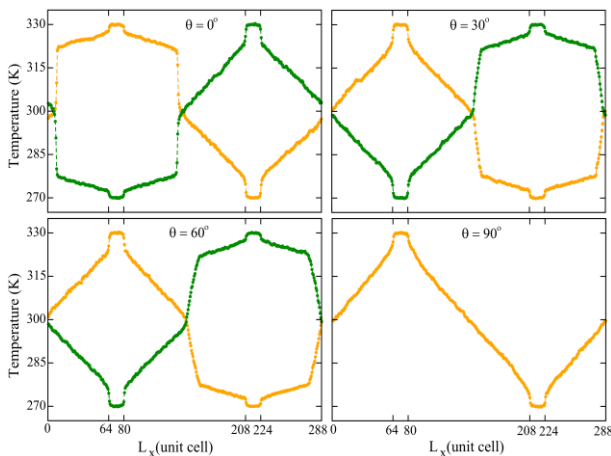**Figure 5.** Temperature profiles of the monolayer h-BN/h-AlN superlattice nanoribbons with $L_x = 288$ unit cells for θ values of 0º, 30º, 60º, and 90º at 300 K. Orange curves for L$_L$: hot region and L$_R$: cold region, and green curves for the reverse.

The temperature profiles of the NEMD simulations for four different angles of h-BN/h-AlN superlattice nanoribbons with L$_x$ = 288 unit cells are presented in Fig. 5. In the figures, the orange curves are the results of the simulations that take account of the energy flow from the hot region to the cold region, while the green curves are the results of the simulations that take into account the energy flow of the cold region to the hot region. For the 0º, 30º, and 60º angles, both materials are located in different temperature regions and therefore it is observed that the temperature profiles exhibit sharp transitions at the interface of the superlattices. While the transitions are sharper at lower angles, the transitions become smoother as the angle values increase. At the θ value of 90º, where the superlattice is like a homogeneous structure, a smooth temperature profile is displayed as expected.

The obtained results for the h-BN and h-AlN superlattice nanoribbons show up that the thermal conductivity of these structures can be controlled by superlattice sample length, temperature, and various geometries. The temperature across the reservoir regions for device applications of materials with high thermal conductivity reaches equilibrium very quickly, and this renders the thermoelectric device useless. Therefore, materials with low thermal conductivity are needed for thermoelectric device applications. The reduction of lattice thermal conductivity by inhibiting phonon propagation is one of the best ways to reduce the thermal conductivity of materials. Results of this study can be interpreted as the h-BN and h-AlN superlattice nanoribbons may be considered as a convenient choice to control the heat flow in thermoelectric device applications.

48

4. DISCUSSION AND CONCLUSION

Consequently, the thermal transport properties of the monolayer h-BN/h-AlN superlattice nanoribbons are analyzed using non-equilibrium molecular dynamics simulations. The thermal conductivities of the superlattices are determined as a function of the different period lengths, geometries, sample lengths, and temperatures. The estimated lattice thermal conductivity values of the superlattice nanoribbons are much lower than those of pristine structures, as expected. The results expose the extremum points in the lattice thermal conductivity that implies wave-like and particle-like phonon transport by controlling the period length of the superlattice nanoribbons. Also, the thermal conductivity of superlattice nanoribbons can be reduced with both decreasing sample lengths and increasing temperature. Besides, the thermal conductivities of the superlattice nanoribbons with non-symmetric geometries have a heat flow difference due to asymmetry in the reverse directions. This difference leads to thermal rectification in the superlattice structures. Especially at low temperatures, it is found out the thermal rectification factor can be increased up to 7% by adjusting the connect geometries. As a conclusion, this study presents detailed information on the thermal transport properties of the monolayer h-BN and h-AlN superlattice nanoribbons which could be used to manipulate the heat flow in thermal management and thermoelectric device applications.

Tr. Doğa ve Fen Derg. Cilt 11, Sayı 3, Sayfa 44-50, 2022

Tr. J. Nature Sci. Volume 11, Issue 3, Page 44-50, 2022

Acknowledgement

REFERENCES

[1]   Taniyasu Y, Kasu M, Makimoto T. An aluminium nitride light-emitting diode with a wavelength 210 nanometers. Nature. 2006;441(7091):325-8.

[2]   Mokkapati S, Jagadish C. III-V compound SC for optoelectronic devices. Materials Today. 2009;12(4):22-32.

[3]   Lu N, Ferguson I. III-nitrides for energy production: photovoltaic and thermoelectric applications. Semiconductor Science and Technology. 2013;28(7):074023.

[4]   Li X, Liu X. Group III nitride nanomaterials for biosensing. Nanoscale. 2017;9(22):7320-41.

[5]   Ambacher O. Growth and applications of group III-nitrides. Journal of Physics D: Applied physics. 1998;31(20):2653.

[6]   Lu H, Guo Y, Robertson J. Chemical trends of Schottky barrier behavior on monolayer hexagonal B, Al, and Ga nitrides. Journal of Applied Physics. 2016;120(6):065302.

[7]   Huang Z, Lü TY, Wang HQ, Yang SW, Zheng JC. Electronic and thermoelectric properties of the group-III nitrides (BN, AlN and GaN) atomic sheets under biaxial strains. Computational Materials Science. 2017;130:232-41.

[8]   Song L, Ci L, Lu H, Sorokin PB, Jin C, Ni J, et al. Large scale growth and characterization of atomic hexagonal boron nitride layers. Nano Letters. 2010;10(8):3209-15.

[9]   Cheng TS, Summerfield A, Mellor CJ, Khlobystov AN, Eaves L, Foxon CT, et al. High-temperature molecular beam epitaxy of hexagonal boron nitride with high active nitrogen fluxes. Materials. 2018;11(7):1119.

[10] Tsipas P, Kassavetis S, Tsoutsou D, Xenogiannopoulou E, Golias E, Giamini S, et al. Evidence for graphite-like hexagonal AlN nanosheets epitaxially grown on single crystal Ag (111). Applied Physics Letters. 2013;103(25):251605.

[11] Mansurov V, Malin T, Galitsyn Y, Zhuravlev K. Graphene-like AlN layer formation on (111) Si surface by ammonia molecular beam epitaxy. Journal of Crystal Growth. 2015;428:93-7.

[12] Zeng H, Zhi C, Zhang Z, Wei X, Wang X, Guo W, et al. "White graphenes": boron nitride nanoribbons via boron nitride nanotube unwrapping. Nano Letters. 2010;10(12):5049-55.

[13] Barone V, Peralta JE. Magnetic boron nitride nanoribbons with tunable electronic properties. Nano Letters. 2008;8(8):2210-4.

[14] Tabarraei A. Thermal conductivity of monolayer hexagonal boron nitride nanoribbons. Computational Materials Science. 2015;108:66-71.

[15] Tian Z, Lee S, Chen G. Heat transfer in thermoelectric materials and devices. Journal of Heat Transfer. 2013;135(6).

[16] Ouyang Y, Zhang Z, Li D, Chen J, Zhang G. Emerging theory, materials, and screening methods: new opportunities for promoting thermoelectric performance. Annalen der Physik. 2019;531(4):1800437.

[17] Feng CP, Wan SS, Wu WC, Bai L, Bao RY, Liu ZY, et al. Electrically insulating, layer structured SiR/GNPs/BN thermal management materials with enhanced thermal conductivity and breakdown voltage. Composites Science and Technology. 2018;167:456-62.

[18] Zhang Z, Ouyang Y, Cheng Y, Chen J, Li N, Zhang G. Size-dependent phononic thermal transport in low-dimensional nanomaterials. Physics Reports. 2020.

[19] Li N, Ren J, Wang L, Zhang G, Hänggi P, Li B. Colloquium: Phononics: Manipulating heat flow with electronic analogs and beyond. Reviews of Modern Physics. 2012;84(3):1045.

[20] Tien C, Chen G. Challenges in microscale conductive and radiative heat transfer. Previews of Heat and Mass Transfer. 1995;2(21):97.

[21] Yao T. Thermal properties of AlAs/GaAs superlattices. Applied Physics Letters. 1987;51(22):1798-800.

[22] Ravichandran J, Yadav AK, Cheaito R, Rossen PB, Soukiassian A, Suresha S, et al. Crossover from incoherent to coherent phonon scattering in epitaxial oxide superlattices. Nature materials. 2014;13(2):168-72.

[23] Cheaito R, Polanco CA, Addamane S, Zhang J, Ghosh AW, Balakrishnan G, et al. Interplay between total thickness and period thickness in the phonon thermal conductivity of superlattices from the nanoscale to the microscale: Coherent versus incoherent phonon transport. Physical Review B. 2018 Feb;97:085306.

[24] Juntunen T, Vänskä O, Tittonen I. Anderson localization quenches thermal transport in aperiodic superlattices. Physical Review Letters. 2019;122(10):105901.

[25] Latour B, Volz S, Chalopin Y. Microscopic de scription of thermal-phonon coherence: From coherent transport to diffuse interface scattering in superlattices. Physical Review B. 2014 Jul;90:014307.

[26] Chowdhury PR, Reynolds C, Garrett A, Feng T, Adiga SP, Ruan X. Machine learning maximized Anderson localization of phonons in aperiodic superlattices. Nano Energy. 2020;69:104428.

[27] Wang X, Wang M, Hong Y, Wang Z, Zhang J. Coherent and incoherent phonon transport in a graphene and nitrogenated holey graphene superlattice. Physical Chemistry Chemical Physics. 2017;19(35):24240-8.

[28] Zhu T, Ertekin E. Phonon transport on two-dimensional graphene/boron nitride superlattices.

Physical Review B. 2014;90(19):195209.

[29] Chen XK, Xie ZX, Zhou WX, Tang LM, Chen KQ. Phonon wave interference in graphene and boron nitride superlattice. Applied Physics Letters. 2016;109(2):023101.

[30] Felix IM, Pereira LFC. Suppression of coherent thermal transport in quasiperiodic graphene-hBN superlattice ribbons. Carbon. 2020;160:335-41.

[31] Chen XK, Xie ZX, Zhang Y, Deng YX, Zou TH, Liu J, et al. Highly efficient thermal rectification in carbon/boron nitride heteronanotubes. Carbon. 2019;148:532-9.

[32] Pei QX, Zhang YW, Sha ZD, Shenoy VB. Carbon isotope doping induced interfacial thermal resistance and thermal rectification in graphene. Applied Physics Letters. 2012;100(10):101901.

[33] Song C, Li S, Bao H, Ju J. Design of thermal diodes using asymmetric thermal deformation of a Kirigami structure. Materials & Design. 2020:108734.

[34] Wang H, Hu S, Takahashi K, Zhang X, Takamatsu H, Chen J. Experimental study of thermal rectification in suspended monolayer graphene. Nature Communications. 2017;8(1):1-8.

[35] Jiang P, Hu S, Ouyang Y, Ren W, Yu C, Zhang Z, et al. Remarkable thermal rectification in pristine and symmetric monolayer graphene enabled by asymmetric thermal contact. Journal of Applied Physics. 2020;127(23):235101.

[36] Lu J, Zheng Z, Yao J, Gao W, Xiao Y, Zhang M, et al. An asymmetric contact-induced self-powered 2D In_2S_3 photodetector towards high-sensitivity and fast-response. Nanoscale. 2020;12(13):7196-205.

[37] Chang CW, Okawa D, Majumdar A, Zettl A. Solid-state thermal rectifier. Science. 2006;314(5802):1121-4.

[38] Duan Z, Liu D, Zhang G, Li Q, Liu C, Fan S. Interfacial thermal resistance and thermal rectification in carbon nanotube film-copper systems. Nanoscale. 2017;9(9):3133-9.

[39] Wang Y, Vallabhaneni A, Hu J, Qiu B, Chen YP, Ruan X. Phonon lateral confinement enables thermal rectification in asymmetric single-material nanostructures. Nano Letters. 2014;14(2):592-6.

[40] Zarghami Dehaghani M, Molaei F, Spitas C, Hamed Mashhadzadeh A. Thermal rectification in nozzle-like graphene/boron nitride nanoribbons: A molecular dynamics simulation. Computational Materials Science. 2022;207:111320.

[41] Plimpton S. Fast parallel algorithms for short-range molecular dynamics. J Computational Physics. 1995;117(1):1 19.

[42] LAMMPS;. http://lammps.sandia.gov.

[43] Karaaslan Y, Yapicioglu H, Sevik C. Assessment of the thermal transport properties of group- III nitrides: A classical molecular dynamics study with transferable Tersoff-type inter-atomic potentials. Physical Review Applied. 2020 Mar;13:034027.

[44] Karaaslan Y. Coherent and incoherent phonon thermal transport in group-III nitride monolayer superlattices with Tersoff type interatomic potential. Physica E: Low-dimensional Systems and Nanostructures. 2022;140:115176.

[45] Müller-Plathe F. A simple nonequilibrium molecular dynamics method for calculating the thermal conductivity. The Journal of Chemical Physics. 1997;106(14):6082-5.

[46] Li Z, Xiong S, Sievers C, Hu Y, Fan Z, Wei N, et al. Influence of thermostatting on nonequilibrium molecular dynamics simulations of heat conduction in solids. The Journal of Chemical Physics. 2019;151(23):234105.

[47] Schelling PK, Phillpot SR, Keblinski P. Comparison of atomic-level simulation methods for computing thermal conductivity. Physical Review B. 2002 Apr;65:144306.

[48] Chen P, Zhang Z, Duan X, Duan X. Chemical synthesis of two dimensional atomic crystals, heterostructures and superlattices. Chemical Society Reviews. 2018;47(9):3129-51.

[49] Karaaslan Y. Thermal transport properties of hexagonal monolayer group-III nitride nanoribbons. Physica B: Physics of Condensed Matter. 2022; 640:414022.

[50] Saha B, Koh YR, Comparan J, Sadasivam S, Schroeder JL, Garbrecht M, et al. Cross-plane thermal conductivity of (Ti,W)N/(Al,Sc)N metal/semiconductor superlattices. Physical Review B. 2016 Jan;93:045311.

50

Türk Doğa ve Fen Dergisi
Turkish Journal of Nature and Science

Evaluation of the Levels of Metalloproteinases as well as Markers of Oxidative Stress and Apoptosis in Lung Tissues After Malathion and Rutin Administrations to Rats

Cihan GÜR[1*], Fatih Mehmet KANDEMİR[2]

[1] Atatürk University, Veterinary Faculty, Biochemistry Department, Erzurum, Türkiye
[2] Aksaray University, Medicine Faculty, Medical Biochemistry Department, Aksaray, Türkiye
Cihan GÜR ORCID No: 0000-0001-6775-7858
Fatih Mehmet KANDEMİR ORCID No: 0000-0002-8490-2479

Corresponding author: cihan.gur@atauni.edu.tr

Abstract: Malathion (MLT) is an important environmental pollutant in the organophosphate class. Rutin (RUT), on the other hand, is one of the flavonoid family members whose effectiveness against various toxic agents has been extensively studied. In the present study, the effects of MLT and RUT treatments on oxidative stress, apoptosis and metalloproteinases in lung tissues of rats were investigated. In this study, MDA, GSH, Nrf2, HO-1, MMP2, MMP9 and caspase-3 levels in lung tissues were analyzed by biochemical or RT-PCR method after rats received MLT and/or RUT treatment for 28 days. The data showed that MLT-induced MDA levels decreased after RUT treatment. Also, it was determined that Nrf2 and HO-1 mRNA transcript levels and GSH levels suppressed by MLT approached the control group levels after RUT treatment. MLT up-regulated the expression of metalloproteinases (MMP2 and MMP9) in lung tissues, while RUT down-regulated the expression of these genes. In addition, it was observed that MLT triggered caspase-3 expression, while RUT exerted an anti-apoptotic effect by suppressing caspase-3. As a result, it was determined that while MLT showed toxic effects in the lung tissues of rats through oxidative stress, apoptosis and metalloproteinases, RUT could alleviate these toxic effects.

51

Ratlara Malathion ve Rutin Uygulamaları Sonrası Akciğer Dokularında Metalloproteinaz Düzeyleri ile Oksidatif Stres ve Apoptoz Belirteçlerinin Değerlendirilmesi

Öz: Malathion (MLT), organofosfat sınıfında yer alan önemli bir çevresel kirleticidir. Rutin (RUT) ise çeşitli toksik ajanlara karşı etkinliği yoğun olarak araştırılan flavonoid aile üyelerinden biridir. Bu çalışmada, MLT ve RUT tedavilerinin sıçanların akciğer dokularında oksidatif stres, apoptoz ve metalloproteinazlar üzerine etkileri araştırıldı. Çalışmada, sıçanlara 28 gün boyunca MLT ve/veya RUT tedavisi verildikten sonra akciğer dokularındaki MDA, GSH, Nrf2, HO-1, MMP2, MMP9 ve kaspaz-3 seviyeleri biyokimyasal veya RT-PCR yöntemi ile analiz edildi. Veriler, MLT ile indüklenen MDA seviyelerinin RUT tedavisinden sonra düştüğünü gösterdi. Ayrıca Nrf2 ve HO-1 mRNA transkript düzeyleri ile MLT tarafından baskılanan GSH düzeylerinin RUT tedavisi sonrası kontrol grubu düzeylerine yaklaştığı belirlendi. MLT, akciğer dokularında metalloproteinazların (MMP2 ve MMP9) ekspresyonunu yukarı doğru düzenlerken, RUT bu genlerin ekspresyonunu aşağı regüle etti. Ayrıca MLT'nin kaspaz-3 ekspresyonunu tetiklediği, RUT'nin ise kaspaz-3'ü baskılayarak anti-apoptotik etki gösterdiği gözlendi. Sonuç olarak, MLT'nin oksidatif stres, apoptoz ve metalloproteinazlar yoluyla sıçanların akciğer dokularında toksik etkiler gösterirken, RUT'nin bu toksik etkileri azaltabileceği belirlendi.

1. INTRODUCTION

Pesticides are defined as chemicals used in agriculture to control weeds, insects and many other pests [1]. 1.8 billion people use 4.6 million tons of pesticides annually, and only less than 5% of these chemicals reach the target organism [2, 3]. Among the reasons for the widespread use of pesticides are the limited arable land and increasing production demand. Additionally, pesticide use becomes inevitable with new pesticide classes released every year to break pesticide resistance. Pesticides are very harmful compounds because they remain in the environment for a long time and have limited decomposition tendency [2].

Organophosphate insecticides (OPIs) are powerful toxicants that target the nervous systems of insects and other pests [4]. OPIs mainly work through inhibition of acetylcholinesterase (AChE), an enzyme that breaks down acetylcholine and causes acetylcholine to accumulate at the neuronal junction. Due to their ability to produce toxicity in non-target species, including humans, through the inhibition of acetylcholinesterase, they are considered sources of serious environmental pollution and health threat [5]. Malathion (MLT) is a broad spectrum organophosphate [OP] insecticide used to control a variety of outdoor insects in both agricultural and veterinary applications [6]. MLT is widely used due to its relatively low acute toxicity compared to other OP insecticides. Extensive studies have been conducted to evaluate the potential health effects of MLT in a variety of biological models, from amphibians to mammals. MLT has been reported to induce toxicity through inhibition of AchE followed by activation of cholinergic receptors [7]. Following exposure to MLT, this chemical can be rapidly absorbed by the skin, mucous membranes, gastrointestinal tract, eyes, and respiratory system. MLT has lipophilic properties which allow to spread rapidly to other tissues and to accumulate AChE in target organs. Apart from this, it has been reported that MLT causes the formation of reactive oxygen species (ROS), weakening of the antioxidant system and, consequently, induction of oxidative stress [8]. Therefore, it is thought that the use of antioxidant compounds may have beneficial effects against MLT-induced pulmonary toxicity.

Flavonoids are potent antioxidant compounds that inhibit lipid peroxidation and platelet aggregation. These compounds directly scavenge ROS, reactive nitrogen species, protect tissue from free radicals and activate antioxidant enzymes [9]. Rutin (RUT) is a quercetin glycone with a flavonol structure. It is predominantly found in citrus fruits such as oranges, grapefruits, lemons and limes. It is a member of bioflavonoids with antioxidant, anti-inflammatory, antiallergenic, antiviral and anticarcinogenic properties [10]. Previous studies have shown that RUT can alleviate the damaging effects of various toxic drugs with its antioxidant properties [11-13]. However, we could not find a study investigating the effect of RUT against MLT-induced lung toxicity. Therefore, the protective properties of RUT against MLT-induced lung toxicity were investigated in the present study.

2. MATERIAL AND METHOD

2.1. Supply, Care and Ethics Committee Approval of Experimental Animals

Sprague Dawley rats used in the study were obtained from Atatürk University Medical Experimental Application and Research Center. Animals were 10-12 weeks old and weighed 220-250 g. The environmental conditions in which the rats were housed had a temperature of $24 \pm 1°C$, a humidity of $45 \pm 5\%$, and a 12-hour light/dark cycle. The animals had access to standard pellet food and water *ad libitum* throughout the treatment. Ethics committee approval was given for the 28-day study by Atatürk University Animal Experiments Local Ethics Committee (Protocol no: 2022-7-112).

2.2. Experiment Design

In the experiment, 35 rats were divided into 5 groups, 7 in each group. The doses of MLT and RUT given to the animals were determined with reference to the previous studies. The groups are designed as given below:

1. Control Group : The animals were given saline orally for 28 days.
2. RUT 100 Group : Animals were given 100 mg/kg/body weight RUT orally for 28 days [14].
3. MLT Group : Animals were given 100 mg/kg/body weight MLT orally for 28 days [15].
4. MLT+RUT 50 Group : Animals were given 50 mg/kg/body weight RUT orally for 28 days, 30 minutes later MLT was administered orally at a dose of 100 mg/kg/body weight.
5. MLT+RUT 100 Group : Animals were given 100 mg/kg/body weight RUT orally for 28 days, 30 minutes later MLT was administered orally at a dose of 100 mg/kg/body weight.

On the 29th day of the study, the rats were decapitated under mild sevoflurane anesthesia and their lung tissues were removed. Tissues were stored at -80 °C until biochemical and molecular analysis.

2.3. Analysis of Malondialdehyde Levels in Lung Tissue

Lung tissues from rats were pulverized in liquid nitrogen by means of a tissue shredder (Tissue Lyser II, Qiagen, The Netherlands). Then the tissues were homogenized in 1.15% KCl buffer at a ratio of 1:10 (weight/volume). The obtained homogenates were centrifuged at 1000xg for 15 minutes at +4 °C. Malondialdehyde (MDA) levels in homogenates was analyzed by the method developed by Placer et al. (1966) [16]. Results are presented as nmol/g tissue.

2.4. Analysis of Glutathione Levels in Lung Tissue

For glutathione (GSH) analysis, homogenates, the preparation of which was explained in the previous

section, were centrifuged at 9000xg at +4 °C. GSH levels were determined in the supernatants obtained afterwards, using the method of Sedlak et al (1968) [17]. Obtained results are presented as nmol/g tissue.

2.5. Total RNA Isolation from Lung Tissue

Total RNA isolation from pulverized lung tissues was performed using hibrizol reagent (HibriGen). For this, 60 mg of pulverized lung tissues were weighed into sterile eppendorf tubes and 2 ml of hybrisol was added. All procedures were carried out in accordance with the manufacturer's instructions. In the last step, after washing the total RNAs with 75% ethanol, they were dissolved with RNase-free water and their concentrations were measured in the nanodrop device.

2.6. cDNA Synthesis from Total RNAs

cDNA synthesis from total RNAs was performed with the iScript™ cDNA Synthesis Kit (BIO-RAD, USA). cDNA synthesis was carried out in strict accordance with the instructions given by the manufacturer.

2.7. RT-PCR

At the RT-PCR stage, the primers of the genes whose sequences are given in Table 1, cDNAs, iTaq Universal SYBR® Green Supermix and a mixture with RNase-DNase-free water were prepared. The reaction was started by entering the temperatures and times specified in the procedure that came with iTaq Universal SYBR® Green Supermix into the ROTOR-GENE Q (Qiagen, Germany) device. At the end of the procedures, the fold changes of the relevant genes were calculated using the $2^{-deltadelatCT}$ method using the CT values obtained from the device [18]. GAPDH was used as internal control.

Table 1: Primer sequences

Gene	Sequences (5'-3')	Length (bp)
MMP2	F: CTCTAGGAGAAGGACAAGTG R: CTCAAAGTTGTACGTGGTGG	158
MMP9	F: AGCTGGCAGAGGATTACCTG R: ATGATGGTGCCACTTGAGGT	230
Nrf2	F: TTTGTAGATGACCATGAGTCGC R: TCCTGCCAAACTTGCTCCAT	161
HO-1	F: ATGTCCCAGGATTTGTCCGA R: ATGGTACAAGGAGGCCATCA	144
Caspase-3	F: ACTGGAATGTCAGCTCGCAA R: GCAGTAGTCGCCTCTGAAGA	270
GAPDH	F: GAGTATGTCGTGGAGTCTAC R: CAGGATGCATTGCTGACAAT	179

2.8. Statistical Analysis

In the statistical analysis of the data, one-way analysis of variance (ANOVA) and Tukey's multiple comparison test were used in SPSS 20.0 program. Results are presented as mean ± SD. P < 0.05 was considered statistically significant.

3. RESULTS

3.1. Oxidative Stress State in Lung Tissue

After MLT and RUT treatments were applied to rats, tissue MDA and GSH levels and nuclear factor erythroid 2-related factor 2 (Nrf2) and heme oxygenase 1 (HO-1) mRNA transcript levels were analyzed to determine the oxidative stress status in lung tissue (Figure 1). It was determined that MLT downregulated the Nrf2 and HO-1 genes, caused the depletion of GSH stores and caused a significant increase in MDA levels (p<0.05). On the other hand, RUT treatment provided activation in Nrf2 and HO-1 genes. In addition, RUT reduced MDA levels by regenerating GSH stores. While there was no difference between the doses of RUT on Nrf2 expression, HO-1 expression was triggered in a dose-dependent manner (p<0.05). Different doses of RUT did not make a statistical difference on MDA and GSH levels.
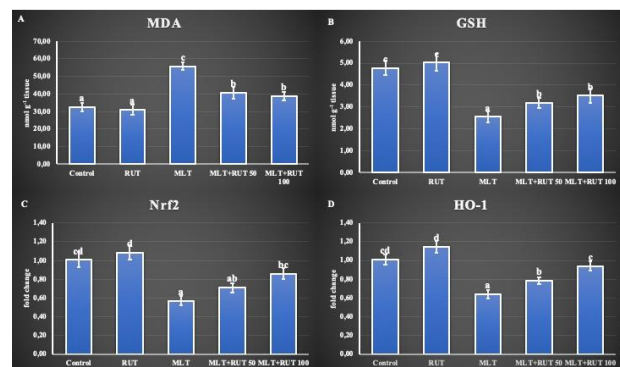
Figure 1. Status of oxidative stress markers in lung tissue after malathion and rutin treatments. (RUT: Rutin, MLT: Malathion, MDA: Malondialdehyde, GSH: Glutathione, Nrf2: Nuclear factor erythroid 2-related factor 2, HO-1: heme oxygenase 1)

3.2. mRNA Transcript Levels of Metalloproteinases in Lung Tissue

When the status of metalloproteinases in lung tissue was evaluated, it was determined that matrix metalloproteinase-2 (MMP2) and matrix metalloproteinase-9 (MMP9) expressions increased after MLT administration. It was observed that MMP expressions were down-regulated in the lung tissues of rats given RUT (p<0.05). In addition, another finding was that there was no difference in MMP2 or MMP9 expressions between MLT+RUT50 and MLT+RUT100 groups. The results are summarized in Figure 2.
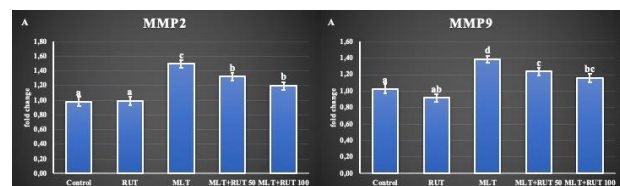

Figure 2. Status of metalloproteinases in lung tissue after malathion and its rutin treatments. (RUT: Rutin, MLT: Malathion, MMP2: matrix metalloproteinase-2, MMP9: matrix metalloproteinase-9)

53

3.3. Apoptotic State in Lung Tissue

After MLT and RUT treatments, mRNA transcript levels of Caspase-3 gene were analyzed by RT-PCR method to detect apoptotic state in lung tissue. According to the results presented in Figure 3, it was observed that MLT could trigger caspase-3 expression and cause apoptosis in lung tissue. On the other hand, it was determined that Caspase-3 expression was significantly suppressed after RUT administration and this was dose-dependent ($p < 0.05$).
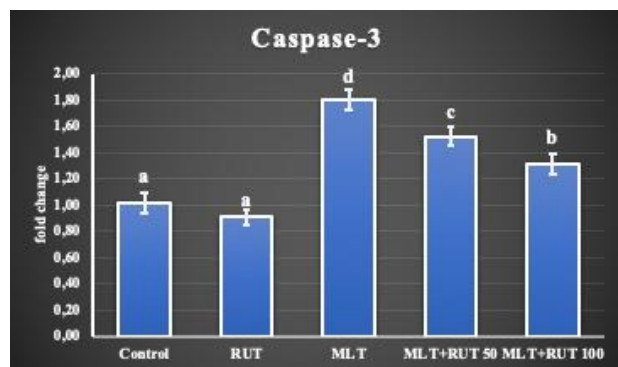

Figure 3. Apoptosis in lung tissue after malathion and rutin treatments. (RUT: Rutin, MLT: Malathion)

4. DISCUSSION AND CONCLUSION

Organophosphate pesticides are at the forefront of toxic substances, and many studies have shown that these compounds are among environmental pollutants that threaten human health. OPs are absorbed into the body through the respiratory system, gastrointestinal tract, and skin. OPs cause respiratory and neuromuscular conduction disorders mainly by inhibiting AChE in the nervous system [19]. MLT has taken its place among these toxic compounds as one of the environmental pollutants that threaten human health. Although many studies have been done against MLT toxicity before, an effective treatment method has not been developed yet [6, 20]. In the present study, the effects of RUT against the lung toxicity of MLT were evaluated, and the data obtained showed that RUT was a promising compound against this disease.

It has been previously reported that oxidative stress, which develops due to excessive increase in reactive oxygen species, is the basic mechanism of many toxic compounds [21-25]. There is evidence of increased oxidative stress in chronic toxicity of several OP compounds, including MLT [19, 26, 27]. However, information on the role of oxidative stress in subacute and chronic OP toxicity remains insufficient. OP is thought to bind directly to proteins and phosphorylate them, creating a pro-oxidative state [28]. In the present study, it was observed that the levels of GSH, a tripeptide antioxidant [29, 30], were significantly reduced in lung tissue after MLT treatment. Moreover, it was observed that decreased GSH levels probably caused a further increase in ROS levels and that these aggressive molecules damaged the membranes of lung tissue cells, causing lipid peroxidation, thereby increasing MDA levels. Previous studies have reported that different flavonoids applied against various pesticide groups alleviate oxidative stress and alleviate the toxic effects of these compounds [31, 32]. In our study, it was determined that RUT treatment suppressed oxidative stress by providing the regeneration of GSH, whose levels were significantly reduced by MLT, and by preventing lipid peroxidation.

Nrf2 is one of the transcription factors that protect cells against oxidative stress [33, 34]. Nrf2 regulates a wide range of genes such as superoxide dismutase, oxidoreductases and heme oxygenases [35, 36]. In a previous study, it was reported that deltamethrin suppressed Nrf2 as well as Cu/Zn SOD, GSH-Px, GST and CAT expressions in the liver and spleen tissue of *Channa argus*, however, significant increases in the mRNA transcript levels of these markers occurred after curcumin treatment [37]. Another study displayed that activating the Nrf2/HO-1 pathway exhibits nephroprotective effects in deltamethrin-induced nephrotoxicity [38]. Similarly, in the current study, it was determined that oxidative stress exacerbated due to the disruption of the Nrf2/HO-1 pathway after MLT treatment, but RUT treatment could activate this pathway and protect the lung tissue from MLT-induced oxidative stress. It is thought that the possible reason for this is the reduction of oxidative stress due to the ROS scavenging property of RUT and thus reducing the suppressive effect of oxidative stress on Nrf2.

Under normal conditions, the pulmonary extracellular matrix (ECM) determines the tissue architecture necessary for lung function. However, defects in the production of ECM are found in the fibrotic response [39]. MMPs are proteolytic enzymes known to be involved in cell migration and tissue remodeling [40]. Among MMPs, MMP2 and MMP9 contribute to tissue remodeling by playing a role in the degradation of collagen and elastase in lung tissue [41]. These endopeptidases have been reported to play an important role in various lung diseases [42]. Unfortunately, little is known about the effects of pesticides on MMPs in lung tissue. Several studies have reported that paraquat may contribute to the development and progression of fibrosis by increasing MMP9 expression [43, 44]. In the present study, it was observed that MLT contributed to pulmonary toxicity by triggering MMP expressions in the lung tissues of rats. On the other hand, it was determined that MMP2 and MMP9 expressions were downregulated with RUT treatment.

Apoptosis induced by factors such as reactive oxygen species is a normal cell death process [45, 46]. ROS production can cause cell damage due to increased membrane permeability and impaired mitochondrial function, resulting in apoptotic cell death [20]. Previous studies have shown that activation of the Nrf2/HO-1 signaling pathway plays a crucial role in inhibiting apoptosis by enhancing oxidative defense [45, 47]. Caspase-3 has an important role in the apoptotic pathway and is widely used as an apoptotic marker in many studies [48-51]. It has been reported that MLT treatment

increases apoptotic proteins in the brain such as Bax, Bak and caspase-3 [52, 53]. In the present study, it was observed that MLT could trigger the apoptotic process by up-regulating caspase-3 expression in lung tissue. On the other hand, it was determined that RUT treatment suppressed caspase-3 expression in anti-parallel with Nrf-2/HO-1 pathway. This supports the relationship between the lung toxicity of MLT and oxidative stress.

As a result, it was observed that oxidative stress and apoptosis were triggered in the lung tissues of rats given MLT, MMPs were activated and significant damage to the tissue could occur as a result. However, it has been determined that RUT treatment can alleviate MLT-induced pulmonary damage through suppression of oxidative stress, apoptosis and MMPs.

Acknowledgement

REFERENCES

[1] Gupta VK, Siddiqi NJ, Ojha AK, Sharma B. Hepatoprotective effect of Aloe vera against cartap- and malathion-induced toxicity in Wistar rats. J Cell Physiol. 2019;234(10):18329-43.

[2] Pandit AA, Gandham RK, Mukhopadhyay CS, Verma R, Sethi R. Transcriptome analysis reveals the role of the PCP pathway in fipronil and endotoxin-induced lung damage. Respir res. 2019;20(1):1-16.

[3] Hassani S, Sepand M, Jafari A, Jaafari J, Rezaee R, Zeinali M, et al. Protective effects of curcumin and vitamin E against chlorpyrifos-induced lung oxidative damage. Hum Exp Toxicol. 2015;34(6):668-76.

[4] Jokanović M. Medical treatment of acute poisoning with organophosphorus and carbamate pesticides. Toxicol lett. 2009;190(2):107-15.

[5] Moore PD, Patlolla AK, Tchounwou PB. Cytogenetic evaluation of malathion-induced toxicity in Sprague-Dawley rats. MRGTEM. 2011;725(1-2):78-82.

[6] Abdel-Daim MM, Abushouk AI, Bungău SG, Bin-Jumah M, El-Kott AF, Shati AA, et al. Protective effects of thymoquinone and diallyl sulphide against malathion-induced toxicity in rats. Environ Sci Pollut Res. 2020;27(10):10228-35.

[7] Geng X, Shao H, Zhang Z, Ng JC, Peng C. Malathion-induced testicular toxicity is associated with spermatogenic apoptosis and alterations in testicular enzymes and hormone levels in male Wistar rats. Environ Toxicol Pharmacol. 2015;39(2):659-67.

[8] Uysal M, Karaman S. In vivo effects of intravenous lipid emulsion on lung tissue in an experimental model of acute malathion intoxication. Toxicol Ind. 2018;34(2):110-8.

[9] Jahan S, Munawar A, Razak S, Anam S, Ain QU, Ullah H, et al. Ameliorative effects of rutin against cisplatin-induced reproductive toxicity in male rats. BMC urology. 2018;18(1):1-11.

[10] Nafees S, Rashid S, Ali N, Hasan SK, Sultana S. Rutin ameliorates cyclophosphamide induced oxidative stress and inflammation in Wistar rats: role of NFκB/MAPK pathway. Chem Biol Interact. 2015;231:98-107.

[11] Zargar S, Wani TA, Alamro AA, Ganaie MA. Amelioration of thioacetamide-induced liver toxicity in Wistar rats by rutin. Int J Immunopathol Pharmacol. 2017;30(3):207-14.

[12] Yeh C-H, Yang J-J, Yang M-L, Li Y-C, Kuan Y-H. Rutin decreases lipopolysaccharide-induced acute lung injury via inhibition of oxidative stress and the MAPK–NF-κB pathway. Free Radic Biol Med. 2014;69:249-57.

[13] Kandemir FM, Caglayan C, Aksu EH, Yildirim S, Kucukler S, Gur C, et al. Protective effect of rutin on mercuric chloride-induced reproductive damage in male rats. Andrologia. 2020;52(3):e13524.

[14] Caglayan C, Kandemir FM, Darendelioğlu E, Yıldırım S, Kucukler S, Dortbudak MB. Rutin ameliorates mercuric chloride-induced hepatotoxicity in rats via interfering with oxidative stress, inflammation and apoptosis. J Trace Elem Med Biol. 2019;56:60-8.

[15] Akbel E, Arslan-Acaroz D, Demirel HH, Kucukkurt I, Ince S. The subchronic exposure to malathion, an organophosphate pesticide, causes lipid peroxidation, oxidative stress, and tissue damage in rats: the protective role of resveratrol. Toxicol res. 2018;7(3):503-12.

[16] Placer ZA, Cushman LL, Johnson BC. Estimation of product of lipid peroxidation [malonyl dialdehyde] in biochemical systems. Anal biochem. 1966;16(2):359-64.

[17] Sedlak J, Lindsay RH. Estimation of total, protein-bound, and nonprotein sulfhydryl groups in tissue with Ellman's reagent. Anal biochem. 1968;25:192-205.

[18] Livak KJ, Schmittgen TD. Analysis of relative gene expression data using real-time quantitative PCR and the 2− ΔΔCT method. methods. 2001;25(4):402-8.

[19] Farkhondeh T, Mehrpour O, Forouzanfar F, Roshanravan B, Samarghandian S. Oxidative stress and mitochondrial dysfunction in organophosphate pesticide-induced neurotoxicity and its amelioration: a review. Environ Sci Pollut Res. 2020;27(20):24799-814.

[20] Ranjbar A, Ghahremani MH, Sharifzadeh M, Golestani A, Ghazi-Khansari M, Baeeri M, et al. Protection by pentoxifylline of malathion-induced toxic stress and mitochondrial damage in rat brain. Hum Exp Toxicol. 2010;29(10):851-64.

[21] Caglayan C, Temel Y, Kandemir FM, Yildirim S, Kucukler S. Naringin protects against cyclophosphamide-induced hepatotoxicity and nephrotoxicity through modulation of oxidative stress, inflammation, apoptosis, autophagy, and DNA damage. Environ Sci Pollut Res. 2018;25(21):20968-84.

55

[22] Gur C, Kandemir O, Kandemir FM. Investigation of the effects of hesperidin administration on abamectin-induced testicular toxicity in rats through oxidative stress, endoplasmic reticulum stress, inflammation, apoptosis, autophagy, and JAK2/STAT3 pathways. Environ Toxicol. 2022;37(3):401-12.

[23] Gur C, Kandemir FM, Darendelioglu E, Caglayan C, Kucukler S, Kandemir O, et al. Morin protects against acrylamide-induced neurotoxicity in rats: an investigation into different signal pathways. Environ Sci Pollut Res. 2021;28(36):49808-19.

[24] Kucukler S, Benzer F, Yildirim S, Gur C, Kandemir FM, Bengu AS, et al. Protective effects of chrysin against oxidative stress and inflammation induced by lead acetate in rat kidneys: a biochemical and histopathological approach. Biol Trace Elem Res. 2021;199(4):1501-14.

[25] Yıldız MO, Çelik H, Caglayan C, Kandemir FM, Gür C, Bayav İ, et al. Neuromodulatory effects of hesperidin against sodium fluoride-induced neurotoxicity in rats: Involvement of neuroinflammation, endoplasmic reticulum stress, apoptosis and autophagy. NeuroToxicology. 2022;90:197-204.

[26] Coban FK, Ince S, Kucukkurt I, Demirel HH, Hazman O. Boron attenuates malathion-induced oxidative stress and acetylcholinesterase inhibition in rats. Drug Chem Toxicol. 2015;38(4):391-9.

[27] Ince S, Arslan-Acaroz D, Demirel HH, Varol N, Ozyurek HA, Zemheri F, et al. Taurine alleviates malathion induced lipid peroxidation, oxidative stress, and proinflammatory cytokine gene expressions in rats. Biomed Pharmacother. 2017;96:263-8.

[28] Vanova N, Pejchal J, Herman D, Dlabkova A, Jun D. Oxidative stress in organophosphate poisoning: role of standard antidotal therapy. J Appl Toxicol. 2018;38(8):1058-70.

[29] Gür C, Genç A, Kandemir Ö. Ratlarda Deltametrin'in Neden Olduğu Dalak Toksisitesine Karşı Rutin'in Potansiyel Koruyucu Etkilerinin Oksidatif Stres, Apoptoz ve İnflamasyon Belirteçleri Üzerinden Araştırılması. Atatürk University J Vet Sci. 17(1):6-10.

[30] Caglayan C, Kandemir FM, Darendelioğlu E, Küçükler S, Ayna A. Hesperidin protects liver and kidney against sodium fluoride-induced toxicity through anti-apoptotic and anti-autophagic mechanisms. Life Sci. 2021;281:119730.

[31] Küçükler S, Çomaklı S, Özdemir S, Çağlayan C, Kandemir FM. Hesperidin protects against the chlorpyrifos-induced chronic hepato-renal toxicity in rats associated with oxidative stress, inflammation, apoptosis, autophagy, and up-regulation of PARP-1/VEGF. Environ Toxicol. 2021;36(8):1600-17.

[32] Anwar M, Muhammad F, Akhtar B, Saleemi MK. Nephroprotective effects of curcumin loaded chitosan nanoparticles in cypermethrin induced renal toxicity in rabbits. Environ Sci Pollut Res. 2020;27(13):14771-9.

[33] Yardim A, Gur C, Comakli S, Ozdemir S, Kucukler S, Celik H, et al. Investigation of the effects of berberine on bortezomib-induced sciatic nerve and spinal cord damage in rats through pathways involved in oxidative stress and neuro-inflammation. Neurotoxicology. 2022;89:127-39.

[34] Yardim A, Kandemir FM, Ozdemir S, Kucukler S, Comakli S, Gur C, et al. Quercetin provides protection against the peripheral nerve damage caused by vincristine in rats by suppressing caspase 3, NF-κB, ATF-6 pathways and activating Nrf2, Akt pathways. Neurotoxicology. 2020;81:137-46.

[35] Hussein RM, Mohamed WR, Omar HA. A neuroprotective role of kaempferol against chlorpyrifos-induced oxidative stress and memory deficits in rats via GSK3β-Nrf2 signaling pathway. Pestic Biochem Physiol. 2018;152:29-37.

[36] Yardim A, Gur C, Comakli S, Ozdemir S, Kucukler S, Celik H, et al. Investigation of the effects of berberine on bortezomib-induced sciatic nerve and spinal cord damage in rats through pathways involved in oxidative stress and neuro-inflammation. Neurotoxicology. 2022;89:127-39.

[37] Kong Y, Li M, Guo G, Yu L, Sun L, Yin Z, et al. Effects of dietary curcumin inhibit deltamethrin-induced oxidative stress, inflammation and cell apoptosis in Channa argus via Nrf2 and NF-κB signaling pathways. Aquaculture. 2021;540:736744.

[38] Shi W, Zhang D, Wang L, Sreeharsha N, Ning Y. Curcumin synergistically potentiates the protective effect of sitagliptin against chronic deltamethrin nephrotoxicity in rats: impact on pro-inflammatory cytokines and Nrf2/Ho-1 pathway. JBMT. 2019;33(10):e22386.

[39] Subbiah R, Tiwari RR. The herbicide paraquat-induced molecular mechanisms in the development of acute lung injury and lung fibrosis. Crit Rev Toxicol. 2021;51(1):36-64.

[40] Zhang W, Fievez L, Cheu E, Bureau F, Rong W, Zhang F, et al. Anti-inflammatory effects of formoterol and ipratropium bromide against acute cadmium-induced pulmonary inflammation in rats. Eur J Pharmacol. 2010;628(1-3):171-8.

[41] Yesildag K, Gur C, Ileriturk M, Kandemir FM. Evaluation of oxidative stress, inflammation, apoptosis, oxidative DNA damage and metalloproteinases in the lungs of rats treated with cadmium and carvacrol. Mol Biol Rep. 2022;49(2):1201-11.

[42] Zhang F, Hu L, Wu Y-x, Fan L, Liu W-t, Wang J, et al. Doxycycline alleviates paraquat-induced acute lung injury by inhibiting neutrophil-derived matrix metalloproteinase 9. Int Immunopharmacol. 2019;72:243-51.

[43] Liu M-w, Liu R, Wu H-y, Li Y-y, Su M-x, Dong M-n, et al. Radix puerariae extracts ameliorate paraquat-induced pulmonary fibrosis by attenuating follistatin-like 1 and nuclear factor erythroid 2p45-related factor-2 signalling pathways through downregulation of miRNA-21 expression. BMC Complement Altern Med. 2015;16(1):1-15.

56

[44] Yao R, Cao Y, He Y-r, Lau WB, Zeng Z, Liang Z-a. Adiponectin attenuates lung fibroblasts activation and pulmonary fibrosis induced by paraquat. PLoS One. 2015;10(5):e0125169.

[45] Yang X, Fang Y, Hou J, Wang X, Li J, Li S, et al. The heart as a target for deltamethrin toxicity: Inhibition of Nrf2/HO-1 pathway induces oxidative stress and results in inflammation and apoptosis. Chemosphere. 2022;300:134479.

[46] Varışlı B, Darendelioğlu E, Caglayan C, Kandemir FM, Ayna A, Genç A, et al. Hesperidin Attenuates Oxidative Stress, Inflammation, Apoptosis, and Cardiac Dysfunction in Sodium Fluoride-Induced Cardiotoxicity in Rats. Cardiovasc Toxicol. 2022;23:1-9.

[47] Hou W, Zhu X, Liu J, Map J. Inhibition of miR-153 ameliorates ischemia/reperfusion-induced cardiomyocytes apoptosis by regulating Nrf2/HO-1 signaling in rats. Biomed Eng Online. 2020;19(1):1-14.

[48] Semis HS, Kandemir FM, Kaynar O, Dogan T, Arikan SM. The protective effects of hesperidin against paclitaxel-induced peripheral neuropathy in rats. Life Sci. 2021;287:120104.

[49] Semis HS, Gur C, Ileriturk M, Kandemir FM, Kaynar O. Evaluation of therapeutic effects of quercetin against Achilles tendinopathy in rats via oxidative stress, inflammation, apoptosis, autophagy, and metalloproteinases. Am J Sports Med. 2022;50(2):486-98.

[50] Kandemir FM, Kucukler S, Caglayan C, Gur C, Batil AA, Gülçin İ. Therapeutic effects of silymarin and naringin on methotrexate-induced nephrotoxicity in rats: Biochemical evaluation of anti-inflammatory, antiapoptotic, and antiautophagic properties. J Food Biochem. 2017;41(5):e12398.

[51] Caglayan C, Kandemir FM, Ayna A, Gür C, Küçükler S, Darendelioğlu E. Neuroprotective effects of 18β-glycyrrhetinic acid against bisphenol A-induced neurotoxicity in rats: involvement of neuronal apoptosis, endoplasmic reticulum stress and JAK1/STAT1 signaling pathway. Metab Brain Dis. 2022;37:1931-40.

[52] Salama OA, Attia MM, Abdelrazek MA. Modulatory effects of swimming exercise against malathion induced neurotoxicity in male and female rats. Pestic Biochem Physiol. 2019;157:13-8.

[53] Dos Santos AA, Naime AA, de Oliveira J, Colle D, Dos Santos DB, Hort MA, et al. Long-term and low-dose malathion exposure causes cognitive impairment in adult mice: evidence of hippocampal mitochondrial dysfunction, astrogliosis and apoptotic events. Arch toxicol. 2016;90(3):647-60.

57

Türk Doğa ve Fen Dergisi
Turkish Journal of Nature and Science
www.dergipark.gov.tr/tdfd

Utilization of Demolition Waste for Treatment of Acid Mine Drainage and Immobilization of Heavy Metals Released from Copper Flotation Tailings

Gulsen TOZSIN[1*], Ercument KOC[1], Banu YAYLALI[2], Haci DEVECI[3]

[1]Ataturk University, Faculty of Engineering, Department of Metallurgical and Materials Engineering, Erzurum, Türkiye
[2]Ataturk University, Faculty of Engineering, Department of Mechanical Engineering, Erzurum, Türkiye
[3]Karadeniz Technical University, Faculty of Engineering, Department of Mining Engineering, Trabzon, Türkiye
Gulsen TOZSIN ORCID No: 0000-0001-5653-9919
Ercument KOC ORCID No: 0000-0002-9804-4620
Banu YAYLALI ORCID No: 0000-0002-9488-3910
Haci DEVECI ORCID No: 0000-0003-4105-0912

*Corresponding author: gulsentozsin@gmail.com

Abstract: In this study, the treatment of acid mine drainage (AMD) and immobilization of heavy metals released from CFT (copper flotation tailings) were investigated using strongly alkaline demolition waste (DW), collected from the urban renewal areas. Shake flask batch tests were conducted to assess the influence of time and different ratios of CFT/DW on the acidity and heavy metal release characteristics of the drainage water. During the tests, samples were collected from filtered leachates at regular intervals to monitor pH, SO_4^{2-} and release of heavy metals. The results indicated that the pH increased from 2.21 (t=0) to 10.37 after 120 minutes of shaking in an orbital shaker. The highest SO_4^{2-} release ($[SO_4^{2-}]$=4558 mg L^{-1}, t=0) was measured at 1:3 dose of CFT:DW application with 257 mg L^{-1} (pH=10.37) at the end of 120 minutes. The addition of DW almost completely reduced the release of heavy metals from CFT due to its high alkaline content. As a result, it was suggested that DW could effectively be used for the treatment of AMD and immobilization of heavy metals released from CFT.

Bakır Flotasyon Atıklarından Ağır Metal Salınımının Önlenmesi ve Asit Maden Drenajının İyileştirilmesi için Yıkıntı Atıklarının Kullanımı

Öz: Bu çalışmada, kentsel dönüşüm alanlarından toplanan güçlü alkali özelliğe sahip yıkıntı atıkları (DW) kullanılarak asit maden drenajının (AMD) iyileştirilmesi ve bakır flotasyon atıklarından (CFT) salınan ağır metallerin önlenmesi araştırılmıştır. Drenaj suyunun asitliği ve ağır metal salınımı üzerinde zamanın ve farklı CFT/DW oranlarının etkisini değerlendirmek için çalkalama testleri yapılmıştır. Testler sırasında pH, SO_4^{2-} ve ağır metal salınımını izlemek için filtrelenmiş sızıntı sularından düzenli aralıklarla numuneler toplanmıştır. Sonuçlar, çalkalayıcıda 120 dakika çalkalandıktan sonra pH'ın 2.21'den (t=0) 10.37'ye yükseldiğini göstermiştir. En yüksek SO_4^{2-} salınımı ($[SO_4^{2-}]$=4558 mg L^{-1}, t=0) 120 dakika sonunda 1:3 doz CFT:DW uygulamasında 257 mg L^{-1} (pH=10.37) olarak ölçülmüştür. DW ilavesi yüksek alkali içeriği nedeniyle CFT'den ağır metal salınımını neredeyse tamamen azaltmıştır. Sonuç olarak, DW'nin AMD iyileştirmesinde ve CFT'den salınan ağır metallerin önlenmesinde etkin bir şekilde kullanılabileceği önerilmiştir.

1. INTRODUCTION

Acid mine drainage (AMD) is an environmental concern due to its adverse effects on the surrounding ecosystem. When sulfide minerals such as pyrite are exposed to oxidation in a humid environment, they can release protons (H$^+$ ions) to the aqueous environment (1). Thus, the water acquires an acidic character with a concomitant decrease in pH and increased release of most heavy metals [1-3]:

58

$$4FeS_2+15O_2+14H_2O \rightarrow 4Fe(OH)_{3\downarrow}+8SO_4^{2-}+16H^+ \quad (1)$$
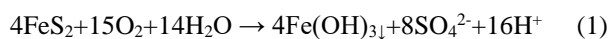
The resulting acidic waters with high metal content are defined as AMD. Once AMD starts, it is very hard to stop and very expensive to control. Therefore, special precautions must be taken to prevent AMD formation [4,5]. Prevention techniques should be designed at the source to reduce or eliminate the drainage of the acidic water. Prevention at the source, i.e., prevention at the acid formation stage, can be possible by increasing the neutralization capacity of the minerals, such as CFT, by applying alkaline material having neutralization potential, such as DW [6,7].

The control and management of solid wastes are one of the biggest problems. Today, although the rates vary depending on the country and the city, construction and demolition wastes have a large share in solid waste [8,9]. More than 90% of waste is generated by demolition, while new construction accounts for less than 10%. In 2015, waste from construction sites accounted for 23.1 million tons and waste from demolition sites accounted for 358.7 million tons globally [10]. The transportation and storage costs of DW are quite high. In addition, very large natural areas are occupied for the storage of these wastes, which may cause the degradation of soil in these areas with the loss of its fertility and hence, agricultural land [11,12]. Therefore, the utilization of DW is of great environmental and economic importance.

In Turkey, the main problem in the urban renewal process is the limited availability of storage facilities where the waste will be safely disposed of after demolition to control its harmful effects on the environment. It is necessary to investigate the potential use of DW as raw material in industrial applications, which will contribute to environmental sustainability and the protection of natural resources. When alkaline materials, such as DW, are added to an acidic environment, they not only increase the pH of the environment but also allow heavy metals in the solution to precipitate and thus, largely eliminate AMD-driven problems leading to severe environmental problems [1,13,14]. Post-mining activities are among the most important conditions for sustainable development, and developed countries successfully perform these activities. It is possible to prevent surface and underground water pollution by eliminating the potential of mining wastes to produce acid by using alkaline materials such as DW. This study investigated the effectiveness of DW utilization for AMD treatment and the precipitation of heavy metals released from CFT.

2. MATERIAL AND METHOD

2.1. Materials

CFT, a waste product of the flotation process used to enrich copper sulfide ores, was obtained from Murgul Copper Mine in Artvin, Turkey. DW was collected from the buildings in Yakutiye district in Erzurum (Turkey), demolished due to the urban renewal within the scope of the Cultural Road Project, which is being carried out with the support of Erzurum Metropolitan Municipality. CFT

particles were smaller than 75 μm in diameter, while DW sample was ground down to 75 μm. Pure $CaCO_3$ powder (pH=9; $CaCO_3$=100% wt) was also used as a reference material (Merck-102066) to compare the effectiveness of DW on the CFT neutralization process.

2.2. Experimental Procedure

Static and kinetic tests were carried out to determine the acid-producing potential (APP) of CFT and the neutralization potential of DW. The acid-base accounting method [15] was used in the static tests to determine APP based on the total sulfide content of CFT (APP = 31.25 x 42(%S)) [16]. DW was utilized as neutralization material to treat CFT at a dose of 1.31 units per unit CFT. This dose was determined using the following stoichiometry of FeS_2 and $CaCO_3$ (2), which predicts the amount of lime required to neutralize all of the potential acids based on the percentage of sulfides present in CFT.
$$FeS_2+2CaCO_3+3.75O_2+1.5H_2O \rightarrow Fe(OH)_3+2SO_4^2+2Ca^{2+}+2CO_2 \quad (2)$$

Kinetic tests are performed to evaluate the acid generation potential and leachate quality of mine waste and process tailings [16]. Shake flask batch tests, one of the kinetic test methods, were conducted to evaluate the effect of mixing ratio of CFT to DW and shaking time on the evolution of pH, the release of SO_4^{2-} and heavy metals into the leachate.

After the required amounts of CFT and DW samples, and distilled water were placed in a flask at the tested dosage of DW, the flask was placed onto an orbital shaker (WiseCube, WIS-20R). Test conditions for shake flask batch tests are given in Table 1. The solid-liquid ratio was set as 2 L kg^{-1} [16]. Using pure $CaCO_3$ instead of DW, a control test without a neutralizing additive, e.g., DW or $CaCO_3$, was also conducted to compare the effect of DW on the CFT neutralization process. Under normal conditions, while it is required to use 1312.5 kg $CaCO_3$ to neutralize 1 ton of waste pyrite containing 42% S, 66 g $CaCO_3$ is required to neutralize 50 g waste pyrite. However, since DW contains $CaCO_3$ by 30.44%, 217 g DW was used instead of 66 g DW to neutralize 50 g CFT at 1:1 dose of CFT:DW application. Based on the purity of DW, it is assumed that DW cannot completely react with CFT and therefore, different doses of DW were also used in the shake flask batch tests (Table 1).

Table 1. Test conditions for shake flask batch tests

Series	CFT	DW	Distilled water
	(g)		(mL)
CFT (control)	50	-	100
CFT+pure $CaCO_3$	50	66	232
CFT+DW (1:1)	50	217	534
CFT+DW (1:0.5)	50	109	318
CFT+DW (1:1.5)	50	326	752
CFT+DW (1:2)	50	434	968
CFT+DW (1:2.5)	50	543	1186
CFT+DW (1:3)	50	651	1042

Samples prepared were shaken in flasks under continuous stirring at 180 rpm (23 ± 2 °C) for a total of 120 minutes. During the leaching period, pH measurements were

performed every 15 minutes. Samples were taken with a syringe every 60 minutes, passed through filter paper. Filtered samples were stored at 4°C for SO_4^{2-} and heavy metals analyses.

2.3. Analytical Procedure

The mineralogical compositions of CFT and DW samples were determined by X-Ray diffraction (XRD) (RIGAKU, D/Max-2000). SO_4^{2-} concentration was analyzed as specified in method 375.4 of EPA [17]. The pH was measured using an Orion 420A + pH/mV/ORP device. The $CaCO_3$ content was determined using a calcimeter [18]. The total sulfide content of CFT was evaluated by using the methods given in the Turkish Standards Institution [19]. Heavy metal concentration was determined using inductively coupled plasma mass spectrometry (ICP-OES; PerkinElmer Sciex Elan). The scanning electron microscopy (SEM, FEI Quanta 400 MK2) coupled with Energy Dispersive X-ray Spectrometry (EDS, EDAX Genesis XM4 Imaging detector) was used for morphological analysis and identification and quantification of elements after 1:3 dose (max) of CFT:DW application.

3. RESULTS AND DISCUSSION

3.1. Characteristics of CFT and DW

The pH value and total sulfide content of CFT obtained from Murgul Copper Mine were measured as 2.21 and 42% respectively. The $CaCO_3$ content of DW obtained from urban renewal areas in Erzurum was determined as 30.44% with a pH of 11.07.
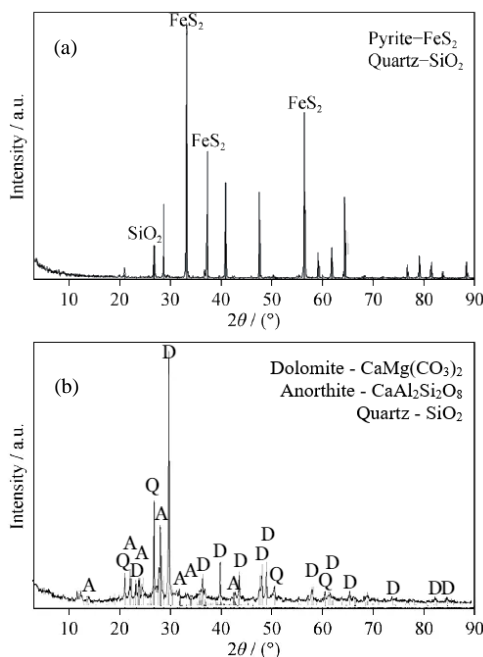

Figure 1. The XRD pattern of a) CFT and b) DW

The XRD analysis results indicate that the major minerals in the CFT sample are pyrite (FeS_2) and quartz (SiO_2); and the major minerals in DW are dolomite ($CaMg(CO_3)_2$), anorthite ($CaAl_2Si_2O_8$) and quartz (SiO_2), respectively (Figure 1).

3.2. Experimental Results

To determine the neutralization potential of DW applied on CFT at different doses, the changes of the leachate pH values over time were investigated (Figure 2). At the end of 120 minutes of shaking, pH remained stable around 2.21 in the control group. Significant increases were observed in the pH values of CFT leachate treated with pure $CaCO_3$ and different doses of DW at the first 15 minutes. No significant changes were observed in the following periods. In the pure $CaCO_3$ applied sample, the pH value of the leachate, which was 2.21 (t=0), increased to 6.60 after 15 minutes of shaking. The greatest pH change occurred at 1:3 dose of CFT:DW application. It was noted that the pH value increased from 2.21 to 10.09 after 15 minutes and 10.37 after 120 minutes of shaking. Johnson and Halberg [20] and Zinc and Griffith [21] stated in their studies that acidity was neutralized by increasing the pH of the environment with alkaline materials like lime or limestone.
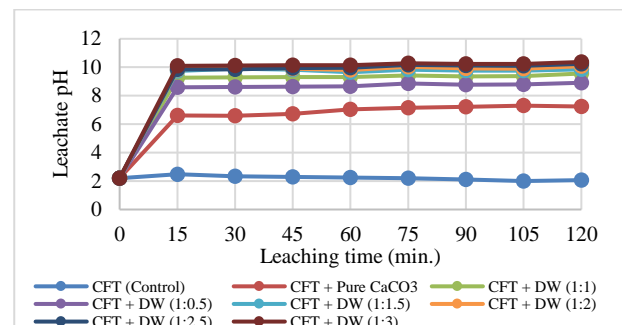
Figure 2. The effect of time on the leachate pH values at different application doses of DW on CFT

After separating the filtered leachate, the solids remaining on the filter paper were dried and examined under SEM-EDS. SEM images and the EDS pattern of the leaching residue obtained after 1:3 dose (max) of CFT:DW application show that the main elements are Si, Ca, Al and Mg due to neutralization of CFT with DW applications (Figure 3).

No significant changes in SO_4^{2-} concentration of the leachates were observed in the control group depending on the pH value, while serious decreases were observed in the SO_4^{2-} value in pure $CaCO_3$ and DW applications after 60 minutes, and not much change was observed at the end of 120 minutes. The SO_4^{2-} value was measured as 982 mg L^{-1} (pH=7.03) and 970 mg L^{-1} (pH=7.23) with pure $CaCO_3$ application at the end of the 60 and 120 minutes, respectively. In DW application, the lowest SO_4^{2-} value was observed at the 1:3 dose of CFT:DW. At this dose application, the SO_4^{2-} value, which was 4558 mg L^{-1} at the beginning (t=0, pH=2.21), was observed as 274 mg L^{-1} (pH=10.14) and 257 mg L^{-1} (pH=10.37) after 60 minutes and 120 minutes, respectively (Table 2). DW application affected the pH value and SO_4^{2-} concentration in the leachate. As the application doses of DW increased, the pH of the leachate increased and SO_4^{2-} concentration decreased due to the neutralization capacity of DW. Since SO_4^{2-} ion precipitated in the form of $CaSO_4$ and its concentration decreased in the environment. Madzivire et al. [22] and Name and Sheridan [23] stated in their studies

Tr. Doğa ve Fen Derg. Cilt 11, Sayı 3, Sayfa 58-62, 2022

Tr. J. Nature Sci. Volume 11, Issue 3, Page 58-62, 2022

that the SO_4^{2-} concentration decreased depending on the increase in pH.

Figure 3. SEM images and EDS pattern of leaching residue obtained after 1:3 dose (max) of CFT:DW application

Table 2. SO_4^{2-} concentration in the leachates

Series	Time (min)	pH	SO_4^{2-} (mg L^{-1})
Start	0	2.21	4558
CFT (control)	60	2.25	4417
	120	2.06	4550
CFT+Pure CaCO₃	60	7.03	982
	120	7.23	970
CFT+DW (1:1)	60	9.31	852
	120	9.56	841
CFT+DW (1:0.5)	60	8.66	757
	120	8.91	748
CFT+DW (1:1.5)	60	9.65	665
	120	9.86	652
CFT+DW (1:2)	60	9.81	443
	120	10.07	426
CFT+DW (1:2.5)	60	9.97	378
	120	10.24	365
CFT+DW (1:3)	60	10.14	274
	120	10.37	257

Depending on their neutralization capacity, the effects of different application doses of DW on heavy metal release from CFT were investigated. Concentrations of the heavy metals in the leachate at the end of 60 and 120 minutes during the shake flask batch tests and standard limits allowed by WHO [24] are given in Table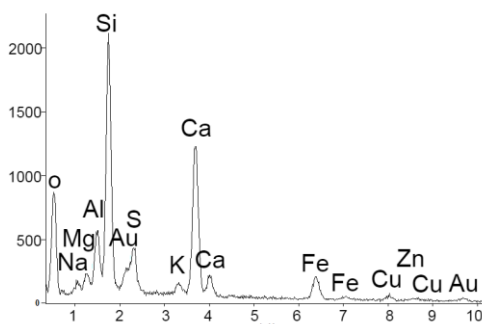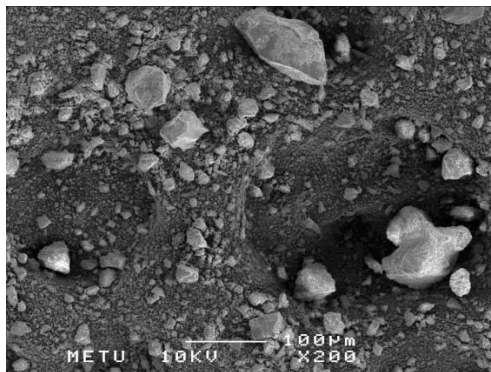 3. No significant changes in Cd, Cr, Cu, Fe and Zn concentrations were observed in the control group in the leachate after 120 minutes of shaking with initial values of 3.45 mg L^{-1}, 2.99 mg L^{-1}, 264 mg L^{-1}, 479 mg L^{-1} and 20.14 mg L^{-1} (t=0), respectively. At the beginning of the tests, the heavy metal concentrations in the leachates were high while they decreased with the addition of pure CaCO₃ and DW application. In pure CaCO₃ application and all dose applications of DW; Cd, Cr, Cu, Fe and Zn values decreased below the limit values of 0.003 mg L^{-1}, 0.05 mg L^{-1}, 2 mg L^{-1}, 0.3 mg L^{-1} and 3 mg L^{-1}, respectively at the

end of 60 minutes. The results indicated that DW reduced the Cd, Cr, Cu, Fe and Zn concentrations in the leachate, due to the alkaline content of DW, which neutralized the acidity, reducing the leachability and solubility of metals under alkaline conditions achieved in the tests [25]. Szymanski and Janowska [26] and Tenodi et al. [27] stated that the decrease in pH might cause an elevated level of heavy metals in the leachate and negatively affect the surrounding ecosystems. Feng et al. [28] and Rose [29] neutralized acid by using DW in similar studies and showed that no iron was found in the leachate due to the precipitation. Cui et al. [30] and Rodriguez-Jorda et al. [31] explained that the release of heavy metals could be prevented by using alkaline materials such as DW.

Table 3. Heavy metal concentrations in the leachate and limit values

Series	Time (min)	Cd	Cr	Cu	Fe	Zn
		(mg L^{-1})				
Start	0	3.45	2.99	264	479	20.14
CFT (control)	60	3.12	3.02	257	496	22.11
	120	4.33	3.01	265	481	21.18
CFT+Pure CaCO₃	60	<0.005	<0.005	0.033	<0.005	0.269
	120	<0.005	<0.005	0.034	<0.005	0.092
CFT+DW (1:1)	60	<0.005	<0.005	0.671	<0.005	<0.005
	120	<0.005	<0.005	0.556	<0.005	<0.005
CFT+DW (1:0.5)	60	<0.005	<0.005	0.744	<0.005	<0.005
	120	<0.005	<0.005	0.871	<0.005	<0.005
CFT+DW (1:1.5)	60	<0.005	<0.005	0.478	<0.005	<0.005
	120	<0.005	<0.005	0.308	<0.005	<0.005
CFT+DW (1:2)	60	<0.005	<0.005	0.114	<0.005	<0.005
	120	<0.005	<0.005	0.161	<0.005	<0.005
CFT+DW (1:2.5)	60	<0.005	<0.005	0.174	<0.005	<0.005
	120	<0.005	<0.005	0.103	<0.005	<0.005
CFT+DW (1:3)	60	<0.005	<0.005	0.076	<0.005	<0.005
	120	<0.005	<0.005	0.068	<0.005	<0.005
Limit values [24]		0.003	0.05	2	0.3	3

4. CONCLUSIONS

This study investigated the utilization of DW for the treatment of AMD and immobilization of heavy metals released from copper flotation tailings. The results showed that as a result of DW applications at different doses on the CFT neutralization process, the greatest pH change was observed at 1:3 dose of CFT:DW application. The pH value increased from 2.21 to 10.37 at the end of 120 minutes. Depending on the increase in pH, SO_4^{2-} concentration decreased from 4558 (t=0, pH=2.21) to 257 mg L^{-1} (pH:10.37) and Cd, Cr, Cu, Fe and Zn concentrations were almost completely reduced in the leachate at 1:3 dose of CFT:DW application after 120 minutes of leaching. Considering the environmental quality and health, neutralizing acidity and removing heavy metals released from CFT is of paramount importance, and it could be achieved using DW generated during demolition activities.

REFERENCES

[1] Akcil A, Koldas S. Acid mine drainage (AMD): causes, treatment and case studies. J Clean Prod. 2006; 14: 1139-1145.

[2] Tozsin G, Arol AI, Cayci G. Evaluation of pyritic tailings from a copper concentration plant for calcareous sodic soil reclamation. Physicochem Probl Miner Process. 2014; 50 (2): 693-704.

[3] Pandey S, Kankeu EF, Redelinghuys J, Kim J, Kang M. Implication of biofilms in the sustainability of acid mine drainage and metal dispersion near coal tailings. Sci Total Environ. 2021; 788: 147851.

[4] Menzel K, Barros L, García A, Figueroa RR, Estay H. Metal sulfide precipitation coupled with membrane filtration process for recovering copper from acid mine drainage. Sep Purif Technol. 2021; 270: 118721.

[5] Silva D, Weber C, Oliveira C. Neutralization and uptake of pollutant cations from acid mine drainage (AMD) using limestones and zeolites in a pilot-scale passive treatment system. Miner Eng. 2021; 170: 107000.

[6] Alcolea A, Vazquez M, Caparros A, Ibarra I, Garcia C, Linares R, Rodriguez R. Heavy metal removal of intermittent acid mine drainage with an open limestone channel. Miner Eng. 2012; 26: 86-98.

[7] Valero AG, Martínez SM, Faz A, Rivera J, Acosta JA. Environmentally sustainable acid mine drainage remediation: use of natural alkaline material. J Water Process Eng. 2020; 33: 101064.

[8] Huang WL, Lin DH, Chang NB, Song K. Recycling of C&D waste via a mechanical sorting process. Resour Conserv Recycl. 2002; 37: 23-37.

[9] Marzouk M, Azab S. Environmental and economic impact assessment of construction and demolition waste disposal using system dynamics. Resour Conserv Recycl. 2014; 82: 41-49.

[10] EPA. Advancing sustainable materials management: Facts and Figures Reports. Assessing trends in material generation, recycling, composting, combustion with energy recovery and landfilling in the United States, July, 1-23; 2018.

[11] Shi M, Ling TC, Gan B, Guo MZ. Turning concrete waste powder into carbonated artificial aggregates. Constr Build Mater. 2019; 199: 178-184.

[12] Gencel O, Erdugmus E, Sutcu M, Oren OH. Effects of concrete waste on characteristics of structural fired clay bricks. Constr Build Mater. 2020; 255: 119362.

[13] Damrongsiri S. Feasibility of using demolition waste as an alternative heavy metal immobilising agent. J Environ Manage. 2017; 192: 197-202.

[14] Giampaolo C, Mastro SL, Polettini A, Pomi R, Sirini P. Acid neutralisation capacity and hydration behaviour of incineration bottom ash-portland cement mixtures. Cem Concr Res. 2002; 32: 769-775.

[15] Sobek AA, Schuller WA, Freeman JR, Smith RM. Field and laboratory methods applicable to overburden and minesoils, EPA 600/2-78-054, 203; 1978.

[16] EPA. Acid mine drainage prediction. EPA Technical Document 530 R 94 036, NTIS PB94-201829, Washington DC, USA; 1994.

[17] EPA. Sulfate turbidimetric. Method 375.4, Methods for the chemical analysis of water and wastes, EPA/600/4–79/020. US Environmental Protection Agency, Washington DC, USA; 1979.

[18] Nelson RE. Carbonate and Gypsum. In: A.L. Page (Editor). Methods of soil analysis. Part 2. Chemical and microbiological properties. American Society of Agronomy. Soil Science Society of America. Publisher. Madison, Wisconsin; 1982. p. 181-196.

[19] Turkish Standards Institution (TSI). Copper and copper alloys, determination of sulfur content-combustion titrimetric method, Ankara, Turkey; 1987.

[20] Johnson DB, Hallberg KB. Acid mine drainage remediation options: a review. Sci Total Environ. 2005; 338 (1-2): 3-14.

[21] Zinck J, Griffith W. Review of mine drainage treatment and sludge management operations. Natural Resources Canada, Mine Environment Neutral Drainage Program. MEND Report 3.43.1; 2013.

[22] Madzivire G, Gitari WM, Vadapalli VRK, Ojumu TV, Petrik LF. Fate of sulphate removed during the treatment of circum-neutral mine water and acid mine drainage with coal fly ash: modelling and experimental approach. Miner Eng. 2011; 24: 1467-1477.

[23] Name T, Sheridan C. Remediation of acid mine drainage using metallurgical slags. Miner Eng. 2014; 64: 15-22.

[24] WHO. Guidelines for drinking-water quality. 4th ed. Incorporating the First Addendum, Geneva, Switzerland; 2017.

[25] Kjeldsen P, Barlaz MA, Rooker AP, Baun A, Ledin A, Christensen TH. Present and long-term composition of MSW landfill leachate: a review. Crit Rev Environ Sci Technol. 2002; 32 (4): 297-336.

[26] Szymanski K, Janowska B. Migration of pollutants in porous soil environment. Arch Environ Prot. 2016; 42 (3): 87–95.

[27] Tenodi S, Krcmar D, Agbaba J, Zrnic K, Mira R. Assessment of the environmental impact of sanitary and unsanitary parts of a municipal solid waste landfill. J Environ Manage. 2020; 258: 110019.

[28] Feng D, van Deventer JSJ, Aldrich C. Removal of pollutants from acid mine wastewater using metallurgical by-product slags. Sep Purif Technol. 2004; 40: 61-67.

[29] Rose AW. Advances in passive treatment of coal mine drainage 1998–2009. In: Proceedings of the 27th ASMR, Pittsburgh, PA; 2010. p. 847–887.

[30] Cui M, Jang M, Cho SH, Khim J, Cannon FS. A continuous pilot-scale system using coal-mine drainage sludge to treat acid mine drainage contaminated with high concentrations of Pb, Zn, and other heavy metals. J Hazard Mater. 2012; 215 (216): 122-128.

[31] Rodriguez-Jorda MP, Garrido F, Garcia-Gonzalez MT. Effect of the addition of industrial by-products on Cu, Zn, Pb and As leachability in a mine sediment. J Hazard Mater. 2012; 213 (214): 46-54.

62

Türk Doğa ve Fen Dergisi
Turkish Journal of Nature and Science
www.dergipark.gov.tr/tdfd

Effect of Alkali Modulus on the Compressive Strength and Ultrasonic Pulse Velocity of Alkali-Activated BFS/FS Cement

Murat DENER[1]

[1] Bingol University, Engineering and Architecture Faculty, Civil Engineering Department, Bingöl, Türkiye
Murat DENER ORCID No: 0000-0001-6430-8854

Corresponding author: mdener@bingol.edu.tr

Abstract: Portland cement, which has been used as an unrivaled binder material since its development has become one of major sources of greenhouse gas emission. Compared with the conventional cement, alkali-activated materials which based on the principle of activating precursor materials by means of alkali activators have comparable engineering properties and lower CO_2 emission during its production. In this study, the effect of alkali modulus on the compressive strength and ultrasonic pulse velocity of granulated blast furnace slag (BFS)/ferrochrome slag (FS)-based alkali-activated cement was investigated. Alkali-activated cement was produced from the mixture of a blast furnace slag and ferrochrome slag in proportion 80% and 20% respectively. Alkali modulus of 0.8, 1.0, 1.2, 1.4 were adopted in the test. Mortar specimens with the alkali modulus of 0.8 and 1 had a compressive strength of 6.43 MPa and 9.75 MPa, respectively, while specimens with the modulus of 1.2 and 1.4 gained approximately half of their 28-day strength in the first three days. The 28-days UPV values of the specimens with alkali modulus of 0.8, 1, 1.2 and 1.4 were 4117, 4032, 3831 and 3697 m/s, respectively.

Alkali Modülünün Alkali-Aktif YFC/FC Çimentosunun Basınç Dayanımı Ve UPV Hızı Üzerindeki Etkisi

Öz: Geliştirildiği günden bu yana rakipsiz bir bağlayıcı malzeme olarak kullanılan Portland çimentosu, sera gazı emisyonunun başlıca kaynaklarından biri haline gelmiştir. Geleneksel çimento ile karşılaştırıldığında, öncü malzemelerin alkali aktivatörler vasıtasıyla etkinleştirilmesi prensibine dayanan alkali-aktif malzemeler, benzer mühendislik özelliklerine sahip olmalarının yanısıra üretiminden kaynaklanan CO_2 emisyonu çok daha düşüktür. Bu çalışmada, alkali modülünün yüksek fırın cürufu/ferrokrom cürufu esaslı alkali-aktif çimentonun basınç dayanımı ve ultrasonik geçiş hızı üzerindeki etkisi araştırılmıştır. Alkali-aktif çimentonun bağlayıcı malzemesi %80 oranında yüksek fırın cürufu, %20 oranında ferrokrom cürufundan oluşmaktadır. Test edilecek alkali modülleri 0.8, 1.0, 1.2, 1.4 olarak belirlenmiştir. Alkali modülü 0.8 ve 1 olan harç numunelerinin basınç dayanımları sırasıyla 6,43 MPa ve 9,75 MPa iken alkali modülü 1.2 ve 1.4 olan numuneler ilk üç günde 28 günlük dayanımlarının yaklaşık olarak yarısını kazanmıştır. Alkali modülü 0.8, 1, 1.2 ve 1.4 olan numunelerin 28 günlük UPV değerleri sırasıyla 4117, 4032, 3831 ve 3697 m/s olarak ölçülmüştür.

1. INTRODUCTION

Cement, used as a binding material in concrete, constitutes around 10% of conventional concrete by mass and is manufactured at a rate of around 4 gigatonnes (Gt) per year [1]. Over the more than past half century, cement consumption has increased tenfold, while steel production has only increased by a factor of three [1], [2]. Cement is responsible for 36% of the 7.7

Gt of CO_2 released globally by construction activities in 2010 [1], [3].

With the increase in infrastructure activities throughout the world, especially in developing countries, the demand for cement has continuously been increasing. Many concerns regarding CO_2 emission, raw materials consumption and energy are incorporated with Portland cement (PC) productions [4]. Although developments in PC production technology provide a reduction in energy

consumption and harmful emissions, PC manufacturing produces approximately 0.8 tons of CO_2 per ton of PC [5], [6]. These reasons have motivated researchers to study on alternative materials to substitute PC. Alkali-activated materials (AAM) are potential alternatives to the traditional cement [5].

The main benefit of AAM is that it significantly reduces CO2 emissions [7]. Besides having good mechanical properties, its chemical resistance is better than PC [4], [8]–[10]. AAMs are manufactured by activating the precursor with alkali activators. High alkalinity conditions are required for AAM production. Some of the precursor materials used in alkali activation systems are blast furnace slag (BFS), fly ash, metakaolin etc. Sodium hydroxide (NaOH) and sodium silicate (Na_2SiO_3) are most used activators to activate these precursor materials. Under high alkali conditions, aluminosilicates dissolve in water and decompose into alumina and silica units. Then these units combine to form polymeric bonds [4], [11], [12].

Alkali-activated slag are considered as alternative binder material to PC that can be activated by alkali activator such as Na_2SiO_3 and NaOH [5]. Early mechanical strengths, low porosity, lower heat of hydration and superior durability are some advantages of alkali-activated slag [13], [14]. The main reaction product formed by alkali activation of blast furnace slag is an aluminum-substituted C-A-S-H-type gel which has a disordered tobermorite-like structure. Regardless of the activator used, the C-A-S-H-type gel has a lower calcium content than a hydrated PC system, whose Ca/Si ratio is usually between 1.5 and 2.0 [15]. There are several factors affecting the properties of alkali-activated slag such as raw materials used, activator type, liqiud to solid ratio, the curing temperature, alkali dosage and modulus etc. [5].

There are many studies [4], [16]–[18] investigating the impact of silicate modulus (Ms) and alkali dosage on the strength of alkali-activated slag. Compressive strength generally increases as the alkali dosage increases, provided that it is between 2% and 8% by slag mass [19]–[21]. The impact of Ms on the strength is more complex. At a constant dosage as the Ms increases the compressive strength increases because of the formation of more silica gel. The optimum Ms is found to be lower when the alkalinity of slag is lower. Above the optimum modulus compressive strength may decrease as the Ms increases [16], [20]. There are several studies [22]–[24] on the usage of ferrochrome slag (FS) to produce alkali-activated cements. Karakoç et al. [25] investigated the effect of silicate modulus on alkali-activated cement produced with FS. More research are needed to investigate the effect of the alkali modulus on the ferrrochrome based alkali-activated cement.

Within the scope of this study, AAM mortars were produced by using 80% BFS and 20% FS as the precursor material. The effect of the alkali modulus on the compressive strength and ultrasonic pulse velocity (UPV) of the mortar specimens was investigated.

2. MATERIAL AND METHOD

2.1. Material

BFS and FS were used in this study as the precursors of alkali-activated cement (AAC) production. The chemical composition of the BFS and FS were given in Table 1.

Table 1. Chemical composition of BFS and FS

Constituent	BFS (%)	FS (%)
SiO_2	40.52	33.8
Al_2O_3	13.74	25.48
Fe_2O_3	1.74	0.61
CaO	33.86	1.1
MgO	7.72	35.88
SO_3	0.17	-
Na_2O	0.66	-
K_2O	0.81	-
Cr_2O_3	-	2.12
Specific gravity	2.8	2.85

The aggregate used for mortar production was natural river sand. The size distribution of the aggregate used is shown in Figure 1.
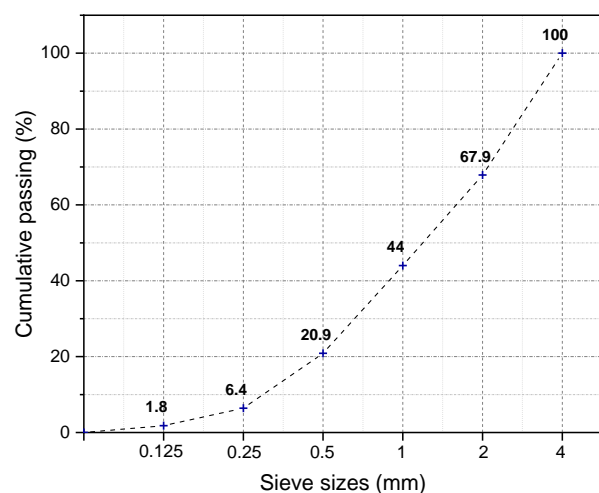
Figure 1. Size distribution of the aggregate

The mixture of NaOH and Na_2SiO_3 were used as an activator for the activation of BFS and FS. The NaOH in the form of pellets with 99% purity was used. NaOH solution was prepared by dissolving NaOH pellets in water. Na_2SiO_3 solution consisted of 28% SiO_2, 9% Na_2O, and 63% H_2O content by mass with a silica modulus of 3.11.

2.2. Mortar preparation and test procedure

A total of four mortar mixtures were prepared to investigate the effect of alkali modulus on BFS/FS based alkali activated cement. The mixture proportions are presented in Table 2.

Table 2. Mix proportions of the produced mortars

Codes	Modulus	w/b	Sand/binder	Na_2O (%)	BFS (%)	FS (%)
M0.8	0.8	0.45	2.75	6	80	20
M1.0	1.0	0.45	2.75	6	80	20
M1.2	1.2	0.45	2.75	6	80	20
M1.4	1.4	0.45	2.75	6	80	20

BFS and FS precursor were used in a mass ratio of 80:20. The precursor-to-aggregate ratio was 1:2.75 and the water-to-precursor (binder) ratio was 0.45. The alkali dosage (Na_2O by mass of the precursor materials) of all mixtures was 6 wt%. A set of mixtures were prepared with four alkali modulus. Alkali modulus refers to the ratio of total SiO_2 (wt %) to total Na_2O (wt %) in the activator mix. Figure 2 shows one of the fresh mortars prepared.

Figure 2. Fresh mortar mixture

Initially, precursor materials and aggregate were blended together for half a minute. Afterward, NaOH and Na_2SiO_3 solutions were added to the dry mixture after mixing together. Mixing continued until a homogeneous mixture (2 minutes) was obtained. Mortar mixtures were poured into steel molds of 50 mm cube. After the fresh mortars were casted, the molds were wrapped with stretch film to prevent water evaporation (Figure 3). Mortar specimens were cured at 50 °C for 24 hours and then kept at room temperature until days of testing. Literature review and preliminary experiments revealed that 50 °C curing temperature was the most suitable curing temperature in terms of compressive strength [26], [27].

Figure 3. Wrapped mold

The compressive strength test was carried out according to ASTM C109 [28]. The ultrasonic pulse velocity test was performed in accordance with ASTM C597 [29]. Figure 4 shows the compressive strength and UPV tests, respectively.

Figure 4. Compressive strength and UPV tests, respectively

3. RESULTS

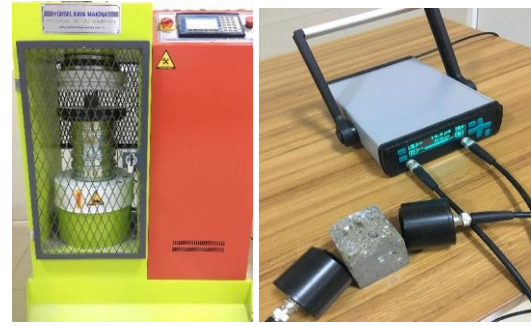### 3.1. Compressive strength results

3-day compressive strength results of mortar specimens are given in Figure 5. The compressive strength increased with the increase of alkali modulus.
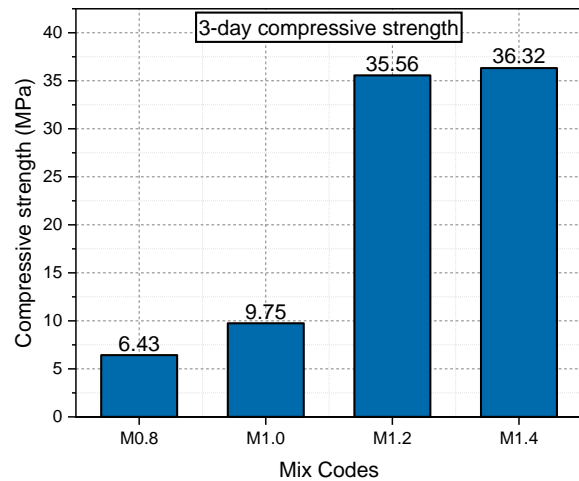
Figure 5. 3-day compressive strength results

The compressive strengths of the specimens with alkali modulus of 0.8 and 1 were considerably lower than the compressive strengths of the specimens with alkali modulus of 1.2 and 1.4. The compressive strengths of the specimens for 0.8, 1, 1.2 and 1.4 modules were measured as 6.43, 9.75, 35.56 and 36.32 MPa, respectively. When the alkali modulus was increased from 1 to 1.2, the 3-day compressive strength increased 2.45 times. It was understood that 1.2 alkali modulus is the critical value in terms of 3-day compressive strength. There was no significant difference between the 3-day compressive strength of the samples with alkali modulus of 1.2 and 1.4. The strength of the sample with an alkali modulus of 1.4 was 2.1% higher than the specimen with a modulus of 1.2. Fang et al. [17] stated that compressive strength increased with the increase of alkali modulus. The increase in compressive strength can be attributed to the high alkalinity of the exposure solution [4]. In the study conducted by Fang et al. [17] it was stated that the difference between the 28-day compressive strength and the 7-day compressive strength generally increased as the alkali modulus decreased. The fact that the 3-day compressive strength is much lower can be attributed to

65

the absence of a strong reaction between the precursor materials and the activator at low alkali modulus.

28-day compressive strength results of mortar specimens are given in Figure 6. As can be seen from the figure, the compressive strength increased as the alkali modulus increased.
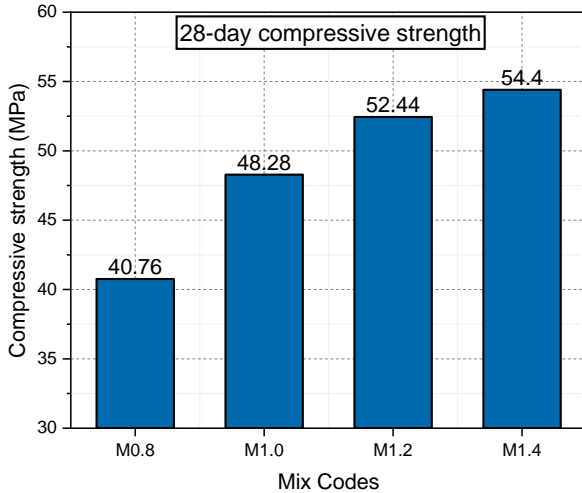
Figure 6. 28-day compressive strength results

The compressive strengths of the specimens for 0.8, 1, 1.2 and 1.4 alkali modules were measured as 40.76, 48.28, 52.44 and 54.4 MPa, respectively. The compressive strength of M1.4 specimen, which the highest strength was obtained, was 33.5% more than the M0.8 specimen, which the lowest compressive strength was obtained. This difference was 464.9% for 3-day compressive strengths. When the alkali modulus of alkali-activated BFS/FS mortar was below 1.2, the 3-day compressive strength was very low compared to the 28-day strength. It was understood that compressive strength development of the specimens with alkali modulus of 0.8 and 1 was quite slow.

Figure 7 represents the changes of the 28-day compressive strength of the mortar specimens compared to the 3-day strength.
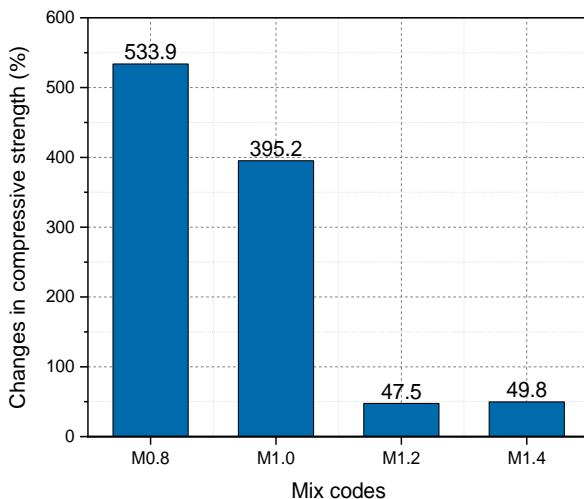
Figure 7. Changes in compressive strength

The 28-day compressive strength of the specimens with alkaline modulus of 0.8 and 1 increased considerably compared to the 3-day strengths. The 28-day strength of the specimens with an alkali modulus of 1.2 and 1.4 was approximately 50% higher than the 3-day strength. Mortar specimens with 1.2 and 1.4 alkali modules gained a very important part of their strength in the first 3 days.

3.1. UPV results

3-day UPV values of mortar specimens are given in Figure 8. The highest UPV value was obtained when the alkali modulus was 1.2.
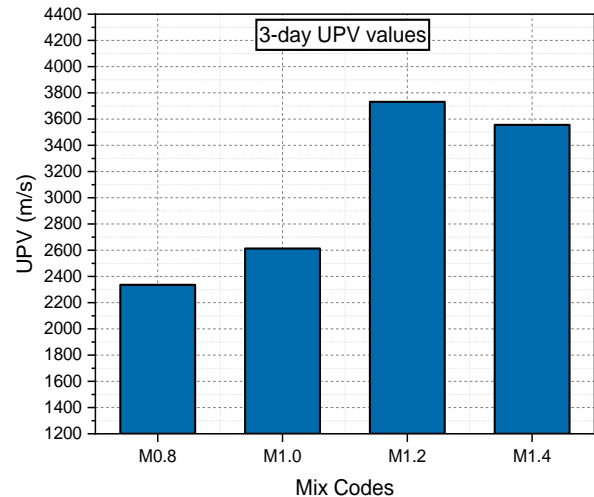
Figure 8. 3-day UPV results

The UPV values of the specimens coded M0.8, M1, M1.2 and M1.4 were 2336, 2616, 3731 and 3556 m/sec, respectively. Consistent with the results measured in the compressive strength test, the UPV values of the M0.8 and M1 coded specimens were considerably low compared to the M1.2 and M1.4 coded samples. While the highest compressive strength was obtained from the specimen coded M1.4, the highest UPV value was measured in the M1.2 coded sample. The UPV value of the M1.2 coded sample was 4.9% higher than that of the M1.4 coded sample.

28-days compressive strength results of mortar specimens are given in Figure 9.
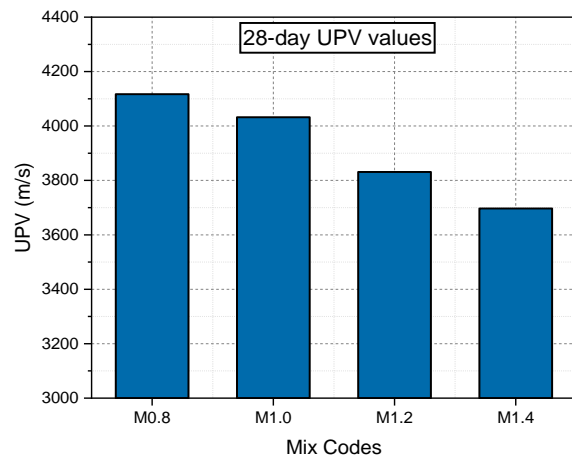
Figure 9. 28-day UPV results

The UPV values of the specimens coded M0.8, M1, M1.2 and M1.4 were 4117, 4032, 3831 and 3697 m/sec, respectively. The UPV values of all specimens increased compared to those obtained after 3 days. At the end of 28 days, the highest UPV value was obtained from the M0.8 coded specimen, while the highest compressive strength was obtained from the M1.4 coded specimen. The specimen with the highest UPV value at the end of 28 days had the lowest 3-day UPV value.

Figure 10 shows the changes of the 28-day UPV values of the mortar specimens according to the 3-day UPV values.
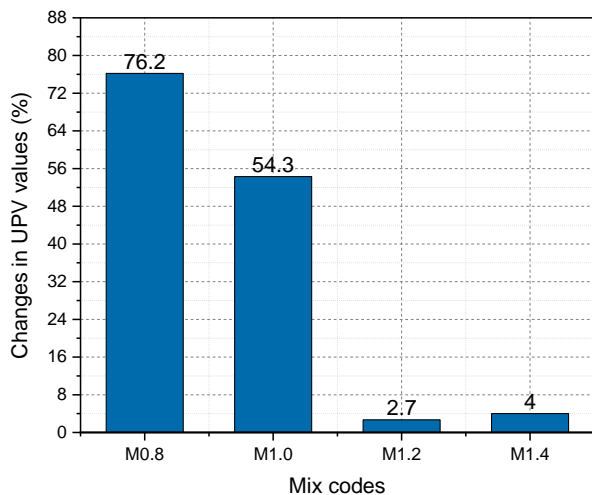
Figure 10. Changes in compressive strength

The 28-day UPV values of the mortar specimens coded M0.8, M1, M1.2 and M1.4 increased by 76.2%, 54.3, 2.7 and 4, respectively, compared to the 3-day UPV values. While the 28-day UPV values of the M1.2 and M1.4 coded mortar specimens did not change notably compared to the 3 days, the UPV values of the M0.8 and M1 coded mortar specimens increased significantly.

4. CONCLUSION

In this study, the effect of alkali modulus on the compressive strength and ultrasonic pulse velocity of granulated blast furnace slag/ferrochrome slag-based alkali-activated cement was investigated. Mortar specimens with alkali modulus 0.8 and 1 had very low compressive strength after 3 days, while mortar specimens with alkali modulus 1.2 and 1.4 gained most of their 28-day strength in the first three days. Especially in cases where early strength is required, the alkali modulus of 1.2 is the limit value in terms of compressive strength. In accordance with the result obtained in the compressive strength test, the 3-day UPV values of the samples with alkali modulus of 0.8 and 1 were lower than the samples with alkali modulus of 1.2 and 1.4. In contrast to the compressive strength results, the 28-day UPV values of the samples with 0.8 and 1 alkali modulus were higher.

REFERENCES

[1] G. Habert *et al.*, "Environmental impacts and decarbonization strategies in the cement and concrete industries," *Nat. Rev. Earth Environ.*, 2020.

[2] P. J. M. Monteiro, S. A. Miller, and A. Horvath, "Towards sustainable concrete," *Nature Materials*. 2017.

[3] B. Bajželj, J. M. Allwood, and J. M. Cullen, "Designing climate change mitigation plans that add up," *Environ. Sci. Technol.*, vol. 47, no. 14, pp. 8062–8069, 2013.

[4] A. E. Abubakr, A. M. Soliman, and S. H. Diab, "Effect of activator nature on the impact behaviour of Alkali-Activated slag mortar," *Constr. Build. Mater.*, vol. 257, p. 119531, 2020.

[5] A. Sedaghatdoost, K. Behfarnia, M. Bayati, and M. sadegh Vaezi, "Influence of recycled concrete aggregates on alkali-activated slag mortar exposed to elevated temperatures," *J. Build. Eng.*, vol. 26, no. July, p. 100871, 2019.

[6] A. Ababneh, F. Matalkah, and R. Aqel, "Synthesis of kaolin-based alkali-activated cement: Carbon footprint, cost and energy assessment," *J. Mater. Res. Technol.*, vol. 9, no. 4, pp. 8367–8378, 2020.

[7] E. Gartner and H. Hirao, "A review of alternative approaches to the reduction of CO2 emissions associated with the manufacture of the binder phase in concrete," *Cement and Concrete Research*, vol. 78. pp. 126–142, 2015.

[8] B. Singh, G. Ishwarya, M. Gupta, and S. K. Bhattacharyya, "Geopolymer concrete: A review of some recent developments," *Construction and Building Materials*, vol. 85. pp. 78–90, 2015.

[9] A. Gruskovnjak, B. Lothenbach, L. Holzer, R. Figi, and F. Winnefeld, "Hydration of alkali-activated slag: Comparison with ordinary Portland cement," *Adv. Cem. Res.*, vol. 18, no. 3, pp. 119–128, 2006.

[10] K. Neupane, "High-Strength Geopolymer Concrete- Properties, Advantages and Challenges," *Adv. Mater.*, vol. 7, no. 2, p. 15, 2018.

[11] M. Karatas, M. Dener, M. Mohabbi, and A. Benli, "A study on the compressive strength and microstructure characteristic of alkali-activated metakaolin cement," *Rev. Mater.*, vol. 24, no. 4, 2019.

[12] M. Dener, M. Karatas, and M. Mohabbi, "Sulfate resistance of alkali-activated slag/Portland cement mortar produced with lightweight pumice aggregate," *Constr. Build. Mater.*, vol. 304, p. 124671, 2021.

[13] M. Dener, M. Karatas, and M. Mohabbi, "High temperature resistance of self compacting alkali activated slag/portland cement composite using lightweight aggregate," *Constr. Build. Mater.*, vol. 290, Jul. 2021.

[14] S. Aydin and B. Baradan, "Effect of activator type and content on properties of alkali-activated slag mortars," *Compos. Part B Eng.*, vol. 57, pp. 166–172, 2014.

67

[15] J. L. Provis and S. A. Bernal, "Geopolymers and Related Alkali-Activated Materials," *Annu. Rev. Mater. Res.*, vol. 44, no. 1, pp. 299–327, 2014.

[16] Z. Shi, C. Shi, S. Wan, and Z. Zhang, "Effects of alkali dosage and silicate modulus on alkali-silica reaction in alkali-activated slag mortars," *Cem. Concr. Res.*, vol. 111, no. July, pp. 104–115, 2018.

[17] S. Fang, E. S. S. Lam, B. Li, and B. Wu, "Effect of alkali contents, moduli and curing time on engineering properties of alkali activated slag," *Constr. Build. Mater.*, vol. 249, 2020.

[18] O. Karahan and A. Yakupoğlu, "Resistance of alkali-activated slag mortar to abrasion and fire," *Adv. Cem. Res.*, vol. 23, no. 6, pp. 289–297, 2011.

[19] F. Puertas, S. Martínez-Ramírez, S. Alonso, and T. Vázquez, "Alkali-activated fly ash/slag cements. Strength behaviour and hydration products," *Cem. Concr. Res.*, vol. 30, no. 10, pp. 1625–1632, 2000.

[20] S. D. Wang, K. L. Scrivener, and P. L. Pratt, "Factors affecting the strength of alkali-activated slag," *Cem. Concr. Res.*, vol. 24, no. 6, pp. 1033–1043, 1994.

[21] C. Duran Atiş, C. Bilim, Ö. Çelik, and O. Karahan, "Influence of activator on the strength and drying shrinkage of alkali-activated slag mortar," *Constr. Build. Mater.*, 2009.

[22] İ. Türkmen, M. B. Karakoç, F. Kantarcı, M. M. Maraş, and R. Demirboğa, "Fire resistance of geopolymer concrete produced from Elazığ ferrochrome slag," *Fire Mater.*, vol. 40, no. 6, pp. 836–847, 2016.

[23] A. Özcan and M. B. Karakoç, "The Resistance of Blast Furnace Slag- and Ferrochrome Slag-Based Geopolymer Concrete Against Acid Attack," *Int. J. Civ. Eng.*, vol. 17, no. 10, pp. 1571–1583, 2019.

[24] M. Mohabbi Yadollahi and M. Dener, "Investigation of elevated temperature on compressive strength and microstructure of alkali activated slag based cements," *Eur. J. Environ. Civ. Eng.*, 2019.

[25] M. B. Karakoç, I. Türkmen, M. M. Maraş, F. Kantarci, R. Demirboɟa, and M. Uɟur Toprak, "Mechanical properties and setting time of ferrochrome slag based geopolymer paste and mortar," *Constr. Build. Mater.*, vol. 72, pp. 283–292, 2014.

[26] T. Bakharev, J. G. Sanjayan, and Y. B. Cheng, "Effect of elevated temperature curing on properties of alkali-activated slag concrete," *Cem. Concr. Res.*, vol. 29, no. 10, pp. 1619–1625, 1999.

[27] B. S. Gebregziabiher, R. J. Thomas, and S. Peethamparan, "Temperature and activator effect on early-age reaction kinetics of alkali-activated slag binders," *Constr. Build. Mater.*, vol. 113, pp. 783–793, 2016.

[28] A. ASTM C109/C109M, "Compressive Strength of Hydraulic Cement Mortars (Using 2-in . or [50-mm] Cube Specimens) 1," *Am. Soc. Test. Mater.*, 2007.

[29] ASTM C597, "Standard Test Method for Pulse Velocity Through Concrete," *American Society for Testing and Materials, West Conshohocken, PA, USA*. 2016.

68

Türk Doğa ve Fen Dergisi
Turkish Journal of Nature and Science
www.dergipark.gov.tr/tdfd

Investigation of the Role of CYP1A1 and CYP1B1 Expressions in Obesity Susceptibility

Fatih POLAT[1], Hakan BULUŞ[2], Pınar KAYGIN[3], Onur DİRİCAN[3*], Gülçin Güler ŞİMŞEK[4], Sezen YILMAZ SARIALTIN[5], Nurdan GÜRBÜZ[3], Can YILMAZ[6], Serpil OĞUZTÜZÜN[3]

[1]University of Health Sciences, Van Training and Research Hospital, General Surgery Department, Van,Türkiye
[2]University of Health Sciences, Keçiören Training and Research Hospital, General Surgery Department, Ankara, Türkiye
[3]Kırıkkale University, Faculty of Science, Department of Biology, Kırıkkale, Türkiye
[4]University of Health Sciences, Gulhane Training and Research Hospital, Department of Pathology, Ankara, Türkiye
[5]Ankara University, Faculty of Pharmacy, Department of Pharmaceutical Toxicology,Ankara, Türkiye
[6]Van Yüzüncü Yil University, Faculty of Science, Department of Molecular Biology and Genetics;Van, Türkiye

Fatih POLAT ORCID No: 0000-0001-5969-9811
Hakan BULUŞ ORCID No: 0000-0001-7439-8099
Pınar KAYGIN ORCID No: 0000-0003-0127-1753
Onur DİRİCAN ORCID No: 0000-0003-0511-6611
Gülçin Güler ŞİMŞEK ORCID No: 0000-0001-7710-4631
Sezen YILMAZ SARIALTIN ORCID No: 0000-0002-8387-4146
Nurdan GÜRBÜZ ORCID No: 0000-0003-1685-4644
Can YILMAZ ORCID No: 0000-0002-0028-6614
Serpil OĞUZTÜZÜN ORCID No: 0000-0002-5892-3735

*Corresponding author: soguztuzun@yahoo.com

69

Abstract: Obesity, a chronic inflammatory disease, needs to be understood with a more multidisciplinary perspective based on metabolic functioning. The rapid increase in the incidence and prevalence of the disease in recent years has caused it to become a global health problem. CYP1A1 is a key enzyme in the metabolization of several exogenous and endogenous substrates including polyunsaturated fatty acids. CYP1B1 plays a regulatory role in metabolic pathways, such as the metabolism of steroid hormones and fatty acids. Therefore, the purpose of our study is to reveal the role of cytochrome p450 (CYP1A1 and CYP1B1) isozymes in obese patients. In addition, this is the first study to examine the effects of CYP1A1 and CYP1B1 in obese patients concerning various hormones, lipids, and also diabetic and whole blood parameters. Patients with obesity who underwent bariatric surgery were included in our study and the expression of CYP1A1 and CYP1B1 in surgery tissues was determined by immunohistochemistry. CYP1A1 was weakly expressed in 33.3%, moderately in 32.5%, and strongly in 21.4% of tissues. Weak CYP1B1 expression was observed only in 28.6% of the tissues while moderate or strong expression was not observed in any of the tissues. No statistically significant differences were found between expression levels of CYP1A1 and CYP1B1 isozymes in obese patients and demographic characteristics (p>0.05).Correlation analyses were also performed between the expression levels and the clinical data of the patients. There was a significant correlation between CYP1A1 expression and hemoglobin levels (p<0.05). A significant correlation was found between CYP1B1 expression and insulin as well as HDL levels (p<0.05). These detoxification enzymes could be considered one of the key targets in obesity. However, higher expressions should be elucidated with other studies, especially in the molecular pathway. Moreover, new approaches are needed to evaluate susceptibility of the disease and obtain effective treatments.

Obezite Duyarlılığında CYP1A1 Ve CYP1B1 Ekspresyonlarının Rolünün Araştırılması

Anahtar Kelimeler
Obezite,
Oksidatif stres,
CYP1A1,
CYP1B1,
Ksenobiyotikler

Öz: Metabolik işleyiş, etkileri ve neden olduğu hastalıklar açısından daha multidisipliner bir bakış açısıyla anlaşılması gereken obezite, son yıllarda prevalansı ve insidansı artan hastalıklardan biri olarak görülmektedir. Bu hastalığın metabolic yolunda önemli enzim gruplarından biri olan sitokrom p450 (CYP1A1 ve CYP1B1) izozimlerinin rolünün ortaya konulması amaçlanmıştır. 2017-2019 yılları arasında Ankara Keçiören Eğitim ve Araştırma Hastanesi Genel Cerrahi Kliniği'nde obezite tanısı konulan ve bariatric cerrahi, ksenobiyotik metabolizması uygulanan 152 hastaya immünohistokimya yöntemiyle CYP1A1 ve CYPB1 izoenzimlerinin ekspresyonu araştırılmıştır. CYP1A1 açısından elde edilen bulgular; 152 kişide CYP1A1 ve CYP1B1 immünohistokimya boyama düzeyleri incelenen dokuların %12.7'sinde CYP1A1 ekspresyonu gözlenmezken; %33.3, %32.5 ve %21.4'te zayıf bir CYP1A1 ifadesi gözlenmiştir. Dokuların %71.4'ünde CYP1B1 ekspresyonu görülmezken, dokuların %28.6'sında zayıf ekspresyon izlenmiştir. Hiçbir dokuda orta veya güçlü CYP1B1 ekspresyonu gözlenmemiştir. Kadın hastalardan alınan dokuların ortalama CYP1A1 ve CYP1B1 boyama seviyeleri erkek hastalardan daha yüksek bulunmuştur. Klinik verilerden diyabet parametresi ($p<0.05$) ile anlamlı olduğu gözlenmiştir. Çalışmamızda elde edilen veriler ışığında obez hastalarda anlamlı CYP1A ve CYP1B1 ekspresyonları gözlenmiş ve detoksifikasyon mekanizması nedeniyle antioksidan metabolizma ve işlevsellik mevcuttur. Obez hastalarda bu enzim düzeyindeki artışın özellikle moleküler yolakta başka çalışmalarla aydınlatılması gerektiği ve benzer çalışmalara yol göstereceği düşünülmektedir.

1. INTRODUCTION

Obesity, whose prevalence and incidence is increasing rapidly, is one of the biggest health problems encountered in recent years [1]. Oxidative stress plays an important role in the emergence of cancer, atherosclerosis, arthritis, neurodegenerative diseases, cardiovascular diseases, diabetes and also metabolic disorders including obesity [2-4]. In obesity, oxidative stress biomarkers are associated with body mass index (BMI), body fat percentage, low-density lipoprotein (LDL) and triglyceride levels. The capacity of the antioxidant defense system decreases according to the level of fat percentage in the body. A diet high in fat and carbohydrates has been shown to induce oxidative stress and inflammation in obese subjects significantly [5]. It has been stated that oxidative stress may cause insulin resistance, which is a common condition in obesity, by disrupting insulin secretion from β-cells in the pancreas and glucose transport in skeletal and adipose tissue [6]. Independent of obesity, the metabolic syndrome also induces oxidative stress alone. Uncontrolled adipokine production induced by oxidative stress is one of the mechanisms contributing to the development of the metabolic syndrome [7]. Obesity appears to cause the presence of oxidative stress [8]. The wide variety of detoxification processes that make these xenobiotics that reach the body less toxic, more polar and easily excreted is called xenobiotic biotransformation or xenobiotic metabolism [9]. Cytochrome P450 (CYP) enzymes play the most prominent role in Phase I xenobiotic metabolism[10]. CYP1A1 is the biomarker that metabolizes polycyclic aromatic hydrocarbons inducible by smoking. CYP1B1 is involved in the estrogen metabolic pathway. Especially, this role is realized by the regulation of 4-hydroxy estradiol in the pathogenesis of breast and endometrial cancer [11]. Investigation of the functionality of metabolic components such as glutathione, superoxide dismutase against oxidative stress and reduction of toxic substances is continued in order to prevent metabolic exposure from causing cellular and tissue damage [12].

In our study, it was aimed to contribute to the understanding of the development of the obesity from an epidemiological point of view by examining the expression status of CYP1A1 and CYP1B1 proteins, which are important ondeoxification mechanisms, based on patients' demographic and clinical characteristics.

2. MATERIAL AND METHOD

2.1.Immunohistochemical Staining

In this study, 149 paraffin tissue blocks of obesity patients were received from the Keçiören Research and Education Hospital. They were stained by immunohistochemistry (IHC) method for CYP1A1 and CYP1B1 isoenzymes.

For immunohistochemistry, the tissue sections were peroxidase-incubated for 10 minutes using 3% hydrogen peroxide in methanol (v/v). After that, the sections were performed for 3 min using a 0.01M citrate buffer, pH 6.0 in a domestic pressure cooker. Sections were incubated at room temperature for 10 min with superblock (SHP125; Scy Tek laboratories, west logan, UT). The sections were then covered with the primary antibodies diluted (1:750 for

CYP1A1; 1:400 for CYP1B1) in TBS at 4 °C. anti-CYP1A1 (sc-20,772) and Anti-CYP1B1 (sc-32,882) were obtained from Santa Cruz Biotechnology Inc., Dallas, TX. After washing for 15 minutes in TBS, the sections were incubated at room temperature with a biotinylated link antibody (SHP125; ScyTek Laboratories) followed by streptavidin/HRP complex (SHP125; ScyTek laboratories). The sections were incubated at room temperature with biotinylated link antibody (SHP125; ScyTek Laboratories) then diaminobenzidine was used to visualize peroxidase activity in tissues. And they were counterstained with hematoxylin. Scoring of immunohistochemically stained sections were performed for each enzyme was: (-), negative (no staining);1, weak staining; 2, moderate staining; 3, strong staining.

2.2.Statistical Analysis

IBM SPSS Version 25.0 (Armonk, NY: IBM Corp) was used for statistical analysis. The numerical variables describing the clinical and demographic characteristics of the patients were expressed as mean±standard deviation or standard error of mean. The categorized variables were described as numbers of patients (n) and percentages (%) based on descriptive statistics. The Shapiro-Wilk test was performed to assess the distribution profiles of the numerical variables. The Levene test was used to assess the homogeneity of variances. The Mann-Whitney U test was used to compare differences between two independent and The Kruskal-Wallis test was three or more independent groups for non-normally distributed variables. Bonferonni correction was performed. The correlation analysis was evaluated by Spearman's rank correlation test.

Differences at the $p<0.05$ level were considered statistically significant.

3. RESULTS

The demographic and clinical characteristics of the patients were categorized and explained in Table 1. A total of 126 obese patients were included in our study. The study group consisted of 111 females (88,1%) and 15 males (11,9%). 35 of the patients (27,8%) were 30 or younger than 30 years old, 60 patients (47,6%) were between 31 and 45 years old, and 31 patients (24,6%) were older than 45 years. All of the patients were obese, so there were no patients with a BMI below 40. Only 3 of the patients (2.4%) had a BMI of 40, and 123 patients (97,6%) had a BMI above 40. 59.5% (75 patients) of the patients were only obese, while 39.7% (50 patients) had additional diseases (comorbidity). 74 of the patients (58.7%) did not use any medication, while 51 patients (40.5%) used some. 72 of the patients (57.1%) underwent surgery, while 54 patients (42.9%) did not undergo surgery. Additionally, a number of other measurements were recorded and classified including patients' white blood cell (WBC), hemoglobin (HGB), platelet (PLT), fasting and postprandial glucose, high-density lipoprotein (HDL), low-density lipoprotein (LDL), total cholesterol, triglyceride, free T3 and T4, thyroid-stimulating hormone (TSH), estradiol, follicle-stimulating hormone (FSH), luteinizing hormone (LH), C-peptide, insulin, cortisol, adrenocorticotropic hormone (ACTH), sex hormone-binding globulin (SHBG) and hemoglobin A1c (HbA1c) levels.

Table 1. Categorized demographic and clinical characteristics of patients

Variables	Category	Number (%)
Gender	Female	111 (%88,1)
	Male	15 (%11,9)
Age	≤30	35 (%27,8)
	31-45	60 (%47,6)
	>45	31 (%24,6)
BMI	≤40	3 (%2,4)
	>40	123 (%97,6)
Comorbidities	Yes	50 (%39,7)
	No	75 (%59,5)
	Missing (unknown)	1 (%0,8)
Medication usage status	Yes	51 (%40,5)
	No	74 (%58,7)
	Missing (unknown)	1 (%0,8)
Surgery status	Yes	72 (%57,1)
	No	54 (%42,9)
WBC	<4,5	0 (%0)
	4,5-11,0	106 (%84,1)
	>11,0	20 (%15,9)

HGB	<11,0	7 (%5,6)
	11-16	110 (%87,3)
	>16	9 (%7,1)
PLT	<130	3 (%2,4)
	130-400	111 (%88,1)
	>400	12 (%9,5)
Glucose (fasting)	<70	1 (%0,8)
	70-105	84 (%66,7)
	>105	41 (%32,5)
Glucose (postprandial)	<140	58 (%46,0)
	140-200	21 (%16,7)
	>200	10 (%7,9)
	Missing (unknown)	37 (%29,4)
Triglyceride	≤150	57 (%45,2)
	>150	61 (%48,4)
	Missing (unknown)	8 (%6,3)
Total cholesterol	≤200	67 (%53,2)
	>200	57 (%45,2)
	Missing (unknown)	2 (%1,6)
Free T3	<1,8	0 (%0)
	1,8-4,6	124 (%98,4)
	>4,6	0 (%0)
	Missing (unknown)	2 (%1,6)
Free T4	<0,9	17 (%13,5)
	0,9-1,7	108 (%85,7)
	>1,7	0 (%0)
	Missing (unknown)	1 (%0,8)
TSH	<0,27	4 (%3,2)
	0,27-4,2	105 (%83,3)
	>4,2	16 (%12,7)
	Missing (unknown)	1 (%0,8)
HbA1C	≤6	80 (%63,5)
	>6	38 (%30,2)
	Missing (unknown)	8 (%6,3)

The results were expressed as n (%).BMI: body-mass index, WBC: white blood cell, HGB: hemoglobin, PLT: platelet, TSH: thyroid-stimulating hormone, HbA1c: hemoglobin A1c.

The patients' demographic and clinical characteristics were shown in Table 2. Patients' age, height, weight and BMI were recorded as demographic data. Patients' WBC, HGB, PLT, fasting and postprandial glucose, HDL, LDL, total cholesterol, triglyceride, free T3 and T4, TSH, estradiol, FSH, LH, C-peptide, insulin, cortisol, ACTH, SHBG, HbA1c levels were recorded as clinical data. Patients' mean age was 37,91 years (16-63), mean weight was 125,10 kg (91-182), and mean BMI was 46,77 kg/m² (40-70.31).

Table 2. The patients' demographic and clinical characteristics

Variable (unit)	Number	Mean±SD
Age (year)	126	37,91 ± 11,01 (16-63)
Height (cm)	126	163,48 ± 8,21 (148-189)
Weight (kg)	126	125,10 ± 19,26 (91-182)
BMI (kg/m²)	126	46,77 ± 6,18 (40-70,31)
WBC	126	8,96 ± 2,00 (5,27-14,90)
HGB	126	13,68 ± 1,55 (9,87-18,40)
PLT	126	290,39 ± 80,71 (34,30-535,00)
Glucose (fasting)	126	111,16 ± 54,50 (69,00-498,00)
Glucose (postprandial)	88	139,35 ± 62,43 (71,00-394,00)
HDL	21	43,19 ± 7,77

		(32,00-60,00)
LDL	15	124,60 ± 34,55 (55,00-168,00)
Triglyceride	118	173,03 ± 85,86 (42,00-545,00)
Total cholesterol	118	215,62 ± 170,75 (108,00-2016,00)
Free T3	124	3,01 ± 0,41 (1,84-4,08)
Free T4	125	1,03 ± 0,14 (0,61-1,55)
TSH	125	2,58 ± 2,17 (0,05-16,28)
Estradiol	56	78,45 ± 62,99 (9,00-247,00)
FSH	75	11,38 ± 15,91 (0,96-75,98)
LH	75	10,54 ± 10,58 (1,07-45,09)
C peptide	117	3,33 ± 1,09 (1,28-6,23)
Insulin	122	19,60 ± 25,31 (1,70-275,60)
Cortisol	122	10,17 ± 4,10 (0,8-20,00)
ACTH	87	29,14 ± 19,10 (5,00-126,00)
SHBG	55	37,80 ± 31,30 (7,51-226,00)
HbA1C	117	6,06 ± 1,36 (4,10-13,10)

The results were expressed as mean±SD (minimum-maximum values). BMI: body-mass index, WBC: white blood cell, HGB: hemoglobin, PLT: platelet, HDL: high-density lipoprotein, LDL: low-density lipoprotein, TSH: thyroid-stimulating hormone, FSH: follicle stimulating hormone, LH: luteinizing hormone, ACTH: adrenocorticotropic hormone, SHBG: sex hormone-binding globulin, HbA1c: hemoglobin A1c.

IHC staining was performed on the tissues as explained in the material and method section. CYP1A1 and CYP1B1 expression levels were evaluated and explained in Table 3. Weak CYP1A1 expression was observed in 33.3% of the tissues. Moderate expression of CYP1A1 was detected in 32.5% of tissues, and strong expression was in 21.4%. Weak CYP1B1 expression was observed in 28.6% of the tissues. There was no moderate or strong expression of CYP1B1 in any of the tissues.

from obesity patients after immunohistochemical analysis are shown in Figure 1.

Table 3. CYP1A1 and CYP1B1 expression levels of the tissues

Expression Level	CYP1A1	CYP1B1
0	16/126[a] (%12,7)	90/126[a] (%71,4)
1	42/126[a] (%33,3)	36/126[a] (%28,6)
2	41/126[a] (%32,5)	0/126[a] (%0)
3	27/126[a] (%21,4)	0/126[a] (%0)
Mean	1,63 ± 0,09[b] (0-3)[c]	0,29 ± 0,04[b] (0-1)[c]

Staining scores were determined according to the staining intensity of the tissues. 0: negative staining, 1: weak staining, 2: moderate staining, 3: strong staining.
a: Number of samples stained at specified level / Total number of samples (percent),
b: Mean staining level ± Standard Error of Mean (SEM)
c: The lowest staining level – The highest staining level

Microscopic images of CYP1A1 and CYP1B1 protein expressions in tissues obtained surgically

Figure 1. Microscopic images of CYP1A1 and CYP1B1 protein expressions in tissues obtained surgically from obesity patients after immunohistochemical analysis.
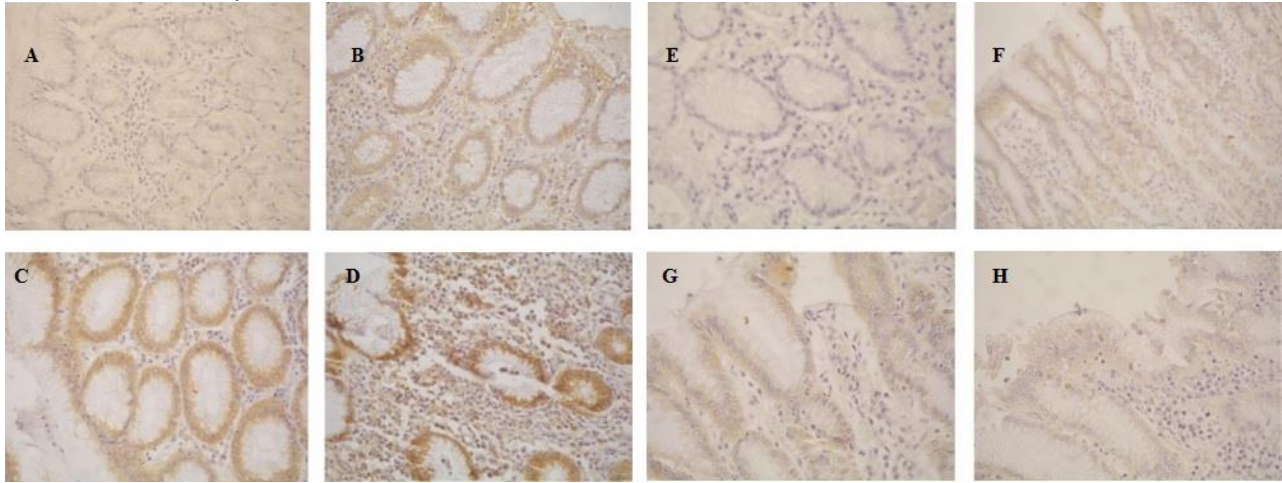
CYP1A1 protein; A: Expression of negative protein in stomach tissue, 40X; **B**: Weak (+1) protein expression in stomach tissue 40X; **C**: Moderate (+2) protein expression in stomach tissue 40X; **D**: Strong (+2) protein expression in stomach tissue protein expression 40X. **CYP1B1 protein;E**: Expression of negative protein in stomach tissue, 40X; **F**: Weak (+1) protein expression in stomach tissue, 20X; **G**: Weak (+1) protein expression in stomach tissue, 40X; **H**: Weak nuclear in stomach tissue (+1) protein expression 40X)

The expression levels of CYP1A1 and CYP1B1 were analyzed based on the patients' demographic characteristics such as gender, age, comorbidities, medication use, and operation status in Table 4.

CYP1A1 and CYP1B1 expression levels were determined based on the patients' age, as shown in Figure 3. The 31-45 age group had the highest CYP1A1 expression levels.

However, there were no statistically significant differences in CYP1A1 staining levels between patients of different age groups (p>0.05). The patients over 45 years of age expressed the highest levels of CYP1B1. However, there were no statistically significant differences in CYP1B1 expression levels among patients in different age groups (p>0.05).

Table 4. CYP1A1 and CYP1B1 expression levels based on patients' demographic characteristics

Variable	CYP1A1	CYP1B1
Gender		
Female	1,65±0,09 [a] (0-3)[b]	0,31±0,04 [a] (0-1)[b]
Male	1,47±0,26 [a] (0-3)[b]	0,13±0,09 [a] (0-1)[b]
p-value	0,545	0,166
Age		
≤30	1,59±0,18 [a] (0-3)[b]	0,29±0,08 [a] (0-1)[b]
31-45	1,78±0,12 [a] (0-3)[b]	0,25±0,06 [a] (0-1)[b]
>45	1,35±0,16 [a] (0-3)[b]	0,35±0,09 [a] (0-1)[b]
p-value	0,154	0,579
Comorbidity		
Yes	1,50±0,12 [a] (0-3)[b]	0,26±0,06 [a] (0-1)[b]
No	1,71±0,12 [a] (0-3)[b]	0,31±0,05 [a] (0-1)[b]
p-value	0,241	0,574
Medication usage		
Yes	1,49±0,12 [a] (0-3)[b]	0,25±0,06 [a] (0-1)[b]
No	1,72±0,12 [a] (0-3)[b]	0,31±0,05 [a] (0-1)[b]
p-value	0,215	0,499
Surgery status		
Yes	1,62±0,11 [a] (0-3)[b]	0,28±0,05 [a] (0-1)[b]
No	1,63±0,14 [a] (0-3)[b]	0,30±0,06 [a] (0-1)[b]
p-value	0,961	0,821

a: Mean ± SEM, b: The minimum-the maximum

CYP1A1 and CYP1B1 expression levels were evaluated in terms of the patients' gender, as shown in Figure 2.Mean CYP1A1 and CYP1B1 expression levels of tissues taken from female patients were higher than those of male patients. However, the difference between the groups was not statistically significant ($p > 0.05$).
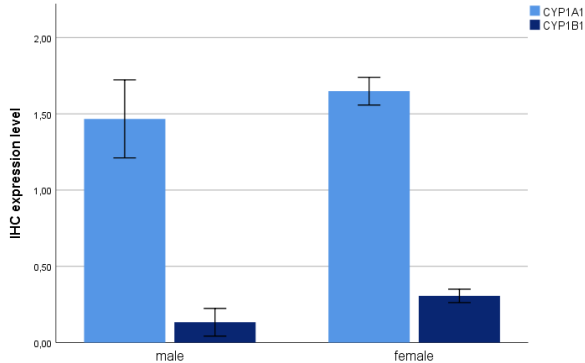
Figure 2. CYP1A1 and CYP1B1 expression levels based on patients' gender
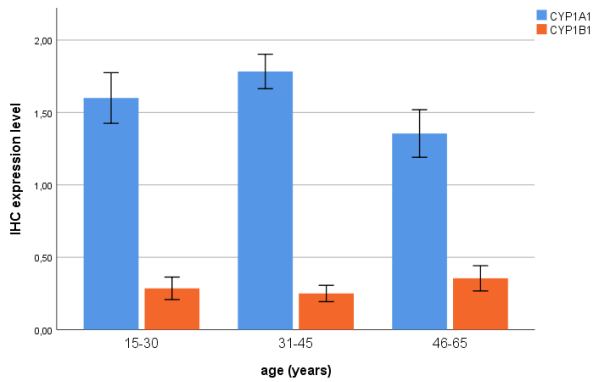
Figure 3. CYP1A1 and CYP1B1 expression levels in terms of patients' age

CYP1A1 and CYP1B1 expression levels were determined in terms of the patients' comorbidities as seen in Figure 4. CYP1A1 and CYP1B1 expression levels of patients without comorbidities were higher than those with comorbidities. However, this difference was not statistically significant in both expressions ($p > 0.05$).
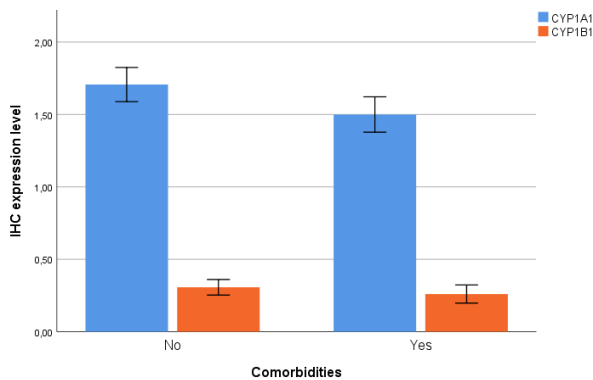
Figure 4. CYP1A1 and CYP1B1 expression levels based on patients' comorbidities

CYP1A1 and CYP1B1 expression levels were assessed with respect to the patients' medication usage status, as illustrated in Figure 5. CYP1A1 and CYP1B1 expression levels were higher in tissues taken from patients not using medications than those using medications. However, the difference was not statistically significant in both expressions ($p > 0.05$).
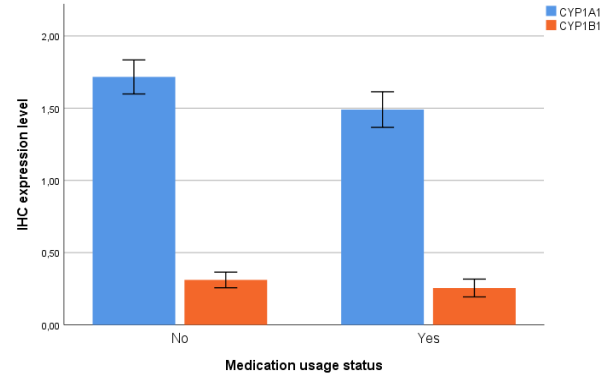
Figure 5. CYP1A1 and CYP1B1 expression levels in terms of patients' medication usage

The expression levels of CYP1A1 and CYP1B1 were analyzed concerning operation status as displayed in Figure 6. There was no statistically significant difference between the patients' operation status and CYP1A1 and CYP1B1 expression levels ($p > 0.05$).
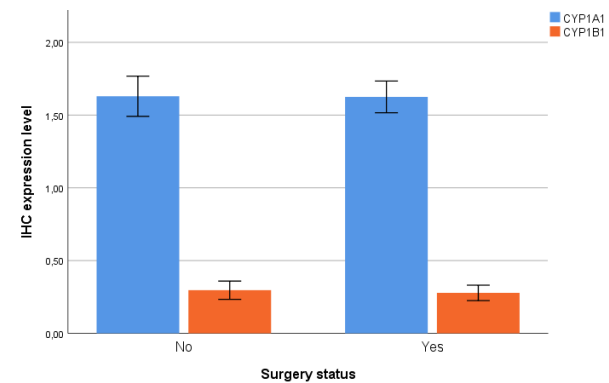
Figure 6. CYP1A1 and CYP1B1 expression levels in terms of patients' surgery status

Correlation analysis was performed between the CYP1A1 and CYP1B1 expression levels and the patients' clinical and demographic characteristics (Table 5). A negative and significant correlation was found between CYP1A1 expression and HGB levels ($p < 0.05$). A negative and significant correlation was observed between CYP1B1 expression and HDL levels ($p < 0.05$). A negative and significant correlation was noted between CYP1B1 expression and insulin levels ($p < 0.05$)

Table 5. Correlation analyzes of patients' clinical and demographic characteristics and CYP1A1 and CYP1B1 expression levels

Variable	CYP1A1		CYP1B1	
	Correlation coefficient	p-value	Correlation coefficient	p-value
Age	-0,125	0,162	0,019	0,830
Height	-0,012	0,891	-0,093	0,301
Weight	-0,038	0,672	-0,059	0,512
BMI	0,020	0,826	-0,024	0,788
WBC	0,087	0,334	-0,134	0,135
HGB	-0,215	0,016*	0,106	0,238
PLT	0,167	0,062	0,019	0,832
Glucose (fasting)	0,136	0,128	-0,010	0,910
Glucose (postprandial)	-0,020	0,850	0,120	0,267
HDL	0,280	0,219	-0,484	0,026*
LDL	0,139	0,622	0,164	0,560
Triglyceride	-0,017	0,856	-0,026	0,779
Total cholesterol	0,128	0,166	0,179	0,053
Free T3	0,104	0,248	-0,005	0,960
Free T4	0,130	0,150	0,095	0,293
TSH	0,148	0,099	0,033	0,712
Estradiol	0,128	0,347	-0,118	0,387
FSH	-0,174	0,136	-0,015	0,900
LH	-0,167	0,153	0,019	0,869
C Peptid	-0,076	0,418	-0,115	0,218
Insulin	-0,005	0,954	-0,228	0,011*
Cortisol	0,129	0,157	0,047	0,607
ACTH	0,094	0,388	-0,077	0,479
SHBG	-0,117	0,394	0,084	0,541
HBA1C	0,086	0,358	0,151	0,104
CYP1A1	1,000	-	0,116	0,196
CYP1B1	0,116	0,196	1,000	-

(*) There is a statistically significant correlation (p<0.05). BMI: body-mass index, WBC: white blood cell, HGB: hemoglobin, PLT: platelet, HDL: high-density lipoprotein, LDL: low-density lipoprotein, TSH: thyroid-stimulating hormone, FSH: follicle stimulating hormone, LH: luteinizing hormone, ACTH: adrenocorticotropic hormone, SHBG: sex hormone-binding globulin, HbA1c: hemoglobin A1c.

4. DISCUSSION AND CONCLUSION

Oxidative stress is associated with the development of obesity, a multifactorial disease that is very common in all over the world. Oxidative stress has been observed to occur with the random production of adipokines from adipose tissue, which usually results in the development of metabolic syndrome [13]. Parameters such as oxidative damage and C-reactive protein (CRP) are higher in obese individuals. Depending on this situation, BMI has a direct correlation withLDL levels and triglyceride ratio [14]. In some obese individuals, antioxidant defense parameters can belower than their fat ratios. The levels of vitamin E, vitamin C, beta carotene and glutathione have been shown to decrease in obese individuals [15]. It was also determined that it resulted in the induction of significant oxidative stress and inflammation in individuals on a carbohydrate and fat diet [16].The published studies showed that long-term obesity cause decreasing in antioxidant sources and in the activities of antioxidant enzymes including super oxide dismutase (SOD) and catalase [17].SOD and glutathione peroxidase activities were decreased in obese individuals compared to healthy individuals [18]. Some endogenous and exogenous sources of obesity are also causes metabolic and hereditary disorders such as DNA damage, tissue damage, mutation, cell aging and even cancer.

Xenobiotic metabolism is classified in three main groups as phase I,phase II and also phase III. Carcinogens are either broken down into non-reactive products and excreted directly from the body or converted to reactive metabolites by Phase I reactions.

In this study, the relationship between obesity and the expression of CYP1A1 and CYP1B1 isozymes, which are important members of the cytochrome P450 (CYP) enzyme system was investigated.Considering that no diet is applied, especially in the development of obesity, significant increases of CYP1A1 and CYP1B1 enzymes in the metabolic pathway to provide reducing roles and removal from the metabolic pathway were observed, as expected. This situation coincides with the epidemiologically guiding confirmed data in terms of causing a metabolic correlation with similar and current studies in the literature and preparing the ground for the formation of other diseases.

Knowing that CYP1A1 and CYP1B1 are among the most important Phase I enzymes with their effects on reactive oxygen compounds in the continuity of the anti-cancer mechanism and with their flovanoid metabolizer role, it is possible to investigate the effects on some types of cancer by inducing cytochrome p450 on cell lines with these compounds. In the study of Surichan et al., 2018, the role of CYP1A1/CYP1B1-mediated enzyme induction in human breast cancer in reducing the 4-hydroxy tangeretin product was revealed [19].

It is encountered in studies that try to reveal the role and functioning principle of CYP1A1 and CYP1B1 enzyme expressions in the metabolic pathway. In the study conducted by Androutsopoulos et al.,2011, the status of cytochrome p450 compounds in the diet-treated samples in terms of flavonoid compounds were investigated comparatively in terms of CYP1A1 and CYP1B1. CYP1A1 and CYP1B1 are two extrahepatic enzymes involved in carcinogenesis and cancer progression. Selective inhibition of CYP1A1 and CYP1B1 by dietary

components, particularly the flavonoids class, has been characterized as a paradigm corresponding to the concept of dietary chemoprevention. The ability of CYP1 enzymes to selectively metabolize dietary flavonoids into transformation products that inhibit cancer cell proliferation has been highlighted. In the study conducted with 14 different flovonoid markers, the status of CYP1A1 and CYP1B1 components was analyzed by HPLC and tried to be rationalized. And the results obtained overlap with the role of these phase I enzymes in the literature, and the states of flovonoids showed homology [20].

All these results indicated that CYP1A1 and CYP1B1 expression was increased in obesity. Significant changes occur in the amount of CYP1A1 and CYP1B1 enzymes in obese people. While these changes may occur as an adaptive response, the findings suggest that oxidative stress observed in obesity may be one of the possible mechanisms underlying this change. Findings contribute to the definition of the physiopathology of obesity are important in the prevention of complications such as cardiovascular diseases that may develop due to obesity. Thus the results of our study can be in the development of preventive approaches.

The results of our study will contribute to the epidemiological examination of obesity and to reveal new solutions. Clarifing the role of enzymes involved in detoxification in the development and progression of the disease could be a key target to cope with this disease. New approaches are needed to evaluate obesity susceptibility and to find effective treatment.

Conflicts of interest

The authors declare no conflicts of interest

Ethical statement

All procedures were conducted in accordance with the Declaration of Helsinki. This study was approved by the Research Ethics Committee of the Keçiören Education and Research Hospital (2012-KAEK-15/2073). Written informed consent was obtained from all parents or guardians.

REFERENCES

[1] Yach D., Stuckler D., Brownell K.D. Epidemiologic and economic consequences of the global epidemics of obesity and diabetes. *Nat. Med.*2006;12:62–66.

[2] Manna, P., & Jain, S. K. Obesity, oxidative stress, adipose tissue dysfunction, and the associated health risks: causes and therapeutic strategies. *Metabolic syndrome and related disorders,* 2015; 13(10): 423-444.

[3] Valko, M., Leibfritz, D., Moncol, J., Cronin, M. T., Mazur, M., &Telser, J. Free radicals and antioxidants in normal physiological functions and human disease.*The international journal of biochemistry & cell biology,* 2007; 39(1): 44–84. https://doi.org/10.1016/j.biocel.2006.07.001

[4] Djordjević V. B. Free radicals in cell biology. *International review of cytology,* 2004; 237:57–89. https://doi.org/10.1016/S0074-7696(04)37002-6

[5] Wellman, N.S., Friedberg, B. Causes and consequences of adult obesity: health, social and economic impacts in the United States. *Asia Pacific Journal of Clinical Nutrition,* 2002;11, S705–S709. https://doi.org/10.1046/j.1440-6047.11.s8.6.x

[6] Furukawa, S., Fujita, T., Shimabukuro, M., Iwaki, M., Yamada, Y., Nakajima, Y., Nakayama, O., Makishima, M., Matsuda, M., & Shimomura, I. Increased oxidative stress in obesity and its impact on metabolic syndrome. *The Journal of clinical investigation,* 2004; 114(12): 1752–1761. https://doi.org/10.1172/JCI21625

[7] Hansel, B., Giral, P., Nobecourt, E., Chantepie, S., Bruckert, E., Chapman, M. J., &Kontush, A. Metabolic syndrome is associated with elevated oxidative stress and dysfunctional dense high-density lipoprotein particles displaying impaired antioxidative activity. *The Journal of clinical endocrinology and metabolism,* 2004; 89(10): 4963–4971. https://doi.org/10.1210/jc.2004-0305

[8] Russell, A. P., Gastaldi, G., Bobbioni-Harsch, E., Arboit, P., Gobelet, C., Dériaz, O., Golay, A., Witztum, J. L., &Giacobino, J. P. Lipid peroxidation in skeletal muscle of obese as compared to endurance-trained humans: a case of good vs. bad lipids? *FEBS letters*, 2003; 551(1-3): 104–106. https://doi.org/10.1016/s0014-5793(03)00875-5

[9] Patterson, A. D., Gonzalez, F. J., & Idle, J. R. Xenobiotic metabolism: a view through the metabolometer. *Chemical research in toxicology,* 2010; 23(5): 851–860. https://doi.org/10.1021/tx100020p

[10] Prakash, C., Zuniga, B., Song, C. S., Jiang, S., Cropper, J., Park, S., & Chatterjee, B. Nuclear Receptors in Drug Metabolism, Drug Response and Drug Interactions. *Nuclear receptor research,* *2015*; 2: 101-178. https://doi.org/10.11131/2015/101178

[11] Anttila, S., Hakkola, J., Tuominen, P., Elovaara, E., Husgafvel-Pursiainen, K., Karjalainen, A., Hirvonen, A., &Nurminen, T. Methylation of cytochrome P4501A1 promoter in the lung is associated with tobacco smoking. *Cancer research,* 2003; 63(24): 8623–8628.

[12] Paluzar, H., &Sagiroglu, A. Effects of Organophosphorus and Pyrethroid Pesticides on Antioxidant Enzymes and Reactivation Effects of Pralidoxime: In vitro Studies. *Kuwait Journal of Science,*2021;https://doi.org/10.48129/kjs.11847

[13] Esposito, K., Ciotola, M., Schisano, B., Misso, L., Giannetti, G., Ceriello, A., &Giugliano, D. Oxidative stress in the metabolic syndrome. *Journal of endocrinological investigation,* 2006; 29(9): 791–795. https://doi.org/10.1007/BF03347372

[14] Pihl, E., Zilmer, K., Kullisaar, T., Kairane, C., Mägi, A., &Zilmer, M. (2006). Atherogenic inflammatory and oxidative stress markers in relation to overweight values in male former athletes. *International journal of obesity*

(2005), 30(1), 141–146. https://doi.org/10.1038/sj.ijo.0803068

[15] Hartwich, J., Góralska, J., Siedlecka, D., Gruca, A., Trzos, M., &Dembinska-Kiec, A. Effect of supplementation with vitamin E and C on plasma hsCRP level and cobalt-albumin binding score as markers of plasma oxidative stress in obesity. *Genes & nutrition,* 2007; 2(1): 151–154. https://doi.org/10.1007/s12263-007-0041-6

[16] Patel, C., Ghanim, H., Ravishankar, S., Sia, C. L., Viswanathan, P., Mohanty, P., &Dandona, P. Prolonged reactive oxygen species generation and nuclear factor-kappaB activation after a high-fat, high-carbohydrate meal in the obese. *The Journal of clinical endocrinology and metabolism,* 2007; 92(11): 4476–4479. https://doi.org/10.1210/jc.2007-0778

[17] Amirkhizi, F., Siassi, F., Minaie, S., Djalali, M., Rahimi, A., &Chamari, M. Is obesity associated with increased plasma lipid peroxidation and oxidative stress in women? *Arya Atherosclerosis*, 2010; 2(4).

[18] Ozata, M., Mergen, M., Oktenli, C., Aydin, A., Sanisoglu, S. Y., Bolu, E., Yilmaz, M. I., Sayal, A., Isimer, A., &Ozdemir, I. C. Increased oxidative stress and hypozincemia in male obesity. *Clinical biochemistry*, 2002; 35(8): 627–631. https://doi.org/10.1016/s0009-9120(02)00363-6

[19] Surichan, S., Arroo, R. R., Tsatsakis, A. M., &Androutsopoulos, V. P. Tangeretin inhibits the proliferation of human breast cancer cells via CYP1A1/CYP1B1 enzyme induction and CYP1A1/CYP1B1-mediated metabolism to the product 4' hydroxy tangeretin. *Toxicology in vitro : an international journal published in association with BIBRA,* 2018; 50: 274–284. https://doi.org/10.1016/j.tiv.2018.04.001

[20] Androutsopoulos, V. P., Papakyriakou, A., Vourloumis, D., &Spandidos, D. A. Comparative CYP1A1 and CYP1B1 substrate and inhibitor profile of dietary flavonoids. *Bioorganic & medicinal chemistry,* 2011;19(9): 2842–2849. https://doi.org/10.1016/j.bmc.2011.03.042

78

Türk Doğa ve Fen Dergisi
Turkish Journal of Nature and Science

www.dergipark.gov.tr/tdfd

Predicting Traffic Accident Severity Using Machine Learning Techniques

Ali ÇELİK[1*], Onur SEVLİ[2]

[1] Burdur Mehmet Akif Ersoy Üniversitesi, Fen-Edebiyat Fakültesi, Fizik Bölümü, Burdur, Türkiye
[2] Burdur Mehmet Akif Ersoy Üniversitesi, Eğitim Fakültesi, Bilgisayar ve Öğretim Teknolojileri Eğitimi Bölümü, Burdur, Türkiye
Ali ÇELİK ORCID No: 0000-0001-8218-6512
Onur SEVLİ ORCID No: 0000-0002-8933-8395

*Corresponding author: ali.celik@cern.ch

Abstract: Road accidents, harming countries' economies, national assets as well as people's lives, are one of the major problems for countries. Thus, investigating contributing factors to the accidents and developing an accurate accident severity prediction model is critical. Using the traffic accident data collected in Austin, Dallas, and San Antonio city of Texas between 2011 and 2021, the primary contributing factors in crashes are probed and the performance of a deep learning model and five different machine learning techniques, such as Logistic Regression, XGBoost, Random Forest, KNN, and SVM, are investigated. The finding shows that the Logistic Regression algorithm shows the best performance among the others with an accuracy of 88% in classifying accident severity.

Makine Öğrenmesi Tekniklerini Kullanarak Trafik Kazalarının Sonucunu Tahmin Etme

Öz: Ülkelerin ekonomilerine, milli varlıklarına zarar verip insanların yaşamlarına sebep olan trafik kazaları, ülkelerin en büyük sorunlarından biridir. Dolayısıyla, kazaların meydana gelmesine katkıda bulunan faktörlerin araştırılması ve doğru bir kaza şiddeti tahmin modelinin geliştirilmesi kritik öneme sahiptir. Bu çalışmada, 2011-2021 yılları arasında Teksas'ın Austin, Dallas ve San Antonio şehirlerinden toplanan trafik kazası verileri kullanılarak, kazalara sebep olan faktörler incelenip, Derin Öğrenme, Lojistik Regresyon, XGBoost, Random Forest, KNN ve SVM gibi 6 farklı makine öğrenme tekniğinin kaza şiddet tahmin performans sonuçları karşılaştırılırdı. Elde edilen bulgular, Lojistik Regresyon algoritmasının kaza şiddetini sınıflandırmada %88 doğrulukla diğerleri arasında en iyi performansı gösterdiğini göstermektedir.

1. INTRODUCTION

Traffic accidents are happening every second worldwide and are causing both people's lives and negative impacts on countries' economies. Although it might be difficult to avoid traffic accidents altogether, reducing the occurrence rate and death rate by taking some pre-measures is possible. As traffic accidents result from road conditions, weather conditions, driver's behavior, or any combinations, machine learning techniques could help model the accidents and classify the severity of the accidents.

Several studies have been conducted on traffic accident classification. Two of them are traffic accident analyses carried out by the same authors with different methods in the studies [1] and [2]. Another study on the classification of traffic accidents is presented in work [3] in Korea. The research [4] probes driver injury severity, which is divided into three classes: no injury, possible injury, and disabling injury, at the signalized intersections in central Florida, while another study reveals the relation between speed limit increase and fatal crash rate in Washington State [5]. A similar study to detect the severity of accidents is conducted with data containing close to 35000 records in Hong Kong using the WEKA tool [6]. Authors of work [7] use the support vector machines to find a pattern in crash injury severity by using collected data from rollover accidents within a

period of two years in New Mexico. Using more than 270000 traffic accident records collected in Michigan, USA, from 2010 to 2016, the study predicts accident severity utilizing machine learning algorithms: Logistic Regression, Random Forest Model, Naïve Bayesian Classifier, AdaBoost Classification Tree [8]. Work [9] presents a case study of traffic accident classification and severity prediction in Spain using data collected over a six-year period (2011–2015) by the Spanish traffic agency. Reference [10] investigated the key factors associated with fatal severity by analyzing 971 accidents in Abu Dhabi in 2014. Authors of [11] investigate prominent factors in traffic accidents in Adana province, Turkey, and classify them according to their injury severity (i.e., fatal, non-fatal). Work [12] conducts a case study in the example of rural roads in Texas. Authors probe crash factor identification and severity prediction in accidents involving teen drivers. The outcomes are evaluated in terms of prediction performance and speed, and XGBoost is concluded to be the best-performing one in both categories.

This paper presents the utilization of deep learning and machine learning algorithms to predict traffic accident severity and identify underlying reasons causing both casualties and damages to national assets. We analyzed data recorded by the Texas Department of Transportation (TxDOT) in Austin, Dallas, and San Antonio cities from 2011 through 2021. Data is accessed through the Crash Records Information System (CRIS) [13]. Deep learning and five different machine learning algorithms, Logistic regression, K-Nearest Neighbors, Support Vector Machine, Random Forest, and XGBoost classifiers, are considered, and their results are compared.

2. MATERIAL AND METHOD

2.1. Dataset and Datamining Process

CRIS database accommodates a variety of traffic accident data from 2011 through 2021 for any city or county in the state of Texas. Dataset can be created with multiple features, such as weather conditions, road surface conditions, light conditions, crash severity, crash time, crash date, location, airbag deployment status, human-related factors contributing to the crash, vehicle-related attributes, and many others. The dataset for this study contains close to 1.1 million accident records. We constructed our data set with attributes; weather conditions, road surface conditions, crash severity, airbag deployment status, human-related factors, and person injury severity. Figure 1 shows the comparison of the number of Fatal/Serious and Other injuries by year from the constructed dataset.

The classification of traffic accident severity is performed in different stages, which involves cleaning, feature selection, and transformation before training each model. We make use of python, deep learning framework Keras [14], machine learning library scikit-learn [15], and pandas [16] for cleaning and training a model. After cleaning the raw data as some of the

attributes have many missing or "unknown" data, all the categorical values are encoded into numerical ones (0-1) using the pandas "get_dummies" function for further processing. The cleaned data set is then split into two as train and test set at a rate of 75% and 25%, respectively. The attributes "Speed limit," "Car_Age," and "Vehicle_Damage_Rating" have values varying in different ranges, and it is an issue for machine learning algorithms as they do not contribute equally to the model. Thus, we used Scikit-learn's "StandardScaler" class to scale all the features with a mean of zero and a standard deviation equal to one.

Figure 1. The number of Fatal/Serious and Other injuries by year. Data from San Antonio city is included partially

Classification algorithms usually perform poorly with imbalanced data sets; hence obtained accuracy results are likely to be misleading. As the classes in our data are distributed unevenly, as seen in Figure 2, the down-sampling method is applied to the majority class using python's resampling library [17] to overcome the performance issue. After getting the data ready for building predictive models for person injury severity, the deep learning classification technique and the scikit-learn library are utilized to implement Random Forest, XGBoost, Logistic Regression, K-Nearest Neighbors, and SVM classifiers algorithms.
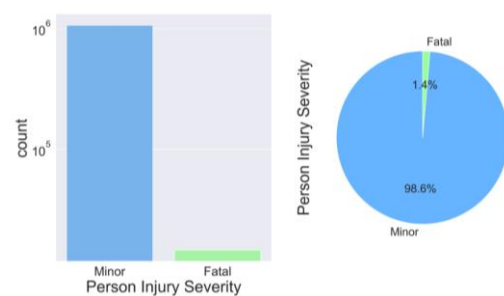
Figure 2. The number of instances corresponding to each class

2.2. Classification Algorithms

2.2.1. Logistic regression (LR)

As opposed to regression in its name, Logistic regression formulated in 1958 by David Cox is a classification model [18]. It is widely used for both binary and multi-class classification problems and achieves excellent performance for linearly separable classes. LR uses the sigmoid function shown below in equation 1, and the y-axis corresponds to the classification's probability.

Tr. Doğa ve Fen Derg. Cilt 11, Sayı 3, Sayfa 79-83, 2022

Tr. J. Nature Sci. Volume 11, Issue 3, Page 79-83, 2022

$$Logistic\ function = \frac{1}{1+e^{-x}} \qquad (1)$$

2.2.2. Random forests (RF)

Random forests [19], a supervised learning algorithm, are an ensemble method of decision trees trained on a subset of the training set. Random forest is widely used for classification and regression tasks. Since RF is a combination of learning models, it performs better than any single predictor itself.

2.2.3. XGBoost

XGBoost [20] algorithm stands for "Extreme Gradient Boosting" and is an implementation of a gradient boosting library. XGBoost is known for a better execution speed on a large number of data set as well as utilizing memory resources efficiently.

2.2.4. K-Nearest neighbors (KNN)

K-Nearest Neighbors [21] algorithm is a supervised machine learning algorithm that can be used for both classification and regression problems. KNN is a distance-based algorithm that predicts to which class an unknown data point might belong.

2.2.5. Support vector machine (SVM)

Support Vector Machine [22] is also a supervised learning model used for both classification and regression tasks. The idea behind how it works is to construct an optimum hyperplane in multi-dimensional space to separate classes and predict which classes a new example belongs to. The optimum hyperplane is obtained when the distance from the hyperplane to the closest data points of any class is maximized. This optimum hyperplane is also called a maximum-margin hyperplane.

2.2.6. Deep learning

Deep learning [23] is a subfield of machine learning that uses neural networks to generate data-learning and prediction-capable models. Neural networks are systems of interconnected nodes, known as neurons, that imitate the functioning of the human brain. A neural network is constructed of layers of nodes, with each layer transforming the incoming data in a unique manner. The input layer accepts unprocessed data as input and transmits it to subsequent processing layers. Each layer computes a function on the previous layer's output and then passes its output to the next layer for further processing. Finally, the outputs from all layers are integrated into a single set that represents the final prediction or classification. In order to minimize prediction errors and achieve higher accuracy in a deep learning model, the back-propagation algorithm, altering the weights of connections between nodes, is made use of.

3. RESULTS

In this section, we present and discuss results from different classification techniques as well as analyze the major contributing factors to the accidents. Figure 3 shows contributing factors to traffic crashes on the roads of Austin, Dallas, and San Antonio. As seen from the histogram, driver's inattention (19%), failing speed control (15%), and following too closely (10%) are some of the major contributing factors. Other minor factors are cell/mobile device use, speeding (over limit), impaired visibility, being under drug influence, and failing to yield right of way to pedestrians. While disregarding the stop signs and traffic lights contributes to crashes 6.5%, speed-related crashes are about 18% overall.
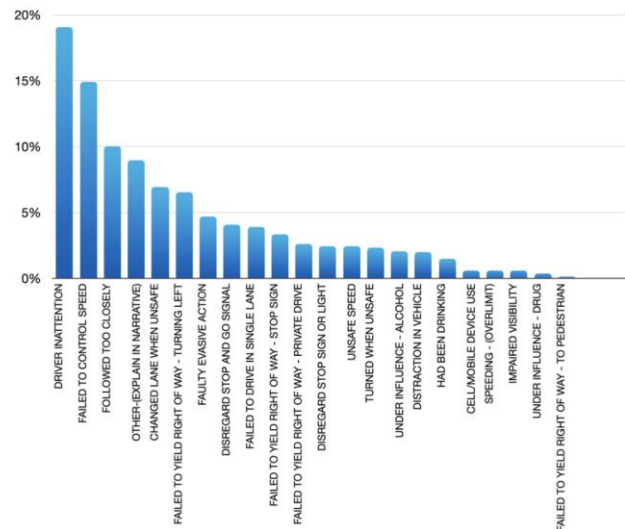
Figure 3. Major contributing factors to crashes in Austin, Dallas, and San Antonio

As the performance measures of the models, we utilized the weighted average for recall, the weighted average for f1-score, the Receiver Operator Characteristic (ROC), and the Area Under the Receiver Operating Characteristic Curve (AUC). Table 1 shows the performance of all classification techniques used in this work. While Figure 4 shows the confusion matrix for the best classifier in this work, Figure 5 and Figure 6 depict ROC comparison and AUC values for each model, respectively. AUC value varies between 0-1, and the bigger AUC indicates how better the model's classification performance is. An AUC value of 1 indicates that the model is excellent, whereas 0.5 or less means the model is poor. An AUC value greater than 0.7 generally indicates that a model has good prediction ability for classification.

81
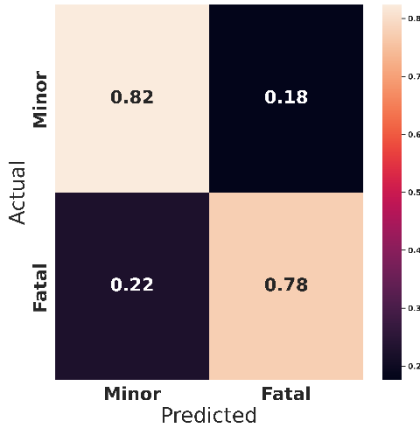
Figure 4. Confusion Matrix for Logistic Regression Model

Although all of the AUC values from different models are fairly close, the LR algorithm outperforms the others with an 88.1% accuracy. XGBoost has a better performance with 87.9% accuracy than SVM with 87.4%. An accuracy of 86.0%, 85.8%, and 80.6% is obtained with deep learning, RF, and KNN, respectively. A comparison of the AUC value for all the classifiers is shown in Figure 6. The result demonstrates that Logistic regression is the best classifier, although the second-best model, XGBoost, performs nearly well.

Table 1. Performance measures with different machine learning techniques

Models	Recall	F1-Score
XGBOOST	81%	88%
KNN	79%	87%
LR	82%	89%
RF	79%	87%
SVM	77%	86%
Deep Learning	81%	88%

Figure 5. ROC distribution for all the trained models

4. DISCUSSION AND CONCLUSION

The second most populated state in the United States [24], Texas also has more than 22 million registered vehicles [25]. These figures indicate that there are approximately 75 vehicles per 100 people, implying that there might be a significant number of vehicles on the roads on a daily 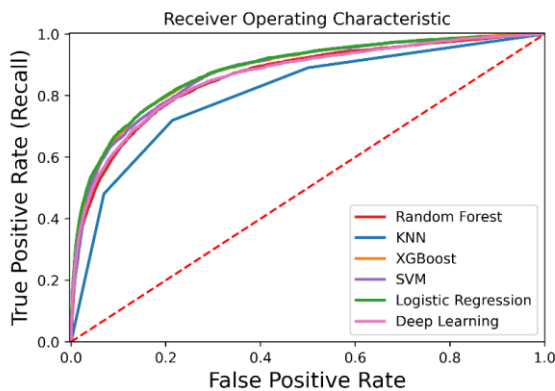basis. In this study, we investigate the primary contributing factors in crashes and forecast crash severity in three major cities: Austin, Dallas, and

San Antonio. According to the findings, driver inattention, failure to manage speed, and following too closely are the top three most common contributing causes in collisions. As one might expect, these three contributing factors might be reasonable findings as there are too many distracting elements around us today, which may cause drivers to lose focus and miss the instructions and traffic signs/warnings on the roads that ultimately trigger accidents. The inability to manage speed and following too close may be the outcome of over-reliance on automobiles and disregarding other considerations since modern vehicles include new features and safety precautions that might mislead the drivers to over-rely on them. Consequently, identifying important factors causing crashes can assist policymakers in developing new road safety policies and engineers in building safer roads. Additionally, predicting accident severity in real-time with our high-accuracy model might assist in taking the necessary prompt action in arriving at the crash scene to reduce the accident's severity. We also probed the performance of different classification techniques in classifying traffic accident severity, grouped into two categories: Fatal/Serious and other injuries. Based on the performance metrics considered in this study, Logistic Regression shows the best performance, with 88.1% accuracy in classifying accident severity (see Figure 6).
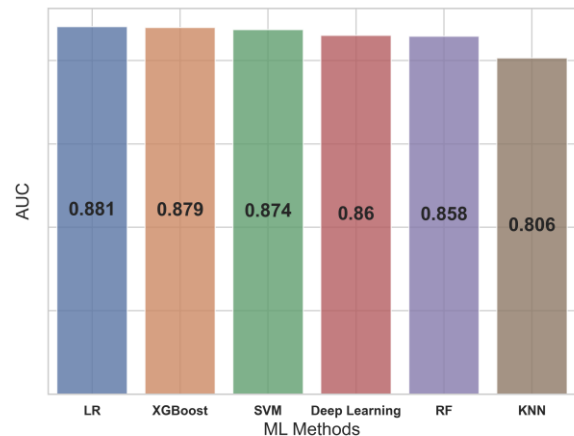
Figure 6. Comparison of AUC values for different trained models

Various research groups conduct similar studies for predicting the severity of accidents. While other works are evaluated with different performance metrics, work [8] adopts AUC as a performance metric to evaluate their findings. For predicting the severity of accidents in the Michigan example, 75.5% accuracy is obtained. However, a better result is presented in this study by analyzing the dataset collected in Texas's three major cities between 2011 and 2021.

REFERENCES

[1] Chong M, Abraham A, Paprzycki M. Traffic accident data mining using machine learning paradigms. In: *Fourth International Conference on Intelligent Systems Design and Applications (ISDA'04), Hungary*. 2004, pp. 415–420.

[2] Chong MM, Abraham A, Paprzycki M. Traffic accident analysis using decision trees and neural networks. *ArXiv Prepr Cs0405050*.

[3] Sohn SY, Lee SH. Data fusion, ensemble and clustering to improve the classification accuracy for the severity of road traffic accidents in Korea. *Saf Sci* 2003; 41: 1–14.

[4] Abdelwahab HT, Abdel-Aty MA. Development of artificial neural network models to predict driver injury severity in traffic accidents at signalized intersections. *Transp Res Rec* 2001; 1746: 6–13.

[5] Ossiander EM, Cummings P. Freeway speed limits and traffic fatalities in Washington State. *Accid Anal Prev* 2002; 34: 13–18.

[6] Krishnaveni S, Hemalatha M. A perspective analysis of traffic accident using data mining techniques. *Int J Comput Appl* 2011; 23: 40–48.

[7] Chen C, Zhang G, Qian Z, et al. Investigating driver injury severity patterns in rollover crashes using support vector machine models. *Accid Anal Prev* 2016; 90: 128–139.

[8] Comparison of Machine Learning Algorithms for Predicting Traffic Accident Severity | IEEE Conference Publication | IEEE Xplore, https://ieeexplore.ieee.org/abstract/document/8717393 (accessed 4 December 2021).

[9] Traffic Accidents Classification and Injury Severity Prediction | IEEE Conference Publication | IEEE Xplore, https://ieeexplore.ieee.org/document/8492545 (accessed 3 January 2022).

[10] Taamneh M, Alkheder S, Taamneh S. Data-mining techniques for traffic accident modeling and prediction in the United Arab Emirates. *J Transp Saf Secur* 2017; 9: 146–166.

[11] Aci C, Ozden C. Predicting the Severity of Motor Vehicle Accident Injuries in Adana-Turkey Using Machine Learning Methods and Detailed Meteorological Data. *Int J Intell Syst Appl Eng* 2018; 6: 72–79.

[12] Lin C, Wu D, Liu H, et al. Factor Identification and Prediction for Teen Driver Crash Severity Using Machine Learning: A Case Study. *Appl Sci* 2020; 10: 1675.

[13] CRIS Query, https://cris.dot.state.tx.us/public/Query/app/home (accessed 4 December 2021).

[14] Chollet F, others. Keras, https://github.com/fchollet/keras (2015).

[15] Pedregosa F, Varoquaux G, Gramfort A, et al. Scikit-learn: Machine Learning in Python. *J Mach Learn Res* 2011; 12: 2825–2830.

[16] McKinney W, others. Data structures for statistical computing in python. In: *Proceedings of the 9th Python in Science Conference*. Austin, TX, 2010, pp. 51–56.

[17] Lemaître G, Nogueira F, Aridas CK. Imbalanced-learn: A python toolbox to tackle the curse of imbalanced datasets in machine learning. *J Mach Learn Res* 2017; 18: 559–563.

[18] Cox DR. The regression analysis of binary sequences. *J R Stat Soc Ser B Methodol* 1958; 20: 215–232.

[19] Ho TK. Random decision forests. In: *Proceedings of 3rd international conference on document analysis and recognition*. IEEE, 1995, pp. 278–282.

[20] XGBoost | Proceedings of the 22nd ACM SIGKDD International Conference on Knowledge Discovery and Data Mining, https://dl.acm.org/doi/10.1145/2939672.2939785 (accessed 26 June 2022).

[21] Peterson LE. K-nearest neighbor. *Scholarpedia* 2009; 4: 1883.

[22] Cortes C, Vapnik V. Support-vector networks. *Mach Learn* 1995; 20: 273–297.

[23] LeCun Y, Bengio Y, Hinton G. Deep learning. *Nature* 2015; 521: 436–444.

[24] US States - Ranked by Population 2022, https://worldpopulationreview.com/states (accessed 18 May 2022).

[25] Motor vehicles in the U.S. - registrations by state. *Statista*, https://www.statista.com/statistics/196505/total-number-of-registered-motor-vehicles-in-the-us-by-state/ (accessed 18 May 2022).

Türk Doğa ve Fen Dergisi
Turkish Journal of Nature and Science
www.dergipark.gov.tr/tdfd

Evaluations on the Use Potential of Some Woody Plants Naturally Growing in Elazığ Flora in Landscape Architecture

Musa Denizhan ULUSAN[1*], Rıdvan POLAT[2]

[1]Süleyman Demirel University, General Secretariat Unit, Isparta, Türkiye
[2]Bingöl University, Faculty of Agriculture, Department of Landscape Architecture, Bingöl, Türkiye
Musa Denizhan ULUSAN ORCID No: 0000-0001-9040-5025
Rıdvan POLAT ORCID No: 0000-0003-0261-3671

Corresponding author: rpolat@bingol.edu.tr

Keywords
Elazığ,
Flora,
Woody Plants,
Landscape

Abstract: In this study, the potential of use in the landscape area of some woody plants that naturally spread in the flora of Elazig was investigated. As a result of the researches, it was determined that 29 genera and 54 natural plant taxa belonging to 18 families in the region have potential landscape plant characteristics. Families with the most taxa; Rosaceae (19 taxa), Salicaceae (4 taxa), and Fagaceae (4 taxa). The genera with the most taxa are; *Crataegus*, *Rosa* and *Quercus* with 4 taxa each, followed by *Acer, Tamarix* and *Sorbus* with 3 taxa each. As a result of the evaluation, the woody plants with landscape potential in the region are used for ornamentation, aesthetics, fence, ground cover, etc. It has been found that it can be used for many purposes.

Elazığ Florasında Doğal Olarak Yetişen Bazı Odunsu Bitkilerin Peyzaj Mimarlığında Kullanım Potansiyeli Üzerine Değerlendirmeler

Anahtar Kelimeler
Elazığ,
Flora,
Odunsu bitkiler,
Peyzaj

Öz: Bu çalışmada Elazığ florasında doğal olarak yayılış gösteren bazı odunsu bitkilerin peyzaj alanında kullanım potansiyelleri incelenmiştir. Araştırmalar sonucunda bölgede 18 familyaya ait 29 cins ve 54 doğal bitki taksonunun potansiyel peyzaj bitkisi özelliklerine sahip olduğu belirlenmiştir. En çok taksona sahip familyalar; Rosaceae (19 takson), Salicaceae (4 takson) ve Fagaceae (4 takson). En çok taksona sahip olan cinslere bakıldığında ise; *Crataegus*, *Rosa* ve *Quercus* 4'er takson, onu 3'er taksonla *Acer*, *Tamarix* ve *Sorbus* takip etmektedir. Değerlendirme sonucunda yörede peyzaj potansiyeli olan odunsu bitkilerin süsleme, estetik, çit, yer örtücü vb. birçok amaçla kullanılabileceği tespit edilmiştir.

1. INTRODUCTION

Flora is considered to be one of most important figure of the landscape. The greenery space design landscape scenery and have productive and eco-stabilizing functions in the landscape area. Trees and shrubs have great influence on the environment and living conditions of the other organisms. Short term changes in ecosystems do not significantly impact their lifecycle and survival. Woody plants are long lived organisms with different adaptability to changes of environmental conditions [1,2].

Trees and shrubs constitute an important element in the cityscape [3]. The natural, graceful shapes of trees provide an architectural transition between human size and the scale of buildings and streets [4,5], and over the ages urban tree plantings have been regarded as a mirror of the prosperity and achievements of society. Trees help reduce the urban heat intensity [6]. Urban trees are capable of reducing storm water runoff and thereby reduce flooding [7]. They act as noise filters and purify the air through capturing particulate matter, carbon dioxide, ozone and other air pollutants originating from traffic and industrial activities [7,8,9]. However, the above-mentioned aesthetic, social and microclimatic ameliorations are only possible if the urban tree stock is vital.

Natural flora is the main source of landscape plants all over the world. Turkey is one of the major floral regions in the world, with more than 12,000 taxa of herbaceous and woody species, of which 3500 species are endemic.

The rich vegetation in Turkey is because of its geographic location, vegetation zones and the different climate and sub - climate types [10].

The aim of this study is to reveal wild woody plants that have the potential to be used for landscaping purposes, which naturally spread in the flora of Elazığ.

2. MATERIAL AND METHOD

2.1. Study Area

Study area was located on the east of Anatolian diagonal, in the skirts of South-Eastern Taurus Mountains [11], in the Upper Euphrates Region of the Eastern Anatolia Region, Elazığ (**Fig. 1**) is under the influence of Irano-Turanian Plant Geography Region and falls within the B7 grid square according to the Grid classification system developed by Davis [12].

Figure 1. Study area

The surface area of the province is 9313 km^2 and is 1067–1225 m high from sea level. It is located on the high plateaus of Eastern Anatolian Region and it is located between 40°21′–38°30′ northern latitudes and 38°17′–39°11′ eastern longitudes. Elazığ has 10 sub-provinces and 544 villages.

2.2. Methods

In this research the potential landscape usages of some of the woody plants in Elazığ Providence have been investigated. In between the years 2019-2021 visits to the field have been made in different vegetation seasons. Identification of plants in the area was made mostly during fieldwork. Plant samples were taken from unidentified species and preserved for later identification. Various floristic works on natural plants were used in the identification of plants [10,12,14-16]. Current scientific names and author names of taxa are arranged according to World Flora Online [17].

In the evaluation phase of the general data, the potential use of plant species in the landscape (aesthetics and visuality, hedge formation, surface covering, shading, emphasis, naturalness, etc.), flowering periods, flower/fruit colors were emphasized. The appearance of some plant taxa in the field, which were determined

during the studies and could come to the fore in landscape use, were photographed.

3. RESULTS

Landscape studies generally consider the characteristics of plants such as emphasis, color, form and aesthetics. There are many woody plant taxa in the flora of Elazığ, which stand out with their color, form and aesthetic features and have the potential to be evaluated in the landscape**.**

As a result of the studies, it was determined that 29 genera and 54 natural plant taxa belonging to 18 families in the region have potential landscape plant characteristics**.** Families with the most taxa; Rosaceae (19 taxa), Salicaceae (4 taxa), and Fagaceae (4 taxa). The genera with the most taxa are; *Crataegus*, *Rosa* and *Quercus* with 4 taxa each, followed by *Acer, Tamarix* and *Sorbus* with 3 taxa each. As a result of the evaluation, the majority of the woody plants are used for more than one purpose (Table 1).

When the data obtained in the study were evaluated, it was determined that many taxa attracted attention with their flower beauty and fruit characteristics (**Fig. 2, 3).** Woody plants with flower characteristics are preferred to create spring coloration in the landscape with their flower characteristics.
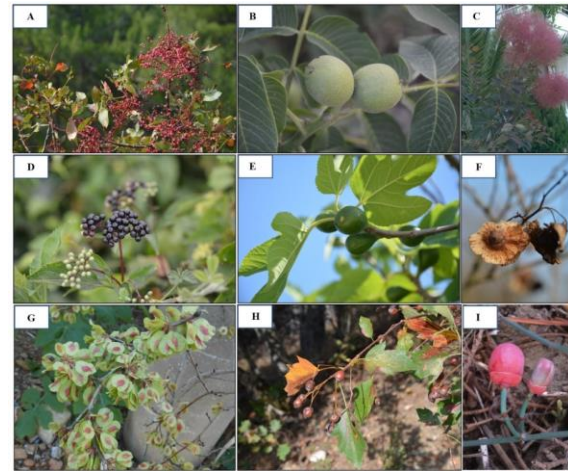

Fiure 2. Some potential taxa with fruit characteristics in Elazığ flora : A) *Pistacia palaestina* Boiss. B) *Juglans regia* L .C) *Cotinus coggygria* Scop. D) *Sambucus nigra* L. E) *Ficus carica* L. subsp. *carica* F) *Paliurus spina-christi* P. Mill. G) *Ulmus minor* Mill. H) *Sorbus torminalis* (L.) Crantz var. *torminalis* I) *Ephedra major* Host. subsp. *major*
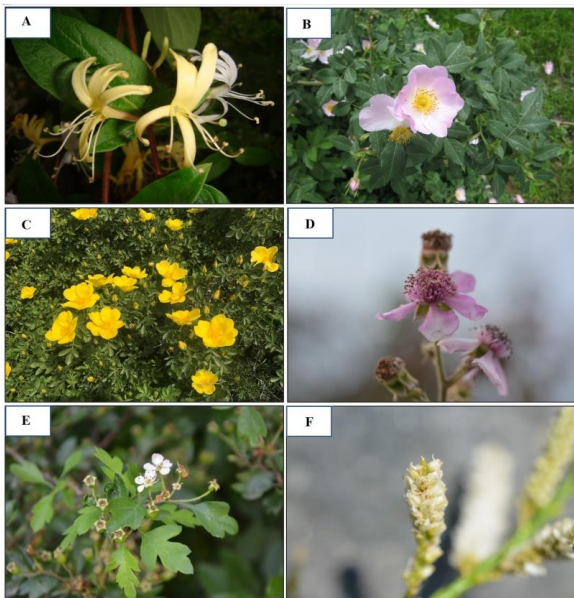
85

Figure 3. Some potential taxa with flower characteristics in Elazığ flora : A) *Lonicera etrusca* Santi var. *etrusca.* B) *Rosa canina* L. C) *Rosa foetida* J. Herrm.. D) *Rubus sanctus* Schreb. .L. E) *Crataegus monogyna* Jacq. F) *Tamarix smyrnensis* Bunge

However, it has been observed that some taxa spreading in the region have the potential to be used as hedges and ground covers as well as ornamentation. In addition to ornamental/aesthetic use, approximately 17 taxa from the plants identified in the studies conducted in the region have also been found to be used as hedges (Table 1). Some of the plant taxa that have the potential to be used as hedges are as follows; *Berberis crataegina*, *Colutea cilicica*, *Ephedra major*, *Genista albida*, *Genista aucheri*, *Lonicera etrusca*, *Glycyrrhiza glabra*, *Tamarix smyrnesis.*

Studies in the research area mention the usage areas of some taxa (13 taxa) distributed in the flora of Elazig as groundcovers in landscape studies. *Sambucus nigra*, *Lonicera etrusca*, *Genista albida*, *Spiraea crenata* and *Tamarix tetrandra* are some of these taxa.

4. DISCUSSION AND CONCLUSION

The selection of proper plants for specific stand conditions is a very important task that effects success in the landscape planning and landscape design. In Europe recent studies [18,19], documented poor diversity of tree genera an species planted in urban areas. A few genera of woody plant (*Acer*, *Aesculus*, *Platanus* and *Tillia*) are used at street trees.

In a study conducted in the Gürün (Sivas) region, which is close to the study area, it was determined that 42 plant taxa were used in urban landscape studies for various purposes [20]. In a study conducted in the Bartın region, it was determined that about 25 woody plants were used in landscape studies [21].The variety of species planted on roadsides, parks, gardens and residential areas in the region is very limited. The number of exotic taxa is high in plants used in landscape studies in Elazig and other province.

Spellenberg and Given [22], reviewed general criteria for tree selection for urban environments. According to their worldwide knowledge, the most important criteria for selecting trees for urban environments are: suitability of taxa to local conditions, low maintenance cost and avoidance of structural problems. Considering these criteria, the importance of local taxa becomes more evident.

In order to have a healthy and sustainable urban landscape tree and shrub population, a high diversity of species and genera is so important. The reflection of potential taxa in the natural flora to the landscape areas in the region will increase the diversity. The diversity in the city's landscape clarifies the distinction between street and green space. The diversity of native and non-native tree species is also of great importance in urban environments in the region [23].

As a result of the studies in Elazığ province, it has been seen that many natural plant taxa that can easily benefit from the landscape in terms of fence, ground cover and similar features, especially visual-form and aesthetics, spread in the region. Indigenous natural taxa should support to increased biodiversity in urban areas with ecologically better-balanced plant communities. Preferring natural taxa suitable for the texture of the city in urban landscape areas will provide important economic advantages as well as solving ecological adaptation problems. The reflection of the rich natural flora of our country on the landscape of the cities, besides increasing the visual diversity, provides the recognition of the flora.

REFERENCES

[1] Bakay L, Paganová V. Evaluation of phenological activity of progenies of true service tree (Sorbus domestica L.) from the locality Jelenec. Acta Horticulturae et Regiotecturae, 2010, 13(2), 38-41.

[2] Sjöman H. Trees for tough urban sites, 2012, 7.

[3] Arnold H.F. Trees in urban design. 2nd edition. 1993, Van Norstrand Reinhold, New York.

[4] Jacobs A.B. Great Streets. 1995, MIT Press, Cambridge, MA

[5] Bell S, Blom D. Rautamäki, M., Castel-Branco, C., Simson, A., Olsen, I.A. Design of Urban Forests. In: Konijnendijk, C.C., K. Nilsson, T.B. Randrup, and J. Schipperijn (Eds.) Urban Forests and Trees, 2005, pp. 149-186. Springer.Ğ

[6] King VJ, Davis C. A case study of urban heat island in the Carolinas. Enviromental Hazards, 2007. 7, 353-359

[7] McPherson E.G, Nowak D, Heisler G, Grimmond S, Souch C, Grant R, Rowntree R. Quantifying urban forest structure, function and value: the Chicago Urban Forest Climate Project. Urban Ecosystems, 1997, 1, 49-61.

[8] Becket K.P, Freer-Smith P, Taylor G. Effective tree species for local air-quality management. Journal of Arboriculture, 2000, 26, 12-19.

[9] Nowak D, Crane D, Stevens J. Air pollution removal by urban trees and shrubs in the United

States. Urban Forestry and Urban Greening, 2006, 4, 115-123.

[10] Güner, A., Aslan, S., Ekim, T., Vural, M. ve Babaç, M.T. Türkiye Bitkileri Listesi (Damarlı Bitkiler). Nezahat Gökyiğit Botanik Bahçesi ve Flora Araştırmaları Derneği Yayınları, İstanbul. 2012.

[11] Çakılcıoğlu U, Türkoğlu İ. Plants used for pass kidney stones by the folk in Elazığ, The Herb Journal of Systematic Botany, 2008, 14, pp. 133-144.

[12] Davis, P H. Flora of Turkey Volume1- 9. Edinburg University Press, Edinburg, 1967.

[13] Yücel E. Çiçekler ve yerörtücüler, Türmatsan Organize Matbaacılık San. Ltd. Şti. Eskişehir, 2012a, 352s.

[14] Yücel E. Ağaçlar ve çalılar I. Türmatsan Organize Matbaacılık San. Ltd. Şti. Eskişehir, 2012b, 277s.

[15] Akkemik Ü. (Editör). Türkiye'nin doğal-egzotik ağaç ve çalıları I, Gymnospermler-Angiospermler (A-G). Orman Genel Müdürlüğü Yayınları, Ankara, 2014a, 736s.

[16] Akkemik Ü. (Editör). Türkiye'nin doğal-egzotik ağaç ve çalıları II, Angiospermler (H-Z). Orman Genel Müdürlüğü Yayınları, Ankara, 2014b, 680s.

[17] Anonymous. The plant list. A working list of a plant species. [Online]. Available: May 2020, http://www.theplantlist.org.

[18] Pauleit S, Ennos R, Golding Y. Modeling the environmental impacts fo urban lands use and land cover change – a study in Merseyside, UK. Landscape and Urban Planning, 2005. 71, 295-310.

[19] Sæbø A, Benedikz T, Randrup T.B. Selection of trees for urban forestry in the Nordic countries. Urban Forestry and Urban Greening, 2, 2003, 101-114.

[20] Bozkurt SG, Akkemik Ü. Gürün (Sivas) ilçesinde tespit edilen odunsu bitkilerin kentsel planlama açısından kullanım olanakları, 2019, Cilt 15, Sayı 2, 137 – 152.

[21] Ekici B. Bartın kenti ve yakın çevresinde yetişen bazı doğal bitkilerin kentsel mekanlarda kullanım olanakları, Süleyman Demirel Üniversitesi Orman Fakültesi 2010, 110-126.

[22] Spongberg S.A. A reunion of trees: Discovery of exotic plants and their introduction into North American and European landscapes. 1995, Harvard University Press, Cambridge, Mass.

[23] Karaköse, M Polat R, Rahman MO, Çakilcioğlu U. Traditional honey production and bee flora of Espiye, Turkey, Bangladesh Journal of Plant Taxonomy,2018, 25 (1), 79-91.

87

Tablo 1. Elazığ Florasında potansiyel peyzaj bitkileri listesi.

Family	Plant name	Turkish Name/Local Name	Life Form	Potential Use in Landscape
Adoxaceae	*Sambucus nigra* L.	Mürver	Small tree	ornamental, fence, ground cover
Anacardiaceae	*Cotinus coggygria* Scop.	Boyacı sumağı, Duman ağacı	Shrub, Small tree	ornamental, aesthetic
Anacardiaceae	*Pistacia palaestina* Boiss.	Çöğre	Small tree	ornamental, aesthetic
Betulaceae	*Betula litwinowii* Doluch.	Huş, Düzük	Tree	ornamental, aesthetic
Betulaceae	*Betula pendula* Roth	Huş ağacı	Tree	ornamental, aesthetic
Berberidaceae	*Berberis crataegina* DC.	Karamuk	Shrub	ornamental, fence, ground cover
Cannabaceae	*Celtis planchoniana* K.I.Chr	Dahum	Small tree	ornamental, aesthetic
Cannabaceae	*Celtis tournefortii* Lam.	Dardagan	Small tree	ornamental, aesthetic
Caprifoliaceae	*Lonicera etrusca* Santi var. *etrusca*	Dokuzdon	Shrub	ornamental, aesthetic, fence
Ephedraceae	*Ephedra major* Host. subsp. *major*	Hum	Shrub	ornamental, fence, ground cover
Fabaceae	*Colutea cilicica* Boiss. & Balansa	Patlangaç	Shrub	ornamental, fence, ground cover
Fabaceae	*Genista albida* Willd.	Ak borcak	Shrub	ornamental, fence, ground cover
Fabaceae	*Genista aucheri* Boiss.	Bayır borçağı	Shrub	ornamental, fence, ground cover
Fabaceae	*Glycyrrhiza glabra* L.	Meyan	Shrub	ornamental, fence, ground cover
Fagaceae	*Quercus brantii* Lindl.	Kara meşe	Small tree	ornamental, aesthetic
Fagaceae	*Quercus cerris* L.	Saçlı meşe	Tree	ornamental, aesthetic
Fagaceae	*Quercus infectoria* Oliv. subsp. *veneris* (A.Kern.) Meikle	Zindiyen	Small tree	ornamental, aesthetic
Fagaceae	*Quercus petraea* (Matt.) Liebl. subsp. *pinnatiloba* (K.Koch) Menitsky	Koca pelit	Tree	ornamental, aesthetic
Juglandaceae	*Juglans regia* L.	Ceviz	Tree	ornamental, aesthetic
Moraceae	*Ficus carica* L. subsp. *carica*	İncir	Tree	ornamental, aesthetic
Moraceae	*Ficus carica* L. subsp. *rupestris* (Hausskn.) Browicz	İt inciri	Tree	ornamental, aesthetic
Rhamnaceae	*Paliurus spina-christi* P. Mill.	Karaçalı	Shrub	ornamental, aesthetic
Rhamnaceae	*Rhamnus alpina* L. subsp. *fallax* (Boiss.) Maire & Petitm.	Dağ cehrisi	Shrub	ornamental, aesthetic
Rhamnaceae	*Rhamnus pallasii* Fisch. & C.A.Mey.	Ala cehri	Shrub	ornamental, aesthetic
Rosaceae	*Amelanchier ovalis* Medik. subsp. *integrifolia* (Boiss. & Hohen.) Bornm.	Tüylü karagöz	Shrub	ornamental, fence, ground cover
Rosaceae	*Amygdalus communis* L.	Badem	Tree	ornamental, aesthetic
Rosaceae	*Amygdalus trichamygdalus* (Hand.-Mazz.) Woronow var. *trichamygdalus*	Haşmet bademi	Small tree	ornamental, aesthetic
Rosaceae	*Cerasus microcarpa* (C.A.Mey.) Boiss. subsp. *tortuosa* (Boiss. & Hausskn.) Browicz	Sarı dağkirazı	Shrub	ornamental, aesthetic
Rosaceae	*Crataegus ambigua* A.K.Becker	Kuşyemişi	Small tree	ornamental, aesthetic
Rosaceae	*Crataegus azarolus* L. var. *azarolus*	müzmüldek	Small tree	ornamental, aesthetic
Rosaceae	*Crataegus monogyna* Jacq.	Alıç, Sez, Sinz	Tree	ornamental, aesthetic
Rosaceae	*Crataegus orientalis* Pall. ex M.Bieb. subsp. *szovitsii* (Pojark.) K.I.Chr.	Koyun alıcı	Small tree	ornamental, aesthetic
Rosaceae	*Pyrus syriaca* Boiss. var. *syriaca*	Çakal armudu	Tree	ornamental, aesthetic
Rosaceae	*Rosa foetida* J.Herrm.	Acem sarısı	Shrub	ornamental, aesthetic
Rosaceae	*Rosa beggeriana* Schrenk	Bağdagül	Shrub	ornamental, aesthetic
Rosaceae	*Rosa canina* L.	Kuşburnu	Shrub	ornamental, aesthetic
Rosaceae	*Rosa hemisphaerica* J. Herrm.	Kadın göbeği	Shrub	ornamental, aesthetic
Rosaceae	*Rosa orientalis* A.Dupont ex DC.	Askergülü	Shrub	ornamental, aesthetic
Rosaceae	*Rubus sanctus* Schreb.	Böğürtlen	Shrub	ornamental, aesthetic
Rosaceae	*Sorbus torminalis* (L.) Crantz var. *torminalis*	Pitlicen	Small tree	ornamental, aesthetic
Rosaceae	*Sorbus umbellata* Fritsch	Geyik elması	Small tree	ornamental, aesthetic
Rosaceae	*Sorbus roopiana* Bordz.	Kanık üvez	Small tree	ornamental, fence, ground cover
Rosaceae	*Spiraea crenata* subsp. *crenata* L.	Keçi sakalı	Shrub	ornamental, fence, ground cover
Salicaceae	*Populus alba* L. var. *alba*	Ak kavak	Tree	ornamental, aesthetic
Salicaceae	*Populus tremula* L. subsp. *tremula*	Titrek kavak	Tree	ornamental, aesthetic
Salicaceae	*Salix alba* L. subsp. *alba*	Aksöğüt	Tree	ornamental, aesthetic
Salicaceae	*Salix caprea* L.	Sorgun	Small tree	ornamental, aesthetic
Sapindaceae	*Acer campestre* L.	Ova Akçaağacı	Tree	ornamental, fence
Sapindaceae	*Acer tataricum* subsp. *tataricum* L.	Akçaağaç	Tree	ornamental, fence
Sapindaceae	*Acer hyrcanum* Fisch. & C.A.Mey. subsp. *hyrcanum*	Akçaağaç	Tree	ornamental, fence
Tamaricaceae	*Tamarix tetrandra* Pall. ex M.Bieb.	Ilgın, Gezik	Shrub	ornamental, fence, ground cover
Tamaricaceae	*Tamarix smyrnensis* Bunge	Ilgın	Shrub	ornamental, fence, ground cover
Tamaricaceae	*Tamarix gracilis* Willd.	İnce ılgın	Tree	ornamental, fence, ground cover
Ulmaceae	*Ulmus minor* Mill.	Ova karaağacı	Tree	ornamental, aesthetic

Türk Doğa ve Fen Dergisi
Turkish Journal of Nature and Science
www.dergipark.gov.tr/tdfd

The Antinociceptive Effect of Adalimumab, A TNF-Alpha Inhibitor, in a Formalin Induced Inflammatory Pain Model in Mice

Mehmet ÖZ[1*], Hasan ŞİMŞEK[1]

[1] Department of Physiology, Faculty of Medicine, University of Aksaray, Aksaray, Türkiye
Mehmet ÖZ ORCID No: 0000-0003-4167-2623
Hasan ŞİMŞEK ORCID No: 0000-0001-5573-4923

Corresponding author: ozmhmt@gmail.com

Abstract: The aim of this study, evaluate the nociceptive effect of adalimumab, a TNF-alpha inhibitor, on formalin-induced inflammatory pain in mice. The antinociceptive activity of adalimumab was determined on adult male BALB-C mice (6 mice in each group) by a formalin-induced inflammatory pain model and hot plate test applied. Diclofenac, which we used as a positive control, showed anti-nociceptive activity in both phases of the formalin test. The effect of the hot plate test at the thirtieth minute was statistically significantly different. Adalimumab was not effective in the neuronal phase of the formalin test but showed an antinociceptive effect in the inflammatory phase. Changes due to adalimumab in the hot plate test did not reach statistical significance. The findings of this study showed that adalimumab, which we applied as a single dose, had antinociceptive activity in the inflammatory phase of the formalin test. This result indicated that the peripheral analgesic effect of adalimumab is stronger.

89

Farelerde Formalin Kaynaklı İnflamatuar Ağrı Modelinde Bir Tnf-Alfa İnhibitörü Olan Adalimumabın Antinosiseptif Etkisi

Öz: Bu çalışma farelerde formalin testiyle uyarılmış inflamatuar ağrı üzerine bir tnf-alfa inhibitörü olan adalimumabın nosiseptif etkisinin değerlendirilmesi amacıyla gerçekleştirildi. Adalimumab'ın anti-nosiseptif aktivitesi formalin ile uyarılmış inflamatuar ağrı modeli ve sıcak tabaka testleri ile erişkin erkek BALB-C ırkı fareler (her grupta 6 fare) kullanılarak gerçekleştirildi. Adalimumab tek doz (10 mg/kg) olarak formalin enjeksiyonundan 120 saat önce uygulandı. Pozitif kontrol olarak uyguladığımız diklofenak sodyum formalin enjeksiyonundan 15 dakika önce 10 mg/kg dozunda uygulandı. Diklofenak sodyum, formalin testinin her iki fazında da anti-nosiseptif aktivite gösterdi. Sıcak plaka testinde otuzuncu dakikadaki etkisi anlamlı olarak farklıydı. Adalimumab, formalin testinin nöronal fazında etkili değildi, inflamatuar fazda antinosiseptif etki gösterdi. Sıcak plaka testinde adalimumaba bağlı değişiklikler anlamlılığa ulaşamadı. Sonuç olarak, tek doz uyguladığımız adalimumabın formalin testinin inflamatuar fazında anti-nosiseptif aktiviteye sahip olduğunu gösterdi. Bu sonuç adalimumabın periferik analjezik etkisinin daha güçlü olduğunu göstermektedir.

1. INTRODUCTION

Pain is one of the global health problems that negatively affect the quality of life and can be defined as excessive neuronal activity caused by the activation of many ion channels and related receptors, which causes depolarization of nociceptive nerve endings and accordingly creates action potentials [1]. Pain is actually a symptom and often does not occur spontaneously, but is accompanied by a chronic metabolic disease such as diabetes and rheumatoid arthritis [2]. It has also been

reported to be associated with anxiety and depression in some societies [3]. It is possible to classify pain into different categories as acute pain and chronic pain according to duration, inflammatory pain and neuropathic pain in terms of pathogenesis, somatic pain and visceral pain according to the region, mild-moderate and severe pain according to intensity [1]. Inflammatory pain occurs in response to tissue damage and inflammation. The sensory nervous system responds to stimuli by undergoing certain changes in its response capacity to repair the affected part of the body. This is sometimes in the form of pain response to normally

Tr. Doğa ve Fen Derg. Cilt 11, Sayı 3, Sayfa 89-93, 2022

Tr. J. Nature Sci. Volume 11, Issue 3, Page 89-93, 2022

harmless stimuli (allodynia) and sometimes in the form of a widening of the response to the stimulus that produces a response (hyperalgesia), and the pain associated with the perception of harmful stimuli is called nociceptive pain [4]. Although non-steroidal anti-inflammatory drugs such as opioids and glucocorticoids are widely used to treat inflammation and related diseases, chronic applications of these drugs bring the use of new drugs to the agenda due to side effects such as stomach irritation and ulcers, hepatotoxicity and kidney failure [5].

While the evidence for the role of proinflammatory cytokines in the formation of inflammation is increasing, it is known that tumor necrosis factor-alpha (TNF-alpha), interleukin 6 (IL-6), and IL-1β take an active role in this process [6]. Adalimumab, an anti-TNF-alpha monoclonal antibody, binds directly to TNF-alpha and blocks its receptor binding or after dissolving to inhibit TNF-alpha binding, it binds to membrane TNF receptors and exerts a bidirectional effect [7]. Although it is used to modify inflammatory responses in rheumatic diseases such as rheumatoid arthritis and ankylosing spondylitis [8], and inflammatory bowel diseases such as Crohn's disease [9], increasing evidence now shows the efficacy of adalimumab in more pathological conditions. Adalimumab, ameliorates cognitive impairment by attenuating neuroinflammation in the mouse model of Alzheimer's disease [10], reduces methotrexate-induced organ toxicity with toxic side effects on tissues and organs [11], limits the production of proinflammatory cytokines in the experimental animal model of acute lung injury, and improves tissue inflammation [12], prevents cognitive impairment and neuroinflammation caused by chronic cerebral hypoperfusion [13], reduces pulmonary edema and histological damage due to mechanical ventilation [14], alleviates endotoxin-induced cardiac damage by modulating cytokine secretion [15], protective effect by reducing blood sugar and cytokine secretion in obese diabetic rats [16], prevents lipid peroxidation caused by spinal cord trauma in rats [17]. It contributes to the regulation of cognitive and emotional processes in response to anti-inflammatory therapy with adalimumab in patients suffering from inflammatory bowel disease [18].
Findings in current studies that adalimumab controls inflammation processes by regulating proinflammatory cytokine release and is therapeutically effective suggest that it may be effective in the inflammatory pain model. For this purpose, this study was planned to evaluate the efficacy of adalimumab in mice with formalin induced inflammatory pain and to compare it with another therapeutic agent with proven efficacy.

2. MATERIAL AND METHOD

2.1. Animals

The mice used in our study were obtained from Selcuk University Experimental Medicine Research and Application Center and the study was carried out in this center. BALB/C male mice weighing 27-30 grams, 8-10 weeks old, were kept in a climate-controlled room with a temperature of 22±2 °C and relative humidity of 50±5% in a 12-hour light and 12-hour dark period. Mice received standard mouse chow and water ad libitum. This study was started after obtaining the necessary permission from the Experimental Medicine Research and Application Center Experimental Animals Local Ethics Committee of Selcuk University (Ethical approval date: 22.05.2022, number: 2022/15).

2.2. Groups and Procedures

Our study consisted of four groups with 6 mice in each group. No drug was administered to the control group. In our second group, 20 microliters (μl) of 1% formalin were injected subcutaneously into the dorsal part of the right hind legs of the mice. The third group received formalin injection as in the second group. Diclofenac sodium (Sigma Aldrich, St Louis, MO, USA), at a dose of 10 mg/kg was injected intraperitoneally (i.p.) 15 minutes before the formalin injection [19]. The fourth group was injected adalimumab (Humira, 40 mg/0.8 ml AbbVie Laboratories, Istanbul, Turkey) with i.p., a TNF-alpha inhibitor at a dose of 10 mg/kg, 5 days before the formalin injection [15]. In order to avoid the placebo effect, the carriers of the drug-administered groups were injected in the same way as the drug-administered groups.

2.3. Formalin Test

All mice were placed in the observation cage 30 minutes before the test and acclimatized to the environment. For the formalin test, nociception was induced by subcutaneous administration of 20 μl of 1% formalin to the dorsal part of the right hind legs of the mice [20]. As soon as the formalin was administered, each mouse was placed in a clear plexiglass box to observe the spontaneous activity of the treated foot. The observable biphasic pain response after subcutaneous formalin injection was evaluated in two time periods, 0-10 (neurogenic phase) and 10-30 (inflammatory phase) minutes. The time spent (in seconds) for the mice to lick or bite the injected hind paw during the respective periods was measured in each experimental group, and this value was considered an indicator of nociceptive behavior.

2.4. Hot Plate Test

Mice were individually placed on a metal hot plate (MAY 9619, Ankara, Turkey) set at 55 ± 1 °C; The time it took either as soon as he started licking his front and back paws or when he tried to jump off the hot plate was recorded and taken from the hot plate. Mice were kept on the hot plate for a maximum of 30 seconds to avoid tissue damage [20]. Mice were allowed to spend some time on the plate one hour before testing to acclimate to the experimental setup.

2.5. Statistical Analysis

The data obtained from our study are presented as mean ± standard error of the mean. One-way analysis of

variance (ANOVA, SPSS v.20.0) and TUKEY multiple comparison tests were used for statistical analysis of the results. A value of p<0.05 was accepted as significant.

3. RESULTS

3.1. Formalin Test Results

Injection of 1% formalin, which we administered 20 µl subcutaneously in mice, produced nociceptive behaviors in both phases of the test (p<0.05). The effect of adalimumab, which we administered as a single dose of 10 mg/kg 5 days before the formalin test, was biphasic. The effect on the neuronal phase (between 0-10 minutes after formalin injection), which is considered the early phase of the formalin test, was not statistically significant (p>0.05). However, in the late phase of the test (in the inflammatory phase-between 10-30 minutes after the formalin injection), adalimumab improved the nociceptive activity due to formalin injection (p<0.05). Mice in the group receiving diclofenac sodium, which we used as a positive control, exhibited (p<0.05) antinociceptive behavior both in the neuronal phase and in the inflammatory phase (Fig. 1A-B)
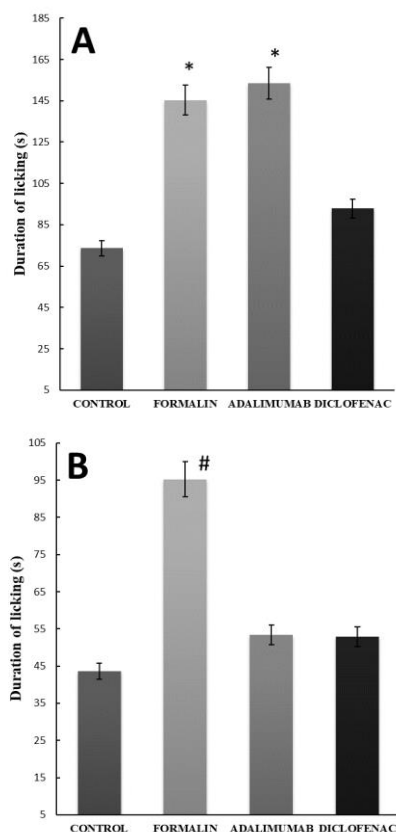

Figure 1. Results of paw-licking test (formalin test). (A) Early phase (0-10 minutes after injection) (B) Late phase (10-30 minutes after injection). The data are expressed as the means ± SD. Asterisk (*) indicates significance compared with Control and Diclofenac groups. Hash (#) indicates significance compared with other groups. p<0.05; one-way ANOVA.

3.2. Hot Plate Test Results

In the hot plate test, measurements were taken before the start of the formalin test (0. minutes) and at the 15th and 30th minutes after it started. There was no significant difference between all groups in the measurements made at the 0th and 15th minutes (p>0.05). The delay response detected in the diclofenac sodium group at the 30th minute was found to be significantly different (p<0.05). Adalimumab-induced changes were not significant (p>0.05) in all measurements of the test in mice with formalin-induced inflammatory pain (Fig. 2).
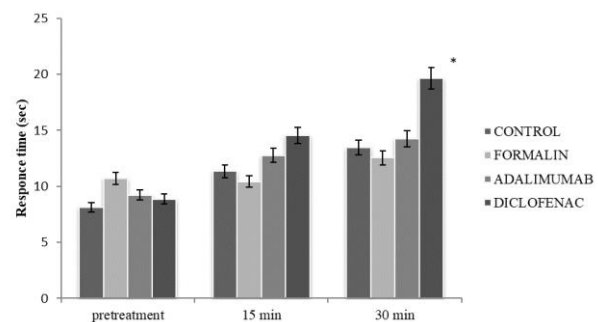
Figure 2. Hot-plate test of the antinociceptive activity of intraperitoneally administered adalimumab in mice. The data are expressed as the means ± SD. Asterisk (*) indicates significance compared with other groups. p<0.05; one-way ANOVA.

4. DISCUSSION AND CONCLUSION

Formalin test in experimental animals is widely used to evaluate the effects of pain relief agents. This study was carried out to evaluate the effect of adalimumab, a TNF-alpha inhibitor, on nociceptive behaviors in inflammatory pain processes in mice with a formalin-induced inflammatory pain model. In this model, diclofenac sodium was used as a positive control. In the second phase of the formalin test, adalimumab reduced paw licking behavior compared to the plain formalin group but was not effective in the neuronal phase. The effects were less pronounced in the hot plate test, and no statistically significant difference was observed between the groups. Our study revealed that adalimumab is effective in the second stage of the formalin test, rather than in the first stage, in which the inflammatory process is evaluated.

The most commonly used experimental animals for nociception and inflammation studies are mice and rats. Some tests used for this purpose include various chemical agents such as formalin, acetic acid and carrageenan, as well as physical stimuli such as hot and cold [21]. The formalin test is used as a model for finding antinociceptive and anti-inflammatory substances [20]. Subcutaneous injection of dilute formalin is given to the dorsal or plantar part of the paw of the experimental animal, causing an inflammatory response characterized by swelling in the rodent's paw [22]. Subsequently, the release of mediator cytokines such as TNF-alpha, IL-1β, and IL-6, which cause inflammation from glial cells in the spinal cord, leads to tissue damage over time [23]. Formalin-induced nociception is an in vivo model of acute pain and leads

91

to characteristic biphasic licking, biting, and pulling behaviors. The initial phase also called the early phase or neurogenic phase, is characterized by central neurogenic pain caused by direct chemical stimulation of C-fiber nociceptors and occurs within the first (0-10 min) minutes of formalin administration. Nociceptive behaviors in this process can be prevented with opioid drugs due to the central effect [20]. The late phase also called the inflammatory phase, is the result of the inflammatory pain response from peripheral mechanisms. It is characterized by an inflammatory process involving mediators such as prostaglandins, neuropeptides and nitric oxide and lasts 10-30 minutes [20], [24]. This information indicates that the two phases observed in the formalin test-induced inflammatory pain model may have different nociceptive mechanisms. In general, centrally acting drugs inhibit both phases, while peripherally acting drugs inhibit only the second phase. In our study, we showed that the nociceptive behaviors observed in the adalimumab group due to the formalin test were not different from the formalin group in the early neuronal phase of the test, but were lower in the inflammatory phase compared to the formalin group. It is not surprising that adalimumab is active in the inflammatory process rather than the neuronal phase. Due to the role of proinflammatory cytokines such as TNF-alpha, IL-1β and IL-6 released from spinal cord glial cells [23], especially in the second phase of the test, inhibition of these cytokines may be associated with the antinociceptive response in the second phase. In addition, TNF-alpha plays a key role in neuronal inflammation [25]. While there are clinical and experimental studies of adalimumab in many pathological conditions associated with inflammation in the literature, to the best of our knowledge, our study is the first report evaluating the nociceptive effect of adalimumab in an inflammatory pain model.

Adalimumab; has curative effects in mood disorders observed in patients suffering from chronic bowel disease [18], contributes to recovery in lipopolysaccharide-induced lung injury by reducing lung tissue TNF-alpha immunoreactivity more effectively than the steroid group [12], cognitive impairment observed in rats in the chronic cerebral hypoperfusion model, TNF-alpha ameliorates by inhibiting IL-6 and NF-kB signaling [13]. We cannot say whether the antinociceptive effect of adalimumab we observed in our study is related to proinflammatory cytokine release, this is the first limitation of our study. Since there has not been such a study before, we cannot make a comparison about the effect of different adalimumab doses and administration regimens. However, a recent review reported that adalimumab reduces pain symptoms associated with the disease in people suffering from hidradenitis suppurativa, without mentioning any mechanism of action [26]. Although the investigation of the underlying mechanism of the antinociceptive effect of adalimumab is the subject of future studies, our study is important as it is the first report showing the antinociceptive effect of adalimumab. Diclofenac sodium showed antinociceptive activity in both the early and late phases, and the findings were consistent with the literature [27], [28]. The hot plate test is used to evaluate

centrally mediated anti-nociceptive and analgesic effects after pain induced by an appropriate method. This test is based on recording the delay in the experimental animal pulling its paw off the hot plate or licking the paw. In our study, adalimumab did not change this effect in all measurements made throughout the hot plate test. The peripheral analgesic effect is mediated by the inhibition of inflammatory mediators, while the inhibition of central pain receptors is related to the central analgesic effect. In our study, the insufficient statistical power of the effect of adalimumab in the hot plate test indicates that it does not have a strong analgesic activity that can be mediated centrally. Our study is the first to evaluate the antinociceptive effect of adalimumab, therefore, it is necessary to better explain the subject and to conduct new studies on how adalimumab has an effect in different doses and different administration regimens, and through which pathways it works in these evaluations.

In conclusion, our study showed that adalimumab has an antinociceptive effect in the formalin test. Because the effect is more pronounced in the inflammatory phase of this test and the effect is weaker in the hot plate test, this indicates that its peripheral analgesic effect is stronger rather than the central effect.

REFERENCES

[1] Wang J. Glial endocannabinoid system in pain modulation. Int J Neurosci 2019;129:94–100. https://doi.org/10.1080/00207454.2018.1503178.

[2] Wang P, Wen C, Olatunji OJ. Anti-Inflammatory and Antinociceptive Effects of Boesenbergia rotunda Polyphenol Extract in Diabetic Peripheral Neuropathic Rats. J Pain Res 2022;15:779–88. https://doi.org/10.2147/JPR.S359766.

[3] Jackson T, Thomas S, Stabile V, Han X, Shotwell M, McQueen KAK. Chronic Pain Without Clear Etiology in Low- and Middle-Income Countries: A Narrative Review. Anesth Analg 2016;122:2028–39.
https://doi.org/10.1213/ANE.0000000000001287

[4] Woolf CJ. What is this thing called pain? J Clin Invest 2010;120:3742–4. https://doi.org/10.1172/JCI45178.

[5] Sloot S, Boland J, Snowden JA, Ezaydi Y, Foster A, Gethin A, et al. Side effects of analgesia may significantly reduce quality of life in symptomatic multiple myeloma: a cross-sectional prevalence study. Support Care Cancer 2015;23:671–8. https://doi.org/10.1007/s00520-014-2358-1.

[6] Medzhitov R. Origin and physiological roles of inflammation. Nature 2008;454:428–35. https://doi.org/10.1038/nature07201.

[7] Horiuchi T, Mitoma H, Harashima S, Tsukamoto H, Shimoda T. Transmembrane TNF-alpha: structure, function and interaction with anti-TNF agents. Rheumatology (Oxford) 2010;49:1215–28. https://doi.org/10.1093/rheumatology/keq031.

[8] Furst DE, Schiff MH, Fleischmann RM, Strand V, Birbara CA, Compagnone D, et al. Adalimumab, a fully human anti tumor necrosis factor-alpha

monoclonal antibody, and concomitant standard antirheumatic therapy for the treatment of rheumatoid arthritis: results of STAR (Safety Trial of Adalimumab in Rheumatoid Arthritis). J Rheumatol 2003;30:2563–71.

[9] Chang C-W, Wei S-C, Chou J-W, Hsu T-C, Chuang C-H, Lin C-P, et al. Safety and Efficacy of Adalimumab for Patients With Moderate to Severe Crohn's Disease: The Taiwan Society of Inflammatory Bowel Disease (TSIBD) Study. Intest Res 2014;12:287–92. https://doi.org/10.5217/ir.2014.12.4.287.

[10] Park J, Lee S-Y, Shon J, Kim K, Lee HJ, Kim KA, et al. Adalimumab improves cognitive impairment, exerts neuroprotective effects and attenuates neuroinflammation in an Aβ1-40-injected mouse model of Alzheimer's disease. Cytotherapy 2019;21:671–82. https://doi.org/10.1016/j.jcyt.2019.04.054.

[11] Bahceci İ, Tumkaya L, Mercantepe T, Aslan N, Duran ÖF, Soztanaci US, et al. Inhibition of methotrexate induced toxicity in the adult rat spleen by adalimumab. Drug Chem Toxicol 2022:1–7. https://doi.org/10.1080/01480545.2022.2029880.

[12] Sarioğlu N, Sunay FB, Yay AH, Korkut O, Erel F, Hişmioğulları AA, et al. Anti-inflammatory effects of adalimumab, tocilizumab, and steroid on lipopolysaccharide-induced lung injury. Turk J Med Sci 2021. https://doi.org/10.3906/sag-2010-303.

[13] Xu J-J, Guo S, Xue R, Xiao L, Kou J-N, Liu Y-Q, et al. Adalimumab ameliorates memory impairments and neuroinflammation in chronic cerebral hypoperfusion rats. Aging 2021;13:14001–14. https://doi.org/10.18632/aging.203009.

[14] Correger E, Marcos J, Laguens G, Stringa P, Cardinal-Fernández P, Blanch L. Pretreatment with adalimumab reduces ventilator-induced lung injury in an experimental model. Rev Bras Ter Intensiva 2020;32:58–65. https://doi.org/10.5935/0103-507x.20200010.

[15] Durmaz S, Kurtoğlu T, Barbarus E, Eliyatkın N, Yılmaz M. TNF-alpha inhibitor adalimumab attenuates endotoxin induced cardiac damage in rats. Acta Cir Bras 2020;35:e202000202. https://doi.org/10.1590/s0102-865020200020000002.

[16] Shuwa HA, Dallatu MK, Yeldu MH, Ahmed HM, Nasir IA. Effects of Adalimumab, an Anti-tumour Necrosis Factor-Alpha (TNF-α) Antibody, on Obese Diabetic Rats. Malays J Med Sci 2018;25:51–62. https://doi.org/10.21315/mjms2018.25.4.5.

[17] Börcek AÖ, Çivi S, Öcal Ö, Gülbahar Ö. Effects of tumor necrosis factor alpha blocker adalimumab in experimental spinal cord injury. J Korean Neurosurg Soc 2015;57:73–6. https://doi.org/10.3340/jkns.2015.57.2.73.

[18] Gray MA, Chao C-Y, Staudacher HM, Kolosky NA, Talley NJ, Holtmann G. Anti-TNFα therapy in IBD alters brain activity reflecting visceral sensory function and cognitive-affective biases. PLoS One 2018;13:e0193542. https://doi.org/10.1371/journal.pone.0193542.

[19] Nurullahoglu KE, Okudan N, Belviranli M, Oz M. The comparison of preemptive analgesic effects of curcumin and diclofenac. Bratisl Lek Listy 2014;115:757–60. https://doi.org/10.4149/bll_2014_146.

[20] Valle-Dorado MG, Hernández-León A, Nani-Vázquez A, Ángeles-López GE, González-Trujano ME, Ventura-Martínez R. Antinociceptive effect of Mansoa alliacea polar extracts involves opioid receptors and nitric oxide in experimental nociception in mice. Biomed Pharmacother 2022;152:113253. https://doi.org/10.1016/j.biopha.2022.113253.

[21] Zadeh-Ardabili PM, Rad SK. Anti-pain and anti-inflammation like effects of Neptune krill oil and fish oil against carrageenan induced inflammation in mice models: Current statues and pilot study. Biotechnol Rep (Amst) 2019;22:e00341. https://doi.org/10.1016/j.btre.2019.e00341.

[22] Damas J, Liégeois JF. The inflammatory reaction induced by formalin in the rat paw. Naunyn Schmiedebergs Arch Pharmacol 1999;359:220–7. https://doi.org/10.1007/pl00005345.

[23] Yin Z-Y, Li L, Chu S-S, Sun Q, Ma Z-L, Gu X-P. Antinociceptive effects of dehydrocorydaline in mouse models of inflammatory pain involve the opioid receptor and inflammatory cytokines. Sci Rep 2016;6:27129. https://doi.org/10.1038/srep27129.

[24] Hunskaar S, Hole K. The formalin test in mice: dissociation between inflammatory and non-inflammatory pain. Pain 1987;30:103–14. https://doi.org/10.1016/0304-3959(87)90088-1.

[25] Torres-Acosta N, O'Keefe JH, O'Keefe EL, Isaacson R, Small G. Therapeutic Potential of TNF-α Inhibition for Alzheimer's Disease Prevention. J Alzheimers Dis 2020;78:619–26. https://doi.org/10.3233/JAD-200711.

[26] Tsentemeidou A, Sotiriou E, Sideris N, Kourouklidou A, Lallas A, Ioannides D, et al. Adalimumab Effect on Pain in Hidradenitis Suppurativa Patients: Systematic Review and Meta-Analysis. Dermatol Pract Concept 2022;12:e2022099. https://doi.org/10.5826/dpc.1202a99.

[27] Jaffal SM, Al-Najjar BO, Abbas MA, Oran SA. Antinociceptive Action of Moringa peregrina is Mediated by an Interaction with α2-Adrenergic Receptor. Balkan Med J 2020;37:189–95. https://doi.org/10.4274/balkanmedj.galenos.2020.2019.11.14.

[28] Mannan MA, Khatun A, Khan MFH. Antinociceptive effect of methanol extract of Dalbergia sissoo leaves in mice. BMC Complement Altern Med 2017;17:72. https://doi.org/10.1186/s12906-017-1565-y.

93

Türk Doğa ve Fen Dergisi
Turkish Journal of Nature and Science

www.dergipark.gov.tr/tdfd

The Use of *Rheum Ribes* (Işğın) Extracts for Copper Protection in Acidic Media

Fatma KAYA[1], Ramazan SOLMAZ[2*], İbrahim Halil GEÇİBESLER[2]

[1] Bingöl University, Science and Letters Faculty, Chemistry Department, 12000, Bingöl, Türkiye
[2] Bingöl University, Health Sciences Faculty, Occupational Health and Safety Department, 12000, Bingöl, Türkiye
Fatma KAYA ORCID No: 0000-0003-0783-5652
Ramazan SOLMAZ ORCID No: 0000-0002-9295-1203
Halil İbrahim GEÇİBESLER ORCID No: 0000-0002-4473-2671

Corresponding author: rsolmaz@bingol.edu.tr; rsolmaz01@gmail.com

Abstract: The extracts of different parts of ışğın such as flower (RRF), leaf (RRL), and root (RRR) were prepared and their protective effects on copper corrosion in an acidic media were investigated in this study. Other components that are not currently in use will thus be able to be transformed into benefits. Extracts from various parts of the plant were dissolved in a 1 M HCl solution at a concentration of 1000 ppm for this purpose. The time variation of open circuit potential (Eocp-t), linear polarization resistance (LPR), electrochemical impedance spectroscopy (EIS), and potentiodynamic polarization (PP) techniques were used to investigate the electrochemical behaviour of copper metal in these solutions. The surface of copper was examined after corrosive medium treatment using a scanning electron microscope (SEM), energy dispersive X-ray spectroscopy (EDX), and contact angle measurements. The results revealed that the effects of extracts obtained from different parts of the RR on the behavior of copper in an acidic medium varied. The best protection was provided by the RRF extract. Despite this, RRR extract failed to protect Cu from corrosive ions in 1 M HCl solution. According to surface analyses, the plant extracts formed an adherent and compact organic film on the Cu surface.

Rheum Ribes (Işğın) Özütlerinin Asidik Ortamda Bakırın Korunması için Kullanılması

Anahtar Kelimeler
Rheum Ribes (Işğın),
Bakır,
Doğal bitki özütleri,
Korozyon inhibitörü

Öz: Bu çalışmada, ışğının çiçek (RRF), yaprak (RRL) ve kök (RRR) gibi farklı bölgelerinin ayrı ayrı özütleri hazırlanarak asidik ortamda bakırın korozyonuna koruma etkileri incelenmiştir. Böylelikle ışğının kullanılmayan diğer kısımlarının da faydaya dönüştürülmesi mümkün olabilecektir. Bu amaçla, RR özütlerinin 1 M HCl çözeltisinde 1000 ppm çözeltileri hazırlanmıştır. Bakır metalinin bu çözeltilerdeki elektrokimyasal davranışları açık devre potansiyelinin zamanla değişimi (Eocp-t), elektrokimyasal impedans spektroskopisi (EIS), lineer polarizasyon direnci (LPR) ve potansiyodinamik polarizasyon (PP) teknikleri ile incelenmiştir. Bakırın korozif ortam ile muamelesi sonrasında yüzeyi taramalı elektron mikroskopu (SEM), enerji dağılımlı X-ışını spektroskopisi (EDX) ve temas açısı ölçümleri ile incelenmiştir. Elde edilen bulgular, RR'nin farklı bölgelerinden elde edilen özütlerin bakırın asidik ortamdaki davranışına etkilerinin farklı olduğunu göstermiştir. En iyi koruma RRF özütünde elde edilmiştir. RRR özütü ise bakırı 1 M HCl çözeltisinde korozyona karşı koruyamamaktadır. Yüzey analizleri bitki özütlerinin metal yüzeyinde koruyucu bir film oluşturduğunu göstermiştir.

1. INTRODUCTION

In 2016, the Council of Higher Education designated Bingöl University as a pilot university under the Regional Development-Oriented Mission Differentiation and Specialization Program of Universities. In terms of flora, Bingöl province is one of our country's most important

regions. In this context, one of the primary goals of this work is to identify and introduce new plants with high economic value into the economy. This is critical for the development of the region. In this context, this study was planned to determine the new usage areas of the RR plant, which is well-known in the region.

94

Copper metal, on the other hand, is one of the most frequently used metals in the industry due to important properties such as high electrical and thermal conductivity [1-3]. Nevertheless, in corrosive environments such as acidic, basic, chloride, humidity, and air, this metal incredibly quickly loses its metallic conductivity [4]. When copper metal corrodes, most of its properties and consequently its industrial use properties are lost [3, 5]. As a result, protecting this metal from corrosion is critical from a strategic standpoint. The use of corrosion inhibitors is the most common and effective method of protecting metals from corrosion. Corrosion inhibitors are classified as either inorganic or organic. Inorganic corrosion inhibitors work by corrosion of metals and forming a protective oxide film on the metal surface or a poorly soluble salt of the metal. However, because of their oxidizing properties, their concentrations in the corrosive environment must be constantly monitored. The majority of them have toxic qualities, which make them extremely harmful to both humans and the environment. Some metal salts, such as those in the lanthanide group, are quite costly.

Organic compounds, which are used as corrosion inhibitors are generally adsorbed on the metal surface and form a barrier between the metal and corrosive media. According to the literature, molecules containing P, N, S, and O atoms, as well as molecules with double or triple bonds, are better adsorbed on the metal surface and thus more effective inhibitors [6-8]. Studies on the use of environmentally friendly molecules are being conducted in this field because the majority of organic inhibitors used are toxic and have negative effects on people and the environment [9-12]. Natural plant extracts have become popular for this purpose in recent years [13-20]. Natural plant extracts or active ingredients are natural and have no adverse effects on humans or the environment. It is natural and its prices are lower than synthetic corrosion inhibitors. For this reason, it is extremely important to concentrate studies on these plants. Natural products are both healthy and economical, and for this purpose, the most important use potential for the future is chemicals [21-22].

Işgın (RR) is found in some countries as well as our country's Eastern Anatolia (Ağrı, Bingöl, Elazığ, Hakkari, Kars, Van, and Sivas) region [23]. Mountainous and flinty terrain is ideal for its flourishing. It is quite common for people to consume the plant fresh. This plant has a sour taste, strengthens the stomach, prevents vomiting, and is constipating [24]. Aside from using the underground parts to treat hemorrhoids and diabetes, this plant is also used to aid digestion in various parts of the country [25]. Due to its low pH value, RR is eaten by peeling and has a sour taste [3,56]. The young roots and stems of RR are used as a preventative against measles and smallpox, as well as an anti-gall agent. In addition to curing diabetes, ulcers, and stomach ailments, its roots have anti-inflammatory properties [25, 26]. Anthraquinones in RR are spotlighted as having antibacterial properties [27, 28]. In terms of vitamin C, this plant is extremely abundant. The RR plant has the following compositional characteristics: 5.59% dry matter, 0.63% total ash, 1.3% protein, 3.75 g/g iron,

1.13 g/g zinc, 0.5 g/g copper, 0.423 g/g manganese, 0.255 g/g vitamin A, 0.614 g/g vitamin E, and 98.6 g/g selenium [29, 30]. RR is a safe and natural plant that can be used to protect metals, as was already mentioned.

Plant-based anticorrosive secondary metabolites may be used to overcome corrosive deformations due to material quality, oxidation reactions, acidic and basic environment exposure. Effective anticorrosive compounds can be isolated and identified from leaves, flowers or roots of plants of natural origin. In some studies, it has been reported that especially the flower parts of the plants are rich in total phenolics, flavonoid alkaloids, terpenoids and glycosides [31, 32]. Therefore, extracts from different parts of plants, which have such a rich variety of secondary metabolites that are economical, environmentally friendly and easily available, could be used for anticorrosive purposes.

The inhibitory effects of the extracts from various RR parts on copper corrosion in 1 M HCl solution were investigated. Several electrochemical techniques were used to accomplish this. Following exposure to corrosive RR extracts, the metal's surface was examined with the help of SEM, EDX, and contact angle measurements. Based on the information gathered, it was determined which area of this plant would best protect the copper. The top extract will be the focus of the next stage of research, and its protective properties will be improved by adjusting a few parameters.

2. MATERIAL AND METHOD

2.1. Preparation of Electrodes

The working electrode was made of Cu with a purity of 99.98-99.99%. The cylindrical copper rods were prepared by embedding them in polyester and leaving out only the lower end of the measurement. The electrode's total surface area in contact with the solution was 0.0707 cm2. The Cu electrodes were cleaned with sandpaper, the last of which was a 2000 grid, using a sanding machine before the measurements. After washing with pure water and absolute ethanol, they were immersed in absolute ethanol in an ultrasonic bath for a set amount of time before being immersed in the test solutions without waiting. Pt sheet with a total surface area of 2 cm2 was utilized as an auxiliary electrode. The reference electrode was Ag/AgCl (3 M KCl).

2.2. Preparation of RR Extracts

This study made use of RR from Bingöl region. The extraction procedure has previously been described in detail [33]. After collecting the RR taxon grown in its natural habitats, the leaf, flower, and root parts were separated and dried on unprinted papers in a sunny place. The dried plant parts were ground to 30 mesh particle size by grinding with a laboratory type mill. Each of the ground plant organs was weighed 100 g and extracted with 2 L methanol. As a result of the extraction process, it was filtered and separated from the extract pulp part. The remaining pulp was extracted two more times with the

same amount of methanol. The methanol in the extract solution obtained as a result of the extraction process was removed with the help of a rotary evaporator at temperatures not exceeding 40°C under low pressure. The dry extract obtained as a result of the evaporation process was taken into an amber colored bottle and stored in the refrigerator at +4 °C.

2.3. Test Solutions

The corrosion tests were performed in 1 M HCl and 1000 ppm extracts containing 1 M HCl solutions. Dilution of 1 M HCl solution produced an analytical grade HCl solution (37%). 1000 mg dried RR extracts were dissolved in pure water and diluted to 1 L in a 1 L flask with distilled water. The temperature of corrosive solutions was kept at 298 K in a water bath during the tests. The experimental set-up was opened to the atmosphere and the solutions were not stirred during the experiments.

2.4. Electrochemical Measurements

Electrochemical behavior of Cu was investigated using computer-controlled CHI 660D and CHI6096 A.C. Electrochemical Analyzers. Pt and Ag/AgCl electrodes were used as counter and reference electrodes. Initially, the working electrodes were immersed in 1 M HCl in the absence and presence of the extracts for 1 hour, and the change in E_{ocp} was plotted against the immersion time. Regarding this exposure time, EIS data were collected in the frequency range from 100 kHz to 0.003 Hz. The amplitude was 10 mV from peak to peak. Upon completion of these tests, LPR experiments were carried out at 0.001 V s^{-1}, ranging from -10 mV more negatively to +10 mV more positively versus E_{ocp}, and an i-E plots were obtained. Polarization resistance was discovered in the formation of these lines. Finally, polarization plots from E_{ocp} to anodic potentials were obtained in the same system at a scan rate of 1 mV s^{-1}.

2.5. Characterization of the Metal Surface

Cu was left in the 1 M HCl solution for 1 hour without and with each extract added. The metal was then removed, cleaned thoroughly with purified water, dried, and stored in a desiccator until measurements were taken. A Jeol model (JEOL 6510) SEM was used to examine their surface structure and appearance. EDX measurements were used to determine the chemical composition of the surface. To determine surface hydrophobic or hydrophilic characters and the guest the orientation of the molecules at the surface contact angle measurements were taken [34, 35]. The sessile water drop theory was used in these experiments.

3. RESULTS AND DISCUSSION

3.1. The Change of Open Circuit Potential with Exposure Time

Changes at the metal/solution interface, as well as the initiation and continuation of copper corrosion, could all cause $E_{ocp\text{-}t}$ variation. These lines could also reveal details

about the reaction mechanism or the dominance of anodic or cathodic processes. Before conducting electrochemical measurements, a constant steady-state open circuit condition is also required. As a result, the change in E_{ocp} of Cu during test solution exposure was initially recorded for 1 h. Figure 1 shows a graphical representation of this information.

Figure 1 shows that the potential of Cu sharply shifts to more negative potentials during the first 80 seconds. This behavior is responsible for copper dissolution. After about a half-hour, the potential shifts to the positive side and nearly remains constant. Copper passivation is caused by $CuCl_{(k)}$ and other copper corrosion products [36]. The addition of the extracts causes the metal's E_{ocp} to abruptly shift into passive regions. This result shows that the molecules of extracts form a surface-protective film that serves as a fundamental physical barrier and prevents the corrosion of Cu by mainly influencing the anodic mechanism. After the addition of the extracts E_{ocp} of the metal shifts to passive regions sharply [37]. The potential changes depending on the type of extract, with RRF having the most passive and stable potential. These differences could be explained by the difference in the chemical composition of each part of the plant. In all cases, the potential approaches steady-state conditions, making electrochemical measurements possible.
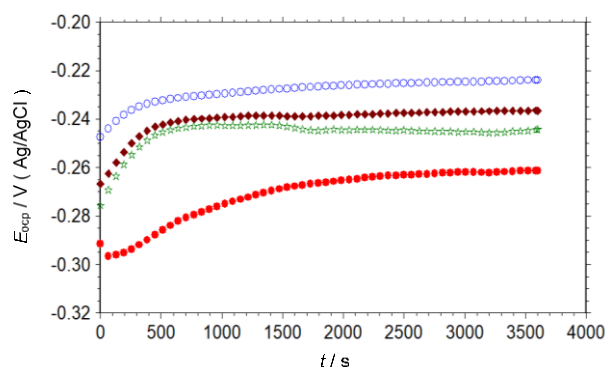
Figure 1. The change of open circuit potential of Cu with immersion time in 1 M HCl (●) and containing 1000 ppm RRF (○), RRL (♦), and RRR (☆) solutions

3.2. Electrochemical Impedance Spectroscopy

EIS is one of the most effective electrochemical methods available today for studying the behavior of metal/solution interfaces because it allows for resistance measurement without polarizing the surface. In order to examine the behavior of the film-modified metal surface/solution interface, the EIS technique was employed. Figure 2 shows related Nyquist and Bode plots of Cu obtained in acidic solutions containing RRF, RRL, and RRR extract. Even though the Nyquist plots (Figure 2a) only define two loops, the Bode plots (Figures 2b and c) show that three time constants appeared. When the plots obtained in uninhibited HCl solution were examined, the high-frequency loop that appeared at high frequencies could be attributed to charge transfer resistance and double layer resistance [38]. The resistance of copper chloride species formed on the surface could be assigned to the second middle-frequency one. At low

frequencies, a straight line appeared, which is generally defined as Warburg impedance [39], This is due to the diffusion resistance of corrosive ions such as $CuCl_2^-$ at the metal/solution interface.

Figure 2. The Nyquist (a), log Z-log f (b), and phase angle-log f (c) (Bode) plots of Cu obtained in 1 M HCl solution without (●) and with the addition of 1000 ppm RRF (○), RRL (♦) and RRR (☆) solutions after 1-hour exposure

The general behavior of Cu did not change when the RR extracts were added to 1 M HCl solution, indicating that the extracts inhibit Cu corrosion without changing the mechanism [37]. However, th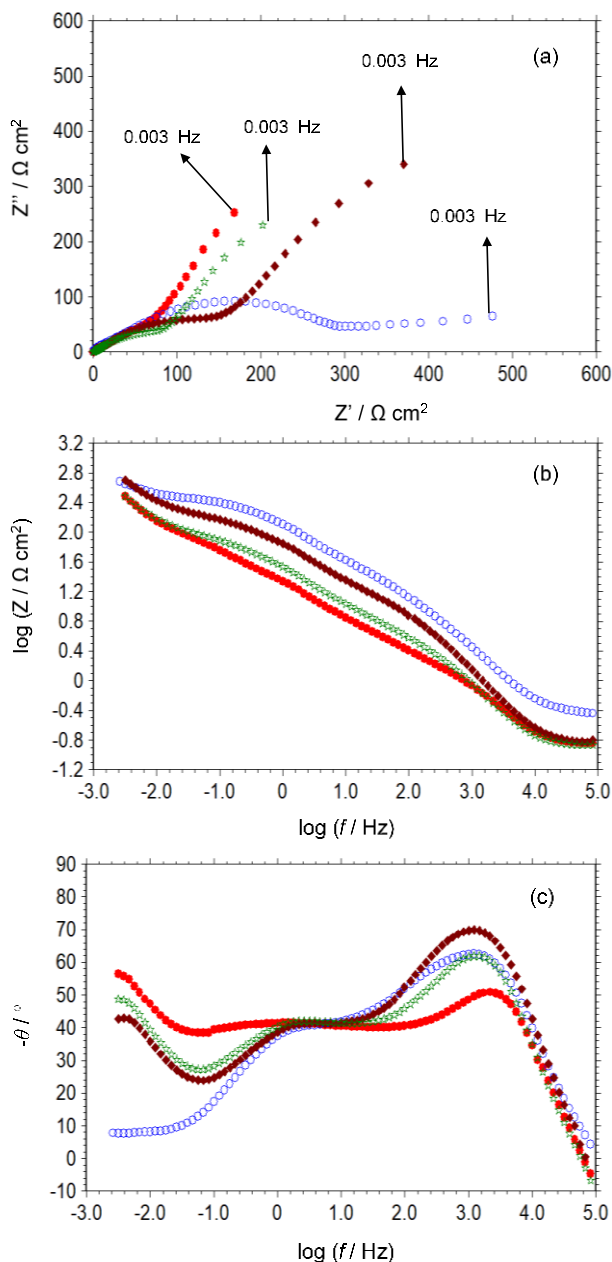e total number of high and middle-frequency loops increased in the order RRF > RRL > RRR. The increased charge transfer resistance and film resistance suggest that the extract molecules form a protective organic film over the Cu surface [39] and protect Cu from acidic corrosion. High and low frequencies are explained in the same way as 1 M HCl. The middle time constant, which corresponds to film resistance, could be assigned to the formation of film at

the surface as well as copper products under the film or film pores. In the presence of the extracts, the angle of the low-frequency line related to the Warburg impedance decreases, reaching its lowest value in the case of RRF. This could be attributed to the formation of a compact and adherent film at the surface, which prevents corrosive ions from diffusing [39]. Polarization resistance was defined as the total resistance of charge transfer resistance, double layer resistance, film resistance, and resistance to corrosive species accumulation at the surface (R_p). Figure 2 shows that the extracts of RRF and RRL inhibit the corrosion rate of Cu and protect it from corrosion. However, the RRR extract was unable to adequately protect the metal in this acidic solution. Therefore, it cannot be advised to use this extract for this purpose. Further research, on the other hand, is required to improve the protection efficiency of RRF or RRL. In the next stage, we intend to improve the protection efficiency by incorporating a suitable organic molecule or KI to create a synergy between the extract molecules and the additive. The extracts' protection ability will also be tested in H_2SO_4 solution because the surface is cleaner in this acid and more molecules are expected to be adsorbed over the surface and perform better protection. The data presented here are preliminary data from this project, and additional studies such as the effect of extract concentration, exposure time, corrosive media type, and synergistic effect of KI to increase protection efficiency, as well as data analyses by a licensed fitting program, are ongoing and will be reported in another study.

3.3. Linear Polarization Resistance

The LPR technique was also used to investigate the extracts' corrosion resistance. Current-potential curves were obtained in 1 M HCl solution in the absence and presence of 1000 ppm of each plant extracts for this purpose. Table 1 shows the R_p values and inhibition efficiencies (η) that were used to generate the data.

The slopes of the $E\text{-}i$ curves were used to calculate R_p values, while the following equation was used to calculate η values:

$$\eta = \left(\frac{R'_p - R_p}{R'_p} \right) \times 100 \qquad (1)$$

In this equation, R'_p and R_p are the polarisation resistances of Cu in 1 M HCl solution with and without RR extracts, respectively. The LPR results are in excellent accordance with the EIS data, as shown in Table 1. Although RRF and RRL could protect the Cu in 1 M HCl solution, RRR almost does not change the corrosion rate of the metal in these conditions and thus cannot be used as a corrosion inhibitor. RRF provides the best protection capability. The best inhibitor (RRF), whose protection ability will be increased by more than 90% in the following section, will be the subject of additional research, as was previously stated.

Table 1. Electrochemical parameters obtained from LPR measurements in 1 M HCl solution in the absence and presence of 1000 ppm RRF, RRL, and RRR at 298 K

97

Inhibitor	R_p (Ω cm^2)	η %
1 M HCl	107	
RRF	270	60.3
RRL	195	45.1
RRR	112	4.7

The ability of RRF and RRL to protect the metal surface could be attributed to the formation of a protective film of extract molecules on the metal surface. Further research into the adsorbed molecules and protection mechanism is ongoing and will be reported later.

3.4. Potentiodynamic Polarization

Semi-logarithmic anodic current potential curves of Cu obtained in 1 M HCl in the absence and presence of the extracts are shown in Figure 3.
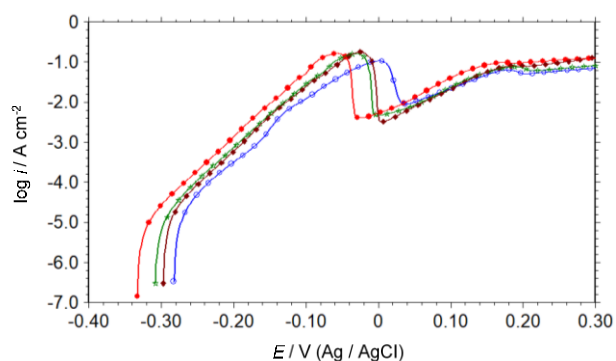

Figure 3. Polarization curves of Cu were obtained in 1 M HCl solution without (●) and with the addition of 1000 ppm RRF (○), RRL (♦), and RRR (☆) solutions after 1-hour exposure

As is seen in Figure 3, E_{ocp} of Cu in 1 M HCl without the extracts was -0.333 V. When the potential of the metal increases in these conditions the current density increases sharply due to the dissolution of Cu [38, 39].

$$Cu \; \rightarrow \; Cu^+ \; + e^- \tag{2}$$

$$Cu^+ \; + \; Cl^- \; \rightarrow \; CuCl_{(s)} \tag{3}$$
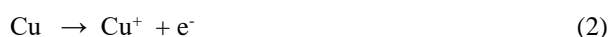
$CuCl_{(s)}$ deposits on the surface and diminishes the dissolution rate when the concentration of copper ions on the surface reaches its resolution constant. A passivation peak appears around -0.056 V as a result of $CuCl_{(s)}$ formation on the surface[38, 39]. Around -0.03 V, full passivation occurs. Because the $CuCl_{(s)}$ is not stable at the surface, the current density remains high. By increasing the potential scan to more positive potentials, the current density increases again, resulting in the formation of soluble cuprous complex $CuCl_2^-$ [39-41]:

$$CuCl_{(s)} \; + \; Cl^- \; \rightarrow \; CuCl_2^-_{\;(aq)} \tag{4}$$
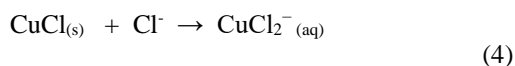
The E_{ocp} of Cu shifts toward more positive regions when the RR extracts are added to the corrosive media, and the

current densities decrease, which is greater at the RRF. These findings are consistent with the E_{ocp-t} measurements. Thus, polarization measurements show that the extracts are mixed-type corrosion inhibitor with a predominantly anodic action [37]. The lines are almost parallel around the Tafel region, indicating that the extracts inhibit corrosion without affecting the dissolution mechanism and that the dissolution reaction is controlled by activation. However, as described in the EIS studies, the overall reaction mechanism is diffusion controlled. Surface extract films work by simply blocking [37].

Table 2. Electrochemical data derived from polarization measurements obtained in 1 M HCl solution in the absence and presence of 1000 ppm RRF, RRL, and RRR at 298 K

Inhibitor	E_{ocp} (V)	$i_{-0.2\,V}$ (μA cm^{-2})
1 M HCl	-0.333	1348
RRF	-0.283	318
RRL	-0.297	592
RRR	-0.308	736

Table 2 contains some electrochemical data derived from these curves (More details will be given in the next studies). The polarization data in Figure 3 and Table 2 also show that RRF provides better corrosion protection. However, RRR's protection ability is very low, making it unsuitable for practical applications. On the other hand, RRF's protection ability needs to be improved for practical applications, and we will conduct additional studies as described above in the following studies.

3.5. Surface Characterization Studies

SEM images of Cu exposed to the extract containing HCl solution for 1 h are shown in Figure 4. Adsorption of the extract molecules results in the formation of compact and adherent organic films over the copper in the presence of the extract. These films act as a physical barrier between the corrosive solution and the metal surface. In the case of RRF, the best film is formed, which could explain the higher corrosion protection efficiency.
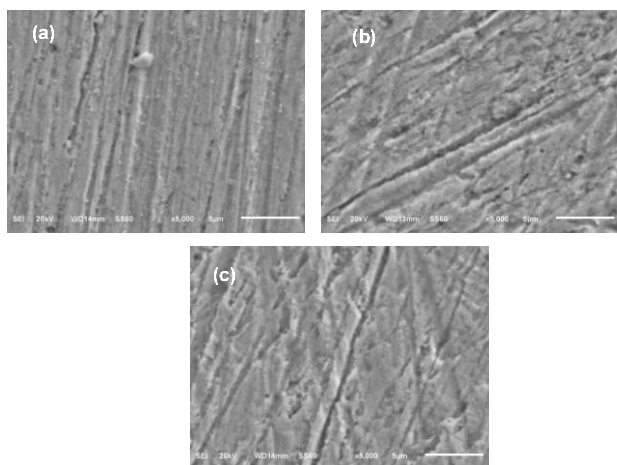
98

Figure 4. SEM images of Cu surface after exposure to 1 M HCl solution in the presence of 1000 ppm RRF (b), RRL (b), and RRR (c)

EDX measurements were used to examine the chemical composition of the same surfaces. Figure 5 depicts the obtained data. Because Cu does not contain C, O, S, N, or P, these metals are derived from the surface film formed by the molecules of plant extract. The presence of Cl- indicates the formation of $CuCl_x$ species on the bare metal regions under the film or in the film pores. There is no linear relationship between an element's composition and inhibition efficiency, which may be due to differences in the chemical composition of different parts of the plant.
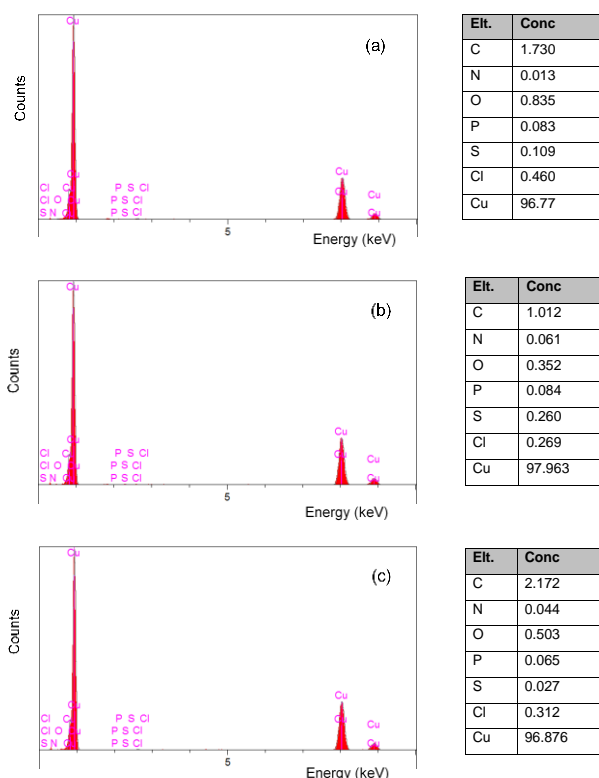

Elt.	Conc
C	1.730
N	0.013
O	0.835
P	0.083
S	0.109
Cl	0.460
Cu	96.77

Elt.	Conc
C	1.012
N	0.061
O	0.352
P	0.084
S	0.260
Cl	0.269
Cu	97.963

Elt.	Conc
C	2.172
N	0.044
O	0.503
P	0.065
S	0.027
Cl	0.312
Cu	96.876

Figure 5. EDX spectrums and elemental composition of Cu surface after exposure to 1 M HCl solution in the presence of 1000 ppm RRF (b), RRL (b), and RRR (c)

Contact angle measurements were used to investigate the hydrophilic or hydrophobic properties of the RRF film formed on the surface, which performed better in terms of protection. The measurements of the other extract films

were not performed even though future studies will only be performed on this extract to improve its protection efficiency. Figure 6 demonstrates the obtained data. Since having to add RRF to the corrosive solution, the surface's contact angle increases. The whole observation implies that the extract molecules are oriented and adsorbed to the surface along with more electronegative sites, and the surface's hydrophobic character tends to increase.

Figure 6. Contact angles of Cu surface after exposing to 1 M HCl solution in the absence and presence of 1000 ppm RRF

4. CONCLUSIONS

The extracts of different parts of ışgın such as flower (RRF), leaf (RRL), and root (RRR) were prepared and their protective effects on copper corrosion in 1 M HCl solution were investigated by electrochemiöl techniques. The surface of the metal after exposure to the test solutions was investigated by SEM, EDX, and contact angle measurements. The following major points could be concluded:

1) The effects of extracts obtained from various parts of the RR on copper behavior in an acidic environment differed.
2) The extracts adsorb on the Cu surface and form a compact and adherent film, which prevents the corrosion of Cu.
3) The RRF extract provided the best corrosion protection.
4) RRR extract was ineffective at protecting Cu from corrosion in 1 M HCl.
5) The extracts contained anodic and mixed-type corrosion inhibitors.
6) The addition of RRF to the corrosive solution increases the surface's hydrophobicity.
7) RRF has a corrosion protection efficiency of more than 60%, but the inhibition efficiency could be better.

More research, on the other hand, is required to improve RRF's protection effectiveness so that it can be used in real-world applications without risk. This study identified the plant part that best protects copper. We intend to improve the protection effectiveness in the following phase by adjusting factors such as extract concentration, exposure time, corrosive media type, and KI's synergistic effects. A licensed fitting program is currently kinetically analyzing data, and the results will be reported in another study.

Acknowledgement

99

and Bingöl University Central Laboratory for characterization measurements.

REFERENCES

[1] Xu Q, Ge K, Zhang S, Tan B.Understanding the adsorption and inhibitive properties of Nitrogen-Doped Carbon Dots for copper in 0.5 M $_{H2SO4}$ solution. J. Taiwan Inst. Chem. Eng. 2021; 125, 23-34.

[2] Li Y, Chen H, Tan B, Xiang B, Zhang S, Luo W, Zhang Y, Zhang J. Three piperazine compounds as corrosion inhibitors for copper in 0.5 M sulfuric acid medium. J. Taiwan Inst. Chem. Eng. 2021; 126, 231-43.

[3] Zeng W, Lia W, Tan B, Liu J, Chen J. A research combined theory with an experiment of 2-amino-6-(methylsulfonyl)benzothiazole as an excellent corrosion inhibitor for copper in an H2SO4 medium. J. Taiwan Inst. Chem. Eng. 2021; 128, 417-29.

[4] Pan YC, Wen Y, Xue LY, Guo XY, Yang HF. Adsorption behavior of methimazole monolayers on a copper surface and its corrosion inhibition. J. Phys. Chem. C. 2012; 116, 3532−38.

[5] Ma HY, Yang C, Chen SH, Jiao YL, Huang SX, Li DG, Luo JL. Electrochemical investigation of dynamic interfacial processes at 1-octadecanethiol-modified copper electrodes in halide-containing solutions. Electrochim. Acta. 2003; 48, 4277–89.

[6] Hajjaji FEL, Salim R, Ech-chihbi E, Titi A, Messali M, Kaya S, El Ibrahimi B, Taleb M. New imidazolium ionic liquids as ecofriendly corrosion inhibitors for mild steel in hydrochloric acid (1 M): Experimental and theoretical approach. J. Taiwan Inst. Chem. Eng. 2021; 123, 346-62.

[7] Khaled F. Corrosion control of copper in nitric acid solutions using some amino acids: A combined experimental and theoretical study. Corros. Sci. 2010; 52, 3225–34.

[8] Amin MA, Ibrahim MM. Corrosion and corrosion control of mild steel in concentrated H2SO4 solutions by a newly synthesized glycine derivative. Corros. Sci. 2011; 53, 873–85.

[9] Wan S, Zhang T, Chen H, Liao B, Guo X. Kapok leaves extract and synergistic iodide as novel effective corrosion inhibitors for Q235 carbon steel in H2SO4 medium. Ind. Crops Prod. 2022; 178, 114649.

[10] Jokar M, Farahani TS, Ramezanzadeh B. Electrochemical and surface characterizations of morus alba pendula leaves extract (MAPLE) as a green corrosion inhibitor for steel in 1M HCl. J. Taiwan Inst. Chem. Eng. 2016; 63, 436-52.

[11] Bedair MA, Soliman SA, Metwally MS. Synthesis and characterization of some nonionic surfactants as corrosion inhibitors for steel in 1.0M HCl (Experimental and Computational study). Ind. Eng. Chem. 2016; 41, 10-22.

[12] Alinejad S, Naderi R, Mahdavian M. Effect of inhibition synergism of zinc chloride and 2-mercaptobenzoxzole on protective performance of an eco-friendly silane coating on mild steel. Ind. Eng. Chem. 2017; 48, 88-98.

[13] Da Silva MVL, de Britto Policarpi E, Spinelli A. Syzygium cumini leaf extract as an eco-friendly corrosion inhibitor for carbon steel in acidic medium. J. Taiwan Inst. Chem. Eng. 2021; 129, 342-9.

[14] El Ibrahimi AJ, Tahar BA, Chadili M, El Issami S, Jbara O, Khallaayoun A, Bazzi L. Application of Zizyphun Lotus-pulpe of jujube extract as green and promising corrosion inhibitor for copper acidic medium. J. Mol. Liq. 2018; 268,102-13.

[15] Rahal C, Masmoudi M, Abdelhedi R, Sabot R, Jeannin M, Bouaziz M, Refait P. Olive leaves extract as natural corrosion inhibitor for pure copper in 0.5 M NaCl solution: A study by voltammetry around OCP. J. Electroanal. Chem. 2016; 769, 53-61.

[16] Deyab MA. Egyptian licorice extract as a green corrosion inhibitor for copper in hydrochloric acid solution. J. Ind. Eng. Chem. 2015; 22, 384-9.

[17] Krishnaveni K, Ravichandran J. Influence of aqueous extract of leaves of Morinda tinctoria on copper corrosion in HCl medium. J. Electroanal. Chem. 2014; 735, 24-31.

[18] Shabani-Nooshabadi M, Hoseiny FS, Jafari Y. Green approach to corrosion inhibition of copper by the extract of Calligonum comosum in strong acidic medium, Metall. Mater. Trans. A. 2015; 46, 293-9.

[19] Shabani-Nooshabadi M, Hoseiny FS, Jafari Y. Corrosion inhibition of copper by Ephedera sacocarpa plant extract as green corrosion inhibitor in strong acidic medium. Anal. Bional. Electrochem. 2014; 6, 341-54.

[20] Raghavendra N. latest exploration on Natural Corrosion Inhibitors for Industrial Important Metals in Hostile Fluid Environments: A comprehensive overview. J. Bio. Tribo. Corros. 2019; 5, 54.

[21] Sanaei Z, Shahrabi T, Ramezanzadeh B. Synthesis and characterization of an effective green corrosion inhibitive hybrid pigment based on Zinc acetate-Cichorium intybus L leaves extract (ZnA-CIL.L): Electrochemical investigations on the synergistic corrosion inhibition of mild steel in aqueous chloride solutions. Dyes Pigm. 2017; 139, 218-32.

[22] Gerengi H, Uygur I, Solomon M, Yildiz M, Goksu H. Evaluation of the inhibitive effect of Diospyros kaki (Persimmon) leaves extract on St37 steel corrosion in acid medium. Sustainable Chem. Pharm. 2016; 4, 57-66.

[23] Davis PH,. Flora of Turkey and The East Aegean Islands. Vol. 2. Edinburg, Edinburgh University Press, 268, 1966.

[24] Baytop T.. Türkiyede Bitkiler ile Tedavi Istanbul, Istanbul Üniversitesi Yayınları, No 3255 - Eczacılık Fakültesi No 40, 358, 1984.

[25] Özbek H, Ceylan E, Kara ÖF, Koyuncu M.. Rheum ribes (Uskun) Kökü Ekstresinin Sağlıklı ve Diyabetli Farelerdeki Hipoglisemik Etkisi, 14. Bitkisel İlaç Hammaddeleri Toplantısı, Bildiriler, 29-31 Mayıs, Eskisehir, 2002.

[26] Tosun F, Akyüz KÇ. Anthraquinones and flavanoids from Rheum ribes. Ankara Ecz. Fak. Derg. 2003; 32(1), 31-5.

[27] Bazzaz BS, Khajenkaramadin M, Shokooheizadeh HR. In vitro antibacterial activity of Rheum ribes

extract obtained from various plant parts against clinical isolates of gram nagative pathogens. Iran. J. Pharm. Res. 2005; 2, 87-91.

[28] Alaaddin AM, Al-Khateb EA, Jager AK.. Antibacterial activity of Iragi Rheum ribes root. Pharm. Bio. 2007; 45(9), 688-90.

[29] Andiç S, Tunçtürk Y, Ocak E, Köse Ş.. Some chamical characteristic of edible wild rhuarb species (Rheum ribes L.). Res. J. Agric. Biol. Sci. 2009; 5(6), 973-7.

[30] Munzuroğlu Ö, Karataş F, Gür N. Işgın (Rheum ribes L.) bitkisindeki A, E ve C vitaminleri ile selenyum düzeylerinin araştırılması. Turk J. Biol. 2000; 24, 397-404.

[31] Gecibesler IH, Kocak A, Demirtas I. (2016). Biological activities, phenolic profiles and essential oil components of *Tanacetum cilicicum* (*Boiss.*) Grierson. Nat. Prod. Res. 2016; 30(24), 2850-55.

[32] Kumar S, Mishra A, Pandey AK. (). Antioxidant mediated protective effect of *Parthenium hysterophorus* against oxidative damage using in vitro models. BMC Comp. Alt. Med. 2013; 13(1), 1-9.

[33] Kaya F, Geçibesler İH, Solmaz R. Corrosion inhibition of mild steel in 1 M HCI solution by *Rheum Ribes L.* (ışgın) flower extracts. XVth International Corrosion Symposium, Hatay, Turkey, 2018, p. 287-95.

[34] Dehghani A, Bahlakeh G, Ramezanzadeh B, Ramezanzadeh M. Potential of Borage flower aqueous extract as an environmentally sustainable corrosion inhibitor for acid corrosion of mild steel: Electrochemical and theoretical studies. J. Mol. Liq. 2019; 277, 895-911.

[35] Asadi N, Ramezanzadeh M, Bahlakeh G, Ramezanzadeh B. Utilizing Lemon Balm extract as an effective green corrosion inhibitor for mild steel in 1M HCl solution: A detailed experimental, molecular dynamics, Monte Carlo and quantum mechanics study. J. Taiwan Inst. Chem. Eng. 2019; 95, 252-72.

[36] Kosec T, Miloš̌ev I, Pihlar B. Benzotriazole as an inhibitor of brass corrosion in chloride solution. Appl. Surf. Sci. 2007; 253, 8863–73.

[37] Sedik A, Lerari D, Salci A, Athmani S, Bachari K, Gecibesler İH, Solmaz R. Dardagan Fruit extract as eco-friendly corrosion inhibitor for mild steel in 1 M HCl: Electrochemical and surface morphological studies. J. Taiwan Inst. Chem. Eng. 2020; 107, 189-200.

[38] Rajkumar G, Sethuraman MG. A study of copper corrosion inhibition by selfassembled films of 3-mercapto-1H-1,2,4-triazole, Res. Chem. Intermed. 2016; 42, 1809–21.

[39] Qiang Y, Fu S, Zhang S, Chen S, Zou X. Designing and fabricating of single and double alkyl-chain indazole derivatives self-assembled monolayer for corrosion inhibition of copper. Corros. Sci. 2018; 140, 111–21.

[40] Liao Q Q, Yue ZW, Yang D, Wang ZH, Li ZH, Ge HH,   Li YJ. Self-assembled monolayer of ammonium pyrrolidine dithiocabamate on copper detected using electrochemical methods, surface enhenced Raman scattering and quantum chemistry calculations. Thin Solid Films. 2011; 519, 6492-8.

[41] Liao QQ, Yue ZW, Yang D, Wang ZH, Li ZH, Ge HH, Li YJ. Inhibition of copper corrosion in sodium chloride solution by the self-assembled monolayer of sodium diethyldithiocarbamate. Corros. Sci.2011; 53, 1999–2005.

101

Türk Doğa ve Fen Dergisi
Turkish Journal of Nature and Science
www.dergipark.gov.tr/tdfd

Determination of Silage Quality of Fenugreek (*Trigonella foenum-graecum* L.) with Oat (*Avena sativa* L.) and Rye (*Secale cereale* L.) Mixtures

Mehmet Arif ÖZYAZICI[1*], Seyithan SEYDOŞOĞLU[1], Semih AÇIKBAŞ[1]

[1]Siirt University, Faculty of Agriculture, Department of Field Crops, Siirt, Türkiye
Mehmet Arif ÖZYAZICI ORCID No: 0000-0001-8709-4633
Seyithan SEYDOŞOĞLU ORCID No: 0000-0002-3711-3733
Semih AÇIKBAŞ ORCID No: 0000-0003-4384-3908

Corresponding author: arifozyazici@siirt.edu.tr

Abstract: In this study, it was aimed to determine the quality of silage mixtures (100:0%, 75:25%, 50:50%, 25:75% and 0:100%) of fenugreek (*Trigonella foenum-graecum* L. cv Berkem) with oat (*Avena sativa* L. cv Faikbey) and rye (*Secale cereale* L. cv Aslım-93). Following the harvest, plants were cut in 2-3 cm sizes, filled in vacuum bags according to the mixing ratios and left for fermentation at 25±2 ºC for 60 days. Physical observations (odor, structure, color), dry matter (DM), pH, crude protein (CP), acid detergent fiber (ADF) and neutral detergent fiber (NDF) analysis were applied to silage samples and relative feed value (RFV) was determined. According to the results obtained, the total physical score of the silages, consisting of the sum of the odor, structure and color scores, ranged between 13.30-19.75 and the physical quality of the silages was ranged between middle-very good class. According to the results of the research, it was determined that the silage DM, ADF and NDF ratios decreased, and the pH, CP and RFV values increased in parallel with the increase in the fenugreek ratio in the mixture. The DM, pH, CP, ADF, NDF and RFV values of the silages varied between 15.67-34.33%, 5.06-5.79%, 6.01-18.17%, 32.03-48.90%, 40.07-74.53% and 63.41-148.48, respectively. As a result, it was concluded that the silage of "25% oats + 75% fenugreek" mixture was superior to the silages of other mixtures, especially when considered the chemical parameters.

Çemen (*Trigonella foenum-graecum* L.) ile Yulaf (*Avena sativa* L.) ve Çavdar (*Secale cereale* L.) Karışımlarının Silaj Kalitesinin Belirlenmesi

Öz: Bu çalışmada, çemen (*Trigonella foenum-graecum* L. cv Berkem) ile yulaf (*Avena sativa* L. cv Faikbey) ve çavdar (*Secale cereale* L. cv Aslım-93) karışımlarının (%100:0, %75:25, %50:50, %25:75 ve %0:100) silaj kalitesinin belirlenmesi amaçlanmıştır. Hasat edilen bitkiler 2-3 cm boyutlarında parçalandıktan sonra karışım oranlarına göre vakum poşetlere doldurulmuş ve 60 gün süre ile 25±2 ºC'de fermantasyona bırakılmıştır. Silaj örneklerinde; fiziksel gözlemler (koku, strüktür, renk) ve kuru madde (KM) analizi ile pH, ham protein (HP), asit deterjanda çözülmeyen lif (ADF) ve nötral deterjanda çözülmeyen lif (NDF) gibi kimyasal analizler yapılmış, silaj materyallerinin nispi yem değeri (NYD) belirlenmiştir. Elde edilen sonuçlara göre, silajların koku, strüktür ve renk puanları toplamından oluşan toplam fiziksel puanı 13.30-19.75 arasında değişmiş ve silajların fiziksel kalitesi orta ile çok iyi sınıfında yer almıştır. Araştırma sonucuna, göre karışımdaki çemen oranının artışına paralel olarak silaj KM, ADF ve NDF oranlarının azaldığı, pH, HP ve NYD değerlerinin arttığı belirlenmiştir. Silajların KM, pH, HP, ADF, NDF ve NYD değerlerinin sırasıyla %15.67-34.33, 5.06-5.79, %6.01-18.17, %32.03-48.90, %40.07-74.53 ve 63.41-148.48 arasında değişim göstermiştir. Sonuç olarak, özellikle kimyasal parametreler dikkate alındığında %25 yulaf+%75 çemen karışımı silajının diğer karışımlardan elde edilen silajlardan daha üstün olduğu sonucuna varılmıştır.

1. INTRODUCTION

A cheap feed source, roughage is very important for farm animals due to its contents of nutrients necessary for the stomach microflora of ruminant animals [1]. In general, high quality roughage sources consist of forage crops grown in pasture-rangelands and field agriculture. In Türkiye, animals are not fed adequately and in a balanced way [2] there is a shortage of approximately 56 million tons of roughage [3]. With the rapid development of animal husbandry, the demand for high-quality green forage throughout the year is also increasing. Increasing the productivity of pasture-rangelands and the cultivation and production of forage crops are of great importance in closing the current forage deficit. In this sense, there was a significant increase in silage production in recent years, especially as a solution to quality roughage problem. Silage is a high-moisture-content forage that is used to feed livestock. Using silage as feed is economically feasible and suitable for cattle management [4]. Silage making is considered to be the most effective and economical method for the preservation of green fodder. Silage production technique plays a role in silage quality, as well as the characteristics of the silage material. For this purpose, many plants can be used to make silage, either sole or in mixtures.

Oat (*Avena sativa*) is an annual crop well known in temperate climates [5] and it is produced for grain and forage in many countries [6]. Oat has multifunctional uses such as forage, fodder, straw for bedding, hay, haylage, silage chaff, human food as rolled or crushed into meal or flour [7]. Oat is a functional food [5] with identified 113 phytochemicals in its content [8]. It contains a spectrum of phenolics and avenanthramides [9]. The mixed-linkage β-glucan is a water-soluble dietary fibre as considered the main biologically active component of many oat products [10]. *Avena sativa* does not only produce highly nutritious grains, but also valuable forage [11]. Oat is a fast growing, palatable, succulent and nutritious fodder crop [12]. Oat is one of the most important winter forage crops grown for livestock in Türkiye.

Rye (*Secale cereale* L.) is a multi-purpose winter cereal mainly grown in Central and Eastern Europe and in Western Canada [13]. It is an important crop used for food, feed and bioenergy [14]. Rye synthesizes benzoxazinoids which are protective special metabolites [15] which regulate aboveground and belowground biotic interactions [16]. Benzoxazinoids play an important role in disease resistance and have anti-bacterial and anti-fungal activity [17]. *Secale cereale* grains are rich in dietary fibre, phenolic acids, lignans and alkylresorcinols [18]. This crop is a high-quality forage plant. At post-heading stage, biomass of rye increases by up to 30%. But lignification of the cell walls result with low fermentation efficiency and digestibility. Also contamination by mycotoxin-producing fungi may impair the quality of the silage [4]. Whole rye crop harvested at pre-maturity stage is a valuable forage for silage production [19].

Fenugreek (*Trigonella foenum-graecum* L.), grown for its seeds, fresh shoots and leaves, is one of the oldest plants belonging to the legume family known for its medicinal and aromatic properties [20]. Fenugreek is native to the eastern Mediterranean zone but is currently cultivated worldwide. The plant has alkaloids, steroids and sapogenins and plant has an important place in traditional medicine to aid digestion and to improve metabolism. Trigonelline and diaszhenin are the most important metabolites of fenugreek in decreasing blood cholesterol [21]. Nowadays, as feed additives, herbs are get incorporated in the animal diets to increase productivity by improving digestibility, nutrient absorption and pathogen elimination in the gut [22]. Fenugreek seeds are used in animal nutrition as powder, oils or extracts due to its therapeutic properties. Leaves of this plant contains carbohydrates, proteins and minerals, low in lipids. Its oils or extracts have antibacterial and antifungal activities. It helps to circulate nutrients into the cells and to remove the toxic materials from the cells. By hormone precursors content, its seeds increase milk secretion in animals. Fenugreek seeds are used in fish, domestic rabbits and ruminant diets [23].

Mixing different species in silage making is a method used to obtain fodder with high nutritional value. Legumes and cereals are generally used for this purpose [2]. Legume monocultures have a low risk of silage fermentation due to their low water soluble carbohydrate and dry matter (DM) content and high buffering capacity [24; 25]. For this reason, grass-legume silage mixtures are preferred in the direction that cereals will provide fermentable carbohydrates and legumes will improve the protein content of silage. Mixing legumes with cereals for ensiling will not just improve quality of silages but also will diversify forage production of enterprices with multifunctional crops, produce rich feeds with functional phytochemicals (β-glucan etc.), help to breed more healthy and diseases tolerant farm animals and produce more nutritious feeds. Therefore, it is also important to determine the best legume-grass combination ratio during the ensiling process. In addition, there is limited information on the nutritional value of the silage of cereals and fenugreek grown in an intermediate crop period.

This study was conducted to determine the quality properties of silages prepared by mixing oats (*A. sativa* L.) and rye (*S. cereale* L.) with different proportions of fenugreek (*T. foenum-graecum* L.).

2. MATERIAL AND METHOD

2.1. Materials

In the study, oats (*A. sativa* L.), rye (*S. cereale* L.) and fenugreek (*T. foenum-graecum* L.) crops were grown in the 2019-2020 vegetation period in Siirt province which has a semi-arid climate located in the Southeastern Anatolia Region of Türkiye (Figure 1) to prepare silages. "Faikbey" oat variety and "Aslım-93" rye variety was obtained from Bahri Dağdaş International Agricultural Research Institute and "Berkem" fenugreek variety was obtained from Dicle University Faculty of Agriculture.
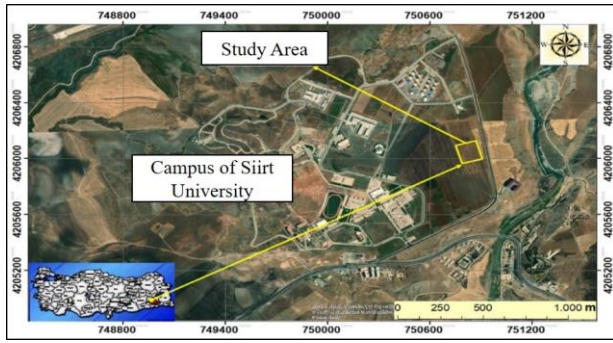
103

Figure 1. Crop growth location of the silaged plant materials

Soils where silage materials are cultivated was clayey in texture, salt-free, slightly alkaline, moderately calcareous, poor in organic matter content, poor in available phosphorus content and rich in available potassium content. According to long term (1990-2020) meteorological data of the Siirt province the current climate in the region is semi-arid. Average temperature was 11.6 °C, annual total precipitation was 632.5 mm, and average relative humidity was 59.9% for the long-term average of the region. Average temperature and total precipitation values for 2019-2020 were above the long term averages, while average relative humidity values were below the long term averages [26].

2.2. Methods

Field trial was established during the winter vegetation period of 2019-2020 with three replications according to the randomized complete blocks design. Row spacing was 20 cm, plot length was 12 m and number of rows was 12 for oats and rye in sowing. Seeding rate was 450 seeds m^{-2} for oats, 500 seeds m^{-2} for rye, and 25 kg ha^{-1} for fenugreek. In the research, 60 kg ha^{-1} nitrogen (N) and 140 kg P$_2$O$_5$ ha^{-1} phosphorus (P) were given as deficient nutrient element for cereals. Half of the N and whole P were applied to the soil one week before sowing. The remaining half of the N was applied to the cereals when plants were at tillering stage [27]. Fenugreek was planted with 25 cm row spacing, 6 rows and 5 m plot length. At sowing, 30 kg ha^{-1} N and 90 kg ha^{-1} P$_2$O$_5$ were applied to fenugreek. Harvest time for silage was pod establishment stage for fenugreek, spike emergence stage for rye and beginning of the clustering period for oats.

Harvested plants were wilted in shade for three hours. The plants, whose wilting processes were completed, were chopped in approximately 2-3 cm dimensions with a branch shredder. The subject of the research was to determine the silage value of the mixtures of fenugreek and oat and rye in different proportions. For this aim, the mixing ratios used in the study were set as 100:0, 75:25, 50:50, 25:75 and for "Rye: Fenugreek" and "Oats: Fenugreek". Plant materials prepared for silage were weighed, mixed, one kg was taken from each mixture and placed in a special vacuum bag after being compressed. All mixtures were kept in a dark and cool environment for 60 days after being silaged. Packs were checked every week to observe the conditions of the materials.

After the fermentation process was completed, the tanks of matured silages were opened and some physical and chemical analyzes were made on the samples. Physical examinations such as odor, structure and color of the samples on the opened silage bags were conducted subjectively by five experts. The scoring method developed by Anonymous [28] was used in the evaluation of physical analyzes. The silage quality class of the silages was determined according to the DLG (Deutsche Landwirtschafts-Gesellschaft) score (Table 1). The DLG score is the total physical score (0-20 points) obtained by the sum of the scores of odour, structure and color [28; 29].

For the determination of the silage DM content (%), 300 g wet samples were taken from the mature silages and dried in an oven at 65 °C for 48 hours. The DM ratio was determined by weighing the dried silage samples on a precision scale and proportioning to the wet weight [30].

For the pH value, a part of silage materials representing the bags was taken from each silage bag, then mixed homogeneously and 25 g wet silage sample from this mixture was weighed on a precision balance before put into a mixer. 250 ml of distilled water was placed on the sample and mixed for 10 minutes, then filtered through filter paper and taken into glass beakers. The pH in the filter of approximately 200 ml material was determined by a pH meter [31]. In order to determine the crude protein (CP) ratios of the silages, the silage samples were dried at 65 °C until they reached a constant weight, then were ground in a mill with a sieve diameter of 1 mm in the laboratory and prepared for the analysis. The total N values of these samples were determined by the Kjehldahl method and the CP ratios were determined by multiplying the N values with the coefficient of 6.25 [30]. Analysis of acid detergent fiber (ADF) and neutral detergent fiber (NDF) in silage applications were determined by using ANKOM 200 Fiber Analyzer according to the principles reported by Van Soest [32] and Van Soest and Wine [33].

The relative feed value (RFV), which is an index for the estimation of the energy value of the roughage by the consumption of the animal, was determined with the help of the following equations developed by Van Dyke and Anderson [34]. To calculate this, digestible dry matter (DDM, %) was calculated with the help of Equation 1, dry matter consumption (DMC, %) was calculated with Equation 2, and RFV was determined with the help of Equation 3.

$$DDM (\%) = 88.9 - (0.779 \times ADF\%) \qquad (1)$$
$$DMC (\%) = 120 / NDF\% \qquad (2)$$
$$RFV (\%) = DDM\% \times DMC\% \times 0.775 \qquad (3)$$

According to the RFV data determined in silages, the quality class reported by Rohweder et al. [35], [RFV>151= Top quality, 125-151= 1st quality (very good), 103-124= 2nd quality (good), 87-102= 3rd quality (medium), 75-86= 4th quality (bad) ve RFV<75= 5th quality (unacceptable)] was used to evaluate the quality of the forage.

The data obtained from the study were subjected to the analysis of variance according to the randomized block experimental design. The differences between the groups according to the F-test results were determined by Tukey's multiple comparison test [36].

Table 1. Physical examination key developed by DLG and silage quality class

Physical examination key	
1. Odor	**Score**
No butter acid odor, slightly sour, fruity and aromatic odor	14
A small amount of butter acid, strong sour odor, and slight escalation	8
Moderate butter acid odor, strong escalation-musty odor	4
Strong butter acid or ammonia odor, very slight sour odor	2
Strong decomposition, ammonia or musty odor	0
2. Structure	
Intact leaves and stems	4
A slightly deteriorated structure of leaves	2
A deteriorated structure of leaves and stems, musty and dirty	1
Rotten leaf and stalk	0
3. Color	
Preserved its color at the moment it was silaged (brown in withered silage)	2
Slightly changed color (yellow to brown)	1
Completely changed color (reseda green)	0
Quality class according to the physical properties of silage	
Quality class	**DLG score**
I- Very good	20-18
II- Good	17-14
III- Medium	13-10
IV- Low (low value)	9-5
V- Corrupted (useless)	4-0

3. RESULTS AND DISCUSSIONS

3.1. Silage Physical Properties

In determining the quality of silage feed, physical methods such as color, odor and structure, which are simple and can be applied under all conditions, are also used, and with this method, preliminary information about the quality of silage can be obtained [37]. The scores and quality class results of the physical observation values (odor, structure and color) of the silages obtained by mixing fenugreek with rye and oats in different proportions are given in Table 2.

Silage odor is one of the most important sensory characteristics used to determine silage quality by physical methods. The average odor value of all applications was determined as 12.28 points, and the odor values of oat, rye and fenugreek silage and their mixtures varied between 9.50-14.00 points. In terms of odor, it was observed that sole fenugreek silage, with a score of 9.50, was close to the "strong sour odor and slightly warming" odor. Other applications have a very good and good silage odor in terms of odor in general. In particular, silage consisting of 75% oats+25% fenugreek gave the best result with 14.00 points (Table 2).

In a good silage, leaves and stems are required to preserve their physical structure. In the study, it was determined that the structure of the leaves in "100% fenugreek" silage was slightly deteriorated and showed low structure characteristics with an average score of 2.50. It was observed that the structure of the leaves and stems of the other silages was not deteriorated in general and the silage structures were at the desired levels. In this sense, it has been determined that fenugreek has the highest structure feature of silages at 50:50 mixing ratios with oats and rye (Table 2). The main factor in the preservation of the structure is the fermentation stage, and since the amount of lactic acid increases in a short time in the successfully fermentated silo feed, deterioration, wear or mold formation does not occur on the leaves and stems.

Another physical feature used to determine the quality of silage is color. As can be seen from Table 2, the average color value of the applications was determined as 1.72 points, and the color score values of the silages varied between 1.30-2.00. These values show that all silage applications generally preserve their color when prepared and physically indicates a good silage. Especially among the mixed silages, "75% oats+25% fenugreek" silage gave the best results in terms of color (Table 2).

Total physical scores (DLG) of silage materials ranged between 13.30-19.75. In terms of DLG, "100% fenugreek" silage was in the "medium" silage quality class, while the other silages were in between "good" and "very good" class. According to the average value of all applications, the physical quality of the silages was found to be "good". In general, when the physical properties and DLG scores are evaluated together, it can be said that better quality silage was obtained from "75% oats+25% fenugreek" mixed silage compared to sole silage materials (Table 2).

It was also been revealed in some other studies that the physical properties of silages obtained by mixing legume forage species and cereals in different proportions differ depending on the mixing ratios. In general, higher scores in terms of DLG were obtained from the mixture of legumes with cereals at low rates, as in the findings of our study. For example, highest DLG scores were reported from silages obtained by mixing white clover with barley at 20%+80% [38], forage peas with barley at 25%+75% [37; 39], grasspea with triticale at 20%+80% [40], common vetch with oats at 25%+75% [41].

Table 2. Average scores and quality class of physical properties of silages of sole and binary mixtures of fenugreek, oat and rye

Applications	Odor	Structure	Color	DLG	Quality class
100% Oats	13.50	3.75	2.00	19.25	Very good
100% Rye	13.00	3.75	1.75	18.50	Very good
100% Fenugreek	9.50	2.50	1.30	13.30	Medium
75% Oats + 25% Fenugreek	14.00	3.75	2.00	19.75	Very good
50% Oats + 50% Fenugreek	13.75	4.00	1.65	19.40	Very good
25% Oats + 75% Fenugreek	11.50	3.50	1.65	16.65	Good
75% Rye + 25% Fenugreek	12.50	3.75	1.90	18.15	Very good
50% Rye + 50% Fenugreek	12.00	4.00	1.60	17.60	Good
25% Rye + 75% Fenugreek	10.75	3.50	1.65	15.90	Good
Mean	**12.28**	**3.61**	**1.72**	**17.61**	**Good**

3.2. Silage Dry Matter Ratio and Some Chemical Properties

The DM ratio and some chemical properties of silages obtained with different ratios of mixtures of fenugreek, oat and rye are given in Table 3. As can be seen from Table 3, the difference between the applications in terms of all silage quality parameters was found to be statistically significant at the p<0.01 level.

The DM ratio is of great importance in the complete realization of chemical events during silage formation, and this ratio is accepted as an important criteria in determining silage quality [42; 43]. In the study, the DM content varied between 15.67% (sole fenugreek)-34.33% (sole rye). It was determined that silage DM ratio increased in parallel with the increase in the ratio of oat

and rye in the mixtures (Table 3). In general, DM contents of grass plants are higher than legumes [37]. This situation led to an increase in the DM ratio in silages obtained by adding cereals to fenugreek, which has a very low DM content. It was also been reported in many research findings that the silage DM ratio increases due to the increase in the cereal ratio in the mixture, and that quality silages were obtained in this sense [37-41; 44]. According to these results, sole silage of fenugreek will reduce silage quality. Therefore, there was a positive relationship between silage quality and DM ratio. Ensiling excessively high moisture content plant affects the lactic acid fermentation in the silo negatively and increases the formation of butter acid [45]. For this reason, the silage material must contain highly soluble carbohydrates per unit dry matter.

Table 3. DM ratio and some chemical properties of silages of sole and binary mixtures of fenugreek, oat and rye[*]

Application	DM (%)	pH	CP (%)	ADF (%)	NDF (%)	RFV
100% Oats	25.33 c	5.50 d	6.01 f	40.27 c	64.83 c	82.55 g
100% Rye	34.33 a	5.06 g	6.62 ef	48.90 a	74.53 a	63.41 i
100% Fenugreek	15.67 g	5.79 a	18.17 a	32.03 f	40.07 i	148.48 a
75% Oats + 25% Fenugreek	23.33 d	5.52 d	6.92 e	40.27 c	58.63 e	91.28 e
50% Oats + 50% Fenugreek	19.67 e	5.59 c	12.30 c	37.40 d	50.90 f	109.23 d
25% Oats + 75% Fenugreek	17.67 f	5.66 b	16.00 b	34.73 e	45.90 h	125.34 b
75% Rye + 25% Fenugreek	29.33 b	5.24 f	7.92 d	46.83 b	68.60 b	71.08 h
50% Rye + 50% Fenugreek	23.67 d	5.45 e	12.63 c	40.57 c	60.62 d	87.94 f
25% Rye + 75% Fenugreek	20.33 e	5.67 b	15.67 b	35.43 e	49.10 g	116.15 c
Mean	**23.26**	**5.50**	**11.36**	**39.60**	**57.02**	**99.50**

*: No significant difference at the p≤0.01 level were determined between the means shown with the same letter.

Silage pH value is one of the main factors affecting the fermentation quality [46-49]. In our study, the highest pH was obtained from sole fenugreek (5.79), and the lowest was obtained from sole rye (5.06) silage (Table 3). It is reported that the silage pH level should be kept at low levels in order to obtain a quality silage [50], while Filya [47] stated that the pH value of a good silage should be below 5. Other researchers [51-54] reported that the pH value of a good silage was between 3.5 and 4.5. It was observed that the pH value was above the desired value in all silage applications examined according to these critical values in the literature. It is thought that this situation is probably due to the lack of good compaction in the silo. However, when Table 3 is examined, reductions in fenugreek ratio in mixtures resulted with reductions in pH values of silages. In other words, as the proportion of cereals included in the mixture increased, the pH value of the silage decreased (Table 3). It has been reported in some research results that the silage pH values of the silages consisting of a mixture of leguminous forage plants and some cereals differ according to the mixing ratios. Silage pH value according to the mixing ratio; was 5.05-5.34 according to Demirel et al. [38] in barley and

white clover mixtures, 3.90-4.00 according to Aykan and Saruhan [37] and Seydoşoğlu [39] in barley and forage pea mixtures, 3.99-4.19 according to Karadeniz et al. [40] in mixtures of triticale and grasspea, 5.03-6.04 according to Görü and Seydoşoğlu [41] in mixtures of some cool season cereals (oat, barley, rye and triticale) and common vetch, 4.51-4.83 according to Gülümser et al. [44] in oat and forage pea mixtures.

Crude protein ratio is considered as an important indicator in determining the quality of forages. In the study, the highest CP rate was determined in sole fenugreek silage with 18.17%. The lowest CP ratio was found in sole oat silage (6.01%). It was observed that the CP values of the silages belonging to the cereal-fenugreek mixtures, where the ratio of silage of cereals and fenugreek was 25%, were in the low group statistically. In other words, silage CP values increased in parallel with the increase in the amount of fenugreek in the mixture (Table 3). This is due to the fact that fenugreek is a legume. In some other studies, in which CP ratios of silages increase with the increase in legume ratios in the mixtures [2; 41; 49; 55-57].

When the ADF and NDF ratios of the silages belonging to the sole and different mixtures of fenugreek, oat and rye are examined, the highest ADF and NDF ratio is sole rye (48.90% and 74.53%, respectively), and the lowest is sole fenugreek (32.03% and 40.07%, respectively) silages (Table 3). This is an expected result. Because the fiber density of leguminous plants is lower than that of grass [58]. In the study, it was also observed that the ADF and NDF contents of the silages obtained decreased as the amount of fenugreek added to the mixture increased (Table 3). This can be explained by the proportional decrease in cell wall substances in mixtures where fenugreek, which is rich in cellular substances such as CP, is a legume. In other words, the low ADF and NDF content of fenugreek was effective in the low ADF and NDF content of the silage it was mixed with. The ratio of ADF and NDF, which are plant cell wall components, is a good indicator of total digestible nutrients, and it is desirable to have a low ratio of ADF and NDF in roughage [59; 60]. As another result of our study, considering the ratio of ADF and NDF, it can be said that silages obtained from fenugreek-oat mixtures produced higher quality roughage than fenugreek-rye mixtures (Table 3). In silages made with different grass-legume mixtures, Can et al. [61] found the ADF ratio to be 29.61-35.88% and the NDF ratio to be 41.66-57.49% in tedera (*Bituminaria bituminosa* L.) and oat mixed silages; Turan [56] found the ADF ratio of 30.19%-33.11% and the NDF ratio to 43.00-47.84% in Hungarian vetch and barley mixtures; Karadeniz et al. [40] found the ADF ratio to be 32.76-34.63% and the NDF ratio to be 46.87-49.70% in the mixtures of grasspea and triticale; Görü and Seydoşoğlu [41] reported the ADF ratio between 31.85-42.99% and NDF ratio between 47.47-68.12% in some cool climate cereals (oat, barley, rye and triticale) and common vetch mixtures. In the same studies, the researchers reported that ADF and NDF ratios of silages decreased with the increase in legume ratios in the mixtures, consistent with the findings of our study.

The RFV of the silages ranged from 63.41 (sole rye) to 148.48 (sole fenugreek) (Table 3). When the RFV values determined in the study were evaluated according to the quality class determined by Rohweder et al. [35]; sole rye and 75% rye+25% fenugreek mixture silages were 5th class, sole oats silage were 4th class, 75% oats+25% fenugreek and 50% rye+50% fenugreek mixtures were 3rd class, 50% oats+50% fenugreek and 25 mixtures of % rye+75% fenugreek were produced 2nd class and sole fenugreek and 25% oats+75% fenugreek mixed silages were produced 1st class quality fodders. Accordingly, it was observed that higher quality silage was obtained as the ratio of fenugreek plant in the mixture increased (Table 3). Similar results were obtained in terms of RFV in silages consisting of legume-grass mixes [39; 41; 49; 56; 61].

4. CONCLUSION

In this study, in which the quality characteristics of the silages of different mixtures of fenugreek, oat and rye were determined, better results were obtained from the mixtures compared to the sole silages of the species. This shows that fenugreek mixed with cereals can be ensiled and it is a promising legume for silage production. According to these results, it was concluded that the silage of 25% oats + 75% fenugreek mixture was superior to the silage obtained from other mixtures, especially when considering the chemical parameters.

REFERENCES

[1] Budak F, Budak F. Quality on forage plants and factors effecting forage quality. Turkish Journal of Scientific Reviews. 2014;7(1):1-6. (In Turkish).

[2] Can M, Acar Z, Ayan İ, Gülümser E, Mut H. Silage quality of chicory binary mixtures with white clover and orchard grass. Journal of the Institute of Science and Technology. 2020;10(4):3076-3083. (In Turkish).

[3] Acar Z, Tan M, Ayan İ, Önal Aşçı Ö, Mut H, Başaran U, Gülümser E, Can M, Kaymak G. Situation of forage crops agriculture and development opportunities in Turkey. Agricultural Engineers of Turkey IX. Technical Congress, 13-17 January, Ankara, Turkey; 2020. (In Turkish).

[4] Kim HS, Han OK, Kim SC, Kim MJ, Kwak YS. Screening and investigation Lactobacillius spp. to improve *Secale cereale* silage quality. Animal Science Journal. 2017;88(10):1538-1546.

[5] Sterna V, Zute S, Brunava L. Oat grain composition and its nutrition benefice. Agriculture and agricultural science procedia. 2016;8:252-256.

[6] Kim KS, Tinker NA, Newell MA. Improvement of oat as a winter forage crop in the Southern United States. Crop Science. 2014;54(4):1336-1346.

[7] Ahmad M, Dar ZA, Habib M. A review on oat (*Avena sativa* L.) as a dual-purpose crop. Scientific Research and Essays. 2014;9(4):52-59.

[8] Raguindin PF, Itodo OA, Stoyanov J, Dejanovic GM, Gamba M, Asllanaj E, Kern H. A systematic review of phytochemicals in oat and buckwheat. Food Chemistry. 2020;127982.

[9] Soycan G, Schär MY, Kristek A, Boberska J, Alsharif SN, Corona G, Spencer JP. Composition and content of phenolic acids and avenanthramides in commercial oat products: Are oats an important polyphenol source for consumers? Food chemistry: X. 2019;3: 100047.

[10] Wang Q, Ellis PR. Oat β-glucan: physico-chemical characteristics in relation to its blood-glucose and cholesterol-lowering properties. British Journal of Nutrition. 2014;112(S2):S4-S13.

[11] Huang CW, Liang WH, Esvelt Klos K, Chen CS, Huang YF. Evaluation of agronomic performance and exploratory genome-wide association study of a diverse oat panel for forage use in Taiwan. Grassland Science. 2020;66(4):249-260.

[12] Irfan M, Ansar M, Sher A, Wasaya A, Sattar A. Improving forage yield and morphology of oat varieties through various row spacing and nitrogen application. JAPS: Journal of Animal & Plant Sciences. 2016;26(6).

[13] Gaikpa DS, Koch S, Fromme FJ, Siekmann D, Würschum T, Miedaner T. Genome-wide association mapping and genomic prediction of

Fusarium head blight resistance, heading stage and plant height in winter rye (*Secale cereale*). Plant Breeding. 2020;139(3):508-520.

[14] Miedaner T, Hübner M, Korzun V, Schmiedchen B, Bauer E, Haseneyer G, Reif JC. Genetic architecture of complex agronomic traits examined in two testcross populations of rye (*Secale cereale* L.). BMC Genomics. 2012;13(1):1-13.

[15] Bakera B, Święcicka M, Stochmal A, Kowalczyk M, Bolibok L, Rakoczy-Trojanowska M. Benzoxazinoids biosynthesis in rye (*Secale cereale* L.) is affected by low temperature. Agronomy. 2020;10(9):1260.

[16] Cotton TA, Pétriacq P, Cameron DD, Al Meselmani M, Schwarzenbacher R, Rolfe SA, Ton J. Metabolic regulation of the maize rhizobiome by benzoxazinoids. The ISME Journal. 2019;13(7): 1647-1658.

[17] Bakera B, Makowska B, Groszyk J, Niziołek M, Orczyk W, Bolibok-Brągoszewska H, Rakoczy-Trojanowska M. Structural characteristics of ScBx genes controlling the biosynthesis of hydroxamic acids in rye (*Secale cereale* L.). Journal of Applied Genetics. 2015;56(3):287-298.

[18] Pihlava JM, Hellström J, Kurtelius T, Mattila P. Flavonoids, anthocyanins, phenolamides, benzoxazinoids, lignans and alkylresorcinols in rye (*Secale cereale*) and some rye products. Journal of Cereal Science. 2018;79:183-192.

[19] Auerbach H, Theobald P. Additive type affects fermentation, aerobic stability and mycotoxin formation during air exposure of early-cut rye (*Secale cereale* L.) silage. Agronomy. 2020;10(9):1432.

[20] Özyazıcı G. Responses of sulfur and phosphorus doses on the yield and quality of fenugreek (*Trigonella foenum-graecum* L.). Applied Ecology and Environmental Research. 2020;18(5):7041-7055.

[21] Bahmani M, Shirzad H, Mirhosseini M, Mesripour A, Rafieian-Kopaei M. A review on ethnobotanical and therapeutic uses of fenugreek (*Trigonella foenum-graecum* L). Journal of Evidence-Based Complementary & Alternative Medicine. 2016;21(1):53-62.

[22] Adil S, Qureshi S, Pattoo RA. A review on positive effects of fenugreek as feed additive in poultry production. International Journal of Poultry Science. 2015;14(12):664.

[23] Dronca D, Pacala N, Stef L, Pet I, Bencsik I, Dumitrescu G, Ahmadi M. Fenugreek-a dietary alternative component in animal feed. scientific papers: Animal Science & Biotechnologies/Lucrari Stiintifice: Zootehnie si Biotehnologii. 2018;51(2).

[24] Kaiser AG, Dear BS, Morris SG. An evaluation of the yield and quality of oat-legume and ryegrass-legume mixtures and legume monocultures harvested at three stages of growth for silage. Australian Journal of Experimental Agriculture. 2007;47(1):25-38.

[25] Denek N, Can A, Avci M, Aksu T, Durmaz H. The effect of molasses-based pre-fermented juice on the fermentation quality of first-cut lucerne silage. Grass Forage Sci. 2011;66:243-250.

[26] Anonymous 2020a. Siirt Province Climate Data. T.C. Ministry of Agriculture and Forestry, General Directorate of Meteorology, Türkiye.

[27] Anonymous 2020b. Ministry of Agriculture and Forestry. Seed Registration and Certification Central Directorate, Cool Climate Cereals Technical Instruction, Ankara, Türkiye.

[28] Anonymous 1987. Bewertung von Grünfutter, Silage und Heu-Deutsche Landwirtschafts-Gesellschaft (DLG), DLG Merkblatt Frankfurt, 224.

[29] Ergün A, Tuncer ŞD, Çolpan İ, Yalçın S, Yıldız G, Küçükersan MK, Küçükersan S, Şehu A, Saçaklı P. Feed, Feed Hygiene and Technology. Ankara University, Faculty of Veterinary Medicine, Extended 5th Edition, Ankara, Turkey, 2013; p448. (In Turkish).

[30] Bulgurlu Ş, Ergül M. Physical, chemical and biological analysis methods of feeds. Ege University Faculty of Agriculture Publications No: 127, 1978. İzmir, Turkey. (In Turkish).

[31] Anonymous 1993. Bestimmung des pH-Wertes. In: Die chemischen Untersuchungen von Futtermitteln. Teil 18 Silage. Abschnit 18.1 Bestimmung des pH-Wertes., Methodenbuch Bd. III., VDLUFAVerlag, Darmstadt.

[32] Van Soest PJ. The use of detergents in the analysis of fibre feeds. II. A rapid method for the determination of fibre and lignin. Journal of the Association of Official Analytical Chemists. 1963;46:829-835.

[33] Van Soest PJ, Wine RH. Use of detergents in the analysis of fibrous feeds. IV. Determination of plant cell-wall constituents. Journal - Association of Official Analytical Chemists. 1967;50:50-55.

[34] Van Dyke NJ, Anderson PM. Interpreting a Forage Analysis. Alabama Cooperative Extension, Circular ANR-890, 2000.

[35] Rohweder DA, Barnes RF, Jorgensen N. Proposed hay grading standards based on laboratory analyses for evaluating quality. Journal of Animal Science. 1978;47(3):747-759.

[36] Açıkgöz N, Açıkgöz N. Common mistakes in the statistical analyzes of agricultural experiments I. Single Factorials. Anadolu. 2001;11(1):135-147. (In Turkish).

[37] Aykan Y, Saruhan V. Determination of Silage Quality Features of Field Pea (*Pisum sativum* L.) and Barley (*Hordeum vulgare* L.) Mixtures Ensiling at Different Rates. The Journal of Faculty of Veterinary Medicine. 2018;11(2):64-70. (In Turkish).

[38] Demirel R, Saruhan V, Baran MS, Andiç N, Şentürk Demirel D. Determination of different ratios of trifolium repens and hordeum vulgare mixtures on silage quality. Yüzüncü Yıl University Journal of Agricultural Sciences. 2010;20(1):26-31. (In Turkish).

[39] Seydoşoğlu S. Investigation of the effect of fodder pea (*Pisum sativum* L.) and Barley (*Hordeum vulgare* L.) herbages mixed at different rates on silage and feed quality, Journal of Agriculture

108

Tr. Doğa ve Fen Derg. Cilt 11, Sayı 3, Sayfa 102-109, 2022

Tr. J. Nature Sci. Volume 11, Issue 3, Page 102-109, 2022

Faculty of Ege University. 2019;56(3):297-302. (In Turkish).

[40] Karadeniz E, Eren A, Saruhan V. Determination of silage quality of grasspea (*Lathrus sativus* L.) and Triticale (xTriticosecale Wittmack) mixtures. ISPEC Journal of Agricultural Sciences. 2020;4(2):249-259. (In Turkish).

[41] Görü N, Seydoşoğlu S. Determination of silage quality of some winter cereals (oat, barley, rye and triticale) mixed with common vetch (*Vicia sativa* L.). Isparta Uygulamalı Bilimler Üniversitesi, Ziraat Fakültesi Dergisi. 2021;16(1):26-33. (In Turkish).

[42] Geren H. Effect of sowing dates on silage characteristics of different maize cultivars grown as second crop under Bornova conditions. Journal of Agriculture Faculty of Ege University, 2001;38(2-3):47-54. (In Turkish).

[43] Çakmak B, Yalçın H, Bilgen H. The effect of packing pressure and storage duration on the crude nutrient content and the quality of silages made from green and fermented corn. Journal of Agricultural Sciences. 2013;19:22-32. (In Turkish).

[44] Gülümser E, Mut H, Başaran U, Çopur Doğrusöz M. determination of quality traits of silages obtained of forage pea and oats in different ratios. Journal of the Institute of Science and Technology. 2021;11(1):763-770.

[45] Filya İ. The effects of lactic acid bacterial inoculants on the fermentation aerobic stability and in situ rumen degradability characteristics of maize and sorghum silages. Turkish Journal Of Veterınary And Animal Scıences. 2002;26:815-823. (In Turkish).

[46] McDonald P, Henderson AR, Heron SJE. The Biochemistry of Silage. Second Edition. Chalcombe Publication, Marlow-England. 1991. p.340.

[47] Filya İ. Silage Technology. Uludağ University, Faculty of Agriculture, Department of Animal Science, Bursa, Turkey. 2001. (In Turkish).

[48] Wang J, Wang JQ, Zhou H, Feng T. Effects of addition of previously fermented juice prepared from alfalfa on fermentation quality and protein degradation of alfalfa silage. Animal Feed Science and Technology. 2009;151:280-290.

[49] Geren H. An ınvestigation on some guality characteristics of ensilaged giant kinggrass (*Pennisetum hybridum*) with different levels of leguminous forages. Journal of Agriculture Faculty of Ege University. 2014;51(2):209-217. (In Turkish).

[50] Liu QH, Shao T, Zhang JG. Determination of aerobic deterioration of corn stalk silage caused by aerobicbacteria. Animal Feed Science and Technology. 2013;183(3-4):124-131.

[51] Danley MM, Vetter RL, Wedin WF. Modified laboratory silo unit for studying the fermentation of corn (*Zea mays* L.) grain. Agronomy Journal. 1973;65:621-624.

[52] Comberg G. Gärfutter: Betriebswirtschaft, Erzeugung, Verfütterung. Verlag Eugen Ulmer Stuttgart, Gerokstraße 19, Printed in Germany. 1974. p.260.

[53] Roth GW. Corn silage productionand management. college of agricultural sciences. Agricultural Research and Coop. Extension, Agronomy Facts. 2001;18.

[54] Kılıç A. Determination of Quality in Roughage. Hasat Publishing, İstanbul, Türkiye. 2006. (In Turkish).

[55] Geren H, Avcioglu R, Soya H, Kir B. Intercropping of corn with cowpea and bean: biomassyield and silage quality. African Journal of Biotechnology. 2008;7(22):4100-4104.

[56] Turan N. Determination of chemical composition and quality properties of silage produced by mixing green hungarian vetch and barley in various proportions. European Journal of Science and Technology. 2019;17:787-793. (In Turkish).

[57] Mut H, Gülümser E. Çopur Doğrusöz M, Başaran U. Effect of different companion crops on alfalfa silage quality. KSU Journal of Agriculture and Nature. 2020;23(4):975-980. (In Turkish).

[58] Önal Aşçı Ö, Acar Z. Quality in Forages. TMMOB Chamber of Agricultural Engineers Publications, Ankara, Türkiye. 2018. p.112. (In Turkish).

[59] Van Soest PJ. Nutritional Ecology of the Ruminant (2nd Ed.). Ithaca, N.Y. Cornell University Press. 1994.

[60] Gürsoy E, Macit M. Determination of in vitro gas production parameters of some grass forages grown as naturally in the pastures of Erzurum. Yüzüncü Yıl University Journal of Agricultural Sciences. 2014;24(3):218-227. (In Turkish).

[61] Can M, Kaymak G, Gülümser E, Acar Z, Ayan İ. Determination of silage quality of Bituminaria bituminosa with oat mixtures. Anadolu Journal of Agricultural Sciences. 2019;34:371-376. (In Turkish).

109

Türk Doğa ve Fen Dergisi
Turkish Journal of Nature and Science

www.dergipark.gov.tr/tdfd

Biosynthesis, Characterization and Determination of Sun Protection Factor (SPF) of Iron Nanoparticles With Bee Bread

Büşra BILDIR[1], Zeynep DEMİRKAN[1], Bülent KAYA[2*]

[1] Bee and Bee Products Department, Institute of Science, Bingöl University, Bingöl, Türkiye
[2] Molecular Biology and Genetics Department, Science and Art Faculty, Bingol University, Bingöl, Türkiye
Büşra BILDIR ORCID No: 0000-0002-5631-1946
Zeynep DEMİRKAN ORCID No: 0000-0002-8101-8194
Bülent KAYA ORCID No: 0000-0002-1216-6441

*Corresponding author: bkaya@bingol.edu.tr

Keywords	**Abstract:** Bee bread is a food product obtained by fermenting bee pollen with honey and storing it in honeycomb cells. In this fermentation, phenolic compounds remain unaffected and unchanged. Bee bread contains approximately; 35% sugar, 24-35% carbohydrate, 20-22% protein, 3.5% lactic acid, 2.43% mineral, 1.6% lipid and 1.6% fat. Within the scope of the study, biocompatible iron nanoparticles were synthesized (BB@FeNPs) by utilizing the potential reducing powers of these components contained in bee bread. The characterization of obtained bee bread-based nanoparticles; was performed using spectroscopic techniques such as ultraviolet-visible light spectrophotometer, fourier transform infrared spectrophotometer, and x-ray diffraction spectrometry. Scanning electron microscopy was used as a microscopic method in the characterization of nanoparticles. In addition, the sun protection factor (SPF) of the synthesized nanoparticles was determined by ultraviolet spectrophotometry. Although the studies in recent years tend to search for bioactive molecules of natural origin, no nanoparticle synthesis with bee bread has been encountered in the literature. This study is important as it is a first in the synthesis of metal nanoparticles with bee bread.
Green synthesis, Metal nanoparticles, Bee bread, Sun protection factor (SPF)	

Arı Ekmeği ile Demir Nanopartiküllerinin Biyosentezi, Karakterizasyonu ve Güneş Koruma Faktörünün (SPF) Belirlenmesi

Anahtar Kelimeler	**Öz:** Arı ekmeği, arı poleninin bal ile fermente edilmesi ve petek gözlerine depolanmasıyla elde edilen bir gıda maddesidir. Bu fermantasyonda fenolik bileşikler etkilenmeden ve değişmeden kalmaktadır. Arı ekmeği içeriğinde yaklaşık olarak; %35 şeker, %24-35 karbonhidrat, %20-22 protein, %3,5 laktik asit, %2,43 mineral, %1,6 lipid ve %1,6 yağ bulunmaktadır. Çalışma kapsamında, arı ekmeğinin içermiş olduğu bu bileşenlerin potansiyel indirgeme güçlerinden yararlanılarak biyouyumlu demir nanopartiküller sentezlenmiştir (BB@FeNPs). Elde edilen arı ekmeği temelli nanopartiküllerin karakterizasyonu; ultraviyole-görünür ışık spektrofotometresi, fourier dönüşümlü kızılötesi spektrofotometresi ve x-ışını kırınım spektrometresi gibi spektroskopik teknikler kullanılarak gerçekleştirilmiştir. Nanopartiküllerin karakterizasyonunda mikroskobik yöntem olarak ise taramalı elektron mikroskobu kullanılmıştır. Ayrıca sentezlenen nanopartiküllerin güneş koruma faktörü (SPF) ultraviyole spektrofotometri ile belirlenmiştir. Son yıllardaki çalışmaların doğal kaynaklı biyoaktif molekülleri araştırma eğiliminde olmasıyla birlikte, literatürde arı ekmeği ile nanopartikül sentezine rastlanılmamıştır. Bu çalışma arı ekmeği ile metal nanopartikül sentezinde bir ilk olması açısından önemlidir.
Yeşil sentez, Metal nanopartiküller, Arı ekmeği, Güneş koruma faktörü (SPF)	

1. INTRODUCTION

It is known that the term nanotechnology was first mentioned by Richard Feynman at the meeting of the American Physical Society (APS) in 1959 [1]. Nanotechnology on the other hand is the science that allows studies such as measurement, modeling, design, processing and arrangement that can be carried out on

materials at 1-100 nm dimensions [2]. Although the word nano basically means one billionth of any unit, it is used as a technical unit of measurement [3]. In this respect, nanoparticles constitute the basic building blocks of nanotechnology [4]. Although the usage area of nanoparticles is quite wide, a few of these areas are as follows; the food, health, aerospace and pharmaceutical and cosmetic industries [5].

There are 3 different synthesis methods for the synthesis of nanoparticles; physical, chemical and biological. The negative effects of physical and chemical synthesis methods are replaced left to the biological synthesis method, which is a less costly and environmentally friendly method [5]. With biological green synthesis, it is possible to synthesize nanoparticles in an environmentally friendly and easy way without the need for toxic chemicals, high temperature, high pressure and high energy [6]. In the green synthesis method, nanoparticles with different content, shape, size and physicochemical properties are synthesized. In this method, nanoparticle synthesis is carried out by using phenolic compounds, amines, proteins, enzymes, pigments, alkaloids and microorganisms in plants as reducing agents [7]. Biological (fungi, plants, algae, bacteria, etc.) natural resources are used for the green synthesis of nanoparticles [5]. Nanoparticles prepared with natural product extracts generally show promising bioactivity as they contain phytocomponents as stabilizing ligands on their surface. In the synthesis of biocompatible nanomaterials, bee products such as honey, pollen, royal jelly, bee venom and beeswax are thought to be a potential product source to prevent nanoparticle aggregation [8].

With the increase in health awareness and interest in functional foods in today's world, bee products bring new perspectives to future productions. In this context, bee bread, which is a bee product, contributes to human health and nutritional values due to its unique chemical content and also having microbial fermentation effect. The abundant presence of compounds such as polyphenols and flavonoids, which are important for the human body, reduces the formation of reactive oxygen species (ROS). All bee products, including bee bread; it has many biological properties such as biodegradation, non-toxic structure and biocompatibility. All these properties pave the way for the use of bee bread as a complementary ingredient in traditional medicines or nanoparticle production. In addition to the prediction that bee bread can be used in the production of nanoparticles, from bee products nanoparticles; it has been stated that it can be used in advanced imaging, probing and cancer treatment [9]. Figure 1 shows a section of the bee bread sample used in the study.

Figure 1. Bee bread samples

Metal oxide nanoparticles are used in many different areas from food packaging to drug delivery systems, from solar cells to cosmetics [10]. The most preferred basic metal oxide nanoparticles are iron oxides (FeO, Fe_2O_3, Fe_3O_4 etc.), zinc oxide (ZnO), titanium dioxide (TiO_2), aluminum oxide (AlO), and cerium oxide (CeO_2) nanoparticles [10, 11]. Thanks to the physicochemical properties of iron oxide nanoparticles, which are among metal oxide nanoparticles, they are frequently used in in vitro and in vivo research [12, 13]. Iron oxides are either naturally found or synthesized under laboratory conditions [14].

Based on all this information, within the scope of the study, green synthesized iron nanoparticles were produced with bee bread. The sun protection factor (SPF) of the synthesized nanoparticles was determined by in vitro method, providing an idea for future studies. Although green synthesis through bee products such as honey, pollen, and propolis has been performed before, no studies using bee bread have been conducted to date. For this reason, the study reveals a first in the literature with metal nanoparticle synthesis using bee bread.

2. EXPERIMENTAL METHODS

2.1. Materials

Bee bread samples were obtained from local beekeepers at Bingöl, Turkey, in 2021. Iron (II) chloride ($FeCl_2$), iron (III) chloride ($FeCl_3$), sodium hydroxide (NaOH), nitric acid (HNO_3) and sodium nitrate ($NaNO_3$) reagents used in nanoparticle synthesis and characterization were of analytical purity.

2.2. Methods

2.2.1. Preparation of bee bread extract

The bee bread obtained from the Bingöl (Turkey) region was weighed approximately 10 g and ground into powder

with the help of a grinder. Powdered bee bread samples were added into 100 mL of distilled water brought to 100 ˚C. The resulting mixture was homogenized at 100 ˚C in a heated magnetic stirrer for 30 minutes. The homogeneous mixture was filtered through filter paper and purified water was added on it so that the final volume was 100 mL. The pH value of bee bread extract was measured as 1.5 and stored in a glass bottle at -18 ˚C to be used in the studies.

2.2.2. Synthesis of BB@Fe nanoparticles

0.01 M $FeCl_2$ solution and 0.02 M $FeCl_3$ solution were prepared in 50 mL distilled water separately and on a magnetic stirrer. Then, the two solutions were combined and mixed in a heated magnetic stirrer until the temperature reached 60°C. On the other hand, the prepared bee bread extract was diluted with distilled water at a ratio of 1:10. While the pH value of the diluted bee bread extract was 7 at the beginning, 1 M NaOH was added to ensure the final pH value was 10. When the temperature of the mixture prepared with $FeCl_2$ and $FeCl_3$ solutions reached 60˚C, 30 mL of diluted bee bread extract was added. Until the pH value of the whole mixture reached 12, 2 M NaOH was added dropwise, and it was mixed in a heated magnetic stirrer until the temperature reached 60˚C. As a result of the precipitation of magnetic nanoparticles, the separation of the supernatant was achieved. Nanoparticles were taken into a petri dish and left to dry in an oven at 40˚C.

2.2.3. Determination of isoelectric point of BB@Fe nanoparticles

It was prepared with 100 mL of 0.1 M $NaNO_3$ distilled water on a magnetic stirrer. 100 mL of $NaNO_3$ solution was divided into 10 beakers in equal amounts. The pH values of the solutions in the beakers were adjusted between 3-12 ($pH_{initial}$). 0.1 M HNO_3 and 0.1 M NaOH solutions were used to adjust the pH values. 10 mg of BB@Fe nanoparticles were added to each of the pH-adjusted solutions. The nanoparticle added solutions were allowed to mix at room temperature for 1 day. At the end of the waiting period, the pH value (pH_{end}) of each solution was measured again and the isoelectric point of the nanoparticles was determined.

2.2.4. Characterization of BB@Fe nanoparticles

Biosynthesis of BB@Fe nanoparticles was observed using Ultraviolet-Visible Light Spectrophotometer, UV-VIS-NIR (SHMADZU UV-3600). Related functional groups in biosynthesis and stabilization of bee bread extract, $FeCl_2$, $FeCl_3$ and BB@FE nanoparticles used in the study were screened using Fourier Transform Infrared Spectrophotometer, FT-IR (Perkin Elmer Spectrum 100). The size and shape of the BB@Fe nanoparticles were determined using X-Ray Diffraction Spectrometer, XRD (RIGAKU ULTIMA IV), and the morphology was determined using Scanning Electron Microscopy, SEM (JEOL JSM 6510).

2.2.5. Determination of sun protection factor (SPF) of BB@Fe nanoparticles

The term sun protection factor (SPF), which is used to evaluate the effectiveness of sunscreens against the UVB effect, is defined as the ratio of the UV dose required to create a minimal erythema reaction after the sunscreen is applied to the skin, to the UV dose required to produce the same erythema in unprotected skin. In short, the SPF value expresses how many times the sunscreen prolongs the time to reach the minimal erythema dose [15]. The equation used in this study to determine the SPF value of nanoparticles biosynthesized with bee bread is given below (1).

$$\text{SPF spectrophotometric} = CF \times \Sigma EE (\lambda) \times I (\lambda) \times Abs (\lambda) \qquad (1)$$

EE= erythemal effect spectrum
I= sun intensity spectrum
CF= confirmation factor
Abs= absorbance

To determine the SPF value of BB@FeNPs; The nanoparticles were weighed 10 mg and dissolved in 10 mL DMSO. Absorption spectra of the samples prepared at 100-1000 ppm concentrations were measured in the range of 290-320 nm against DMSO. The results were calculated according to the Mansur equation and the SPF values of the nanoparticles were determined [16, 17]. The EE x I values determined by Sayre et al. [18], are constant and are given in Table 1.

3. RESULTS AND DISCUSSION

3.1. Isoelectric Point of BB@FeNPs

Similar charged particles in the same liquid repel each other, while differently charged particles attract each other. These push-pull forces of the particle are defined as the zeta potential [19]. The zeta potential value takes different values according to the pH value of the solution in which the particle is located. The pH value, where these values intersect with the zero axis, is defined as the "isoelectric point". Amino acids and proteins are cationic at low pH values, anionic at high pH values, and neutral at isoelectric points [20]. At the isoelectric point, the positive (+) and negative (–) charges being equal to each other result in the formation of attraction instead of electrostatic repulsion between the same molecules and the collapse of proteins [21]. Measurements of the pH value to detect the surface charge of BB@FeNPs are given in Figure 2. According to this figure, the isoelectric point of BB@Fe nanoparticles was found to be 7.8.
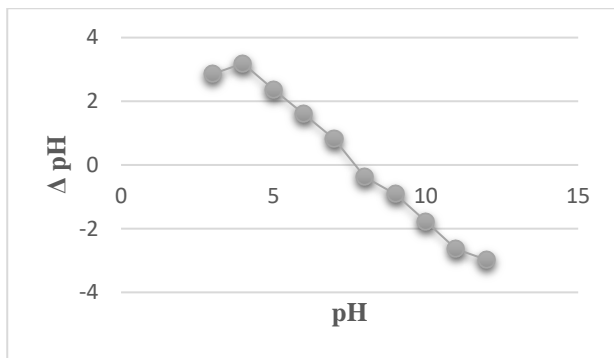
Figure 2. Graph of BB@FeNPs isoelectric point

Considering the acidic nature of bee bread samples, it is expected that the isoelectric point of BB@FeNPs is close to neutral compared to iron nanoparticles in the literature [22, 23].

3.2. UV-VIS-NIR Spectrophotometer

UV-VIS-NIR absorption spectrum of iron nanoparticles synthesized with bee bread showed a peak around 242 and 273 nm (Figure 3). According to Mirza et al. [24], reported that iron oxide nanoparticles peaked at 248 and 278 nm through extracts of *Agrewia optiva* and *Prunus persica*, similar to our study.
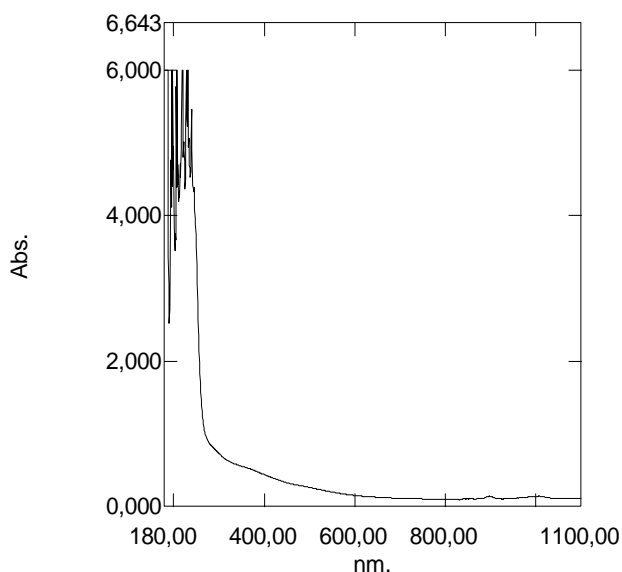

Figure 3. UV-VIS-NIR spectra of BB@FeNPs

3.3. FT-IR Spectrophotometer

FT-IR analysis was performed to determine the bond relationship and functional groups in BB@FeNPs with bee bread sample. FT-IR spectra of bee bread, BB@FeNP, FeCl$_3$ and FeCl$_2$ samples are given in Figure 4.
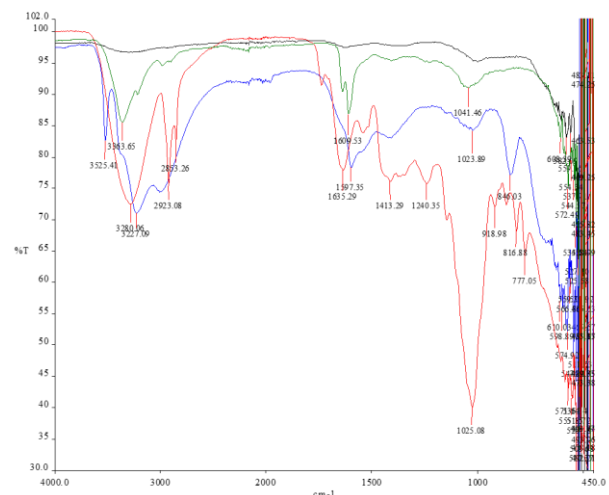

Figure 4. FT-IR spectra of bee bread (red), BB@FeNP (black), FeCl$_3$ (blue) and FeCl$_2$ (green)

Spectra of bee bread sample showed strong bands at 3655.17, 3280.06, 3000.00, 2923.08, 2853.26, 1733.42, 1635.29, 1488.34, 1413.29, 1297.01, 1240.35, 1127.18, 1025.08, 918.98, 816.88, 777.05 cm^{-1}; BB@FeNPs showed strong bands at 3659.48, 3340.51, 2969.82, 2159.48, 1926.90, 1737.72, 1634.53, 1402.35, 1174.47, 1004.64, 815.46, 660.67 cm^{-1}. The peak at about 3300 cm^{-1} is due to the O\H stretching vibrations of phenolic groups, while the peak at 1600 cm^{-1} is thought to be due to the C=O stretching vibrations of carboxylic acids. This situation is also observed in similar studies [24, 25]. In addition, C\H stretching vibrations of the aromatic compound of the samples were observed at around 2900 cm^{-1}, C\O stretching vibrations were observed at 1000-1100 cm^{-1} and C\O\C stretching vibrations at 1400 cm^{-1} peaks [26]. Apart from the defined bands, there are a few more bands in both bee bread and iron nanoparticles synthesized with bee bread. Finding these specific peaks may vary depending on the type of bee bread and the extraction method. Multiple peaks appearing in BB@Fe nanoparticles indicate the presence of Fe in accordance with the literature [24, 25]. According to the FT-IR analysis results, it can be assumed that the phenolic compounds in bee bread can provide closure and stabilization of BB@FeNPs.

3.4. XRD Spectrophotometer

The estimation of the crystal sizes of iron nanoparticles synthesized using bee bread characterized by XRD is shown in Figure 5. The main diffraction peaks of BB@FeNPs are 32°(220), 36°(311), 45°(422), 57°(511) and 63°(440). These peaks are standard JCPDS NO. The 85-1436 data can be compared with the standard XRD model of Fe$_3$O$_4$ NPs in the database.
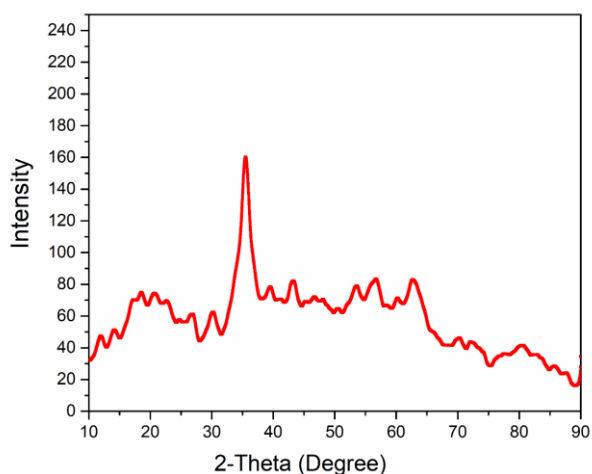
113

Figure 5. XRD spectra of BB@FeNPs

In the literature, Fe_3O_4 nanoparticles used for magnetic resonance imaging and hyperthermia [27], Fe_3O_4 nanoparticles coated with fucan polysaccharides [28], and aqueous extracts of food processing wastes Fe_3O_4 nanoparticles [29] XRD spectra are similar to our study.

3.5. SEM and EDX Analysis

In the characterization of BB@FeNPs, nanoparticles were observed under scanning electron microscopy (SEM) and the morphological analysis results are shown in Figure 6. In addition, energy dispersive X-ray (EDX) spectroscopy, shown in Figure 6, confirmed that the synthesized nanoparticles contained Fe [29].
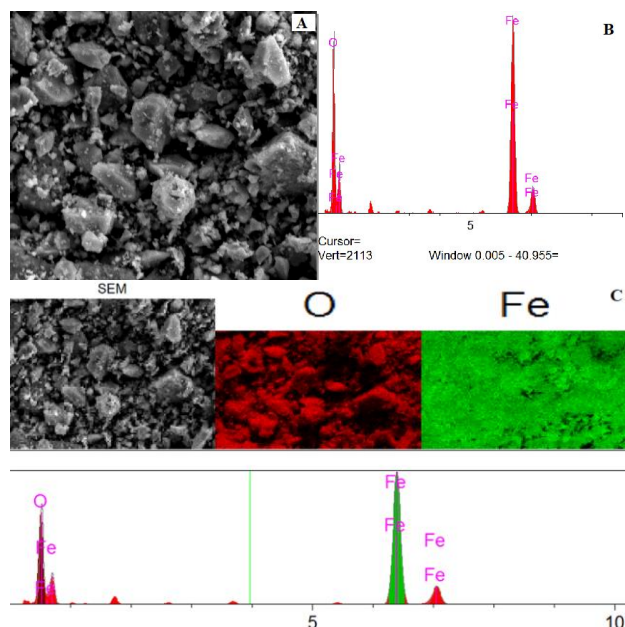

Figure 6. SEM image of BB@FeNPs (A), EDX spectra of BB@FeNPs (B), elemental mapping of BB@FeNPs (C)

3.6. Sun Protection Factor (SPF) of BB@Fe Nanoparticles

UV radiation from the sun can cause skin burning, inflammation, and other serious side effects such as skin cancer [30]. For this reason, various sunscreen formulations have been developed to protect the skin from harmful UV rays from the sun. The effectiveness of

sunscreen formulations is universally evaluated for sun protection factor (SPF) [31]. Nanoparticles are known to be carriers that enhance the protective effects of various natural sunscreen agents [32]. Permission for the use of nanoparticles in sunscreens has been granted by the Food and Drug Administration (FDA) [33]. Therefore, nanoparticles based on titanium dioxide (TiO_2) and zinc oxide (ZnO) are widely used as SPF enhancers in sunscreen formulation [34]. However, studies have shown that ZnO nanoparticles form free radicals and cause oxidative stress and cytotoxicity [35-37]. In addition, the Scientific Committee for Consumer Safety (SCCS) recommended avoiding the use of photocatalytically active TiO_2 in sunscreen and cosmetic products [38]. Among the materials examined as an alternative; there are metal oxide nanoparticles containing ceria (CeO_2) [39-45], tin oxide (SnO_2) [46], iron oxide (Fe_2O_3) [47-48]. Iron oxides are used in cosmetic products, especially foundations and eye shadows. It has even been known to be added to sunscreens to give them a brown tint [49]. Iron oxide nanoparticles have more commercialization potential in this field due to their low cost and high volume. In this study, the SPF value of metal nanoparticles biosynthesized with bee bread for sunscreen formulations was determined in vitro (Table 1). Determination of the SPF value by the in vitro method is now universally accepted due to the simplicity of the analysis and the reproducibility of the results [16].

According to the findings given in Table 1, SPF values of BB@FeNPs were evaluated between 100-1000 ppm. It is observed that the SPF value of BB@FeNPs increases with increasing concentrations. The highest SPF value was found at the highest concentration with 18.82. This value encourages the use of safer and environmentally friendly materials to be used in commercial sunscreen formulations on the market.

114

4. CONCLUSIONS

Bee bread is a bee product obtained by an anaerobic fermentation process by storing bee pollen in honeycombs with the help of honey and digestive enzymes. The high nutritional value of bee bread and its richness in bioactive substances enabled the production of nanoparticles by the green synthesis method. The characterization of the synthesized nanoparticles was carried out and the sun protection factor was determined.

Sun rays have negative effects on skin aging. Sunscreens positively affect the formation of photo-aging and sunburn, especially in the melanoma layer. The reason for the increase in skin cancer cases in recent years is seen as unprotected sun exposure. People with light skin color and people who blush quickly in the sun are at a higher risk of developing skin cancer. With this study, it has been demonstrated that iron nanoparticles are an alternative to sunscreen instead of dangerous titanium dioxide and zinc oxide nanoparticles.

REFERENCES

[1] Feynman RP. There's plenty of room at the bottom. Eng Sci. 1960; 23: 22-36.

[2] Beykaya M, Çağlar A. Bitkisel özütler kullanılarak gümüş-nanopartikül (AgNP) sentezlenmesi ve antimikrobiyal etkinlikleri üzerine bir araştırma. AKU-J Sci Eng. 2016; 16(3): 631-641.

[3] Crane M, Handy RD, Garrod J, Owen R. Ecotoxicity test methods and environmental hazard assessment for engineered nanoparticles. Ecotoxic. 2008; 17(5): 421-437.

[4] Nagarajan R. Nanoparticles: Building blocks for nanotechnology. In: Nanoparticles: Synthesis, Stabilization, Passivation, and Functionalization. American Chemical Society. Chapter 1, 2008. p. 2-14.

[5] Erdoğan Ö, Birtekocak F, Oryaşın E, Abbak M, Demirbolat GM, Paşa S et al. Enginar yaprağı sulu ekstraktı kullanılarak çinko oksit nanopartiküllerinin yeşil sentezi, karakterizasyonu, anti-bakteriyel ve sitotoksik etkileri. Duz Med J. 2019; 21(1): 19-26.

[6] Karnani RL, Chowdhary A. Biosynthesis of silver nanoparticle by eco-friendly method. Ind J Sci. 2013; 1(2): 25-31.

[7] Çiftçi H, Er Çalışkan Ç, Öztürk K, Yazıcı B. Yeşil yöntemle sentezlenen biyoaktif nanopartiküller. BSJ Eng Sci. 2021; 4(1): 29-42.

[8] Marin S, Vlasceanu GM, Tiplea RE, Bucur IR, Lemnaru M, Marin MM et al. Applications and toxicity of silver nanoparticles: A recent review. Curr Top Med Chem. 2015; 15(16): 1596-1604.

[9] Khalifa SAM, Elashal M, Kieliszek M, Ghazala NE, Farag MA, Saeed A et al. Recent insights into chemical and pharmacological studies of bee bread. Trends Food Sci Technol. 2020; 97: 300-316.

[10] Ju-Nam Y, Lead JR. Manufactured nanoparticles: An overview of their chemistry, interactions and potential environmental implications. Sci Total Environ. 2008; 400(1-3): 396-414.

[11] Johnston BD, Scown TM, Morger J, Cumberland SA, Baalousha M, Linge K, et al. Bioavailability of nanoscale metal oxides TiO_2, CeO_2, and ZnO to fish. Environ Sci Technol. 2010; 44(3):1144-1151.

[12] Sadeghi L, Tanwir F, Babadi VY. In vitro toxicity of iron oxide nanoparticle: Oxidative damages on HepG2 cells. Exp Toxico Pathol. 2015; 67(2): 197-203.

[13] Caro C, Egea-Benavente D, Polvillo R, Royo JL, Leal MP, Garcia-Martin ML. Comprehensive toxicity assessment of PEGylated magnetic nanoparticles for in vivo applications. Colloids Surf B: Biointerfaces. 2019; 177: 253-259.

[14] Dale L. Synthesis, properties, and applications of iron nanoparticles. Small: Nano Micro. 2005; 1(5): 482-501.

[15] Diffey BL. Sunscreens, suntans and skin cancer: People do not apply enough sunscreen for protection. BMJ. 1996; 313(7062): 942.

[16] Mansur JS, Breder MNR, Mansur MCA, Azulay RD. Determinaçao do fator de proteçao solar por espectrofotometria. An Bras Dermatol. 1986; 61(3): 121-124.

[17] Fonseca AP, Rafaela N. Determination of sun protection factor by UV-Vis Spectrophotometry. Health Care Curr Rev. 2013;1(1):108.

[18] Sayre RM, Agın PP, Levee GJ, Marlowe E. Comparison of in vivo and in vitro testing of sun screening formulas. Photochem Photobiol. 2008; 29(3): 559-566.

[19] Baalousha M, Lead JR. Characterization of natural aquatic colloids by flow field flow fraction and atomic force microscopy. Environ Sci Technol. 2007; 41(4): 1111-1117.

[20] Aydoğan Ö, Bayraktar E, Mehmetoğlu Ü. Ters misel sistemi ile L-aspartik asit ekstraksiyonu. PAJES. 2009; 15(2): 284-290.

[21] Novák P, Havlí V. Protein extraction and precipitation. In: Proteomic Profiling and Analytical Chemistry (Second Edition). 2016. p. 52-62.

[22] Üzüm Ç, Shahwan T, Eroğlu AE, Hallam KR, Scott TB, Lieberwirth I. Synthesis and characterization of kaolinite-supported zero-valent iron nanoparticles and their application for the removal of aqueous Cu^{2+} and Co^{2+} ions. Appl Clay Sci. 2009; 43(2): 172-181.

[23] Çiftçi H, Ersoy B, Evcin A. Synthesis, characterization and Cr(VI) adsorption properties of modified magnetite nanoparticles. Acta Phys Pol A. 2017; 132(3): 564-569.

[24] Mirza AU, Kareem A, Nami SAA, Khan MS, Rehman S, Bhat SA et al. Biogenic synthesis of iron oxide nanoparticles using *Agrewia optiva* and *Prunus persica* phyto species: Characterization, antibacterial and antioxidant activity. J Photochem Photobiol B, Biol. 2018; 185: 262-274.

[25] Jegadeesan GB, Srimathi K, Santosh Srinivas N, Manishkanna S, Vignesh D. Green synthesis of iron oxide nanoparticles using *Terminalia bellirica* and *Moringa oleifera* fruit and leaf extracts: Antioxidant, antibacterial and thermoacoustic properties. Biocatal Agric Biotechnol. 2019; 21: 101-354.

[26] Chavan RR, Bhinge SD, Bhutkar MA, Randive DS, Wadkar GH, Todkar SS et al. Characterization, antioxidant, antimicrobial and cytotoxic activities of green synthesized silver and iron nanoparticles using alcoholic *Blumea eriantha* DC plant extract. Mater Today Commun. 2020; 24: 101320.

[27] Wang YM, Cao X, Liu GH, Hong RY, Chen YM, Chen XF et al. Synthesis of Fe_3O_4 magnetic fluid used for magnetic resonance imaging and hyperthermia. J Magn Magn Mater. 2011; 323(23): 2953-2959.

[28] Silva VAJ, Andrade PL, Silva MPC, Bustamante DA, Valladares LDLS, Aguiar JA. Synthesis and characterization of Fe_3O_4 nanoparticles coated with fucan polysaccharides. J Magn Magn Mater. 2013; 34: 138-143.

[29] Patra JK, Baek K. Green biosynthesis of magnetic iron oxide (Fe_3O_4) nanoparticles using the aqueous extracts of food processing wastes under photo catalyzed condition and investigation of their antimicrobial and antioxidant activity. J Photochem Photobiol B, Biol. 2017; 173: 291-300.

[30] Sax BW. Educating consumers about sun protection. Pharmacy Times. New York. 2000; 66(5): 48-50.

115

[31] Stockdale M. Sun protection factors. Int J Cosmet Sci. 1985; 7(5): 235-246.

[32] He H, Li A, Li S, Tang J, Li L, Xiong L. Natural components in sunscreens: Topical formulations with sun protection factor (SPF). Biomed Pharmacother. 2021; (134): 111161.

[33] Newman MD, Stotland M, Ellis JI. The safety of nanosized particles in titanium dioxide-and zinc oxide-based sunscreens. J Am Acad Dermatol. 2009; 61(4): 685-692.

[34] Singh P, Nanda A. Enhanced sun protection of nano-sized metal oxide particles over conventional metal oxide particles: an in vitro comparative study. Int J Cosmet Sci. 2014; (363): 273-283.

[35] Gu T, Yao C, Zhang K, Li C, Ding L, Huang Y et al. Toxic effects of zinc oxide nanoparticles combined with vitamin C and casein phosphopeptides on gastric epithelium cells and the intestinal absorption of mice. RSC Advan. 2018; 8(46): 26078-26088.

[36] Wong SWY, Zhou GJ, Leung PTY, Han J, Lee JS, Kwok KWH et al. Sunscreens containing zinc oxide nanoparticles can trigger oxidative stress and toxicity to the marine copepod *Tigriopus japonicus*. Mar Pollut Bull. 2020; 154: 111078.

[37] Krol A, Pomastowski P, Rafińska K, Railean-Plugaru V, Buszewski B. Zinc oxide nanoparticles: Synthesis, antiseptic activity and toxicity mechanism. Adv Colloid Interface Sci. 2017; 249: 37-52.

[38] SCCS, Chaudhry Q. Opinion of the scientific committee on consumer safety (SCCS)- Revision of the opinion on the safety of the use of titanium dioxide, nano form, in cosmetic products. Regul Toxicol Pharmacol. 2015; 73(2): 669-670.

[39] Truffault L, Ta MT, Devers T, Konstantinov K, Harel V, Simmonard C et al. Application of nanostructured Ca doped CeO_2 for ultraviolet filtration. Mater Res Bull. 2010; 45(5): 527-535.

[40] Truffault L, Winton BR, Choquenet B, Andreazza-Vignolle C, Simmonard C, Devers T et al. Cerium oxide based particles as possible alternative to ZnO in sunscreens: Effect of the synthesis method on the photoprotection results. Mater Lett. 2012; 68: 357-360.

[41] Truffault L, Yao QW, Wexler D, Nevirkovets IP, Konstantinov K, Devers T et al. Synthesis and characterization of Fe doped CeO_2 nanoparticles for pigmented ultraviolet filter applications. J Nanosci Nanotechnol. 2011a; 11(5): 4019-4028.

[42] Zholobak NM, Ivanov VK, Shcherbakov AB, Shaporev AS, Polezhaeva OS, Baranchikov AY et al. UV-shielding property, photocatalytic activity and photocytotoxicity of ceria colloid solutions. J Photochem Photobiol B, Biol. 2010; 102(1): 32-38.

[43] Yabe S, Sato T. Cerium oxide for sunscreen cosmetics. J Solid State Chem. 2003; 171(1-2): 7-11.

[44] Boutard T, Rousseau B, Couteau C, Tomasoni C, Simonnard C, Jacquot C et al. Comparison of photoprotection efficiency and antiproliferative activity of ZnO commercial sunscreens and CeO_2. Mater Lett. 2013; 108: 13-16.

[45] Caputo F, Nicola MDe, Sienkiewicz A, Giovanetti A, Bejarano I, Licoccia S et al. Cerium oxide nanoparticles, combining antioxidant and UV shielding properties, prevent UV-induced cell damage and mutagenesis. Nanoscale. 2015; 7(38): 15643-15656.

[46] Morlando A, Cardillo D, Devers T, Konstantinov K. Titanium doped tin dioxide as potential UV filter with low photocatalytic activity for sunscreen products. Mater Lett. 2016; 171: 289-292.

[47] Cardillo D, Konstantinov K, Devers T. The effects of cerium doping on the size, morphology, and optical properties of α-hematite nanoparticles for ultraviolet filtration. Mater Res Bull. 2013; 48(11): 4521-4525.

[48] Truffault L, Choquenet B, Konstantinov K, Devers T, Couteau C, Coiffard LJM. Synthesis of Nano-hematite for possible use in sunscreens. J Nanosci Nanotechnol. 2011b; 11(3): 2413-2420.

[49] Serpone N, Dondi D, Albini A. Inorganic and organic UV filters: Their role and efficacy in sunscreens and suncare product. Inorg Chim Acta. 2007; 360(3): 794-802.

Appendices

Table 1. SPF values of BB@FeNPs at different concentrations

Compound	Concentration	Wavelength	CF	EE*I	Abs	SPF
BB@FeNP	1000 ppm	290	10	0,0015	1,955	18,81973
		295	10	0,0817	1,906	
		300	10	0,2874	1,888	
		305	10	0,3278	1,878	
		310	10	0,1864	1,872	
		315	10	0,0839	1,863	
		320	10	0,0180	1,859	
	500 ppm	290	10	0,0015	0.981	9,732117
		295	10	0,0817	0.974	
		300	10	0,2874	0.971	
		305	10	0,3278	0.973	
		310	10	0,1864	0.974	
		315	10	0,0839	0.975	
		320	10	0,0180	0.975	
	200 ppm	290	10	0,0015	0.654	6,516159
		295	10	0,0817	0.650	
		300	10	0,2874	0.648	
		305	10	0,3278	0.652	
		310	10	0,1864	0.654	
		315	10	0,0839	0.655	
		320	10	0,0180	0.660	
	100 ppm	290	10	0,0015	0.490	4,920233
		295	10	0,0817	0.486	
		300	10	0,2874	0.491	
		305	10	0,3278	0.492	
		310	10	0,1864	0.494	
		315	10	0,0839	0.495	
		320	10	0,0180	0.498	

117

Türk Doğa ve Fen Dergisi
Turkish Journal of Nature and Science
www.dergipark.gov.tr/tdfd

Influence of Layer Thickness on Magnetoresistance Properties of Multilayered Thin Films

Taner KALAYCI[1*]

[1] Bandırma Onyedi Eylül University, Medical Services and Technique Department, Bandırma, Türkiye
Taner KALAYCI ORCID No: 0000-0002-6374-2373

Corresponding author: tanerkalayci@bandirma.edu.tr

	Abstract: In this study, the magnetoresistance properties of multilayered structures consisting of five different combinations of Pt and Co thin layers were studied in the room temperature range. Thin films were prepared by using magnetron sputtering techniques in ultra-high vacuum conditions. It has been found that the percentage of MR decreases as the thickness of the spacer layer thickness increases. For 3 nm thickness, 0.16% MR ratio is obtained, while for 4 and 5 nm these values are 0.15% and 0.10% respectively. In addition, as reference layer thickness increases, MR values are 0.10%, 0.11% and 0.15%, respectively. These results show that the prepared thin film sets can be used in technological applications such as MR based sensors and spin field transistors.

Katman Kalınlığının Çok Katmanlı İnce Filmlerin Manyetodirenç Özelliklerine Etkisi

	Öz: Bu çalışmada, beş farklı Pt ve Co ince tabaka kombinasyonundan oluşan çok tabakalı yapıların manyetodirenç özellikleri oda sıcaklığı aralığında incelenmiştir. İnce filmler, ultra yüksek vakum koşullarında magnetron püskürtme teknikleri kullanılarak hazırlandı. Ara tabaka kalınlığı arttıkça MR yüzdesinin azaldığı tespit edilmiştir. 3 nm kalınlık için %0.16 MR oranı elde edilirken, 4 ve 5 nm için bu değerler sırasıyla %0.15 ve %0.10'dur. Ayrıca referans katman kalınlığı arttıkça MR değerleri sırasıyla %0.10, %0.11 ve %0.15'tir. Bu sonuçlar, hazırlanan ince film setlerinin MR tabanlı sensörler ve spin alan transistörleri gibi teknolojik uygulamalarda kullanılabileceğini göstermektedir.

1. INTRODUCTION

Magnetic thin film structures, which consist of ferromagnetic layers separated by nonmagnetic metallic spacer, are widely used in magnetic recording media, spin field-effect transistors and magnetic sensors [1]. One of the main factors affecting the sensitivity of magnetoresistance (MR) based sensors is the interlayer coupling and its novel applications combining interfacial Dzyaloshinskii-Moriya interaction [2,3]. It is known that interlayer coupling strongly depends on quality of ferromagnet/spacer interfaces and electronic transport through the spacer.

The giant magnetoresistance (GMR) phenomenon is observed in magnetic multilayer structures where the magnetic layers of Iron (Fe), Cobalt (Co) and other magnetic metals are separated by non-magnetic layers (Chromium, Platinum, Iridium) several nanometers thick [4-8]. The thicknesses of these non-magnetic layers are chosen so that the exchange interaction between the spins of the ferromagnetic layers has an effective antiferromagnetic character. Thanks to this interaction, the magnetizations of adjacent ferromagnetic layers are oriented in opposite directions to each other (antiferromagnetic configuration). When this structure is placed in an external magnetic field, the magnetizations of the layers begin to align in parallel (ferromagnetic configuration), resulting in a significant change in electrical resistance. With nano-sized multilayer structures, the magnetoresistance reaching values above 100% at low temperatures in total determines the suitability conditions to produce next-generation magnetic sensors, read heads, magneto-resistive random-access memories, and other spintronic devices [9–11].

Ultrathin magnetic films and multilayer structures show the dimensional dependence of magnetic properties on film thickness, which is a transition from the two-dimensional behavior of films of 4-6 single-layer

thickness to certain bulk values of films with tens of single-layer thickness [12–14]. Moreover, the properties of ultrathin magnetic films and nanostructures show high sensitivity to the effects of anisotropy created by the crystal field of a substrate or non-magnetic layers, and to the single-ion anisotropy and dipole-dipole interaction of the magnetic moments of atoms in the films [15–17]. The dimensional and anisotropy properties of these nano systems can be detected in their critical behavior because the properties of critical behavior of magnetic systems such as critical temperature and critical exponents are most sensitive to dimensional changes and the effect of magnetic anisotropy [14,18].

Here, we investigated the magnetoresistance properties of [Pt/Co]$_6$(2.4 nm)/Pt (x nm)/Co (y nm) (3≤x≤5, 2≤y≤4 nm) sample sets changing the spacer and Co layer thicknesses.

2. MATERIAL AND METHOD

2.1. Experimental Procedure

The Silicon (Si) substrates were cleaned with an ultrasonic cleaner in acetone for 15 min and then in ethanol for 15 min, followed by washing with deionized water. Five different stacks with the following structures were fabricated (the numbers in parentheses denote the layer thickness in nm). Our sample set can be summarized as follows:

Sample 1: [Pt/Co]$_6$(2.4 nm)/Pt (3 nm)/Co(2 nm)
Sample 2: [Pt/Co]$_6$(2.4 nm)/Pt (4 nm)/Co(2 nm)
Sample 3: [Pt/Co]$_6$(2.4 nm)/Pt (5 nm)/Co(2 nm)
Sample 4: [Pt/Co]$_6$(2.4 nm)/Pt (5 nm)/Co(3 nm)
Sample 5: [Pt/Co]$_6$(2.4 nm)/Pt (5 nm)/Co(4 nm)

The substrates were annealed at 750 K for 90 min to clean the surface before deposition. All layers were deposited by using an ultrahigh vacuum magnetron sputtering unit on the Si (100) substrate with lateral dimensions of 10 mm × 10 mm. At the bottom of the multilayer system Pt buffer layer was grown with a thickness of 40 Å. Finally, the multilayer system was covered with 40 Å Pt cap layer against to the oxidation. The base pressure of the sputter chamber is $2x10^{-9}$ mbar and during the deposition Argon (Ar) pressure was $5x10^{-3}$ mbar. Pt layers were grown by DC generators while Co layers were grown by RF generators. The deposition rates for Pt and Co layers were 8.75 and 0.44 Å min^{-1}, respectively [19].

2.2. Magnetoresistance Measurements

Magnetoresistance measurements of multilayer magnetic thin films were made through four-point probe method at a constant applied current of 5 mA. Wire bonder was used for some of the contacts while silver cake was used for some. In magnetoresistance measurements, the film is placed in a sample container and the voltage values on the film are recorded in response to the current passing through the sample.
The schematic representation of the four-point measurement technique used in measuring the resistors of the prepared samples and the corresponding equivalent

resistance circuits are given below in Figure 1. When the contact is received using four-point technique, the current is given from the external contacts and the voltage values are read from the internal contacts. In this way, only the resistance value from the example itself is read.
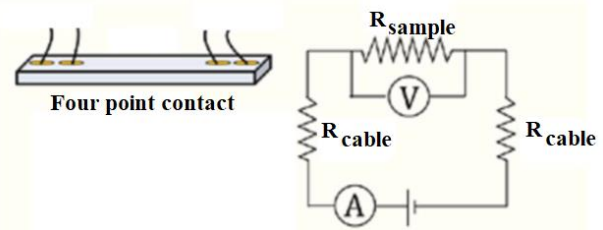

Figure 1. Schematic representation of four-point resistance measurement and circuit

In measurements such as anisotropic magnetoresistance (AMR) and giant magnetoresistance (GMR), contact points must be linear on magnetic films. For measurements such as anomalous Hall effect (AHE) and Planar Hall effect (PHE), contact points must be perpendicular to each other at the corners of the sample. To determine AMR and GMR behavior of the samples we prepared, four-point measurement techniques were applied, and measurements were performed in parallel and perpendicular geometries in the current and magnetic field plane.

The experimental system in which MR measurements are performed consists of electromagnets, computers, voltmeters that can read voltage at nanoscale, sample container and direct current power source. PCB (Printed Circuit Board) was used as a sample container. The two outer contacts on the circuit are prepared to apply current, while the two inner contacts are prepared to read voltage. The electromagnet, which is a magnetic field generator, is controlled by the computer while the voltage values are recorded from the nanovoltmeter.

3. RESULTS

The rate of resistance changes in samples (MR %) is calculated as follows,

$$MR(\%) = \frac{R(H) - R(\min)}{R(min)} x100 \qquad (1)$$

Resistance on applied magnetic field is represented by R(H) and resistance on zero magnetic field is represented by R(min).

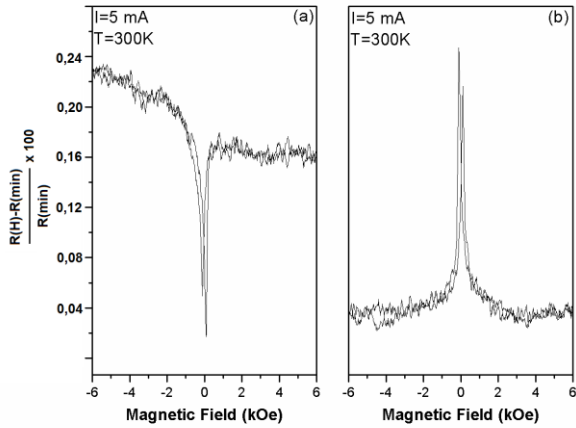Figures 2-6 below are MR measurements obtained, respectively:

Figure 2. [Pt/Co]₆ (2,4 nm)/Pt(**3 nm**)/Co(2 nm) Magnetoresistance measurement in thin film a) Current and magnetic field parallel to each other b) Current and magnetic field perpendicular to each other
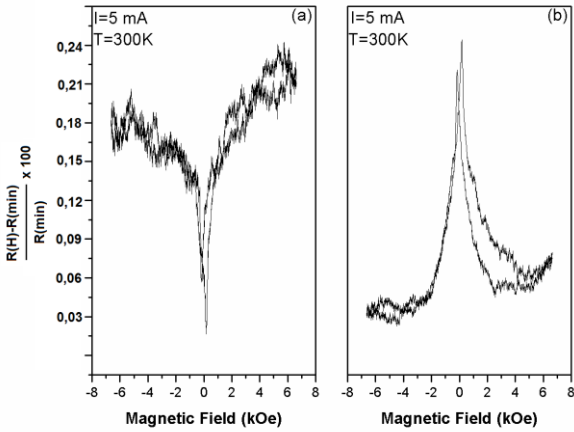
Figure 3. [Pt/Co]₆ (2,4 nm)/Pt(**4 nm**)/Co(2 nm) Magnetoresistance measurement in thin film a) Current and magnetic field parallel to each other b) Current and magnetic field perpendicular to each other
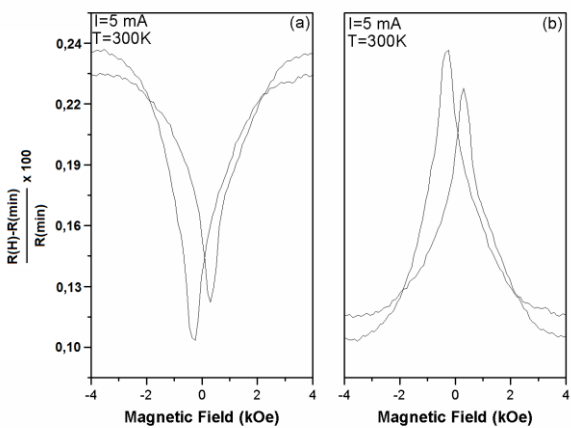
Figure 4. [Pt/Co]₆ (2,4 nm)/Pt(**5 nm**)/Co(**2 nm**) Magnetoresistance measurement in thin film a) Current and magnetic field parallel to each other b) Current and magnetic field perpendicular to each other

Figure 5. [Pt/Co]₆ (2,4 nm)/Pt(5 nm)/Co(**3 nm**) Magnetoresistance measurement in thin film a) Current and magnetic field parallel to each other b) Current and magnetic field perpendicular to each other

Figure 6. [Pt/Co]₆ (2,4 nm)/Pt(5 nm)/Co(**4 nm**) Magnetoresistance measurement in thin film a) Current and magnetic field parallel to each other b) Current and magnetic field perpendicular to each other
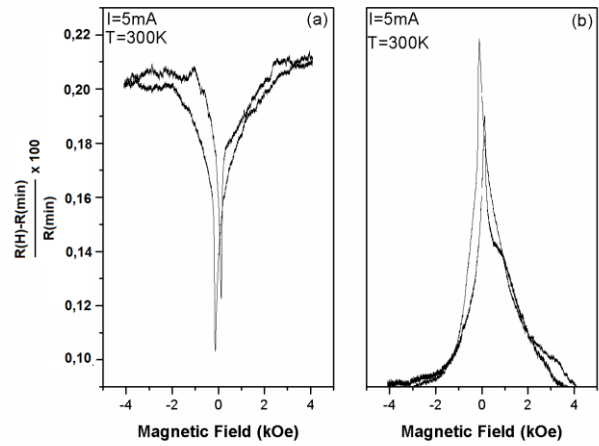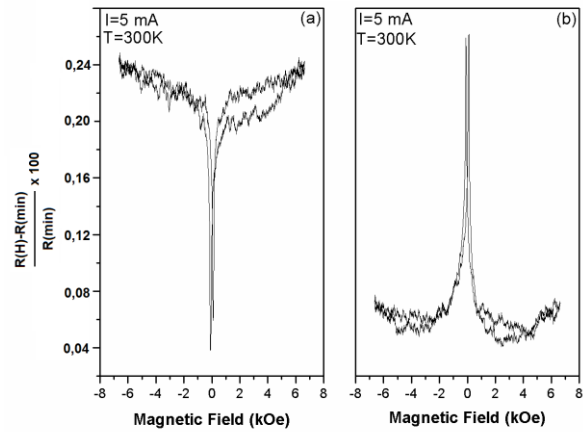
120

5 mA of current was applied to the samples during the measurements. And measured voltage values were recorded depending on the magnetic field. Resistance values were obtained by dividing the read voltage values into the applied current values. It is seen that the resistance values are not symmetrical on the vertical axis relative to the origin due to the geometry of the contacts prepared. Because all contacts cannot be placed in the film plane in order, besides the MR effect, anormal Hall effect and Planar Hall effect contributions can also be added to the measurement results. Since it is known that these contributions do not change coercive field values, there was no need to correct the shifts.

Coercive field values of 130 Oersted (Oe) for 3 nm Pt thickness, 312 Oe for 4 nm Pt thickness, 184 Oe for 5 nm Pt and 2 nm Co thickness, 135 Oe for 3 nm Co thickness, 110 Oe for 4 nm Co thickness were measured. These values clearly show that the thin films we prepared can be used in magnetic sensor applications.

In such multilayer systems, there are two advantages of having the thickness of ferromagnetic layers close to each other (low net moment). Low net moment limits the

dipole areas arising from the interaction of the reference and free layer. Second, the low moment allows the reference layer to interact weakly with the external field.

As stated in Equation 1, the MR ratios obtained when applied for figures 2, 3, 4, 5 and 6 were obtained as 0.16, 0.15, 0.10, 0.11 and 0.15, respectively. It is seen in the above figures that the percentage of MR decreases as the thickness of the spacer layer thickness increases. The exponential variation of the MR amplitude is related to the flow of polarized conduction electrons across the interlayer from one ferromagnetic layer to the next. For 3 nm thickness, 0.16% MR ratio is obtained, while for 4 and 5 nm these values are 0.15% and 0.10%, respectively. In addition, as reference layer thickness increases, MR values are 0.10%, 0.11% and 0.15% respectively [20, 21]. It can be seen from figures 4, 5 and 6 that the MR amplitude increases significantly when the thickness of the Co layer we use as the reference layer increases.

4. DISCUSSION AND CONCLUSION

Spacer layer thickness (Pt) increased from 3 nm to 5 nm and the magnetoresistance decreases gradually. This indicates that magnetoresistance is due to the exchange of polarized electrons transferred from one ferromagnetic layer to another [22]. The exponential variation of the MR amplitude is related to the flow of polarized conduction electrons through the decency from one ferromagnetic layer to another. Scattering on the interface reduces current perpendicular to the surface and therefore also decays MR amplitude. When the thickness of the Co layer we use as the reference layer increases, it is seen that the MR amplitude increases conspicuously.

The magnetic field sensitivity provided by the GMR structure consists of two layers, the hard reference layer, and the soft layer, which are not sensitive to the external field. The relative angle of the magnetization vectors of the two layers controls the resistance of the device.

In general, spin transfer torque and the GMR effect are closely related. So, to obtain one, you must obtain the other. For a GMR magnetic sensor and reading header, one of the magnetic layers is less sensitive to the external magnetic field (the reference layer), while the other is sensitive to the external field (the free layer). For such a design, the current depends only on the relative angles of the magnetizations of the two layers through the GMR effect i.e. the change in resistance and affect magnetization through the formation and warming of Oersted fields.

As a result, with tuning the thickness of these types of thin films or nanostructures, it is seen that thin films we have prepared can be used in technological devices such as magnetic sensor applications and reading heads.

REFERENCES

[1] Grünberg P, Layered magnetic structures: history, highlights, applications, Phys. Today 2001; 54: 31–38.

[2] Chung K H, Kim S N, Lim S H, Magnetic parameters in giant magnetoresistance spin valve and their roles in magnetoresistance sensitivity, Thin Solid Films. 2018; 650: 44–50.

[3] Prudnikov A, Li M, De Graef M, Sokalski V, Towards simultaneous control of interlayer exchange coupling and the interfacial Dzyaloshinskii-Moriya interaction in Ru-based synthetic antiferromagnets, IEEE Magn. Lett. 2018; 1–4.

[4] Grünberg P, Schreiber R, Pang Y, Brodsky M B, Sowers H, Layered Magnetic Structures: Evidence for Antiferromagnetic Coupling of Fe Layers across Cr Interlayers. Phys. Rev. Lett. 1986; 57: 2442.

[5] Baibich M N, Broto J M, Fert A, et al., Giant Magnetoresistance of (001)Fe/(001)Cr Magnetic Superlattices. Phys. Rev. Lett. 1988; 61: 2472.

[6] Binash G, Grunberg P, Saurenbach F, Zinn W, Enhanced magnetoresistance in layered magnetic structures with antiferromagnetic interlayer exchange. Phys. Rev. B 1989; 39: 4828.

[7] Barthelemy A, Fert A, Theory of the magnetoresistance in magnetic multilayers: Analytical expressions from a semiclassical approach. Phys. Rev. B 1991; 43: 13124.

[8] Parkin S S P, Giant Magnetoresistance in Magnetic Nanostructures. Annu. Rev. Mater. Sci. 1995; 25: 357.

[9] Parkin S, More N, Roche K P, Oscillations in exchange coupling and magnetoresistance in metallic superlattice structures: Co/Ru, Co/Cr, and Fe/Cr. Phys. Rev. Lett. 1990; 23: 130.

[10] Bland J A C, Heinrich B, Ultrathin Magnetic Structures IV, Springer, Berlin, 2005; p. 257.

[11] Bader S D, Parkin S S P, Spintronics. Annu. Rev. Condens. Matter Phys. 2010; 1: 71.

[12] Huang F, Kief M T, Mankey G J, Willis R F, Magnetism in the few-monolayers limit: A surface magneto-optic Kerr-effect study of the magnetic behavior of ultrathin films of Co, Ni, and Co-Ni alloys on Cu(100) and Cu(111). Phys. Rev. B 1994; 49: 3962.

[13] Li Y, Baberschke K, Dimensional crossover in ultrathin Ni(111) films on W(110). Phys. Rev. Lett. 1992; 68: 1208.

[14] Vaz C A F, Bland J A C, Lauhoff G, Magnetism in ultrathin film structures. Rep. Prog. Phys. 2008; 71: 056501.

[15] Heinrich B, Cochran J F, Ultrathin metallic magnetic films: magnetic anisotropies and exchange interactions. Adv. Phys. 1993; 42: 523.

[16] Heinrich B, Monchesky T, Urban R, Role of interfaces in higher order angular terms of magnetic anisotropies: ultrathin film structures. J. Magn. Magn. Mater. 2001; 236: 339.

[17] Johnson M T, Bloemen P J H, Den Broeder F J A, De Vries J J, Magnetic anisotropy in metallic multilayers. Rep. Prog. Phys. 1996; 59: 1409.

[18] Pelissetto A, Vicari E, Critical phenomena, and renormalization-group theory. Phys. Rep. 2002; 368: 549.

[19] Kalaycı T, Deger C, Akbulut S, Yildiz F, Tuning magnetic properties of non-collinear magnetization configuration in Pt/[Pt/Co]6/Pt/Co/Pt multilayer structure. J. Magn. Magn. Mater. 2017; 436: 11-16.

[20] Wenbo Z, Weichuan H, Chuanchuan L, Chuangming H, Zhiwei C, Yuewei Y, and Xiaoguang L, Electric-Field-Controlled Nonvolatile Magnetization Rotation and Magnetoresistance Effect in Co/Cu/Ni Spin Valves on Piezoelectric Substrates. ACS Appl. Mater. Interfaces 2018; 10: 21390−21397.

[21] Avci C O, Lambert C, Sala G, Gambardella P, A two-terminal spin valve device controlled by spin–orbit torques with enhanced giant magnetoresistance. Appl. Phys. Lett. 2021; 119: 032406.

[22] Dieny B, Speriosu V S, Metin S, Parkin S S P, Gurney B A, Magnetotransport properties of magnetically soft spinvalve structures. J. Appl. Phys. 1991; 69: 4774.

Türk Doğa ve Fen Dergisi
Turkish Journal of Nature and Science
www.dergipark.gov.tr/tdfd

A Generalized Thermoelastic Behaviour of Isotropic Hollow Cylinder

Mehmet EKER[1]*, Durmuş YARIMPABUÇ[2]

[1] Tarsus University, Faculty of Engineering, Department of Mechanical Engineering, Mersin, Türkiye
[2] Osmaniye Korkut Ata University, Faculty of Arts and Sciences, Department of Mathematics, Osmaniye, Türkiye
Mehmet EKER ORCID No: 0000-0002-6785-1710
Durmuş YARIMPABUÇ ORCID No: 0000-0002-8763-1125

*Corresponding author: mehmeteker@tarsus.edu.tr

Abstract: In this study, the thermoelastic behavior of a thick-walled homogeneous cylinder based on Lord-Shulman theory is investigated. It is assumed that the inner and outer surfaces of the cylinder are traction-free, and the outer surface is maintained at a reference temperature while the inner surface is subjected to a time-dependent internal temperature load. The governing equations in coupled form are solved with the pseudospectral Chebyshev method. The numerical approach is validated with benchmark results in the literature. The temperature, radial and tangential stress distributions are examined for three different nondimensional times to represent the time-varying effects of the applied instantaneous temperature load. The effect of the coupled term in Lord-Shulman theory for different high temperatures is examined and the difference between the coupled and uncoupled solution in different time periods is tabulated and the difference is highlighted.

123

İzotropik İçi Boş Silindirin Genelleştirilmiş Termoelastik Davranışı

Öz: Bu çalışmada, içi boş homojen bir silindirin Lord-Shulman teorisine dayalı termoelastik davranışı incelenmiştir. Silindirin iç ve dış cidarlara etki eden etki eden mekanik bir yükün olmadığı, dış cidarda sabit bir sıcaklık, iç cidarın ise zamana bağlı bir iç sıcaklık yüküne maruz kaldığı varsayılmıştır. Bağlaşımlı formdaki bünye denklemleri, pseudospektral Chebyshev yöntemiyle çözülmüştür. Kullanılan sayısal yaklaşım, literatürde mevcut referans sonuçlarla doğrulanmıştır. Sıcaklık, radyal ve teğetsel gerilme dağılımları, uygulanan anlık sıcaklık yükünün zamanla değişen etkilerini temsil etmek için üç farklı zaman için incelenmiştir. Lord-Shulman teorisinde yer alan bağlaşımlı terimin farklı yüksek sıcaklıklar için etkisi incelenmiştir. Farklı zamanlar için bağlaşımlı ve bağlaşımsız çözümler arasındaki fark vurgulanmış ve tablo olarak sunulmuştur.

1. INTRODUCTION

In the advanced applications, engineering structures can work under challenging thermal shock loads such as in the nuclear blast environment, pulsed laser and electromagnetic radiation. Thermal stresses and deformations would develop from a sudden increase in temperature in an elastic medium, significantly altering the mechanical behavior of thermo-elastic materials. As a result, in thermoelastic problems, the coupling between the temperature and displacement fields becomes critical [1]. The conventional heat conduction equation is the foundation of the classical (uncoupled) thermoelasticity theory. The theory was established by Biot [2]. Because

of its parabolic character of the energy equation, the conventional heat conduction theory posits that thermal disturbances propagate at infinite speeds. This prediction may be appropriate for most engineering purposes, but it is a physically unfeasible assumption, especially at extremely low temperatures near absolute zero or for extremely short time periods. In order to overcome physical discrepancy of infinite speed prediction for thermal disturbances, the generalized theories of thermoelasticity were formulated. These theories offer the wave type heat propagation with finite speed. This phenomenon is mostly described as second sound [3]. The Lord–Shulman (LS) theory [4], which modifies Fourier's law of heat conduction by introducing one

thermal relaxation time, is one of the well-known generalized theories. In the theory, the parabolic type heat equation is replaced by a hyperbolic one which ensures finite speeds of propagation for both heat and elastic waves. The detail for the other generalized thermoelastic theories and recent studies can be found Shakeriaski et al.'s review in [5].

Reformulation of classical thermoelastic equations by Lord-Shulman dates back to 1967. They presented waveform thermal equation instead of the law of Fourier and defined the term relaxation time. The relaxation time represents the needed time-lag to establish steady state heat conduction in a volume element if the element is exposed to thermal shock. Derivation of thermoelastic formulation based on generalized thermoelasticity was done by Furukawa et al. [6-7] for an infinite body with a circular cylindrical hole and for an infinite solid cylinder. They obtained the temperature and thermal stresses with one relaxation time. A coupled thermoelastic problem in finite domain was analyzed by Hosseini Tehrani and Eslami [8-9] with boundary element method. They studied the effect of relaxation times and coupling coefficient on the thermal and elastic wave propagation. Bases on generalized coupled thermoelasticity, a disk problem solved by Bagri and Eslami [10] by utilizing transfinite element method. They obtained the thermal and stress wave propagation through the radius of disk and illustrated the coupling coefficient effect on the results. A unified coupled thermoelasticity formulation was proposed by same authors [11] based on the Lord–Shulman (L–S), Green–Lindsay (G–L), and Green–Naghdi (G–N) models for isotropic homogeneous cylinders and spheres. The structures are considered as subject to thermal shock on their inner walls. The governing equations were solved analytically into Laplace domain and transformed to the time domain by a numerical Laplace inversion. Application of Lord-Shulman theory was also extended to functionally graded cylinders. In this respect, Bagri and Eslami [12] utilized transfinite element method and the numerical inverse Laplace technique under uniform thermal shock to introduce unified formulation based on Lord Shulman, Green-Lindsay and Green-Naghdi methods. The dynamic response of functionally graded thermoelastic thick-walled hollow cylinders due to time-dependent heat flux studied by Sharma et al. [13] with an analytical method. They studied the effect of inhomogeneity for strains, stresses, displacement and temperature by the help of Lord-Shulman theory. The theory was also used for the thermoelastic problem of clamped axisymmetric infinite hollow cylinders under thermal shock with variable thermal conductivity by Zenkour [14]. He investigated effects of variable thermal conductivity and time parameters on radial displacement, temperature, and stresses. Thermoelastic interactions in the context of Lord-Shulman theory of a hollow cylinder compared the optimal homotopy analysis solution to the exact solution by Abbas and Abd-elmaboud [15]. They illustrated temperature, displacement and radial stress distribution graphically and discussed the effect of the relaxation time on the results.

Performing the thermoelastic behaviour analyzes in the literature, some researchers neglected the coupled terms, while others made calculations by taking these terms into account. However, the field of study examining the differences between stresses in these two different analyzes in the literature remained untouched. The originality of this work is that it examines the difference between stresses in analyzes with and without coupled terms. In this study, coupled thermoelastic behavior of a hollow homogeneous copper cylinder subjected to a time dependent internal temperature load is carried out. Among the generalized thermoelastic theories, Lord-Shulman theory with one relaxation time is used. The non-dimensional governing equations are obtained in coupled form and solved numerically with pseudospectral Chebyshev method (PCM). The temperature, radial and tangential stress distributions are presented graphically for three different nondimensional times. The effect of the coupled term in the Lord-Shulman theory on the solution for different high temperatures is examined and the difference between the coupled and uncoupled solution in different time periods is emphasized.

2. GOVERNING EQUATIONS

In the framework of Lord-Shulman theory, a linear, homogeneous thermoelastic continuum governing equations is employed for an isotropic thick-walled cylinder with $a \leq r \leq b$. Here a and b are the inner and outer radius respectively. The schematic illustration of the cylinder is given in Figure 1. Under the plane strain condition and cylindrical symmetry consideration, the equation of motion in the absence of body forces is given by [15],

$$\frac{\partial \sigma_{rr}}{\partial r} + \frac{1}{r}(\sigma_{rr} - \sigma_{\theta\theta}) = \rho \frac{\partial^2 u}{\partial t^2} \tag{1}$$
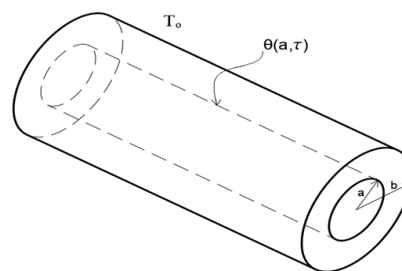
Figure 1. Schematic illustration of the homogeneous hollow cylinder

where ρ is the mass density, u displacement component, r radius. σ_{rr} and $\sigma_{\theta\theta}$ are the radial and circumferential stresses respectively.

$$\sigma_{rr} = (\lambda + 2\mu)\frac{\partial u}{\partial r} + \lambda\frac{u}{r} - \gamma(T - T_0) \tag{2}$$

$$\sigma_{\theta\theta} = \lambda\frac{\partial u}{\partial r} + (\lambda + 2\mu)\frac{u}{r} - \gamma(T - T_0) \tag{3}$$

where T is the absolute temperature, T_0 the reference uniform temperature of the body, λ, μ are elastic parameters, γ the thermal elastic coupling tensor in

124

which $\gamma = (3\lambda + 2\mu)\alpha$. Since cylindrical symmetry is taken into account under plane strain conditions, the only nonzero component of the displacement vector is u_r, and u can be represented by $u_r = u(r,t)$.

The energy equation without heat sources is given as below [15],

$$
k\left(\frac{\partial^2 T}{\partial r^2} + \frac{1}{r}\frac{\partial T}{\partial r}\right) = \left(\frac{\partial}{\partial t} + \tau_0 \frac{\partial^2}{\partial t^2}\right)\left(\rho c_e T + T_0 \gamma \left(\frac{\partial u}{\partial r} + \frac{u}{r}\right)\right) \quad (4)
$$

where c_e is the specific heat at constant strain, k the thermal conductivity and τ_0 is relaxation time proposed by Lord-Shulman theory.

For convenience, the following non-dimensional variables are introduced [15]:

$$
\eta = c_1 \chi\, r, \quad U = c_1 \chi\, u, \quad \tau = c_1{}^2 \chi\, t,
$$

$$
\bar{\tau}_0 = c_1{}^2 \chi\, \tau_0, \quad S_{rr} = \frac{1}{\lambda + 2\mu}\sigma_{rr}, \quad S_{\theta\theta} = \frac{1}{\lambda + 2\mu}\sigma_{\theta\theta}, \quad (5)
$$

$$
\theta = \frac{T - T_0}{T_0}, \quad c_1 = \sqrt{\frac{\lambda + 2\mu}{\rho}}, \quad \chi = \frac{\rho c_e}{k}
$$

The aforementioned governing equations are reduced to following equations in considerations of the non-dimensional variables described in Equation (5).

$$
\frac{\partial^2 U}{\partial \eta^2} + \frac{1}{\eta}\frac{\partial U}{\partial \eta} - \frac{U}{\eta^2} - \beta \frac{\partial \theta}{\partial \eta} = \frac{\partial^2 U}{\partial \tau^2} \quad (6)
$$

$$
\frac{\partial^2 \theta}{\partial \eta^2} + \frac{1}{\eta}\frac{\partial \theta}{\partial \eta} = \left(\frac{\partial}{\partial \tau} + \bar{\tau}_0 \frac{\partial^2}{\partial \tau^2}\right)\left(\theta + \epsilon\left(\frac{\partial U}{\partial \eta} + \frac{U}{\eta}\right)\right) \quad (7)
$$

in a similar way stress equations can be obtained as,

$$
S_{rr} = \frac{\partial U}{\partial \eta} + \xi \frac{U}{\eta} - \beta\, \theta \quad (8)
$$

$$
S_{\theta\theta} = \xi \frac{\partial U}{\partial \eta} + \frac{U}{\eta} - \beta\, \theta \quad (9)
$$

where $\beta = \frac{T_0 \gamma}{\rho c_1{}^2}$, $\epsilon = \frac{\gamma}{\rho c_e}$, $\xi = \frac{\lambda}{\rho c_1{}^2}$. The boundary conditions in which the inner and outer surfaces of the cylinder are traction-free and the outer surface is maintained at a reference temperature, while the inner surface is subjected to a time-dependent internal temperature load, are given in dimensionless form as follows:

$$
S_{rr}(a, \tau) = 0, \quad \theta(a, \tau) = \theta_1 e^{-\alpha\tau}
$$

$$
S_{rr}(b, \tau) = 0, \quad \theta(b, \tau) = 0 \quad (10)
$$

where θ_1 is constant and α is an exponent of diminished heat flux.

3. SOLUTION PROCEDURE

The solution of physical variables can be performed by following the decomposition methodology below [15].

$$
U(\eta, \tau) = U(\eta)\, e^{\omega\tau}, \quad \theta(\eta, \tau) = \theta(\eta)\, e^{\omega\tau}
$$

$$
S_{rr}(\eta, \tau) = S_{rr}(\eta)\, e^{\omega\tau}, \quad S_{\theta\theta}(\eta, \tau) = S_{\theta\theta}(\eta)\, e^{\omega\tau} \quad (11)
$$

where ω is the angular frequency. After decomposition, the system of differential equations can be rewritten in the following form.

$$
\frac{\partial^2 U}{\partial \eta^2} + \frac{1}{\eta}\frac{\partial U}{\partial \eta} - \frac{U}{\eta^2} - \omega^2 U - \beta \frac{\partial \theta}{\partial \eta} = 0 \quad (12)
$$

$$
\frac{\partial^2 \theta}{\partial \eta^2} + \frac{1}{\eta}\frac{\partial \theta}{\partial \eta} - (\omega + \bar{\tau}_0 \omega^2)\left(\theta + \epsilon\left(\frac{\partial U}{\partial \eta} + \frac{U}{\eta}\right)\right) = 0 \quad (13)
$$

$$
S_{rr} = \frac{dU}{d\eta} + \xi \frac{U}{\eta} - \beta\, \theta \quad (14)
$$

$$
S_{\theta\theta} = \xi \frac{dU}{d\eta} + \frac{U}{\eta} - \beta\, \theta \quad (15)
$$

and the boundary conditions will take following form

$$
S_{rr}(a) = 0, \quad \theta(a) = \theta_1 e^{-(\omega + \alpha)\tau}
$$

$$
S_{rr}(b) = 0, \quad \theta(b) = 0 \quad (16)
$$

Then, the system of ordinary differential equations given in Equation (12-16) is solved with pseudospectral Chebyshev method in coupled form.

3.1. Coupled Solution

In the Lord Shulman's approach, it is presumed that if the body is strained, transient stress change will accompany these strains, and interrelatedly, the temperature changes induce thermal strains [16]. For this reason, the equation of motion for the displacement and the heat conduction equation have to be solved simultaneously. Then, the coupled form of these dimensionless equations may be expressed in compact form as:

$$
\frac{\partial^2 Y}{\partial \eta^2} + L_\eta \frac{\partial Y}{\partial \eta} - L_C Y = 0 \quad (17)
$$

where $Y = [\theta\ U]^T$ and the linear coefficient matrices (L_η, L_C) are,

125

$$L_\eta = \begin{bmatrix} \dfrac{1}{\eta} & -\epsilon(\omega + \bar{\tau}_0\omega^2) \\ -\beta & \dfrac{1}{\eta} \end{bmatrix},$$

$$L_C = \begin{bmatrix} -(\omega + \bar{\tau}_0\omega^2) & \dfrac{-\epsilon(\omega + \bar{\tau}_0\omega^2)}{\eta} \\ 0 & -\dfrac{1}{\eta} - \omega^2 \end{bmatrix}$$

(18)

3.2. Numerical Solution of the Problem

The pseudospectral Chebyshev approach is based on first-kind Chebyshev polynomials. In the method, a solution is found in the interval specified in the problem. Chebyshev Gauss-Lobatto points, which have a denser point distribution at the boundary points than the midpoints, are used for obtaining high accuracy results. In accordance with the equation below, these points are evenly spaced on the semicircle.

$$\eta_j = \cos\left(\frac{j\pi}{n}\right), \qquad (j = 0,1,\dots,n) \qquad (19)$$

The pseudospectral Chebyshev Model is employed to perform the coupled thermoelastic analysis of hollow cylinders under the time depended temperature loading by referring to the study of Trefethen [17], Fornberg [18] and Gottlieb [19] that depends on discretization of the governing equation (17) with respect to the spatial variable using the pseudospectral Chebyshev method. With reference to collocation points, the first order $(n + 1)x(n + 1)$ Chebyshev differentiation matrix will be created and denoted by D. First-order Chebyshev differentiation matrix D provides highly precise approximation to $U'(\eta_j)$, $\theta'(\eta_j)$, $U''(\eta_j)$, $\theta''(\eta_j)$ ..., simply by multiplying the differential matrix with vector data $U'(\eta_j) = (D\,U)_j$, $\theta'(\eta_j) = (D\,\theta)_j$, $u''(\eta_j) = (D^2\,U)_j$, $\theta''(\eta_j) = (D^2\,\theta)_j$ suchlike where $U = [U_0,\dots,U_n]^T$ and $\theta = [\theta_0,\dots,\theta_n]^T$ discrete vectors data at positions η_j. The Chebyshev differentiation matrix computing process and codes as an m-file can be found in prominent references see e.g., (Trefethen, [17]), where the collocation points η_j are numbered from right to left and defined in $[-1,1]$. The approach may be used to any interval with a minor modification. Accordingly, the coupled linear thermoelastic equation for the cylinder (17) is simply converted into a linear system by using the pseudospectral Chebyshev collocation approach as below:

$$L\,Y = 0 \qquad (20)$$

where

$$L = D^2 + L_\eta D - L_c. \qquad (21)$$

Boundary conditions (16) are imposed to this linear system (20) by only replacing the first and last row of the system matrix L with the appropriate values. Then, the non-trivial solution of the dimensionless temperature

and displacement distributions can be found by solving the linear system with any decomposition method.

4. RESULTS AND DISCUSSION

In this study, thermoelastic interactions of a hollow copper cylinder based on Lord-Shulman theory are analyzed by the pseudospectral Chebyshev method. It is assumed that the outer surface is kept at the reference temperature while the inner surface is subject to temperature degradation over time. Analyzes are made by increasing the internal temperatures up to $T_1 = 500\,K$, which is the elastic limit of the copper material ($T_0 = 293\,K$). In the numerical calculations, following physical properties are used for copper [15],

Table 1. Mechanical and thermal material properties of copper

Pro	Value	Unit	Pro	Value	Unit
λ	$7.76\ x\ 10^{10}$	$kg\ ms^{-2}$	c_e	$3.831\ x\ 10^2$	$m^2 K^{-1} s^{-2}$
μ	$3.86\ x\ 10^{10}$	$kg\ ms^{-2}$	ρ	$8.954\ x\ 10^3$	$kg\ m^{-3}$
K	$3.68\ x\ 10^2$	$kg\ m\ K^{-1} s^{-3}$	α	$17.8\ x\ 10^{-6}$	$1\ K^{-1}$

The other quantities for the numerical calculation are chosen as $\omega = 5$, $\alpha = 3$, $\Omega = 5$ and $\tau_0 = 0.02$ [15]. Before proceeding to solution of the current problem, the numerical method is tested with the benchmark solution [15] available in the literature. The dimensionless temperature and radial stress distributions at certain times are compared on the graph (Figure 2) with analytical results. In comparison, the PCM solution results obtained using 16 data points are found to be in good agreement with the analytical results. According to these results, the solution to the current problem is continued with PCM.
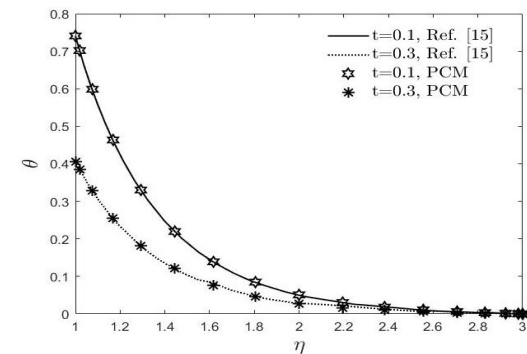
(a)   Temperature distribution
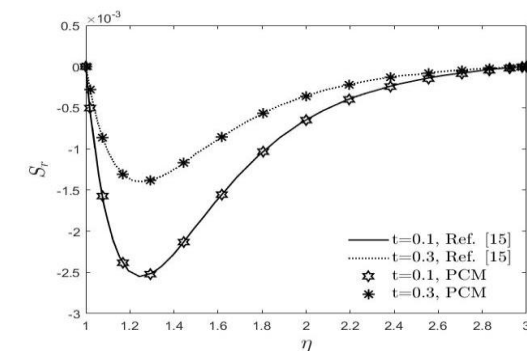
(b) Radial stress distribution
Figure 2. Distribution of temperature and radial stress in a hollow cylinder along the thickness at certain times

The non-dimensional numerical results of temperature, and stresses are given graphically for different values of time in Figure 3 for coupled and noncoupled (NC) conditions. In order to see the time-varying effect of the applied temperature load as the boundary condition, all results are plotted at $t = 0.02, 0.1$ and 0.3 time frames. These frames depict the various phases of the temperature load. In Figure 3(a), nondimensional temperature distributions are shown. In the early stage of loading $(t = 0.02)$ the inner wall temperature is almost at the highest value that can be reached with the applied load. It is observed that this value decreases as time progresses to $t = 0.1$ and 0.3 nondimensional times. The dimensionless temperature distribution along the wall thickness decreases exponentially and reaches to zero at the outer wall in accordance with the boundary conditions. Since the results are given graphically, the difference between the coupled and uncoupled results is not clearly observed at this stage. The radial stress distributions satisfying the traction-free boundary conditions at both ends are presented in Figure 3(b). It is seen from the figure that the stress magnitudes are proportional to the temperature distributions. It is observed that the highest stress values occur at the beginning of loading (t=0.02) and after a certain period of time, these values decrease. The stresses reach their highest values in the first quarter of the wall $(\eta \cong 1.25)$ from the inside to the outside. Similarly, it is observed in Figure 3(c) that the greatest tangential stress occurs on the inner wall in the provinces where the temperature effect is greatest. With the advancing time, the slope of the tangential stress curve decreases with the wall thickness. It can be also observed that all stress results occur in the compression direction Figure 3(b-c) as the cylinder is subjected to internal thermal load.
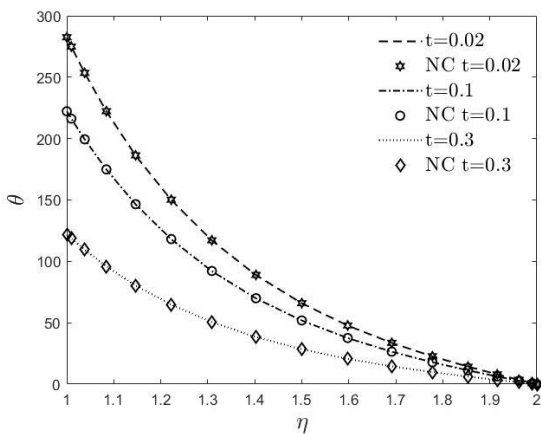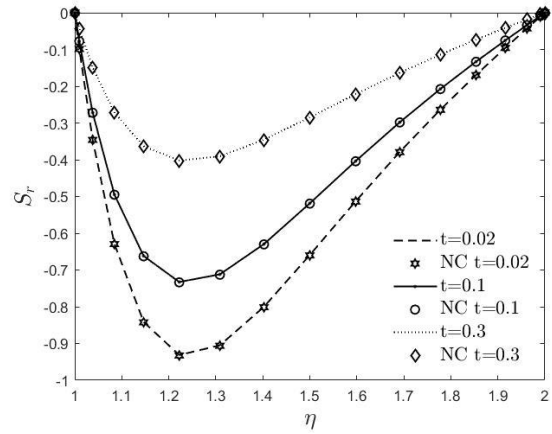
(b) Radial stress distribution
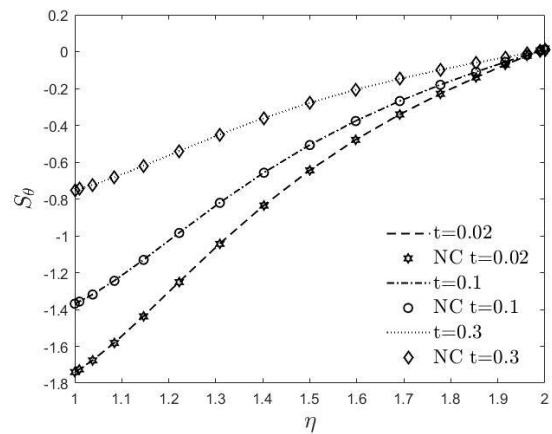
(c) Tangential stress distribution

Figure 3. Distribution of temperature, radial and tangential stresses in a hollow cylinder along the thickness at certain times

(a) Temperature distribution

Further research is done to see the effect of the coupled term on the results. The infinity norm is used to calculate the maximum difference between the results obtained from the coupled and uncoupled solutions $(\|S_{coupled} - S_{uncoupled}\|_\infty)$ at three different temperatures $(\theta = 300, 400, 500)$ and at different time periods $(t = 0.02, 0.1, 0.2)$. The gradient variation of the coupled terms of radial and tangential stresses are given in Table 2 and Table 3, respectively. As can be seen from the Table 2-3, the stress values are larger in the calculations made by including the coupled terms, so to stay on the safe side in the analysis, the coupled terms should be included in the analysis. In the early stages of thermal loading, the differences are greatest for all time periods and for temperature magnitudes. In addition, as the temperature effect increased $(T = 500\ K)$, it is observed that the difference between the coupled and the uncoupled solution increased. This indicates the need for coupled solutions under sudden loading conditions. This difference tends to decrease as time progresses $(for\ t = 0.1, 0.2)$.

Table 2. The gradient variation of the coupled terms to radial stress

Time	$\theta = 300$	$\theta = 400$	$\theta = 500$
	$\sigma_r x 10^{-4}$	$\sigma_r x 10^{-4}$	$\sigma_r x 10^{-4}$
0.02	13.080977	17.441303	21.801629
0.1	10.289861	13.719815	17.149768
0.3	5.647195	7.529594	9.411992

Table 3. The gradient variation of the coupled terms to tangential stress

Time	$\theta = 300$	$\theta = 400$	$\theta = 500$
	$\sigma_\theta x 10^{-4}$	$\sigma_\theta x 10^{-4}$	$\sigma_\theta x 10^{-4}$
0.02	17.624611	23.499481	29.374352
0.1	13.864010	18.485347	23.106683
0.3	7.608730	10.144973	12.681217

5. CONCLUSION

This article examines the combined thermoelastic behavior based on the Lord-Shulman theory of a hollow homogeneous copper cylinder whose inner surface is subjected to a time dependent internal temperature load. The coupled governing equations are solved by using the pseudospectral Chebyshev method. The dimensionless temperature, radial and tangential stress variation along the radius of the cylinder and in some time frames are obtained and shown in the figures. The influence of coupled and uncoupled conditions is demonstrated on the thermoelastic responses of the copper cylinder at different times, which determines the intensity of the thermal load. It has been noticed that in all cases, the highest temperature and stress values occur at the beginning of the instantaneous thermal loading and these values decrease with time. When the differences between the coupled and uncoupled solution results are revealed with the help of the infinity norm, it is observed that the stress values are higher in the calculations made by including the coupled terms. According to this analysis, the highest difference in the results is obtained in the early times of the instantaneous highest thermal loading, while the lowest difference is obtained in the later time period at the lowest temperature. For a more precise analysis, it may be recommended to choose the coupling analysis for problems involving instantaneous loading or high temperature difference. Besides, it can be stated that the PCM is a useful, sensitive numerical solution method and can be adopted simply for solving such problems.

REFERENCES

[1] Ai ZY, Ye ZK, Yang JJ. Thermo-mechanical behaviour of multi-layered media based on the Lord-Shulman model. Comput Geotech. 2021;129.

[2] Biot MA. Thermoelasticity and irreversible thermodynamics. J. Appl. Phys. 1956;27:240–253.

[3] Zamani A, Hetnarski RB, Eslami MR. Second sound in a cracked layer based on Lord–Shulman theory. J. Therm. Stresses. 2011;34(3):181-200.

[4] Lord HW, Shulman Y. A generalized dynamical theory of thermo-elasticity. J. Mech. Phys. Solids. 1967;15(5):299–309.

[5] Shakeriaski F, Ghodrat M, Escobedo-Diaz J, Behnia M. Recent advances in generalized thermoelasticity theory and the modified models: a review. J. Comput. Des. Eng. 2021;8(1):15-35.

[6] Furukawa T, Noda N, Ashida F. Generalized thermoelasticity in an infinite solid with a hole. J. Therm. Stresses. 1989;12(3):385–402.

[7] Furukawa T, Naotake N, Fumihiro A. Generalized thermoelasticity for an infinite solid cylinder. JSME Int J., Ser. A. 1991;34(3):281-286.

[8] Hosseini-Tehrani P, Eslami MR. Boundary element analysis of coupled thermoelasticity with relaxation times in finite domain. AIAA Journal. 2000;38(3):534–41.

[9] Hosseini-Tehrani P, Eslami MR. Boundary element analysis of finite domains under thermal and mechanical shock with the Lord-Shulman theory. J. Strain Anal. Eng. Des. 2003;38(1):53–64.

[10] Bagri A, Eslami MR. Generalized coupled thermoelasticity of disks based on the Lord–Shulman model. J. Therm. Stresses. 2004;27(8):691–704.

[11] Bagri A, Eslami MR. A unified generalized thermoelasticity; solution for cylinders and spheres. Int. J. Mech. Sci. 2007;49(12):1325–35.

[12] Bagri A, Eslami MR. A unified generalized thermoelasticity formulation; application to thick functionally graded cylinders. J. Therm. Stresses. 2007;30(9-10):911-930.

[13] Sharma JN, Sharma PK, Mishra KC, Dynamic Response of Functionally Graded Cylinders due to Timedependent Heat Flux. Meccanica. 2016;51(1):139-154.

[14] Zenkour, AM. Generalized thermoelasticity theories for axisymmetric hollow cylinders under thermal shock with variable thermal conductivity. J. Mol. Eng. Mater. 2018;6(3-4):1850006.

[15] Abbas IA, Abd elmaboud Y. Analytical solutions of thermoelastic interactions in a hollow cylinder with one relaxation time. Math. Mech. Solids. 2017;22(2):210-223.

[16] Carter JP, Booker JR. Finite element analysis of coupled thermoelasticity. Comput Struct. 1989;31(1):73-80.

[17] Trefethen, LN. Spectral Methods in Matlab, 10, SIAM, Philadelphia, PA, 2000.

[18] Fornberg, B. A Practical Guide to Pseudospectral Methods, 1, Cambridge University Press, Cambridge, 1998.

[19] Gottlieb D. The Stability of Pseudospectral-Chebyshev Methods. Math. Comput. 1981;36(153):107-118.

Türk Doğa ve Fen Dergisi
Turkish Journal of Nature and Science
www.dergipark.gov.tr/tdfd

Topographic, Morphological and Morphometric Investigation of Mandible in Norduz Sheep

Semine DALGA[1*], Uğur AYDIN[2], Tansel ÇAL[1]

[1]Kafkas University, Veterinary Faculty, Anatomy Department, Kars, Türkiye
[2]Kafkas University, Veterinary Faculty, Surgery Department, Kars, Türkiye
Semine DALGA ORCID No: 0000-0001-7227-2513
Uğur AYDIN ORCID No: 0000-0001-5756-4841
Tansel ÇAL ORCID No: 0000-0002-3034-5814

*Corresponding author: seminedalga@kafkas.edu.tr

Keywords
Anatomy,
Mandible,
Osteometry,
Surgery,

Abstract: In order to contribute to animal welfare, veterinary maxillofacial surgery is a branch of science that requires a thorough understanding of a region's anatomy. Therefore, the purpose of this study was to define the mandible by using macroanatomical, morfometric and topographic methods to better understand the morphophysiology of the mandible in Norduz sheep. In this study ten male Norduz sheep mandibles were used. The mandibles were initially examined using classical morphometric and topographic methods. The mandible was observed to be composed of corpus, ramus and angulus parts. It was observed that the mental foramen was oval and round in shape and varied in number on the lateral edge of the mandible. The mandible foramen was found to be elliptical. According to the statistical analysis, mandible length was measured as 149.12±4.75 mm, on the right side and 148.12±4.50 mm, on the left side in Norduz sheep. Mandible height was determined as 160.81±4.72 mm, on the right and 160.74±5.11 mm, on the left side. The distance from the mandible foramen to the infradental space was 127.85±4.62 mm, on the right and 125.31±4.11 mm, on the left side. Diastema length was found to be 38.05±1.34 mm, on the right and 40.87±2.81 mm, on the left side. The length of the premolar and molar teeth on the margo alveolaris of the mandible was 56.69±2.38 mm, on the right side and 54.13±2.73 mm, on the left side. The distance from the foramen mentale to the gonion caudale was analyzed as 118.34±4.22 mm, on the right and 118.90±4.12 mm, on the left side. According to the statistical analysis, the length of mandible foramen (L17) was statistically significant (p<0.05) when measured over the right (8.74±0.47 mm) and left (6.61±0.69 mm) mandibles.

129

Norduz Koyununda Mandibulanın Topografik, Morfolojik ve Morfometrik Olarak İncelenmesi

Anahtar Kelimeler
Anatomi,
Mandibula,
Osteometri,
Cerrahi,

Öz: Hayvan refahına katkıda bulunmak için veteriner çene cerrahisi uzmanlık alanları içerisinde bölge ile ilgili derin anatomik bilgi sahibi olmayı gerektiren bilim alanlarındandır. Bu nedenle, bu çalışmada Norduz koyununda mandibula'nın morfofizyolojisinin anlaşılması için makroanatomik, morfometrik ve topografik yöntemler kullanılarak mandibula'nın tanımlanması amaçlandı. Çalışmada on adet erkek hayvana ait Norduz koyun mandibula'sı kullanıldı. Mandibulalar önce klasik morfometrik ve topografik yöntemlerle incelendi. Mandibula'nın corpus, ramus ve angulus bölümlerinden oluştuğu görüldü. Foramen mentale'nin oval ve yuvarlak şekilde olduğu, değişik sayılarda mandibula'nın lateral kenarında bulunduğu saptandı. Foramen mandibula'nın eliptik bir şekilde olduğu gözlendi. Yapılan istatistiksel analize göre Norduz koyununda mandibula uzunluğu sağ tarafta 149.12±4.75 mm, sol tarafta 148.12±4.50 mm, olarak ölçüldü. Mandibula yüksekliği sağ tarafta 160.81±4.72 mm, sol tarafta 160.74±5.11 mm, olarak analiz edildi. Foramen mandibula'nın infradental aralığa uzaklığı sağ tarafta 127.85±4.62 mm, sol tarafta 125.31±4.11 mm, olarak belirlendi. Diastema uzunluğu sağ tarafta 38.05±1.34 mm, sol tarafta 40.87±2.81 mm, olarak analiz edildi. Mandibula'nın margo alveolaris'i üzerinde premolar ve molar dişlerin uzunluğu sağ tarafta 56.69±2.38 mm, sol tarafta 54.13±2.73 mm, olarak belirlendi. Foramen mentale'nin gonion caudale'ye olan uzaklığı sağ tarafta 118.34±4.22 mm, sol tarafta 118.90±4.12 mm, olarak analiz edildi. Yapılan istatistiksel analize göre sağ (8.74±0.47 mm) ve sol (6.61±0.69 mm) mandibulalar üzerinden ölçülen, foramen mandibula'nın uzunluğu (L17) istatistiksel olarak anlamlıydı (p<0.05).

1. INTRODUCTION

Behavioral biology, physiology, and morphology provide ecological information on how animals interact in their natural environment and captivity [1]. Because oral disease has an effect on systemic health [2,3], veterinary dentistry is one of the most promising fields for improving animal welfare [2,4]. Early diagnosis and treatment of oral diseases are critical to reducing individual morbidity and mortality [2,5,6]. Deep topographic and anatomical knowledge of the area to be treated is necessary in order to avoid any intervention that may adversely affect animal welfare during the correct treatment [2,7,8].

The formations found in the cranium and mandible as a whole are the distinguishing features of each animal, allowing for differentiation not only between races and species, but also within species. Sex-related differences are strongly evident in the head skeletons of ruminant animals within a species [9]. Numerous research on the bones that comprise the skull in an integral way has made significant contributions to both comparative anatomy and clinical applications [10-23]. It can be utilized to determine the characteristics of bones obtained in excavation studies as well as morphometric research used as a reference for comparative anatomy and practical applications. The data obtained during the zooarchaeological excavations carried out for this purpose can provide insight into the history and livestock conditions of that time. In such investigations, morphological determinations are made based on morphometric results [24]. In addition, the differences in the skull and mandible and the measured parameters are examined for intraspecies variations and sex analysis. [25,26]. Norduz sheep are a type of domestic sheep that is bred in rural areas in the region called Norduz, Gürpınar district of Van province [27].

Therefore, this study aims to contribute to a better understanding of local morphophysiology, the interpretation of imaging studies, and the improvement of anesthetic and clinical status during surgical techniques in live adult species; it also aims to define it morphologically, morphometrically, and topographically.

2. MATERIAL AND METHOD

In this study, ten male Norduz sheep mandibles were utilized. The study was approved by the Animal Experiments Local Ethics Committee of Kafkas University (KAÜ-HADYEK/2022-066). Study materials were obtained from the Gürpınar district of Van province. Dissection procedures were performed on the supplied materials. After separating the skin and muscles from the mandibles, they were subjected to a controlled maceration process. In order to bleach the bones, the materials were kept in hydrogen peroxide, following which the drying process was undergone. Mandibles were morphologically examined bilaterally. For the morphometric evaluation, 21 parameters were measured on the materials with the help of a Digital Caliper (28) (Figure 1). Six parameters were measured to determine

the topographic location of the foramen mandible and foramen mentale for clinical applications (Figure 2). For statistical analysis, the data were subjected to Independent-Samples T Test, using the SPSS 22.0 software package (Table 1). After the materials were photographed, they were written down in accordance with Nomina Veterinaria Anatomica [29].

3. RESULTS

The mandible of Norduz sheep was seen to be composed of ramus, corpus and angulus parts. The processus coronoideus was seen to extend beyond the processus condylaris and to curve backwards with a distinct arc. The width of the processus condyaris varied between the materials. It was observed that certain materials were narrowly bent backwards, while others were curved by broadening. The materials of the foramen mentale were observed to be in the form of two holes in 30% and round or oval in shape.

Twenty one reference points were measured morphometrically over the mandibles. According to the statistical analysis, mandible length was measured as 149.12 ± 4.75 mm, on the right and 148.12 ± 4.50 mm, on the left side in Norduz sheep. Mandible height was analyzed as 160.81 ± 4.72 mm, on the right and 160.74 ± 5.11 mm, on the left side. The distance from the foramen mandible to the infradental space was 127.85 ± 4.62 mm on the right and 125.31 ± 4.11 mm, on the left side. Diastema length was analyzed as 38.05 ± 1.34 mm, on the right and 40.87 ± 2.81 mm, on the left side. The length of the premolar and molar teeth on the margo alveolaris of the mandible was 56.69 ± 2.38 mm, on the right and 54.13 ± 2.73 mm, on the left side. The distance from the foramen mentale to the gonion caudale was analyzed as 118.34 ± 4.22 mm, on the right and 118.90 ± 4.12 mm, on the left side. According to the statistical analysis results, the length of the foramen mandible (L17) was significantly different in direction between the materials (p<0.05).
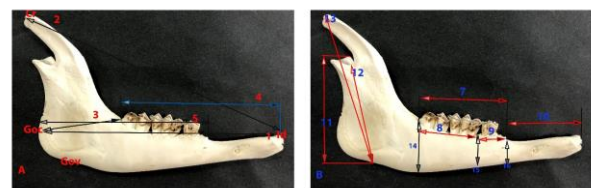
Figure 1. Condylion (cnd); the caudal endpoint of processus condylaris, Cr (coronion); the caudal endpoint of processus coronideus, Gonionventrale (Gv); The inferior endpoint of the angular mandible, Gonioncaudale (Gc); The caudal endpoint of processus angularis, Infradentale (Id); The rostro-superior point of the alveoli between incisive teeth, A: Length 1(1): lenght between gonion caudale and infradentale, Length 2(2): length between infradentale and aboral edge of condylar process, Length 3(3): length between gonion caudale and aboral alveolar edge of 3rd molar tooth, Length 4(4): length between infradentale and aboral alveolar edge of 3rd molar tooth, Length 5(5): length between gonion caudale and rostral alveolar edge of 2nd premolar tooth, B: Length 7(7): length between first premolar tooth and last molar tooth, Length 8(8): length between first and last molar teeth, Length 9(9): length between first and last premolar teeth, Length 10(10): length of diestema, Length 11(11): length between gonion ventrale and condylion, Length 12(12): length between gonion ventrale and the deepest point of incisura mandibulae, Length 13(13): length between gonion ventrale and coronion, Length 14(14): height of

mandible level of alveolar edge of 3rd molar tooth, Length 15(15): height of mandible level of rostral alveolar edge of 1st molar tooth, Length 16(16): height of mandible level of rostral alveolar edge of 2nd premolar tooth.
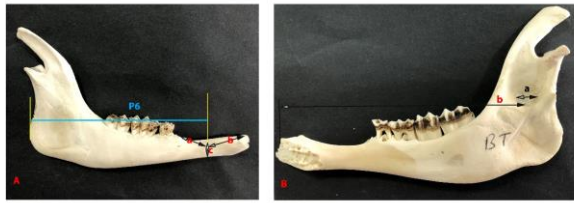

Figure 2. Measured reference points for anesthesia administration of foramen mandible and foramen mentale, **A; Length 6 (P6):** length between gonion caudale and aboral edge of mental foramen, **Length 19(a):** Distance between first premolar tooth and mental foramen, **Length 20(b):** Distance between lateral incisor tooth and mental foramen, **Length 21(c):** Distance between the base of the mandible and mental foramen, **B; Length 17(a):** The length of mandible foramen, **Length 18(b):** Distance between foramen mandible and infradental

Table 1. Table containing the statistical analysis of the parameters taken and evaluated from the mandible

Parameters	Right(mean±st. error)	Left (mean±st. error)
Length 1	149.12±4.75	148.12±4.50
Length 2	160.81±4.72	160.74±5.11
Length 3	47.83±1.39	48.12±1.21
Length 4	99.71±3.00	100.07±3.76
Length 5	104.06±3.58	102.55±2.99
Length 6	118.34±4.22	118.90±4.32
Length 7	56.69±2.38	54.13±2.73
Length 8	26.61±1.91	25.73±3.17
Length 9	28.53±0.81	30.11±1.25
Length 10	38.05±1.34	40.87±2.81
Length 11	62.99±2.31	62.99±1.99
Length 12	55.25±3.60	63.45±3.42
Length 13	84.53±3.08	83.52±6.29
Length 14	31.50±0.82	31.26±1.16
Length 15	22.61±0.72	20.91±1.06
Length 16	14.42±0.50	14.50±0.42
Length 17	8.74±0.47	6.61±0.69
Length 18	127.85±4.62	125.31±4.11
Length 19	16.83±0.79	17.32±1.09
Length 20	20.46±0.64	21.70±0.47
Length 21	6.79±0.22	7.09±0.24

4. DISCUSSION AND CONCLUSION

In this study, the mandible of male Norduz sheep was examined morphologically, topographically, and morphometrically.

According to the literature review, the length of the mandible was 167.8 mm, in Hemşin sheep [14], 152.4 mm, in Morkaraman sheep [30], 147.8 mm, in Tuj sheep [30], 157.6 mm, in Mehra-ban sheep [12], 181.6 mm, in Barbados sheep [13], 198.0±0.28 mm, in Yankasa sheep [32], and 186.30±9.30 mm, in Hasmer sheep [33]. Avdic et al. [2013] reported this value as 176.0 mm, in their study on sheep in Sarajevo, and 185.91±13.33 mm, for Sharri sheep [22] . Mandible length in Norduz sheep was discovered as 149.12±4.75 mm, on the right side and 148.12±4.50 mm, on the left side. According to this data, the Norduz sheep mandible was slightly longer than that of Tuj sheep, but significantly shorter than the other breeds.

The height of the mandible has also been reported to be 94.2 mm, for Hemşin sheep [14], 87.0 mm, for

Morkaraman sheep [30], 85.4 mm, for Tuj sheep [30], 95.7 mm, for Mehra-ban sheep [12], 107.9 mm, for Barbados sheep [13], 129.0±0.57 mm, for Yankasa sheep [32], and 108.68±2.36 mm, for Hasmer sheep [33]. It was 99.6 mm, according to Avdic et al. [2013][34], in their study on sheep in Sarajevo. Mandible height in Norduz sheep was determined to be 160.81±4.72 mm, on the right and 160.74±5.11 mm, on the left side. Mandible height was found to be higher in male Norduz sheep compared to other sheep breeds.

In Norduz sheep, the height of the mandible at the level of the last molar tooth [P14] was analyzed as 31.50±0.82 mm, on the right and 31.26±1.16 mm, on the left side. This parameter was reported to be 37.47±3.25 mm, in Hasmer sheep [33], 37.93 mm, in Hemşin sheep [14], and 38.88 mm, in Morkaraman sheep [30]. This parameter was reported as 36.75 mm, in females and 35.61 mm, in males in Abaza goats [19]. It was observed that the mandible height was lower in male Norduz sheep compared to other sheep breeds.

In Norduz sheep, the mean distance between gonion ventral and processus condylaris was 62.99±2.31 mm, on the right and 62.99±1.92 mm, on the left side. The same parameter was reported as 68.52 mm, in Hemşin sheep [14], 74.58±1.75 mm, in Hasmer sheep [33], and 77.50 mm, in Mehra-ban sheep [12]. The same parameter was reported as 63.57 mm, in female and 63.33 mm, in male Abaza goats [19]. This parameter was found to be lower in male Norduz sheep compared to other sheep breeds.

The length of the molar teeth [P8] on the margo alveolaris of the mandible in Norduz sheep was measured to be an average of 26.61±1.91 mm, on the right and 25.73±3.17 mm, on the left side. This parameter was reported as 57.2 mm, in Hemşin sheep [14], 49.26±3.11 mm, in Hasmer sheep [33], and 53.12 mm, in Morkaraman sheep [30]. It was observed that the molar tooth length in Norduz sheep was quite small compared to other sheep breeds analyzed in the literature. In a study conducted on Abaza goats [19] , this parameter was measured as 58.28 mm, in females and 53.66 mm, in males. Margo interalveolaris (Diastema) length was reported as 43.54±3.48 mm, [33] and 43.74 mm, [14] in Hasmer sheep; 45.81±3.73 mm, in Sharri sheep [22] and 45.81±3.73 mm, in female and 45.98±3.87 mm, in male Bardhoka sheep [26]. In the mandibles of Awassi sheep [41], this parameter was reported as 46.27±3.29 mm, in females and 48.97±5.82 mm, in males. Diastema length (P10) in male Norduz sheep was analyzed as 38.05±1.34 mm, on the right and 40.87±2.81 mm on the left side.

The distance between foramen mentale and gonion caudale (6); was reported as 137.4 mm, in Mehraban sheep[12], 152.3 mm, in Barbados sheep[13], 165.0 mm, in Yankasa sheep[32], 112.9 mm, in Iranian domestic sheep [35], and 149.40±11.02 mm, in Hasmer sheep [33].

In studies on goats in the literature, the same parameter was found to be 128.87 mm, in female, 118.84 mm, in male Abaza goats [19], 125.30±8.49 mm, in female,

151.31±0.5 mm, in male Gurcu goats [42], 43±0,08 cm, in Blackbucks [36], 11.69±0.40 cm, [37], in Black Bengal goats, 9.26±0.49 cm, [38] in GVD goats, 15.23±1.46 cm, [31] in Barbados black belly sheep, and 11.8±0.89 cm, [39] in Black Bengal goats.

The blockage of the mandibular nerve is important in all surgical procedures affecting the mandible's incisive, premolar, and molar teeth. The blockage of the mental nervus, which is a continuation of the nervus mandibularis and passes through the foramen mentale, is also very important. Three reference points for the blockade of the relevant nerve passing through the foramen mentale in Norduz sheep were identified and measured.

The mean distance between the 1st premolar tooth and the foramen mentale (P19) was found to be 1.68±0.79 cm, on the right and 1.73±1.09 cm, on the left side. This parameter was reported as 2.25±0.38 cm, in Barbados black belly [31] sheep, 1.98±0.21 cm, in Hemşin sheep [18], and 1.46±0.09 cm, in Black bengal goats [39].

The distance between the foramen mentale and the lateral incisor teeth (P20) was measured as 2.04±0.64 cm, and 2.17±0.47 cm, on the left side in Norduz sheep. This parameter was found to be 2.11±0.17 cm, in Black bengal goats [37], 2.25±0.31 cm, in Barbados black belly sheep [31], 1.58±0.19 cm in Gwembe Valley dwarf goats [38], 2.01±0.05 cm, in Black bengal goats [39], 1.56±0.22 cm, in West African dwarf goats [40], and 2.40±0.37 cm in Hemsin sheep [18].

The distance between the foramen mentale and margo ventralis (P21) was measured as 0.67±0.22 cm on the right and 0.70±0.24 cm on the left side in Norduz sheep. This parameter was reported as 0.70±0.18 cm in Barbados black belly sheep [31], 0.69±0.13 cm in Hemşin sheep [18], 2.35±0.26 cm in Gwembe Valley dwarf goats [38], and 0.77±0.04 cm, in Black bengal goats [39].

The findings of this study are significant in many ways; morphologically, morphometrically, and most important clinically, during surgical interventions in the head area. Due to the lack of information in the current literature regarding the parameters investigated in this sheep breed, the available data provide a solid foundation for comparative anatomy with other ruminant animals and further research in other fields such as zooarchaeology and animal welfare.

REFERENCES

[1] Moura C.E.B, Albuquerque JFG, Magalhaes MS, Silva NB, Oliveira MF, Papa PC. Analise comparativa da origem do plexo braquial de catetos [Tayassutajacu]. Pesq. Vet. Bras. 2007; 27, 357–362.

[2] Niemiec B, Gawor J, Nemec A, Clarke D, McLeod K, Tutt C, et al. World small animal veterinary associationglobal dental guidelines. JSAP. 2020;61,E36–E161.

[3] Pachaly JR, Gioso MA. The oral cavity, 457–463. In M. E. Fowler & Z. L. Cubas (Eds.), Biology, medicine and surgery of south American wild animals. 2001; Iowa State University Press.

[4] Pachaly JR. Odontoestomatologia, 1068–1091. In Z. S.Cubas, J. C. R. Silva, & J. L. Catao-Dias (Eds.), 2007; Tratado de Animais Selvagens. Roca.

[5] Enlund KB, Karlsson M, Brunius C, Hagman R, Höglund OV, Gustås P, et al. Professional dental cleaning in dogs: Clinical routines among Swedish veterinarians and veterinary nurses. *Acta Veterinaria Scandinavica*, 2020; 62, 61

[6] Glatt SE, Francl KE, Scheels JL. A survey of current dental problems and treatments of zoo animals. International Zoo Yearbook, 2008; (42), 206–213.

[7] Beckman B, Legendre L. Regional nerve blocks for oral surgery in companion animals. Compendium on Continuing Education for the Practising Veterinarian, 2002; (24), 439–444.

[8] Moura AG, Bernardino JR, Severino RS, Teixeira CS. Topografia dos forames mentonianos laterais em suínos das linhagens Agroceres e Seghers genetics do Brasil. Bioscience Journal, 2006; (22), 119–123.

[9] Kobryńczuk F, Krasińska M, Szara T. Sexual dimorphism in skulls of the lowland European bison, *Bison bonasus bonasus*. Ann Zool Fennici, 2008; (45):335–340. https:// doi. org/ 10. 5735/ 086. 045.0415

[10] Wehausen JD, Ramey RR. Cranial morphometric and evolutionary relationships in the northern range of *Ovis canadensis*. J Mammal, 2000; (81):145–161. https:// doi. org/ 10. 1644/ 1545

[11] Ozcan S, Aksoy G, Kurtul I, Aslan K, Ozudogru Z. A comparative morphometric study on the skull of the Tuj and Morkaraman sheep. Kafkas Univ Vet Fak Derg. 2010; (16):111–114. https:// doi. org/ 10. 9775/ KVFD. 2009. 518

[12] Karimi I, Onar V, Pazvant G, Hadipour M, Mazaheri Y. The cranial morphometric and morphologic characteristics of Mehraban sheep in Western Iran. Glob Vet, 2011; (6):111–117.

[13] Mohamed R, Driscoll M, Mootoo N. Clinical anatomy of the skull of the Barbados Black Belly sheep in Trinidad. Int J Curr Res Med Sci. 2016; (2) :8–19.

[14] Dalga S, Aslan K, Kırbaş G. Hemşin Koyunu mandibulası üzerinde morfometrik bir çalışma. Atatürk Üniv Vet Bil Derg. 2017; 12(1): 22-7.

[15] Dalga S, Aslan K, Akbulut Y. A morphometric study on the skull of the adult Hemshin sheep. Van Vet J, 2018; (29):125–129

[16] Magalhaes HIR, Romao FB, Paula YH, Luz MM, Barcelos JB, Silva Z, et al. Morphometry of the mandibular foramen applied to local anesthesia in hoary fox (*Lycalopex vetulus*). Pesq. Vet. Bras. 2019; (39), 278–285.

[17] Dalga S.Topographic and morphometric study of the mental foramina of Abaza goats with its clinical implication for regional anesthesia Folia Morphologica. 2020; (79), No. 3, pp. 576–579 DOI: 10.5603/FM.a2019.0122

[18] Dalga S, Aslan K. Topographic and morphometric study on mental foramen in Hemshin sheep for local anesthesia. MJAVL. 2020; (10):93–97.

[19] Dalga S, Aslan K. Morphological and Osteometric Analysis of the Skull in Abaza goats (Capra aegagrus), Dicle Üniv Vet Fak Derg. 2021;14(1):35-38 DOI: 10.47027/duvetfd.883353

[20] Özkan E, Jashari T, Gündemir O, Gezer İnce N. Morphometric analysis of the mandible of Bardhoka autochthonous sheep in Kosovo. Anat Histol Embryol. 2020; 49:737–741. https://doi.org/10. 1111/ahe.12568

[21] Yılmaz B, Demircioglu İ. İvesi Koyunlarda (Ovis aries) Kafatasının Morfometrik Analizi. Fırat Üniversitesi Sağlık Bilimleri Veteriner Dergisi, 2020; 34:01–06

[22] Jashari T, Duro S, Gündemir O, et al. Morphology, morphometry and some aspects of clinical anatomy in the skull and mandible of Sharri sheep. Biologia (2021). https://doi.org/10.1007/s11756-021-00955-y

[23] Ribeiro LDA, Magalhaes HIR, Silva AF, Silva FOC. Macroscopic, morphometric, and tomographic features of the mandible of the collared peccary (Pecari tajacu) applied to clinical morpho-physiology and imaging. The Anatomical Record. 2022;1–14. https://doi.org/10.1002/ar.24897

[24] Onar V, Pazvant G, Pasicka E, Armutak A, Alpak H. Byzantine horse skeletons of Theodosius Harbour: 2. Withers height estimation. Rev Med Vet. 2015; 166:30–42

[25] Marzban AB, Hajian O, Rahmati S. I nvestigating the morphometric characteristics of male and female Zell sheep skulls for sexual dimorphism. ASJ. 2018; (15):13–20

[26] Gundemir O, Duro S, Jashari T, Kahvecioğlu O, Demircioğlu İ, Mehmeti H. A study on morphology and morphometric parameters on skull of the Bardhoka autochthonous sheep breed in Kosovo. Anat Histol Embryol. 2020; 49:365–371. https://doi.org/10.1111/ahe.12538

[27] Koyuncu M: Sheep Breeding. Dora Publishing Distribution Ltd. Şti. 1st edn., 42, Bursa, 2019.

[28] Von den Driesch, A. A guide to the measurement of animal bones from archaeological sites: as developed by the Institut fur Palaeoanatomie, Domestikationsforschung und Geschichte der Tiermedizin of the University of Munich (Vol. 1). Peabody Museum Press, 1976.

[29] Nomina Anatomica Veterinaria: International Committee on Veterinary Gross Anatomical Nomenclature: General Assembly of the World Association of Veterinary Anatomists. 6thedition, Gent, 2017.

[30] Demiraslan Y, Gülbaz F, Özcan S, Dayan MO, Akbulut Y. Morphometric analysis of the mandible of Tuj and Morkaraman sheep. J Vet Anat. 2014; (7): 75-86.

[31] Mohamed R, Drisco M, Mootoo N. Clinical Anatomy of the skull of the Barbados Black Belly Sheep in Trinidad. International Journal of Current Research in Medical Science. 2016; 2(8): 8-19.

[32] Shehu SA, Bello A, Sonfada ML, Suleiman HM, Umar AA, Danmaigoro A, et al. Morphometrical study of the mandibular bone of female Yankasa sheep. International Journal of Current Science and Multidisciplinary Journal. 2019; 2(1): 1-10

[33] Özüdoğru Z, İlgün R, Özdemir D. Hasmer koyunu mandibula'sı üzerinde makroanatomik ve morfometrik incelemeler. Erciyes Üniv Vet Fak Derg. 2019; 16(3): 218-223.

[34] Avdic R, Hadziomerovic N, Tandir F, Pamela B, Velida C. Analysis of morphometric parameters of the Roe deer mandible (Capreolus capreolus) and mandible of the sheep (Ovis aries). Veterinaria. 2013; 62: 1-9.

[35] Monfared AL. Clinical anatomy of the skull of Iranian native sheep. Glob Vet. 2013; 10:271–275. https:// doi. org/ 10. 5829/ idosi. gv. 2013. 10.3. 7253

[36] Choudhary OP, Singh I. Applied anatomy of the maxillofacial and mandibular regions of the Indian blackbuck (Antelope cervicapra). J Anim Res. 2015; 5(3): 497-500.

[37] Uddin MM, Ahmed SSU, Islam KN, Islam MM. Clinical anatomy of the head region of the Black Bengal goat in Bangladesh. International Journal of Morpholology. 2009; 27(4): 1269-1273.

[38] Kataba A, Mwaanga ES, Simukoko H, Pares CPM. Clinical anatomy of the head Region of Gwembe Valley dwarf goat in Zambia. International Journal of Veterinary Science. 2014; 3(3): 142-146.

[39] Poddar S, Faruq AA, Dey T, Kibria ASMG, Uddin MM. Topographic and Morphometric Anatomy of Mental Foramen of Black Bengal goat (Capra hircus) in Bangladesh with its Clinical Implication for Regional Anesthesia. Int J Zoo Animal Biol. 2018; 1(1):000102.

[40] Olopade JO, Onwuka SK. An osteometric study of the skull of the West African Dwarf goat from South Eastern Nigeria. II- Mandibular and Maxillofacial features (Short Communication). Nigerian Veterinary Journal. 2005; 27(2): 66-70.

[41] Yılmaz B. Morphometric Evaluation of the Mandible in the Awassi Sheep (Ovis aries). Harran Üniv Vet Fak Derg. 2020; 9 (2): 189-193.

[42] Dalga S, Aslan K. Applied anatomy to the Gurcu goat's mandible in Kafkas and its clinical significance in regional anesthesia, TJVR. 2021; 5 (2): 51-56.

133

Türk Doğa ve Fen Dergisi
Turkish Journal of Nature and Science

www.dergipark.gov.tr/tdfd

On Travelling Wave Solutions of Dullin-Gottwald-Holm Dynamical Equation and Strain Wave Equation

Seyma TULUCE DEMIRAY[1*], Merve DAVARCI YALCIN[2]

[1] Osmaniye Korkut Ata University, Department of Mathematics, Osmaniye, Türkiye
[2] Osmaniye Korkut Ata University, Department of Mathematics, Osmaniye, Türkiye
Seyma TULUCE DEMIRAY ORCID No: 0000-0002-8027-7290
Merve DAVARCI YALCIN ORCID No: 0000-0002-4862-7836

*Corresponding author: seymatuluce@gmail.com

Abstract: In this study, extended trial equation method (ETEM) is implemented to obtain exact solutions of the Dullin-Gottwald-Holm Dynamical equation (DGHDE) and the strain wave equation. We constitute some exact solutions such as soliton solutions, rational, Jacobi elliptic, periodic wave solutions and hyperbolic function solutions of these equations via ETEM. Then, we present results that we obtained by using this method.

134

Dullin-Gottwald-Holm Denklemi ve Gergin Dalga Denkleminin Hareketli Dalga Çözümleri Üzerine

Öz: Bu çalışmada, Dullin-Gottwald-Holm Dinamik denkleminin ve gergin dalga denkleminin kesin çözümlerini elde etmek için genişletilmiş deneme denklem metodu uygulanmıştır. Bu denklemlerin soliton çözümleri, rasyonel, Jacobi eliptik, periyodik dalga çözümleri ve hiperbolik fonksiyon çözümleri gibi bazı kesin çözümleri genişletilmiş deneme denklem metodu ile elde edilmiştir. Daha sonra bu yöntemi kullanarak elde ettiğimiz sonuçlar sunduk.

1. INTRODUCTION

In recent years, travelling wave solutions are substantially significant subject matter in biophysics, geophysical sciences, chemical kinematics, optical fibers, the technology of space, elastic media and some issues in nonlinear sciences. Recently many scientists have applied various methods to obtain travelling wave solutions of NLEEs (nonlinear evolution equations) such as Hirota's direct method [1], Jacobi elliptic function method [2], new version of the trial equation method [3], (G'/G)–expansion method [4], tanh-coth method [5] etc. In this work, the ETEM [6,7] will be performed to get exact solutions of the DGHDE and the strain wave equation.
Firstly, we tackle the following the DGHDE [8]

$$u_t + h_1 u_x - h_2^2 \left(u_{xxt} + u u_{xxx} + 2 u_x u_{xx} \right) + 3 u u_x + h_3 u_{xxx} = 0, \, t \geq 0, \tag{1}$$

where fluid velocity of system is symbolized by u in spatial direction x.

$h_2^2 (h_2 > 0)$ and $\dfrac{h_1}{h_3}$ indicate squares of length scales, and $h_1 = \sqrt{gh}$ (where $h_1 = 2\omega$) demonstrates the linear wave speed for undisturbed water at rest at spatial infinity. G. M. Octavian has submitted the analysis of wave-breaking solutions to Eq. (1) [9]. M. H. Raddadi et al. have obtained solitary wave solutions of Eq. (1) by using new extended direct algebraic method [10]. R. K. Gupta and B. Anupma have found exact solutions of Eq. (1) via Lie Classical method [11].

Secondly, we investigate the strain wave equation given below [12]:

$$u_{tt} - u_{xx} - \gamma \left(\alpha_1 \left(u^2 \right)_{xx} - \alpha_3 u_{xxxx} + \alpha_4 u_{xxtt} \right) = 0, \tag{2}$$

where γ shows elastic strain, α_1, α_3 and α_4 are arbitrary constants. Kumar et al. have found new exact solitary wave solutions of Eq. (2) by using generalized exponential rational function method [13]. M. G. Hafez and M. A. Akbar have obtained multiple explicit and exact traveling wave solutions of this equation by using an exponential expansion method [14].

The arrangement of this study was done as follows. In Sec. 2, we perform ETEM on DGHDE and strain wave equation. In Sec. 3, the results acquired using this method are expressed.

2. FUNDAMENTALS OF THE ETEM

Step 1. For a known nonlinear partial differential equation

$$P\left(u, u_t, u_x, u_{xx}, \ldots\right) = 0 \tag{3}$$

we get the wave transformation as

$$u\left(x_1, x_2, \ldots, x_N, t\right) = u(\eta), \ \eta = \lambda \left(\sum_{j=1}^{N} x_j - ct \right), \tag{4}$$

where $\lambda \neq 0$, $c \neq 0$. Accommodating Eq. (4) into Eq. (3) satisfies a nonlinear ordinary differential equation,

$$N\left(u, u', u'', \ldots\right) = 0. \tag{5}$$

Step 2. Presume that the trial equation of Eq. (5) can be indicated as following:

$$u = \sum_{i=0}^{\delta} \tau_i \Gamma^i, \tag{6}$$

where

$$\left(\Gamma'\right)^2 = \Lambda(\Gamma) = \frac{\phi(\Gamma)}{\psi(\Gamma)} = \frac{\xi_\vartheta \Gamma^\vartheta + \ldots + \xi_1 \Gamma + \xi_0}{\zeta_\varepsilon \Gamma^\varepsilon + \ldots + \zeta_1 \Gamma + \zeta_0}. \tag{7}$$

Considering relations (8) and (9), we can have

$$\left(u'\right)^2 = \frac{\phi(\Gamma)}{\psi(\Gamma)} \left(\sum_{i=0}^{\delta} i \tau_i \Gamma^{i-1} \right)^2, \tag{8}$$

$$u'' = \frac{\phi'(\Gamma)\psi(\Gamma) - \phi(\Gamma)\psi'(\Gamma)}{2\psi^2(\Gamma)} \left(\sum_{i=0}^{\delta} i \tau_i \Gamma^{i-1} \right) + \frac{\phi(\Gamma)}{\psi(\Gamma)} \left(\sum_{i=0}^{\delta} i(i-1) \tau_i \Gamma^{i-2} \right), \tag{9}$$

135

where $\phi(\Gamma)$ and $\psi(\Gamma)$ are polynomials. Putting these terms into Eq. (5) ensures an equation of polynomial $\Omega(\Gamma)$ of Γ :

$$\Omega(\Gamma) = \sigma_s \Gamma^s + \ldots + \sigma_1 \Gamma + \sigma_0 = 0. \tag{10}$$

In accordance with balance principle, we can describe a relation of ϑ, ε and δ . We can find some values of ϑ, ε and δ .

Step 3. Letting the coefficients of $\Omega(\Gamma)$ all be zero will satisfy an algebraic equations system:

$$\sigma_i = 0, \quad i = 0, \ldots, s. \tag{11}$$

Solving equation system (11), we will define the values of $\xi_0, \ldots, \xi_\vartheta; \ \zeta_0, \ldots, \zeta_\varepsilon$ and $\tau_0, \ldots, \tau_\delta$.

Step 4. Simplify Eq. (7) to elementary integral shape,

$$\pm(\eta - \eta_0) = \int \frac{d\Gamma}{\sqrt{\Lambda(\Gamma)}} = \int \sqrt{\frac{\psi(\Gamma)}{\phi(\Gamma)}} d\Gamma. \tag{12}$$

Applying a complete discrimination system for polynomial to classify the roots of $\Omega(\Gamma)$, we solve the infinite integral (12) and categorize the exact solutions for Eq. (3).

3. IMPLEMENTATIONS OF THE ETEM

In this chapter, we implement the ETEM to the DGHDE and the strain wave equation, respectively.

3.1. Implementation on the DGHDE

In an attempt to find travelling wave solutions of Eq. (1), we take the transformation

$$u(x,t) = U(\eta), \ \eta = x - vt, \ v \neq 0. \tag{13}$$

Then, we get

$$vh_2^2 (U'')' - vU' + h_1 U' - h_2^2 U (U'')' + h_3 (U'')' + 3UU' - 2h_2^2 U'U'' = 0. \tag{14}$$

Also, integrating Eq. (14) according to η and getting the integration constant to zero, we attain

$$U'' \left(h_2^2 (-v) - h_3 + h_2^2 U \right) - (h_1 - v)U - \frac{3U^2}{2} + \frac{1}{2} h_2^2 (U')^2 = 0. \tag{15}$$

Embedding Eqs. (8) and (9) into Eq. (15), and utilizing the balance principle, we gain

$$\vartheta = \varepsilon + 2. \tag{16}$$

Then, we procure the corollaries as follows:

Case 1: If we choose $\varepsilon = 0, \ \delta = 1$ and $\vartheta = 2$, then,

$$(u')^2 = \frac{\tau_1^2 \left(\xi_0 + \Gamma \xi_1 + \Gamma^2 \xi_2 \right)}{\zeta_0}, \tag{17}$$

$$u'' = \frac{\tau_1 \left(\xi_1 + 2\Gamma \xi_2 \right)}{2\zeta_0}, \tag{18}$$

where $\xi_2 \neq 0,\ \zeta_0 \neq 0$. Substituting Eq. (6), Eq. (17) and Eq. (18) into Eq. (15), we get an algebraic equation system. Then, by using Wolfram Mathematica 12, $\xi_0,\ \xi_1,\ \xi_2, \zeta_0$ and v coefficients are obtained as following

$$\xi_0 = \xi_0\ ,\ \xi_1 = \xi_1,\ \xi_2 = \frac{h_2^2 \xi_1 \tau_1}{h_3 + h_2^2 \left(h_1 + 2\tau_0\right)},$$

$$\tau_0 = \tau_0,\ \tau_1 = \tau_1,\ \zeta_0 = \frac{h_2^4 \xi_1 \tau_1}{h_3 + h_2^2 \left(h_1 + 2\tau_0\right)},$$

$$v = \frac{-\xi_1\left(h_3 + h_2^2 h_3 \tau_0 + h_2^4 \tau_0^2 + h_1 h_2^2 \left(h_3 + h_2^2 \tau_0\right)\right)}{h_2^2 \left(h_1 h_2^2 + h_3\right)\xi_1} +$$

$$\frac{h_2^2\, \xi_0 \left(h_3 + h_2^2\left(h_1 + 2\tau_0\right)\right)\tau_1}{h_2^2 \left(h_1 h_2^2 + h_3\right)\xi_1},$$

(19)

Embedding Eq. (19) into Eqs. (7) and (12), we acquire

$$\pm\left(\eta - \eta_0\right) = A \int \frac{d\Gamma}{\sqrt{\dfrac{\xi_0}{\xi_2} + \dfrac{\xi_1}{\xi_2}\Gamma + \Gamma^2}},$$

(20)

where $A = \sqrt{\dfrac{\zeta_0}{\xi_2}} = h_2$.

Integrating Eq. (20), we gain the solutions of Eq. (1) as follows

$$\left(\eta - \eta_0\right) = A \ln\left(\Gamma - \alpha_1\right) \tag{21}$$

$$\pm\left(\eta - \eta_0\right) = 2A \ln\left[\sqrt{\Gamma - \alpha_1} + \sqrt{\Gamma - \alpha_2}\right], \alpha_2 > \alpha_1. \tag{22}$$

Moreover, α_1 and α_2 are the roots of the polynomial equation,

$$\Gamma^2 + \frac{\xi_1}{\xi_2}\Gamma + \frac{\xi_0}{\xi_2} = 0. \tag{23}$$

Embedding Eq. (21) and Eq. (22) into Eq. (6), we can find the following exact traveling wave solutions for Eq. (1), respectively:

$$u\left(x,t\right) = \tau_0 + \tau_1\left(\alpha_1 + e^{\pm\frac{\left((x-vt)-\eta_0\right)}{h_2}}\right), \tag{24}$$

$$u\left(x,t\right) = \tau_0 + \frac{\tau_1}{4}\left(\begin{array}{l} 2\left(\alpha_1 + \alpha_2\right) + e^{\pm\frac{\left((x-vt)-\eta_0\right)}{h_2}} \\ + \left(\alpha_1 - \alpha_2\right)^2 e^{\pm\frac{\left((x-vt)-\eta_0\right)}{h_2}} \end{array}\right), \tag{25}$$

where

$$v = \frac{-\xi_1\left(h_3 + h_2^2 h_3 \tau_0 + h_2^4 \tau_0^2 + h_1 h_2^2 \left(h_3 + h_2^2 \tau_0\right)\right)}{h_2^2 \left(h_1 h_2^2 + h_3\right)\xi_1} + \frac{h_2^2\, \xi_0 \left(h_3 + h_2^2\left(h_1 + 2\tau_0\right)\right)\tau_1}{h_2^2 \left(h_1 h_2^2 + h_3\right)\xi_1}.$$

For simplicity, we take $\eta_0 = 0, \tau_0 = -\tau_1 \alpha_1$, then Eq. (24) is reduced to the single king solution,

$$u(x,t) = \left(\tilde{A} e^{\tilde{B}(x-vt)} \right), \tag{26}$$

where $\tilde{A} = \tau_1$, $\tilde{B} = \pm \dfrac{1}{A}$.

For simplicity, we take $\eta_0 = 0, \alpha_1 = 1, \alpha_2 = 0,$ then Eq. (25) is reduced to the hyperbolic function solution,

$$u(x,t) = \tau_0 + \frac{\tau_1}{2}\left(1 + \cosh\left(\tilde{B}(x-vt) \right) \right), \tag{27}$$

where

$$v = \frac{-\xi_1\left(h_3 + h_2^2 h_3 \tau_0 + h_2^4 \tau_0^2 + h_1 h_2^2 \left(h_3 + h_2^2 \tau_0 \right) \right)}{h_2^2 \left(h_1 h_2^2 + h_3 \right)\xi_1} + \frac{h_2^2 \, \xi_0 \left(h_3 + h_2^2 \left(h_1 + 2\tau_0 \right) \right)\tau_1}{h_2^2 \left(h_1 h_2^2 + h_3 \right)\xi_1}.$$

Case 2: If we choose $\varepsilon = 0, \ \delta = 2$ and $\vartheta = 2,$ then

$$\left(u' \right)^2 = \frac{\left(\tau_1 + 2\Gamma \tau_2 \right)^2 \left(\xi_0 + \Gamma \xi_1 + \Gamma^2 \xi_2 \right)}{\zeta_0}, \tag{28}$$

$$u'' = \frac{4\tau_2 \left(\xi_0 + \Gamma \xi_1 + \Gamma^2 \xi_2 \right) + \left(\xi_1 + 2\Gamma \xi_2 \right)\left(\tau_1 + 2\Gamma \tau_2 \right)}{2\zeta_0}, \tag{29}$$

where $\xi_2 \neq 0, \ \zeta_0 \neq 0$.

Solving algebraic equation system (11), we find

$$\xi_0 = \xi_0, \ \ \xi_1 = \xi_1, \ \ \xi_2 = -\frac{h_2^2 \xi_1^2 \tau_1}{3\left(h_1 h_2^2 + h_3 \right)\xi_1 - 4h_2^2 \xi_0 \tau_1}, \zeta_0 = -\frac{h_2^4 \xi_1^2 \tau_1}{3\left(h_1 h_2^2 + h_3 \right)\xi_1 - 4h_2^2 \xi_0 \tau_1},$$

$$\tau_0 = -2h_1 - \frac{2h_3}{h_2^2} + \frac{2\xi_0 \tau_1}{\xi_1}, \tau_1 = \tau_1, \ \ \tau_2 = 0, \ \ v = -2h_1 - \frac{3h_3}{h_2^2} + \frac{3\xi_0 \tau_1}{\xi_1}. \tag{30}$$

Setting these results into Eqs. (7) and (12), we have

$$\pm(\eta - \eta_0) = A_1 \int \frac{d\Gamma}{\sqrt{\dfrac{\xi_0}{\xi_2} + \dfrac{\xi_1}{\xi_2}\Gamma + \Gamma^2}}, \tag{31}$$

where $A_1 = \sqrt{\dfrac{\zeta_0}{\xi_2}} = h_2$.

Integrating Eq. (31), we obtain the solutions of Eq. (1) as following:

$$\pm(\eta - \eta_0) = A_1 \ln\left(\Gamma - \alpha_1 \right), \tag{32}$$

$$\pm(\eta - \eta_0) = 2A_1 \ln\left[\sqrt{\Gamma - \alpha_1} + \sqrt{\Gamma - \alpha_2} \right], \alpha_2 > \alpha_1. \tag{33}$$

138

Furthermore, α_1 and α_2 are the roots of the polynomial equation,

$$\Gamma^2 + \frac{\xi_1}{\xi_2}\Gamma + \frac{\xi_0}{\xi_2} = 0. \tag{34}$$

Setting Eqs. (32) and (33) into Eq. (6), we find travelling wave solutions of Eq. (1) as

$$u(x,t) = \left[\begin{array}{l} \tau_0 + \tau_1 h_1 + \tau_1 e^{\pm\frac{(x-vt-\eta_0)}{h_2}} \\ + \tau_2 \left(h_1 + e^{\pm\frac{(x-vt-\eta_0)}{h_2}} \right)^2 \end{array} \right], \tag{35}$$

$$u(x,t) = \left[\begin{array}{l} \tau_0 + \dfrac{\tau_1}{4}\left(\begin{array}{l} 2(h_2+h_1) + e^{\pm\frac{(x-vt-\eta_0)}{h_2}} \\ + (h_1-h_2)^2 e^{\mp\frac{(x-vt-\eta_0)}{h_2}} \end{array} \right) \\[1em] + \dfrac{\tau_2}{16}\left(\begin{array}{l} 2(h_2+h_1) + e^{\pm\frac{(x-vt-\eta_0)}{h_2}} \\ + (h_1-h_2)^2 e^{\mp\frac{(x-vt-\eta_0)}{h_2}} \end{array} \right)^2 \end{array} \right]. \tag{36}$$

For simplicity, we take $\eta_0 = 0,$ then Eq. (35) is reduced to the single king solution,

$$u(x,t) = \left[\sum_{i=0}^{2} \tau_i \left(\alpha_1 + e^{B\left(x - \left(-2h_1 - \frac{3h_3}{h_2^2} + \frac{3\xi_0\tau_1}{\xi_1}\right)t\right)} \right)^i \right], \tag{37}$$

where $B = \pm\dfrac{1}{A_1}$, $v = -2h_1 - \dfrac{3h_3}{h_2^2} + \dfrac{3\xi_0\tau_1}{\xi_1}$.

For simplicity, we take $\eta_0 = 0, \alpha_1 = 1, \alpha_2 = 0,$ then Eq. (36) is reduced to the hyperbolic function solution,

$$u(x,t) = \left[\sum_{i=0}^{2} \frac{\tau_i}{2^i}\left(1 + \cosh\left(B(x-vt)\right)\right)^i \right], \tag{38}$$

where $v = -2h_1 - \dfrac{3h_3}{h_2^2} + \dfrac{3\xi_0\tau_1}{\xi_1}$.

Case 3: If we choose $\varepsilon = 1,\ \delta = 1$ and $\vartheta = 3$ then

$$(u')^2 = \frac{\tau_1^2\left(\xi_0 + \Gamma\xi_1 + \Gamma^2\xi_2 + \Gamma^3\xi_3\right)}{\zeta_0 + \Gamma\zeta_1}, \tag{39}$$

$$u'' = \frac{\left(\zeta_0 + \Gamma\zeta_1\right)\left(\xi_1 + 2\Gamma\xi_2 + 3\Gamma^2\xi_3\right)\tau_1}{2\left(\zeta_0 + \Gamma\zeta_1\right)^2} - \frac{\zeta_1\left(\xi_0 + \Gamma\xi_1 + \Gamma^2\xi_2 + \Gamma^3\xi_3\right)\tau_1}{2\left(\zeta_0 + \Gamma\zeta_1\right)^2}, \tag{40}$$

where $\xi_3 \neq 0,\ \zeta_1 \neq 0$. Consecutively, resolving the algebraic equation system (11) yields

$$\xi_1 = \frac{h_2^4 \xi_2^2 \tau_0 \left(2h_3 + h_2^2 \left(2h_1 + \tau_0\right)\right)}{\zeta_1 \left(h_3 + h_2^2 \left(h_1 + 2\tau_0\right)\right)^2},\ \ \xi_2 = \xi_2,\ \ \xi_3 = \frac{\zeta_1}{h_2^2},\ \ \zeta_0 = 0, \zeta_1 = \zeta_1,$$

$$\tau_0 = \tau_0,\ \ \tau_1 = \frac{\zeta_1 \left(h_3 + h_2^2 \left(h_1 + 2\tau_0\right)\right)}{h_2^4 \xi_2}, v = -\frac{h_3}{h_2^2} + \tau_0.$$

(41)

Embedding these corollaries into Eqs. (7) and (12), we gain

$$\pm\left(\eta - \eta_0\right) = A_2 \int \frac{\sqrt{\dfrac{\zeta_0 + \Gamma}{\zeta_1}}}{\sqrt{\dfrac{\xi_0}{\xi_3} + \dfrac{\xi_1}{\xi_3}\Gamma + \dfrac{\xi_2}{\xi_3}\Gamma^2 + \Gamma^3}} d\Gamma,$$

(42)

where $A_2 = \sqrt{\dfrac{\zeta_1}{\xi_3}} = h_2$.

Integrating Eq. (42), we get the solutions of Eq. (1) as following:

$$\pm\left(\eta - \eta_0\right) = 2A_2 \left(\ln\left|\sqrt{\frac{\zeta_0 + \zeta_1 \Gamma}{\zeta_1}} + \sqrt{\Gamma - \alpha_1}\right| - \sqrt{\frac{\zeta_0 + \zeta_1 \Gamma}{b_1 \left(\Gamma - \alpha_1\right)}} \right),$$

(43)

$$\pm\left(\eta - \eta_0\right) = \frac{2A_2}{\sqrt{\zeta_1 \left(\alpha_2 - \alpha_1\right)}} \left\{ \sqrt{\zeta_0 + \zeta_1 \alpha_1}\ \arctan\left[\sqrt{\frac{\left(\zeta_0 + \zeta_1 \alpha_1\right)\left(\Gamma - \alpha_2\right)}{\left(\zeta_0 + \zeta_1 \Gamma\right)\left(\alpha_2 - \alpha_1\right)}}\right] + \sqrt{\alpha_2 - \alpha_1}\ \ln\left|\sqrt{\frac{\zeta_0 + \zeta_1 \Gamma}{\zeta_1}} + \sqrt{\Gamma - \alpha_2}\right| \right\},$$

(44)

$$\pm\left(\eta - \eta_0\right) = \frac{2A_2 \left(\left(\zeta_0 + \zeta_1 \alpha_1\right) F\left(\varphi, l\right)\right)}{\sqrt{\zeta_1 \left(\alpha_1 - \alpha_2\right)\left(\zeta_0 + \zeta_1 \alpha_3\right)}} + \frac{2A_2 \left(\left(\alpha_3 - \zeta_1 \alpha_1\right)\pi\left(\varphi, n, l\right)\right)}{\sqrt{\zeta_1 \left(\alpha_1 - \alpha_2\right)\left(\zeta_0 + \zeta_1 \alpha_3\right)}},$$

(45)

where

$$F\left(\varphi, l\right) = \int_0^\varphi \frac{d\psi}{\sqrt{1 - l^2 \sin^2 \psi}},$$

$$\pi\left(\varphi, n, l\right) = \int_0^\varphi \frac{d\psi}{\left(1 + n\sin^2 \psi\right)\sqrt{1 - l^2 \sin^2 \psi}},$$

(46)

and

140

$$\varphi = \arcsin \sqrt{\frac{(\Gamma - \alpha_3)(\alpha_2 - \alpha_1)}{(\Gamma - \alpha_1)(\alpha_2 - \alpha_3)}},$$

$$n = \frac{\alpha_3 - \alpha_2}{\alpha_1 - \alpha_2}, \ l^2 = \frac{(\zeta_0 + \zeta_1 \alpha_1)(\alpha_3 - \alpha_2)}{(\zeta_0 + \zeta_1 \alpha_3)(\alpha_1 - \alpha_2)}. \tag{47}$$

Also, α_1, α_2 and α_3 are the roots of the polynomial equation,

$$\Gamma^3 + \frac{\xi_2}{\xi_3} \Gamma^2 + \frac{\xi_1}{\xi_3} \Gamma + \frac{\xi_0}{\xi_3} = 0. \tag{48}$$

Remark 1. The solutions of Eq. (1) were attained by using ETEM and these obtained solutions were checked in Wolfram Mathematica 12.

3.2. Implementation of the Strain Wave Equation

In an attempt to find travelling wave solutions of Eq. (2), we take the transformation
$u(x,t) = U(\eta), \ \eta = x - kt,$ where k is an arbitrary constant. Then, we acquire

$$(k^2 - 1)U'' - \gamma \alpha_1 (U^2)'' + \gamma (\alpha_3 - \alpha_4 k^2) U^{(4)} = 0, \tag{49}$$

Also, integrating Eq. (49) according to η twice and getting the integration constant to zero, we get

$$\gamma (\alpha_3 - \alpha_4 k^2) U'' + (k^2 - 1)U - \gamma \alpha_1 U^2 = 0. \tag{50}$$

Embedding Eqs. (8) and (9) into Eq. (50), and using the balance principle, we find

$$\vartheta = \delta + \varepsilon + 2. \tag{51}$$

After this solution procedure, we get the results as follows:

Case 1: If we take $\varepsilon = 0, \ \delta = 1$ and $\vartheta = 3$, then

$$(u')^2 = \frac{\tau_1^2 (\xi_3 \Gamma^3 + \xi_2 \Gamma^2 + \xi_1 \Gamma + \xi_0)}{\zeta_0}, \tag{52}$$

$$u'' = \frac{\tau_1 (3\xi_3 \Gamma^2 + 2\xi_2 \Gamma + \xi_1)}{2\zeta_0}, \tag{53}$$

where $\xi_3 \neq 0, \ \zeta_0 \neq 0$. Respectively, solving the algebraic equation system (11) yields

$$\xi_0 = \xi_0, \ \xi_1 = \xi_1, \ \xi_2 = \xi_2, \ \xi_3 = \frac{\tau_1 (2\xi_2 \tau_0 - \xi_1 \tau_1)}{3\tau_0^2},$$

$$\zeta_0 = \frac{-2\xi_2 \tau_0 (-\alpha_3 + \alpha_4 (1 + \gamma \alpha_1 \tau_0))}{2\alpha_1 \tau_0^2} + \frac{\xi_1 (-\alpha_3 + \alpha_4 (1 + 2\gamma \alpha_1 \tau_0)) \tau_1}{2\alpha_1 \tau_0^2}, \tag{54}$$

$$\tau_0 = \tau_0, \ \tau_1 = \tau_1, \ k = \sqrt{\frac{-2\xi_2 \tau_0 (1 + \gamma \alpha_1 \tau_0) + \xi_1 (1 + 2\gamma \alpha_1 \tau_0) \tau_1}{-2\xi_2 \tau_0 + \xi_1 \tau_1}}.$$

Tr. Doğa ve Fen Derg. Cilt 11, Sayı 3, Sayfa 134-149, 2022

Tr. J. Nature Sci. Volume 11, Issue 3, Page 134-149, 2022

Embedding these results into Eqs. (7) and (12), we have

$$\pm\left(\eta-\eta_{0}\right)=\sqrt{A_{3}}\int\frac{d\Gamma}{\sqrt{\Gamma^{3}+\frac{\xi_{2}}{\xi_{3}}\Gamma^{2}+\frac{\xi_{1}}{\xi_{3}}\Gamma+\frac{\xi_{0}}{\xi_{3}}}}.\tag{55}$$

Integrating Eq. (55), we get the solutions to the Eq. (2) as follows:

$$\pm\left(\eta-\eta_{0}\right)=-2\sqrt{A_{3}}\,\frac{1}{\sqrt{\Gamma-\alpha_{1}}},\tag{56}$$

$$\pm\left(\eta-\eta_{0}\right)=2\sqrt{\frac{A_{3}}{\alpha_{2}-\alpha_{1}}}\arctan\sqrt{\frac{\Gamma-\alpha_{2}}{\alpha_{2}-\alpha_{1}}},\alpha_{2}>\alpha_{1},\tag{57}$$

$$\pm\left(\eta-\eta_{0}\right)=\sqrt{\frac{A_{3}}{\alpha_{2}-\alpha_{1}}}\ln\left|\frac{\sqrt{\Gamma-\alpha_{2}}-\sqrt{\alpha_{1}-\alpha_{2}}}{\sqrt{\Gamma-\alpha_{2}}+\sqrt{\alpha_{1}-\alpha_{2}}}\right|,\alpha_{1}>\alpha_{2},\tag{58}$$

$$\pm\left(\eta-\eta_{0}\right)=2\sqrt{\frac{A_{3}}{\alpha_{1}-\alpha_{3}}}F\left(\varphi,l\right),\alpha_{1}>\alpha_{2}>\alpha_{3},\tag{59}$$

where

$$A_{3}=\frac{\zeta_{0}}{\xi_{3}}=\frac{3\left(-2\xi_{2}\tau_{0}\left(-\alpha_{3}+\alpha_{4}\left(1+\gamma\alpha_{1}\tau_{0}\right)\right)\right)}{2\alpha_{1}\tau_{1}\left(2\xi_{2}\tau_{0}-\xi_{1}\tau_{1}\right)}+\frac{3\xi_{1}\left(-\alpha_{3}+\alpha_{4}\left(1+2\gamma\alpha_{1}\tau_{0}\right)\right)\tau_{1}}{2\alpha_{1}\tau_{1}\left(2\xi_{2}\tau_{0}-\xi_{1}\tau_{1}\right)},$$

$$F\left(\varphi,l\right)=\int_{0}^{\varphi}\frac{d\psi}{1-l^{2}\sin^{2}\psi},\tag{60}$$

and

$$\varphi=\arcsin\sqrt{\frac{\Gamma-\alpha_{3}}{\alpha_{2}-\alpha_{3}}},\quad l^{2}=\frac{\alpha_{2}-\alpha_{3}}{\alpha_{1}-\alpha_{3}}.\tag{61}$$

Also α_{1}, α_{2} and α_{3} are the roots of the polynomial equation,

$$\Gamma^{3}+\frac{\xi_{2}}{\xi_{3}}\Gamma^{2}+\frac{\xi_{1}}{\xi_{3}}\Gamma+\frac{\xi_{0}}{\xi_{3}}=0.\tag{62}$$

Substituting the solutions (56-59) into Eq. (6), we can get the following exact traveling wave solutions such as rational function solution, hyperbolic function solutions and Jacobi elliptic function solutions of Eq. (2), respectively:

$$u(x,t)=\tau_{0}+\tau_{1}\alpha_{1}+\frac{4\tau_{1}A_{3}}{\left(x-kt-\eta_{0}\right)^{2}},\tag{63}$$

$$u(x,t)=\tau_{0}+\tau_{1}\alpha_{1}+\tau_{1}\left(\alpha_{2}-\alpha_{1}\right)\tanh^{2}\left(\frac{1}{2}\sqrt{\frac{\alpha_{1}-\alpha_{2}}{A_{3}}}\left(x-kt-\eta_{0}\right)\right),\tag{64}$$

142

$$u(x,t) = \tau_0 + \tau_1\alpha_1 + \tau_1(\alpha_1 - \alpha_2)\operatorname{csch}^2\left(\frac{1}{2}\sqrt{\frac{\alpha_1 - \alpha_2}{A_3}}(x - kt)\right), \tag{65}$$

and

$$u(x,t) = \tau_0 + \tau_1\alpha_3 + \tau_1(\alpha_2 - \alpha_3)sn^2\left(\pm\frac{1}{2}\sqrt{\frac{\alpha_1 - \alpha_3}{A_3}}(x - kt - \eta_0), \frac{\alpha_2 - \alpha_3}{\alpha_1 - \alpha_3}\right), \tag{66}$$

where

$$k = \sqrt{\frac{-2\xi_2\tau_0(1 + \gamma\alpha_1\tau_0) + \xi_1(1 + 2\gamma\alpha_1\tau_0)\tau_1}{-2\xi_2\tau_0 + \xi_1\tau_1}}.$$

If we take $\tau_0 = -\tau_1\alpha_1$ and $\eta_0 = 0$ for simpleness, then the solutions (63)-(65) can degrade to rational function solution

$$u(x,t) = \left(\frac{2\sqrt{\tilde{A}_1}}{x - kt}\right)^2, \tag{67}$$

1-soliton solution

$$u(x,t) = \frac{A_4}{\cosh^2[B_1(x - kt)]}, \tag{68}$$

143

singular soliton solution

$$u(x,t) = \frac{A_5}{\sinh^2[B_1(x - kt)]}, \tag{69}$$

where

$$k = \sqrt{\frac{-2\xi_2\tau_0(1 + \gamma\alpha_1\tau_0) + \xi_1(1 + 2\gamma\alpha_1\tau_0)\tau_1}{-2\xi_2\tau_0 + \xi_1\tau_1}}, \tilde{A}_1 = \tau_1 A_3, A_4 = \tau_1(\alpha_2 - \alpha_1),$$

$$A_5 = \tau_1(\alpha_1 - \alpha_2), B_1 = \pm\frac{1}{2}\sqrt{\frac{\alpha_1 - \alpha_2}{A_3}}.$$

Here, A_4 and A_5 are the amplitudes of the solitons, while k is the velocity and B_1 is the reverse width of the solitons. Thus, we can say that the solitons exist for $\tau_1 > 0$.

In addition, if we receive $\tau_0 = -\tau_1\alpha_3$ and $\eta_0 = 0$, Eq. (66) is converted into the Jacobi elliptic function solution

$$u_i(x,t) = A_6 sn^2\left[B_i(x - kt), \frac{\alpha_2 - \alpha_3}{\alpha_1 - \alpha_3}\right], \tag{70}$$

where

$$k = \sqrt{\frac{-2\xi_2\tau_0\left(1+\gamma\alpha_1\tau_0\right)+\xi_1\left(1+2\gamma\alpha_1\tau_0\right)\tau_1}{-2\xi_2\tau_0+\xi_1\tau_1}}, \quad A_6 = \tau_1\left(\alpha_2-\alpha_3\right), \; B_i = \frac{(-1)^i}{2}\sqrt{\frac{\alpha_1-\alpha_3}{A_3}}, \; (i=1,2).$$

Remark 2. When the modulus $l \to 1$, Eq. (70) can be converted into dark soliton solutions

$$u_i(x,t) = A_6 \tanh^2\left[B_l\left(x-kt\right)\right], \tag{71}$$

where

$$\alpha_1 = \alpha_2$$

and $k = \sqrt{\dfrac{-2\xi_2\tau_0\left(1+\gamma\alpha_1\tau_0\right)+\xi_1\left(1+2\gamma\alpha_1\tau_0\right)\tau_1}{-2\xi_2\tau_0+\xi_1\tau_1}}$ represents the velocity of the dark soliton.

Case 2: If we take $\varepsilon = 0$, $\delta = 2$ and $\vartheta = 4$, then

$$\left(v'\right)^2 = \frac{\left(\tau_1+2\tau_2\Gamma\right)^2\left(\xi_4\Gamma^4+\xi_3\Gamma^3+\xi_2\Gamma^2+\xi_1\Gamma+\xi_0\right)}{\zeta_0}, \tag{72}$$

$$v'' = \frac{\left(\tau_1+2\tau_1\Gamma\right)\left(4\xi_4\Gamma^3+2\xi_3\Gamma^2+2\xi_2\Gamma+\xi_1\right)}{2\zeta_0}+\frac{2\tau_2\left(\xi_4\Gamma^4+\xi_3\Gamma^3+\xi_2\Gamma^2+\xi_1\Gamma+\xi_0\right)}{\zeta_0}, \tag{73}$$

where $\xi_4 \neq 0$, $\zeta_0 \neq 0$.

Respectively, solving the algebraic equation system (11) outputs as follows:

$$\xi_0 = \frac{\dfrac{\alpha_1\zeta_0\tau_1^6}{\alpha_3-k^2\alpha_4}-24\xi_1\tau_1^3\tau_2^2+\dfrac{-36\left(-1+k^2\right)^2\zeta_0^2\tau_1^2\tau_2^2+576\gamma^2\left(\alpha_3-k^2\alpha_4\right)\xi_1^2\tau_2^4}{\gamma^2\alpha_1\left(\alpha_3-k^2\alpha_4\right)\zeta_0}}{288\tau_1^2\tau_2^3},$$

$$\xi_1 = \xi_1, \; \xi_2 = \frac{\xi_1\tau_2}{\tau_1}+\frac{\alpha_1\zeta_0\tau_1^2}{6\tau_2\left(\alpha_3-k^2\alpha_4\right)}, \; \xi_3 = \frac{\alpha_1\zeta_0\tau_1}{3\left(\alpha_3-k^2\alpha_4\right)}, \; \xi_4 = \frac{\alpha_1\zeta_0\tau_2}{6\left(\alpha_3-k^2\alpha_4\right)},$$

$$\tag{74}$$

$$\tau_0 = \frac{1}{12}\left(\frac{\tau_1^2}{\tau_2}+\frac{6\left(\dfrac{-1+k^2}{\gamma}+\dfrac{4\left(\alpha_3-k^2\alpha_4\right)\xi_1\tau_2}{\zeta_0\tau_1}\right)}{\alpha_1}\right), \; \tau_1 = \tau_1, \; k = k.$$

Embedding these results into Eqs. (7) and (12), we have

$$\pm\left(\eta-\eta_0\right) = A_7\int \frac{d\Gamma}{\sqrt{\Gamma^4+\dfrac{\xi_3}{\xi_4}\Gamma^3+\dfrac{\xi_2}{\xi_4}\Gamma^2+\dfrac{\xi_1}{\xi_4}\Gamma+\dfrac{\xi_0}{\xi_4}}}, \tag{75}$$

where $A_7 = \sqrt{\dfrac{6\alpha_3-6k^2\alpha_4}{\alpha_1\tau_2}}$.

Integrating Eq. (75), we get the solutions to the eq. (2) as follows

Tr. Doğa ve Fen Derg. Cilt 11, Sayı 3, Sayfa 134-149, 2022

Tr. J. Nature Sci. Volume 11, Issue 3, Page 134-149, 2022

$$\pm\left(\eta-\eta_0\right)=-\frac{A_7}{\Gamma-\alpha_1}, \tag{76}$$

$$\pm\left(\eta-\eta_0\right)=\frac{2A_7}{\alpha_1-\alpha_2}\sqrt{\frac{\Gamma-\alpha_2}{\Gamma-\alpha_1}}, \quad \alpha_1>\alpha_2, \tag{77}$$

$$\pm\left(\eta-\eta_0\right)=\frac{A_7}{\alpha_1-\alpha_2}\ln\left|\frac{\Gamma-\alpha_1}{\Gamma-\alpha_2}\right|, \tag{78}$$

$$\pm\left(\eta-\eta_0\right)=\frac{2A_7}{\sqrt{\left(\alpha_1-\alpha_2\right)\left(\alpha_1-\alpha_3\right)}}\ln\left|\frac{\sqrt{\left(\Gamma-\alpha_2\right)\left(\alpha_1-\alpha_3\right)}-\sqrt{\left(\Gamma-\alpha_3\right)\left(\alpha_1-\alpha_2\right)}}{\sqrt{\left(\Gamma-\alpha_2\right)\left(\alpha_1-\alpha_3\right)}+\sqrt{\left(\Gamma-\alpha_3\right)\left(\alpha_1-\alpha_2\right)}}\right|, \quad \alpha_1>\alpha_2>\alpha_3, \tag{79}$$

$$\pm\left(\eta-\eta_0\right)=\frac{2A_7}{\sqrt{\left(\alpha_1-\alpha_3\right)\left(\alpha_2-\alpha_4\right)}}F\left(\varphi,l\right), \quad \alpha_1>\alpha_2>\alpha_3>\alpha_4, \tag{80}$$

where

$$A_7=\sqrt{\frac{6\alpha_3-6k^2\alpha_4}{\alpha_1\tau_2}}, \quad \varphi=\arcsin\sqrt{\frac{\left(\Gamma-\alpha_1\right)\left(\alpha_2-\alpha_4\right)}{\left(\Gamma-\alpha_2\right)\left(\alpha_1-\alpha_4\right)}}, \quad l^2=\frac{\left(\alpha_2-\alpha_3\right)\left(\alpha_1-\alpha_4\right)}{\left(\alpha_1-\alpha_3\right)\left(\alpha_2-\alpha_4\right)}. \tag{81}$$

Also α_1, α_2, α_3 and α_4 are the roots of the polynomial equation,

145

$$\Gamma^4+\frac{\xi_3}{\xi_4}\Gamma^3+\frac{\xi_2}{\xi_4}\Gamma^2+\frac{\xi_1}{\xi_4}\Gamma+\frac{\xi_0}{\xi_4}=0. \tag{82}$$

Substituting the solutions (76)-(80) into Eq. (6), we have

$$u\left(x,t\right)=\tau_0+\tau_1\alpha_1\pm\frac{\tau_1A_7}{x-kt-\eta_0}+\tau_2\left(\alpha_1\pm\frac{A_7}{x-kt-\eta_0}\right)^2, \tag{83}$$

$$u\left(x,t\right)=\tau_0+\tau_1\alpha_1+\frac{4A_7^2\left(\alpha_2-\alpha_1\right)\tau_1}{4A_7^2-\left[\left(\alpha_1-\alpha_2\right)x-kt-\eta_0\right]^2}+\tau_2\left(\alpha_1+\frac{4A_7^2\left(\alpha_2-\alpha_1\right)}{4A_7^2-\left[\left(\alpha_1-\alpha_2\right)x-kt-\eta_0\right]^2}\right)^2, \tag{84}$$

$$u\left(x,t\right)=\tau_0+\tau_1\alpha_2+\frac{\left(\alpha_2-\alpha_1\right)\tau_1}{\exp\left[\frac{\left(\alpha_1-\alpha_2\right)}{A_7}\left(x-kt-\eta_0\right)\right]-1}+\tau_2\left(\alpha_2+\frac{\left(\alpha_2-\alpha_1\right)}{\exp\left[\frac{\left(\alpha_1-\alpha_2\right)}{A_7}\left(x-kt-\eta_0\right)\right]-1}\right)^2, \tag{85}$$

$$u\left(x,t\right)=\tau_0+\tau_1\alpha_1+\frac{\left(\alpha_1-\alpha_2\right)\tau_1}{\exp\left[\frac{\left(\alpha_1-\alpha_2\right)}{A_7}\left(x-kt-\eta_0\right)\right]-1}+\tau_2\left(\alpha_1+\frac{\left(\alpha_1-\alpha_2\right)}{\exp\left[\frac{\left(\alpha_1-\alpha_2\right)}{A_7}\left(x-kt-\eta_0\right)\right]-1}\right)^2, \tag{86}$$

$$u(x,t) = \tau_0 + \tau_1\alpha_1 - \frac{2(\alpha_1-\alpha_2)(\alpha_1-\alpha_3)\tau_1}{2\alpha_1-\alpha_2-\alpha_3+(\alpha_3-\alpha_2)\cosh\left[\dfrac{\sqrt{(\alpha_1-\alpha_2)(\alpha_1-\alpha_3)}}{A_7}(x-kt-\eta_0)\right]}$$

$$+\tau_2\left(\alpha_1 - \frac{2(\alpha_1-\alpha_2)(\alpha_1-\alpha_3)}{2\alpha_1-\alpha_2-\alpha_3+(\alpha_3-\alpha_2)\cosh\left[\dfrac{\sqrt{(\alpha_1-\alpha_2)(\alpha_1-\alpha_3)}}{A_7}(x-kt-\eta_0)\right]}\right)^2, \tag{87}$$

$$u(x,t) = \tau_0 + \tau_1\alpha_2 + \frac{\tau_1(\alpha_1-\alpha_2)(\alpha_4-\alpha_2)}{\alpha_4-\alpha_2+(\alpha_1-\alpha_4)\,sn^2\left[\dfrac{\sqrt{(\alpha_1-\alpha_3)(\alpha_2-\alpha_4)}}{2A_7}(x-kt-\eta_0),\dfrac{(\alpha_2-\alpha_3)(\alpha_1-\alpha_4)}{(\alpha_1-\alpha_3)(\alpha_2-\alpha_4)}\right]}$$

$$+\tau_2\left(\alpha_2 + \frac{\tau_1(\alpha_1-\alpha_2)(\alpha_4-\alpha_2)}{\alpha_4-\alpha_2+(\alpha_1-\alpha_4)\,sn^2\left[\dfrac{\sqrt{(\alpha_1-\alpha_3)(\alpha_2-\alpha_4)}}{2A_7}(x-kt-\eta_0),\dfrac{(\alpha_2-\alpha_3)(\alpha_1-\alpha_4)}{(\alpha_1-\alpha_3)(\alpha_2-\alpha_4)}\right]}\right)^2. \tag{88}$$

For simplicity, if we take $\eta_0 = 0$, then we can write the solutions (83)-(88) as follows:

$$u(x,t) = \sum_{i=0}^{2}\tau_i\left(\alpha_1 \pm \frac{A_7}{x-kt}\right)^i, \tag{89}$$

$$u(x,t) = \sum_{i=0}^{2}\tau_i\left(\alpha_1 + \frac{4A_7^{\,2}(\alpha_1-\alpha_2)}{4A_7^{\,2}-\left[(\alpha_1-\alpha_2)(x-kt)\right]^2}\right)^i, \tag{90}$$

$$u(x,t) = \sum_{i=0}^{2}\tau_i\left(\alpha_2 + \frac{\alpha_2-\alpha_1}{\exp\left[B_2(x-kt)\right]-1}\right)^i, \tag{91}$$

$$u(x,t) = \sum_{i=0}^{2}\tau_i\left(\alpha_1 + \frac{\alpha_1-\alpha_2}{\exp\left[B_2(x-kt)\right]-1}\right)^i, \tag{92}$$

$$u(x,t) = \sum_{i=0}^{2}\tau_i\left(\alpha_1 - \frac{2(\alpha_1-\alpha_2)(\alpha_1-\alpha_3)}{2\alpha_1-\alpha_2-\alpha_3+(\alpha_3-\alpha_2)\cosh\left[C(x-kt)\right]}\right)^i, \tag{93}$$

$$u(x,t) = \sum_{i=0}^{2} \tau_i \left(\alpha_2 + \frac{(\alpha_1 - \alpha_2)(\alpha_4 - \alpha_2)}{\alpha_4 - \alpha_2 + (\alpha_1 - \alpha_4) sn^2(\varphi, l)} \right)^i,$$ (94)

where

$$A_7 = \sqrt{\frac{6\alpha_3 - 6k^2\alpha_4}{\alpha_1 \tau_2}}, \quad B_2 = \frac{k(\alpha_1 - \alpha_2)}{A_7}, \quad C = \frac{k\sqrt{(\alpha_1 - \alpha_2)(\alpha_1 - \alpha_3)}}{A_7},$$

$$\varphi = \frac{k\sqrt{(\alpha_1 - \alpha_3)(\alpha_2 - \alpha_4)}}{2A_7}(x - kt), l^2 = \frac{(\alpha_2 - \alpha_3)(\alpha_1 - \alpha_4)}{(\alpha_1 - \alpha_3)(\alpha_2 - \alpha_4)}.$$

Here, A_7 is the amplitude of the soliton, while k is the velocity and B_2 and C are the inverse width of the solitons.

Remark 3. The solutions of Eq. (2) were reached by using ETEM and these obtained solutions were checked in Wolfram Mathematica 12.
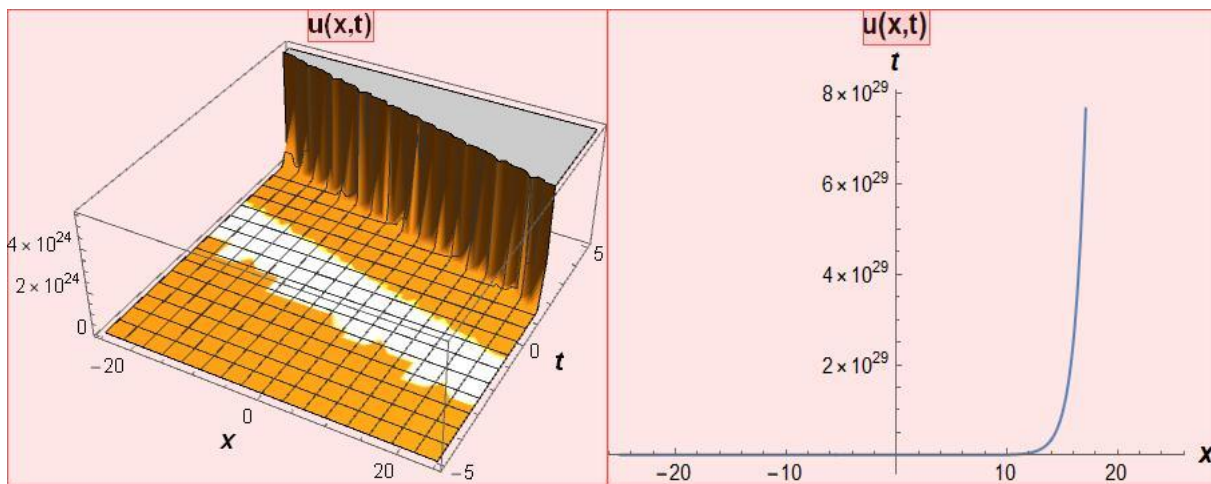

Figure 1. Graph of the solution (26) is indicated at $\tau_0 = 1, \tau_1 = 2, h_1 = 2, h_2 = 1, h_3 = -1, \xi_0 = 3, \xi_1 = -1, -25 \leq x \leq 25,$ $-5 \leq t \leq 5$ and the second graph denotes the exact solution of Eq. (26) for $t = 3$.
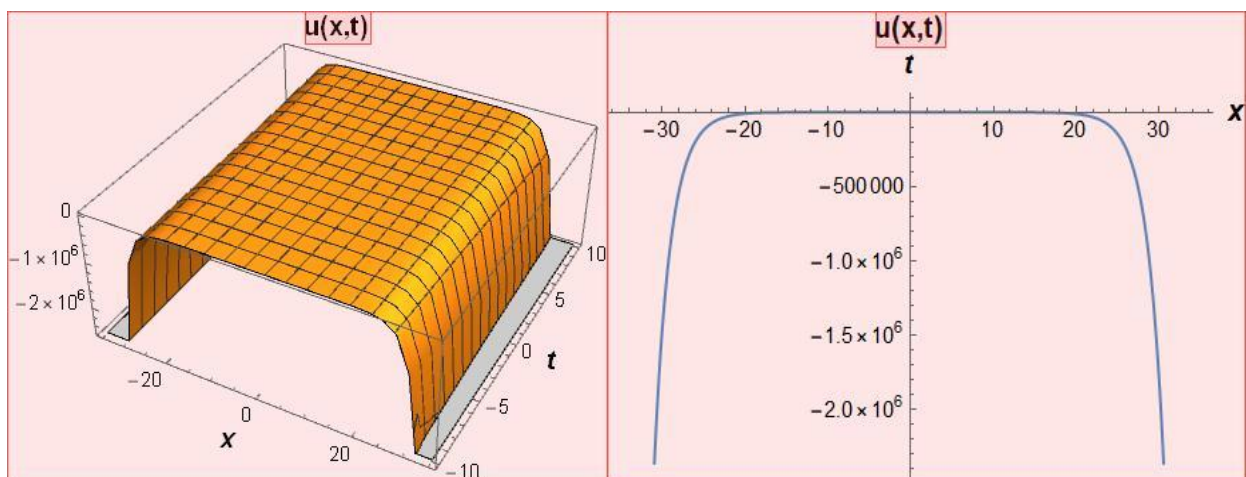

Figure 2. Graph of the solution (27) is indicated at $\tau_0 = 1, \tau_1 = -2, h_1 = -2, h_2 = 2, h_3 = 1, \xi_0 = -2, \xi_1 = -1,$ $-35 \leq x \leq 35, -10 \leq t \leq 10$ and the second graph denotes the exact solution of Eq. (27) for $t = 2$.
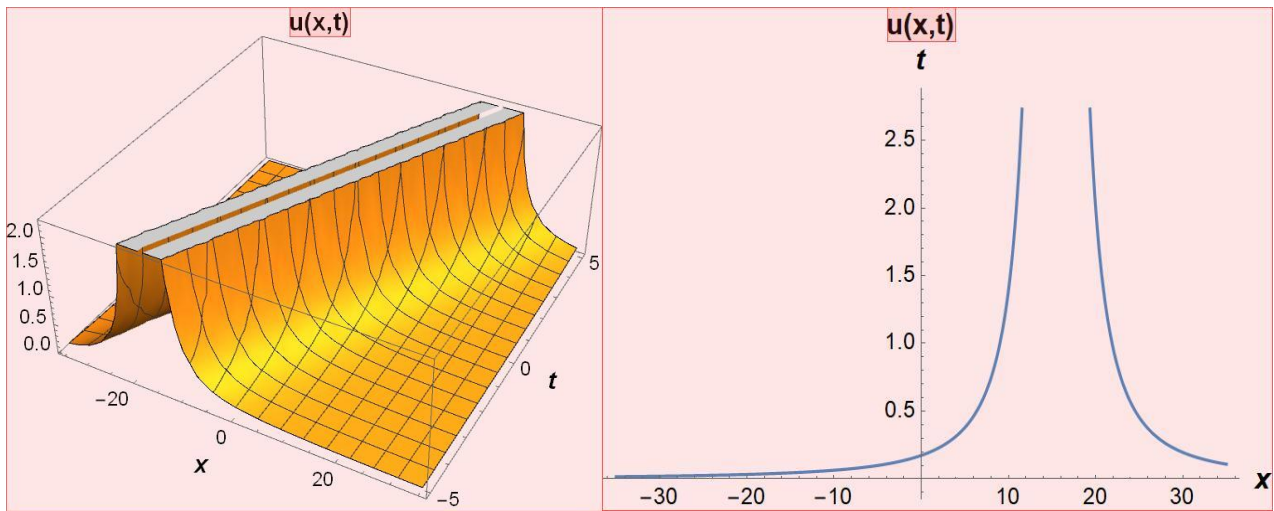
Figure 3. Graph of the solution (67) is indicated at $\tau_0 = -1$, $\tau_1 = 2$, $\xi_1 = 4$, $\xi_2 = 1$, $\alpha_1 = -2$, $\alpha_3 = -2$, $\alpha_4 = 1$, $\gamma = 3$, $-35 \leq x \leq 35$, $-5 \leq t \leq 5$ and the second graph denotes the exact solution of Eq. (67) for $t = 4.5$.
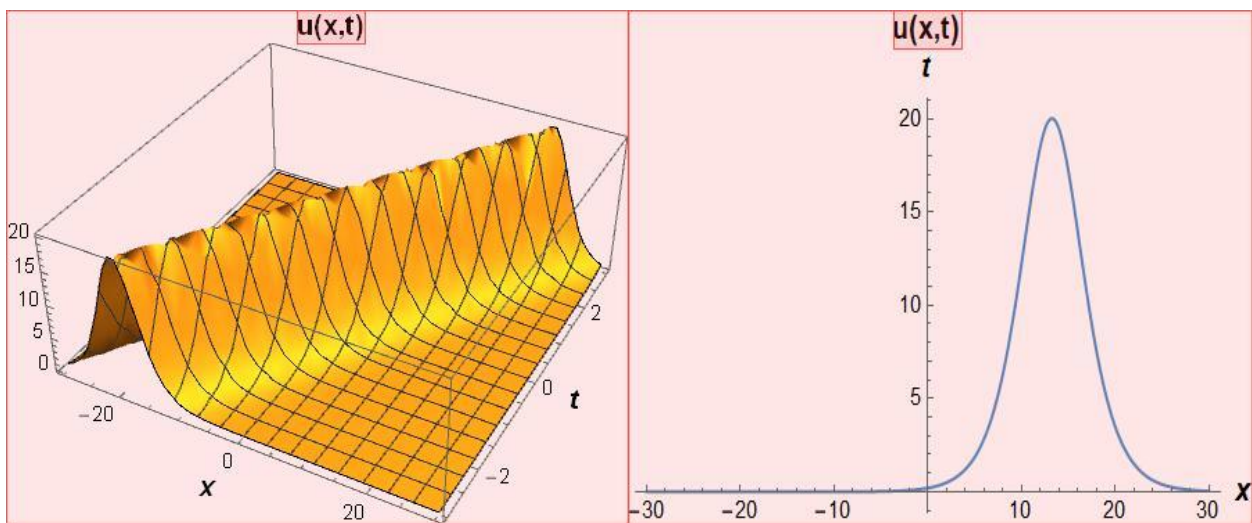
148

Figure 4. Graph of the solution (68) is indicated at $\tau_0 = -2$, $\tau_1 = 5$, $\xi_1 = 3$, $\xi_2 = 1$, $\alpha_1 = -3$, $\alpha_2 = 1$, $\alpha_3 = -1$, $\alpha_4 = 2$, $\gamma = 4$, $-30 \leq x \leq 30$, $-3 \leq t \leq 3$ and the second graph denotes the exact solution of Eq. (68) for $t = 2$.
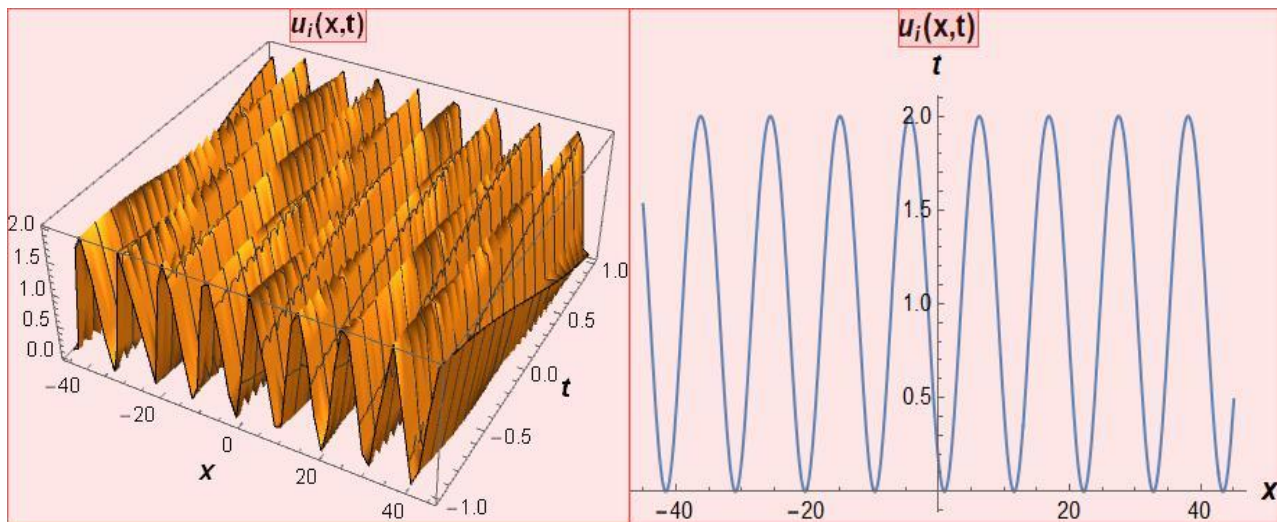
Figure 5. Graph of the solution (70) is indicated at $\tau_0 = -1,\ \tau_1 = 1,\ \xi_1 = 2,\ \xi_2 = 4,\ \alpha_1 = -1,\ \alpha_2 = 5,\ \alpha_3 = -3,\ \alpha_4 = 3,$ $\gamma = 2,\ -45 \le x \le 45,\ -1 \le t \le 1$ and the second graph denotes the exact solution of Eq. (70) for $t = 0.5$.

4. CONCLUSIONS

In this work, we get travelling wave solutions of the DGHDE and strain wave equation by using ETEM. It is necessary to note that ETEM presents powerful mathematical tool for finding the exact solutions of these equations and this method is highly efficient in the matter of seeking for new solutions such as soliton solutions, rational, Jacobi elliptic, periodic wave solutions and hyperbolic function solutions.

5. REFERENCES

[1] Wazwaz AM. The Hirota's direct method and the tanh–coth method for multiplesoliton solutions of the Sawada–Kotera–Ito seventh-order equation, Applied Mathematics and Computation. 2008;199:133–8.

[2] Pelap F, Kamga J, Fomethe A, Kenfack A, Faye M. Wave dynamics in a modified quintic complex Ginzburg-Landau system. Phys. Lett. A. 2009;373:1015-8.

[3] Pandir Y, Ekin A. Dynamics of combined soliton solutions of unstable nonlinear Schrodinger equation with new version of the trial equation method. Chinese Journal of Physics. 2020;67:534-43.

[4] Rizvi STR, Ali K, Sardar A, Younis M, Bekir A. Symbolic computation and abundant travelling wave solutions to KdV-mKdV equation. Pramana. 2017;88(16):1-6.

[5] Irshad A, Mohyud-Din ST. Tanh-Coth Method for Nonlinear Differantial Equations. *Studies in Nonlinear Sciences*, 2012;3(1):24-48.

[6] Pandir Y, Gurefe Y, Kadak U, Misirli E. Classification of exact solutions for some nonlinear partial differential equations with generalized evolution. Abstract and Applied Analysis. 2012;2012:1-16.

[7] Bulut H, Pandir Y. Tuluce Demiray S. Exact Solutions of Nonlinear Schrodinger's Equation with Dual Power-Law Nonlinearity by Extended Trial Equation Method. Waves in Random and Complex Media. 2014;24(4):439-51.

[8] Younas U, Seadawy AR, Younis M, Rizvi STR. Dispersive of propagation wave structures to the dullin-GottwaldHolm dynamical equation in a shallow water waves. Chinese Journal of Physics. 2020;68:348-64.

[9] Octavian GM. Global conservative solutions of the Dullin-Gotwald-Holm Equation. Dıscrete and contınuous. 2007;19(3):575-94.

[10] Raddadi MH, Younis M, Seadawy AR, Rehman SU, Bilal M, Rizvi STR, Althobaiti A. Dynamical behaviour of shallow water waves and solitary wave solutions of the Dullin-Gottwald-Holm dynamical system. Journal of King Saud University-Science. 2021;33(101627):1-9.

[11] Gupta RK, Anupma B. The Dullin-Gottwald-Holm Equation: Classical Lie Approach and Exact Solutions. International Journal of Nonlinear Science. 2010;2(10):146-52.

[12] Ayati Z, Hosseini K, Mirzazadeh M. Application of Kudryashov and functional variable methods to the strain wave equation in microstructured solids. Nonlinear Engineering. 2017;6(1):25–9.

[13] Kumar S, Kumar A, Wazwaz AM. New exact solitary wave solutions of the strain wave equation in microstructured solids via the generalized exponential rational function method. The European Physical Journal Plus. 2020;135(870):1-17.

[14] Hafez MG, Akbar MA. An exponential expansion method and its application to the strain wave equation in microstructured solids. Ain Shams Engineering Journal. 2015;6:683-90.

149

Türk Doğa ve Fen Dergisi
Turkish Journal of Nature and Science
www.dergipark.gov.tr/tdfd

Railway Security System Design Using Unmanned Aerial Vehicle Image Processing and Deep Learning Methods

Muzaffer EYLENCE[1], Mehmet YÜCEL[1], M. Melikşah ÖZMEN[1], Bekir AKSOY[1*]

[1] Isparta University of Applied Sciences, Technology Faculty, Mechatronic Engineering Department, Isparta, Türkiye

Muzaffer EYLENCE ORCID No: 0000-0001-7299-8525
Mehmet YÜCEL ORCID No: 0000-0002-4100-5831
Mustafa Melikşah ÖZMEN ORCID No: 0000-0003-3585-0518
Bekir AKSOY ORCID No: 0000-0001-8052-9411

Corresponding author: bekiraksoy@isparta.edu.tr

Keywords
Deep Learning,
Image Processing,
Unmanned Aerial Vehicle

Abstract: With the developing technology, technological blessings make human life easier and help them every day. Unmanned aerial vehicles (UAV), which is one of the technological blessings, have shown themselves in many fields, especially in fields such as the military, defence industry, photography, and hobby. With the development of defence systems with UAVs, the security of railways has also been left to UAVs. In this study, while the foreign matter separation is made on the railway by using the deep learning model in real-time, the image taken on the UAV is simultaneously controlled by using the image processing method. The fact that the deep learning model has a 0.99 mAP rate increases the reliability of the model.

150

İnsansız Hava Aracı ile Görüntü İşleme ve Derin Öğrenme Yöntemleri Kullanılarak Demiryolu Güvenlik Sistemi Tasarımı

Anahtar Kelimeler
Derin Öğrenme,
Görüntü İşleme,
İnsansız Hava Aracı

Öz: Gelişen teknoloji ile her geçen gün teknolojik nimetler insan hayatını kolaylaştırmakta ve onlara yardım etmektedir. Teknolojik nimetlerden olan insansız hava araçları (İHA) askeri, savunma sanayi, fotoğrafçılık ve hobi gibi alanlar başta olmak üzere birçok alanda kendisini göstermiştir. İHA ile savunma sistemlerinin gelişmesiyle birlikte demiryollarının güvenliği de İHA'lara bırakılmaya başlanılmıştır. Bu çalışmada İHA üzerinden alınan görüntü gerçek zamanlı olarak derin öğrenme modeli kullanılarak demiryolu üzerinde yabancı madde ayrımı yapılırken eş zamanlı olarak görüntü işleme metodu kullanılarak demiryolunun sağlamlığı kontrol edilmektedir. Derin öğrenme modelinin 0.99 mAP oranına sahip olması modelin güvenirliliğini artırmaktadır.

1. INTRODUCTION

Today, the use of public transportation vehicles is increasing with the decrease in energy resources and the increase in costs [1]. Among the public transport vehicles, rail transport is the most efficient, cost-effective, and convenient means of transportation. It has lower fuel costs, can carry large loads, is environmentally friendly, and is safer because it is not affected by weather conditions as in air transportation [2]. Therefore, rail transport has become the backbone of every developing country. One of the most important components that make rail transport safe is its infrastructure. The railway infrastructure usually consists of sleepers installed at regular intervals between them and steel rails supported

by the ballast structure. Steel rails in train transportation directly affect passenger safety and comfort as transportation infrastructure. The deterioration of the railway line, the wear of the materials on the lines over time, foreign materials falling on the railway, and deliberate sabotage on the railway put the safety of railway passengers at risk. Considering all these factors, a fast and efficient inspection system is required to ensure the safety of railways [3-5].

Railway inspection is of critical importance to ensure the safety of railway traffic and protect human health [6]. Most of the inspection processes in use today are done visually. In this method, which is traditionally called, the detection of any damage to the railway components or a

Tr. Doğa ve Fen Derg. Cilt 11, Sayı 3, Sayfa 150-154, 2022

Tr. J. Nature Sci. Volume 11, Issue 3, Page 150-154, 2022

foreign substance is carried out by the assigned people walking along the rail [7]. However, performing this process manually with an auditor is slow, costly, dangerous, and labour-intensive. As a result of the increase in the number of railway networks, the frequency of inspection studies with traditional methods is decreasing [2]. This situation creates a risk in transportation by causing the defects in the railway not to be detected in a timely manner. Therefore, to eliminate these risks, the disadvantages of traditional methods should be overcome. Compared to traditional methods, ultrasonic, acoustic, emission, and eddy current-based techniques are also used. However, such techniques can be applied with train movement and cannot provide information about the size of the defect [8,9].

Recently, rail companies around the world have been working on autonomous inspection systems that can more efficiently inspect railroad defects. With the development of autonomous control systems, more advanced control techniques have been designed to overcome the shortcomings of traditional methods [10, 11]. Among these techniques is the use of UAVs. Unmanned aerial vehicles are systems that can fly controlled or autonomously without the need for a pilot. Today, it is frequently preferred in military, health, commercial, scientific studies, and civil aviation studies. In addition, more efficient systems can be designed by integrating deep learning and image processing techniques into unmanned aerial vehicles [12]. Deep learning is based on the principle that a set of pictures, video, or audio data is analyzed with certain algorithms to give an estimated value as output. Applications such as product classification, object counting, and face recognition can be given as examples of deep learning study areas [10,13].

In line with this study, an autonomous system has been developed with the UAV by using deep learning and image processing techniques. The system is flying along a railway and collecting images via the camera on it. While the collected images are checked for the integrity of the railway bypassing through histogram equalization and gaussian filtering processes, the same images are simultaneously analyzed with YOLO v5, one of the deep learning algorithms, to check whether there is a foreign substance on the railway. As a result of the deep learning output, it can be determined whether there are defects in the railway and whether there is any sabotage situation [14].

2. MATERIAL AND METHOD

The methods used in the study, the creation of the data set, the deep learning algorithm, and performance evaluation metrics were examined as three sub-titles and discussed in detail below. The method part of the study was carried out as shown in the workflow diagram given in Figure 4.

2.1. Material

In the study, a system proposal developed by using image processing methods based on an artificial intelligence system was made in order to detect foreign materials on the train tracks and to control the integrity of the rails. In the study, it was trained with the data set obtained using the YOLOv5 deep learning network. The accuracy of the deep learning network, whose training was completed, was evaluated according to the mAP, precision, and recall metrics.

2.1.1. Create datasets

The data set was carried out by taking pictures of foreign materials placed on the railways in different locations in Isparta province with a drone. The photographs were collected in different time periods at different angles and at different distances. Figure 1 shows some photos of the data set. The data set includes a total of 785 photographs of foreign substances. At the same time, there is a video of 3 minutes and 23 seconds in which the drone flies on the railway to check the image processing methods and the stability of the train tracks in the dataset.

Figure 1. Datasets

2.1.2. Yolo v5

YOLO v5 network is the latest version among YOLO architectures as of 2022. It gives fast and high accuracy compared to other versions [15]. YOLO networks are algorithms used for object recognition using convolutional neural networks developed by Joseph Redmon in 2016 [16]. There is no official article for YOLO v5 at the time of preparation of this article, as the YOLO v5 network is published by different developers and not by the official publisher [17]. The YOLO v5 network uses the spine, neck, and head structure that we frequently encounter in object recognition processes. While the objects trained on ImageNet are used as backbones, the bounding boxes of the objects are called heads, and the YOLO, which is used for object detection, is called the spine [18]. The YOLOv5 network is presented in 4 different models. These are YOLOv5s, YOLOv5l, YOLOv5m, and YOLOv5x [19]. Figure 2 shows the YOLOv5 architecture.
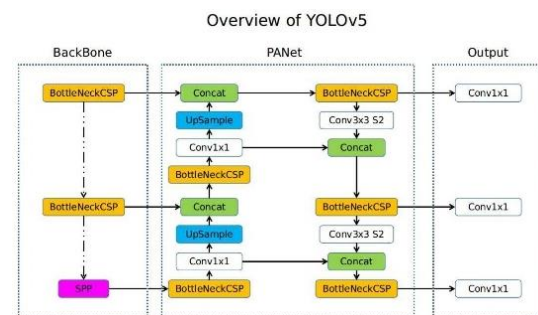
Figure 2. Yolo v5 Architecture

2.1.1. Histogram equalization

Images taken from the camera have RGB color space. The pixel values of an image in the RGB color space have three elements, so the images are converted to gray format, that is, the pixel values between 0-255, to perform the operations quickly in computer vision processes [20]. Histogram equalization is used to provide color distribution by distributing the clustered pixels in the images equally to all sides [21]. With histogram equalization method, it is a method that is frequently used to reveal the shapes that are not clear on the image, with low brightness or in the dark region [20]. In Figure 3, the original image is shown with the histogram equalization method applied on an image.
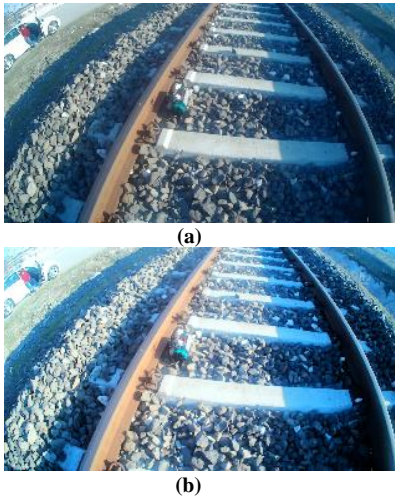

(a)

(b)

Figure 3. Histogram Equalization (a) Original Image b) Histogram Equalized Image

2.1.1. Gussian filter

It is the method used for blurring the picture. The blurring process is used to reduce the noise on the picture and to determine the edges. It is obtained by multiplying the two-dimensional convolution matrix with the image pixels [22]. With the Gussian filter, it is aimed to equalize the frequency on the image and increase the view on the image [23]. It is the method used for blurring the picture. The blurring process is used to reduce the noise in the picture and to determine the edges. It is obtained by multiplying the two-dimensional convolution matrix with the image pixels. The formula for the Gaussian filter is given in equation 1.

$$G(x) = \frac{1}{\sqrt{2\pi\sigma}} e^{-\frac{x^2}{2\sigma}} \tag{1}$$

2.1.1. Performance evaluation metrics

Deep learning results are evaluated according to certain metric values. Details about mAP, precision, and recall being used in this study are given below. The mAP value is the value that measures the accuracy of the location of the bounding boxes to evaluate the object recognition algorithms between 0-1 [24,25]. It means the average of the AP value. The closer the mAP value is to 1, the more accurate the model is found to make predictions. The equation of the mAP metric is given in equation 2 [24].

$$mAP = \frac{1}{N} \sum_i AP_i \tag{2}$$

Precision is the metric that gives us how many of the values we consider positive in the confusion matrix. Precision value is used to evaluate the closeness between the measured value and the actual value. In Equation 3, the equation of the precision metric is given.

$$Precision = \frac{TP}{TP + FP} \tag{3}$$

The recall is the value that gives how many of the images we evaluate positive are positive. It represents the ratio between the samples taken and the samples detected. In Equation 4, the equation of the recall metric is given.

$$Recall = \frac{TP}{TP + FN} \tag{4}$$

2.2. Methods

The workflow diagram of the study is given in Figure 4. First, the dataset was created to feed and train the YOLO v5 network. Labelling was performed on the dataset on the roboflow framework. The data set, which was prepared for the training phase, was put into training on Google Collab, and the weights trained in the YOLO v5 network were downloaded to the computer. At the same time, an image processing system to control the integrity of the railway was prepared, and the two methods were combined. The real-time image is simultaneously inserted into both the image processing method and the deep learning network, and the results are displayed in an interface.

152

Figure 4. Workflow diagram

3. RESULTS

The findings obtained as a result of the study are given below. YOLO v5 network training results are based on mAP, precision, and recall values. 785 images were used in the data set. The images were separated as test and training data after labelling. While 628 images were used in the training dataset, 157 images were used in the test dataset. Figure 5 shows the mAP graph of the YOLO v5 network. A precision graph of YOLO v5 network is given in Figure 6. Figure 7 shows the recall graph of the YOLO v5 network.
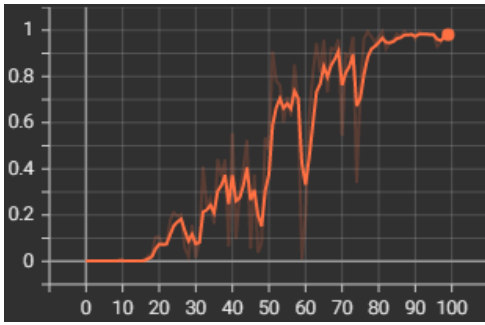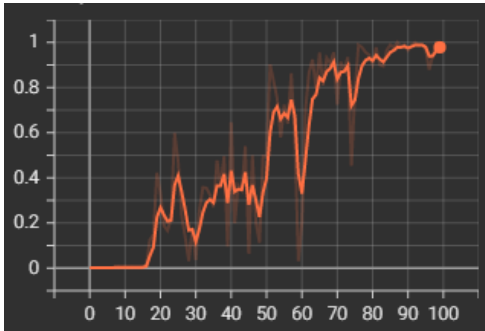
Figure 5. mAP graph
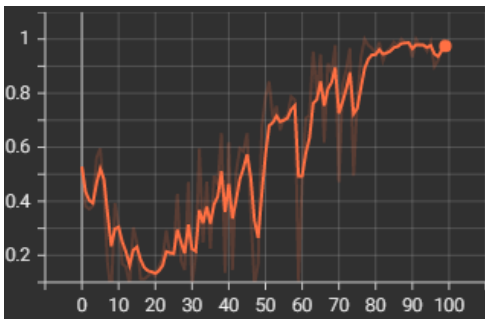

Figure 6. Precision graph

Figure 7. Recall graph

The table where the graphic values are given is shown in Table 1 below.

Table 1. Performance Evaluation Metrics

Metrics	Value
MAP	0.995
PRECISION	0.978
RECALL	1

When the training result values of the YOLO v5 network are examined, it is observed that the trained model performs the prediction process with high accuracy.

4. DISCUSSION AND CONCLUSION

As a result of the work done, it is a tiring and time-consuming process to determine the soundness of the railway and the detection of foreign matter by walking thousands of kilometres. In our proposed system, a UAV has been developed to detect foreign materials on the railway by flying along the railway and to warn the officials by checking the soundness of the railway. Future studies it is aimed to train on new models by increasing and diversifying the number of images in the data set. At the same time, it is aimed to carry out new studies on the integrity of the railway by using deep learning methods.

REFERENCES

[1] Sonay Görgülü Balcı. Hafif raylı sistemlerde lazerli engel algılayıcı sistem tasarımı [dissertation]. Kırıkkale üniversitesi; 2014.

[2] Feng H, Jiang Z, Xie F, Yang P, Shi J, Chen L. Automatic Fastener Classification and Defect Detection in Vision-Based Railway Inspection Systems. IEEE Transactions on Instrumentation and Measurement. 2014;63(4):877-888.

[3] Shah A, Bhatti N, Dev K, Chowdhry B. Muhafız: IoT-Based Track Recording Vehicle for the Damage Analysis of the Railway Track. IEEE Internet of Things Journal. 2021;8(11):9397-9406.

[4] Aydin I, Sevi M, Sahbaz K, Karakose M. Detection of Rail Defects with Deep Learning Controlled Autonomous UAV. Sakheer, Bahrain: Sakheer, Bahrain; 2021.

[5] Kaya V, Baran A, Tuncer S. Dinamit Destekli Terör Faaliyetlerinin Önlenmesi İçin Derin Öğrenme Temelli Güvenlik Destek Sistemi. European Journal of Science and Technology. 2021;.

[6] Shafique R, Siddiqui H, Rustam F, Ullah S, Siddique M, Lee E et al. A Novel Approach to Railway Track Faults Detection Using Acoustic Analysis. Sensors. 2021;21(18):6221.

[7] Aydın I, Güçlü E, Akın E. Mask R-CNN Algoritmasını Kullanarak Demiryolu Travers Eksikliklerinin Tespiti İçin Otonom İHA Tasarımı. Fırat Üniversitesi Mühendislik Bilimleri Dergisi. 2022.

[8] Zhang H, Jin X, Wu Q, Wang Y, He Z, Yang Y. Automatic Visual Detection System of Railway Surface Defects With Curvature Filter and Improved Gaussian Mixture Model. IEEE Transactions on Instrumentation and Measurement. 2018;67(7):1593-1608.

[9] Singh M, Singh S, Jaiswal J, Hempshall J. Autonomous Rail Track Inspection using Vision Based System. 2006 IEEE International Conference on Computational Intelligence for Homeland Security and Personal Safety. 2006.

[10] Faghih-Roohi S, Hajizadeh S, Nunez A, Babuska R, De Schutter B. Deep convolutional neural networks for detection of rail surface defects. 2016 International Joint Conference on Neural Networks (IJCNN). 2016.

[11] Jing, G., Qin, X., Wang, H., & Deng, C. (2022). Developments, challenges, and perspectives of railway inspection robots. Automation in Construction, 138, 104242.

[12] Mardiana, S., Hamdani, D., Chaniago, M. B., Wahyu, A. P., Heryono, H., & Suhendri, S. (2022). Information System for Railway Inspection using Drone and Image Processing.

[13] Bayhan E, Ozkan Z, Namdar M, Basgumus A. Deep Learning Based Object Detection and Recognition of Unmanned Aerial Vehicles. 2021 3rd International Congress on Human-Computer Interaction, Optimization and Robotic Applications (HORA). 2021.

[14] Gasparini, R., D'Eusanio, A., Borghi, G., Pini, S., Scaglione, G., Calderara, S., ... & Cucchiara, R.

153

(2021, January). Anomaly Detection, Localization and Classification for Railway Inspection. In 2020 25th International Conference on Pattern Recognition (ICPR) (pp. 3419-3426). IEEE.

[15] Yan B, Fan P, Lei X, Liu Z, Yang F. A Real-Time Apple Targets Detection Method for Picking Robot Based on Improved YOLOv5. Remote Sensing. 2021;13(9):1619.

[16] Redmon, J., Divvala, S., Girshick, R., & Farhadi, A. You only look once: Unified, real-time object detection. In Proceedings of the IEEE conference on computer vision and pattern recognition 2016. p. 779-788.

[17] GitHub - ultralytics/yolov5: YOLOv5 🚀 in PyTorch > ONNX > CoreML > TFLite [Internet]. GitHub. 2022 [cited 20 Apr. 2022]. Available from: https://github.com/ultralytics/yolov5

[18] Murat S. İnsansız Hava Aracı Görüntülerinden Derin Öğrenme Yöntemleriyle Nesne Tanıma [YL]. Maltepe Üniversitesi; 2021.

[19] Wang Z, Wu L, Li T, Shi P. A Smoke Detection Model Based on Improved YOLOv5. Mathematics. 2022;10(7):1190.

[20] Bulut F. Değiştirilmiş Ayrık Haar Dalgacık Dönüşümü ile Yeni Bir Histogram Eşitleme Yöntemi. Mühendislik Bilimleri ve Tasarım Dergisi. 2022;10(1):188-200.

[21] Jebadass J, Balasubramaniam P. Low light enhancement algorithm for color images using intuitionistic fuzzy sets with histogram equalization. Multimedia Tools and Applications. 2022;81(6):8093-8106.

[22] Cifci, M. (2022). Derin Öğrenme Metodu Kullanarak BT Görüntülerinden Akciğer Kanseri Teşhisi . Dokuz Eylül Üniversitesi Mühendislik Fakültesi Fen ve Mühendislik Dergisi , 24 (71) , 487-500 . DOI: 10.21205/deufmd.2022247114

[23] Öztürk, A. İ. , Yıldırım, O. , Ateş, Y. & Kuru, A. (2022). Böbrek Görüntülerinde Filtreleme Tekniği Kullanarak Kist Belirlenmesi . Avrupa Bilim ve Teknoloji Dergisi , (38) , 198-204 . DOI: 10.31590/ejosat.1086788

[24] Cartucho J, Ventura R, Veloso M. Robust Object Recognition Through Symbiotic Deep Learning In Mobile Robots. 2018 IEEE/RSJ International Conference on Intelligent Robots and Systems (IROS). 2018.

[25] Qi J, Liu X, Liu K, Xu F, Guo H, Tian X et al. An improved YOLOv5 model based on visual attention mechanism: Application to recognition of tomato virus disease. Computers and Electronics in Agriculture. 2022;194:106780.

154

Türk Doğa ve Fen Dergisi
Turkish Journal of Nature and Science

www.dergipark.gov.tr/tdfd

New Amino Acid Chalcone Conjugates: Synthesis, Characterization and Dielectric Properties

Eray ÇALIŞKAN*1

1Bingol University, Faculty of Science and Arts, Chemistry Department, Bingöl, Türkiye
Eray ÇALIŞKAN ORCID No: 0000-0003-2399-4100

*Corresponding author: ecaliskan@bingol.edu.tr

Abstract: In this study, two novel amino acid chalcone compounds were synthesized through a reaction of Fmoc group-protected L-phenylalanine and two amino chalcone derivatives. Target compounds contain dimethoxy and trimethoxy substitutions. The structures of the synthesized compounds were characterized by elemental analysis, 1H and 13C APT NMR spectroscopy techniques. Dielectric parameters such as dielectric constant, dielectric loss and ac conductivity were measured and the results showed that dielectric constant of trimethoxy conjugate was two times higher than dimethoxy conjugate.

Yeni Amino Asit Kalkon Konjugatları: Sentez, Karakterizasyon ve Dielektrik Özellikler

Öz: Bu çalışmada, Fmoc grubu korumalı L-fenilalanin ve iki amino kalkon türevinin reaksiyonu yoluyla iki yeni amino asit kalkon bileşiği sentezlendi. Hedef bileşikler, dimetoksi ve trimetoksi sübstitüe kalkon yapılarını barındırmaktadır. Sentezlenen bileşiklerin yapıları element analiz, 1H ve 13C APT NMR spektroskopi teknikleri ile aydınlatılmıştır. Bileşiklere ait dielektrik sabiti, dielektrik kayıp ve ac iletkenlik gibi dielektrik parametreler ölçülmüş ve sonuçlar trimetoksi taşıyan konjugatın dielektrik sabitin dimetoksili konjugattan yaklaşık iki kat yüksek olduğunu göstermektedir.

155

1. INTRODUCTION

Chalcone derivatives are one of the subgroups of compounds called flavonoids in the 15-carbon 1,3-diphenylpropane skeleton with the basic structure of two phenyls and one propane chain combined [1-4]. Different members of flavonoids can be obtained by arranging this 15-carbon skeleton in different ways and by attaching different substituents to the rings. Studies have highlighted chalcone compounds as one of the most important members of flavonoids [5-7]. Chalcone and its derivatives have great importance in the field of chemistry and physics due to their photophysical and photochemical properties [8]. Several compounds containing natural and synthetic chalcone rings have broad fluorescence activity in the visible region. That is why chalcones and their derivatives have been used in several application areas due to their strong fluorescence in the UV and visible regions [9-11].

Amino acid conjugates are the name given to new compounds obtained as a result of the chemical bonding of amino acids with another group of organic compounds [12-15]. Amino acids are biologically very important compound groups. Therefore, it is aimed to obtain more effective compounds by interacting with compound groups such as vitamins, hormones, heterocyclic compounds, and drugs [16-19]. In addition to their biological importance, they can be used in different application areas by interacting with physically active compounds.

In this study, two new hybrid compounds were obtained by the reaction of Fmoc-protected phenylalanine with chalcones bearing dimethoxy and trimethoxy groups. Dielectric parameters of the target compounds were measured and compared to each other. The results indicate that trimethoxy substituted conjugate has higher dielectric constant than dimethoxy conjugates.

## 2. MATERIAL AND METHOD

2-chloro-4,6-dimethoxy-1,35-triazine (CDMT), N-methyl morpholine (NMM), sodium hydroxide (NaOH), ethanol (EtOH) and acetonitrile (MeCN) were purchased from Sigma-Aldrich used in the synthesis steps, DMSO-d6 used in NMR analysis were obtained from Merck.

The structures were characterized by using NMR Spectra Bruker Avance III–400. The dielectric analysis was recorded using a QuadTech 7600 LRC impedance analyzer. The elemental analysis data were obtained using a LECO CHNS elemental analyzer.

2.1. General Synthesis Method

4-amino acetophenone (1.0 eq) was taken into a reaction flask that contained 50 ml of ethanol and stirred until completely dissolved. 30% of NaOH solution was added to the flask and color change was observed. After 15 minutes, aromatic aldehyde (1.0 eq.) was added to the reaction mixture. The reaction was monitored by thin layer chromatography (TLC) and after the completion of the reaction, the solvent of the mixture was removed and the residue dissolved small amount of acetone (10 ml). The residue was added to water to obtain a precipitate. Yellow color solid was formed, filter and dried [20]. Yields were up to 90%. The general synthesis way was given in Scheme 1.
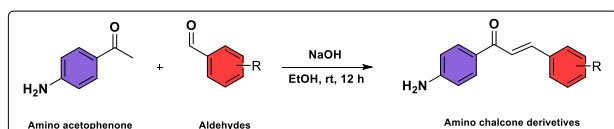
Scheme 1. General synthesis method of chalcones

Fmoc group protected-amino acid (1.00 mmol), CDMT (1.1 mmol), and the amino chalcone derivative were added to the one-necked reaction flask that contain acetonitrile (80 ml). At room temperature, N-methyl morpholine (1.5 mmol) is added dropwise to the reaction mixture. The reaction is followed by thin layer chromatography. The solvent of the terminated reaction is removed under reduced pressure. Precipitation is observed after the reaction mixture was added in water and in the first stage mixture was completely dissolved. After a while, the precipitation occurred. The target product, which is separated from the mixture by filtration, is left to dry. Yellow color solids were obtained with up to %85 yields [21].
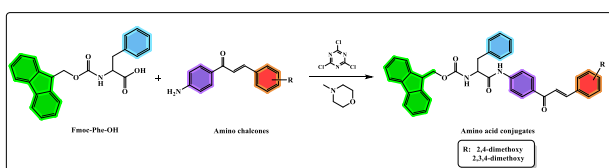
Scheme 2. General synthetic route for amino acid conjugates

(E)-1-(4-aminophenyl)-3-(2,4-dimethoxyphenyl)prop-2-en-1-one
1H NMR (400 MHz, DMSO-d6) δ 3.84 (s, 3H, -OCH$_3$), 3.90 (s, 3H, -OCH$_3$), 6.09 (s, 2H), 6.65 – 6.60 (m, 4H), 7.72 – 7.67 (d, J = 17.0 Hz, 1H), 7.89 – 7.86 (m, 3H). 13C APT NMR: 56.1, 56.6, 99.8, 106.2, 115.6, 118.3, 121.6, 128.2, 130.5, 133.3, 141.2, 143.6, 155.2, 160.1, 188.7. Elemental Analysis: (theoretical) C, 72.07; H, 6.05; N, 4.94, (experimental) C, 72.14; H, 6.12; N, 4.98.

## (E)-1-(4-aminophenyl)-3-(2,3,4-trimethoxyphenyl)prop-2-en-1-one
^{1}H NMR (400 MHz, DMSO-d$_6$) δ 3.79 (s, 3H, -OCH$_3$), 3.86 (s, 3H, -OCH$_3$), 3.87 (s, 3H, -OCH3), 6.13 (s, 2H), 6.64 – 6.62 (m, 2H), 6.92 – 6.90 (d, J = 8.8 Hz, 1H), 7.79 – 7.72 (m, 3H), 7.91 – 7.89 (m, 2H). ^{13}C APT NMR: 56.5, 59.9, 60.1, 104.0, 115.2, 121.6, 122.9, 128.3, 133.1, 134.0, 141.4, 143.3, 149.7, 155.6, 156.0, 188.1. Elemental Analysis: (theoretical) C, 69.00; H, 6.11; N, 4.47; (experimental) C, 69.05; H, 6.16; N, 4.50

(9H-fluoren-9-yl)methyl(E)-(1-oxo-3-phenyl-1-((4-(3-(2,3,4-trimethoxyphenyl)acryloyl)phenyl)amino)propan-2-yl)carbamate
^{1}H NMR (400 MHz, DMSO-d$_6$) δ 10.55 (s, 1H), 8.16 (d, J = 8.4 Hz, 2H), 7.97 – 7.85 (m, 6H), 7.84 – 7.79 (m, 3H), 7.68 (t, J = 8.3 Hz, 2H), 7.45 – 7.37 (m, 4H), 7.31 (t, J = 6.0 Hz, 4H), 7.23 (d, J = 7.5 Hz, 1H), 6.94 (d, J = 9.0 Hz, 1H), 4.48 (td, J = 9.2, 4.5 Hz, 1H), 4.21 (q, J = 6.0, 5.0 Hz, 2H), 3.88 (d, J = 3.3 Hz, 6H), 3.85 (s, 1H), 3.79 (s, 3H), 3.09 (dd, J = 13.9, 4.6 Hz, 1H), 2.93 (dd, J = 13.7, 10.2 Hz, 1H). ^{13}C NMR (DMSO-d$_6$) δ 188.01, 171.77, 156.48, 156.16, 154.21, 153.54, 144.22, 143.58, 142.24, 141.15, 138.33, 138.24, 136.26, 133.19, 131.42, 130.24, 129.40, 128.60, 128.11, 127.77, 127.52, 126.91, 125.83, 125.76, 123.86, 121.87, 121.56, 121.34, 120.81, 119.16, 113.19, 108.94, 66.18, 62.01, 60.95, 57.55, 56.55, 47.03, 37.76. Elemental Analysis: (theoretical) C, 73.88; H, 5.61; N, 4.10; (experimental) C, 73.93; H, 5.66; N, 4.15.

(9H-fluoren-9-yl)methyl(E)-(1-((4-(3-(2,4-dimethoxyphenyl)acryloyl)phenyl)amino)-1-oxo-3-phenylpropan-2-yl)carbamate
^{1}H NMR (400 MHz, DMSO-d$_6$) δ 10.55 (s, 1H), 8.14 (d, J = 8.3 Hz, 2H), 8.01 (d, J = 15.6 Hz, 1H), 7.95 (dd, J = 8.3, 4.7 Hz, 2H), 7.89 (d, J = 7.6 Hz, 3H), 7.85 – 7.76 (m, 3H), 7.68 (t, J = 8.3 Hz, 2H), 7.43 – 7.37 (m, 3H), 7.30 (dd, J = 9.6, 4.5 Hz, 3H), 7.23 (d, J = 7.3 Hz, 1H), 6.65 (d, J = 8.9 Hz, 2H), 6.21 (d, J = 67.1 Hz, 1H), 4.48 (td, J = 9.6, 4.5 Hz, 1H), 4.20 (d, J = 5.4 Hz, 2H), 3.91 (d, J = 7.5 Hz, 3H), 3.85 (d, J = 6.2 Hz, 3H), 3.09 (dd, J = 13.8, 4.6 Hz, 1H), 2.94 (dd, J = 13.6, 10.3 Hz, 1H). ^{13}C NMR (DMSO-d$_6$) δ 188.08, 171.75, 163.49, 160.39, 156.48, 154.06, 144.23, 144.21, 143.43, 141.15, 138.66, 138.24, 136.62, 133.43, 131.30, 130.50, 130.12, 129.74, 129.40, 128.59, 128.10, 127.52, 126.90, 125.75, 121.86, 120.57, 119.18, 116.51, 113.19, 106.81, 98.78, 66.19, 57.55, 56.31, 56.01, 47.04, 37.79. Elemental Analysis: (theoretical) C, 75.44; H, 5.56; N, 4.29; (experimental) C, 75.49; H, 5.61; N, 4.33.
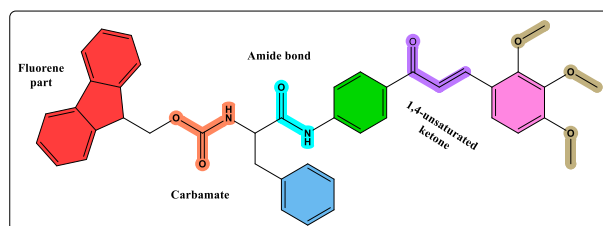
Scheme 3. General structural representation and functional parts of amino acid-chalcone conjugate

3. RESULTS AND DISCUSSION

3.1. Chemistry

In the ^{1}H NMR spectrum of the trimethoxy amino chalcone compound in figure 1a, it is seen that the peak of the three methoxy CH$_3$ protons in the chalcone structure resonates as a singlet at 3.79, 3.86, and 3.87 ppm, and the total number of aromatic and olefinic protons is compatible with the structure. In addition, when the NMR spectrum of the dimethoxy chalcone derivative in Figure 1b is examined, the presence of two methoxy CH$_3$ protons as a singlet at 3.84 and 3.90 ppm and the compatibility of the number of aromatic protons with the structure can be shown as proof of the formation of compounds. When the ^{1}H NMR spectrum of the trimethoxy-containing conjugate is evaluated (Figure 2a), first of all, the presence of 9 chalcone methoxy protons in the aliphatic region, diastereotopic CH$_2$ protons of phenylalanine in the range of 2.90 to 3.11 ppm, and 2 protons of the Fmoc group at 4.18-4.23 ppm indicate that the structure was formed. Therefore, ^{13}C NMR of the same compound is examined, the specific carbonyl of the chalcone compound appeared at 188.01 ppm, the amide carbonyl at 177.77 ppm, and the carbonyl of the Fmoc group appeared at 156.48 ppm. The phenylalanine CH$_2$ carbon at 37.76 ppm and the CH$_2$ carbon belonging to the Fmoc group at 66.18 ppm in the aliphatic region indicate that the target structure was formed.
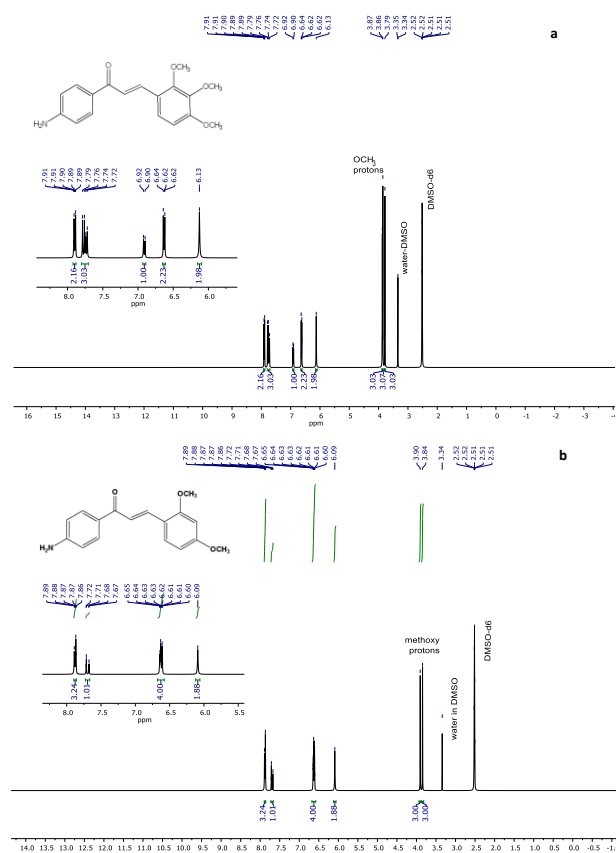

Figure 1. ^{1}H NMR spectra of dimethoxy amino chalcone (a) and trimethoxy (b) compounds
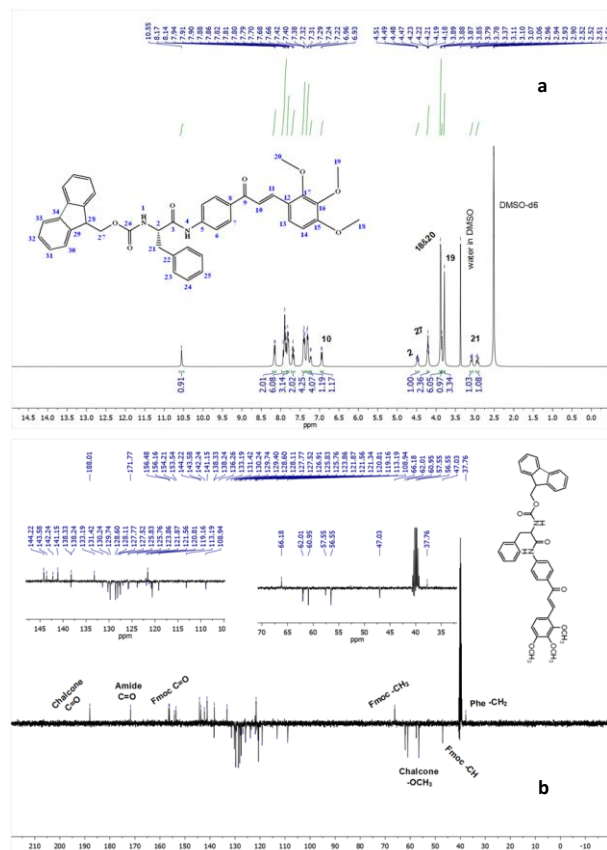

Figure 2. ^{1}H (a) and ^{13}C APT (b) NMR spectra of trimethoxy chalcone conjugates

3.2. Dielectric Studies

Dielectric is a type of insulating material that can be polarized by placing it in an electric field, but unlike a conductor, the electric charge contained in the dielectric does not flow but causes dielectric polarization to occur. Although the term "insulator" also means low electrical conductivity, the term dielectric is often used for insulating materials with a high level of polarization, the magnitude of which is represented by the dielectric constant. The dielectric coefficient (dielectric constant) can be defined as the ratio of the permittivity of the medium to the permittivity of the free space. The higher the permeability, the more the material tends to reduce the area created. If the polarization created by applying an electric field is high for a dielectric material, the dielectric constant will also be high. This is also true for high resistance to electric current flow [22, 23].

Table 1. Dielectric parameters of conjugates at 1KHz frequency

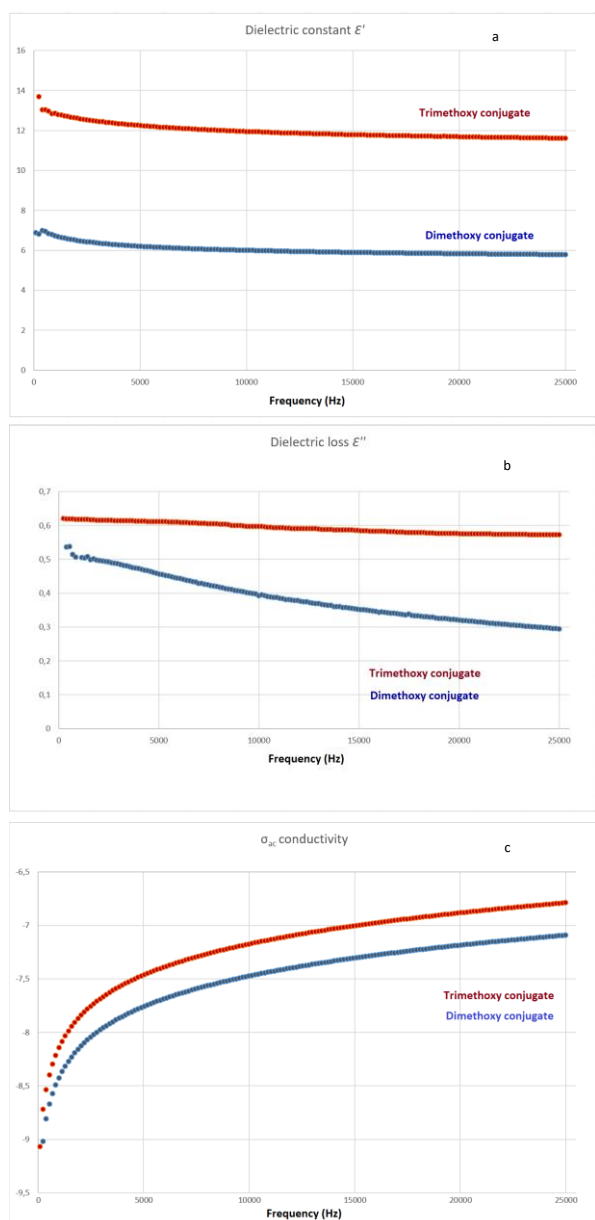| Entry	Dielectric constant (Ɛ')	Dielectric loss (Ɛ'')	Conductivity σ_{ac} (S cm^{-1})
Fmoc-Phe-trimethoxy-chalcone	11.93	0.596	6.64 x 10^{-8}
Fmoc-Phe-dimethoxy-chalcone	5.98	0.392	3.34 x 10^{-8}

Figure 3. (a) dielectric constant, (b) dielectric loss, (c) ac conductivity results of target compounds

Dielectric parameters of organic and inorganic compounds in which different chalcone structures are substituted were studied. In studies conducted by Koran et al., dielectric constants of methoxy chalcone compounds bonded to phosphazene compounds as hexa-substituted were determined in the range of 1.5 to 2.8. On the other hand, in another study [24], the dielectric properties of methacrylate polymers with chalcone in the side chain were examined and the dielectric constant was found to be 3.33. Compared to the results obtained in other studies [19, 25-31], trimethoxy and dimethoxy conjugates showed considerable dielectric properties. The presence of an extra methoxy group caused extra polarization in the compound and the dielectric constant was higher than the dimethoxy derivative.

4. CONCLUSION

In this work, the synthesis of new amino acid conjugates was successfully completed by following the triazine methodology in high yields. It seems possible that the target compounds have promising dielectric properties and can be used in application areas such as capacitors with various modifications. The obtained compounds have the potential to be used in optical and physical applications.

STATEMENT OF CONFLICT OF INTEREST

The author declared no conflict of interest regarding this article.

REFERENCES

[1] Irfan R, Mousavi S, Alazmi M, Saleem RSZ. A Comprehensive Review of Aminochalcones. Molecules. 2020;25(22):5381.

[2] Lu C-F, Wang S-H, Pang X-J, Zhu T, Li H-L, Li Q-R, et al. Synthesis and Biological Evaluation of Amino Chalcone Derivatives as Antiproliferative Agents. Molecules. 2020;25(23):5530.

[3] Zhuang C, Zhang W, Sheng C, Zhang W, Xing C, Miao Z. Chalcone: A Privileged Structure in Medicinal Chemistry. Chemical reviews. 2017;117(12):7762-810.

[4] Dimmock JR, Elias DW, Beazely MA, Kandepu NM. Bioactivities of chalcones. Curr Med Chem. 1999;6(12):1125-49.

[5] Dan W, Dai J. Recent developments of chalcones as potential antibacterial agents in medicinal chemistry. European Journal of Medicinal Chemistry. 2020;187:111980.

[6] Rozmer Z, Perjési P. Naturally occurring chalcones and their biological activities. Phytochemistry Reviews. 2016;15(1):87-120.

[7] Singh P, Anand A, Kumar V. Recent developments in biological activities of chalcones: A mini review. European Journal of Medicinal Chemistry. 2014;85:758-77.

[8] Das M, Manna K. Chalcone Scaffold in Anticancer Armamentarium: A Molecular Insight. Journal of Toxicology. 2016;2016:7651047.

[9] Yun S-W, Kang N-Y, Park S-J, Ha H-H, Kim YK, Lee J-S, et al. Diversity Oriented Fluorescence Library Approach (DOFLA) for Live Cell Imaging Probe Development. Accounts of Chemical Research. 2014;47(4):1277-86.

[10] Sebti Sd, Solhy A, Smahi A, Kossir A, Oumimoun H. Dramatic activity enhancement of natural phosphate catalyst by lithium nitrate. An efficient synthesis of chalcones. Catalysis Communications. 2002;3(8):335-9.

[11] Wang M, Xu S, Wu C, Liu X, Tao H, Huang Y, et al. Design, synthesis and activity of novel sorafenib analogues bearing chalcone unit. Bioorganic & Medicinal Chemistry Letters. 2016;26(22):5450-4.

[12] Clifford MN, Knight S. The cinnamoyl–amino acid conjugates of green robusta coffee beans. Food Chemistry. 2004;87(3):457-63.

158

[13] Bhuniya S, Park SM, Kim BH. Biotin–Amino Acid Conjugates: An Approach Toward Self-Assembled Hydrogelation. Organic Letters. 2005;7(9):1741-4.

[14] Ishii H, Minegishi M, Lavitpichayawong B, Mitani T. Synthesis of chitosan-amino acid conjugates and their use in heavy metal uptake. International Journal of Biological Macromolecules. 1995;17(1):21-3.

[15] Yoshinaga N, Alborn HT, Nakanishi T, Suckling DM, Nishida R, Tumlinson JH, et al. Fatty Acid-amino Acid Conjugates Diversification in Lepidopteran Caterpillars. Journal of Chemical Ecology. 2010;36(3):319-25.

[16] Urbańska K, Pawlicki M. Porphyrin–Amino Acid Conjugates. The Journal of organic chemistry. 2020;85(12):8196-202.

[17] Knights KM, Sykes MJ, Miners JO. Amino acid conjugation: contribution to the metabolism and toxicity of xenobiotic carboxylic acids. Expert Opinion on Drug Metabolism & Toxicology. 2007;3(2):159-68.

[18] Li J, Sha Y. A Convenient Synthesis of Amino Acid Methyl Esters. Molecules. 2008;13(5):1111-9.

[19] Çalışkan E, Biryan F, Koran K, Akman F, Görgülü AO, Çetin A. Synthesis of Cinnamoyl-Amino Acid Ester Derivatives and Structure-Activity Relationship Based on Thermal Stability, Dielectric, and Theoretical Analysis. ChemistrySelect. 2022;7(20):e202200895.

[20] Farooq S, Ngaini Z. Recent Synthetic Methodologies for Chalcone Synthesis (2013-2018). Current Organocatalysis. 2019;6(3):184-92.

[21] Garrett CE, Jiang X, Prasad K, Repič O. New observations on peptide bond formation using CDMT. Tetrahedron Letters. 2002;43(23):4161-5.

[22] Fiedziuszko SJ, Hunter IC, Itoh T, Kobayashi Y, Nishikawa T, Stitzer SN, et al. Dielectric materials, devices, and circuits. IEEE Transactions on Microwave Theory and Techniques. 2002;50(3):706-20.

[23] Pethig R. Dielectric and Electrical Properties of Biological Materials. Journal of Bioelectricity. 1985;4(2):vii-ix.

[24] Çelik T, Coşkun MF. Dielectric and thermal properties of the methacrylate polymer bearing chalcone side group. Journal of Molecular Structure. 2018;1157:239-46.

[25] Biryan F, Çalışkan E, Koran K. Kinetic analysis and dielectric properties of tyrosine-based tripeptide side groups carrying novel methacrylate polymers. Journal of Polymer Research. 2022;29(10):415.

[26] Çalışkan E. Chemoselective Synthesis of Tyrosine-Based Polymers and Comparison of Their Thermal, Kinetic, and Dielectric Properties. ChemistrySelect. 2022;7(29):e202202010.

[27] Özdemir M, Biryan F, Koran K, Yalçın B, Görgülü AO. Synthesis, structural characterization, therotical and electrical properties of novel sulpho-coumarin based methacrylate polymer. Journal of Polymer Research. 2022;29(5):190.

[28] Çalışkan E, Koran K, Görgülü AO, Çetin A. Electrical properties of amino acid substituted novel cinnamic acid compounds. Journal of Molecular Structure. 2020;1222:128830.

[29] Koran K, Görgülü AO. Structural characterizations, thermal behavior, and electrical measurements of the amidosulfonic acid catalyzed thermal ring-opening polymerization of substituted cyclotriphosphazene in 1,2,4-trichlorobenzene solution. Advances in Polymer Technology. 2018;37(8):3229-39.

[30] Koran K, Özen F, Biryan F, Görgülü AO. Synthesis, structural characterization and dielectric behavior of new oxime-cyclotriphosphazene derivatives. Journal of Molecular Structure. 2016;1105:135-41.

[31] Koran K, Özen F, Torğut G, Pıhtılı G, Çil E, Orhan Görgülü A, et al. Synthesis, characterization and dielectric properties of phosphazenes containing chalcones. Polyhedron. 2014;79:213-20.

159

Türk Doğa ve Fen Dergisi
Turkish Journal of Nature and Science

www.dergipark.gov.tr/tdfd

Fabric Defect Detection Using Customized Deep Convolutional Neural Network for Circular Knitting Fabrics

Mahdi HATAMI VARJOVI[*1], Muhammed Fatih TALU [1], Kazım HANBAY[2]

[1] Inonu University, Engineering Faculty, Computer Engineering Department, Malatya, Türkiye
[2] Inonu University, Engineering Faculty, Software Engineering Department, Malatya, Türkiye
Mahdi HATAMI VARJOVI ORCID No: 0000-0001-6442-7175
Muhammed Fatih TALU ORCID No: 0000-0003-1166-8404
Kazım HANBAY ORCID No: 0000-0003-1374-1417

*Corresponding author: mahdi.hatami.v@gmail.com

Abstract: Visual inspection is a main stage of quality assurance process in many applications. In this paper, we propose a new network architecture for detecting the fabric defects based on convolutional neural network. Four different pre-trained and customized model network architectures have compared in terms of performance. Results have been evaluated on a fabric defect dataset which consist of 13820 images. Among the existing Inception V3, MobileNetV2, Xception and ResNet50 methods, the InceptionV3 model has achieved 78% classification success. Our designed deep network model could achieve 97% success rate. The experimental works show that the designed deep model is effective in detecting the fabric defects.

160

Yuvarlak Örgü Kumaşları İçin Özelleştirilmiş Derin Evrişimsel Sinir Ağı Kullanarak Kumaş Hatası Tespiti

Öz: Görsel denetim, birçok uygulamada kalite güvence sürecinin ana aşamasıdır. Bu çalışmada kumaş hatalarının tespiti için derin evrişimsel ağa dayalı yeni bir ağ mimarisi önerdik. Önceden eğitilmiş ve özelleştirilmiş 4 farklı ağ mimarisi performans açısından karşılaştırılmıştır. 13820 görüntü içeren kumaş hatası veri tabanı üzerinde sonuçlar değerlendirilmiştir. Mevcut Inception V3, MobileNetV2, Xception ve ResNet50 metotları arasında, InceptionV3 modeli %78 sınıflandırma başarısı elde etmiştir. Bizim dizayn ettiğimiz derin ağ modeli %97 başarı elde etmiştir. Deneysel çalışmalar dizayn edilen derin modelin kumaş hatalarını tespit etmede etkili olduğunu göstermiştir.

1. INTRODUCTION

Fabric defects are a significant challenge in the textile industry when it comes to assessing quality control. One of the most essential approaches for evaluating fabric quality is detecting the defect and then classification for those defects. The classification of fabric defects is an important step in the quality assurance process. The machine could alter and enhance its processing technique by supplying defect information. The primary challenges to defect detection are: 1) commonalities between various types of defects. It could be difficult to discriminate between broken picks and slub defects. 2) Classification of various fabrics and extraction of features for the same defect across multiple fabrics takes

a long time. 3) Low-resolution, low-contrast defects. 4) Defects of various scales.

Defect identification is now done in most production utilizing human inspection and conventional feature extraction for each fabric. Fabric surface defect detection algorithms could not successfully identify and distinguish different types of fabric defects due to the complexity of textile defects. Visual inspection by skilled employees using man-made classification criteria is used to assess fabric problems. Due to the limited separation capability of the handicraft features, traditional detection algorithms are less accurate and efficient in distinguishing diverse fabric defects.

Furthermore, traditional algorithms are frequently unable to generalize diverse inspection processes.

Model-based, statistical, and spectral are the three types of classic fabric defect detection methods. Approaches that use models: This approach is appropriate for fabric pictures with surface variations related to defects like yarn breakage and needle breakage. Model-based defect detection techniques have the benefit of being able to generate fabric textures that are similar to the observed fabric textures [1]. Statistical methods: Defect detection seeks to divide the inspection picture into statistically distinct sections. Textural characteristics derived from fractal dimensions, co-occurrence matrix, edge detection, cross correlation, first-order statistics, eigen filters, morphological operations, and a variety of local linear transforms are all included in this class [2].

Spectral approaches: The location of the fabric defect must be determined using spatial domain information. A wide range of studies on fabric defect detection have focused on spectral techniques. The intention of spectral techniques is to remove the fundamentals of image texture and by doing that they were able to generalize the fundamentals of texture using spatial layout. Many standard low-level statistical methods, such as detecting an edge, fail to detect a variety of fabric defects, which appear as minor intention transitions. As a result, it's vital to look into additional reliable computer-vision algorithms for recognizing fabric defects [3].

In computer vision applications, deep convolutional neural networks (CNN) being used for a variety of use cases, including image classification and object recognition [4,5]. Recent researches have created CNN-based algorithms for fabric defect detection in the textile sector, which were inspired by the applications. Bing Wei [6] suggested an approach for improving accuracy in fabric defect samples using a small portion of defective instances and CNN to classify features space using compressive sampling. To detect defective photos, Mei Zhang [7] proposed a deep convolution neural network-based one-class classifier, to train the neural network model, they created a loss function with a correction term based on Euclidean distance. Zhao [8] proposes that an integrated CNN model based on visual long-short-term memory (VLSTM) might alleviate the problem of fabric defects that are difficult to distinguish against a textural background. The strategy they offer is based on human visual perception and memory mechanism. Generative adversarial network (GAN)-based framework is suggested by Liu [9] for defect detection which able to learn existing fabric defected test results and automatically adapt itself to various fabric textures during different situations of application. The proposed method can detect different defect types by optimizing a deep semantic segmentation network. According to gray histogram back-projection, Guodong [10] developed a fast defect-detection-framework (Fast-DDF), To address the problem of adjusting network model parameters and long training time, an end-to-end multi convoluted network model is used for defect classification, as well as batch normalization of samples and a network fine tuning process. Jing [11] introduces a

deep convolutional neural network-based (CNN) detection approach for autonomous fabric defect detection. There are three key steps to it. The fabric image is first divided into local patches, which are labeled. The labeled patches are subsequently given to a deep CNN that has been pre-programmed for transfer learning. Eventually, during the inspection step, the whole image is moved using the trained model, and defects are recognized, as well as the category and position of each defect. Investigating deep Convolutional Neural Network (CNN) design configurations and the impact of different hyper parameter settings for improved defect detection findings, Weimer [12] investigates a new machine learning paradigm, called deep learning. They propose that CNN can automatically produce powerful features from enormous numbers of training data using hierarchical learning algorithms with minimum human involvement.

To use a pre-trained network that has been trained on a big dataset is a frequent and successful technique to deep learning on small datasets, usually a large-scale image categorization. Large picture datasets were commonly used to train CNN architectures such as InceptionV3 [13], VGG16 [14,15], AlexNet [16], and ResNet [17]. This research compares an FCN-based fabric defect detection system with a custom-designed neural network architecture. On a circular knitting machine fabric picture dataset [15, 18, 19], they begin by analyzing and comparing various pre-trained deep CNN architectures for image classification with our own CNN developed model. Then, utilizing flawed and defect-free fabric photos, the suggested method performance is confirmed.

2. RELATED WORKS

2.1. Methodology

We might be able to find some advanced convolutional neural network models and use them to classify fabric defects. The state-of-the-art model topology, on the other hand, is frequently excessively complicated. The ResNet, for example, has excellent classification accuracy but has too many layers, making it difficult to train and evaluate. The GoogleNet model, on the other hand, has many fewer parameters but still can reach excellent classification accuracy. For both fabric defects, an FCN is trained from end -to-end to classify an image of a defect in to the "defected" and "defect-free" pixels. On a circular knitting machine fabric picture dataset, tests are first done to assess the performance of several pre-trained CNNs for classification tasks. The FCN network's backbone will be the pre-trained model that has been chosen. Annotated database pictures with defects are used to train deep models in this research. The FCN is trained on a subset of the same dataset that includes fabric images that have been labeled.

2.2. Defect Classification Using Pre-Trained Neural Networks

(CNNs) are multi-layer neural networks that assess visual inputs and perform tasks including image

categorization, segmentation, and object recognition. A convolutional layer, a pooling layer, and an activation unit are all included in each layer. The convolution layer applies convolution to the output of the preceding layers, utilizing filters or kernels to extract important features for image categorization. Two convolutional blocks are used in some previous network architectures, such as LeNet-5. CNN designs have recently become more complex, including VGG16, Inception, and ResNet, which have enhanced layer configurations.

The majority of past research has presented defect detection approaches based on network training from the scratch. Transfer learning, on the other hand, has also been shown to boost the defect classifier's training efficiency and accuracy.

The accuracy of four distinct pre-trained CNN models, including InceptionV3, VGG16, AlexNet, and ResNet, was tested in this research. ResNet has 152 layers of residual nets, which is 8 times more than the VGG model. Despite of having a simpler model than ResNet, the VGG model outperformed ResNet in classification contests such as ILSVRC 2015 and ILSVRC & COCO 2015 [14]. The models' structures are depicted in Figure 1. The network depth and parameter configuration of the models have been shown in Table 1.

Table 1. Number of parameters and depth of networks

Model	Number of parameters	Depth
InceptionV3	23.851.784	159
ResNet50	25.636.712	152
MobileNetV2	3.538.984	88

For transfer learning, first we need to normalize the fabric images then separate images into train and test folders after that images divided into 80% train and 20% for the test purpose. After the data has been prepared, we are loading a pre-trained model.

Deep neural networks are multi-layered structures with numerous tunable hyperparameters. The initial layers' role is to capture generic features, whereas the later layers focus more on the explicit task at hand. We can retrain some of the model's layers while leaving others frozen in training. A binary cross-entropy loss is used to construct the model. As an optimizer, the rmsprop technique is utilized. Our Fabric defect classifiers are trained on Nvidia 2080 TI GPU with the Keras framework and TensorFlow backend which is an open-source machine learning framework [20].
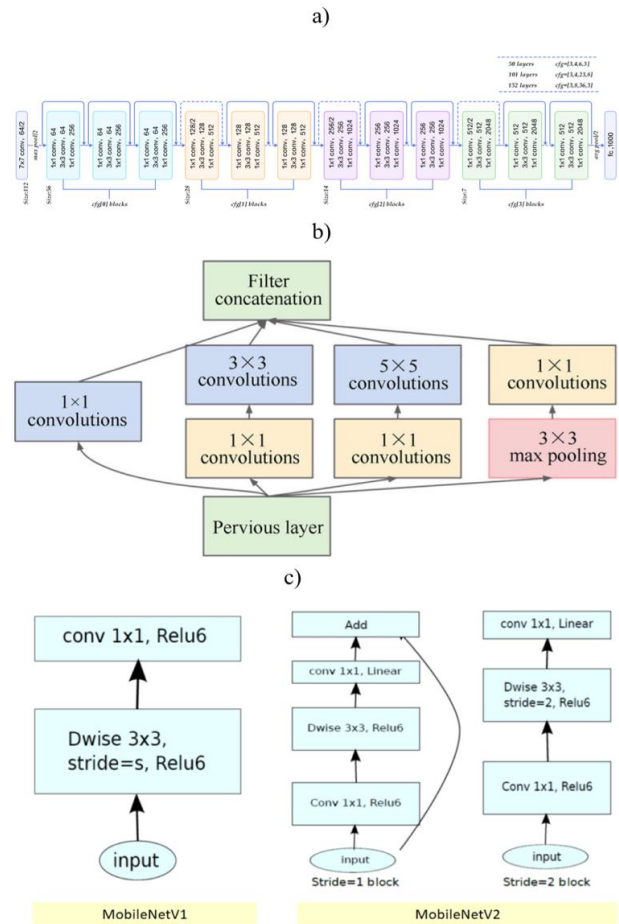
Figure 1. a) ResNet b) Inception c) MobileNet network architectures

2.3. Fabric Image Dataset

The dataset of fabric images which has the total 13820 images organized according to a list of 2 categories on circular knitting machine. Image size is 250x256 pixels [15, 19] where 10820 are defect-free and 3000 are defected images for classification process. The sample images are shown in Figure 2.
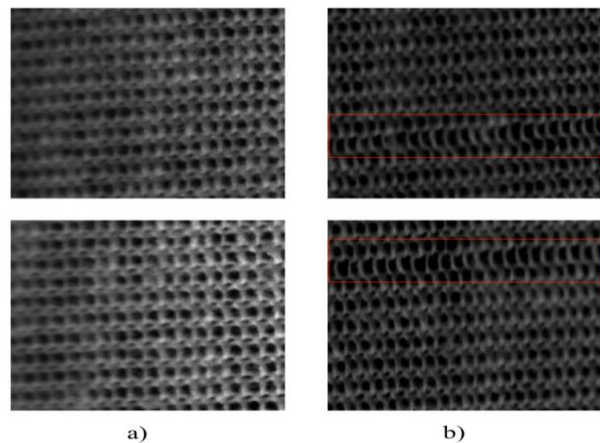

Figure 2. a) defect-free b) defected fabric images

162

3. RESULTS

3.1. Classification of Defected Images Using Pre-Trained Networks

In this part, we'll compare the pre-trained and customized models in terms of performance. We utilize the same environment and database to provide a proper comparison. We did the same thing with the pre-trained weights, setting them as the model's initial value and then training it. The pre-trained models: InceptionV3, MobileNetV2, Xception, and ResNet50 are primarily fine-tuned for model training. All of the models utilize the same training datasets.

Table 2. Classification performances of different deep architectures

Model	Epoch	Accuracy (%)	Image Size
Our Model	14	97%	250 x 256
InceptionV3	20	78%	250 x 256
MobileNetV2	20	49%	250 x 256
Xception	20	69%	250 x 256
ResNet50	20	22%	250 x 256

The customized model classifier is trained for 20 epochs which has batch size of 64 and 0.9 is used for momentum term, while training with datasets, InceptionV3 classifier achieved over 78% accuracy higher than other pre-trained networks, ResNet based classifier produces the minimum accuracy between all models and all results. Our designed model could be considered one block VGG model which consist of one convolution layer followed by max pooling then output of previous layer flattened and connected to ReLU activation function and finally one layer of Soft-max which predict the classes for defected and defect-free classification. The custom designed model provided in Figure 3 and the accuracy of all classifiers shown in Table 2.
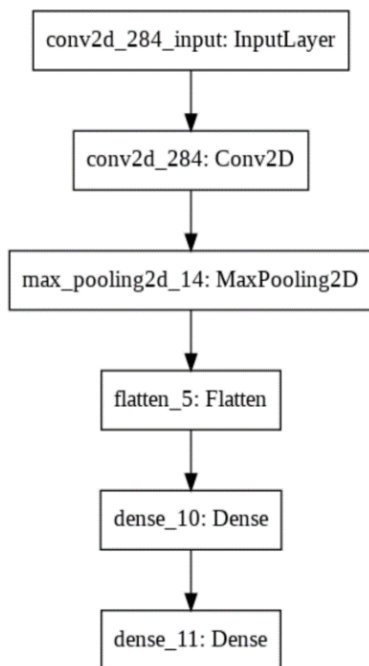

Figure 3. The proposed convolutional neural network architecture

3.2. Fully Convolutional Network Training

The pre-trained weights of ImageNet are used to generate the weights of all layers of fully convolutional networks. We used the circular knitting machine fabric image dataset to train the model. Figure 4 displays the result of validation accuracy and validation loss. By looking at the results, we can see the simple in-depth network could achieve good results. In some cases, adding the one layer of dropout regularization could help the overall accuracy but for our classification problem we have 250x256 image size which by adding the dropout layer our feature sets do reduced and caused lower accuracy. Another important factor in FCN is the over-fitting, we observed that training for higher epochs could cause over-fitting in model training, in our case 14 epoch is the optimal number for our model to achieve higher accuracy.
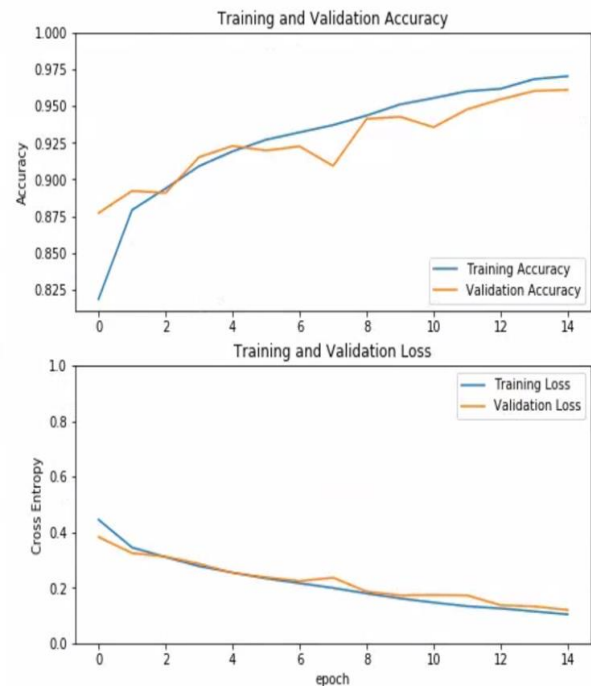
Figure 4. The classification results of the base-model in terms of accuracy and loss

Adding more layers will help the network to extract more features and do better classification for specific recognition tasks but we could do that up to a certain extent. After we surpass the threshold, instead of extracting more features we are getting in to the over-fitting phase. Overfitting could lead to errors in some or the other form like false positives. We tried to add more layer to the model and by adding additional layer to our base model after 10 epochs our model start to produce the sign of over-fitting as shown in Figure 5.
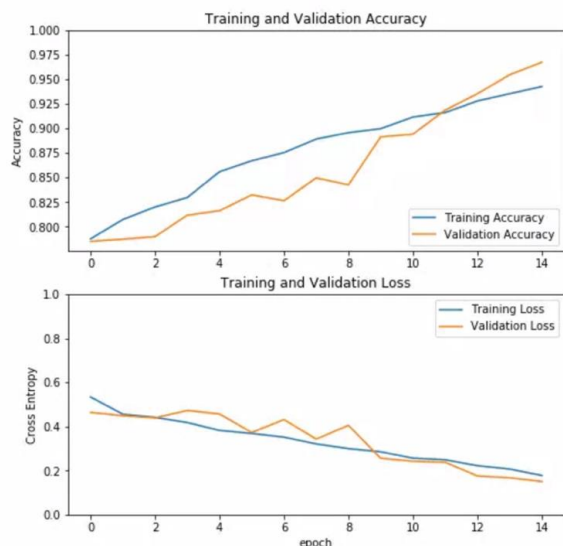
Figure 5. The classification results of the additional layer on top of base-model in terms of accuracy and loss

3.3. Testing

The database is divided into two folders, one for defect images and another for defect-free images. The class numbers are the same as the name convention which is 2. In a dataset including 600 defective fabric images, 562 defected images and 38 defect-free images were recognized, with a TNR of 96.3 %. Overall, the system has a 97% detection accuracy, and each input image is detected in an average of 15.4 milliseconds. Table 3 compares the performance of the InceptionV3 to that of the original.

**Table 3.** TNR: True Negative Rages; TPR; True Positive Rates

Model	TNR	TPR	Model size
Our Network	96.3	98.3	70 MB
InceptionV3	79.9	80.5	95 MB

4. DISCUSSION AND CONCLUSION

For fabric defect identification and accuracy evaluation, a vision-based technique based on deep convolutional networks is suggested in this paper. For fabric-defect recognition, we compared the accuracy of a pre-trained neural network and a customized neural network model. Then we trained all network with same database and examined the custom designed model with smaller in-depth and lower in-params could achieve better results than pre-trained neural networks with much deeper and much higher parameters. We proposed a simpler model that can be applied to detect fabric defects which produced via circular knitting machine in factory. As a result, applications of the proposed fully connected neural network in circular knitting machine fabric manufacturing should be researched further. Although the suggested approach has successfully collected defected images, quantifying defect for various textiles remains a challenge. As a result, future research should concentrate on how to enhance the suggested approach in order to make defect detection more robust on various fabric sorts and noisy defects.

REFERENCES

[1] Hanbay K, Talu MF, Özgüven ÖF. Fabric defect detection systems and methods—A systematic literature review. Optik. 2016 Dec 1;127(24):11960–73.

[2] Mahajan P, Kolhe S R, Patil P M. A review of automatic fabric defect detection techniques. Advances in Computational Research. 2009. 1(2): 18-29.

[3] Kumar A. Computer-Vision-Based Fabric Defect Detection: A Survey. IEEE TRANSACTIONS ON INDUSTRIAL ELECTRONICS. 2008.55(1): 348-363.

[4] Fanga B, Lia Y, Zhanga H,. Chan J C-W. Collaborative learning of lightweight convolutional neural network and deep clustering for hyperspectral image semi-supervised classification with limited training samples. ISPRS Journal of Photogrammetry and Remote Sensing. 2020.161:164-178.

[5] Sezer A, Sezer H B. Deep Convolutional Neural Network-Based Automatic Classification of Neonatal Hip Ultrasound Images: A Novel Data Augmentation Approach with Speckle Noise Reduction. Ultrasound in Medicine & Biology. 2020. 46(3): 735-749.

[6] Wei B, Hao K, Tang X, Ding Y. A new method using the convolutional neural network with compressive sensing for fabric defect classification based on small sample sizes. Textile Research Journal. 2019. 89(17): 3539-3555.

[7] Zhanga M, Wu J, Lina H, Yuan P, Song Y. The Application of One-Class Classifier Based on CNN in Image Defect Detection. Procedia Computer Science. 2017. 114: 341-348.

[8] Zhao Y, Hao K, He H, Tang X, Wei B. A visual long-short-term memory based integrated CNN model for fabric defect image classification. Neurocomputing. 2020, 380: 259-270.

[9] Liu J, Wang C, Su H, Du B, Tao D. Multistage GAN for Fabric Defect Detection. IEEE Transactions on Image Processing. 2019. 29:3388-3400.

[10] SUN G, ZHOU Z, GAO Y, XU Y, XU L, LIN S. A Fast Fabric Defect Detection Framework for Multi-Layer Convolutional Neural Network Based on Histogram Back-Projection. IEICE Transactions on Information and Systems. 2019. 102(12): 2504-2514.

[11] Jing J-F, Ma H, Zhang H-H. Automatic fabric defect detection using a deep convolutional neural network. Coloration Technology. 2019. 135(3): 213-223.

[12] Weimer D, Scholz-Reiter B, Shpitalni M. Design of deep convolutional neural network architectures for automated feature extraction in industrial

inspection. CIRP Annals - Manufacturing Technology. 2016. 1481:4.

[13] Szegedy C, Vanhoucke V, Ioffe S, Shlens J, Wojna Z. Rethinking the Inception Architecture for Computer Vision. Computer Vision and Pattern Recognition. 2016. 1-10.

[14] Simonyan K, Zisserman A. Very Deep Convolutional Networks for Large-Scale Image Recognition. In: 3rd International Conference on Learning Representations, ICLR 2015 - Conference Track Proceedings. International Conference on Learning Representations, ICLR;

[15] Hanbay, K, Detecting of Circular Knitting Fabric Defects Using VGG16 Architecture, Tr. J. Nature Sci. 11(2), 125-129. 2022.

[16] Krizhevsky A, Sutskever I, Hinton G E. Imagenet classification with deep con- volutional neural networks. Adv. Neural Inf. Proces. Syst. 2012. 60(6): 1097-1105.

[17] He K, Zhang X, Ren S, Sun, J. Deep residual learning for image recognition. In Proceedings of the IEEE conference on computer vision and pattern recognition. 2016. 770-778.

[18] Hanbay K, Talu M F, Özgüven Ö F, Öztürk D. Fabric defect detection methods for circular knitting machines. 23nd Signal Processing and Communications Applications Conference (SIU), Malatya, 2015. 735-738.

[19] Hanbay K, Fatih Talu M, Özgüven ÖF, Öztürk D. Real-Time Detection of Knitting Fabric Defects Using Shearlet Transform. Tekst ve Konfeksiyon. 29(1):2019. 3-10.

[20] Chollet, F. (2015) keras, GitHub. https://github.com/fchollet/keraserences

165

Türk Doğa ve Fen Dergisi
Turkish Journal of Nature and Science

www.dergipark.gov.tr/tdfd

Evaluation of the Biological Activities of Royal Jelly on Prostate and Breast Cancer Cells

Adnan AYNA[1]*, Ekrem DARENDELİOĞLU[2]

[1] Bingöl University, Science and Letter Faculty, Chemistry Department, Bingöl, Türkiye
[2] Bingöl University, Science and Letter Faculty, Molecular Biology and Genetics Department, Bingöl, Türkiye
Adnan AYNA ORCID No: 0000-0001-6801-6242
Ekrem DARENDELİOĞLU ORCID No: 0000-0002-0630-4086

*Corresponding author: aayna@bingol.edu.tr

Abstract: Due to their high toxicity to healthy body cells, chemotherapy drugs used to treat cancer pose a serious threat to the organism. Recent studies have encouraged the utilization of bee products to prevent and treat the cancer. The specific food for the queen honeybee larva (*Apis mellifera*), royal jelly (RJ) is a yellow, milky, cremy product of the bee which is stowed from the mandibular and hypopharyngeal glands of the worker honeybee. According to the reports, RJ may have cytotoxic effects in animal models. However, RJ's cytotoxic and antioxidant properties on PC-3 prostate cancer and MCF-7 breast cancer cell lines have yet to be thoroughly investigated at the cellular level. Therefore, the antioxidant and anti-proliferative activities of RJ in PC-3 prostate cancer cells and MCF-7 breast cancer cells were evaluated to investigate a chemopreventive strategy to increase cancer therapy efficacy. WST-1 assay was used to measure cell proliferation, and levels of reactive oxygen species (ROS) and lipid peroxidation (LPO) were analyzed to look at antioxidant activities. According to the data of this research, RJ act as prooxidants in PC-3 and MCF-7 cancer cell lines by lessening cellular viability and raising ROS and LPO formation.

166

Arı Sütünün Prostat ve Meme Kanseri Hücreleri Üzerindeki Biyolojik Aktivitelerinin Değerlendirilmesi

Anahtar Kelimeler
Arı sütü,
WST-1 testi,
Prostat kanseri,
Meme kanseri,
Lipid
peroksidasyonu

Öz: Kanser tedavisinde kullanılan kemoterapi ilaçları, sağlıklı vücut hücrelerine yüksek toksisiteleri nedeniyle organizma için ciddi bir tehdit oluşturmaktadır. Son zamanlarda yapılan çalışmalar, kanserin önlenmesi ve tedavisi için arı ürünlerinin kullanımını teşvik etmiştir. Kraliçe bal arısı larvası (*Apis mellifera*), arı sütü için özel gıda, işçi bal arısının çene ve hipofarenks bezlerinden salgılanan sarımsı, sütlü, kremsi bir arı ürünüdür. Literatür verilerine göre, RJ'nin hayvan modellerinde sitotoksik etkilerinin olduğu söylenebilir. Bununla birlikte, arı sütünün PC-3 prostat kanseri ve MCF-7 meme kanseri hücre dizileri üzerindeki sitotoksik ve antioksidan özellikleri henüz hücresel düzeyde tam olarak araştırılmamıştır. Bu nedenle, bu çalışmada arı sütünün PC-3 prostat kanseri hücrelerinde ve MCF-7 meme kanseri hücrelerinde antioksidan ve anti-proliferatif aktiviteleri araaşrırılmıştır. Çalışmada, hücre proliferasyonunu analiz etmek için WST-1 testi kullanıldı ve antioksidan aktivitelerini analiz etmek için reaktif oksijen türlerinin (ROS) ve lipid peroksidasyonunun (LPO) seviyeleri analiz edildi. Bu araştırmanın verilerine göre arı sütü hücre canlılığını azaltarak ve ROS ve LPO oluşumunu artırarak PC-3 ve MCF-7 kanser hücre hatlarında prooksidan görevi görmektedir.

1. INTRODUCTION

Royal Jelly (RJ) contains primarily proteins (between 27 and 41 percent). More than 80% of these are soluble proteins. These proteins are thought to be the key macromolecules behind the unique physiological functions of RJ during the growth of the queen honeybee. In earlier investigations, RJ proteins were found to stimulate cell proliferation [1-3]. Sebacic acid (SEA), 10-hydroxydecanoic acid (10-HDAA), and trans-

10-hydroxy-2-decenoic acid (10-H2DA) are three commonly occurring fatty acids in RJ.

The biophysiological properties of RJ comprise anti-cancer, anti-microbial, immune-modulatory, anti-oxidative and anti-hypertensive impacts. They also work in conjunction with proteins to contribute to these biological activities [4-8]. RJ also contains phenolic acids, carotenoids, flavonoids, organic acids [9], vitamins, and minerals [10-11]. The antioxidant action of RJ is mostly attributed to the phenolic and flavonoids found in it, including chrysin, acacetin, apigenin, quercetin, hesperidin and kaempferol [10-12]. Due to their strong anti-oxidative capacity and their ability to alter a number of signaling pathways, containing the inhibition of cell viability, stimulation of apoptotic pathways, and cell cycle arrest, flavonoids also have anticancer properties [13-16,11].

Recent studies have encouraged the utilization of the important products of bee (ie. honey, propolis) for preventing and treating the cancer [17-18]. RJ's antioxidant and anticancer properties on PC-3 prostate cancer and MCF-7 breast cancer cell lines, however, have not yet been thoroughly investigated at the molecular level. For that reason, the goal of this research was to examine RJ's anti-oxidant and anti-cancer effects on PC-3 prostate cancer and MCF-7 breast cancer cell lines as well as the mechanisms behind these effects.

2. MATERIAL AND METHOD

2.1. Materials

PC-3 and MCF-7 cancer cell lines were kindly provided by Tokat Gaziosmanpasa University. Local beekeepers who are members of the Bingöl Beekeepers Association provided Royal Jelly. Local beekeepers produced RJ in the spring of 2019 in Bingöl and kept it at -20 °C. Malondialdehyde bis and 2′,7′-Dichlorofluorescein diacetate (DCFH-DA) were purchased from Merck.

2.2. Cell Culture

In full endothelial growth media with 10% fetal bovine serum and 1% penicillin-streptomycin (10000 units/ml, 10 mg/ml streptomycin), HUVEC, human PC-3 prostate and MCF-7 breast cancer cells were cultured. A humidified incubator with 5 percent CO_2 was used to culture the cells, and it was monitored every two to three days. Using the EZPCR mycoplasma test kit, cells were examined for mycoplasma contamination (Biological Industries).

2.3. Cell Proliferation Assay

The cytotoxicity of Turkish RJ was tested on PC-3 and MCF-7 cells using a Water Soluble Tetrazolium-1 (WST-1) cell proliferation assay kit from Clontech Laboratories in the United States. The supplier's recommended protocol was followed during the experiments. In a 96-well plate, 10.000 PC-3 and MCF-7 cells were first grown. The cells were then exposed to RJ

at concentrations ranging from 0.02 to 0.64 mg/ml. 5 µl of WST-1 was then injected into each well. Using a SpectraMax Plus 384 Microplate Reader, each well's absorbance was measured at 450 nm (the reference wavelength is 630 nm) following a 4-hour incubation [19] (Molecular Devices, USA).

2.4. ROS Assay

Using a 2′-7′ dichlorodihydrofluorescein diacetate (DCFH-DA) test kit bought from Abcam, MA, USA, cellular ROS production was assessed [19]. The cells were handled as it is explained in cell culture section. 1000000 HUVEC, PC-3 and MCF-7 cells were collected after treatment and cell growth, and 1 h at 37 °C in the presence of 2 M DCFH-DA was used to measure the fluorescence.

2.5. Measurement of Malondialdehyde Levels

A small modification to the previously published methodology was used to measure the malondialdehyde (MDA) level in RJ-exposed HT-29 cells [20]. In cell culture, the cells were grown as instructed. Centrifugation of the cells was carried out for 5 min. at 30,000 rpm. The LPO assay mixture was then added to the cell suspensions, which were then and there incubated for 0.5 hours at 95 °C with 1 ml of 0.8 percent w/v thiobarbituric acid and 70 percent w/v trichloroacetic acid. The solution was then chilled on an ice bath for about five minutes, and the cell suspensions were then centrifugated at 15×10^3 rpm for ten minutes. At 532 nm, the supernatant's absorbance was measured.

2.6. Statistical Analysis

At least three times each of the experiments were repeated. With the aid of GraphPad Prism 5, statistical analysis and comparable data groups were evaluated using the one-way ANOVA Newman-Keuls post-hoc Test; $p < 0.05$ was regarded as significant.

3. RESULTS

3.1. Cell Proliferation Assay

On the human prostate cancer cell line PC-3, the growth inhibition of the PC-3 cells by various doses of RJ (0.02 mg/ml, 0.04 mg/ml, 0.16 mg/ml and 0.64 mg/ml) was investigated. RJ substantially and concentration-dependently decreased the viability of prostate cancer cells (Figure 1a). The most effective concentration of RJ on PC-3 cells were determined to be 0.02 mg/ml. We also looked into how RJ affected the viability of MCF-7 breast cancer cell line at the same concentrations of RJ, and the findings revealed that there was no significant impact on the cell proliferation at the tested concentrations except at concentration of 0.02 mg/ml of RJ (Figure 1b).
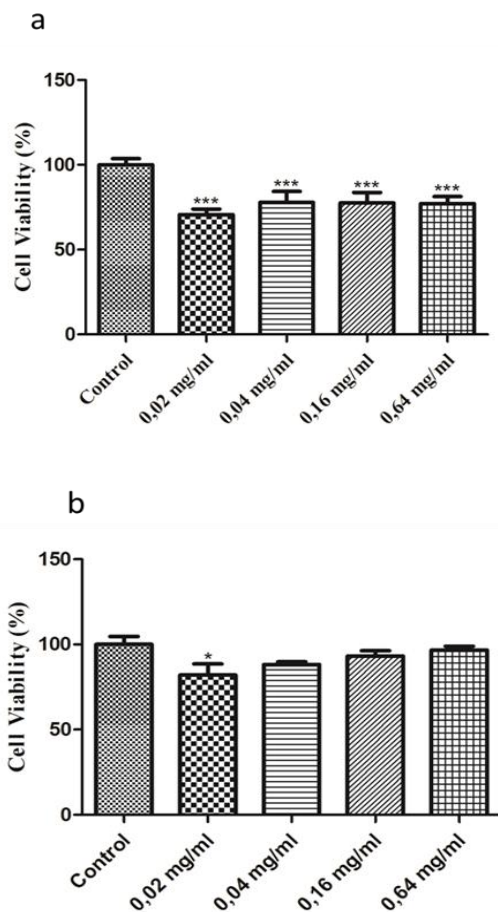
a

b

Figure 1. Effects of various Turkish RJ concentrations on the growth of PC-3 (a) and MCF-7 (b) cells. By using the WST-1 assay, the cell proliferation was evaluated. Experimental data are shown as mean SEM (three replicate treatments). ***p < 0.001, *p < 0.05 indicates statistically significant differences between Cont and other groups

3.2. ROS Assay

In PC-3 cells, the effects of RJ administration on ROS production were assessed. The findings showed that RJ dramatically enhanced ROS levels in PC-3 cells at a concentration of 0.02 mg/ml (Figure 2). The effects of RJ treatment on MCF-7 cell line were also examined within scope of this study. The findings revealed that 0.02 mg/ml of RJ significantly increased ROS generation in MCF-7 and HUVEC cells in comparison to the control (Figure 2).
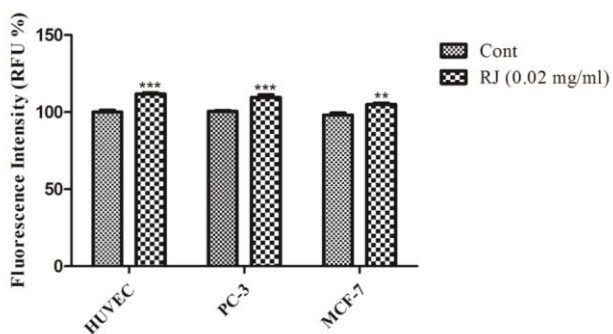

Figure 2. The impacts of RJ exposure on ROS production on PC-3 and MCF-7 cells. Experimental data are shown as mean SEM (three replicate treatments). ***p < 0.001, **p < 0.01 indicates statistically significant differences between Cont and other groups

3.3. Lipid Peroxidation Assay

Malondialdehyde (MDA) levels in controls, HUVEC, PC-3 and MCF-7 cells were measured using a lipid peroxidation technique to evaluate oxidative stress. The amount of thiobarbituric acid reactive substances (TBARS) produced by malondialdehyde was measured as part of the LPO assay (MDA). MDA concentration was evaluated in 0.02 mg/ml RJ treated HUVEC, PC-3 and MCF-7 cells to see whether RJ induced MDA formation in these cells. The results of our study indicated that 0.02 mg/ml of RJ significantly increased MDA generation in HUVEC, PC-3 and MCF-7 cells in comparison to the control (Figure 3).
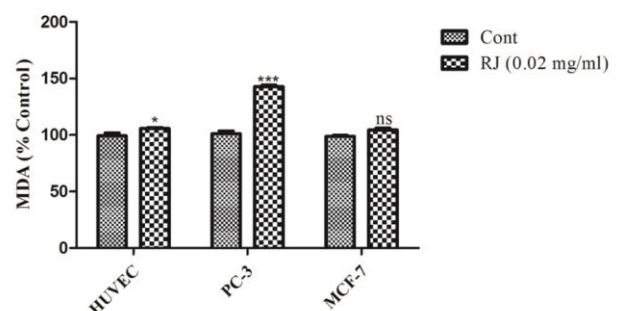

Figure 3. The impacts of RJ exposure on MDA production on PC-3 and MCF-7 cells. Experimental data are shown as mean SEM (three replicate treatments). Data were expressed as mean ± SEM, n = 4. ***p < 0.001, *p < 0.05, ns: nonsignificant indicates statistically significant differences between Cont and other groups

4. DISCUSSION AND CONCLUSION

168

Traditional medicine has long employed bee products extensively. Intriguing bioactivities, such as antimicrobial [21-22], anti-inflammatory [23], and anti-cancer [24] properties, have been demonstrated for the components, water or ethanolic extrats, and izolated biologicaly active ingredients from these products. Along with treating some tumors, bee products have also been widely used to treat a number of immune-related disorders [25]. Numerous malignant cell lines, including those from the prostate, breast, lung, and liver malignancies, have shown evidence of in vitro cellular apoptosis being induced by bee products. Thus, these biologically active natural compounds may prove useful as a component of cutting-edge, underfunded therapy for certain malignancies [16].

According to reports, RJ may have anticancer effects in mice [26,27]. Studies showed that RJ had anticancer properties because it caused tumor cells to develop apoptotic and antiproliferative pathways [12]. Biochemical methods are taken into consideration as a treatment option for cancer, whether it is colon, breast, prostate or another type. Nevertheless, anti-oxidant-rich products of bee species were utilized as bio-therapeutics to lessen cancer patients' risk of recurrence and side effects [28]. To our knowledge, there was no information related to the cytotoxic activity of RJ on PC-3 and MCF-7 cells, according to a thorough literature search. The purpose of this study was to examine the impact of

various RJ concentrations on PC-3 and MCF-7 cell viability, ROS production, and MDA levels.

The investigation into the anti-proliferative and cytotoxic activities of RJ against colon cancer cells revealed that, it might inhibit the physiologic development of the cancerous cells in a concentration-dependent manner with a discernment to cancerous and sarcoma cells. Leukaemia cells were not affected, but sarcoma cells were shown to respond therapeutically to Turkish RJ [29]. According to the extent of the exposure and the RJ concentrations, RJ has been shown to have an immune-stimulating impact via prevention the myelosuppression brought on by tumor evolution [30].

We show that RJ caused an increase in ROS and LPO levels, which is necessary to understand if the cellular processes of RJ treatment on cell survival can be connected to certain induction patterns of ROS and LPO. SOD, CAT, and glutathione are components of the anti-oxidant defence system in the human body, which maintains the balance between the neutralisation and creation of ROS [31]. Nevertheless, oxidative injury, which starts the evolution of cancer, is caused by an inequity between the generation of ROS and the anti-oxidant defence mechanisms [32]. According to [33], ROS have also been linked to the apoptotic pathway, which is essential for eliminating damaged cells during the course of cancer treatment.

Another study's findings showed that Bingöl RJ at a dose of 0.3 mg/ml dramatically increased the amount of ROS in SH-SY5Y cells, whereas RJ at a concentration of 0.5 mg/ml had essentially no influence on ROS levels. While 0.5 mg/ml RJ had no discernible effect on MDA levels in SH-SY5Y cells, the addition of 0.3 mg/ml RJ significantly enhanced the levels of malondialdehyde in those cells. The findings demonstrated that RJ treatment at 0.3 mg/ml dramatically decreased SOD and CAT activity while having little to no effect at 0.5 mg/ml, suggesting that RJ could protect cell membranes from radical-mediated cell damage [34, 35].

The biophysiological properties of RJ comprise anti-cancer, anti-microbial, immune-modulatory, anti-oxidative effects. The purpose of this study was to examine the impact of various RJ concentrations on PC-3 and MCF-7 cell viability, ROS production, and MDA levels. In this study, RJ treatment of these cancer cells reduced cell growth as demonstrated by WST-1 assay. ROS and LPO levels revealed to increase after the RJ treatment at a concentration of 0.02 mg/ml in both cancer cell lines suggesting RJ acts as a prooxidant in our study.

REFERENCES

[1] Filipič B, Gradišnik L, Rihar K, Šooš E, Pereyra A, Potokar J. The influence of royal jelly and human interferon-alpha (HuIFN-αN3) on proliferation, glutathione level and lipid peroxidation in human colorectal adenocarcinoma cells in vitro. Arhiv Za Higijenu Rada i Toksikologiju. 2015;66 (4): 269-274.

[2] Ramanathan ANKG, Nair AJ, Sugunan VS. A review on Royal Jelly proteins and peptides. Journal of Functional Foods. 2018; 44: 255-264.

[3] Dobritzsch D, Aumer D, Fuszard M, Erler S, Buttstedt A. The rise and fall of major royal jelly proteins during a honeybee (Apis mellifera) workers' life. Ecology and Evolution. 2019; 9 (15): 8771-8782.

[4] Coutinho D, Karibasappa SN, Mehta DS. Royal jelly antimicrobial activity against periodontopathic bacteria. Journal of Interdisciplinary Dentistry. 2018;8 (1): 18.

[5] Park HG, Kim BY, Park MJ, Deng Y, Choi YS et al. Antibacterial activity of major royal jelly proteins of the honeybee (Apis mellifera) royal jelly. Journal of Asia-Pacific Entomology. 2019;22 (3): 737-741.

[6] Ahmad S, Campos MG, Fratini F. Altaye SZ, Li J. New insights into the biological and pharmaceutical properties of royal jelly. International Journal of Molecular Sciences. 2020;21 (2): 382- 407.

[7] Park MJ, Kim BY, Deng Y, Park HG, Choi YS et al. Antioxidant capacity of major royal jelly proteins of honeybee (Apis mellifera) royal jelly. Journal of Asia-Pacific Entomology. 2020;23 (2): 445-448.

[8] Guo J, Wang Z, Chen Y, Cao J, Tian W et al. Active components and biological functions of royal jelly. Journal of Functional Foods. 2021;82: 104514.

[9] Lercker G, Capella P, Conte LS, Ruini F, Giordani G. Components of royal jelly: I. Identification of the organic acids. Lipids. 1981;16 (12): 912-919.

[10] Viuda-Martos M, Ruiz-Navajas Y, Fernández-López J, Pérez-Álvarez JA. Functional properties of honey, propolis, and royal jelly. Journal of Food Science. 2008;73 (9): 117-124.

[11] Pasupuleti VR, Sammugam L, Ramesh N, Gan SH. Honey, propolis, and royal jelly: a comprehensive review of their biological actions and health benefits. Oxidative Medicine and Cellular Longevity. 2017;2017.

[12] Kocot J, Kiełczykowska M, Luchowska-Kocot D, Kurzepa J, Musik I. Antioxidant potential of propolis, bee pollen, and royal jelly: possible medical application. Oxidative Medicine and Cellular Longevity. 2018;2018; 1-29.

[13] Liu HL, Jiang WB, Xie MX. Flavonoids: recent advances as anticancer drugs. Recent Patents on Anti-cancer Drug Discovery. 2010;5 (2): 152-164.

[14] Zhang HW, Hu JJ, Fu RQ, Liu X, Zhang YH et al. Flavonoids inhibit cell proliferation and induce apoptosis and autophagy through downregulation of PI3Kγ mediated PI3K/AKT/mTOR/p70S6K/ULK signaling pathway in human breast cancer cells. Scientific Reports. 2018;8 (1): 11255.

[15] Hazafa A, Rehman, KU, Jahan N, Jabeen Z. The role of polyphenol (flavonoids) compounds in the treatment of cancer cells. Nutrition and Cancer. 2019;72 (3): 386-397.

[16] Premratanachai P, Chanchao C. Review of the anticancer activities of bee products. Asian Pacific Journal of Tropical Biomedicine. 2014;4 (5): 337-344.

[17] Badolato M, Carullo G, Cione E, Aiello F, Caroleo MC. From the hive: Honey, a novel weapon against cancer. European Journal of Medicinal Chemistry. 2017;142: 290-299.

[18] Farooqi AA, Romero MA, Aras A, Qureshi MZ, Wakim LH. Honey and popolis-mediated regulation of protein networks in cancer cells. Nutraceuticals and Natural Product Derivatives: Disease Prevention & Drug Discovery. 2019;137-144.

[19] Aykutoglu G, Tartik M, Darendelioglu E, Ayna A, Baydas G. Melatonin and vitamin E alleviate homocysteine-induced oxidative injury and apoptosis in endothelial cells. Molecular Biology Reports. 2020;47 (7): 5285-5293.

[20] Özbolat SN, Ayna A. Chrysin suppresses HT-29 cell death induced by diclofenac through apoptosis and oxidative damage. Nutrition and Cancer. 2021;73 (8): 1419-1428.

[21] Fontana R, Mendes MA, De Souza BM, Konno K, César LMM et al. Jelleines: a family of antimicrobial peptides from the Royal Jelly of honeybees (Apis mellifera). Peptides. 2004;25 (6): 919- 928.

[22] Bengü AŞ, Ayna A, Özbolat SN, Tunç A, Aykutoğlu G et al. Content and antimicrobial activities of Bingol Royal Jelly. Türk Tarım ve Doğa Bilimleri Dergisi. 2020;7 (2): 480-486.

[23] Yang YC, Chou WM, Widowati DA, Lin IP, Peng CC. 10-hydroxy-2-decenoic acid of royal jelly exhibits bactericide and anti-inflammatory activity in human colon cancer cells. BMC Complementary and Alternative Medicine. 2018;18 (1): 202.

[24] Miyata Y, Sakai H. Anti-cancer and protective effects of royal jelly for therapy-induced toxicities in malignancies. International Journal of Molecular Sciences. 2018;19 (10): 3270-3285.

[25] Al-Kushi AG, Header EA, ElSawy NA, Moustafa RA, Alfky NAA. Antioxidant effect of royal jelly on immune status of hyperglycemic rats. Pharmacognosy Magazine. 2018;14 (58):528.

[26] Takahama H, Shimazu T. Food-induced anaphylaxis caused by ingestion of royal jelly. The Journal of Dermatology. 2006;33 (6): 424-426.

[27] Kimura Y. Antitumor and antimetastatic actions of various natural products. In Studies in Natural Products Chemistry. 2008;34: 35-76.

[28] Turan I, Demir S, Misir S, Kilinc K, Mentese A et al. Cytotoxic effect of Turkish propolis on liver, colon, breast, cervix and prostate cancer cell lines. Tropical Journal of Pharmaceutical Research. 2015;14 (5): 777-782.

[29] Taniguchi Y, Kohno K, Inoue SI, Koya-Miyata S, Okamoto I et al. Oral administration of royal jelly inhibits the development of atopic dermatitis-like skin lesions in NC/Nga mice. International Immunopharmacology. 2003;3 (9): 1313-1324.

[30] Bincoletto C, Eberlin S, Figueiredo CA, Luengo MB, Queiroz ML. Effects produced by Royal Jelly on haematopoiesis: relation with host resistance against Ehrlich ascites tumour challenge. International Immunopharmacology. 2005;5 (4): 679-688.

[31] Paulsen CE, Carroll KS. Cysteine-mediated redox signaling: chemistry, biology, and tools for discovery. Chemical Reviews. 2013;113 (7): 4633-4679.

[32] Klaunig JE, Xu Y, Isenberg JS, Bachowski S, Kolaja KL et al. The role of oxidative stress in chemical carcinogenesis. Environmental Health Perspectives. 1998;106 (suppl 1): 289-295.

[33] Jafari M, Rezaei M, Kalantari H, Hashemitabar M. Determination of cell death induced by lovastatin on human colon cell line HT29 using the comet assay. Jundishapur Journal of Natural Pharmaceutical Products. 2013;8 (4): 187-191.

[34] Çalışkan E, Ayna A, Tunç A, Özbolat S, Bengü AŞ, Aykutoğlu G, Çiftci M, Darendelioğlu E. Antioxidant Activities of Bingöl Royal Jelly on SH-SY5Y Cells. International Journal of Nature and Life Sciences. 2021;5(2):61-9.

[35] Ayna A, Tunc A, Özbolat S, Bengü AŞ, Aykutoğlu G, Canli D, Polat R, Ciftci M, Darendelioğlu E. Anticancer, and antioxidant activities of royal jelly on HT-29 colon cancer cells and melissopalynological analysis. Turkish Journal of Botany. 2021;45(8):809-19.

Türk Doğa ve Fen Dergisi
Turkish Journal of Nature and Science
www.dergipark.gov.tr/tdfd

Viscometric Investigation of Compatibilizer Effect on Polyvinyl chloride/Polystyrene Blends

Ersen YILMAZ[1*], Ali BOZTUĞ[2]

[1] Munzur University, Tunceli Vocational School, Machinery Department, Tunceli, Türkiye
[2] Cumhuriyet University, Science Faculty Chemistry Department, Sivas, Türkiye
Ersen YILMAZ ORCID No: 0000-0002-8567-1668
Ali BOZTUĞ ORCID No:　 0000-0003-2922-4481

*Corresponding author: ersenyilmaz@munzur.edu.tr

Abstract: In this study, polyvinyl chloride (PVC) and polystyrene (PS) polymers, which do not form a compatible blend with each other in certain concentration ranges and are widely used on an industrial scale, were used. The concentration range in which these two polymers do not form a compatible blend were determined viscometrically, and maleic anhydride-styrene (MAS) copolymer was added as a compatibilizing agent in this concentration range. The concentration range in which the polymer pair did not form a compatible blend was determined as 1.5 and 2.0 g dL^{-1}. In this concentration range, 5.0 and 10.0 % MAS copolymer was added to the polymer couple and its compatibilizing effect was investigated. It was determined by viscometric method that the MAS copolymer was a good compatibilizer in the range where the polymer pair did not form a compatible blend.

171

Polivinilklorür/Polistiren Karışımlarına Uyumlaştırıcı Etkisinin Viskozimetrik İncelenmesi

Öz: Bu çalışmada belirli derişim aralıklarında birbirleriyle uyumlu karışım oluşturmayan ve endüstriyel ölçekte yaygın kullanıma sahip polivinilklorür (PVC) ve polistiren (PS) polimerleri kullanıldı. Bu iki polimerin uyumlu karışım oluşturmadığı derişim aralığı viskozimetrik yolla belirlenerek bu derişim aralığında maleik anhidrit-stiren (MAS) ko-polimeri uyumlaştırıcı ajan olarak eklendi. Polimer çiftinin uyumlu karışım oluşturmadığı derişim aralığı 1.5 ve 2.0 g dL^{-1} olarak saptandı. Bu derişim aralığında polimer çiftine % 5.0 ve 10.0 oranlarında MAS ko-polimeri eklenerek uyumlaştırıcı etkisi araştırıldı. Eklenen ko-polimerin PVC/PS polimer çifti için iyi bir uyumlaştırıcı olduğu belirlendi.

1. INTRODUCTION

A polymer blend is analogous to metal alloys, in which at least two polymers are combined to create a new material with different physical properties. Mostly, the polymer blends are immiscible in nature while some are miscible. In the immiscible polymer blends, the polymers exist in different phases, whereas single phases are observed in miscible or homogeneous polymer blends due to having the same chemical structure [1]. Polymer blends can be classified according to the physical properties of their constituents as plastic, thermoplastic, elastomer, and so on. However, since the ultimate properties of a polymer blend will depend on the final morphology, miscibility and phase behavior of polymer blends needs to be taken into account. In the other words, polymer blending can be practicable only when the selected polymers are miscible

or can be made miscible by a selected compatibilizer [2,3]. Blends are usually made in two ways. The first way is to dissolve the two polymers in the same solvent and then evaporate the solvent. When the solvent has completely evaporated; If the two polymers are miscible, a homogeneous blend is observed, if not phase separations are observed. The second way is to heat the two polymers together above the glass transition temperatures of both polymers. This is often done in extruders [4].

Compatibilizers are utilized in polymer chemistry to improve the mechanical properties of multicomponent polymer blends. The process of compatibilization is meant to reduce polymer particle interfacial tension, facilitate chain dispersion, stabilize morphology against severe melt processing conditions, and enhance adhesion between two phases [5]. There are compatibilizers with

different blending mechanisms. Examples of reactive compatibilizers: acrylic functions grafted on polyolefin, polyethylene and PP, allow compatibilization with PAs, EVOH, polybutylene terephthalate (PBT), PET. Acrylic functions are often maleic anhydride, glycidyl methacrylate. Such compatibilizers are marketed, for example, as Amplify GR-MA (Dow), Elvaloy PTW and Fusabond (DuPont). Examples of nonreactive compatibilizers: Ethylene–ethylacrylate (EEA) copolymers for PP/PA recycling, ethylene–butylacrylate (EBA), and ethylene methacrylate (EMA) copolymer for compatibilization of PP, PE, PBT, PA, ABS, PC. PMMA or polystyrene grafted on PP (Interloy) can compatibilize polypropylene with PMMA, SAN, ASA, ABS, PVC, PC, PPE. Acrylic–imide copolymers (Paraloid) can compatibilize PPE/PA, PC/PE. Styrenic block copolymers can compatibilize PP/HDPE, PPE/PA, olefins and styrenics SB, PS, ABS [6].

The preparation of polymer blends and the use of these blends in different application areas are closely related to the miscibility of polymers. In this way, blends were formed by using miscible polymers and used for different purposes [7-11]. In order to form compatible polymer blends with each other, there must first be secondary interactions between them, such as dipole-dipole interactions or hydrogen bonds. However, most polymers are not miscible because they cannot interact with each other in this way. For polymers that do not mix with each other to become miscible, the interactions mentioned here must occur [12].

Interactions and interfacial adhesion between polymers with dissimilar chemical structures cannot be effective enough to form blends. Therefore, such polymers must be compatibilized in order to form miscible blends [13,14]. Compatibilization is the addition of a small amount of an interfacing agent to immiscible polymer blends. These agents are called compatibilizers. A compatibilizer is a polymer that, when added to an immiscible polymer pair, increases the degree of compatibility between the polymer pair. Such compatibilizing polymer may be a homopolymer as well as usually a co- or terpolymer. The compatibilizer reduces the interface tension by strengthening the adhesion between the polymers in the blend [15]. For PS and PVC; although both are vinylic polymers, interfacial adhesions of benzene and chlorine side groups are high. Therefore, they do not form compatible blends and a compatibilizer is required.

Polystyrene and PVC polymers do not form compatible blends [16]. The thermal properties of polystyrene are relatively good. It is also a well-known commercial polymer that is radiation resistant. Polystyrene is produced and used in a wide variety of forms. The benzene ring in its chain provides flame resistance and solvent resistance. The polystyrene used in the industry is a highly tactical polystyrene and has an amorphous structure. Its UV radiation resistance and insolubility in many solvents cause environmental problems [17]. PVC polymer is one of the most important industrial polymers that is widely used commercially and preferred in many materials. Polyvinylchloride polymer also has a large

commercial use like polystyrene. It is a thermoformable, mostly amorphous polymer with a linear chain [3].

An additional method of polymer modification is through blending; a procedure that involves the mixing of the main polymer in interest with other components to provide a composite mixture or a blend is used, with improved properties [18]. Blending of polymers is becoming increasingly important in different applications to enhance properties, improve processing, or decrease the cost of production [19]. Blending may also involve the addition of a different class of materials to polymers, such as compatibilizers [20-22]. Polymer blending is also achieved through the mixing of two or more different polymers in the liquid phase [23]. Mixing polymers of different classes may result in miscible blends [24]. Polymer blend miscibility is assessed by viscometry, which also provides information about the interactions of the polymers with each other through blending [25,26].

Although there are different techniques to determine whether polymers are miscible or not, the viscometric method, which can provide important information about polymer-polymer miscibility, still remains a simple and inexpensive method. In this respect, it will continue to be a preferred method in laboratories in examining the behavior of polymer blends. It seems that the Krigbaum-Wall equation will continue to be the most widely used equation for those who are looking for an inexpensive and easy method to evaluate the results obtained by the viscometric method of polymer blends.

Non-miscible polymer pairs were compatibilized using various type of compatibilizers and were studied. There are studies showing that the mechanical and thermal properties of polymer blends compatibilized using compatibilizers are improved [27-29]. In most studies, co- or terpolymers based on maleic anhydride have been used as compatibilizing agents [30-34, 17]. A maleic anhydride based compatibilizer is able to reduce the interfacial tension. As the result of this phenomenon, the interfacial between both phases is strong and the direct effect correspond to the improvement of compatibility [35]. In this research article authors used maleic anhydride-styrene (MAS) for compatibilization of PVC/PS blends. MAS is a reactive synthetic random copolymer made up of styrene and maleic anhydride. Copolymers with maleic anhydride make the blend system miscible by establishing secondary chemical interactions between immiscible polymer pairs. Because of its high reactivity and efficiency, it is widely used as a compatibilizer with most of the blend systems [36].

Many studies have been carried out for blending of PS and PVC [16, 37,38]. In these studies, different copolymers containing maleic anhydride were used and remarkable results were obtained.

In this study, solutions containing 1:1 by weight of polyvinyl chloride (PVC) and polystyrene (PS) with concentrations of 0.5, 1.0, 1.5 and 2.0 g.dL^{-1} were prepared. In the solution medium, it was determined by viscometric method at which concentrations a compatible

blend was formed or not. The concentration range in which this polymer pair did not form a compatible blend was found to be 1.5 and 2.0 g.dL^{-1}. Then, the compatibilizing effect was investigated by adding 5 and 10% by mass of MAS copolymer to the solution containing an equal weight of polymer pairs in this concentration range. As a result, it was found that MAS copolymer can be used as a compatibilizer for PVC and PS blends at 1.5 and 2.0 g.dL^{-1} concentrations.

2. MATERIAL AND METHOD

2.1. Chemicals

Polyvinyl cloride (PVC): The PVC used in this study is a polymer produced by Petkim(Turkey) under the name Petvinyl and with code number P38/74.

Polystyrene (PS): PS used in this study is a polymer produced by Petkim(Turkey) under the name Petren and with code number K-560.

Tetrahydrofuran (THF): The THF used in this study is of analytical grade and is Lab-Scan branded and produced by Labscan Ltd.

Maleic anhydride-Styrene (MAS) copolymer: This copolymer was synthesized in our laboratory.

Styrene: Analytical grade, a Sigma-Aldrich product.

Benzene: Analytical grade, a Sigma-Aldrich product.

Azobisisobutyronitrile (AIBN): % 99 purity, a Merck product.

1-Propanol: Analytical grade, a Merck product.

2.2. Experimental

In this study the miscibility and immiscible concentration range of the polymers were determined. Since PS, PVC and MAS polymers are all soluble in THF, polymer solutions were prepared using THF.

2.2.1. Synthesis of MAS copolymer

With a molar ratio of 1:1; 10 mL of styrene and 9.8 grams of maleic anhydride were taken into a reaction flask. Monomers were dissolved by adding 50 mL of benzene. 0.02 g of AIBN initiator was added to this solution and reacted for 90 minutes at 65 °C. The copolymer was precipitated by adding propyl alcohol to the resulting viscous solution. The copolymer dried at room temperature.

2.2.2. Viscometric measurements

In this study the flow times of pure polymer and polymer solutions were measured to calculate the miscibility parameter. Relative (ηr), and specific (ηsp) viscosities of each solution were calculated. These measurements were made with the Cannon-Fenske type viscometer.

All polymer solutions were prepared in 25 mL volumes, in concentrations and ratios where they were immiscible.The prepared solutions were poured into the viscometer and the flow times were recorded.

The interaction parameters of a polymer blend is defined by Krigbaum and Wall by Equation (Eq.1 and 2) [39].

$$b^{id}_{blend} = b_{AA}W^2_A + b_{BB}W^2_B + 2b^{id}_{AB}W_AW_B \qquad (1)$$

$$b^{id}_{AB} = \sqrt{bAA \ x \ bBB} \qquad (2)$$

where : b_{AA}, b_{BB}, b_{AB} are the interaction parameters of first polymer, second polymer and polymer blend respectively. W represents the weight fraction of the polymers.

The interaction parameters (b) of polymers can be determined using dilute solutions, and this parameter can be used as a criterion for miscibility. This method is based on comparing ideal (b^{id}) and experimental interaction (b^{exp}) parameters. It is possible to calculate these two values from the reduced viscosity value ([η]) – concentration (C) graph [40].

$$\frac{\eta sp}{c} = [\eta] + bC \qquad (3)$$

$$\Delta b_{blend} = b^{exp}_{blend} - b^{id}_{blend} \qquad (4)$$

When Δb is positive;
Polymers are said to be miscible. However, if it is negative, it is assumed that the polymers are not compatible.

From the viscometric flow times of the polymers and blends all the parameters mentioned above are calculated and given in the Tables 1, 2, 3 and 4.

3. RESULTS AND DISCUSSION

Table 1. Calculated $\eta_{sp/c}$ values of polymers

C /g dL^{-1}	$\eta_{sp/c}$ values	
	PVC	PS
0.5	1.314	1.016
1.0	1.449	0.986
1.5	2.090	1.441
2.0	2.594	1.527

Table 2. Calculated ideal interaction parameters (b^{id}) of PVC, PS and PVC/PS

C / g dL^{-1}	$b_{11 (PVC)}$	$b_{22 (PS)}$	$b^{id}_{(PVC/PS)}$
0.5	1.360	0.250	0.583
1.0	0.817	0.094	0.277
1.5	0.970	0.330	0.595
2.0	0.980	0.319	0.557

Table 3. Calculated experimental interaction parameters (b^{exp}) of PVC/PS blends

C / g.dL^{-1}	b^{exp}
0.5	0.861
1.0	0.528
1.5	0.347
2.0	0.281

Table 4. Calculated miscibility criterion (Δb) of PVC/PS blends

C /g.dL^{-1}	Δ_b
0.5	0.278
1.0	0.251
1.5	-0.248
2.0	-0.276

Table 5. Flow times of solutions added MAS copolymer

C /g dL^{-1}	Flow times / s		
	% 0 MAS	% 5 MAS	% 10 MAS
1.5	1200	1330	1391
2.0	1621	1760	1864

When Table 4, which was created with the data in Tables 1, 2 and 3, is examined, it can be seen that PVC and PS mix with each other at relatively low concentrations. However, as the concentration increases, they begin to not mix (due to negative Δb). In order to better monitor this relationship, the calculated miscibility parameter (Δb) values for PVC/PVS blends are plotted against concentration and given in Figure 1. It is understood from Figure 1 that the PS/PVC blend does not miscible at 1.5 and 2.0 g.dL^{-1} concentrations. By taking note of these two experimentally determined concentrations, 5 and 10 percent maleic anhydride-styrene (MAS) copolymer was added to the solutions containing 1:1 PS/PVC couple by weight at these two immiscible concentrations. The flow times of these blends with compatibilizer added, measured by viscometer, are shown in Table 5.

By using the flow times in Table 5, the relative, specific and $\eta sp/c$ values of the solution which do not have compatibilizer and the solutions containing 5 and 10 percent MAS compatibilizer were calculated and given in Table 6. In order to determine whether the added MAS copolymer is a good compatibilizer, it is necessary to look at the interaction parameter (b^{exp} and b^{exp}) calculated via the data in Table 6 with equations 1, 2 and 3. Relevant calculations have been made and given in Table 7. When Table 7 is examined, it is seen that the b^{exp} values of the polymer blends increase as the MAS copolymer is added. However, b values alone are not sufficient as proof that polymers become miscible. For this reason, the miscibility criterion (Δb) should be checked at the relevant concentrations. For this, (Δb) values of the blends were calculated from equation 4 and given in Table 8. It can be read from Table 8 that Δb values of PVC/PS polymer couple increase as MAS copolymer compatibilizer is added. It can also be read from Table 8 that the miscibility increases with the addition of the compatibilizer at a relatively high value. In particular at the rate of 10 percent, the added compatibilizer made the immiscible PVC/PS couple miscible. Figure 2 shows the SEM images of PVC/PS and PVC/PS/MAS containing % 10 MAS blends. The SEM micrographs show clearly that the PVC/PS blend has a separate two-phase morphology.

Table 6. Different viscosity values of solutions added MAS copolymer

C /g dL^{-1}	Viscosity values								
	% 0 MAS			% 5 MAS			% 10 MAS		
	η_b	η_{sp}	$\eta_{sp/c}$	η_b	η_{sp}	$\eta_{sp/c}$	η_b	η_{sp}	$\eta_{sp/c}$
1.5	3.243	2.243	1.495	3.594	2.594	1.730	3.639	2.639	1.760
2.0	4.381	3.381	1.691	4.757	3.757	1.878	5.038	4.038	2.019

Table 7. b values of MAS added polymer couple solutions

C /g dL^{-1}	b^{exp} values			b^{id} values
	% 0 MAS	% 5 MAS	% 10 MAS	(from Table.2)
1.5	0.347	0.620	0.660	0.595
2.0	0.281	0.469	0.610	0.557

Table 8. Δb values of immiscible blends containing MAS

C /g dL^{-1}	Δb values		
	% 0 MAS (from Table 4)	% 5 MAS	% 10 MAS
1.5	-0.248	0.025	0.065
2.0	-0.276	-0.088	0.053

In particular, the PVC-PS blend reveals the polarity differences, and high interfacial tension induces the heterogeneity in the matrix. The appearance of voids and sporadic chain sizes and shapes is due to the inconsistency between the two incompatible polymers. In contrast, the (PVC/PS/MAS) blend has a single-phase morphology. Addition of MAS copolymer results in thermodynamic compatibility through addition of compatibilizer. The smooth surface with fewer fissures and better morphological characteristics is evidence of moved forward attachment between the two incompatible

polymers. This situation observed in Figure 2 showed that the MAS copolymer is a good compatibilizer for these two commercial polymers.
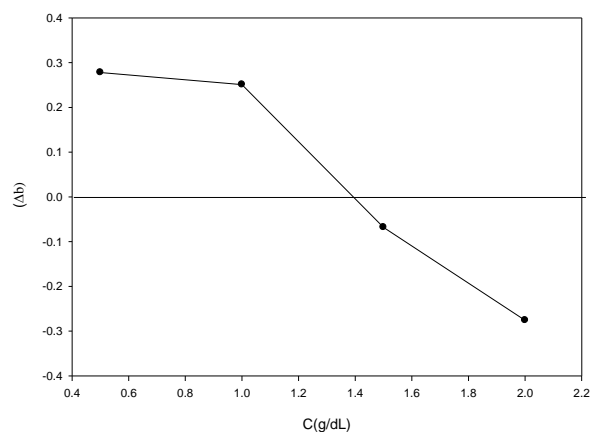
Figure 1. Change of miscibility parameter ($\Delta bmix$) for PVC/PS blend
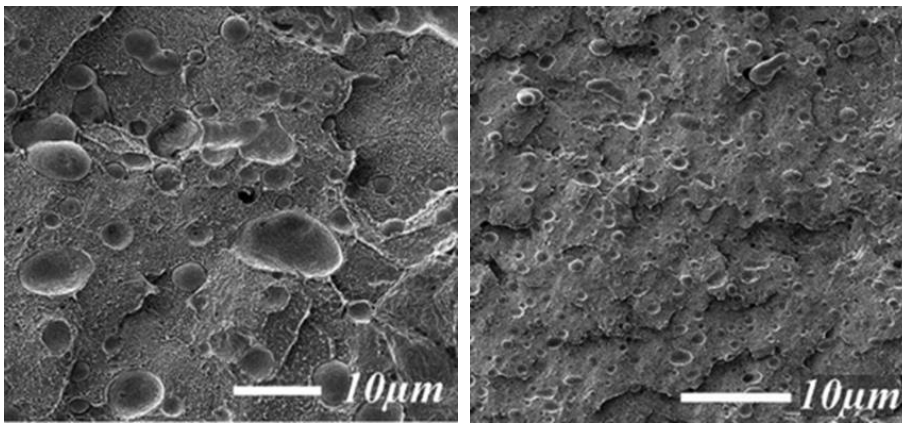
Figure 2. SEM Images of the polymer blends: (left) PVC/PS, (right) PVC/PS/MAS
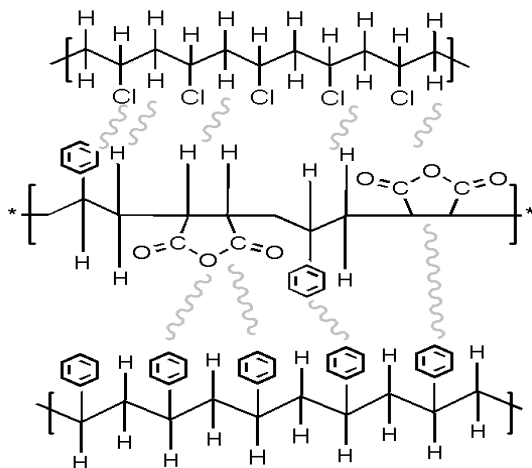

Figure 3. Possible secondary interactions between the polymers and compatibilizer

The factor that makes the two polymers miscible is largely the secondary interactions between the compatibilizer and the components of the blend. Maleic anhydride is an electron donor monomer. The anhydride groups in the compatibilizer make dipole-dipole interactions with the electron donor benzene rings in the polystyrene chain. They also interact with the hydrogen atoms in the PVC backbone due to the electron withdrawal of the -Cl group in the PVC chain. The benzene rings in the copolymer will also interact with the polystyrene chain due to the similarity in chemical structure and will strengthen the bridge established by the copolymer between the two polymers. Such possible secondary interactions are given in Figure 3.

As a result, it can be said that the MAS copolymer is a good compatibilizing agent like other similar copolymers [41-43] in preparing compatible blends of various commercial polymers.

This research have shown that improved compatibility and morphological properties of PS/PVC blends compatibilized by MAS copolymer. MAS copolymer has formed a superior adhesion between the PVC and the PS phases. Due to this effective compatibilization, this copolymer, which we synthesized in our laboratory, can be selected as a compatibilizer in applications where these two important commercial polymers are used.

4. CONCLUSION

As mentioned earlier in this article, compatibilized blending of polymers is one of the only implies of getting an assortment of physical and chemical properties from the constituent polymers. The pick-up in superior properties of polymers depends on their degree of compatibility or miscibility at an atomic degree. Moreover, blending of polymers is a productive approach to the accomplishment of modern combinations of wanted properties without having to synthesize new polymeric materials. This study, in which two very important commercial polymers such as PS and PVC are made into a compatible blend, will contribute to the literature in line with these purposes.

Further studies involving thermal, mechanical and durability testing of MAS-compatibilized PS/PVC blends can be performed to identify potential applications in which these blends could be used.

Acknowledgement

REFERENCES

[1] Jayakumar A., Radoor S., Radhakrishnan E.K., Nair I. C., Siengchin S., Parameswaranpillai J., 3 - Soy protein-based polymer blends and composites, Editor(s): Sanjay Mavinkere Rangappa, Jyotishkumar Parameswaranpillai, Suchart Siengchin, M. Ramesh, In Woodhead Publishing Series in Composites Science and Engineering, Biodegradable Polymers, Blends and Composites,Woodhead Publishing, 2022, Pages 39-57.

[2] Sabzi F., Chapter 24 - Gas Transport Through Polymer Blends, Editor(s): Sabu Thomas, Runcy Wilson, Anil Kumar S., Soney C. George, Transport Properties of Polymeric Membranes, Elsevier, 2018, Pages 517-532, ISBN 9780128098844.

[3] Yilmaz E. Compatibilization of polyvinyl chloride - polymethyl methacrylate polymer blends with maleic anhydride-styrene-methyl methacrylate

175

terpolymer. *J. Appl. Polym. Sci.,* 2022, 139(10), 51745.

[4] Imren Koç D., Koç M. L. Fuzzy viscometric analysis of polymer-polymer miscibility based on fuzzy regression. *Chemometr. Intell. Lab. Syst.*, 2016, 157, 58-66.

[5] Siskey R., Smelt H., Boon-Ceelen K., Persson M., 22 - UHMWPE Homocomposites and Fibers, Editor(s): Steven M. Kurtz, UHMWPE Biomaterials Handbook (Third Edition), William Andrew Publishing, 016, Pages 398-411, ISBN 9780323354011.

[6] Biron M., 3 - Recycling: The First Source of Renewable Plastics, Editor(s): Michel Biron, In Plastics Design Library, Industrial Applications of Renewable Plastics, William Andrew Publishing, 2017, Pages 67-114, ISBN 9780323480659.

[7] Huang JY. and Jiang WC. Effects of chemical composition and structure of unsaturated polyester resins on the miscibility, cured sample morphology and mechanical properties for styrene/unsaturated polyester/low-profile additive ternary systems. 1: Miscibility and cured sample morphology. *Polymer,* 1998, 39(25), 6631-6641.

[8] Imren D., Boztug A., Basan S. Investigation Of Miscibility Of Poly(vinyl chloride) With Poly(ethylene-co-vinyl acetate) By Viscosimetric Method. *Mater. Res. Innov.,* 2006, 10(2), xlvii-xlviii.

[9] Bensemra NB., Bedda A., Belaabed A. Study of the properties of rigid and plasticized PVC/PMMA blends. *Macromol. Symp.*, 2003, 202, 151-165.

[10] Krache R., Benachour D., Pötschke P. Binary and ternary blends of polyethylene, polypropylene, and polyamide 6,6: The effect of compatibilization on the morphology and rheology. *J. Appl Polym. Sci*., 2004, 94 (5), 1976-1985.

[11] Sivalingam G., Madras G. Thermal degradation of ternary blends of poly(ε-caprolactone)/poly(vinyl acetate)/poly(vinyl chloride). *J. Appl. Polym. Sci.,* 2004, 93(3), 1378-1383.

[12] Boztug A., Yilmaz E. Effects of reactive terpolymer containing maleic anhydride on thermomechanical properties of poly(vinyl chloride) based multicomponent blends. *Mater. Res. Innov*, 2007, 11(3), 158-160.

[13] Ubonnut L., Thongyai S., Praserthdam P. Interfacial adhesion enhancement of polyethylene–polypropylene mixtures by adding synthesized diisocyanate compatibilizers. *J. Appl. Polym. Sci*., 2007, 104(6), 3766-3773.

[14] Imren Koç D., Özel Ergün N., Koç M. L. Prediction of miscibility of sodium alginate/poly(ethylene glycol) blends by fuzzy systems. *J. Fac. Eng. Archit. Gazi Univ.* 2019, 34(2), 635-646.

[15] Villarreal ME., Tapia M., Nuño-Donlucas, SM., Puig, JE., González-Núñez, R. Mechanical properties of polystyrene/polyamide 6 blends compatibilized with the ionomer poly(styrene-co-sodium acrylate). *J. Appl. Polym. Sci,* 2004, 92(4), 2545-2551.

[16] Imren D. Compatibilization of immiscible poly(vinyl chloride) (PVC)/polystyrene (PS) blends

with maleic anhydride–styrene–vinyl acetate terpolymer (MAStVA), *J. Mol. Struct.,* 2010, 963(2-3), 245-249.

[17] Tol RT., Groeninckx G., Vinckier I., Moldenaers P., Mewis J. Phase morphology and stability of co-continuous (PPE/PS)/PA6 and PS/PA6 blends: effect of rheology and reactive compatibilization. *Polymer,* 2004, 45(8), 2587-2601.

[18] Paul DR. and Barlow JW. A brief review of polymer blend technology, *Advances in Chemistry*, 1979, 176, 315–335.

[19] Visakh PM., Gordana M., and Daniel P. Recent Developments in Polymer Macro, Micro and Nano Blends: Preparation and Characterization, Woodhead Publishing, Sawston, U.K. 2016.

[20] Fu X., and Qutubuddin S. Polymer-clay nanocomposites: exfoliation of organophilic montmorillonite nanolayers in polystyrene. *Polymer*, 2001, 42(2), 807–813.

[21] Vasanth CS., Chongchen X., and Nikhil G. In Hybrid and Hierarchical Composite Materials, Springer, Cham, Switzerland. 2015.

[22] Gupta RK., and Bhattacharya SN. Polymer-clay nanocomposites: current status and challenges. *Indian Chem. Eng.*, 2008, 50, 242–267.

[23] Paul DR., and Barlow JW. Polymer blends. *J. Macromol. Sci., Part C*, 1980, 18(1), 109–168.

[24] Lizymol PP., and Thomas S. Miscibility studies of polymer blends by viscometry methods. *J. Appl Polym. Sci.*, 1994, 51(4), 635–641.

[25] Fekete E., Földes E., and Pukánszky B. Effect of molecular interactions on the miscibility and structure of polymer blends. *Eur. Polym. J.,* 2005, 41(4), 727–736.

[26] Jukic A., Rogosic M., Franjic I., and Soljic I. Molecular interaction in some polymeric additive solutions containing styrene-hydrogenated butadiene copolymer. *Eur. Polym. J.,* 2009, 45, 2594–2599.

[27] Tanrattanakul V., Petchkaew A. Mechanical properties and blend compatibility of natural rubber –chlorosulfonated polyethylene blends. *J. Appl Polym. Sci.,* 2006, *99(1)*, 127-140.

[28] Wiebking HE. Increasing the flexural modulus of rigid PVC at elevated temperatures. *J. Vinyl Addit. Technol.,* 2006, *12(1),* 37-40.

[29] Genovese A., Shanks RA. Dynamic Mechanical Properties of Poly(propylene) Blends with Poly[ethylene-co-(methyl acrylate)]. *Macromol. Mater. Eng.,* 2004, *289(1),* 20-32.

[30] Lai S.-M., Li H.-C., Liao Y.-C. Properties and preparation of compatibilized nylon 6 nanocomposites/ABS blends: Part II – Physical and thermal properties. *Eur. Polym. J.,* 2007, 43(5), 1660-1671.

[31] Mounir A., Darwish NA., Shehata A. Effect of maleic anhydride and liquid natural rubber as compatibilizers on the mechanical properties and impact resistance of the NR-NBR blend. *Polym. Adv. Technol.,* 2004, 15(4), 209-213.

[32] Ismail H., Supri, Yosuf, AMM. Blend of waste poly(vinylchloride) (PVCw)/acrylonitrile butadiene-rubber (NBR): the effect of maleic

anhydride (MAH). *Polym. Test.,* 2004, 23(6), 675-683.

[33] Araujo EM., Hage E. & Carvalho AJF. Morphological, mechanical and rheological properties of nylon 6/acrylonitrile-butadiene-styrene blends compatibilized with MMA/MA copolymers. *J. Mater. Sci.,* 2003, **38,** 3515–3520.

[34] Cassu SN., & Felisberti MI. In situ compatibilization of polystyrene and polyurethane blends by using poly(styrene-co-maleic anhydride) as reactive compatibilizer. *J. Appl Polym. Sci.,* 2001, *82,* 2514-2524.

[35] Mahendra I.P., Wirjosentono B., Tamrin. The influence of maleic anhydride-grafted polymers as compatibilizer on the properties of polypropylene and cyclic natural rubber blends. *J Polym Res* 2019, 26**,** 215.

[36] Kameshwari Devi SH., Hatna S. The effect of styrene maleic anhydride compatibilizer on the performance of polycarbonate/acrylonitrile butadiene styrene blends, *Mater. Today: Proc.,* 2021, 46(7), 2510-2514.

[37] Braun D., Fischer M. Mechanical behaviour of PWPVC blends compatibilized with block-graft copolymers based on poly(styrene-block-butadiene). *Angew. Makromol. Chem.* 1995, 233, 77-87.

[38] Abdelghany AM., El-Damrawi G., ElShahawy AG., Altomy NM. Structural Investigation of PVC/PS Polymer Blend Doped with Nanosilica from a Renewable Source. *Silicon,* 2018, **10,** 1013–1019.

[39] Krigbaum WR, Wall FT. Viscosities of binary polymeric mixtures. *J. Polym. Sci.* 1950, 1950(5),505–514.

[40] Lewandowska K. The miscibility of poly(vinyl alcohol)/poly(N-vinylpyrrolidone) blends investigated in dilute solutions and solids. *Eur. Polym. J.* 2005, 41:55–64.

[41] Dimitrova TL., La Mantia F.P., Pilati F., Toselli M., Valenza A., Visco A. On the compatibilization of PET/HDPE blends through a new class of copolyesters. *Polymer,* 2000, 41(13):4817-4824.

[42] Hausmann K., Chou RT., Lee CY. Novel functionalised ethylene acrylate copolymers as polymer modifiers. *Polym. Polym. Compos.,* 2004, 12, 119–125.

[43] Fung KL., Li RKY. Mechanical properties of short glass fibre reinforced and functionalized rubber-toughened PET blends. *Polym. Test.,* 2006, 25(7), 923-931.

177

Türk Doğa ve Fen Dergisi
Turkish Journal of Nature and Science
www.dergipark.gov.tr/tdfd

Comparison of traditional Zivzik pomegranate vinegar against commercial pomegranate vinegar: antioxidant activity and chemical composition

Abdulkerim AYBEK[1], Ebru AKKEMİK[1,2]*

[1] Siirt University, Faculty of Engineering, Food Engineering Department, Siirt, Türkiye
[2] Siirt University, Science and Technology Application and Research Center, Siirt, Türkiye
Abdulkerim AYBEK ORCID No: 0000-0002-9543-8659
Ebru AKKEMİK ORCID No: 0000-0002-4177-4884

*Corresponding author: eakkemik@siirt.edu.tr

Abstract: The vinegar, which is well-known for its health benefits, changes its application potential and chemical qualities depending on the raw material from which it is made. In this study, physicochemical properties, total phenolic, total flavonoid, and total anthocyanin content, organic acid, sugar, and phenolic acid composition by high performance liquid chromatography (HPLC), elemental analysis by inductively coupled plasma-optical emission spectrometer (ICP-OES), and antioxidant properties of Zivzik pomegranate vinegar (ZPV) produced using traditional methods from Zivzik pomegranate varieties were compared to commercial pomegranate vinegar (CPV). Total monomeric anthocyanin, total phenolic content and total flavonoid content of ZPV was determined to be 32.39±2.6425 (mg cyanidin-3-glucoside L−1), 1823.529±124784 (mg GAE L−1) and 2.7571±0.2603 (mg rutin mL−1), respectively. Total monomeric anthocyanin, total phenolic content, and total flavonoid content of CPV was determined to be 1.136±0.6054 (mg cyanidin-3-glucoside L−1), 5764.706±848.365 (mg GAE L−1) and 1.3932±0.0349 (mg rutin mL−1), respectively. K is the most abundant element in both vinegar samples. Acetic acid is the most common organic acid found in both forms of vinegar. While chlorogenic acid was determined to be the most prevalent phenolic compound in commercial pomegranate vinegar, gallic acid was shown to be the most prevalent in Zivzik pomegranate vinegar. As a result, while it was determined that the origin and type of the raw material had a direct impact on the product quality, it was also shown that vinegar made using traditional methods was healthier than commercial vinegar.

178

Geleneksel Zivzik Nar Sirkesinin Ticari Nar Sirkesi ile Karşılaştırılması: Antioksidan Aktivite ve Kimyasal Bileşim

Öz: Sağlık için oldukça faydalı olduğu bilinen sirkenin, elde edildiği hammaddeye göre kullanım potansiyeli ve kimyasal özellikleri değiştirmektedir. Bu çalışmada, nar çeşitlerinden biri olan Zivzik narından, geleneksel yöntemlerle üretilen Zivzik nar sirkesinin, fizikokimyasal özellikleri, antioksidan özellikleri, toplam fenolik, toplam flavonoid ve toplam antosiyanin içeriği, HPLC yardımıyla organik asit, şeker ve fenolik asit bileşimi ICP-OES ile element analizi yapılarak ticari nar sirkesi ile karşılaştırılmıştır. Çalışma sonucunda Zivzik nar sirkesinin ticari sirkeye göre daha fazla antioksidan olduğu bulunmuştur. Her iki sirke örneğinde de K baskın element olarak belirlenmiştir. Benzer şekilde, asetik asit, her iki sirke türünde de tespit edilen baskın organik asittir. Ticari nar sirkesinde klorojenik asit baskın fenolik bileşik iken, Zivzik nar sirkesinde gallik asidin baskın olduğu belirlendi. Sonuç olarak hammaddenin menşei ve çeşidinin elde edilen ürün kalitesine doğrudan etkisi olduğu belirlenirken, geleneksel yöntemlerle elde edilen sirkenin sağlık açısından ticari sirkeye göre daha faydalı olduğu sonucuna varıldı.

1. INTRODUCTION

With a history dating back to 3000 B.C vinegar [1] is defined as a liquid produced by ethyl alcohol and acetic acid fermentation of different raw materials [2]. As in the past, vinegar is a favorite material for health and cosmetic purposes as food stuff or disinfectant [3]. In addition, it has been known that vinegar, has antitumor [4], antibacterial [5], antidiabetic [6], antiviral properties [7] and has dermatological benefits [5].

Different fruits, vegetables and grains are used as raw materials in vinegar making. Dimrit grape [8], black carrot [9], black mulberry [10], persimmon [11], rice [12], Trebbiano or Lambrusco grapes (balsamic vinegar) [13], and pomegranate [14] are various raw materials for vinegar making.

The quality of the vinegar depends directly on the raw material. The composition of raw materials is influenced by factors such as cultivation techniques, climate, soil, variety, etc [15]. Besides, it has been stated that vinegar could have different effects on health depending upon the raw material used. For example, it was mentioned that rice vinegar regulates blood pressure, grape vinegar facilitates and smooths digestion and grain vinegar has appetizing property [16].

There have been studies in literature dealing with the effects of factors such as fruit variety, growing conditions and harvest time on product quality. In addition to the studies investigating the effects of grape varieties on wine quality [17], there have been studies reporting that the composition of the phenolic substances in the wine produced is influenced by the variety [18]. Pomegranate has a history as old as that of vinegar [19] and has gained more recognition and importance with advances in growing techniques and food technology, especially with the advances in transportation and storage. Thus, production, consumption and trade of the pomegranate have been steadily increasing. Pomegranate is usually consumed for table, but it also has considerable consumption as sour sauce, molasses, concentrate and vinegar. Nevertheless, there have been limited number of studies on pomegranate vinegar.

The pomegranate vinegar obtained from Gapsi pomegranate, a pomegranate variety grown in Tunisia, was compared with juice, wine and commercial vinegar [14]. Another study examined phenolic substance content, antioxidant properties and color parameters of the vinegar produced from Northern Greek pomegranate genotype [20]. Antioxidant, color and phenolic substance profiles were investigated in vinegar samples obtained from Hicaz and Beynar pomegranate varieties21. All of these studies aimed to reveal the effect of the fruit varieties used on the product content. Raw material is the most important quality factor in vinegar production, but the cultivated variety of a certain type of plant material also has a considerable effect on the quality. Vinegar made from different varieties of the same fruit could have different quality characteristics. Even if their aromas are similar or the same, vinegars produced from different varieties may have different compositions. As a result, the type of fruit used as raw materials would affect the final vinegar product depending upon its composition. In the present study, vinegar production was made from Zivzik pomegranate variety for the first time. Antioxidant and chemical compositions of the vinegar produced were compared to a commercial vinegar. Thus, the potential health benefits of both vinegars were compared.

2. MATERIAL AND METHOD

2.1. Material

The Zivzik Pomegranate that we used as a material in the study was purchased from pomegranate producers in Siirt in November. In addition, Saccharomyces cerevisiae for alcohol fermentation and vinegar mother for acid fermentation were obtained from the market. Acetonitrile, Diphenyl-2-picryl hydrazine, AlCl3, routine, gallic acid, Folin, Ciocalteu reagent, and K-Phosphate were provided from either Sigma – Aldrich or E. Merck. All the other chemical substances used were of analytical grade and obtained from either Sigma–Aldrich or E. Merck.

2.2. Vinegar Production

Zivzik pomegranate vinegar was traditionally produced according to the Kırcı (2017) method [22]. Alcoholic fermentation was carried out by adding 0.25 gL-1 Saccharomyces cerevisiae to the fruit juice obtained by pressing the method from Zivzik pomegrane. Alcohol fermentation was terminated when the alcohol content was 7%. Later, 5% vinegar mother was added to the pomegranate solution for acid fermentation. The pomegranate solution was brought into contact with air to decrease the alcohol content and accelerate the fermentation. Fermentation was terminated when the alcohol content of the pomegranate solution was below 0.5%.

2.3. Physicochemical Analysis in Vinegar Samples

The total acidity according to the titrimetric method was made [23, 24]. Dry matter dissolved in water was read as %brix value. For this, a refractometer (HANNA-HI 96801-Refractometer) was used [24, 25]. Total dry matter analysis was done by drying in the incubator (POL-EKO-APARATURE-SLN-53-std) [8, 24]. The color analysis was measured with a colorimeter (Pencolorart USB models, 1L, Istanbul-Turkey) [24, 26].

2.4. Analysis of total monomeric anthocyanin, total phenolic substance, and total flavonoid in vinegar samples

Total monomeric anthocyanin analysis was made by modifying the pH differential method used by Fuleki & Francis (1968) [27]. Total flavonoid analysis was performed by modifying the colorimetric method of AlCl3 in accordance with our laboratory conditions. The readings were performed at 510 nm wavelength with the Multiskan Go (Thermo 1424-7028) device. Flavonoid content was calculated as mg rutin equivalent (QE) [28,

29]. The total phenolic content of the vinegar samples was determined by used Folin and Ciocalteu reagent at 760 nm with Multiskan Go device (Thermo 1424-7028) as gallic acid equivalent [30, 31].

2.5. Organic Acid, Sugar, and Phenolic Acid Analyses with HPLC in Vinegar Samples

The relevant study was carried out by the Siirt University, Science and Technology Application and Research Center, by receiving service. Organic acid analysis in HPLC has been used in accordance with our laboratory conditions by modifying the Tormo and Izco (2004) method [32]. 0.5 mL of vinegar sample was diluted 1-1 ratio with 10 mM K-Phosphate pH 2.4 buffer, passed through a micropore filter (0.22 μm) and transferred to vials. HPLC-DAD (Thermo/DIONEX Ultimate 3000 series, Thermo Fisher Scientific, the US) device was used for the quantitative analysis of organic acids. Reverse phase column (C-18 Inertsil ODS-3 column, 5 μm particle, 4.6 × 250 mm ID) was used for the analysis of organic acids. In the chromatographic distinction, the mobile phase A (10 mM K-Phosphate pH 2.4) and mobile phase B (acetonitrile) were used. The column flow rate was set at 1 mL min-1 and the column temperature was set to 28°C throughout the analysis. Sample injection volume was adjusted to 50 μL. Standard injection volume was adjusted to 20 μL. During the elution, changes were made to obtain a gradient of A %90, B %10 (1 min; 1mL min-1), A %90, B %10 (12 min; 0.75 mL min-1), and A %25, B %75 (0.75 min; 35mL min-1). The chromatograms of the study were analyzed at 210 nm wavelengths. The phenolic content of the vinegar samples was made according to Akkemik et al., (2019) [33]. Vanillic acid, chlorogenic acid, gallic acid, caffeic acid, and hydroxybenzoic acid were used as standards. Organic sugar analysis of vinegar samples was determined according to TS 13359 method [34]. The study was repeated three times.

2.6. Analysis of Macro Micronutrients with ICP-OES in Vinegar Samples

The relevant study was carried out by the Siirt University, Science and Technology Application and Research Center, by receiving service. 0.5 mL of vinegar samples were taken and placed in teflon decomposition tubes. 6 mL of 65% nitric acid and 2 mL of 30% hydrogen peroxide were added on them. It was kept in the fume hood for 2 hours until the gas output was completed. Then the lids of the tubes were closed and placed in a microwave oven (Berghof Speedwave MWS-2). The microwave oven was operated in three different stage. In the first stage, it was terminated by waiting at 180°C for 10 minutes (99% power), in the second stage at 180°C for 15 minutes (99% power) and at 25°C for 5 minutes (80% power) in the last stage [35]. All samples were then placed in the ICP-OES autosampler unit (Device Perkin Elmer ICP-OES Optima 2100 DV ICP-OES; Plasma power, 1300 W; nebulizer flow, 0.80 L min-1; Plasma flow, 15 L min-1; auxiliary flow, 0.2 L min-1; Plasma View, Axial; Sample Flow Rate, 1.50 mL min-1; Delay Time, 60 sec; Source Equilibration Delay, 15 sec; Plasma Conditions,

Same for All Elements; Nebulizer Start-up, Instant). Calibration solutions were prepared at five different concentrations ranging from 25.00 to 1000.00 ppb using [36].

2.7. Antioxidant Analysis in Vinegar Samples

Free radical removal activity of DPPH (Diphenyl-2-picryl hydrazine) in vinegar samples was performed according to the Blois method in accordance with our laboratory conditions [37]. FRAP (Ferric reducing antioxidant power) analysis in vinegar samples [38, 39] was measured in Multiskango (Thermo, serial no: 1424-7028) device at 593 nm wavelength with minor modifications. Cuprac analysis based on the reduction principle of Cu2+ ions [40] was modified in accordance with our laboratory conditions, and the absorbance values at 450 nm wavelength were determined with the Multiskango (Thermo serial no: 1424-7028) device.

2.8. Statistical Analysis

Microsoft Excel program was used for statistical analysis of the obtained data. The mean values and standard errors of all data were calculated.

3. RESULTS AND DISCUSSION

3.1. Physicochemical Analyses in Vinegar Samples

Average pH value during acetic acid fermentation was 2.93±0.850 in vinegar samples produced from Zivzik pomegranate. In commercial pomegranate vinegar, on the other hand, the pH value was 2.83±0.10 (Table 1). pH values were reported to be between 2.61±0.04 and 3.03±0.10 for different pomegranate vinegars [14, 20, 21]. Thus, pH value of vinegar produced from Zivzik pomegranate was similar to the values reported in the literature.

Table 1. Physicochemical analysis of vinegar samples

PHYSICOCHEMICAL ANALYSIS		ZIVZIK POMEGRANATE VINEGAR	COMMERCIAL POMEGRANATE VINEGAR
pH		2.95±0.1	2.83±0.1
TSS (ºB)		4.80±0.100	12.17±0.058
Total dry matter (%)		2.686±0.088	7.834±0.129
g acetic acid L^{-1}		24±0.6	41.2±0.92
Color analysis	L	8.4133±0.5992	8.1467±0.1380
	a*	1.5567±0.2318	1.6400±0.3477
	b*	-4.6300±0.5524	-4.0767±1.4008

TSS, *Total soluble dry matter, L, brightness; a*, green-red color coordinate; b*, blue-yellow color coordinate*

In terms of total acidity calculated based on milliequivalent weight of acetic acid, Zivzik pomegranate vinegar had an equivalent weight of 24±0.6 g L-1 while commercial pomegranate vinegar had an acetic acid equivalent weight of 41.2±0.92 g L-1 (Table 1). The total acidity of Zivzik pomegranate juice was reported to be 0.9753±0.0532 [41]. During the fermentation, acetic acid forms. However, if fermentation of the vinegar continues, vinegar bacteria break down the acetic acid and lead to upper oxidation. For this reason, fermentation is stopped when the acidity rate of vinegar drops to the level of 0.5%

alcohol [42, 43]. In the present study, when the alcohol content was 0.5% or below, the process was stopped. However, the expected acidity rate was not reached in vinegar sample produced from Zivzik pomegranate. The reason for this could be the break-down of the acetic acid during the experiment. In a study comparing vinegar samples produced by traditional (19 samples) and industrial methods (6 samples), it was found that all but one of the vinegars produced by traditional methods had total acidity levels of less than 40 g L-1 but that the vinegars produced by industrial methods had acidity levels equal to or above 40 g L-1 [24]. Similar results were also obtained in the present study.

The total dry matter and water-soluble dry matter contents of the Zivzik pomegranate vinegar appeared to be lower compared to commercial pomegranate vinegar (Table 1). The total and water-soluble dry matter contents of the vinegars produced by traditional methods were generally low in previous studies, but these contents in the vinegar produced from the Zivzik pomegranate were similar to the values reported in the literature [5, 10, 24]. It is thought that the reason for the high water-soluble dry matter and total dry matter of commercial pomegranate vinegar is due to additives used during the production of the vinegar. L, a and b values of Zivzik pomegranate vinegar and commercial vinegar were generally close to each other, and both vinegars were pale and red in color.

3.2. Total Monomeric Anthocyanin, Total Phenolic Content, and Total Flavonoid Analyses in Vinegar Samples

Zivzik pomegranate vinegar had 32.39 ± 2.6425 mg of cyanidine 3-glucoside L-1 equivalent while commercial pomegranate had 1.136 ± 0.6054 mg cyanidine 3-glucoside L-1 equivalent (Table 2). Although the color analyses of Zivzik pomegranate vinegar and commercial vinegar were similar, about 30 times difference was found between the two vinegars for anthocyanin rate. This finding suggests that coloring or clarification additives are used to create the red color property of the commercial vinegar sample. Rutin was used as standard to determine the flavonoid content of Zivzik pomegranate vinegar and commercial pomegranate vinegar. Zivzik pomegranate vinegar and commercial pomegranate vinegar were found to have 2.7571 ± 0.2603 and 1.3932 ± 0.0349 mg rutin equivalent mL-1 (Table 2). Although the flavonoid content was low in the two vinegar samples examined in the present study, Zivzik pomegranate vinegar had somewhat higher flavonoid content than that of the commercial vinegar. The total phenolic matter contents of Zivzik pomegranate vinegar and commercial pomegranate vinegar were determined based on the gallic acid standard (Table 2). Furthermore, the high content of the total phenolic matter in the commercial vinegar sample compared to the Zivzik pomegranate vinegar suggested that there could be a preservative in the commercial vinegar. The total phenolic substance content was between 710.40 and 4448.0 mg gallic acid equivalent L-1 in [14, 20, 21] different variety pomegranate vinegar. Literature analysis indicated that the variety is effective on phenolic matter content of pomegranate vinegar.

Table 2. Total monomeric anthocyanin, total flavonoid, and total phenolic content in vinegar samples

	TOTAL MONOMERIC ANTHOCYANIN (MG CYANİDİN-3-GLUCOSİDE L^{-1})	TOTAL PHENOLIC CONTENT (MG GAE L^{-1})	TOTAL FLAVONOID CONTENT (MG RUTİN ML^{-1})
Zivzik pomegranate vinegar	32.39 ± 2.6425	1823.529 ± 124.784	2.7571 ± 0.2603
Commercial pomegranate vinegar	1.136 ± 0.6054	5764.706 ± 848.365	1.3932 ± 0.0349

3.3. Organic Acid, Sugar, and Phenolic Acid Analyses with HPLC in Vinegar Samples

The dominant organic acid in vinegar samples was acetic acid (Table 3). However, the ratio of acetic acid in commercial pomegranate vinegar was higher. These findings confirmed the results with the titratable acetic acid. It was reported that traditional vinegar samples generally had titratable acetic acid levels of less than 40 gL-1 [24]. In a study comparing the malic, citric, oxalic, and tartaric acid contents of pomegranate juice samples of different pomegranate varieties including Zivzik, it was reported that citric acid was dominant in all varieties and that the highest malic acid content was measured in Zivzik variety [41]. It was mentioned that ecological conditions and fruit maturity level were responsible for the organic acid contents in juices of different pomegranate varieties [41, 44]. Fructose, glucose and saccharose sugar contents were determined and compared in vinegar samples (Table 3). The results showed that Zivzik pomegranate vinegar had no saccharose while its fructose and glucose contents were higher than the commercial pomegranate vinegar. This once again proved that the composition of vinegar

depends on raw materials. It is well acknowledged that various plants and fruits including pomegranate are the main sources of natural compounds behaving as exogenous antioxidants that strengthen body intrinsic antioxidant machineries for the protection of the organism against ROS-mediated damages. Gallic acid, chlorogenic acid, hydroxybenzoic acid, caffeic acid, quercetin, chrysin and ferulic acid (most of them were identified within the content of pomegranate in our study) are promising bioactive compounds mainly found in plants and fruits with strong antioxidant activities (45-48). Gallic acid, hydroxybenzoic acid, caffeic acid, vanillic acid and chlorogenic acid were used as standards to determine the phenolic acid contents of Zivzik pomegranate vinegar and commercial pomegranate vinegar. The phenolic acid with the highest content in Zivzik pomegranate vinegar was gallic acid while in commercial pomegranate vinegar chlorogenic acid had the highest content (Table 3). Gallic acid was reported to be the predominant organic acid in vinegar samples produced from Beynar and Hicaz pomegranates while chlorogenic acid could not be detected in both vinegar samples [21]. These findings also pointed out the variety as an important factor in the

composition of vinegar. The findings of that study were similar to those in the present study, and very high amount

of chlorogenic acid in commercial vinegar suggested that external preservatives were added.

Table 3. Analysis of organic acid, sugar, and phenolic matter by HPLC in vinegar samples

	STANDARDS	ZIVZIK POMEGRANATE VINEGAR (PPM)	COMMERCIAL POMEGRANATE VINEGAR (PPM)
Organic acid	Tartaric acid	1444.4776±5.6134	109.4413±1.2913
	Malic acid	1306.5262±1.1746	2499.4736±4.0208
	Ascorbic acid	0.3104±0.0023	64.0754±3.7547
	Acetic acid	9553.8308±29.25	34674.5943±49.2736
	Citric acid	27.6851±0.1589	89.3851±21.825
	Total	12332.83±25.13	37436.97±71.13
Sugar	Fructose	77.0365±14.1585	14.9497±0.7483
	Glucose	87.0598±18.1468	33.3640±9.554
	Sucrose	-	7.2872
	Total	164.0962	55.6009
Phenolic acid	Gallic acid	285.4568±1.4886	131.0446±0.4778
	Chlorogenic acid	14.1489±0.1515	257.7429±1.2573
	Hydroxybenzoic acid	1.0345±0.0425	12.2285±0.0629
	Caffeic acid	1.4037±0.0005	0.6894±0.0059
	Vanillic acid	1.7866±0.0124	0.0912±0.0067
	Total	313.7477±1.8105	299.3256±7.7694

3.4. Analysis of Macro Micronutrients with ICP-OES in Vinegar Samples

In our study, the highest amount of mineral in Zivzik pomegranate vinegar was K (2382.55 ± 58.050 ppm), followed by P (94.7460 ± 4.0080 ppm), Mg (60.7500 ± 2.0160 ppm), Na (50.8960 ± 8.4870 ppm) and Ca (15.8720 ± 6.6990 ppm) (Table 4). Commercial pomegranate vinegar, on the other hand, had 2085 ± 133.652 ppm K, 211.5 ± 3.1113 ppm P, 84.323 ± 5.287 ppm Na, 62.887 ± 0.144 ppm Mg and 46.963 ± 10.892

ppm Ca (Table 4). Thus, mineral contents of the Zivzik pomegranate vinegar and commercial pomegranate vinegar were similar. Both vinegar samples had high K contents. In both vinegar samples, some metals that pose a risk factor for human health such as Ni, Pb, Fe and Cu, were found in trace amounts, while the commercial vinegar sample was also found to have Al, Cd and Cr. The presence of these heavy metals in vinegar samples emphasized the importance of soil and environmental conditions where pomegranates grow.

182

Table 4. Macro-microelement analysis in vinegar samples

Element	Zivzik pomegranate vinegar (ppm)	Commercial pomegranate vinegar (ppm)
Al (Aluminum)	-	13.503±2.235
K (Potassium)	2382.55±58.050	2085±133.652
P (Phosphorus)	94.7460±4.0080	211.5 ±3.1113
Mg (Magnesium)	60.7500±2.0160	62.887 ±0.144
Na (Sodium)	50.8960±8.4870	84.323 ±5.287
Cd (Cadmium)	-	0.040± 0.0070
Cr (Chrome)	-	0.0608±0.0185
Ca (Calcium)	15.8720±6.6990	46.963 ±10.892
Ni (Nickel)	5.7703±0.2516	5.74567 ±0.113
B (Boron)	1.3887±0.9777	2.873±0.26200
Pb (Lead)	1.1486±0.0832	0.7462 ±0.0517
Zn (Zinc)	0.7175±0.2071	1.6257 ± 0.184
Fe (Iron)	0.2384±0.0446	5.179 ±2.9260
Sn (Tin)	0.1778±0.0036	-
Cu (Copper)	0.1746±0.0436	0.1156 ±0.044
Bi (Bismuth)	0.0991±0.1171	-
Mn (Manganese)	0.0839±0.0127	0.2372 ± 0.032
Sb (Antimony)	0.0710±0.0249	-
Mo (Molybdenum)	0.0656±0.0082	-
Sr (Strontium)	0.0265±0.0436	0.3097 ± 0.0690
Ba (Barium)	0.0172±0.0128	0.0730 ± 0.0202
Li (Lithium)	0.0101±0.0000	0.9247 +0.0209

3.5. Antioxidant analysis in vinegar samples

Antioxidant properties of vinegar samples were determined using DPPH, Cuprac and FRAP methods (Table 5). DPPH radical scavenging and copper reduction activity levels of Zivzik pomegranate vinegar were higher

than those of the commercial vinegar, while iron reduction activities of the two vinegar samples were similar. Thus, pomegranate vinegar produced by traditional methods was found to have higher antioxidant capacity than commercial vinegar.

Table 5. Antioxidant analysis of vinegar samples

	DPPH (MG TROLOX E ML⁻¹)	CUPRAC (MG TROLOX E ML⁻¹)	FRAP (MG TROLOX E ML⁻¹)
Zivzik pomegranate vinegar	10.875±0.215	51.763±3.042	18.889±1.798
Commercial pomegranate vinegar	6.2297±0.405	37.225±2.044	26.683±5.256

4. CONCLUSION

There are few studies on pomegranate vinegar in the 183iteratüre. The scope of this study, Zivzik pomegranate vinegar and commercial pomegranate vinegar were compared for physicochemical properties, total phenolic, total flavonoid, and total anthocyanin content, organic acid, sugar, and phenolic acid composition by HPLC, elemental analysis by ICP-OES, total monomeric anthocyanin, total phenolic content and total flavonoid content. K is the most abundant element in both vinegar samples. Acetic acid is the most common organic acid found in both forms of vinegar. While chlorogenic acid was determined to be the most prevalent phenolic compound in commercial pomegranate vinegar, gallic acid was shown to be the most prevalent in Zivzik pomegranate vinegar. As a result of the study, it was found that vinegar produced by traditional methods had a much better composition in terms of nutritional value. In addition to the importance of raw materials in vinegar production, it was revealed in the present study that the variety, ecological conditions, and fermentation process are also effective on the nutritional value of vinegars.

Acknowledgment

We thank the Science and Technology Application and Research Center at Siirt University for their contribution

Conflict of Interest

Authors declare no conflict of interest

Author(s) Contribution

All the authors contributed equally. This study is a part of the master's thesis prepared by Abdulkerim AYBEK under the supervision of Dr. Ebru AKKEMIK.

REFERENCES

[1] Yetiman AE. Identification of acetic acid bacteria in vinegar microflora by molecular techniques. Graduate School of Natural and Applied Sciences, Kayseri: University of Erciyes; 2012.

[2] Turkey National Standard-TSE, Vinegar-product made from liquids of agricultural origin - definitions, requirements, marking (Vol. TS 1880 EN 13188/D1:2016), Ankara. 2016.

[3] Muller MF. Gençlik ve Sağlık Iksiri Sirke. Dharma Yayınları, Istanbul, 2009.

[4] Abe K, Kushibiki T, Matsue H, Furukawa K.I, Motomura S. Generation of Antitumor Active Neutral Medium-Sized α-Glycan in Apple Vinegar Fermentation. Bioscience, Biotechnology and Biochemistry. 2007;71(9):2124-2129.

[5] Kadaş Z. Determination of bioactive properties and metabolic effectsof hawthorn vinegar. Graduate School of Natural and Applied Sciences, Bolu: University of Abant İzzet Baysal; 2011.

[6] Johnston CS, Quagliano S, White S. Vinegar ingestion at mealtime reduced fasting blood glucose concentrations in healthy adults at risk for type 2 diabetes. Journal of Functional Foods, 2013;5(4):2007-2011.

[7] Samanidou VF, Antoniou CV, Papadoyannis IN. Gradient Rf-Hplc Determination of Free Phenolic Acids in Wines and Wine Vinegar Samples After Spe, With Photodiode Array Identification. Journal of Liquid Chromatography & Related Technologies, 2001;24 (14):2161–2176.

[8] Unal E. A study on vinegar production from Dimrit grape by different methods. Graduate School of Natural and Applied Sciences, Adana: Çukurova University; 2007.

[9] Öztürk S. A research on the production of vinegar from black carrot. Graduate School of Natural and Applied Sciences, Ankara: Ankara University; 2015.

[10] Marangoz FI. Effect on bioactive compounds and antioxidant properties of mulberry fruit of vinegar product processing. Graduate School of Natural and Applied Sciences, Çanakkale: Çanakkale Onsekiz Mart University; 2016.

[11] Sakanaka S, Ishihara Y. Comparison of antioxidant properties of persimmon vinegar and some other commercial vinegars in radical scavenging assays and on lipid oxidation in tuna homogenates. Food Chemistry, 2008;107 (2):739-744.

[12] Nishidai S, Nakamura Y, Torikai K, Yamamoto M, Ishihara N. et al., Kurosu, a traditional vinegar produced from unpolished rice. Suppresses lipid peroxidation in vitro and in Mouse ski. Bioscience Biotechnology and Biochemistry, 2000;64 (9):1909-1914.

[13] Anonymous, https://s3.amazonaws.com/gourmet-living/Balsamic+Vinegar+FAQ.pdf Last Accessed: 30 June 2019.

[14] Kharchoufi S, Gomez J, Lasanta C, Castro R, Sainz F. et al., Benchmarking laboratory-scale pomegranate vinegar against commercial wine vinegars: antioxidant activity and chemical composition. Journal of the Science of Food and Agriculture, 2018;98(12):4749-4758.

[15] Morales ML, Tesyafe W, Garcia-Parrilla MC, Casas JA, Troncoso AM. Sherry wine vinegar: Physicochemical changes during the acetification process. Journal of the Science in Food and Agriculture, 2001;81:611-619.

[16] Budak N, Güzel-Seydim ZB. Sirke üretimi ve bazı fonksiyonel özellikleri. Gıda Teknolojisi, 2010;14(11):85-88.

[17] Bekar T. The Effects of Grape Growing on Quality Wine, Turkish Journal of Agricultural and Natural Sciences, 2016;3(4):255–264.

[18] Kelebek H. Researches on the phenolic compounds? profile of öküzgözü, bogazkere and kalecik karasi cultivars grown in different regions and their wines. Graduate School of Natural and Applied Sciences, Adana: Çukurova University; 2009.

[19] Godara NR, Godara RK. Assesment of New Germplast of Pomegranate at Hisar. Haryana Journal of Horticultural Sciences. 1991; 20 (3-4):197-202.

[20] Ordoudi SA, Mantzouridou F, Daftsiou E, Malo C, Hatzidimitriou E. et. al., Pomegranate juice functional constituents after alcoholic and acetic acid fermentation. Journal of Functional Foods, 2014;(8): 161-168.

[21] Budak HN. Antioxidant activity and phenolic contents Pomegranate vinegar, Agro FOOD Industry Hi Tech. 2015;26(5):68-72.

[22] Şengül H. Functional vinegar production from güvem (Prunus spinosa) fruit. Graduate School of Natural and Applied Sciences, Tekirdağ: Namik Kemal University; 2017.

[23] Cemeroğlu B. Gıda Analizleri, Genişletilmiş 2. Baskı. Gıda Teknolojisi Derneği Yayınları, No:34 Bizim Grup Basımevi. Ankara, 2010.

[24] Ibrahim MZ. Physicochemical and microbiological properties of industrial and traditional homemade vinegar. Graduate School of Natural and Applied Sciences, Kahramanmaras: Kahramanmaras Sutcu Imam University; 2019.

[25] Akbaş M, Cabaroğlu T. A Research on The Determination of Compositions of Grape Vinegars Produced in Turkey and Their Conformity to Food Legislation. Gida. 2009;35(3):183-188.

[26] Şengün IY, Kılıç G. Microflora, Bioactive Components and Health Effects of Various Kinds of Vinegars. Akademik Gıda 2019;17(1):89-101.

[27] Fuleki T, Francis F. Quantitative methods for anthocyanins. Journal of Food Science, 1968;33:72-83.

[28] Park YS, Jung ST, Kang SG, Heo BK, Arancibia-Avila P. et. al., Antioxidants and proteins in ethylene-treated kiwifruits. Food Chemistry, 2008;107(2):193-206.

[29] Dörtkardeş M. Determination of antioxidant capacities of Salvia Hasankeyfensis Dirmenci, Celep & O.Güner, Stachys Mardinensis (Post) R.R. Mill, Ferulago Bernardii L.Tomkovich & M.Pimenov ve Hymenocrater Bituminosus Fisch. & C.A.Mey. Graduate School of Natural and Applied Sciences, Siirt: Siirt University; 2019.

[30] Singleton VL, Rossi JA. Colorimetry of total phenolics with phosphomolybdic- phosphotungstic acid reagents. American Journal of Enology and Viticulture, 1965;16:144-158.

[31] Slinkard K, Singleton VL. Total Phenol Analyses: Automationand Comparison with Manual Methods, American Journal of Enologyand Viticulture, 1977;28:49-55.

[32] Tormo M, Izco JM. Alternative reversed-phase high-performance liquid chromatography method to analyse organic acids in dairy products, Journal of Chromatography A, 2004;1033:305–310.

[33] Akkemik E, Aybek A, Felek I. Effects of Cefan Melon (Cucumıs Melo L.) Seed Extracts on Human Erythrocyte Carbonıc Anhydrase I-II Enzymes, Applied Ecology and Environmental Research, 2019;17(6):14699-14713.

[34] Turkey National Standard-TSE, TS 13359, Honey-Fructose, glucose, sucrose, turanose and maltose content determination - High performance liquid chromatography (hplc) method, Ankara, 2008.

[35] Anonymous http://www.onlinecas.com/Berghof/mWS3/Micro-onde%20MWS2/applications%20MWS2/AR_MWS-2_Food-Pharma-Cosmetics_140405.pdf 14.07.20-15:30

[36] Anonymous https://www.perkinelmer.com/PDFs/downloads/ATL_BarnesFoodAtomicSpec.pdf 14.07.20-15:32

[37] Blois MS. Antioxidant determinations by the use of a stable free radical. Nature, 1958;29:1199-1200.

[38] Benzie IFF, Strain JJ. Ferric reducing ability of plasma (FRAP) as a measure of antioxidant power: The FRAP assay. Analytical Biochemistry, 1996;239:70-76.

[39] Benzie IFF, Szeto YT. Total antioxidant capacity of teas by the ferric reducing/antioxidant power (FRAP) assay. Journal of Agricultural and Food Chemistry, 1999;47:633–636.

[40] Apak R, Güçlü K, Demirata B, Özyürek M, Çelik S.E. et al., Comparative evaluation of varius total antioxidant capacity assays applied to phenolic compounds with the cuprac assay. Molecules, 2007;12:1496-1547.

[41] Vardin H, Karaaslan M, Yılmaz F, İzol G, Cesur Ö. et al., Zivzik ve Görümlü Narlarının Özelliklerinin ve Katma Değerli Ürünlere İşlenebilirliğinin Belirlenmesi Projesi. Şanlıurfa. 2012.

[42] Turker I. Sirke Teknolojisi ve Teknikte Laktik Asit Fermantasyonları. Ankara Üniversitesi Basımevi, Ankara. 1963.

[43] Özkaya H, Şahin E, Türker İ, Gıda Bilimi ve Teknolojisi, Ankara Üniversitesi Ziraat Fakültesi Yayınları, Ders Kitabı, Ankara, 1991.

[44] Saxena AK, Manan J.K, Berry SK. Pomegranades; postharvest Technology, Chemistry and Processing. Indian Food Packer. 1987;41(4):43-60.

[45] Kucukler, S., Darendelioğlu, E., Caglayan, C., Ayna, A., Yıldırım, S., & Kandemir, F. M. (2020). Zingerone attenuates vancomycin-induced hepatotoxicity in rats through regulation of oxidative stress, inflammation and apoptosis. Life Sciences, 259, 118382.

[46] Aykutoglu, G., Tartik, M., Darendelioglu, E., Ayna, A., & Baydas, G. (2020). Melatonin and vitamin E alleviate homocysteine-induced oxidative injury and apoptosis in endothelial cells. Molecular Biology Reports, 47(7), 5285-5293.

[47] Ayna, A., Özbolat, S. N., & Darendelioglu, E. (2020). Quercetin, chrysin, caffeic acid and ferulic acid ameliorate cyclophosphamide-induced toxicities in SH-SY5Y cells. Molecular Biology Reports, 47(11), 8535-8543.

184

[48] Caglayan, C., Kandemir, F. M., Darendelioğlu, E., Küçükler, S., & Ayna, A. (2021). Hesperidin protects liver and kidney against sodium fluoride-induced toxicity through anti-apoptotic and anti-autophagic mechanisms. Life Sciences, 281, 119730.

185

Türk Doğa ve Fen Dergisi
Turkish Journal of Nature and Science
www.dergipark.gov.tr/tdfd

Sweet Plant Proteins and Their Recombinant Production

Shokoufeh Yazdanıan ASR[1], **Nergiz YÜKSEL[2,3]**, **Seyhan İÇİER[3]**, **Burcu KAPLAN TÜRKÖZ*[4]**

[1]Ege University, Graduate School of Natural and Applied Sciences, Department of Food Engineering, İzmir, Türkiye
[2]Aydın Adnan Menderes University Germencik Yamantürk Vocational School Aydın, Türkiye
[3]Ege University, Graduate School of Natural and Applied Sciences, Department of Biotechnology, İzmir, Türkiye
[4]Ege University, Faculty of Engineering, Department of Food Engineering, İzmir, Türkiye
Shokoufeh Yazdanıan ASR ORCID No: 0000-0002-3468-7045
Nergiz YÜKSEL ORCID No: 0000-0002-1334-051X
Seyhan İÇİER ORCID No: 0000-0002-0627-733X
Burcu KAPLAN TÜRKÖZ ORCID No: 0000-0003-3040-3321

*Corresponding author: burcu.kaplan.turkoz@ege.edu.tr

Abstract: There is a growing interest and increasing awareness of consumers towards natural food products, therefore there is a shift in food industry to produce foods with natural ingredients. On the other hand, high amount of sweetener use in food industry is another health concern. An interesting group of natural sweeteners are sweet proteins, which have hundreds/thousands times higher sweetness than sucrose. Sweet proteins have high sweetness but low calorie values and are of interest as they can be used as healthy alternatives to natural or artificial sweeteners. Known plant sweet proteins are produced by tropical plants and this limits the amount of protein that can be obtained. In order to increase the amount of protein, many studies have been carried out on the recombinant production of plant sweet proteins using different expression systems. In this article, sources, types, physicochemical and structural properties of sweet plant proteins and studies on their recombinant production are reviewed with insights to future studies.

186

Tatlı Bitkisel Proteinler ve Rekombinant Üretimleri

Öz: Tüketicilerin doğal gıda ürünlerine karşı olan ilgisi ve artan bilinçleri nedeniyle, gıda endüstrisi doğal içeriklere sahip gıdalar üretmeye yönelmiştir. Öte yandan gıda endüstrisinde yüksek miktarda tatlandırıcı kullanımı da bir diğer sağlık sorunudur. Tatlı proteinler, sakkarozdan yüzlerce/binlerce kat daha fazla tatlılığa sahip ilgi çekici doğal tatlandırıcılardır. Tatlı proteinler, yüksek tatlılığa ancak düşük kalori değerlerine sahiptir ve doğal veya yapay tatlandırıcılara sağlıklı alternatifler olarak kullanım potansiyelleri yüksektir. Bilinen bitki tatlı proteinleri tropik bitkiler tarafından üretilir ve bu, elde edilebilecek protein miktarını sınırlar. Protein miktarını arttırmak için farklı ekspresyon sistemleri kullanılarak bitkisel tatlı proteinlerin rekombinant üretimi üzerine birçok çalışma yapılmıştır. Bu makalede, tatlı bitki proteinlerinin kaynakları, türleri, fizikokimyasal ve yapısal özellikleri ve rekombinant üretimi ile ilgili çalışmalar derlenmiş ve yeni yapılabilecek çalışmalar üzerinde durulmuştur.

1. INTRODUCTION

Nowadays, the importance of nutrition and a balanced diet for protection of public health is increasing. In recent years, there has been a growing interest in reducing the sugar content in food products by both consumers and producers with the increase in health problems caused by high amounts of sugar consumption.

Attempts to reduce the sugar content in food products led the food industry to use artificial sweeteners however, there are still discussions about the negative health effects of those; including toxic and carcinogenic effects of aspartame and acesulfame K [1], [2]. Although some synthetic sweeteners derived from cyclamic acid and cyclamate are still allowed in USA, but not in EU due to consumer demands. Market research results in developed countries show that many consumers prefer

natural foods [3]. Following these, studies have focused on finding alternatives obtained from natural sources such as sweeteners from plants [4] and sweet plant proteins, which were discovered many years ago have gained importance again. These sweet plant proteins with naturally sweet or taste-modifying properties are seen as natural and healthy alternatives to existing synthetic low-calorie sweeteners.

To date, six sweet plant proteins have been identified all from tropical plants; brazzein, curculin (neoculin), mabinlin, miraculin, monellin and thaumatin [5]. The main advantage of these proteins over carbohydrate based sweeteners is that, they have extremely high sweetness index with an insignificant amount of calories. Several research studies showed that sweet plant proteins do not have allergic or toxic effects [6].In this article, the physicochemical and structural properties of sweet plant proteins, their interactions with the human taste receptor, their current production strategies with an emphasis on recombinant production are reviewed.

1.1. Sweet Plant Proteins

All known sweet plant proteins have been discovered from tropical plants (Figure 1); mabinlin from China, curculin from Malaysia, and other sweet plant proteins are isolated from fruits of plants growing in the rainforests of Africa [5]. The comparison of amino acid sequences of these proteins show that there is no considerable sequence similarity [7]; these proteins have different number of amino acid sequences with almost no homology. The three-dimensional atomic structures of all sweet plant proteins were solved by X-ray crystallography or NMR and it was revealed that there are also no structural similarities among sweet plant proteins. In addition the level of sweetness of sweet plant proteins are also different from each other (Table 1).

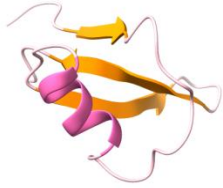**Figure 1.** Plant sources of sweet proteins and initial isolation studies[8]–[13]
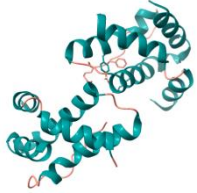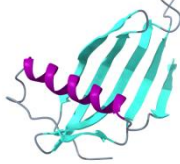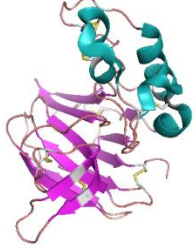
1.1. 1. Thaumatin

The sweet protein thaumatin, obtained from the *Thaumatococcus danielli Benth* fruit is the first approved and commercialized sweet plant protein. Thaumatin is metabolized similarly to other proteins, this protein is suitable for use by patients with diabetes due to its very

low caloric value. Several studies showed that thaumatin does not have any toxic, allergic or other harmful effects in the amounts used as sweetener [14].

Thaumatin has been approved for use as a food additive (E957) by European Union since 1984 [21]. The use of thaumatin for modification and enhancing of flavors has

Table 1. Structural features of sweet proteins

Protein	Source	Comparison of sucrose with sweetness on a molar basis [15]	Molecular weight (kDa) and amino acid content	Three-dimensional structure and PDB code
Brazzein	*Pentadiplvera brazzeana*	17,000	6.5 kDa 54 aa	2BRZ[16]
Curculin	*Curculigo latifolia*	-	24,9 kDa 114 aa	2DPF[17]
Mabinlin II	*Capparis masaikai*	~400	12.4 kDa 105 aa	2DS2[18]
Monellin	*Dioscoreophyllum cumminsii*	100,000	10.7 kDa 94 aa	3MON[19]
Thaumatin	*Thaumatococcus daniellii*	100,000	22.2 kDa 207 aa	3WOU [20]

also been approved by the Food and Drug Administration (FDA) (FEMA GRAS Number 3732) and is marketed in the USA under the trade name Talin. Thaumatin is used as a sweetener and flavor enhancer in candies, chewing gums, soft drinks, dairy products and ice cream in the food industry in Europe and Japan [7], [21]. Furthermore, thaumatin is used as a sweetener in toothpastes and to suppress the bitter taste of some drugs and food supplements. Although thaumatin has a very high sweetness level, its taste is different and more dominant than sucrose and fructose, so it leaves an undesirable sweetness effect in the mouth. For this reason, it is usually used in combination with other sweeteners [14]. Thaumatin has two isoforms; I and II, and commercial thaumatin extracted from the plant consists of a mixture of these two isoforms [14]. Thaumatin isoforms differ only at four amino acid positions, and their three-dimensional structures are almost identical. There are 16 cysteine amino acids in the thaumatin amino acid sequence, resulting in eight intramolecular disulfide bridges. The high number of disulfide bridges give thaumatin high thermal stability [22]. Thaumatin has been shown to be resistant to pasteurization, cooking, and other similar high-temperature processes when pH is 5.5 and lower [23].

However, at neutral pH and above, thaumatin loses its stability and sweetness [14], due to its basic nature with an isoelectric point of around 7.5.

1.1. 2. Brazzein

Brazzein is obtained from fruits of *Pentadiplandra brazzeana Baillo* and is the smallest of sweet plant proteins. Brazzein has a high degree of heat stability due to presence of four disulfide bridges in its structure [11], [24]. Brazzein has high potential in different food applications as it is water-soluble and retains its sweetness in a wide pH range [25]. Brazzein is ready to be commercialized as a sugar replacer and awaits approval from FDA [3].

1.1. 3. Monellin

Monellin, obtained from the fruit of *Dioscoreophyllum cumminsii diels*, consists of two polypeptide chains. These polypeptide chains fold into two different domains, one completely helical and one formed by beta sheets (Table 1). These two domains are held together by noncovalent bonds, therefore the structure of monellin is highly unstable. Monellin denatures at temperatures above 50°C, and loses its sweetness completely[15].

1.1. 4. Mabinlin

The sweet plant protein mabinlin, obtained from the fruit of *Capparis masakai Levl*, consists of two polypeptides, similar to monellin. However, unlike monellin, the mabinlin structure has completely alpha helix folding. In addition, strong disulfide bonds hold the two chains together, and therefore mabinlin has high thermal stability. There are four types of mabinlin isoforms in nature; I, II, III and IV. Among them, the sweetness of mabinlin II has been shown to be around 400 times higher than sucrose [26]. It has been reported in studies that the sweetness of mabinlin-III and -IV did not change after 1 hour at 80 °C, and mabinlin-II did not change even after 48 hours of incubation at the boiling point [2], [11]. Mabinlin does not yet have legal status with the European Food Safety or FDA and is not commercially used as a sweetener in food production.

1.1.5. Curculin and Miraculin

Curculin, isolated from the fruit of *Curculingo latifolia*, is not directly sweet, but at acid pH values have the ability to transform sour flavors into sweet ones [5]. Curculin's sweetness is almost equal to sucrose on a molar basis and is not durable to temperatures above 50°C [27]. There are two isoforms of curculin, and these two isoforms come together to form a heterodimeric structure, called neoculin. While neoculin has very little sweetness at neutral pH values, its sweetness effect increases at acidic pH values and becomes a sweet protein. Therefore, neoculin has important potential use, especially in fruit juices and nectars with low pH and soft drinks.

Miraculin, a sweet plant protein derived from the fruit of *Richadella dulcifica*, is a taste modifying protein, similar to curculin, that can change the sour taste to sweet taste in acidic pH environments. The structure of the miraculin protein is not yet resolved [28].

1.2. Interactions of Sweet Proteins with The Taste Receptor T1R2/T1R3

Humans can detect five basic tastes: sweet, salty, umami, bitter (bitter) and sour. Taste processing takes place first at the level of taste receptor cells. There are four types of taste receptor cells, including the immature Type IV. Mature cells Type I, Type II, Type III; detect salty, sweet-umami-bitter taste and sour taste; respectively[29]. Class C G protein receptors (GPCR) in type II taste cells initiate the molecular pathway that enables the detection of sweet, umami and bitter taste. Sweet taste receptors have been shown to exist in heterodimeric form and the receptor has been identified as T1R2 / T1R3 [30].

When the T1R2/T1R3 receptor binds to the sugar molecule, taste is perceived with the initiation of signal transduction within the cell, and sweet plant proteins create the same effect when they bind to the receptor [5]. In studies examining the three-dimensional structures of known sweet proteins, it has been observed that all of them, except mabinlin, contain beta sheets (Table 1). However, a common "sweet" structural region could not be identified in [15]. For this reason, studies are still ongoing to understand how exactly sweet proteins bind to the receptor in order to mimic sugar molecules at the molecular level [5].

1.3. Recombinant Sweet Plant Proteins Production Studies

The importance of using sweet plants proteins instead of carbohydrate or artificial sweeteners in designing healthy foods is clear. However, due to the fact that these proteins are produced by tropical plants, access to these plants is limited, and the amount of protein obtained from the plant depends on the plant quality[14]. Therefore alternative methods have been investigated and attempts have been made to produce sweet plant proteins using various transgenic plants. Recombinant protein production levels have been observed to be quite low from genetically modified plants [15]. Although studies on recombinant production with transgenic plants or animals have increased in recent years [31]–[34], these approaches are still controversial in terms of economics, sustainability and ethical terms. Numerous studies have been conducted on recombinant production of sweet plant proteins from microorganisms [14].

Table 2. Sweet plant proteins produced recombinantly from different expression systems

Protein	Microorganism	Protein production efficiency	Reference
Brazzein	*Picha pastoris*	44-345 mg/L	[36]
Brazzein	*Kluyveromyces lactis*	238.9 g/L	[37]
Brazzein	*Kluyveromyces lactis*	170 mg/L	[38]
Brazzein	*Bacillus licheniformis*	5mg/L	[39]
Brazzein	*Kluyveromyces lactis*	107 mg/L	[40]
Brazzein	*Escherichia coliBL21(DE3)* *Escherichia coliSHuffle T7*	1.8 - 2.3 mg/L 7.2 - 8.4 mg/L	[41]
Brazzein	*Kluyveromyces lactis*	30-100 mg/L	[42]
Brazzein	*Lactococcus lactis*	1,20-1,65- mg/L	[43]–[45]
Brazzein	*Lactobacillus spp*	N.D	[46]
Brazzein	*Pichia pastoris*	90 mg/L	[47]
Mabinlin II	*Lactococcus lactis*	32,5-59,1 mg/L	[48]
Monellin	*Escherichia coli*	500 mg/L	[49]
Monellin	*Pichia pastoris*	262~271 mg/L	[50]
Monellin	*Lactococus lactis*	0,40 mg /L	[51]
Monellin	*Pichia pastoris*	150 mg/L	[52]
Monellin	*Saccharomyces cerevisiae*	675 mg/L	[53].
Monellin	*Saccharomyces cerevisiae*	410 mg/L	[54].
Thaumatin	*Picha pastoris*	5,6 mg/L	[55]
Thaumatin	*Pichia pastoris*	0.129- 0.399 mg/L	[56]
Thaumatin	*Aspergillus awamori*	5-25 mg/L	[57]
Thaumatin	*Picha pastoris*	100 mg/L	[58]
Thaumatin	*Escherichia coli*	40 mg/L	[59]

Although progress has been made in the production and purification of thaumatin, problems have been encountered in adequate production of other proteins in bacteria, yeast and mold cells [35]. Almost 50 years have passed since the discovery of these proteins, yet optimization studies for recombinant production are still ongoing.

The selection of the expression system in the production of recombinant proteins is very important in terms of protein quality, functionality, productivity and yield. Studies have been carried out on the recombinant production of sweet plant proteins using different microorganisms and expression systems and these are summarized in Table 2.

In studies using *Escherichia coli*, one of the organisms most used in recombinant protein production, it has been observed that sweet plant proteins are generally produced in small amounts, similarly, the efficiency of protein production with *Lactococcus* species is low. Higher recombinant protein amounts are achieved using yeast expression systems.

A great deal of research has been done on the recombinant production and engineering of sweet plant proteins. Among these proteins, thaumatin is the most studied protein, whose sweetness and heat stability have been improved by different methods [2], [14]. In most of the studies conducted before 2000 on recombinant thaumatin [60]–[64]protein yield was reported to be low. In a study conducted in 2000, protein production efficiency was increased by optimizing the gene encoding thaumatin II according to *E.coli* codon usage.

In this study, the produced recombinant thaumatin protein was indistinguishable from natural thaumatin in terms of biochemical, spectroscopic and organoleptic properties [59].Very successful results have been obtained from *Pichia pastoris* expression system for the recombinant production of thaumatin. It has been shown that protein production efficiency is increased by cloning with the extracellular secretion signal naturally found in thaumatin protein sequence and transferring three gene copies instead of one [58]. In another study, protein disulfide isomerase enzyme was also cloned together with thaumatin and it was shown that the production efficiency of recombinant thaumatin increased in the presence of this chaperone [55].

Due to the difficulties and limitations of obtaining brazzein protein from its natural source, numerous attempts have also been made to produce brazzein from microorganisms. Studies on brazzein expression in *E. coli* showed that recombinant brazzein is localized in the insoluble fraction and requires denaturing conditions for purification [7], [65]. In subsequent studies, recombinant brazzein gene was synthesized by optimizing *Bacillus subtilis* codon preference, and recombinant protein was successfully produced from *E. coli* and *Bacillus licheniformis* cells with this synthetic gene, and both recombinant proteins were shown to have sweetness properties. A purification procedure was established for recombinant brazzein produced by *B. licheniformis*, and approximately 5 mg/L brazzein of high purity was obtained [39]. In another, in order to optimize the expression of brazzein protein from *E. coli*, codon-optimized gene was cloned into two different strains and results showed that the strain used had an effect on protein yield [41]. Use of different lactic acid bacteria were also investigated for expression of recombinant

brazzein, but low amounts of recombinant protein were produced[43], [46], [66].

Studies using *Pichia pastoris* show that recombinant brazzein is obtained in active form with a yield of approximately 30−90 mg/L [67]. In a study examining the extracellular secretion of recombinant brazzein from *P. pastoris*, brazzein was cloned with seven different signal peptides and three of these tested signal peptides increased the protein production efficiency. These signal peptides have been reported to be natural signal peptides of chicken lysozyme, *Aspergillus niger* alpha-amylase and Saccharomyces cerevisiae alpha-mating factor proteins [36]. In the study with *Kluyveromyces lactis*, which is used as a different yeast expression system, 107 mg/L of recombinant brazzein was obtained [40]. In another study using *K. lactis*, the effect of co-expression of chaperones involved in the formation of disulfide bonds with brazzein was examined and recombinant brazzein was produced in the range of 30-100 mg / L [42].

In another study performed on the *K. lactis* expression system, conditions such as pH, temperature, expression time, concentration of the inducer and carbon source, and induction time were optimized to increase brazzein production, and 1:2 (w/w) glucose: galactose induction at 25°C was resulted in an 2.5 fold increase in protein production [38]. Therefore, *K. lactis* will be a suitable expression system for recombinant brazzein by optimizing the pH, temperature, ratio of carbon source and nitrogen source, time of induction, as well as inducer, yeast extract and glycerol concentration [40]. Among the sweet plant proteins, the least studied protein is mabinlin. Mabinlin has less sweetness than other proteins and therefore has attracted less attention. Mabinlin structure consists of two independent polypeptides, and chain B was shown to be adequate for the sweetness of mabinlin [68]. The recombinant mabinlin II chain B produced from *E.coli* expression system has a sweet taste; however, it has been reported that the protein can only be purified from the inclusion body by the denaturation/renaturation method. In experiments using *L. lactis* expression system, recombinant mabinlin was produced and secreted out of the cell, albeit in very low amounts. This study is the first step towards the production of mabinlin II from the food grade *L. lactis* system[48].

Different studies have been carried out using *E.coli*, *L.lactis, P.pastoris* and *S.cerevisiae* expression systems for the production of recombinant monellin. In a study with *L.lactis*, it was shown that the use of codon-optimized gene produced a low amount of monellin [51]. In studies with *S. cerevisiae*, another microorganism with a safe expression system for use in foods, 410-675 mg/L recombinant monellin could be produced with low yields [53], [54]. The tendency of monellin to denature at high temperatures limits the use of recombinant protein in food applications [7]. To overcome this situation, amino acid mutations were made in monellin sequence and 150 mg/L protein could be produced using the *P. pastoris* expression system [52]. In another study

using *P. pastoris*, the effect of cell density on monellin production was examined and highest protein levels; 270 mg/L; were obtained with lower cell density fermentations [50].

2. CONCLUSION

Sweet proteins have been the focus of attention of food industry for many years. However, they have not been widely used due to their limited availability. The successful transformation of these proteins for recombinant production will increase their use in food industry as a low calorie replacer for sweeteners and sugars. Apart from the six sweet plant proteins that have been studied so far, the identification of other similar plant proteins is one of the current research topics. By using bioinformatic tools and databases, the identification of new proteins that are similar to sweet proteins both in terms of primary sequence and tertiary structure will accelerate and enlarge the studies in this field. In addition, studies on increasing the sweetness level and recombinant production yields of these proteins with protein engineering approaches are still ongoing. In addition to all these, determining the physicochemical, functional, textural and sensory effects of sweet proteins on the food matrix to which they are added are important research topics in terms of creating new food formulations. It is predicted that in the coming years, sweet proteins will be produced on large scale and used more widely in the food industry as natural sweeteners.

REFERENCES

[1]　Carocho M, Morales P, and Ferreira I. C. F. R. Natural food additives: Quo vadis? Trends Food Sci. Technol.2015;45,(2):284–295.

[2]　Kant R. Sweet proteins - Potential replacement for artificial low calorie sweeteners.Nutr.J., 2005; 4 :1–6.

[3]　Saraiva A, Carrascosa C, Raheem D, Ramos F, and Raposo A. Natural sweeteners: The relevance of food naturalness for consumers, food security aspects, sustainability and health impacts. Int. J. Environ. Res. Public Health.2020; 17(17):1–22.

[4]　Khan T. A, SievenpiperJ. L.Controversies about sugars: results from systematic reviews and meta-analyses on obesity, cardiometabolic disease and diabetes," Eur. J.Nutr.2016;55(s2):25–43.

[5]　Zhao X, Wang C, ZhengY, Liu B . New Insight Into the Structure-Activity Relationship of Sweet-Tasting Proteins: Protein Sector and Its Role forSweet Properties. Front. Nutr.2021;8(June):1–7.

[6]　Gwak M, Chung S, KimY. J., LimC. S.Relative Sweetness and Sensory Characteristicsof Bulk and Intense Sweeteners,2012; 21(3):889–894.

[7]　Faus I. Recent developments in the characterization and biotechnological production of sweet-tasting proteins. Appl. Microbiol. Biotechnol.2000;53(2):145–151.

[8] Harada S, Otani H, Maeda S, Kai Y, Kasai N, Kurihara Y. Crystallization and Preliminary X-ray Diffraction Studies of Curculin: A New Type of Sweet Protein Having Taste-modifying Action, J. Mol. Biol. Apr. 1994;238(2):286–287.

[9] Inglett G. E, May J.F. Serendipity Berries–Source of a New Intense Sweetener. J. Food Sci.1969; 34(5):408–411.

[10] Liu X, Maeda S, Z. Hu, AiuchiT, Nakaya K, Kurihara Y. Purification complete amino acid sequence and structural characterization of the heat-stable sweet protein. mabinlin II. Eur. J. Biochem.1993; 211(1–2): 281–287.

[11] Ming D, Hellekant G . Brazzein, a new high-potency thermostable sweet protein from *Pentadiplandra brazzeana* B.FEBS Lett. Nov. 1994; 355(1):106–108.

[12] Van der wel H, Loeve K. Isolation and Characterization of Thaumatin I and 11. the Sweet - Tasting Proteins from *Thaumatococcus daniellii Bent* h. Eur. J. Biochem.1972;31(1972):221–221.

[13] Takahashi N, Hitotsuya H, Hanzawa H, Arata Y, Kurihara Y. Structural study of asparagine-linked oligosaccharide moiety of taste-modifying protein, miraculin. J. Biol. Chem.1990;265(14):7793–7798.

[14] Joseph J. A, Akkermans A, Nimmegeers P, Van Impe J. F. M. Bioproduction of the recombinant Sweet protein thaumatin: Current state of the art and perspectives. Front. Microbiol.2019; 10(APR):1–19.

[15] Picone D, Temussi P. A. Dissimilar sweet proteins from plants: Oddities or normal components? Plant Sci. 2012;195:135–142.

[16] Caldwell J, Abildgaard F, Džakula Ž, et al. Solution structure of the thermostable sweet-tasting protein brazzein. Nat Struct Mol Biol. 1998; 5: 427–431.

[17] Kurimoto E, Suzuki M, Amemiya E, Yamaguchi, Y, Nirasawa S, Shimba N, Kato. Curculin exhibits sweet-tasting and taste-modifying activities through its distinct molecular surfaces. Journal of Biological Chemistry. 2007; 282(46): 33252–33256.

[18] Li D F, Jiang P, Zhu D Y, Hu Y, Max M, Wang D C. Crystal structure of Mabinlin II: A novel structural type of sweet proteins and the main structural basis for its sweetness. Journal of Structural Biology. 2008; 162(1): 50–62.

[19] Kim S H, de Vos A, Ogata C.. Crystal structures of two intensely sweet proteins. Trends in Biochemical Sciences. 1998; 13(1): 13–15.

[20] Masuda T, Mikami B, Tani F. Atomic structure of recombinant thaumatin II reveals flexible conformations in two residues critical for sweetness and three consecutive glycine residues. Biochimie. 2014; 106:33-38.

[21] Mortensen A. Sweeteners permitted in the European Union: Safety aspects. Scand. J. Food Nutr., 2006; 50(3) :104–116.

[22] Masuda T, Mikami B, Tani F, Atomic structure of recombinant thaumatin II reveals flexible conformations in two residues critical for sweetness and three consecutive glycine residues. Biochimie. 2014; 106; 33–38.

[23] Gibbs B. F, Alli I, Mulligan C.Sweet and taste-modifying proteins: A review.Nutr. Res.1996;16(9):1619–1630.

[24] Izawa H, Ota M, Kohmura M, Ariyoshi Y.Synthesis and characterization of the sweet protein brazzein. Biopolymers.1996; 39(1):95–101.

[25] Tang C. H.Assembly of food proteins for nano-encapsulation and delivery of nutraceuticals (a mini-review). Food Hydrocoll. 2021;117(December 2020):106710.

[26] Kohmura M, Ariyoshi Y. Chemical synthesis and characterization of the sweet protein mabinlin II .Biopolymers. 1998; 46(4): 215–223.1998.

[27] Fawibe, O.O., Ogunyale, O.G. Ajiboye, A.A. and Agboola, D.A. Botanical and protein sweetener.J. Advanced Lab, Res. in Biology V(iv), 2014; 169-187.

[28] Wintjens R, Melody T, Ngoc V, Mbosso E, Huet J .Plant Science Hypothesis / review : The structural basis of sweetness perception of sweet-tasting plant proteins can be deduced from sequence analysis. 2011; 181:347–354.

[29] Lee A. A, Owyang C. Sugars, Sweet Taste Receptors, and Brain Responses. Nutrients. 2017;9(7):653.

[30] Liu B, Jiang H, Wang H, Yang L. Removal of the N-terminal methionine improves the sweetness of the recombinant expressed sweet-tasting protein brazzein and its mutants in Escherichia coli. J. Food Biochem.2021; 45(3):1–6.

[31] Kelada K. D, Tusé D, Gleba Y, McDonald K. A, Nandi S. Process simulation and techno-economic analysis of large-scale bioproduction of sweet protein Thaumatin II. Foods. 2021; 10(4): 1–17.

[32] Lu R, Li X, Wang Y, Jin L. Expression of functional plant sweet protein thaumatin II in the milk of transgenic mice. Food Bioprod. Process.2021;125:222–227.

[33] Park Y. J, Han J. E, Lee H, Lee J. Y, Ho T. T, Park S. Y. Production of recombinant miraculin protein in carrot callus via Agrobacterium-mediated transformation. Plant Cell. Tissue Organ Cult. Feb.2021; 1–9.

[34] Yamamoto T et al. Improvement of the transient expression system for production of recombinant proteins in plants. Sci. Rep.2018; 8(1);1–10.

[35] Masuda T, Kitabatake N. Developments in biotechnological production of sweet proteins. J. Biosci. Bioeng.2006;102(5): 375–389.

[36] Neiers F, Belloir C, Poirier N, Naumer C, Krohn M, Briand L,Comparison of different signal peptides for the efficient secretion of the sweet-tasting plant protein brazzein in *Pichia pastoris*. Life.2021;11(1): 1–12.

[37] Han J. E, Park Y. J., Lee H., Jeong Y. J, Park S. Y.Increased brazzein expression by abiotic stress and bioreactor culture system for the production of sweet protein, brazzein, Plant Biotechnol. Rep.2020;14(4): 459–466.

[38] Lee H. M., Park S. W., Lee S. J., Kong K. H. Optimized production and quantification of the tryptophan-deficient sweet-tasting protein brazzein

in *Kluyveromyces lactis*. Prep. Biochem. Biotechnol.2019; 49(8): 790–799.

[39] Hung C.Y, Cheng L. H, Yeh C. M. Functional expression of recombinant sweet tasting protein brazzein by *Escherichia coli* and *Bacillus licheniformis*.Food Biotechnol. 2019; 33(3): 251–271.

[40] ParkS. W.et al. Efficient brazzein production in yeast *(Kluyveromyces lactis)* using a chemically defined medium .Bioprocess Biosyst. Eng.2021;44(4): 913–925.

[41] Jafarian V, Bagheri K, Zarei J, Karami S, Ghanavatian P. Improved expression of recombinant sweet-tasting brazzein using codon optimization and host change as new strategies. Food Biotechnol. 2020; 34(1): 62–76.2020.

[42] Yun C. R, Kong J. N, Chung J. H., Kim M. C, Kong K. H. Improved Secretory Production of the Sweet-Tasting Protein. Brazzein, in *Kluyveromyces lactis*," J. Agric. Food Chem. 2016; 64(32): 6312-6316.

[43] Berlec A, Jevnikar Z, Majhenič A. Č, RogeljA. Č., Štrukelj B .Expression of the sweet-tasting plant protein brazzein in *Escherichia coli* and *Lactococcus lactis*: A path toward sweet lactic acid bacteria.Appl. Microbiol. Biotechnol.2006; 73(1) :158–165.

[44] Berlec A, Štrukelj B. Large increase in brazzein expression achieved by changing the plasmid/strain combination of the NICE system in *Lactococcus lactis*. Lett. Appl. Microbiol. 2009; 48(6): 750–755.

[45] Berlec A, Štrukelj B. Generating a custom TA-cloning expression plasmid for *Lactococcus lactis*. Biotechniques.2021; 52(1) :51–53.

[46] LeeY. W., KimK. Y., HanS. H., KangC. H., SoJ. S.Expression of the sweet-tasting protein brazzein in *Lactobacillus spp*. Food Sci. Biotechnol. 2012; 21(3):895–898.

[47] Poirier N, Roudnitzky N, Brockhoff A, Belloir C, Maison M, Thomas-Danguin T, et al. Efficient production and characterization of the sweet-tasting brazzein secreted by the yeast pichia pastoris. J Agric Food Chem. 2012;60(39):9807–14.

[48] Gu W, Xia Q, Yao J, Fu S, Guo J, Hu X. Recombinant expressions of sweet plant protein mabinlin II in *Escherichia coli* and food-grade *Lactococcus lactis*. World J. Microbiol. Biotechnol.2015; 31(4): 557–567.

[49] Rega, M.F., Siciliano, A., Gesuele, R. et al. Ecotoxicological survey of MNEI and Y65R-MNEI proteins as new potential high-intensity sweeteners. Environ Sci Pollut Res. 2017; 24: 9734–9740.

[50] Jia L, Tu T, Huai Q, Sun J, Chen S, Li X, et al. Enhancing monellin production by Pichia pastoris at low cell induction concentration via effectively regulating methanol metabolism patterns and energy utilization efficiency. PLoS ONE. 2018; 13(7): e0201085

[51] Boumaiza M, Colarusso A, Parrilli E, Garcia-Fruitós E, Casillo A, Arís A, et al. Getting value from the waste: Recombinant production of a sweet protein by Lactococcus lactis grown on cheese whey. Microb Cell Fact. 2018;17(1):126.

[52] Cai C, Li L, Lu N, Zheng W, Yang L, Liu B. Expression of a high sweetness and heat-resistant mutant of sweet-tasting protein, monellin, in Pichia pastoris with a constitutive GAPDH promoter and modified N-terminus. Biotechnol. Lett.2016; 38 (11):1941–1946.

[53] Liu J, zhong Yan D, jun Zhao S. Expression of monellin in a food-grade delivery system in *Saccharomyces cerevisiae*. J. Sci. Food Agric.2015; 95(13): 2646–2651.

[54] Chen Z, Li Z, Yu N, Yan N. Expression and secretion of a single-chain sweet protein, monellin, in *Saccharomyces cerevisiae* by an α-factor signal peptide. Biotechnol. Lett.2011; 33(4):721–725.

[55] Healey R. D., Lebhar R. D., Hornung S, Thordarson P, Marquis C. P. An improved process for the production of highly purified recombinant thaumatin tagged-variants .Food Chem.. 2017; 237: 825–832. 2017.

[56] Torres P, Saa P. A, Albiol P. A., Ferrer P, Agosin E. Contextualized genome-scale model unveils high-order metabolic effects of the specific growth rate and oxygenation level in recombinant *Pichia pastoris*," Metab. Eng. Commun., 2019; 9(July):e00103.

[57] Lombraña M, Moralejo P. A., Pinto R, Martín J. F. Modulation of *Aspergillus awamori* thaumatin secretion by modification of bipA gene expression. Appl. Environ. Microbiol. 2004; 70(9): 5145–5152.

[58] Masuda T, Ide L, Ohta K, Kitabatake. High-yield secretion of the recombinant sweet-tasting protein thaumatin I. Food Sci. Technol. Res.2010;16(6): 585–592.

[59] Daniell S, Mellits K. H, Faus I, Connerton I. Refolding the sweet-tasting protein thaumatin II from insoluble inclusion bodies synthesised in *Escherichia coli*. Food Chem.2000; 71 (1):105–110.

[60] Edens L, van der Wel H. Microbial synthesis of the sweet-tasting plant protein thaumatin. Trends Biotechnol.1985; 3(3) :61–64 1985.

[61] Illingworth C, Larson G, Hellekant G. Secretion of the sweet-tasting plant protein thaumatin by *Bacillus subtilis*. Biotechnol. Lett.1988; 10(8):587–592.

[62] Lee J et al. Expression of Synthetic Thaumatin Genes in Yeast. Biochemistry, 1988;27(14):5101–5107.

[63] Hahm Y. T, Batt C. A. Expression and secretion of thaumatin from Aspergillus oryzae.Agric. Biol. Chem.1990; 54(10):2513–2520 .

[64] Faus I et al. Expression of a synthetic gene encoding the sweet-tasting protein thaumatin in the filamentous fungus Penicillium roquefortii.Biotechnol. Lett.1997;19 (12):1185-1191.

[65] Assadi-Porter F. M. Aceti D. J., Cheng H., Markley J. L. Efficient Production of Recombinant Brazzein, a Small, Heat-Stable, Sweet-Tasting Protein of Plant Origin. Arch. Biochem. Biophys. Apr. 2000; 376(2):252–258.

193

[66] De Ruyter P. G. G. A., Kuipers O. P. De Vos W. M. Controlled gene expression systems for Lactococcus lactis with the food- grade inducer nisin. Appl. Environ. Microbiol. 1996; 62 (10):3662–3667.

[67] Poirier N et al. E ffi cient Production and Characterization of the Sweet-Tasting Brazzein Secreted by the Yeast Pichia pastoris.2012.

[68] LiD. F, Jiang P, Zhu D. Y, Hu Y, Max M, Wang D. C. Crystal structure of Mabinlin II: A novel structural type of sweet proteins and the main structural basis for its sweetness. J. Struct. Biol. Apr. 2008;162(1): 50–62.